Modeling and experimental design to characterize permeation and gettering of hydrogen isotopes in fusion materials

by

Sebastian Johannes Hendricks

A dissertation submitted by in partial fulfillment of the requirements for the degree of Doctor of Philosophy in

Materials Science and Engineering

Universidad Carlos III de Madrid

Advisors:

Dr. Elisabetta Carella
Dr. Joaquín Mollá Lorente

June 2023

Diese Doktorarbeit widme ich meiner Mutter, meinem Vater und meinen Geschwistern Roman, Delia und Julian.

ACKNOWLEDGMENTS

Writing this dissertation would not have been possible without the scientific, technical, and moral support of colleagues, friends, and family that I have received throughout my time as a Ph.D. student. I would like to express special thanks:

- to Elisabetta Carella and Joaquín Mollá, my thesis directors, for their incredibly helpful, motivating and competent way. Through their expertise and the experience they have shared with me along the way, I have learned a lot that will be of great benefit to me in my future path as a scientist. In my opinion, both of my thesis advisors have found the perfect balance between providing the necessary guidance and allowing me the creative freedom to decide how to conduct the research to achieve the scientific goals of my thesis. I would like to thank both of them for their constant advice and for having always been available to answer my questions. It was only through their support and organization that I was able to participate in conferences and research visits that I will never forget.

- to David Rapisarda for believing in me and for all the opportunities that he has made possible for me. His competent, friendly and personal manner as well as his ability to deeply think through and find solutions to any scientific or technological problem I had impressed and motivated me many times.

- to Iole Palermo for her constant interest in my work and all the useful advice she has given me all along the way. Her competent, positive and reassuring manner makes it a pleasure and a great honor to be part of the Breeding Blanket Technology Group with her as group leader.

- to David Jiménez, Juan Manuel García, Julián Patiño and Julia Navas for the time they devoted to helping me develop the experimental devices addressed in this work. But most of all, I would like to thank them for their positive, fun and easy manner, which made the time we spent working together very enjoyable.

- to Fernando Roca and Carlos Moreno for answering millions of my questions about tritium transport modeling. Without their help, I would have never been able to develop the numerical part of this thesis. I really enjoyed our frequent discussions about the physical mechanisms involved.

- to Marta Malo for having introduced me to the physics and technology of permeation experiments and our fruitful and interesting discussions about possible experimental procedures. I am looking forward to great teamwork during the upcoming experimental campaigns.

- to Belit Garcinuño, Angela García, and Alfonso de Castro for having shared with me their broad knowledge and experience about liquid metals technology which was of incredible benefit to my work.

- to Iván Fernandez for introducing me to CATIA and ANSYS and for clarifying so many technical doubts I encountered during my work. His knowledge and competence fascinated me every time.

- to Marcelo Roldán for the fun and delightful moments in the lab and for so much time you spent helping me with sample preparation and surface analysis.

- to María Sánchez for having taken work off my hands while I was writing my thesis and for creating an incredibly pleasant working atmosphere through her exceptionally friendly and competent way.

- to Luis Alberto Bueno and the team of the "Taller de Fusión" for taking the time to manufacture the components of the experimental devices developed in this thesis with the highest quality. Without their skills, none of the experimental devices would have been able to be put into operation.

- to Juan Mauricio García, Jose Ángel Noguerón and Daniel Alegre for being the best office mates you could ever have. Their positive and friendly personalities created an incredibly pleasant workspace.

- to my Ciemat friends Gianluca D'Ovidio, Dhaval Gadariya, Darío Andrés Cruz and David Regidor. Their funny and uplifting nature gave me so much positive energy over the past few years and made me love my work at Ciemat even more.

I would also like to thank all my friends, especially Robert Löf, for all the laughs, good mood and support they gave me during my Ph.D. studies.

Finally, I would like to thank my mother, father, and siblings, Roman, Delia, and Julian. It is only through their constant support and positivity that I have been able to write this thesis. You can't imagine how much you mean to me!

PUBLISHED AND SUBMITTED CONTENT

List of published scientific articles as first author:

1. **S. J. Hendricks**, J. Molla, F. R. Urgorri, E. Carella

   Impact of yttrium hydride formation on multi-isotopic hydrogen retention by a getter trap for the DONES lithium loop

   Nuclear Fusion 63 (2023) 056012

   https://doi.org/10.1088/1741-4326/acc31a

   - The author of this dissertation is the first author of this publication. He owns, together with the co-authors, the copyright of the submitted article.
   - The author of this dissertation has performed the writing, investigation, visualization, conceptualization and organized the methodology of this work.
   - The material contained in this article is wholly included in chapter 7 of this dissertation.
   - The inclusion in the thesis of material from this source is specified in a footnote to each chapter where an inclusion occurs.
   - Whenever material from this source is included in this thesis, it is singled out with typographic means and an explicit reference.

2. **S. J. Hendricks**, E. Carella, D. Jimenez, J. M. Garcia, J. Molla

   Design of a multi-isotopic hydrogen co- and counter-permeation experiment for HCPB related tritium mitigation studies

   Fusion Engineering and Design 175 (2022) 112991

   https://doi.org/10.1016/j.fusengdes.2021.112991

   - The author of this dissertation is the first author of this publication. He owns, together with the co-authors, the copyright of the submitted article.
   - The author of this dissertation has performed the writing, investigation, visualization, conceptualization and organized the methodology of this work.
   - The material contained in this article is wholly included in chapter 6 of this dissertation.
   - The inclusion in the thesis of material from this source is specified in a footnote to each chapter where an inclusion occurs.
   - Whenever material from this source is included in this thesis, it is singled out with typographic means and an explicit reference.

3. **S. J. Hendricks**, E. Carella, C. Moreno and J. Molla

   Numerical investigation of hydrogen isotope retention by an yttrium pebble-bed from flowing liquid lithium

   Nuclear Fusion 60 (2020) 106017

   https://doi.org/10.1088/1741-4326/aba672

   - The author of this dissertation is the first author of this publication. He owns, together with the co-authors, the copyright of the submitted article.
   - The author of this dissertation has performed the writing, investigation, visualization, conceptualization and organized the methodology of this work.
   - The material contained in this article is partly included in chapter 7 of this dissertation.
   - Whenever material from this source is included in this thesis, it is singled out with typographic means and an explicit reference.

OTHER RESEARCH MERITS

List of published chapters in books:

1. **S. J. Hendricks**

   H-isotopes trapping technologies

   In book *Technofusion III CM programme - The extended abstracts to the* 8° *annual workshop*, M. González Viada, Madrid, Spain, 2020, pp. 65-68

   ISBN: 978-84-09-35035-3

Contributions to international conferences:

1. D. Rapisarda, D. Alegre, F. Arranz, E. Carella, G. D'Ovidio, I. Fernández, R. Fernández, B. Garcinuño, A. García, J. M. García, M. González, **S. J. Hendricks**, T. Hernández, J. Herranz, D. Jiménez-Rey, M. Malo, F. Martin-Fuertes, J. Molla, J. Navas, J. Patiño, A. Quejido, F. R. Urgorri, R. Román, M. Sánchez

   Oral presentation: *The Liquid Metals Laboratory for fusion applications at CIEMAT*

   7th International Symposium on Liquid Metals Applications for Fusion (ISLA-7), Chubu University, Kasugai, Aichi, Japan. December 12-16, 2022

2. **S. J. Hendricks**, E. Carella, C. Moreno, F. R. Urgorri, D. Jimenez, J. Molla

   Oral presentation: *The effect of hydrogen co- and counter-permeation on tritium transport in HCPB and WCLL breeding blankets*

   13th International Conference on Tritium Science and Technology (Tritium 2022), Bucharest, Rumania. October 16-21, 2022

3. E. Carella, **S. J. Hendricks**, M. Roldán

   Poster presentation: *Evaluation of different techniques for surface treatments as oxide barrier: a review of its effect on light ion's permeation*

   32nd Symposium on Fusion Technology (SOFT), Dubrovnik, Croatia. September 18-23, 2022

4. **S. J. Hendricks**, E. Carella, D. Jimenez, C. Moreno, F. R. Urgorri, J. Molla

   Poster presentation: *Experimental and numerical investigation of multi-isotopic transport phenomena and their effect on tritium permeation in HCPB breeding blankets*

   20th International Conference on Fusion Reactor Materials (ICFRM-20), Madrid, Spain. October 25-29, 2021

5. D. Rapisarda, E. Carella, G. D'Ovidio, B. Garcinuño, A. García, M. González, **S. J. Hendricks**, T. Hernández, J. Herranz, A. Ibarra, D. Jiménez, M. Malo, J. Molla

   Oral presentation: *Recent CIEMAT experimental activities on liquid metals for fusion applications*

   Technology of Fusion Energy (TOFE) 2020, Virtual Meeting. November 17, 2020

Contributions to national conferences:

1. **S. J. Hendricks**, J. Molla, E. Carella, C. Moreno, J. Serna, A. Rueda

   Oral presentation: *Formación de hidruros de itrio y su influencia en la retención de hidrógeno por una trampa getter en litio líquido fluyente*

   46ª Reunión Anual de la SNE (Sociedad Nuclear Española), Granada, Spain. October 06-08, 2021

Contributions to national and international workshops and seminars:

1. **S. J. Hendricks**, J. Molla, D. Jimenez, J. Patiño, J. M. Garcia, M. Sánchez

   Oral presentation: *LYDER - Lithium purification experiment at laboratory scale*

   EUROfusion WP Early Neutron Source, 14th Technical Meeting - Lithium Systems, Virtual Meeting. November 24, 2022

2. **S. J. Hendricks**, J. Molla, D. Jimenez, J. M. García, E. Carella

   Oral presentation: *LYDER - La nueva infraestructura del Laboratorio de Metales Líquidos del CIEMAT*

   3ª Asamblea General Anual del Programa Technofusión(III)-CM, Madrid, Spain. November 22, 2021

3. **S. J. Hendricks**, E. Carella, C. Moreno, J. Molla

   Oral presentation: *Experimentos de retención de hidrogeno disuelto en litio líquido para una trampa de itrio*

   2ª Asamblea General Anual del Programa Technofusión(III)-CM, Madrid, Spain. November 18, 2020

4. **S. J. Hendricks**, E. Carella, C. Moreno, J. Molla

   Oral presentation: *Progress in the H-trap validation activities*

   EUROfusion WP Early Neutron Source, 9th Technical Meeting - Lithium Systems, Virtual Meeting. June 8, 2020

5. **S. J. Hendricks**, J. Molla, C. Moreno, E. Carella

   Oral presentation: *Numerical and experimental investigation of yttrium as a getter material for the hydrogen hot-trap for DONES*

   EUROfusion WP Early Neutron Source, 8th Technical Meeting - Lithium Systems, Frascati, Italy. November 19-21, 2019

6. **S. J. Hendricks**, E. Carella, C. Moreno, J. Molla

   Oral presentation: *Tritium transport in DEMO-oriented Neutron Source*

   TRANSAT 1st Workshop on Tritium Transport Modeling in Nuclear Fission and Fusion, Madrid, Spain. October 21-22, 2019

7. **S. J. Hendricks**, on behalf of the Ciemat tritium modeling group

   Oral presentation: *Numerical and experimental investigation of yttrium metal as a getter material for the hydrogen hot trap of IFMIF/DONES*

   TRANSAT 1st Tritium School 2019, Ljubljana, Slovenia. March 25-28, 2019

8. **S. J. Hendricks**, on behalf of the Ciemat tritium modeling group

   Oral presentation: *Numerical modeling of permeation barrier experiments using EcosimPro*

   CN-EU Workshop on Tritium Permeation Barrier, Chengdu, China. November 12-15, 2018

List of official technical reports for EUROfusion:

1. E. Carella, **S. J. Hendricks**

   Evaluation of different techniques for surface treatments

   WP Breading Blanket, EFDA_D_2PUM5E (2022)

   https://idm.euro-fusion.org/?uid=2PUM5E

2. **S. J. Hendricks**, E. Carella

   Procedure for co and counter permeation measurements

   WP Breading Blanket, EFDA_D_2PVZQH (2022)

   https://idm.euro-fusion.org/?uid=2PVZQH

3. **S. J. Hendricks**, E. Carella

   Comparison and simulation of co-permeation in different breeding blankets

   WP Breading Blanket, EFDA_D_2PNLGB (2021)

   https://idm.euro-fusion.org/?uid=2PNLGB

4. **S. J. Hendricks**, E. Carella

   Co-permeation experiments with different gas compositions on Eurofer samples: material characterization and main results

   WP Breading Blanket, EFDA_D_2PNCBY (2021)

   https://idm.euro-fusion.org/?uid=2PNCBY

5. **S. J. Hendricks**, J.Molla

   Design and execution of experiments to validate yttrium as a getter material for the hydrogen hot trap of DONES

   WP Early Neutron Source, EFDA_D_2P7Q8A (2021)

   https://idm.euro-fusion.org/?uid=2P7Q8A

6. C. Moreno, **S. J. Hendricks**, J. Molla

   Evaluation of tritium inventories and permeation in the lithium systems

   WP Early Neutron Source, EFDA_D_2NUCEP (2021)

   https://idm.euro-fusion.org/?uid=2NUCEP

7. **S. J. Hendricks**, E. Carella

   Evaluation of tritium permeation in the He coolant from the HCPB considering various scenarios of hydrogen partial pressures in the cooling gas

   WP Breading Blanket, EFDA_D_2P4A5H (2020)

   https://idm.euro-fusion.org/?uid=2P4A5H

8. C. Moreno, **S. J. Hendricks**, J. Molla

   Update of the evaluation of tritium production and permeation in the loop

   WP Breading Blanket, EFDA_D_2NQB2S (2019)

   https://idm.euro-fusion.org/?uid=2NQB2S

Participation in national and international research projects:

1. Title: Lazo Litio Ciemat
   Financing Entity: Fusion Technology Division (Ciemat)
   Reference: 19_13
   Dates: 06/2020 - 12/2022
   Participating entities: CIEMAT
   Principal Investigator: **S. J. Hendricks** (CIEMAT)

2. Title: Technofusión(III)-CM
   Financing Entity: Comunidad de Madrid
   Reference: P2018/EMT-4437
   Dates: 01/2019 - 12/2022
   Amount of the subsidy: 998.200 €
   Participating entities: CIEMAT, CSIC-CAR, CSIC, UC3M, UCM, UNED, UPM
   Principal Investigator: M. González (CIEMAT)

3. Title: DONES-PRIME
   Financing Entity: Ministry of Science and Innovation, Spain
   Dates: 06/2019 - 12/2023
   Amount of the subsidy: 16.800 €
   Participating entities: CIEMAT
   Principal Investigator: A. Ibarra (CIEMAT)

4. Title: EUROfusion WP Early Neutron Source
   Financing Entity: EURATOM
   Dates: 01/2021 - 12/2022 (EUROfusion Horizon Europe)
   Amount of the subsidy: 6.589.602 €
   Participating entities: CIEMAT, ENEA, RBI, CCFE
   Principal Investigator: Angel Ibarra (CIEMAT)

5. Title: TRANSAT
   Financing Entity: EURATOM Reference: NFRP-2016-2017-1
   Dates: 09/2017 - 09/2021
   Amount of the subsidy: 5.068.134,27 €
   Participating entities: CIEMAT, CEA, AMU, CORIA, DH PHE, ENEA, IFIN HH, IIT, INFLPR, IRSN, JSI, KIT, LGI, RATEN, SCK-CEN, UKAEA, UNIPV, UOP
   Principal Investigator: C. Grisolia (CEA)

6. Title: EUROfusion WP Breeding Blanket
   Financing Entity: EURATOM
   Dates: 01/2021 - 12/2024 (EUROfusion Horizon Europe)
   Amount of the subsidy: 19.179.378 €
   Participating entities: CIEMAT, CEA, ENEA, UKAEA, IAP
   Principal Investigator: Lorenzo Boccaccini (KIT)

7. Title: EUROfusion WP Early Neutron Source Definition and Design
   Financing Entity: EURATOM
   Dates: 01/2014 - 12/2020 (EUROfusion Horizon 2020)
   Amount of the subsidy: 26.578.121 €
   Participating entities: CIEMAT, ENEA, RBI, CCFE
   Principal Investigator: Angel Ibarra (CIEMAT)

8. Title: EUROfusion WP Breeding Blanket
   Financing Entity: EURATOM
   Dates: 01/2014 - 12/2020 (EUROfusion Horizon 2020)
   Amount of the subsidy: 37.666.427 €
   Participating entities: CIEMAT, CEA, CCFE, ENEA, IPP.CR
   Principal Investigator: Lorenzo Boccaccini (KIT)

9. Title: CiClo
   Financing Entity: MINECO, FEDER
   Reference: ENE2013-43650-R
   Dates: 01/2017 - 09/2019
   Amount of the subsidy: 135.000 €
   Participating entities: CIEMAT
   Principal Investigator: D. Rapisarda (CIEMAT)

10. Title: Collaboration on CFETR/EU-DEMO Blankets
    Financing Entity: EUROfusion
    Dates: 03/2018 – 07/2021
    Participating entities: CIEMAT, ENEA, KIT, ICSI, CAEP, SWIP, SYSU, ASIPP
    Principal Investigator: T. Hernández (CIEMAT)

CONTENTS

ABSTRACT

The roadmap towards fusion electricity includes the construction of an experimental fusion reactor called DEMO (DEMOnstration power plant). A critical element of DEMO is the tritium breeding blanket. Amongst others, two breeding blanket designs are currently under investigation: the HCPB (helium-cooled pebble bed) and the WCLL (water-cooled lithium-lead) breeding blanket. In an HCPB breeding blanket, tritium is bred in lithium-containing ceramic pebble beds rinsed by a helium purge gas flowing past helium coolant channels. In a WCLL breeding blanket, a flowing lithium-lead breeder fluid is penetrated by water coolant pipes. In both designs, it is inevitable that radioactive tritium permeates from the breeder zone through Eurofer'97 steel walls into the adjacent coolant. To ensure a safe operation of DEMO, finding methods that mitigate tritium contamination of the coolant is essential. Previous experimental observations suggest that the addition of protium to the breeder fluid or coolant of the breeding blankets might, under certain conditions, reduce the tritium permeation flux. However, there is insufficient information in the literature that would allow the evaluation of this technique as a suitable tritium mitigation method.

For this purpose, in the first part of this thesis, a theoretical study of multi-isotopic hydrogen gas-to-gas (relevant to an HCPB breeding blanket) and liquid metal-to-water (relevant to a WCLL breeding blanket) co- and counter-permeation is conducted in which the cause of the permeation flux altering effect of multi-isotopic permeation is revealed. Algebraic formulas are derived that allow expressing the tritium permeation flux as a function of the concentration of simultaneously co- or counter-permeating protium. Numerical system-level hydrogen transport models of the HCPB and WCLL breeding zones are developed which allow simulation of the occurring tritium permeation fluxes for different protium concentrations in the respective breeder fluid and the coolant. According to the simulations, an addition of protium to the coolant of an HCPB breeding blanket only leads to a reduction in tritium permeation when the protium concentration is too high to be technically feasible. However, adding protium to the HCPB purge gas is found to indeed result in a significant reduction in tritium permeation flux at still relatively low protium concentrations and should therefore be considered as a tritium mitigation method for HCPB breeding blankets. It is found that an increased concentration of protium in the lithium-lead or water coolant of a WCLL breeding blanket can only lead to an increase in tritium permeation and should hence be avoided. The numerical model and derived algebraic formulas describing gas-to-gas counter-permeation are experimentally validated by reproducing experimental data.

To enable additional on-site experimental verification of gas-to-gas co- and counter permeation effects with Eurofer'97 as membrane material a new experimental facility is developed from scratch, called COOPER (CO- and cOunter-permeation) experiment.

This thesis presents the experimental design and commissioning of the COOPER facility as well as preliminary mono-isotopic permeation measurements in which hydrogen transport coefficients such as the diffusivity, permeability and Sieverts' constant of deuterium in Eurofer'97 are determined. Moreover, detailed experimental procedures for performing co- and counter-permeation flux measurements with the COOPER experiment are presented. The described procedures are supported by numerical simulations of multi-isotopic permeation measurements taking into account the geometry and experimental conditions of the COOPER device.

Another key research facility to be built on the path to fusion power is DONES (DEMO-Oriented Neutron Source), an experimental neutron irradiation facility for fusion-relevant materials. It consists of a deuterium beam colliding with a liquid lithium target that is part of a lithium loop system. Nuclear stripping reactions occur between the deuterons and the lithium, producing neutrons, but also protium, deuterium and tritium, which accumulate in the lithium. To comply with hydrogen concentration limits in lithium, an yttrium-based hydrogen getter trap will be installed. However, the physical processes that determine the absorption dynamics and the getter capacity of such a trap have not yet been sufficiently studied to allow a reliable trap design.

For this reason, the second part of this thesis is devoted to the numerical and experimental investigation of hydrogen capture in DONES with the objective of defining trap design conditions that ensure meeting DONES safety limits. A numerical tool is developed from scratch capable of simulating multi-isotopic hydrogen transport in the DONES lithium loop connected to an arbitrary yttrium pebble bed. It includes the physical mechanisms of lithium and yttrium hydride formation, which is a novelty in system-level hydrogen transport modeling. A thermodynamic analysis of the lithium-yttrium-hydrogen system is carried out which reveals the solubility of hydrogen in different yttrium hydride phases exposed to hydrogen-loaded lithium. Moreover, an approximate concentration-dependent relationship of hydrogen diffusivity in yttrium is derived and incorporated into the model. Simulations are performed to analyze the dynamics of hydrogen purification processes during different operating phases of DONES by varying design parameters of the trap. It is found that yttrium dihydride formation greatly increases the gettering capacity of the trap and prevents the concentration in the lithium to increase above a critical value. Moreover, algebraic formulas are derived that allow calculating the required yttrium pebble bed mass and trap replacement period at any given temperature to comply with DONES safety requirements. Finally, the model is validated by a numerical reproduction of experimental results.

To allow future experimental validation of the developed model, a new experimental lithium system is developed and put into operation. It is called the LYDER (Lithium system for Yttrium-based DEeuterium Retention) experiment, the design and construction of which are presented in this thesis. The LYDER system is designed to allow the loading of 100 mL of molten lithium with a controlled concentration of deuterium. The design foresees creating a pressure differential in two argon-filled tanks which moves the

deuterium-loaded lithium through a thin pipe system connected to an yttrium-based deuterium trap. The LYDER system is equipped with a lithium sample extraction system and a thermal desorption spectroscopy branch with the purpose of analyzing the extracted samples for their deuterium content. Numerical hydrogen transport models of the developed lithium system and the deuterium injection system are created and simulation results are discussed in this thesis.

RESUMEN

El camino hacia la energía de fusión incluye la construcción de un reactor de fusión experimental denominado DEMO (DEMOnstration power plant). Un elemento crítico de DEMO es la envoltura reproductora de tritio (de ahora en adelante breeding blanket) donde se produce el combustible tritio. Entre otros, se están investigando intensamente dos diseños de breeding blankts: el HCPB (helium-cooled pebble bed) y el WCLL (water-cooled lithium-lead) breding blanket. En el HCPB breeding blanket, el tritio se genera en lechos de pebbles cerámicos antes de ser arrastrado por un gas de purga de helio que fluye a lo largo de canales de refrigeración de helio. En el WCLL breeding blanket el tritio se produce en litio-plomo líquido que fluye a través de tubos refrigerados por agua. En ambos diseños, es inevitable que el tritio radiactivo generado permea desde la zona de su producción, a través de las paredes de acero de Eurofer'97, hacia el refrigerante. Para garantizar un funcionamiento seguro de DEMO, es esencial encontrar métodos que mitiguen la contaminación del refrigerante por tritio. Resultados experimentales previos sugieren que, en determinadas condiciones, la inyección de protio a la zona de producción de tritio o al refrigerante podría reducir el flujo de permeación de tritio al refrigerante. Sin embargo, hoy en día no existe suficiente información en la literatura que permita evaluar esta técnica como método de mitigación de tritio.

Con este fin, en la primera parte de esta disertación se lleva a cabo un estudio teórico de la co- y contra-permeación multi-isotópica de gas-a-gas (relevante para un breeding blanket HCPB) y de metal líquido-a-agua (relevante para un breeding blanket WCLL). De esta manera se revela la causa de la alteración del flujo de permeación por efectos multi-isotópicas. Se derivan fórmulas algebraicas que permiten expresar el flujo de permeación de tritio en función de la concentración de protio que simultáneamente co- o contra-permea. Además, en esta tesis, se presenta el desarollo de modelos numéricos del transporte de hidrógeno a nivel de sistema de las zonas de producción de tritio en los breeding blankets HCPB y WCLL que permiten simular los flujos de permeación de tritio para diferentes concentraciones de protio añadido. De acuerdo con las simulaciones, la inyección de protio al refrigerante de un breeding blanket HCPB solamente resulta en una reducción de la permeación de tritio cuando la concentración de protio es demasiado alta para ser técnicamente viable. Sin embargo, se ha comprobado que la adición de protio al gas de purga del HCPB produce una reducción significativa a concentraciones de protio relativamente bajas, por lo cual se debería considerar como un posible método de mitigación de tritio, eficaz y barato. Se ha descubierto que una mayor concentración de protio en el refrigerante de litio-plomo o agua de un breeding blanket WCLL sólo puede resultar en un aumento de la permeación de tritio y, por lo tanto, debe evitarse. El modelo numérico y las fórmulas algebraicas derivadas que describen la contra-permeación gas-a-gas se validan mediante datos experimentales.

Para permitir una verificación experimental adicional in situ de los efectos predichos tanto de la co-permeación gas-a-gas como de la contra-permeación gas-a-gas con Eurofer'97 como material de membrana, se desarrolla una nueva instalación experimental desde cero, denominada experimento COOPER (CO- and cOunter-PERmeation). Esta tesis presenta el diseño experimental y la puesta en marcha de la instalación COOPER, así como mediciones preliminares de permeación mono-isotópica en las que se determinan coeficientes de transporte de hidrógeno como la difusividad, la permeabilidad y la constante de Sievert de deuterio en Eurofer'97. Además, se presentan procedimientos experimentales detallados para realizar mediciones de flujo de co-permeación y contra-permeación con el experimento COOPER. Los procedimientos descritos están respaldados por simulaciones numéricas, teniendo en cuenta la geometría característica y las condiciones experimentales del experimento COOPER.

Otra instalación de investigación clave que se construirá en el camino hacia la energía de fusión es DONES (DEMO-Oriented Neutron Source), una instalación experimental de irradiación neutrónica de materiales para la fusión. DONES consiste en un haz de deuterio que colisiona con un blanco de litio líquido que forma parte de un lazo de litio. Reacciones nucleares entre los deuterones y el litio producen neutrones, pero también protio, deuterio y tritio, que se acumulan en el litio. Para respetar los límites de concentración de isotopos de hidrógeno en el litio, se instalará una trampa captadora de hidrógeno a base de itrio. Hasta ahora, los procesos físicos que determinan la dinámica de absorción y la capacidad de captación de una trampa de este tipo no se han investigado lo suficiente como para poder diseñar una trampa fiable.

Por esta razón, la segunda parte de esta tesis se dedica a la investigación numérica y experimental de los mecanismos físicos implicados con el objetivo de definir los parámetros de diseño de la trampa apropiados para DONES. Se desarrolla desde cero una herramienta numérica capaz de simular el transporte de hidrógeno que se produce en el lazo de litio de DONES conectado a un lecho de pebbles de itrio. El modelo incluye los mecanismos físicos de la formación de hidruros de litio e itrio, lo que constituye una novedad en la modelado del transporte de hidrógeno a nivel de sistema. Se lleva a cabo un análisis termodinámico del sistema litio-itrio-hidrógeno que revela la solubilidad de los isótopos de hidrógeno en diferentes fases de hidruro de itrio expuesto a litio cargado de hidrógeno. Además, se deriva una relación aproximada de la difusividad de hidrógeno en itrio dependiente de la concentración de hidrógeno que está incorporado en el modelo. Se realizan simulaciones para analizar la dinámica de los procesos de purificación de isótopos de hidrógeno durante diferentes fases de operación de DONES variando los parámetros de diseño de la trampa. Se observa que la formación de dihidruro de itrio aumenta en gran medida la capacidad de absorción de la trampa y evita que la concentración en el litio aumente por encima de un valor crítico. Además, se derivan fórmulas algebraicas que permiten calcular la masa necesaria del lecho de pebbles de itrio y el periodo de sustitución de la trampa para cumplir los requisitos de seguridad de DONES. El modelo se valida mediante una reproducción numérica de resultados experimentales.

Para facilitar la futura validación experimental del modelo creado, se ha desarrollado y puesto en funcionamiento un nuevo sistema experimental de litio en el marco de esta tesis. Se trata del experimento LYDER (Lithium system for Yttrium-based DEeuterium Retention), cuyo diseño y construcción se presentan en esta tesis. El sistema LYDER está diseñado para permitir la carga de 100 mL de litio fundido con una concentración controlada de deuterio. El diseño prevé la creación de un diferencial de presión entre dos tanques presurizados con argón que mueve el litio cargado de deuterio a través de una linea de tuberías que pasa por una trampa experimental de deuterio. El sistema LYDER está equipado con un sistema de extracción de muestras de litio y una rama de espectroscopia de desorción térmica con el objetivo de analizar las muestras extraídas para determinar su contenido de deuterio. Además, se presentan modelos numéricos del transporte de deuterio en el sistema de litio y del sistema de inyección de deuterio de LYDER. Los resultados de las simulaciones están analizados en esta disertación.

LIST OF ABBREVIATIONS

TABLE I
GENERAL ABBREVIATIONS.

Abbreviation	Meaning
AC	Antechamber
BB	Breeding blanket
BCC	Body centered cubic
BI	Breeder interface
BL	Boundary layer
BP	Backing pump
CAD	Computer aided design
CCG	Cold cathode pressure gauge
CF	Core flow
CFETR	China Fusion Engineering Test Reactor
CG	Coolant gas
CI	Coolant interface
CIC	Coolant inlet channel
CL	Calibrated leak
COC	Coolant outlet channel
CPS	Coolant purification system
COOPER	CO- and cOunter-PERmeation experiment
DEMO	DEMOnstration Power Plant
DG	Capacitance diaphragm gauge
DIS	Deuterium injection system
DT	Dump tank of the LYDER experiment
d.IN	EcosimPro© diffusion port inlet
d.OUT	EcosimPro© diffusion port outlet
DI	Downstream interface
DL	Diffusion-limited
DONES	DEMO-oriented Neuron Source
EDX	Energy dispersive X-ray spectroscopy
EH	Electric heater
FCC	Face centered cubic
EFDA	European Fusion Development Agreement
f.IN	EcosimPro© flow port inlet

Abbreviation	Meaning
f.OUT	EcosimPro© flow port outlet
FP	Fuel pin
GB	Glove box
GDP	Gross domestic product
GMT	Gas mixing tank
GPS	Glove box purification system
HCP	Hexagonal closed packed
HCPB	Helium-cooled pebble bed
HEBT	High energy beam transport
HTR	Heat transfer ring
HyF	Hydride formation
HFTM	High flux test module
HTR	Heat transfer ring
HT	Hydrogen trap
HV	High vacuum
HX	Heat exchanger
IFMIF	International Fusion Materials Irradiation Facility
IL	Isotope-limited
ITER	International Thermonuclear Experimental Reactor
JET	Joint European Tokamak
LD	Leak detector
LEBT	Low energy beam transport
LET	Left expansion tank
LM	Liquid metal
LML	Liquid metals laboratory
LP	Leak path
LS	Lithium sensor
LT	Left tank of the LYDER experiment
LYDER	Lithium system for Y-based DEuterium Retention experiments
MHD	Magnetohydrodynamics
MS	Mass spectrometer
MEBT	Medium energy beam transport
MSR	Molten salt reactor
OP	Open path
O-site	Octahedral site
OW	Outer purge gas wall
OVC	Outer vacuum chamber
PC	Permeation cell

Abbreviation	Meaning
PT	Permeation tube
PCI	Pressure-composition isotherm
PFD	Process flow diagram
PG	Purge gas
PG.IN	Purge gas inlet of an HCPB fuel pin
PG.OUT	Purge gas outlet segment of an HCPB fuel pin
PHTS	Primary heat transfer system
PiG	Pirani gauge
PI	Purge gas interface
PCS	Power conversion system
PSU	Power supply unit
PWR	Pressurized water reactor
QMS	Quadrupole mass spectrometer
RFQ	Radio Frequency Quadrupole
RET	Right expansion tank
RT	Right tank of the LYDER experiment
SC	Sample container
SD	Sample disk
SEM	Scanning electron microscope
SL	Surface-limited
SM	Solid metal
SP	Dry scroll pump
SPARC	Soonest/Smallest Possible ARC
SST-2	Steady State Superconducting Tokamak
SRF Linac	Super conducting Radio Frequency Linear accelerator
T-site	Tetrahedral site
TC	Thermocouple
TDS	Thermal desorption spectroscopy
TBM	Test Blanket Module
TBR	Tritium breeding ratio
TJ-II	Tokamak de la Junta II
TES	Tritium extraction system
TMP	Turbomolecular pump
UHV	Ultra high vacuum
UI	Upstream interface
V	Valve
VC	Vacuum chamber
WCLL	Water-cooled lithium lead

TABLE II

ABBREVIATIONS FOR PARTICLES, ELEMENTS, MOLECULES AND MATERIALS.

Abbreviation	Material
αFe	α-iron
$\overline{\nu}_e$	Anti-neutrino
Al	Aluminum
Ar	Argon
As	Arsenic
Be	Beryllium
C	Carbon
Ca	Calcium
Co	Cobalt
Cr	Chromium
Cu	Copper
e^-	Electron
E97	Eurofer'97
Fe	iron
FKM	Fluoroelastomer
^{i}H	^{i}H, ^{j}H, ^{k}H $\in \{^1\text{H}, ^2\text{H}, ^3\text{H}\}$ where $i = j$ or $i \neq j$ but $k \neq i, j$
^{1}H	Protium
^{2}H	Deuterium
^{3}H	Tritium
^{3}He	Helium-3
^{4}He	Helium-4
I600	Inconel®600
K	Potassium
KALOS	Karlsruhe Lithium Orthosilicate
Li	Lithium
Me^a	Metal of type a
Mn	Manganese
Mo	Molybdenum
n	Neutron
N	Nitrogen
Na	Sodium
Nb	Niobium
Ni	Nickel
O	Oxygen
OFHC copper	Oxygen free high conductivity copper

Abbreviation	Material
RAFM steel	Reduced activation ferritic/martensitic steel
Sb	Antimony
Si	Silicon
Sn	Tin
SS	Stainless steel
Ta	Tantalum
Ti	Titanium
V	Vanadium
W	Tungsten
Y	Yttrium
Zr	Zirconium

LIST OF PHYSICAL QUANTITIES

TABLE III

PHYSICAL QUANTITIES INTRODUCED IN CHAPTER 1.

Symbol	Name	SI unit
t	Time	s
E	Energy	J
E_{NB}	Nuclear binding energy of an atomic nucleus	J
m	Mass	kg
Δm_{MD}	Mass defect of an atomic nucleus	J
$ç$	Speed of light in vacuum ($ç = 299\,792\,458\,\mathrm{m\,s^{-1}}$)	$\mathrm{m\,s^{-1}}$
Δm_{fis}	Mass difference between fission reactants and products	kg
ΔE_{fis}	Energy liberated in a fission reaction	J
Δm_{fus}	Mass difference between fusion reactants and products	kg
ΔE_{fus}	Energy liberated in a fusion reaction	J
T	Temperature	K
σ_{NF}	Fusion reaction cross section	$\mathrm{m^2}$
Q	Fusion energy gain factor	-
C_{e}	Number concentration of electrons in plasma	$\mathrm{m^{-3}}$
τ_{E}	Plasma confinement time	s
$\vec{E}$	Electric field	$\mathrm{V\,m^{-1}}$
$\vec{B}$	Magnetic field	T
R_0	Major radius of a torus	m
V	Volume	$\mathrm{m^3}$
p	Total pressure	Pa
r	Radius	m
TBM	Tritium breeding ratio	-

TABLE IV

PHYSICAL QUANTITIES INTRODUCED IN CHAPTER 2.

Symbol	Name	SI unit
G	Gibbs energy	J
H	Enthalpy	J
S	Entropy	J

Symbol	Name	SI unit
μ	Chemical potential	J
N_s	Number of particles of species s	-
$\overline{H}_s^n$	Enthalpy change per particle s added to subsystem n	J
$\overline{S}_s^n$	Entropy change per particle s added to subsystem n	J
$\mathrm{d}\xi$	Infinitesimal number of particles	-
$\Delta\overline{H}_s$	Enthalpy of solution of species s	J
$\Delta\overline{S}_s$	Entropy of solution of species s	J
$\mathfrak{F}$	Helmholtz free energy	J
Z_n	Canonical partition function of subsystem n	-
k_B	Boltzmann constant ($k_\mathrm{B} = 1.381 \times 10^{-23}\,\mathrm{J\,K^{-1}}$)	$\mathrm{J\,K^{-1}}$
$\vec{p}$	Canonical phase space coordinate of momentum	$\mathrm{kg\,m\,s^{-1}}$
$\vec{q}$	Canonical phase space coordinate of position	m
$\epsilon(\vec{p},\vec{q})$	Energy of a molecule in a certain energy state	J
$\hbar$	Reduced Planck constant ($\hbar = 1.055 \times 10^{-34}\,\mathrm{J\,s}$)	J s
$\vec{\mathfrak{M}}$	Angular momentum of a diatomic hydrogen molecule	$\mathrm{kg\,m^2\,s^{-1}}$
Θ	Moment of inertia of a diatomic hydrogen molecule	$\mathrm{kg\,m^2}$
ϵ_b	Bond dissociation energy per molecule	J
p_s	Partial pressure of species s	Pa
p°	Standard-state pressure ($p^\circ = 101\,325\,\mathrm{Pa}$)	Pa
μ°	Chemical potential at standard-state	J
$\overline{H}^\circ$	Enthalpy change per added particle at standard-state	J
$\overline{S}^\circ$	Entropy change per added particle at standard-state	J
$\Delta\overline{H}^\circ$	Standard-state enthalpy of solution	J
$\Delta\overline{S}^\circ$	Standard-state entropy of solution	J
K_{ij+kk}^{ik+jk}	Equilibrium constant: ${}^i\mathrm{H}^k\mathrm{H} + {}^j\mathrm{H}^k\mathrm{H} \rightleftharpoons {}^i\mathrm{H}^j\mathrm{H} + {}^k\mathrm{H}_2$	-
ϵ_s	Average energy of non-interacting isotopes in a lattice gas	J
N_sites	Number of available interstitial sites	-
ϵ_HH	Interaction energy per H-H pair in a lattice gas	J
N_adj	Number of nearest neighbor sites around an interstitial	-
E_LG	Total energy of a lattice gas	J
Ω	Number of permutations of N_i isotopes over N_sites sites	-
θ_b	Fraction of occupied interstitial sites	-
N_Me	Number of metal atoms	-
x	Number of dissolved isotopes per metal atom	-
x_max	Number of available interstitial sites per metal atom	-
N_A	Avogadro constant ($N_\mathrm{A} = 6.022 \times 10^{23}\,\mathrm{mol^{-1}}$)	$\mathrm{mol^{-1}}$
ρ	Density	$\mathrm{kg\,m^{-3}}$
M	Molar mass	$\mathrm{kg\,mol^{-1}}$

Symbol	Name	SI unit
c_s	Molar concentration of species s	$\mathrm{mol\,m^{-3}}$
μ_{ex}	Excess contribution to the chemical potential per isotope	J
$\overline{H}_{\mathrm{ex}}$	Excess contribution to the enthalpy change per isotope	J
$\overline{S}_{\mathrm{ex}}$	Excess contribution to the entropy change per isotope	J
$\Delta\overline{H}_{\mathrm{s}}$	Sieverts' enthalpy of solution	J
$\Delta\overline{S}_{\mathrm{s}}$	Sieverts' entropy of solution	J
k_{s}	Sieverts' constant	-
k_{s}^0	Pre-exponential factor of the Sieverts' constant	-
K_{ik}^{ex}	Equilibrium constant: $2^i\mathrm{H}^k\mathrm{H} \rightleftharpoons {}^i\mathrm{H}_2 + {}^k\mathrm{H}_2$	-
K_{s}	Sieverts' constant expressed with molar concentration	$\mathrm{mol\,m^{-3}\,Pa^{-\frac{1}{2}}}$
K_{s}^0	Pre-exponential factor of the molar Sieverts' constant	$\mathrm{mol\,m^{-3}\,Pa^{-\frac{1}{2}}}$
$K_{\mathrm{D},0}^{a-b}$	Low conc. distribution coefficient in a Me^a-Me^b-H system	-
θ^{ν}	Fraction of phase ν when two hydride phases coexist	-
x_{ν}	Concentration of phase ν when two hydride phases coexist	-
p_{dec}	Decomposition plateau pressure	Pa
g	Gibbs energy per metal atom of a metal-hydrogen solution	J
$\Delta\overline{H}^{\circ}_{\nu\rightarrow\nu'}$	Enthalpy of hydride formation of $\nu \rightarrow \nu'$ phase transition	J
$\Delta\overline{S}^{\circ}_{\nu\rightarrow\nu'}$	Entropy of hydride formation of $\nu \rightarrow \nu'$ phase transition	J
T_{c}	Max. temperature where two hydride phases can coexist	K
α_{int}	Distance between interstitial sites	m
E_{m}	Energetic height of potential barriers in a metal lattice	J
r	Radial distance	m
$\left\langle r_n^2 \right\rangle$	Mean square distance a lattice atom passes after n jumps	$\mathrm{m^2}$
$f_{\mathrm{m}}(r,t)$	Probability for an atom to migrate a distance r after time t	-
D	Intrinsic diffusion coefficient or diffusivity	$\mathrm{m^2\,s^{-1}}$
ϖ	Jump frequency of a lattice atom in any possible direction	Hz
ω	Jump frequency of a lattice atom towards a specific site	Hz
γ_{int}	Lattice and interstitial site specific geometrical factor	-
a_0	Cubic lattice parameter	m
ΔG_{m}	Gibbs energy of migration	J
ΔH_{m}	Enthalpy of migration	J
ΔS_{m}	Entropy of migration	J
ν_0	Attempt rate of a lattice atom to jump into a specific site	Hz
D^0	Pre-exponential factor of the intrinsic diffusion coefficient	$\mathrm{m^2\,s^{-1}}$
z	Spacial axis oriented perpendicularly into a metal surface	m
B	Mobility of diffusing hydrogen isotopes	$\mathrm{s\,kg^{-1}}$
$\vec{u}$	Velocity vector	$\mathrm{m\,s^{-1}}$
$\vec{u}_{\mathrm{m}}$	Average drift velocity of diffusing hydrogen isotopes	$\mathrm{m\,s^{-1}}$

Symbol	Name	SI unit
$\vec{\mathcal{F}}_{\mathrm{m}}$	Driving force of diffusion	$\mathrm{kg\,m\,s^{-2}}$
$\vec{J}$	Atomic flux of hydrogen isotopes	$\mathrm{mol\,m^{-2}\,s^{-1}}$
$\vec{J}_{\mathrm{dif}}$	Atomic diffusion flux of hydrogen isotopes	$\mathrm{mol\,m^{-2}\,s^{-1}}$
$\overline{D}$	Chemical diffusion coefficient	$\mathrm{m^2\,s^{-1}}$
$\varkappa_s$	Mole number of particles of species s	mol
A_{per}	Surface area of a permeation membrane	$\mathrm{m^2}$
ς	Molar particle generation/consumption rate per volume	$\mathrm{mol\,m^{-3}\,s^{-1}}$
E_{t}	Binding energy difference between a trap and a lattice site	J
$\mathcal{N}^{\mathrm{T}}$	Molar density of trap sites	$\mathrm{mol\,m^{-3}}$
$\mathcal{N}^{\mathrm{L}}$	Molar density of regular lattice sites	$\mathrm{mol\,m^{-3}}$
c^{T}	Molar concentration of hydrogen isotopes in trap sites	$\mathrm{mol\,m^{-3}}$
c^{L}	Molar concentration of hydrogen isotopes in lattice sites	$\mathrm{mol\,m^{-3}}$
$\theta_{\mathrm{b}}^{\mathrm{T}}$	Fraction of occupied trap sites	-
$\theta_{\mathrm{b}}^{\mathrm{L}}$	Fraction of occupied lattice sites	-
μ^{T}	Chemical potential of hydrogen isotopes in trap sites	J
μ^{L}	Chemical potential of hydrogen isotopes in lattice sites	J
$\overline{D}_{\mathrm{eff}}$	Effective chemical diffusion coefficient	$\mathrm{m^2\,s^{-1}}$
μ_{int}	Chemical potential of hydrogen isotopes at a metal surface	J
c_{int}	Molar hydrogen isotope concentration at a metal surface	$\mathrm{mol\,m^{-3}}$
$J_{\mathrm{dif,int}}$	Atomic interface diffusion flux normal to a metal surface	$\mathrm{mol\,m^{-2}\,s^{-1}}$
$\vec{u}_{\mathrm{int}}$	Flow velocity at a metal interface	$\mathrm{m\,s^{-1}}$
d_{BL}	Concentration boundary layer width in a liquid metal flow	m
J_{MT}	Atomic mass transfer flux in the BL of a liquid metal flow	$\mathrm{mol\,m^{-2}\,s^{-1}}$
c_{CF}	Molar concentration in the core flow of a liquid metal flow	$\mathrm{mol\,m^{-3}}$
α_{MT}	Mass transfer coefficient of solutes into a liquid metal flow	$\mathrm{m\,s^{-1}}$
Sh	Sherwood number	-
L_{f}	Characteristic length of a flow environment	m
α_{s}	Sticking coefficient	-
α_{s}^{0}	Pre-exponential factor of the sticking coefficient	-
E_{d}	Activation energy of dissociation	J
θ_{c}	Fraction of occupied surface sites	-
ν_{s}	Number of surface sites	$\mathrm{mol\,m^{-2}}$
j_{d}	Molecular dissociation flux normal to the metal surface	$\mathrm{mol\,m^{-2}\,s^{-1}}$
J_{d}	Atomic dissociation flux normal to the metal surface	$\mathrm{mol\,m^{-2}\,s^{-1}}$
σ	Surface roughness factor	-
Γ	Flux of impinging molecules onto a metal surface	$\mathrm{mol\,m^{-2}\,s^{-1}}$
$f^{\vec{u}}$	Maxwell-Boltzmann velocity distribution	$\mathrm{s^3\,m^{-3}}$
k_{d}	Dissociation rate coefficient	$\mathrm{mol/m^2/s/Pa}$

Symbol	Name	SI unit
ν_i	Areal molar density of occupied surface sites by species i	$\mathrm{mol\,m^{-2}}$
J_{sb}	Atomic flux of chemisorbed isotopes entering the bulk	$\mathrm{mol\,m^{-2}\,s^{-1}}$
k_{sb}	Jump rate per isotope from the surface into the bulk	$\mathrm{mol\,s^{-1}}$
k_{sb}^0	Attempt rate of an isotope to pass the surface-bulk barrier	$\mathrm{mol\,s^{-1}}$
E_{a}	Absorption energy barrier	J
E_{ss}	Subsurface energy barrier	J
δ_{L}	Distance of the order of the lattice parameter	m
J_{bs}	Flux of subsurface isotopes emerging to the surface	$\mathrm{mol\,m^{-2}}$
k_{bs}	Jump rate per isotope from the bulk to the surface	$\mathrm{mol\,s^{-1}}$
k_{bs}^0	Attempt rate of an isotope to pass the bulk-surface barrier	$\mathrm{mol\,s^{-1}}$
K_ν	Equilibrium constant for surface-subsurface equilibrium	m
k_{r}'	Rate coefficient for recombination of two surface atoms	$\mathrm{m^2\,s^{-1}}$
j_{r}'	Molecular flux due to recombination of two surface atoms	$\mathrm{mol\,m^{-2}\,s^{-1}}$
k_{r}''	Rate coefficient for surface-subsurface recombination	$\mathrm{m^2\,s^{-1}}$
j_{r}''	Molecular flux due to surface-subsurface recombination	$\mathrm{mol\,m^{-2}\,s^{-1}}$
k_{r}	Recombination rate coefficient	$\mathrm{m^4\,mol^{-1}\,s^{-1}}$
j_{r}	Molecular recombination flux	$\mathrm{mol\,m^{-2}\,s^{-1}}$
J_{r}	Atomic recombination flux	$\mathrm{mol\,m^{-2}\,s^{-1}}$
j_{net}	Molecular net flux	$\mathrm{mol\,m^{-2}\,s^{-1}}$
J_{net}	Atomic net flux	$\mathrm{mol\,m^{-2}\,s^{-1}}$
$r_{ik+jk}^{\mathrm{f,ex}}$	Forward reaction rate of the reaction (2.10)	$\mathrm{mol\,m^{-3}\,s^{-1}}$
$r_{ij+kk}^{\mathrm{b,ex}}$	Backward reaction rate of the reaction (2.10)	$\mathrm{mol\,m^{-3}\,s^{-1}}$
$\varsigma_s^{\mathrm{ex}}$	Rate of formation of species s from reaction (2.10)	$\mathrm{mol\,m^{-3}\,s^{-1}}$
$k_{ik+jk}^{\mathrm{f,ex}}$	Forward rate coefficient of the reaction (2.10)	$\mathrm{m^3\,s^{-1}\,mol^{-1}}$
$k_{ij+kk}^{\mathrm{b,ex}}$	Backward rate coefficient of the reaction (2.10)	$\mathrm{m^3\,s^{-1}\,mol^{-1}}$
K_{H}	Henry's constant for hydrogen molecules in water	$\mathrm{mol\,m^{-3}\,Pa^{-1}}$
K_n^{w}	Equilibrium constants of reactions n: (2.113) - (2.117)	-
$r_{n,ik}^{\mathrm{f,w}}$	Forward reaction rates of reactions n: (2.113) - (2.117)	$\mathrm{mol\,m^{-3}\,s^{-1}}$
$r_{n,ik}^{\mathrm{b,w}}$	Backward reaction rates of reactions n: (2.113) - (2.117)	$\mathrm{mol\,m^{-3}\,s^{-1}}$
$k_{n,ik}^{\mathrm{f,w}}$	Forward rate coefficients of reactions n: (2.113) - (2.117)	$\mathrm{m^3\,s^{-1}\,mol^{-1}}$
$k_{n,ik}^{\mathrm{b,w}}$	Backward rate coefficients of reactions n: (2.113) - (2.117)	$\mathrm{m^3\,s^{-1}\,mol^{-1}}$
ς_s^{w}	Formation rate of species s from reactions (2.113) - (2.117)	$\mathrm{mol\,m^{-3}\,s^{-1}}$
p_s^{UI}	Partial pressure of species s at an upstream interface	Pa
p_s^{DI}	Partial pressure of species s at a downstream interface	Pa
d	Thickness of a permeation membrane	m
$c_{\mathrm{UI},i}$	Molar concentration of species i at an upstream interface	$\mathrm{mol\,m^{-3}}$
$c_{\mathrm{DI},i}$	Molar concentration of species i at a downstream interface	$\mathrm{mol\,m^{-3}}$
$J_{\mathrm{net,UI}}$	Net flux of isotopes penetrating an upstream interface	$\mathrm{mol\,m^{-2}\,s^{-1}}$

Symbol	Name	SI unit
$J_{\mathrm{net,DI}}$	Net flux of isotopes leaving a downstream interface	$\mathrm{mol\,m^{-2}\,s^{-1}}$
J_{per}	Atomic permeation flux	$\mathrm{mol\,m^{-2}\,s^{-1}}$
$\overline{J}_{\mathrm{per}}$	Atomic steady-state permeation flux	$\mathrm{mol\,m^{-2}\,s^{-1}}$
$c_{\mathrm{UI,eq}}$	Equilibrium concentration at an upstream interface	$\mathrm{mol\,m^{-3}}$
$c_{\mathrm{DI,eq}}$	Equilibrium concentration at a downstream interface	$\mathrm{mol\,m^{-3}}$
$\overline{J}^{\mathrm{dl}}_{\mathrm{per}}$	Diffusion-limited atomic steady-state permeation flux	$\mathrm{mol\,m^{-2}\,s^{-1}}$
Φ_s	Permeability of species s	$\mathrm{mol/m/s/Pa^{\frac{1}{2}}}$
$\overline{J}^{\mathrm{sl}}_{\mathrm{per}}$	Surface-limited atomic steady-state permeation flux	$\mathrm{mol\,m^{-2}\,s^{-1}}$
W_s	Permeation number of species s	-
λ_{r}	Reduced concentration regarding an upstream interface	-
ζ_{r}	Reduced concentration regarding a downstream interface	-
τ_{TL}	Permeation time-lag	$\mathrm{mol\,m^{-2}}$
c_{tot}	Total molar concentration including all isotopes	$\mathrm{mol\,m^{-3}}$
c_{in}	Concentration at inner interface of a cylindrical wall	$\mathrm{mol\,m^{-3}}$
c_{out}	Concentration at outer interface of a cylindrical wall	$\mathrm{mol\,m^{-3}}$
r_{in}	Inner radius of a cylindrical wall	m
r_{out}	Outer radius of a cylindrical wall	m
$\overline{J}^{\circledcirc}_{\mathrm{in}}$	Particle flux through inner interface of cylindrical wall	$\mathrm{mol\,m^{-2}\,s^{-1}}$
$\overline{J}^{\circledcirc}_{\mathrm{out}}$	Particle flux through outer interface of cylindrical wall	$\mathrm{mol\,m^{-2}\,s^{-1}}$
$f^{\mathrm{c}}_{\mathrm{in}}$	Correction factor for inner side of cylindrical membrane	-
$f^{\mathrm{c}}_{\mathrm{out}}$	Correction factor for outer side of cylindrical membrane	-
$f^{\mathrm{c}}_{\mathrm{UI}}$	Correction factor for inner or outer upstream interface	-
$f^{\mathrm{c}}_{\mathrm{DI}}$	Correction factor for inner or outer downstream interface	-

TABLE V

PHYSICAL QUANTITIES INTRODUCED IN CHAPTER 3.

Symbol	Name	SI unit
$\overline{\lambda}$	Mean free path of molecules in a gas	m
L_{VC}	Characteristic wall distance in a vacuum chamber	m
Kn	Knudsen number	-
q_{pV}	Particle flow in a gas chamber	$\mathrm{mbar \cdot L/s}$
Δp_{c}	Critical pressure difference leading to a chocked flow	Pa
C_{sec}	Conductance of a gas chamber section	$\mathrm{L\,s^{-1}}$
$C_{\mathrm{pipe,vis}}$	Conductance of a pipe section in the viscous flow regime	$\mathrm{L\,s^{-1}}$
$C_{\mathrm{pipe,mol}}$	Conductance of a pipe section in the molecular flow regime	$\mathrm{L\,s^{-1}}$

Symbol	Name	SI unit
C_{tot}	Total conductance of a system of pipes	$\text{L}\,\text{s}^{-1}$
$q_{\text{pV}}^{\text{add}}$	Total flow of particles entering or leaving a gas chamber	$\text{mbar} \cdot \text{L/s}$
$q_{\text{pV}}^{\text{leak}}$	Flow of particles leaking into or out of a gas chamber	$\text{mbar} \cdot \text{L/s}$
$q_{\text{pV}}^{\text{per}}$	Flow of particles permeating into or out of a gas chamber	$\text{mbar} \cdot \text{L/s}$
$q_{\text{pV}}^{\text{degas}}$	Flow of particles degassing from the chamber walls	$\text{mbar} \cdot \text{L/s}$
$q_{\text{pV}}^{\text{pump}}$	Flow of particles into a vacuum pump	$\text{mbar} \cdot \text{L/s}$
S_{pump}	Internal pumping speed of a vacuum pump	$\text{L}\,\text{s}^{-1}$
S_{eff}	Effective pumping speed	$\text{L}\,\text{s}^{-1}$
p_{in}	Intake pressure at a pump inlet	Pa
p_{VC}	Pressure in a vacuum vessel	Pa
$p_{\text{VC}}^{\text{min}}$	Ultimate pressure in a vacuum chamber	Pa
$p_{\text{out}}^{\text{max}}$	Maximum allowable outlet pressure of a TMP	Pa
$S_{\text{BP}}^{\text{min}}$	Minimum required pumping speed of a backing pump	$\text{mbar} \cdot \text{L/s}$
U_{V}	Voltage	V
T_{ref}	Reference ambient temperature of a thermocouple	K
$I_{\text{prod,tot},s}^{+}$	Total ion current originating from ionization of species s	A
γ_s	Ion source constant of species s	Pa^{-1}
σ_s	Differential ionization effect cross section of species s	$\text{m}^{-1}\,\text{Pa}^{-1}$
l_{e}	Mean path length of an electron in an ion source	m
I_{IS}^{-}	Electron current emitted from the cathode of an ion source	A
RIP_s	Relative ionization probability of molecular species s	-
$I_{\text{prod},\kappa,s}^{+}$	Current of ions with certain κ from parent species s	A
κ	Dimensionless mass-to-charge ratio of an ion	-
$\text{CF}_{\kappa,s}$	Cracking fraction of ion with certain κ from parent species s	-
U_0	Offset voltage applied to the rods of a QMS	V
V_{QMS}	Amplitude of the voltage applied to the rods in a QMS	V
ω_{QMS}	Angular frequency of voltage applied to the rods in a QMS	Hz
r_{QMS}	Radius of the central tunnel between the rods in a QMS	m
$\text{TF}_{\kappa,s}$	Transmission factor of a QMS	-
$I_{\text{cup},\kappa,s}^{+}$	Ion current with certain κ from species s hitting Faraday cup	A
$I_{\text{meas},\kappa,s}^{+}$	Measured ion current with certain κ from species s	A
$I_{\text{meas},\kappa}^{+}$	Measured ion current of mass-to-charge ratio κ	A
$f_{\kappa,s}^{\text{cal}}$	QMS calibration factor to measure $q_{\text{pV},s}^{\text{per}}$ at a certain κ	$\text{mbar} \cdot \text{L/s/A}$

TABLE VI

PHYSICAL QUANTITIES INTRODUCED IN CHAPTER 4.

Symbol	Name	SI unit
$p_{\mathrm{eff},i}$	Effective pressure of species ${}^{i}\mathrm{H} \in \{{}^{1}\mathrm{H}, {}^{2}\mathrm{H}, {}^{3}\mathrm{H}\}$	Pa
Ψ_s	Multi-isotopic permeation flux factor of species s	-
Λ_s	Normalized multi-isotopic permeation flux factor	-
c_{eff}	Effective concentration	$\mathrm{mol\,m^{-3}}$

TABLE VII

PHYSICAL QUANTITIES INTRODUCED IN CHAPTER 5.

Symbol	Name	SI unit
Δt	Discretized time step for EcosimPro simulation	s
$\mathcal{M}$	Number of discretization segments in fluid flow direction	-
y	Distance in flow direction of flow material component	m
Δy	Discretization length in fluid flow direction	m
l_{flow}	Length of EcosimPro flow material component	m
F	Volume flow rate	$\mathrm{m^3\,s^{-1}}$
A_{cs}	Cross section area of a flow material component	$\mathrm{m^2}$
A_n	Area assigned to diffusion port n of flow component	$\mathrm{m^2}$
$\dot{m}$	Mass flow rate	$\mathrm{kg\,s^{-1}}$
J_s^n	Diffusion flux through area A_n of flow component	$\mathrm{mol\,m^{-2}\,s^{-1}}$
f_{sp}	Splitting fraction of a splitter component	-
N_{split}	Number of channels a flow is split by divider component	-
$\eta_{\mathrm{TES},s}$	Particle extraction efficiency of species s	-
$\mathcal{Q}$	Number of discretization segments in diffusion direction	-
$\Delta z/\Delta r$	Discretization length in diffusion direction	m
l_{FP}	Length of a fuel pin in an HCPB BB	m
$\dot{\varkappa}_{s,\mathrm{gen}}^{\mathrm{FP}}$	Average generation rate of species s per HCPB fuel pin	$\mathrm{mol\,s^{-1}}$
p_{PG}	Total pressure of the purge gas of an HCPB BB	Pa
$\dot{m}_{\mathrm{PG}}$	Mass flow rate of the helium purge gas of an HCPB BB	$\mathrm{kg\,s^{-1}}$
V_{PG}	Total volume of the helium purge gas of an HCPB BB	$\mathrm{m^3}$
$\dot{m}_{\mathrm{PG}}^{\mathrm{FP}}$	Mass flow rate of the purge gas through an HCPB fuel pin	$\mathrm{kg\,s^{-1}}$
ε	Void fraction of a pebble-bed	-
d_{IW}	Thickness of inner E97 wall of pebble bed cladding of FP	m
d_{OW}	Thickness of outer E97 wall of pebble bed cladding of FP	m
η_{CPS}	Extraction efficiency of a BB coolant purification system	-

Symbol	Name	SI unit
d_{pipe}	Total thickness of a pipe wall	m
$p_{11,\text{c}}^{\text{CG}}$	Critical $^1H_2$ pressure in coolant to reduce ^{3}H permeation	Pa
Re	Reynolds number	-
Sc	Schmidt number	-
ϱ_{LM}	Dynamic viscosity of a liquid metal flow	$\text{kg m}^{-1}\,\text{s}^{-1}$
$p_s^{\text{UI.IN}}$	Pressure at the UI of the pipe inlet of Takeda's experiment	Pa
$p_s^{\text{DI.IN}}$	Pressure at the DI of the pipe inlet of Takeda's experiment	Pa

TABLE VIII

PHYSICAL QUANTITIES INTRODUCED IN CHAPTER 6.

Symbol	Name	SI unit
C_{OP}	Conductance of the open path of the COOPER experiment	L s^{-1}
C_{OVC}	Conductance of the OVC of the COOPER experiment	L s^{-1}
$p_{\text{init}}^{\text{GMT-A}}$	Pressure in gas mixing tank A prior to gas injection	Pa
$p_{\text{inj}}^{\text{PC-A}}$	Pressure in permeation cell A after gas injection	Pa
α_{inj}	Factor to convert $p_{\text{init}}^{\text{GMT-A}}$ into the resulting value of $p_{\text{inj}}^{\text{PC-A}}$	-

TABLE IX

PHYSICAL QUANTITIES INTRODUCED IN CHAPTER 7.

Symbol	Name	SI unit
F_{main}	Li volume flow rate through main loop	$\text{m}^3\,\text{s}^{-1}$
F_{trap}	Li volume flow rate through hydrogen trap	$\text{m}^3\,\text{s}^{-1}$
F_{BP}	Li volume flow rate through bypass	$\text{m}^3\,\text{s}^{-1}$
V_{Li}	Total volume of liquid Li	m^3
$c_{s,\text{main}}^{\text{Li}}$	Concentration of species s at position y' in Li main loop	mol m^{-3}
U	Number numerical discretization nodes of the main loop	-
$\dot{\varkappa}_{\text{gen},s}$	Isotope generation rate of species s	mol s^{-1}
$V_{\text{Li,main}}$	Volume of liquid Li in main loop	m^3
$V_{\text{Li,trap}}$	Volume of liquid Li in hydrogen trap	m^3
d_{trap}	Diameter of hydrogen trap container	m
N_{peb}	Number of yttrium pebbles in hydrogen trap	-
r_{peb}	Radius of an yttrium pebble in hydrogen trap	m
d_{peb}	Diameter of an yttrium pebble in hydrogen trap	m

Symbol	Name	SI unit
A_{peb}	Surface area of an yttrium pebble in hydrogen trap	m^2
A_{Y}	Surface area of all yttrium pebbles in hydrogen trap	m^2
l_{trap}	Length of hydrogen trap container	m
V_{trap}	Internal volume of hydrogen trap container	m^3
V_{Y}	Total volume of yttrium in hydrogen trap	m^3
$c^{\text{Li}}_{s,\text{trap}}$	Concentration of species s at position y in hydrogen trap	$\text{mol}\,\text{m}^{-3}$
J_{ret}	Atomic hydrogen isotope retention flux into Y getter bed	$\text{mol}\,\text{m}^{-2}\,\text{s}^{-1}$
$\dot{\varkappa}^{\text{Y}}_i$	Trap retention rate of hydrogen isotope species i	$\text{mol}\,\text{s}^{-1}$
$\dot{\varkappa}^{\text{Y}}$	Total hydrogen isotope retention rate of a trap	$\text{mol}\,\text{s}^{-1}$
δ	Width of the center and last shell of a discretized pebble	m
V_q	Volume of shell q in the discretized pebble	m^3
$\dot{\varkappa}^{\text{shell}}_i$	Moles of isotopes i crossing a pebble shell per second	$\text{mol}\,\text{s}^{-1}$
$c_{\nu\text{-start}}$	Concentration in metal at start of phase ν	$\text{mol}\,\text{m}^{-3}$
$c_{\nu\text{-end}}$	Concentration in metal at end of phase ν	$\text{mol}\,\text{m}^{-3}$
$p_{\nu\text{-start}}$	Equilibrium pressure at start of phase ν	Pa
$p_{\nu\text{-end}}$	Equilibrium pressure at end of phase ν	Pa
$f^{\nu\nu'}$	Equilibrium pressure increase factor at $\nu \rightarrow \nu'$ transition	-
$s_{\nu\nu'}$	Slope of the PCIs of a metal hydrogen system	-
a_n	Fitting coefficients for T-c diagram of Y-H system	-
c^{Li}_{-}	Minimum concentration in Li to trigger YH_2 formation	$\text{mol}\,\text{m}^{-3}$
c^{Li}_{+}	Concentration in Li once Y surface reaches δ-$YH_{2\pm x}$ phase	$\text{mol}\,\text{m}^{-3}$
K^{a-b}_{D}	General distribution coefficient in a Me^a-Me^b-H system	-
$c^{\text{Li}}_{\text{init}}$	Initial concentration in Li prior to purification	$\text{mol}\,\text{m}^{-3}$
$c^{\text{Me}}_{\text{eq}}$	Concentration in metal Me at equilibrium	$\text{mol}\,\text{m}^{-3}$
$\varkappa^{\text{Li}}_{\text{init}}$	Initial mole number of isotopes in Li prior to purification	mol
$\varkappa^{\text{Me}}_{\text{eq}}$	Mole number of isotopes in metal Me at equilibrium	mol
T^{-}_{crit}	Max. T for YH_2 to form at a given concentration	K
T^{+}_{crit}	Min. T for YH_2 to not form at a given concentration	K
AR	Aspect ratio of hydrogen trap container	-
$m^{\text{Li}}_{3,\text{limit}}$	Mass limit of dissolved tritium in the Li of DONES	kg
$m^{\text{Y}}_{3,\text{limit}}$	Mass limit of dissolved tritium in the Y getter of DONES	kg
$\dot{\varkappa}^{\text{Me}}_{i,\alpha}$	Increase rate of isotope mole number in Me in α phase	$\text{mol}\,\text{s}^{-1}$
$\dot{c}^{\text{Me}}$	Increase rate of concentration in metal Me	$\text{mol}\,\text{m}^{-3}\,\text{s}^{-1}$
$\varkappa^{\text{Me}}_{\text{HF}}$	Mole number of isotopes dissolved in Me during HyF	mol
τ_{HF}	Period during which YH_2 forms before trap exhaustion	s
$\dot{\varkappa}^{\text{Me}}_{\text{HF}}$	Increase rate of isotope mole number in Me in during HyF	$\text{mol}\,\text{s}^{-1}$
$\varkappa^{\text{Me}}_{\text{sat}}$	Mole number of isotopes dissolved in Me after saturation	mol
$\dot{\varkappa}^{\text{Me}}_{\text{sat}}$	Increase rate of isotope mole number in Me after saturation	$\text{mol}\,\text{s}^{-1}$

Symbol	Name	SI unit
$m_{3,\mathrm{max}}^{\mathrm{Me}}$	Maximum mass of dissolved tritium in metal Me	kg
$m_{3,\mathrm{eq}}^{\mathrm{Me}}$	^{3}H mass in Me after trap is exchanged and in equilibrium	kg
τ_{trap}	Trap replacement period	s
$\tau_{\mathrm{trap}}^{\mathrm{max}}$	Maximum permissible trap replacement period	s
$m_{\mathrm{Y}}^{\mathrm{min}}$	Min. required trap mass to meet DONES tritium limits	kg

TABLE X

PHYSICAL QUANTITIES INTRODUCED IN CHAPTER 8.

Symbol	Name	SI unit
$m_{\mathrm{Y}}^{\mathrm{max}}$	Maximum yttrium capacity of a hydrogen trap	kg
$r_{\mathrm{in}}^{\mathrm{40CF}}$	Inner radius of a DN40CF nipple	m
$z_{\mathrm{Li}}^{\mathrm{max}}$	Max. height of the lithium column in the LYDER system	m
g_{E}	Gravitational acceleration on Earth ($g_{\mathrm{E}} = 9.81\,\mathrm{m\,s^{-2}}$)	$\mathrm{m\,s^{-2}}$
$V_{\mathrm{Li}}^{\mathrm{SC}}$	Volume of an extracted lithium sample in LYDER	$\mathrm{m^3}$
Δz_{LS}	Distance between level sensors in the right tank	m
V_{PC}	Inner volume of the permeation chamber in LYDER	$\mathrm{m^3}$
z_{tube}	Total height of the permeation membrane in LYDER	m
Δz_{16CF}	Thickness of the ring-shaped 16CF flange ring in LYDER	m
Δz_{roof}	Thickness of the roof of the α-iron membrane in LYDER	m
Δz_{per}	Length of the effective permeation area in LYDER	m
z_{surf}	Height of the lithium column in the right tank	m
$r_{\mathrm{in}}^{\alpha\mathrm{Fe}}$	Inner radius of the α-iron tube in LDYER	m
$r_{\mathrm{out}}^{\alpha\mathrm{Fe}}$	Outer radius of the α-iron tube in LDYER	m
$V_{\mathrm{Li}}^{\mathrm{side}}$	Lithium volume beside the α-iron tube	$\mathrm{m^3}$
A_{40CF}	Interior cross-sectional area of a DN40CF nipple	$\mathrm{m^2}$
$q_{\mathrm{pV}}^{\mathrm{desorb}}$	Flow of particles desorbing from a metal sample	$\mathrm{mbar \cdot L/s}$
$\varkappa_{\mathrm{i,meas}}^{\mathrm{Li}}$	Measured number of desorbed deuterium isotopes	mol
$\varkappa_{\mathrm{i,init}}^{\mathrm{Li}}$	Number of deuterium isotopes initially in the lithium	mol
$\varkappa_{\mathrm{i,final}}^{\mathrm{Li}}$	Number of deuterium isotopes remaining in the lithium	mol

LIST OF TECHNICAL SYMBOLS

TABLE XI
SYMBOLS OF TECHNICAL COMPONENTS.

Symbol	Meaning
	Thermocouple
	Heater
	Turbomolecular pump
	Dry scroll pump
	Diaphragm pressure gauge
	Pirani pressure gauge
	Blower
	Cold cathode pressure gauge
	General open/close valve
	Manually operated open/close valve
	Manually operated regulation valve
	Gas dosing valve
	Pneumatically operated open/close valve
	Electrically operated open/close valve
	Gas cylinder

LIST OF FIGURES

LIST OF TABLES

1. INTRODUCTION AND OBJECTIVES

The first chapter sets out the research context for the scientific work carried out within the scope of this dissertation. First, the need for nuclear fusion as a clean and potentially cheap energy source is justified in the context of humanity's future energy needs. This is followed by an introduction to the physical principles and current technological concepts of nuclear fusion power plants as well as fusion-relevant materials. It includes an overview of currently planned experimental fusion research facilities as part of the roadmap to fusion energy. Finally, tritium safety issues in these facilities are discussed which leads to the description of the objectives and structure of this thesis.

1.1. Energetic scenario and motivation

Advances in agriculture and improvements in medical treatment during the Industrial Revolution in the late 1800s led to a significant decline in infant mortality and an accelerated increase in the world's population. In the wake of economic and technological growth around the globe, the human population experienced its strongest growth in the mid-20th century and has continued to rise ever since (see the top left-hand plot of figure 1.1) [1]. Both population growth and rising gross domestic product (GDP) are accompanied by an increase in energy consumption. This becomes apparent when comparing the upper graphs of figure 1.1. Despite the development of new energy sources such as nuclear fission, solar, wind, and other renewables, about 80 % of the energy consumed today still originates from fossil fuels [2].

It is assumed that the burning of fossil fuels is the main cause of the increase in greenhouse gas concentrations in the Earth's atmosphere, contributing to global warming [5]. Moreover, they contain radioactive materials that are released into the atmosphere after combustion [6]. The use of fossil fuels is also partly responsible for atmospheric aerosols, smog, and acid rain. All of these problems have serious consequences for human health and the environment [7], [8]. Therefore, a transition to cleaner energy sources such as renewable energy or nuclear fission is essential. Current simulations indicate that in the most likely scenario, population growth, and thus global energy demand, will continue to increase at almost the same rate over the next thirty years. Although the global community has agreed to reduce greenhouse gas emissions [9], conservative estimates [3] predict that the share of fossil fuels will only decline from 80 % to 70 % by 2050, despite the increasing availability of renewable energy sources (see lower left graph in figure 1.1).

Expanding the exploitation of nuclear fission energy would be one way to reduce fossil fuel dependency. In contrast to renewable energy sources, nuclear fission is a base-load energy source and does not rely on the development of new energy storage technologies. As can be seen from the lower right-hand graph in figure 1.1, nuclear fission reactors

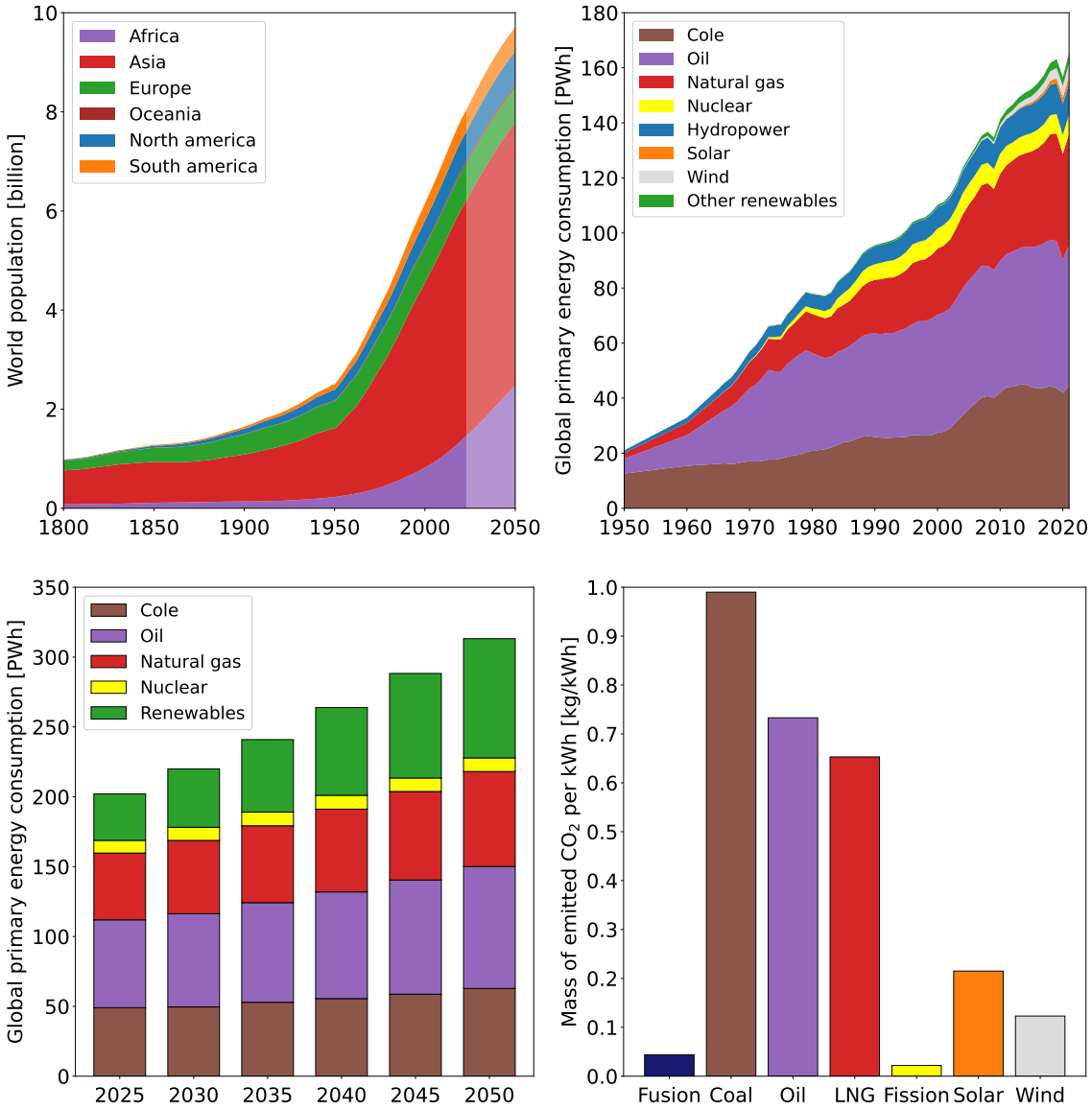

Fig. 1.1. [Top left] Development of the world population extrapolated into the future (median) [1]. [Top right] Global primary energy consumption by energy source [2]. [Lower left] Predicted global primary energy consumption by energy source over the next 30 years [3]. [Lower right] Mass of CO_2 emitted per kW h of electricity produced by a fusion power plant compared to that of other energy sources [4].

have among the lowest CO_2 emission rates of all available energy sources. Nevertheless, despite the development of new generation fission power plants, such as the 4^{th} generation molten salt reactor (MSR), the risk of nuclear accidents like in Chernobyl or Fukushima is ever-present [10], [11]. Another safety concern is that nuclear fission energy relies on the mining and production of radioactive fuel, which is burned and then stored as radioactive waste in sealed containers. The particularly long decay times of the fission products require the waste to be isolated for tenth of thousands of years. Unfortunately, no final disposal concept has been developed so far. In conclusion, the pros and cons of this technology suggest that it is well-suited as a transitional energy source, but should be

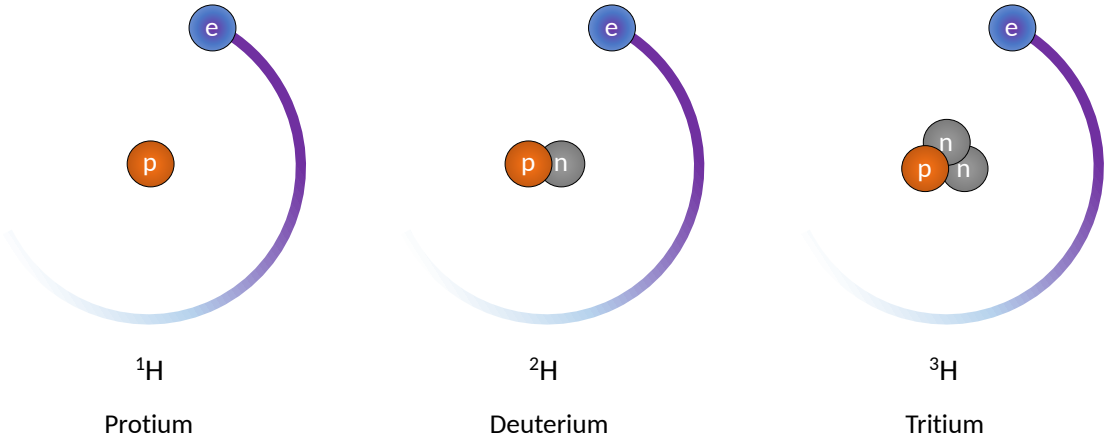

Fig. 1.2. Atomic structure of the hydrogen isotopes protium (^{1}H), deuterium (^{2}H) and tritium (^{3}H).

replaced by a safer alternative in the future.

A promising alternative base-load energy source currently under development is nuclear fusion energy. Like fission reactors, fusion reactors would contribute to CO_2 emissions that are negligible compared to fossil fuel power plants (see the lower right-hand plot of figure 1.1) [4]. In addition, fusion reactors need a lot less fuel to produce the same amount of electricity as reactors fueled by coal, oil, or natural gas. In fact, it is estimated that a 1 GW fusion power plant will require only about 250 kg of fusion fuel per year. In comparison, a coal-fired power station with the same energy output consumes an annual fuel amount of approximately 2.7×10^9 kg [12].

First-generation fusion reactors will rely on the hydrogen isotopes deuterium and tritium as fusion fuel components. Hydrogen is the lightest of all elements and is a collective term for the three hydrogen isotopes, protium (^{1}H), deuterium (^{2}H), and tritium (^{3}H). In the ground state, all three hydrogen isotopes contain a single proton in the nucleus surrounded by an electron in the 1s orbital. While protium has zero, deuterium has one, and tritium has two neutrons (n) bound to the proton in the nucleus (see figure 1.2).

Deuterium is a stable isotope and makes up about $3.5{\times}10^{-3}$ % of the hydrogen isotopes in Earth's water. In water, it is mainly bound in ^{1}H^{2}HO molecules from which it can be easily extracted after processes of chemical enrichment and distillation. Consequently, deuterium is a highly available raw material.

Tritium on the other hand is extremely rare in nature due to its radioactive instability. It undergoes a β^- decay of the form

$$^3\mathrm{H} \longrightarrow {}^3\mathrm{He} + \mathrm{e}^- + \overline{\nu}_\mathrm{e} + 18.6\,\mathrm{keV} \tag{1.1}$$

where $\overline{\nu}_\mathrm{e}$ labels an anti-neutrino. Tritium has a relatively short half-life of only 12.32 years. About 5.7 keV of the energy released is carried by the electron and therefore is not energetic enough to penetrate human skin. If inhaled or ingested tritium poses a serious threat to human life [13]. Like deuterium, tritium is easily incorporated into water molecules through isotope exchange reactions. Tritiated water entering groundwater reservoirs is

a serious safety issue. The main source of tritium today are deuterium-uranium fission reactors of CANDU type which generate small amounts of tritium from heavy water [14]. Over the past decades, the annual demand for tritium has remained relatively low because it is used for only a small number of technological applications, such as ^{3}He production, nuclear weapons, or self-powered lighting induced by tritium radioluminescence. Because of the low tritium production rate, it is planned to breed the necessary tritium inside the fusion reactor by means of lithium spallation. Consequently, the first-generation fusion power plants will rely on the lithium as a raw material.

Lithium is an alkali metal with a melting temperature at atmospheric pressure of $T = 453.54\,\mathrm{K}$ and a boiling temperature of $T = 1616\,\mathrm{K}$ [15]. It accounts for approximately 6×10^{-3} % of Earth's crust where it occurs as ^{6}Li (natural abundance: 7.42 %) and ^{7}Li (natural abundance: 92.58 %) bound to stable minerals or salts [16]. It is mainly recovered from mines or brine pools located in Argentina, Australia, Bolivia, Chile, and China whose reserves are estimated to be approximately 22×10^6 t [17]. Due to the development of lithium batteries and the proceeding transition towards electric vehicles, its recovery has significantly increased in the past decade. Nevertheless, it is estimated that the lithium deposits on Earth are large enough to last at least for several hundred or even thousands of years [16], [18].

Fusion power plants do not produce radioactive waste in the form of burned fuel like fission reactors do. In fact, the only direct fusion product which leaves the reactor as a residual is inert helium (^{4}He) posing no danger to humans or the environment. The second fusion product is high-energy neutrons. These impact the plant's structural material and, over time, cause it to become radioactive through the process of neutron activation. Nevertheless, by making use of reduced-activation ferritic/martensitic (RAFM) steels, like Eurofer97 (E97), the half-lives of the generated radioactive isotopes are significantly shorter compared to the radioactive waste of nuclear fission plants [19]. Figure 1.3 shows a conservative estimate of the total radiotoxicity of the components of a RAFM steel-based fusion reactor after its shutdown compared to that of a pressurized water fission reactor (PWR) of the 2$^{\mathrm{nd}}$ generation, a modern MSR fission reactor and the ash of a coal-fired power plant, normalized to $1\,\mathrm{GW_e}$ electricity production [20]. It can be seen that the anticipated radiotoxicity of a fusion reactor falls to several orders of magnitude below that of fission reactors within about a human lifetime, and over time even drops below the radiotoxicity of the ash emitted by coal-fired plants. The use of vanadium alloys or SiC/SiC materials for critical fusion reactor components would lead to an even further reduction in radiotoxicity. As a result, there is no need for a long-term disposal concept for dismantled reactor components and no burden is placed on future generations.

Indeed, a key advantage of fusion reactors over fission reactors is the impossibility of an uncontrolled power excursion in which the reactor temperature rises in a runaway process. A fusion reactor is thermally stable. Any uncontrolled increase in temperature or pressure would cause the fusion reactions to cease. This eliminates the risk of a nuclear accident in which the activated structural material is released into the environment. More-

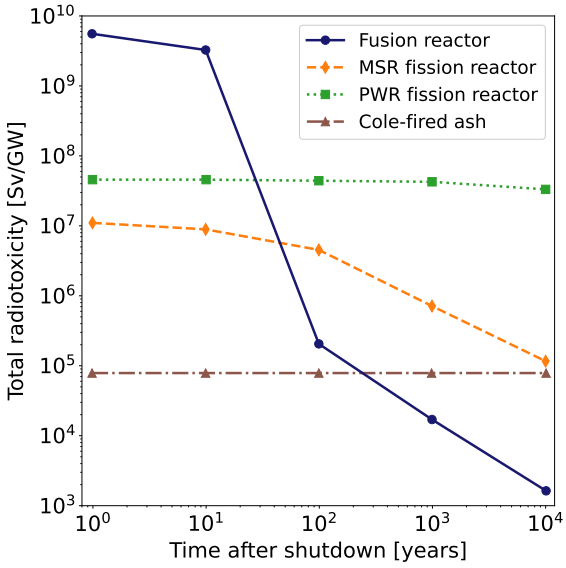

Fig. 1.3. Approximate total radiotoxicity of a fusion reactor after its shutdown compared to fission reactors (2^{nd} generation PWR, 4^{th} generation MSR) and to the ash of a coal-fired power plant, normalized to $1\,\text{GW}_\text{e}$ electricity production [20].

over, since tritium is produced inside the reactor at about the same rate as it is burned off, the total amount of tritium contained in the reactor remains small and therefore poses no severe threat to the outside environment.

However, there are still many scientific and technological challenges to overcome before fusion can be made to work and produce electricity.

1.2. Nuclear fusion technology

Negatively charged electrons and positively charged atomic nuclei are bound to each other by the electromagnetic force. This force is also responsible for chemical bonds between atoms and molecules and stores the energy released in exothermic chemical reactions.

Atomic nuclei are made up of protons and neutrons called nucleons. Despite the repulsive electrostatic force between positively charged protons, nucleons are found to be strongly bound together. This is due to an additional attractive interaction, the nuclear force. According to the theory of quantum chromodynamics, the nuclear force is a residual force that acts between nucleons as a result of the strong interaction between the quarks that form the nucleons [21]. It has a relatively short range but exceeds the repulsive electromagnetic force below a distance of about 2.5×10^{-15} m. This results in a dominant attraction between nucleons within this range.

The nuclear binding energy E_{NB} defines the work that must be done against the nuclear force to decompose and separate a whole nucleus. According to the principle of equivalence between mass and energy, first discovered by Albert Einstein [22], the work expended in such a separation process manifests itself as a condensation of energy into mass. As a result, the summed mass of the individual constituents of an atomic nucleus is by a value $\Delta m_{\text{MD}} = E_{\text{NB}}/ç^2$ heavier than the mass of the nucleus in its bound state. Here, $ç$ labels the speed of light in vacuum and Δm_{MD} is called the mass defect. Figure

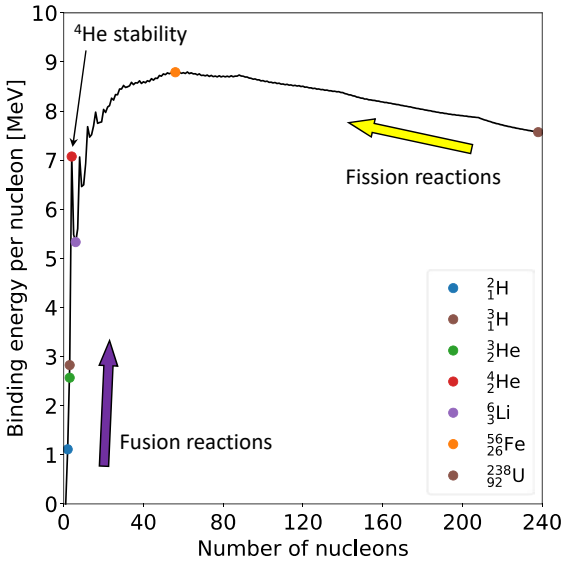

Fig. 1.4. Binding energy per nucleon as a function of the total nucleon number of different isotopes [23].

1.4 presents the binding energy per nucleon as a function of the nucleon number [23]. It is found that for light elements the binding energy per nucleon experiences an overall increase with increasing nucleon number before reaching a maximum and slowly decreases for heavier elements. This tendency suggests that generally, two types of exothermic nuclear reactions exist, nuclear fission and nuclear fusion.

Nuclear fission usually occurs if the bound structure of a very heavy parent nucleus is disturbed for example by an impacting neutron and is split into two or sometimes three lighter daughter fragments. This process is exothermic if, after the fission process, the summed mass defect of the daughter nuclei is greater than the mass defect of the parent nucleus. In this case, the total mass of the produced fission fragments is by a certain value Δm_{fis} smaller than that of the parent nucleus causing the energy $\Delta E_{\text{fis}} = \Delta m_{\text{fis}} \cdot ç^2$ to be liberated.

Nuclear fusion, on the other hand, usually describes a reaction in which two light parent nuclei collide and fuse to form a heavier daughter nucleus. Depending on the individual fusion process, it may involve conversion between protons and neutrons and lead to an additional release of secondary particles like lighter nuclei, neutrons, positrons, neutrinos, and gamma photons. As figure 1.4 shows, the fusion of two very light nuclei to a heavier parent nucleus mostly implies an increase in the binding energy and thus in the mass defect of the daughter nucleus. The increase in binding energy and mass defect after the fusion reaction results in a reduction of the total mass of the reaction products by a value Δm_{fus} compared to the mass of the parent nuclei. This is associated with an energy release of $\Delta E_{\text{fus}} = \Delta m_{\text{fus}} \cdot ç^2$. In most fusion reactions, the energy released is distributed among the fusion products in the form of kinetic energy, but can also be partially dissipated as electromagnetic radiation by a gamma photon. It can be seen that light nuclei with certain nucleon numbers have a particularly high binding energy per nucleon, higher than their nearest neighbors on the nucleon number scale. This effect is most prominent in ^{4}He nuclei which are therefore exceptionally stable.

Figure 1.4 reveals that the difference in binding energy per nucleon increases strongest between the nuclei ^{1}H, ^{2}H, ^{3}H, ^{3}He and ^{4}He which suggests that a nuclear fusion between two of these isotopes into one of the others releases a particularly high amount of energy per fusion reaction. This is one of the reasons why the following nuclear fusion reactions are of special importance for the technical application of fusion energy.

$$^2\mathrm{H} + {}^3\mathrm{H} \longrightarrow {}^4\mathrm{He}\,(3.5\,\mathrm{MeV}) + \mathrm{n}\,(14.1\,\mathrm{MeV}) \tag{1.2}$$

$$^2\mathrm{H} + {}^3\mathrm{He} \longrightarrow {}^4\mathrm{He}\,(3.6\,\mathrm{MeV}) + {}^1\mathrm{H}\,(14.7\,\mathrm{MeV}) \tag{1.3}$$

$$^2\mathrm{H} + {}^2\mathrm{H} \longrightarrow {}^3\mathrm{H}\,(1.01\,\mathrm{MeV}) + {}^1\mathrm{H}\,(3.02\,\mathrm{MeV}) \quad (\sim 50\,\%) \tag{1.4}$$

$$\longrightarrow {}^3\mathrm{He}\,(0.82\,\mathrm{MeV}) + \mathrm{n}\,(2.45\,\mathrm{MeV}) \quad (\sim 50\,\%) \tag{1.5}$$

Both, the deuterium-tritium and the deuterium-^{3}He reactions lead to the formation of ^{4}He and a neutron that carries most of the liberated energy. Due to the little lower nuclear binding energy of ^{3}He compared to tritium, the second reaction has a slightly higher energy output. Moreover, neither the fuel nor the products of the second reaction are radioactive, which makes it very attractive for technological use. Like tritium, however, ^{3}He is a very rare isotope on Earth and would have to be artificially produced by lithium spallation. In terms of fuel abundance and accessibility, the last two deuterium-deuterium reactions appear to be of particular interest. Both reactions occur with almost equal probability. Despite their relatively low amount of liberated energies the produced nuclei could subsequently undergo the first two high-energy fusion reactions and terminate as ^{4}He.

Whether a particular fusion reaction is technologically feasible, however, depends on another crucial factor. For fusion to occur, the parent nuclei must collide and have sufficient kinetic energy to tunnel or overcome their repulsive Coulomb potential, allowing the attractive nuclear force to act and the nuclei to fuse. The probability of this happening is represented by the fusion cross section σ_{NF}. It is a measure of the rate at which a given fusion reaction occurs and varies with the kinetic energy of the involved particles. Figure 1.5 shows a plot of the cross sections of the fusion reactions (1.2) - (1.5) as a function of the kinetic energy of ^{2}H and the associated temperature [24]. It should be noted that the plot of the deuterium-deuterium cross section refers to both reactions (1.4) and (1.5) as they are approximately equally probable. The graph clearly shows that above about $T = 3 \times 10^9$ K the cross sections of all plotted reactions are of the same order of magnitude and therefore similarly probable. However, keeping a particle system confined and stable at such high temperatures is not feasible with current technology. The only reaction with an even higher cross section at lower temperatures is the deuterium-tritium reaction. Here, its cross section exceeds that of the other reactions by several orders of magnitude. Therefore, the current fusion research program especially focuses on this reaction as the most technologically accessible reaction for the first generation of future power plants. However, apart from the presence of radioactive tritium, a drawback of this reaction is that most of the energy released is converted into kinetic energy of the neutrons, which have the unfortunate property of activating irradiated material. Moreover, it is particularly

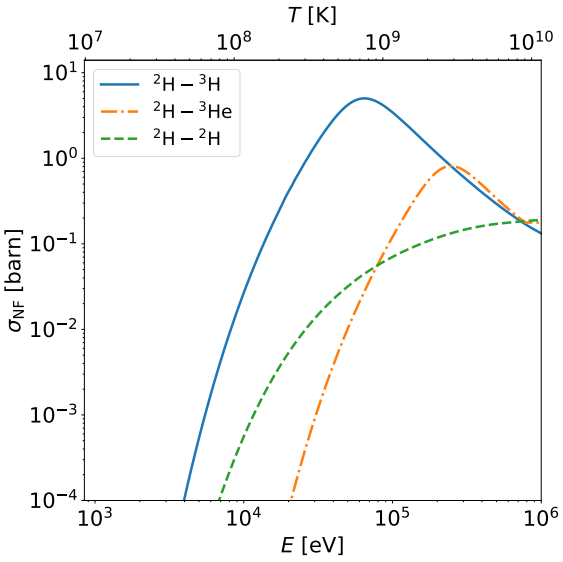

Fig. 1.5. Probability cross section for different nuclear fusion reactions as a function of the kinetic energy of the deuterium nuclei [24].

difficult to efficiently absorb this energy by a cooling system which is necessary to generate electricity. Nevertheless, it will be demonstrated in the following sections the progress of materials research and technology is making great strides in tackling these problems with success.

In order to bring a system of ^{2}H and ^{3}H isotopes to temperatures associated with a sufficiently high deuterium-tritium reaction cross section (see figure 1.5) it must be heated by external heating systems and confined in a relatively dense state. In this process, the atoms ionize and turn into a plasma of free-charged nuclei and electrons. For an economically viable fusion reactor, it is essential that the fusion energy output exceeds the injected energy to keep the fusion reactions running. The ratio between these two quantities is known as the fusion energy gain factor Q which must be greater than unity in order to ensure the required power gain. The condition $Q > 1$ is certainly satisfied if the proportion of the generated fusion power carried by the produced ^{4}He nuclei exceeds the power losses of the plasma. Once this is achieved, the helium collisions in the plasma occur frequently enough so that the plasma temperature is maintained and the external heating systems could, in theory, be switched off. This scenario is called ignition. In 1955, J. D. Lawson first formulated a condition for certain plasma parameters that must be satisfied in order for ignition to occur, the Lawson criterion [25]. For a deuterium-tritium plasma at a temperature of about 14 keV or 1.62×10^8 K the Lawson criterion writes

$$C_e \cdot \tau_E \cdot T \geq 3.5 \times 10^{28}\,\mathrm{s\,K\,m^{-3}} \tag{1.6}$$

when assuming that the plasma densities of deuterium and tritium nuclei are equal. In this expression, C_e is the number concentration of the plasma electrons and τ_E is the plasma confinement time. Both higher or lower temperatures result in an increased triple product and therefore pose a higher challenge for the technological realization of fusion ignition [26]. However, for an economically feasible fusion power plant satisfying the Lawson criterion is indispensable.

In 2022, for the first time in history, apart from thermonuclear fusion weapons, a fusion process with an energy gain factor of $Q > 1$ was experimentally realized [27]. The technique used for this achievement was inertial confinement fusion. It describes an artificial nuclear fusion process in which the fuel components (typically deuterium and tritium) are contained in small millimeter-sized pellets. By compressing the pellets with an extremely high, well-distributed external heat source (for example lasers), the fuel components are compressed to such an extent that their temperature reaches sufficiently high values to satisfy the Lawson criterion. This allows the fuel in the pellets to be completely burned and more fusion power to be generated than is injected by the heat source.

Nevertheless, despite the major scientific breakthrough it has provided, viable fusion reactor concepts based on inertial confinement fusion are only just beginning to emerge [28]. Instead, the first grid-connected fusion power plants will most likely be based on another highly sophisticated nuclear fusion technology which has been the subject of decade-long research. What is meant is magnetic confinement fusion.

1.2.1. Magnetic confinement fusion

Magnetic confinement fusion is a technology in which deuterium and tritium are injected into a vacuum chamber and heated to temperatures where the Lawson criterion is met and fusion ignition occurs. During the heating process, the deuterium and tritium atoms lose their electrons and become a plasma. The plasma is confined to a fixed volume inside the vacuum chamber by a strong magnetic field that prevents the plasma from contacting the chamber walls. This is possible because, as a consequence of the principle of relativity [29], charged particles experience a force perpendicular to a magnetic field and to their direction of motion, the so-called Lorentz force. As a result, in addition to their primary direction of motion, the high-energy plasma particles undergo a superimposed tight circular gyromotion around a point called the guiding center, perpendicular to the magnetic field lines. The trajectory of the guiding center is therefore bound to a certain extent to the direction of the magnetic field lines. Therefore, technically shaping the magnetic field lines allows, in principle, to confine the space in which the movement of the plasma particles mainly takes place. Unfortunately, doing so is complicated by the fact that electric fields $\vec{E}$ and inhomogeneous magnetic fields $\vec{B}$ in the plasma lead to drifts ($\vec{E} \times \vec{B}$ drift, polarization drift, Grad-B drift, and curvature drift [26]) of the particle guiding centers perpendicular to the magnetic field lines out of the confined plasma space [30]. Only very precise and specifically shaped magnetic fields can compensate for these drifts and force the particles back into confinement, keeping the particle escape rate low. Yet, designing and building the right configuration of electromagnets is a physical and technological challenge.

Notwithstanding, there are two reactor designs that have proven to be particularly efficacious in terms of maintaining plasma confinement for a relatively long period of time: the tokamak and the stellarator. Illustrations of the electromagnetic coil systems

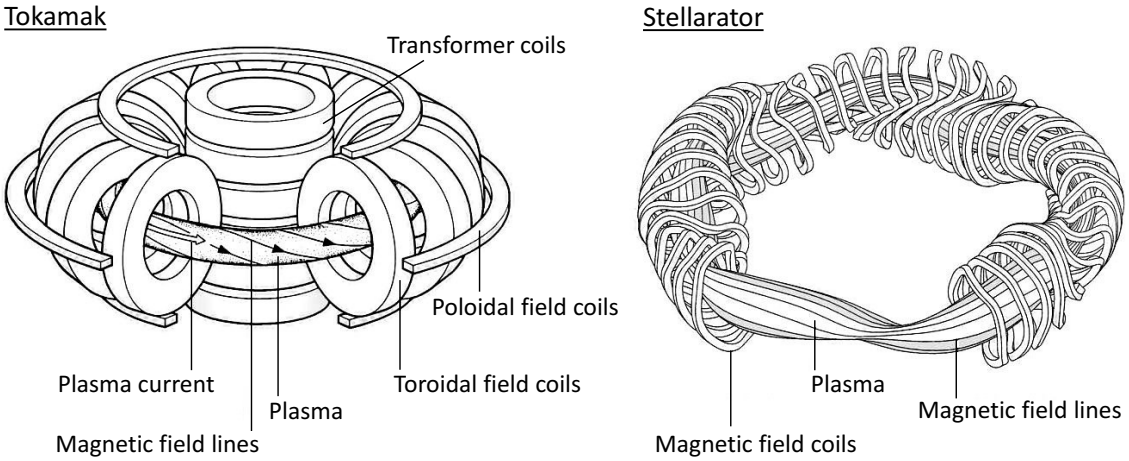

Fig. 1.6. [Left] Magnetic field coil and plasma configuration in a tokamak [31]. [Right] Magnetic field coil and plasma configuration in a stellarator [31].

and induced magnetic fields of both devices are shown in figure 1.6. Both designs are based on an electromagnetic arrangement that encloses the magnetic field lines into a ring-shaped space.

The initial idea of the tokamak came from Austrian-born Ronald Richter [32], [33]. It was later conceptualized by the Soviet scientists Andrei Sacharow and Igor Tamm [34]. In a tokamak, toroidally-arranged electromagnets generate a self-contained magnetic field that runs around the torus in the perpendicular direction to the coils. A second electromagnet, a transformer coil, is located in the center of the torus (see figure 1.6). By continuously changing the intensity of the magnetic field in time, it induces a toroidal plasma current. The current then generates a second transient magnetic field that encircles the plasma current perpendicular to the toroidal direction. The superimposition of both magnetic fields results in helical magnetic field lines that twist around the plasma column on closed magnetic surfaces. This particular magnetic field is necessary to compensate for the particle drifts and thus enables an adequate plasma confinement time. The transformer field is changed over time by repeatedly ramping up the field strength at fixed intervals. However, since the transformer must be discharged after each ramp-up phase before it can be powered up again, modern tokamaks can only operate in pulsed mode. To control the position and shape of the induced plasma current a third coil system is needed, the poloidal field coils (see figure 1.6). This is important because in a tokamak the ohmic resistance of the plasma current is exploited as a plasma heating method [26]. In addition, poloidal field coils allow the plasma to be forced into a D-shaped geometry. This has the advantage of reducing the tension between the toroidal field coils on the inside of the toroidal curvature and allowing impurity particles to be deflected out of the plasma in a pre-determined direction.

The stellarator was invented in 1958 by the American theoretical physicist Lyman Spitzer [35]. In this device, the twisted magnetic field required for plasma confinement is generated solely by magnetic field coils arranged in a complex circular pattern around

the plasma column. Therefore, a stellarator does not depend on a transformer current and can, in principle, be operated in a steady state of permanent plasma confinement. As a consequence, current-induced plasma instabilities do not occur and poloidal field coils are not needed to stabilize the plasma motion. This implies a higher degree of freedom to shape the plasma ring and optimize its properties for its potential use in a future fusion reactor.

Numerous experimental tokamak and stellarator devices have been built over the past decades. Their operation has led to major breakthroughs in understanding and controlling the complex behavior of magnetically confined plasmas. However, none have been designed to generate electricity.

An example of an experimental stellarator device that has led to major advances in stellarator research is the TJ-II (Tokamak de la Junta II) machine. It has been in operation since 1997 at the Ciemat Institute in Madrid, Spain [36]. The largest stellarator in service today is called Wendelstein 7-X and was inaugurated in 2015 [37]. Wendelstein 7-X was designed with the goal of eventually answering the question of whether stellarators might be a simpler reactor concept for future fusion plants than tokamaks. Nevertheless, compared to tokamaks, research on stellarators is still at a relatively early stage.

Since their invention, tokamaks have been optimized several times, as more and more plasma instabilities were discovered that had to be taken into account in the new designs. The largest tokamak in operation and capable of operating with a deuterium-tritium fuel mixture is called JET (Joint European Tokamak). It is located at the Culham Centre for Fusion Energy in Oxfordshire, UK. An illustration of the JET tokamak is shown in the left-hand image in figure 1.7 [26]. It has a plasma volume of $V = 80\,\mathrm{m}^3$, a major plasma radius of $R_0 = 2.96\,\mathrm{m}$ and began operation in 1983. In 1997, it achieved $Q = 0.67$, the highest fusion energy gain of any magnetic confinement fusion device to date. Moreover, it holds the record for the highest fusion power generated of $P_{\mathrm{fus}} = 16\,\mathrm{MW}$ [39], [40].

A considerably larger tokamak called ITER (International Thermonuclear Experimental Reactor) [41] is currently under construction in Cadarache, France (see the central image in figure 1.7). Its designed plasma volume is $V = 840\,\mathrm{m}^3$ with a major radius of $R_0 = 6.2\,\mathrm{m}$. ITER uses superconducting magnetic field coils that operate at cryogenic temperatures. Therefore, the entire coil system is built inside a vacuum cryostat. Indeed, it will be the largest vacuum system and the largest superconducting coil system ever built. ITER is a new generation tokamak whose design is based on the combined knowledge obtained from previous tokamak experiments. It shall demonstrate the feasibility of fusion power as a potential future energy source. Therefore, ITER aims to achieve a fusion energy gain factor as high as $Q = 10$ and maintain a plasma pulse for up to 8 min. In addition, several tritium breeding technologies will be validated during the ITER TBM (Test Blanket Module) program [42]. This is a crucial step on the way towards tritium self-sufficiency of future fusion power plants. The first deuterium plasma is planned for 2027 when construction is expected to be completed and the commissioning phase to

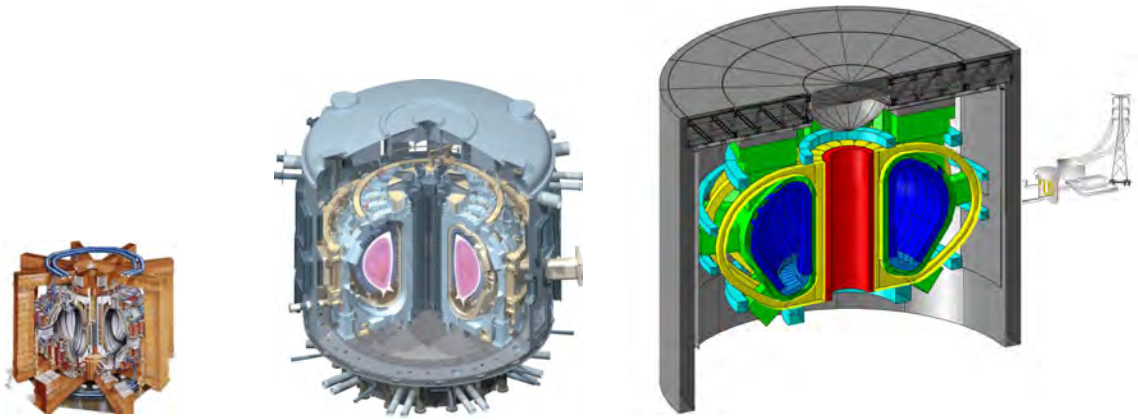

JET

First plasma: 1983

- $Q = 0.67$
- $P_{\text{fus}} = 16$ MW
- $R_0 = 2.96$ m
- $V = 80$ m^3

ITER

First plasma: ~ 2025

- $Q = 10$
- $P_{\text{fus}} = 500$ MW
- $R_0 = 6.20$ m
- $V = 840$ m^3

DEMO

First plasma: ~ 2050

- $Q \approx 25$
- $P_{\text{fus}} \approx 2000$ MW
- $R_0 \approx 9$m
- $V \approx 2500$m^3

Fig. 1.7. Comparison between the sizes and performances of the experimental nuclear fusion devices JET (in operation) [26], ITER (under construction) [38] and DEMO (in the design stage) [39].

begin. Full deuterium-tritium operation is planned for the period after 2035 and the experimental test blanket program is scheduled to start in 2037 [43]. It is worth noting that other new-generation tokamaks with the goal of reaching $Q > 1$ have completed the design phase, the American SPARC [44], the Indian SST-2 [45] and the Chinese CFETR [46]. Their construction is scheduled to begin within the next few years.

ITER is a key research facility on the roadmap towards fusion electricity [47]. This roadmap provides a well-defined and structured path toward the commercialization of fusion energy. It is an agreement between numerous research institutions and forms the programmatic basis for the EUROfusion consortium, which was founded in 2014 as the successor to the European Fusion Development Agreement (EFDA) [48]. EUROfusion establishes and coordinates European fusion research activities and is currently funded by the Euratom Horizon 2020 programme.

According to the EURfusion roadmap, the next step on the path towards a commercial fusion power plant is the DEMO tokamak (DEMOnstration Power Plant) which is already at a relatively advanced stage of conceptual design [49], [50]. The primary goal of DEMO is to demonstrate stable power generation from a nuclear fusion device. Its engineering design phase is expected to start after 2029 and will be adapted to the knowledge gained during the ITER deuterium-tritium operation phase and the subsequent TBM program [43]. A 3D image of the 2017 DEMO design and its currently foreseen dimensions and performance data are shown on the right in figure 1.7. [39], [40], [51]. With a plasma volume of $V \approx 2500\,\text{m}^3$ and a major radius of $R_0 \approx 9\,\text{m}$, DEMO will be significantly larger than ITER [49]. This is necessary to achieve an even higher fusion energy gain

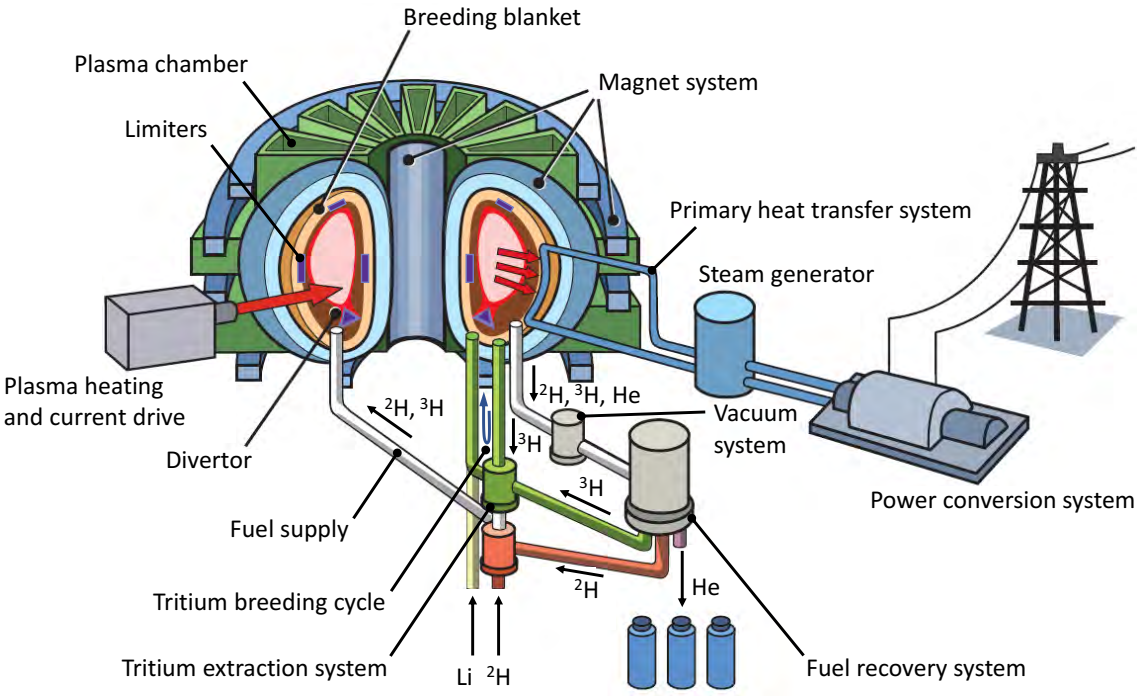

Fig. 1.8. Configuration of a conceptual nuclear fusion power plant [38].

factor of $Q \approx 25$ and plasma pulses of longer than two hours.

DEMO will likely be the first thermonuclear fusion reactor to incorporate all the necessary tokamak components and ancillary systems of a grid-connected fusion power plant which are illustrated in figure 1.8. These can be divided into different subsystems: In-vessel components, cryostat and superconducting magnets, plasma heating and current drive systems, remote maintenance system, plasma diagnostics, vacuum systems, fuel cycle, primary heat transfer system (PHTS) and power conversion system (PCS) [52]. Section 1.2.3 will focus more closely on one specific part of the fuel cycle, the tritium breeding blanket which is penetrated by the PHTS. It is beyond the scope of this dissertation to describe all the other systems in detail, as most of them are not relevant to the research carried out. Nevertheless, the reader can find outlines of their different functions and tasks in the references [53]–[59].

The heart of the DEMO tokamak is the primary vacuum vessel. It has the form of a D-shaped hollow torus with an inner volume of $V \approx 6400\,\mathrm{m}^3$ and an outer radius of $r \approx 18\,\mathrm{m}$. It surrounds the plasma column and contains the in-vessel components such as the breeding blanket and the divertor [60] together with a system of plasma limiters [61] that are subjected to the highest heat load. The vacuum vessel is subdivided into 16 segments with three ports each, an upper port, an equatorial port, and a lower port. A 3D image of the vacuum vessel and its port structure is presented in figure 1.9. The vacuum vessel has the function of maintaining a primary vacuum of $p = 1 \times 10^{-5}\,\mathrm{Pa}$ that is required prior to fuel injection. Moreover, it shields the exterior magnets from the extensive neutron irradiation from the plasma. Through the lower ports, it is connected to a system of different vacuum pumps responsible for the primary vacuum and for the

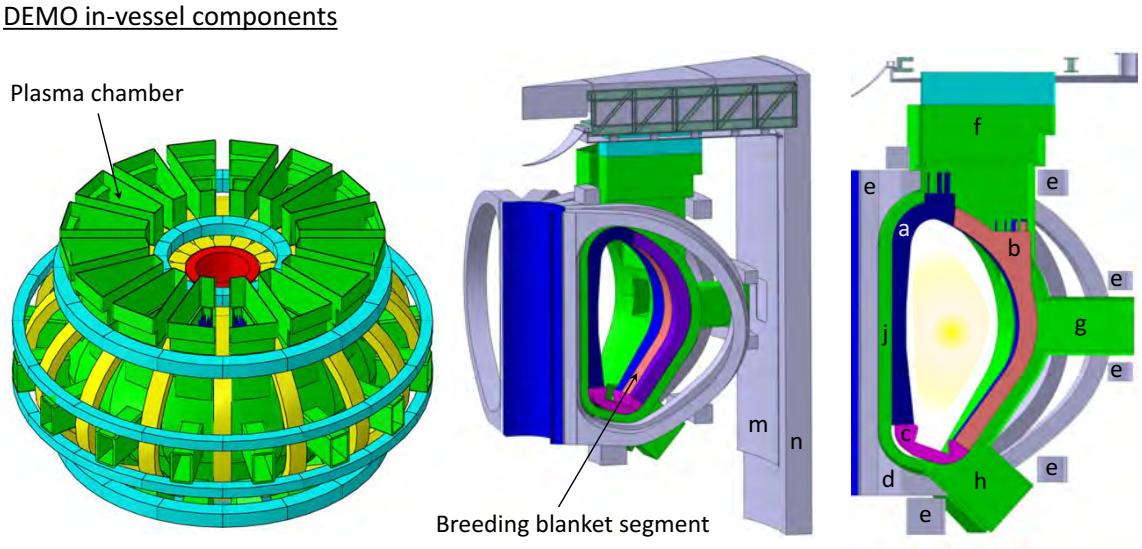

Fig. 1.9. [Left] Primary vacuum vessel of the DEMO tokamak consisting of 16 segments [39]. [Center] Position of a breeding blanket segment inside the vacuum vessel. [Right] Reactor components of the DEMO tokamak; a) inboard blanket segment, b) outboard blanket segment, c) divertor, d) toroidal field coils, e) poloidal field coils, f) upper maintenance port and outlet for service pipes that feed coolant and breeder fluid. g) equatorial port, h) lower port, j) vacuum vessel, m) cryostat, n) bio-shield [39], [62].

removal of exhausted gas particles.

1.2.2. Fusion materials

The DEMO program will include electricity production, tritium self-sufficiency, and plasma operation for several full-power years, its realization depends on new, more advanced materials. These are referred to as fusion materials. Of special importance for the research carried out in this thesis are the fusion-relevant structural material, hydrogen getter materials, and breeding blanket materials.

Structural material

Structural material is the primary material used for components that support the basic structure of the reactor. In general, it must be able to sustain high loads and be corrosion-resistant to coolant or other corrosive fluids. Outside the primary vacuum chamber, conventional 316 or 304 stainless steel can meet these requirements. However, the structural components inside the chamber are much more demanding. Here, in addition to heavy loads the material is subjected to intense thermo-mechanical stresses due to extreme temperature fluctuations and high operating temperatures of $T \leq 823\,\mathrm{K}$. During continuous operation of DEMO, the material in the vacuum vessel is expected to be exposed to neutron irradiation doses greater than 70 dpa (displacements per atom), two orders of magnitude higher than in ITER [53]. Therefore, the structural material selected for the in-vessel

TABLE 1.1

SPECIFIED COMPOSITION REQUIREMENTS FOR THE FE-BASED ALLOY EUROFER'97 GIVEN IN [wt %]. NOT LISTED ELEMENTS MUST HAVE AN IMPURITY CONTENT OF BELOW 5×10^{-3} wt % [64].

Cr	C	Mn	V	W	Ta	Si
8.5 – 9.5	0.09 – 0.12	0.20 – 0.60	0.20 – 0.25	1.0 – 1.2	0.06 – 0.09	< 0.05

N_2	O_2	Ti	Al	Mo	Ni	As + Sn + Sb + Zr
0.015 – 0.045	< 0.01	< 0.01	< 0.01	< 0.01	< 0.01	< 0.01

components should be sufficiently resistant to neutron damage and helium bubble generation. Since it will constitute the majority of the fusion reactor's radioactive waste after shutdown, the in-vessel structural material must not be susceptible to neutron activation. In addition, it should have a low tritium permeability to prevent tritium contamination of the external environment.

To meet these constraints, the European Union Fusion Materials Community has developed a new reduced activation martensitic steel called Eurofer'97 which has been the focus of intensive research over the last two decades [63]. The defined composition requirements for the Fe-based alloy are shown in table 1.1 [64]. It contains a rather high percentage of chemical elements (Fe, Cr, C, V, W, Si, Ti) that are less prone to neutron activation [65]. A significant part of this dissertation is devoted to the numerical and experimental investigation of the hydrogen isotope permeation characteristics of Eurofer'97 at temperatures relevant to the in-vessel components of DEMO.

Hydrogen getter materials

A family of materials that plays an important role in this thesis is hydrogen getter materials. They allow for high-density storage of excess hydrogen isotopes during the operating phases of nuclear fusion devices, thus enabling the regulation of the tritium concentration in the corresponding gas or fluid system. Hydrogen getter materials are exothermic hydride-forming metals arranged in getter beds with a high free surface area to ensure rapid hydrogen absorption. They can be roughly divided into two groups, those that allow the absorbed hydrogen isotopes to be released and reused by thermal treatment, and those whose metal hydrides are too stable to allow tritium recovery after uptake, as the required desorption temperature would be too high to be technologically feasible.

Examples of the first group are uranium and ZrCo. Both of these materials have a high tritium storage capacity and allow the tritium to outgas up to a partial pressure of about $p = 1 \times 10^5$ Pa at desorption temperatures of below $T < 773$ K [66]. Hydrogen getter materials of the first group could find application in fuel cycles of future fusion devices

for the temporary storage of excess fusion fuel.

An example of a hydrogen getter material belonging to the second group is the lanthanide yttrium. For hydrogen-loaded yttrium to provide a hydrogen gas pressure of $p = 1 \times 10^5$ Pa, a desorption temperature of $T \approx 1600$ K would be required [67], which is close to the melting point of the material and too high to be technologically practical [66], [68]. It turns out that yttrium dihydride is the most stable of all metal hydrides in terms of decomposition temperature. This makes it an excellent candidate as a getter material where only hydrogen isotope capture is required, or as a safe long-term tritium disposal material from which the tritium degassing rate is negligible when exposed to the environment. Another advantage of yttrium as a hydrogen getter material is its chemical compatibility with highly corrosive materials like liquid lithium [69].

Breeding blanket materials

Due to insufficient tritium production from external sources, it is essential for a fusion reactor to produce its own tritium in a closed fuel cycle inside the plant. One method of tritium generation is particularly suitable for this purpose, as it exploits the high flux and energy of the fusion products, the neutrons. The idea is to breed tritium in nuclear spallation reactions between fusion neutrons and lithium. In such a reaction, both stable lithium isotopes ^{6}Li and ^{7}Li transmute into tritium and ^{4}He by undergoing the reactions

$$^6\mathrm{Li} + \mathrm{n} \longrightarrow {}^3\mathrm{H} + {}^4\mathrm{He} + 4.8\,\mathrm{MeV} \tag{1.7}$$

$$^7\mathrm{Li} + \mathrm{n} \longrightarrow {}^3\mathrm{H} + {}^4\mathrm{He} + \mathrm{n'} - 2.5\,\mathrm{MeV}\,. \tag{1.8}$$

It can be seen that while reaction (1.8) is endothermic absorbing a significant amount of energy of the impacting neutron, the reaction (1.7) is exothermic and heats the surrounding material. Obviously, the removal of the heat generated by a cooling system would contribute greatly to the power generation of the reactor, which remains the primary objective. This is one reason why it is more convenient for a power plant to produce tritium mainly with the first reaction.

The left-hand plot of figure 1.10 displays the reaction cross sections of the two spallation reactions (1.7) and (1.8) as a function of the neutron energy [24]. The plot shows that the probability of ^{6}Li undergoing a tritium-producing reaction is relatively high in the entire relevant neutron energy range, while ^{7}Li reacts almost exclusively with neutrons of energies close to the maximum neutron energy of 14.1 MeV. The reason why it is important for the lithium breeder to be able to react with a wide range of neutron energies, and not just those produced in the plasma, can be seen from the following.

Tritium losses will be unavoidable in the breeding and fuel cycle. To compensate for this, it is important that a fusion reactor breeds slightly more tritium than it burns. Indeed, it has been estimated that the tritium breeding ratio (TBR) of a fusion reactor should

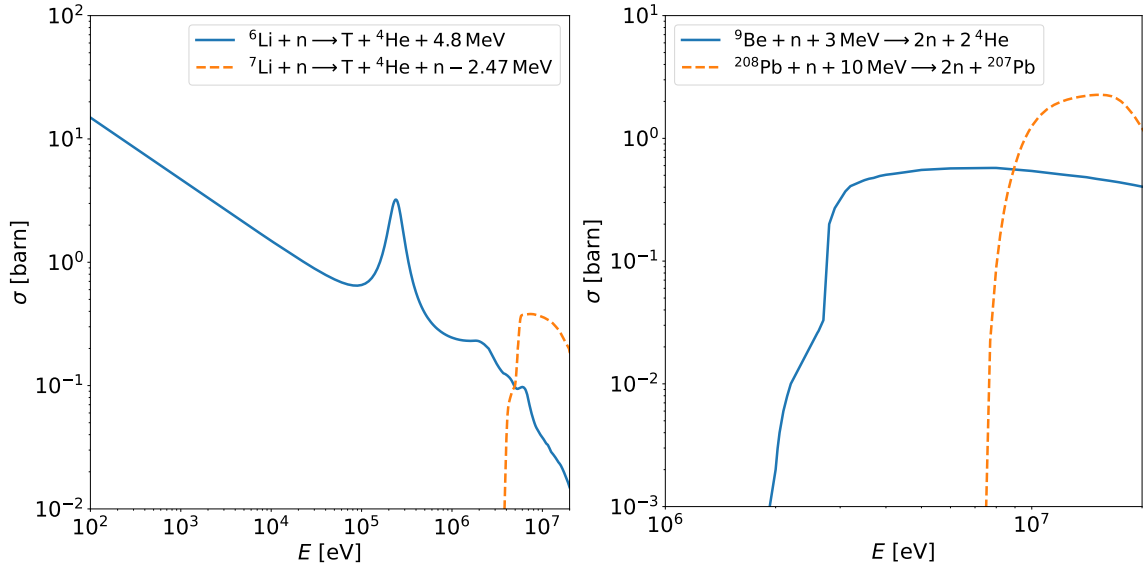

Fig. 1.10. [Left] Probability cross section for tritium breeding reactions of a neutron with different lithium isotopes as a function of the neutron energy [24]. [Right] Probability cross section for (n,2n) reactions of a neutron and different neutron multiplier materials to be used in breeding blankets as a function of the neutron energy [24].

approximately satisfy the condition [70]

$$\text{TBR} \equiv \frac{\text{tritium bred}}{\text{tritium burnt}} > 1.15\,. \tag{1.9}$$

By logic, for this condition to be met, more neutrons need to be available to produce a tritium nucleus than neutrons produced in the fusion reactions. In principle, during the second reaction (1.8) the neutron is not lost as a new less energetic neutron is produced. However, due to its overall small reaction cross section and endothermic nature, another more suitable solution is found to ensure that the condition (1.9) is satisfied, namely the use of a neutron multiplier material. For breeding blankets, the most promising neutron multiplier materials are lead (^{9}Be) and beryllium (^{208}Pb). Both of these two isotopes have the property to produce two neutrons after reacting with a single neutron, according to

$$^9\text{Be} + \text{n} \longrightarrow 2\,^4\text{He} + \text{n'} + \text{n''} - 3\,\text{MeV} \tag{1.10}$$

$$^{208}\text{Pb} + \text{n} \longrightarrow {}^{207}\text{Pb} + \text{n'} + \text{n''} - 10\,\text{MeV}\,. \tag{1.11}$$

Their reaction cross sections are shown in the right-hand plot in figure 1.10 [24]. It can be seen that the two reactions are particularly probable for neutrons with energies close to those of the fusion neutrons produced (14.1 MeV) and are therefore well suited to fusion applications. As can be seen from the reactions (1.10) and (1.11), both reactions are endothermic and consume a large amount of energy. The two neutrons produced are therefore much less energetic than the one struck. The multiplied number of neutrons produced can then react with the tritium breeding material, such that the condition TBM > 1.15 is satisfied. However, since only ^{6}Li has a reasonable reaction cross section for the wide energy range of neutrons produced in the neutron multiplier reactions, it may be

necessary to use predominantly ^{6}Li. As the fraction of naturally occurring ^{6}Li is relatively small compared to ^{7}Li, it is considered to enrich the ^{6}Li for its use as a breeder material.

1.2.3. Breeding blanket

As mentioned above, demonstrating electricity generation with the DEMO tokamak requires complete tritium self-sufficiency and a system that converts the kinetic energy of the fusion neutrons into heat. The breeding blanket (BB) has the purpose of accomplishing both of these tasks. It is an approximately one-meter-deep shell consisting of 16 segments that cover almost the entire inside wall of the vacuum chamber and therefore directly surrounds the plasma. As illustrated in the center of figure 1.9, one segment is located below each of the top ports of the vacuum chamber. Since it is subjected to intense neutron irradiation, its structure is made of Eurofer'97, whose plasma-facing side is covered with thin tungsten armor. Each of the 16 segments consists of an inboard and outboard segment that are highlighted in blue and red in the right-hand image in figure 1.9, respectively.

Among other intensively studied concepts, two breeding blanket designs being considered for DEMO are of particular importance to the research conducted in this dissertation. They are referred to as the WCLL (water-cooled lithium lead) breeding blanket and the HCPB (helium-cooled pebble bed) breeding blanket. Both blankets have completely different internal designs and rely on different neutron multiplier materials and lithium-based tritium-breeding materials. The two concepts are briefly described in the following.

HCPB breeding blanket

The design of the HCPB breeding blanket is shown in figure 1.11. In this breeding blanket concept, the lithium breeding material is a ceramic pebble bed consisting of a solid solution of Li_4SiO_4 and Li_2TiO_3, known as KALOS (Karlsruhe Lithium Orthosilicate) [72]–[74]. The pebble bed is contained within double-cylinder Eurofer'97 claddings, that merge together at one end. Each pebble bed cladding is inserted into a second cylindrical Eurofer'97 envelope. The system consisting of the ceramic breeder, the pebble bed cladding and the envelope is called a fuel breeder pin. Figure 1.11 depicts the shape and orientation of the fuel breeder pins arranged radially around the plasma chamber. The figure shows a breeder module as part of an outer segment containing several fuel pins [71]. Hexagonal $Be_{12}Ti$ neutron multiplier blocks are located between the fuel pins. Therefore, an HCPB breeding blanket relies on ^{9}Be as the neutron multiplier material. Both the neutron multiplier blocks and the fuel pins protrude from a double-walled hollow backplate.

As indicated by the arrows in figure 1.11, a helium coolant gas, which is part of the PHTS, flows through a coolant manifold behind the rear back plate of the breeder module. In its low-temperature state, it first enters small channels that pass through the first wall just behind the tungsten armor before re-entering the coolant manifold on the other side

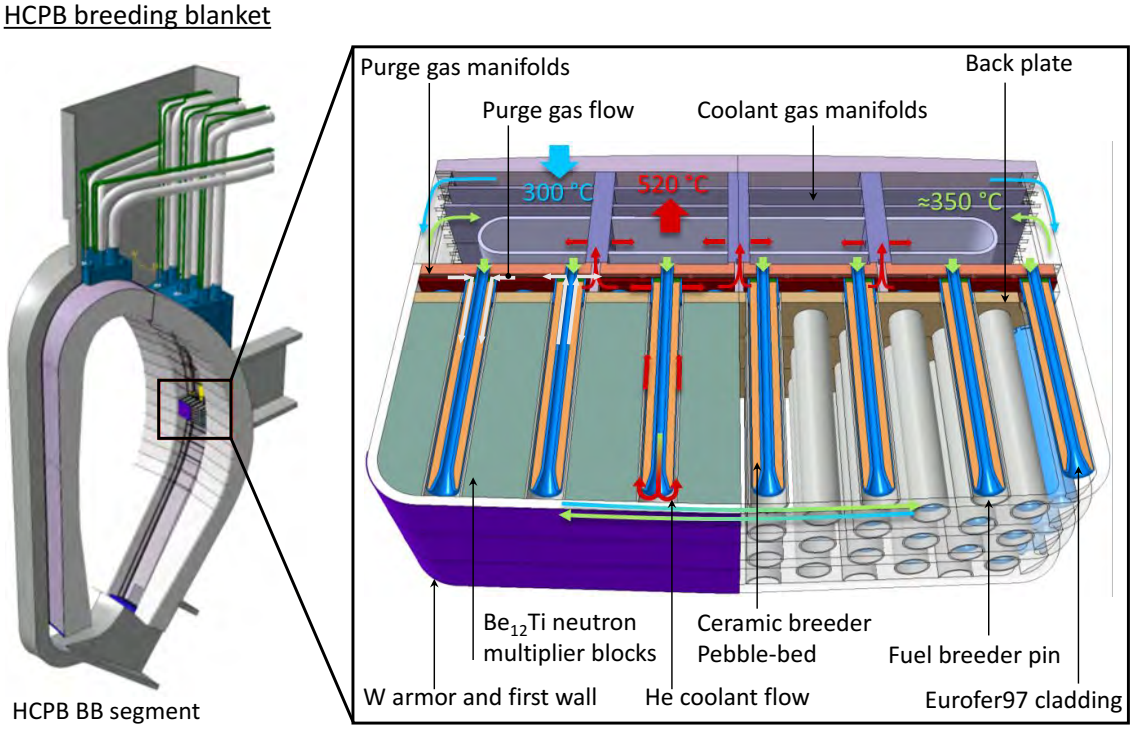

Fig. 1.11. Design of a helium-cooled pebble bed breeding blanket segment [71].

of the module. The slightly warmed gas then enters the fuel pins through the inner tunnel surrounded by the inner wall of the pebble bed cladding and moves towards the first wall. There it turns and exits the fuel pins back into the manifold (see red arrows). This coolant path allows efficient removal of the heat generated in the lithium breeder reactions and of those neutrons that lose their kinetic energy in other structures of the breeder module.

A He + $^1H_2$ purge gas enters the KALOS pebble bed through the gap between the two back plates, flushes the pebble bed and, then leaves the fuel pins through small thin channels made in the inner cladding wall. From here, the purge gas flow leaves the breeding blanket segment through feed tubes that pass through the upper port of the primary vacuum vessel. At the pebble surfaces and grain boundaries, isotopic exchange reactions occur between the H_2 of the purge gas and the generated tritium bound to the ceramic material, causing the tritium to leave the pebbles into the purge gas [75]–[78]. The purge gas loop is connected to a tritium extraction system [79] where a certain fraction of the generated tritium is removed and fed to the fuel supply system. The purge gas is part of the tritium breeding cycle, which in turn is part of the plant's fuel cycle (see figure 1.8).

WCLL breeding blanket

The WCLL breeding blanket design is illustrated in figure 1.12 [80], [81]. Although the external appearance of the breeding blanket segments is very similar to that of the HCPB blanket, its internal structure is fundamentally different. It is based on eutectic liquid lithium-lead (PbLi) as the tritium breeding material, with the lead acting as the neutron

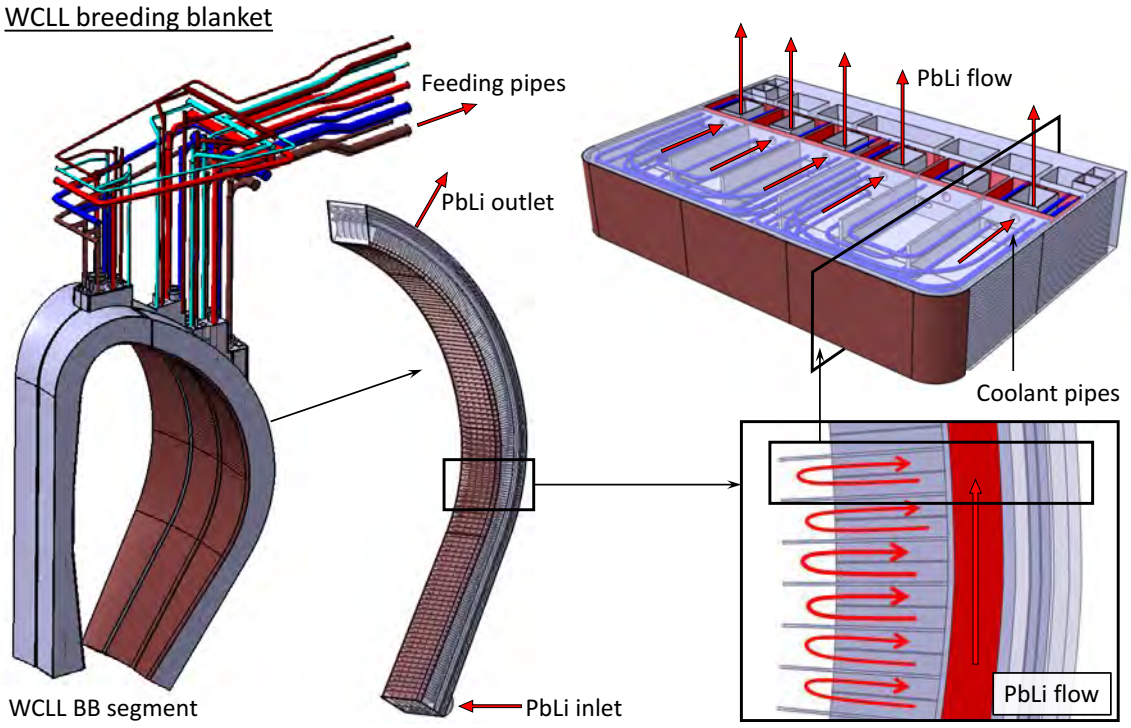

Fig. 1.12. Design of a water-cooled lithium lead breeding blanket segment [80], [81].

multiplier. The lithium content of this eutectic liquid metal mixture is approximately 17 at.% lithium with a melting point at 508 K [82]. The corrosion and hydrogen transport properties of liquid PbLi are currently under intense investigation in the liquid metals laboratory (LML) of the Ciemat Institute [83], [84].

The liquid PbLi enters the segment from behind through an inlet at the bottom. It rises in the rear part of the segment through rectangular channels close to a back plate that separates the PbLi manifold from the breeding zone, which is located on the left, closer to the first wall. As shown in the lower right-hand corner of figure 1.12, the breeding zone consists of stacked rectangular channels arranged radially around the plasma chamber. The channels are connected to the PbLi manifold by tubes. Liquid PbLi coming from the manifold enters the radially arranged channels through the tubes, flows towards the first wall, rises, and flows back through the back plate into the PbLi manifold (see figure 1.12). The bred tritium is generated in the liquid metal in atomic form and thus transported to a tritium extraction system. As part of the PHTS system U-shaped Eurofer'97 coolant water pipes penetrated the WCLL breeding zones. They dissipate the heat generated and thus allow for electricity production of the power plant.

1.2.4. Tritium mitigation in breeding blankets

In fact, the escape of tritium from the plasma chamber or the fuel cycle to external areas is a serious safety issue for future fusion reactors. Therefore, measures must be taken to keep the escape rate as low as possible. Nevertheless, probably the greatest hazard associated

with a potential tritium escape is the problem of tritium permeating from the breeder zone of a breeding blanket into the coolant. In both the WCLL and HCPB breeding blanket design, the respective coolant passes directly through the tritium breeder zones, where they are separated only by very thin Eurofer'97 walls.

Unfortunately, due to its small atomic size, tritium easily penetrates the Eurofer'97 metal lattice and diffuses towards the coolant. The lack of tritium in the coolant creates a tritium concentration gradient in the metal bulk, resulting in a net flux of permeating tritium from the breeder zone into the coolant. Because the temperatures of the partition walls in the breeder zone are significantly higher than the tube walls in other parts of the tritium fuel cycle, the tritium diffusivity in the breeder zone is disproportionately larger. This results in significantly higher tritium permeation rates to the exterior environment compared to other areas of the plant. Although a tritium purification system is planned for the coolant, the possibility of serious tritium contamination of the coolant remains. This is particularly problematic because the PHTS is connected to further external heat transfer systems and a steam generator, allowing the permeated tritium to migrate to the natural environment and, in the worst case, to groundwater reservoirs as tritiated water. It is therefore indispensable for future fusion reactors to employ methods that enable reducing the tritium permeation flux into the coolant as much as possible. Finding such methods has been the subject of intensive research during the past decades.

One possible technique that would serve this purpose is the use of so-called tritium permeation barriers coated on the free Eurofer'97 coolant walls on the side of the corresponding breeder fluid [85]–[87]. Currently, it is considered to be implemented in the WCLL design. Although only a thin coated layer, the low hydrogen isotope diffusivity and low surface recombination kinetics of a ceramic permeation barrier material significantly reduces the total permeation flux into the coolant. However, preventing corrosion damage to the coatings over long periods of exposure to the breeder fluid remains a technological challenge and requires further investigation before their successful application in future fusion power plants can be assured. For this reason, alternative methods to reduce the permeation flux to the coolant are needed.

Slightly more than two decades ago, the first experimental campaigns were conducted to measure the deuterium permeation flux from an upstream to a downstream side of a metal membrane in the presence of a protium counter-flow [88]–[90]. A permeation process involving more than one hydrogen isotope species is here referred to as multi-isotopic permeation. A general evaluation of the observed results leads to the conclusion that, under certain sample material-specific pressure conditions, an increase in the partial pressure of $^1H_2$ on the downstream side of the membrane reduces the deuterium permeation flux from the upstream to the downstream side. This leads to the assumption that a controlled injection of $^1H_2$ gas to the coolant of an HCPB breeding blanket could serve as a method to reduce tritium permeation into the coolant. However, despite the generally observed permeation flux-reducing nature of counter-permeation, the experimental results obtained in the above-mentioned measurement campaigns differ widely.

The references [88]–[90] each present a counter-permeation measurement in which $^2H_2$ gas was injected on the upstream side and $^1H_2$ gas was injected on the downstream side of a sample permeation membrane made of palladium, nickel, and Inconel®600, respectively. All three studies include deuterium permeation flux measurements at very low partial pressures of the added $^1H_2$ gas. The measurements performed by Kizu *et al* suggest that the deuterium permeation flux slightly decreases with increasing $^1H_2$ partial pressure. On the other hand, Takeda *et al* observed the opposite effect, that at very low $^1H_2$ partial pressures, the deuterium permeation flux increases with increasing $^1H_2$ partial pressure and starts to decrease only when the $^1H_2$ pressure on the downstream side exceeds a critical value. The difference in the results shows that understanding the pressure conditions and magnitude at which counter-permeation effects occur is far from trivial. In addition, Kizu *et al* performed co-permeation measurements in which both $^2H_2$ and $^1H_2$ gas was injected on the upstream side. The results showed a slight increase in deuterium permeation flux with increasing $^1H_2$ partial pressure [91]. However, these measurements were made at very low $^1H_2$ partial pressures. Whether, as in Takeda's counter-permeation measurements, the permeation flux in a co-permeation flux measurement would begin to decrease above a certain critical $^1H_2$ partial pressure remains to be observed experimentally. If this is found to be the case, an additional injection of protium into the purge gas of an HCPB breeding blanket may also be considered as a potential permeation mitigation method.

Moreover, several theoretical models were presented in the references listed above. They allow, to a certain extent, the reproduction of the experimental results obtained in the corresponding studies. However, the presented models differ greatly and are based on extreme simplifications. Therefore, it is reasonable to say that the published literature, both experimental and theoretical, does not sufficiently describe the process of co- and counter-permeation to decide whether it could serve as a tritium mitigation technique in breeding blankets.

None of the experimental campaigns carried out so far have performed multi-isotopic permeation measurements using Eurofer'97 as a membrane material. Neither has multi-isotopic permeation through Eurofer'97 been analyzed in a theoretical study that would allow a theoretical estimation of its effect on the tritium permeation in a real breeding blanket. Furthermore, only multi-isotope gas-to-gas permeation experiments relevant to HCPB blankets were performed in the past. The effect of varying the protium concentration in the water or the PbLi of a WCLL blanket on the tritium permeation flux into the water coolant has not been investigated to this date. The lack of research in this field is one of the primary motivations for the work conducted in this thesis.

1.2.5. IFMIF-DONES

Section 1.2.2 highlights the particularly extreme demands that will be placed on materials used for in-vessel components such as RAFM structural steels. These materials will

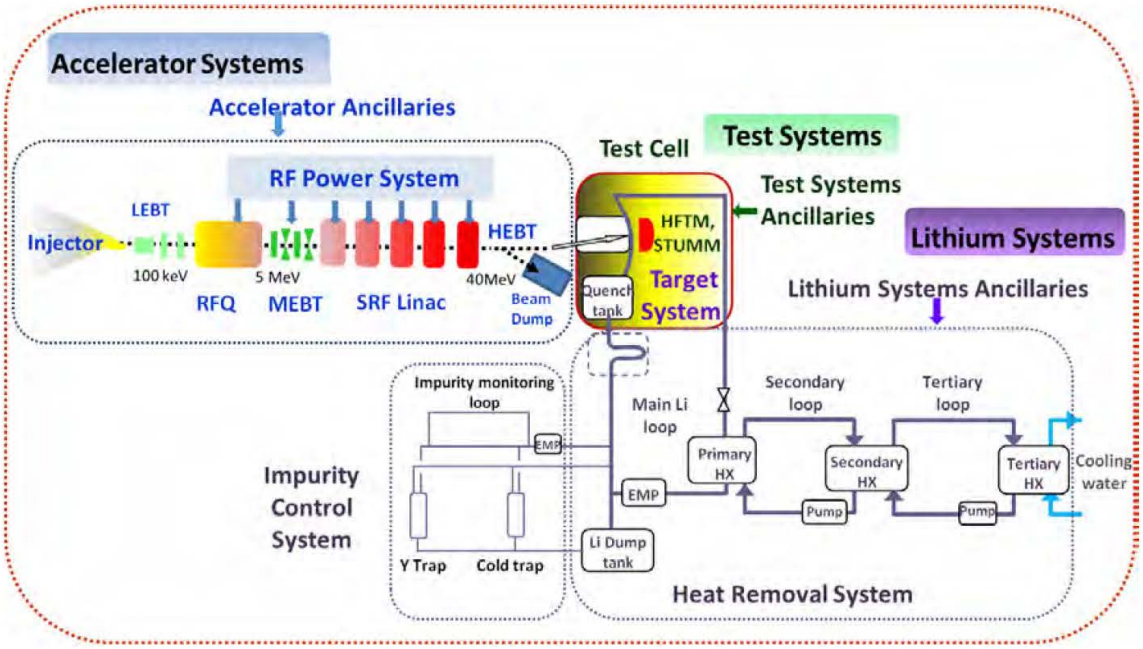

Fig. 1.13. Simplified process flow diagram of the DONES facility highlighting the accelerator systems, the test systems and the lithium systems [92].

be exposed to a neutron radiation field with neutron energies as high as 14.1 MeV. This is expected to strongly affect the microstructure, mechanical properties, and radioactive activation of these materials. Current knowledge of neutron irradiation damage in metals allows estimation of the magnitude of damage that certain materials would experience under such conditions. However, there is an urgent need for an experimental neutron irradiation database established under fusion-relevant conditions. Only by subjecting newly designed plasma facing and structural materials to intense neutron irradiation, such as that expected to be encountered in DEMO, would sufficient data be available to proceed with the engineering design of DEMO.

For this reason, the EUROfusion roadmap towards fusion electricity involves the construction of an experimental high-energy neutron irradiation facility that will generate a neutron beam with fusion-relevant energies. The facility will be mounted in two phases. First, a scaled-down version will be put into operation called DONES (DEMO-Oriented Neutron Source) which is already under construction in Escúzar, Spain. A simplified process flow diagram of the DONES experimental system including its numerous ancillary systems is presented in figure 1.13 [92].

DONES involves of a particle accelerator that produces a beam of 40 MeV deuterium nuclei [93]. The accelerator systems consist of an injector, where deuterium gas is injected and ionized. The deuterium nuclei are subsequently accelerated by passing several accelerator ancillaries such as the LEBT (Low Energy Beam Transport), RFQ (Radio Frequency Quadrupole), MEBT (Medium Energy Beam Transport), SRF Linac (Superconducting Radio Frequency Linear accelerator), and the HEBT (High Energy Beam Transport), before impacting a flowing liquid lithium target in the so-called test cell (see figure

1.13) [92]. Here, the deuterons undergo the following nuclear stripping reactions with the flowing ^{6}Li and ^{7}Li isotopes [24]

$$^{2}\mathrm{H} + {}^{7}\mathrm{Li} \longrightarrow {}^{7}\mathrm{Li} + {}^{1}\mathrm{H} + \mathrm{n} \tag{1.12}$$

$$^{2}\mathrm{H} + {}^{7}\mathrm{Li} \longrightarrow {}^{4}\mathrm{He} + {}^{3}\mathrm{H} + {}^{1}\mathrm{H} + \mathrm{n} \tag{1.13}$$

$$^{2}\mathrm{H} + {}^{7}\mathrm{Li} \longrightarrow {}^{7}\mathrm{Be} + 2\,\mathrm{n} \tag{1.14}$$

$$^{2}\mathrm{H} + {}^{6}\mathrm{Li} \longrightarrow {}^{7}\mathrm{Be} + \mathrm{n}\,. \tag{1.15}$$

Each of these reactions contributes to the production of a high-energy neutron beam that exits the other side of the target toward the HFTM (High Flux Test Module), where material samples can be positioned for study.

In a future phase of the EUROfusion roadmap, the experimental facility will be equipped with a second accelerator [47]. At this stage, the facility will be called IFMIF (International Fusion Materials Irradiation Facility) [93], [94].

1.2.6. Tritium capture in DONES

The lithium flowing through the test cell is part of a closed liquid lithium loop system with an operating temperature of the order of $T = 526\,\mathrm{K}$ that slightly varies in different loop components. The loop is coupled to additional heat exchanger circuits to remove the heat generated in the target. As a result of the nuclear stripping reactions, protium, tritium and ^{7}Be impurities will over time accumulate in the liquid lithium [see equations (1.12) - (1.15)]. Most of the deposited impurities will, however, be non-reacted deuterium originating from the impacting particle beam [95], [96].

As for DEMO, a particular threat to the safety of the liquid lithium system is the production of radioactive ^{3}H. It could be released into the environment in the event of an accident or as a result of permeation and leakage through the piping components of the loop [97]–[99]. Moreover, hydrogen isotopes and other nonmetallic impurities such as C, N, and O lead to increased corrosion of the structural loop material and erosion of the settling solid compounds [100]. Therefore, a DONES safety evaluation concluded that it was necessary to establish strict contamination limits to be met by installing an impurity control and monitoring side loop system connected in parallel to the main loop [101]. The impurities O, C, and part of the accumulating ^{7}Be are removed by a cold trap [95], [102] while N is retained by a titanium getter in the lithium dump tank [103]. To meet safety constraints on hydrogen isotope concentrations in the loop, it was decided to use a separate yttrium pebble bed as a hydrogen getter trap [104].

Yttrium metal has a significantly higher hydrogen isotope solubility than lithium [105]. As a result, in spite of its much smaller volume the yttrium pebbles absorb a significant fraction of the dissolved isotopes from the passing lithium [95]. The rate at which the hydrogen isotopes are absorbed by the pebble bed is greatly reduced in N- or O-contaminated lithium [106]. This is yet another reason why it is essential to purify

the lithium from these impurities. Radiation safety requires that the tritium inventory be kept below 0.3 g in both the yttrium and lithium [99], in addition to the corrosion-related maximum allowable total hydrogen isotope concentration of 10 wppm in the lithium [95].

Although it has been experimentally demonstrated in the past that yttrium metal absorbs hydrogen isotopes from lithium with great efficiency [107]–[112], the exact processes that determine the hydrogen retention dynamics and the getter capacity for a given yttrium volume and operating temperature are still not well enough understood to begin the engineering design of the hydrogen hot trap for DONES. The experimental results in the mentioned references suggest that even the slightest change in the experimental conditions (mass, temperature, initial hydrogen concentration in the lithium, shape of the yttrium pebbles, lithium flow conditions, etc.) leads to a large difference in the experimental results. The only way to fully understand the response of an yttrium getter bed to specific conditions in the lithium is to perform a detailed numerical study of the relevant processes. Such a numerical study should be validated by an in-situ experimental liquid lithium system, which allows to perform deuterium retention experiments using an yttrium getter trap. The necessity for these tasks to be accomplished is another primary motivation for the work conducted in this thesis.

1.3. Research objectives

Realizing the established EUROfusion roadmap to fusion energy fully depends on the construction of the planned research facilities DEMO and IFMIF-DONES. However, their safe operation can only be ensured if methods to tackle the discussed tritium safety issues in these devices are successfully implemented as reliable radiation safety measures. Of particular interest are the possible exploitation of multi-isotopic transport to reduce tritium permeation into the coolant of a DEMO breeding blanket and the use of an yttrium pebble bed as a tritium trap in DONES. However, to date, the available scientific literature does not provide sufficient experimental or theoretical analysis to define the technical conditions under which a successful application of these methods could be guaranteed.

This dissertation is dedicated to the theoretical, numerical, and experimental study of the physical processes that determine the tritium mitigating effects of multi-isotopic transport in DEMO and of yttrium as a tritium getter material for DONES. The general objective of this thesis is the development of the theoretical frameworks that allow defining the conditions under which each of these techniques could function as a reliable tritium mitigation method. For this purpose, new theoretical and numerical models that describe multi-isotopic transport in breeding blankets and tritium capture in DONES are developed and detailed numerical simulations are performed. With the objective of validating the developed models in the future, two new experimental devices are developed from scratch and put into operation.

Following the discussion in section 1.2.4, it can be concluded that the analysis of

protium co- or counter-permeation as a potential tritium mitigation method for DEMO would be greatly facilitated by a deeper theoretical and numerical investigation of the physical processes involved. The accomplishment of this task is the first objective of this thesis. For this purpose, a theoretical study is carried out in which the consequences of multi-isotope transport in both a gas-to-gas (for HCPB applications) and a liquid metal-to-water (for WCLL applications) environment are analyzed analytically. Focusing on a pure co- and a pure counter-permeation scenario allows deriving new algebraic formulas. They enable calculating the permeation flux decrease that occurs for a given hydrogen isotope species as a function of the concentration of the second hydrogen isotope species involved. This study provides an overall understanding of the multi-isotopic transport effects and their origin.

The analytical study is supported by numerical simulation using the simulation software EcosimPro© [113]. The simulations are executed with the aim to simulate the effect an injection of different protium concentrations into the coolant or the breeder fluid of HCPB and WCLL breeding blankets has on the total tritium permeation flux into the respective coolant fluid. Therefore, this thesis includes the creation of detailed numerical hydrogen transport models of the fuel pins as part of the HCPB purge gas system and of a water coolant pipe inside an elementary cell of a WCLL breeding blanket. In this way, the exact pressure conditions under which the flux of the tritium permeation is reduced or increased are defined. For each breeding blanket design, an analysis is performed to critically evaluate the feasibility of multi-isotropic permeation as a tritium mitigation method. Furthermore, the simulation results are reproduced by means of the derived algebraic formulas with the aim of validating the theoretical model.

To experimentally validate both the numerical and the theoretical model, they are used to reproduce the measurement data of the counter-permeation experiment performed by Takeda *et al*. However, as Takeda's experiment employs Inconel®600 and no fusion-relevant structural material as sample membrane material, the experimental validation of the models remains incomplete. A complete experimental validation would require a successful reproduction of co- and counter-permeation measurements through Eurofer'97 as the membrane material in partial pressure regimes that are relevant for real breeding blanket applications.

For this purpose, within the scope of this work, a new experimental device called COOPER (CO- and cOunter PERmeation) experiment has been developed and put into operation. The experiment enables quantitative deuterium permeation flux measurements from an upstream gas chamber filled with $^2H_2$ gas through a Eurofer'97 disk into a downstream chamber. Co- and counter-permeation scenarios under HCPB conditions can be experimentally recreated by injecting additional $^1H_2$ gas to either the up or the downstream side. In contrast to similar previous experimental devices, the hot permeation cells of the COOPER experimental set-up are mounted inside an exterior vacuum chamber. In this way, leakages and permeation of atmospheric gases into the interior of the permeation chambers are drastically reduced and efficient degassing is guaranteed. Furthermore,

the COOPER experiment is designed to allow for the experimental determination of general hydrogen transport parameters like the permeability, the diffusion coefficient, the Sieverts' constant as well as surface rate constants of hydrogen isotopes in the sample disk material. Measuring these physical quantities for Eurofer'97 is drastically needed as these parameters mainly determine the tritium permeation flux into the coolant of a breeding blanket. At this point, the COOPER experiment has passed the commissioning phase in which the accessible measurement parameter ranges are determined, and its successful operation is confirmed. Moreover, calibration and permeation flux measurement procedures are developed. This is showcased in this work by the execution of preliminary mono-isotopic permeation measurements in which deuterium transport parameters in Eurofer'97 are measured.

With the objective of providing a contribution to the design of the hydrogen trap of DONES, part of the work conducted within the framework of this dissertation is dedicated to the development of a numerical simulation tool that is capable of realistically modeling the transport of hydrogen isotopes from the liquid lithium flow of DONES into an arbitrarily sized yttrium getter bed. It allows dynamic simulations of the hydrogen isotope concentrations in the pebble bed and in the surrounding loop system. Under DONES relevant conditions the hydrogen isotope concentration in the lithium likely exceeds critical values which makes a formation of yttrium dihydride during DONES operation very probable. The formation of yttrium dihydride strongly determines the thermodynamics of metal-hydrogen systems and thus the hydrogen isotope absorption behavior of an yttrium getter trap [68], [114]. The inclusion of the hydride formation mechanism complicates the development of the model drastically but is considered relevant due to its anticipated influence on the optimal design parameters of the trap. In order to incorporate hydride formation processes in the model, complete pressure-composition isotherms of the Li-H and Y-H metal hydrogen systems are mathematically reconstructed using recent data from the literature [115], [116]. The conditions for the formation of YH_2 are derived by determining the solubility of hydrogen isotopes in different yttrium hydride phases as a function of the concentration in the lithium. In addition, the model accounts for the theoretical determination of the concentration dependency of the hydrogen isotope diffusivity in different yttrium hydride phases. Integrating the metal hydride formation processes into a dynamic hydrogen transport model is, to the best of the author's knowledge, a novelty and demonstrated for the first time in this thesis. The created model is used to simulate the temporal evolution of the hydrogen isotope concentrations during different DONES operation phases. Thus, the parameters for optimal trap design for DONES as a function of the lithium temperature are determined and suitable operating modes for the trap to meet the tritium safety requirements are presented.

Future experimental validation of this simulation tool requires the development of a new in-situ experimental liquid lithium system. This is another goal of this dissertation. The developed experiment is called LYDER (Lithium system for Yttrium-based DEeuterium Retention experiments) and consists of two liquid lithium tanks connected

by a piping system with an integrated yttrium-based deuterium trap. One tank contains a custom-designed deuterium injection system using an α-iron membrane as a permeation window. By measuring the pressure decrease of $^2H_2$ on the gas side of the window, the amount of deuterium injected into the lithium can be estimated. In a future experimental campaign, it is planned to set the liquid metal in a controlled motion through the tube system by manipulating the pressures in the two argon-filled tanks. While the lithium flows through the yttrium bed, the deuterium concentration will decrease until thermodynamic equilibrium between the two metal hydrogen systems is reached. LYDER is equipped with a lithium sample extraction system that will allow the deuterium concentration in the lithium to be measured offline using an internal experimental branch for thermal desorption measurements or an external chemical dissolution measuring device. In the best case, future experiments will enable measuring the getter capacity of yttrium in deuterium-loaded liquid lithium which is the most important experimental input parameter for the model and the engineering design of the hydrogen trap of DONES.

1.4. Thesis structure

Based on the research objectives described above, the dissertation is structured as follows.

Chapter 1 introduces the scientific and technological context that defines the main motivation of this thesis. It justifies the need for fusion energy as an alternative future energy source. This is followed by an introduction to current fusion technology and fusion-relevant materials. Special emphasis is given to the description of the tritium safety issues encountered in the HCPB and WCLL breeding blankets concepts as well as in the IFMIF-DONES neutron irradiation facility as they are the center of the research carried out in this thesis.

Chapter 2 familiarizes the reader with the physical concepts and equations on which the theoretical and numerical analyses as well as the experimental techniques presented in this dissertation, are based.

Chapter 3 introduces the fundamentals and working principles of different experimental components and techniques which are used for the experimental work carried out within the scope of this thesis.

Chapter 4 presents a theoretical study of multi-isotopic co- and counter-permeation conducted by the author of this dissertation. The analysis focuses on two different permeation environments: multi-isotopic permeation from gas through a metal membrane to gas (relevant for HCPB-related applications) and multi-isotopic permeation from liquid PbLi through a metal membrane to water (relevant for WCLL-related applications). For both cases, new algebraic formulas are derived which provide the dependence of the permeation flux of the less abundant hydrogen isotope species on the partial pressure of the other species involved.

Chapter 5 is devoted to the development of system-level numerical hydrogen transport

models of the breeder zones of the HCPB and WCLL breeding blankets. The models are used to numerically validate the algebraic formulas for co- and counter-permeation derived in Chapter 4. Furthermore, the possible injection of protium into the coolant or breeder fluid as a tritium mitigation method is critically discussed. Finally, the considered theoretical description of multi-isotopic hydrogen transport is tested against measurement data from a previous counter-permeation experiment by reproducing the experimental results with a developed numerical hydrogen transport model and the derived algebraic formulas.

Chapter 6 is dedicated to the description of the experimental design and construction of the COOPER experiment. The commissioning phase of the COOPER experiment is described and preliminary mono-isotopic permeation flux measurements are presented in which hydrogen transport parameters are experimentally determined. Moreover, an experimental procedure for co- and counter-permeation measurements with the COOPER experiment is presented which is supported the numerical simulation of experimental results.

Chapter 7 presents a new numerical tool developed from scratch to simulate hydrogen transport from the liquid lithium system of DONES into a hydride-forming yttrium-based getter trap. The tool is applied to simulate the time-evolving hydrogen isotope concentrations in the DONES lithium loop encountered during a proposed initial purification run and throughout the DONES operation phase. In addition, the underlying theoretical model is used to derive conditions for the optimal pebble bed mass and suitable operating modes to meet tritium safety requirements during the different phases of DONES operation. Finally, the simulation tool is experimentally validated by reproducing measured data that are taken from the literature.

Chapter 8 is dedicated to the description of the design and commissioning of the LYDER experiment developed within the scope of this work. Numerical simulations of experimental processes are performed and planned measurement procedures are presented.

The dissertation is completed by the conclusion of the scientific goals achieved throughout the work for this thesis. The developed numerical and experimental systems presented in this work offer a wide range of possible future research applications, which are proposed and discussed.

A list of references cited in this thesis is included at the end of this document.

2. FUNDAMENTALS OF HYDROGEN IN METALS

Numerically and experimentally investigating multi-isotopic hydrogen permeation and gettering in fusion-relevant materials requires deeply understanding the kinetics and thermodynamics of hydrogen dissolved in metals and its transport across gas-metal interfaces. The governing physical processes which determine the occurring particle fluxes and time-evolving concentrations in such systems are discussed in this chapter.

2.1. Thermodynamics of metal-hydrogen systems

The spontaneous behavior of a multi-particle system in which different phases co-exist and chemical reactions may occur is well described using the thermodynamic concept of the Gibbs free energy [117]

$$G = H - ST = \sum_s \mu_s N_s \,. \tag{2.1}$$

In this definition, H is the enthalpy, S is the entropy and T is the temperature. The total Gibbs energy of a system is the sum of the Gibbs energies of its subsystems [118]. It may be determined by adding up the products of the chemical potentials μ_s and the number of particles N_s for each species s which constitute the system. The differential of the Gibbs energy is given by

$$\mathrm{d}G = V\mathrm{d}p + S\,\mathrm{d}T + \sum_s \mu_s \mathrm{d}N_s \tag{2.2}$$

This allows defining the chemical potential as follows

$$\mu_s = \left(\frac{\partial G}{\partial N_s}\right)_{p,T,N'} = \left(\frac{\partial H}{\partial N_s}\right)_{p,T,N'} - T\left(\frac{\partial S}{\partial N_s}\right)_{p,T,N'} \equiv \overline{H}_s - T\overline{S}_s \,. \tag{2.3}$$

The quantities μ_s, $\overline{H}_s$ and $\overline{S}_s$ describe the changes of the systems Gibbs energy, enthalpy and entropy if a single particle of species s is added to or removed from the system in which the total pressure p, the temperature T and the particle numbers N' of all species other than s are kept constant. Using the thermodynamic Maxwell relations derived from equation (2.2) leads to the following relations for $\overline{H}_s$ and $\overline{S}_s$

$$\overline{S}_s = -\left(\frac{\partial \mu_\mathrm{s}}{\partial T_s}\right)_{p,N} \qquad \& \qquad \overline{H}_s = \mu_s - T\left(\frac{\partial \mu_\mathrm{s}}{\partial T_s}\right)_{p,N} \,. \tag{2.4}$$

Of particular interest for this work is the general scenario in which a system of pure metals $\mathrm{Me}^a, \mathrm{Me}^b \in \{\mathrm{Me1}, \mathrm{Me2}, \mathrm{Me3}, \ldots\}$ is exposed to a gas phase containing a mixture of multi-isotopic hydrogen gas molecules ${}^i\mathrm{H}^j\mathrm{H} \in \{{}^1\mathrm{H}_2, {}^2\mathrm{H}_2, {}^3\mathrm{H}_2, {}^1\mathrm{H}^2\mathrm{H}, {}^1\mathrm{H}^3\mathrm{H}, {}^2\mathrm{H}^3\mathrm{H}\}$ as illustrated in figure 2.1. In the described configuration, the molecules ${}^i\mathrm{H}^j\mathrm{H}$ of the gas would dissociate and dissolve into the different metal bulks as separated hydrogen

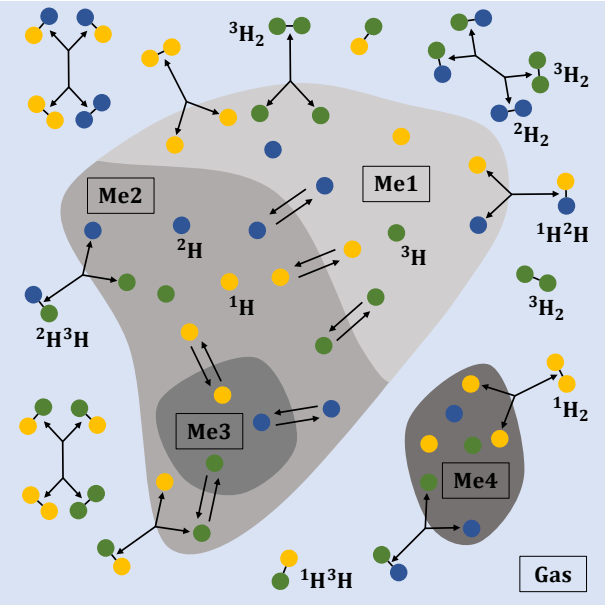

Fig. 2.1. Illustration of hydrogen transport processes and isotope exchange reactions occurring in a system of different metals surrounded by multi-isotopic hydrogen gas.

isotopes ${}^{i}\mathrm{H}, {}^{j}\mathrm{H}, {}^{k}\mathrm{H} \in \{{}^{1}\mathrm{H}, {}^{2}\mathrm{H}, {}^{3}\mathrm{H}\}$ while already dissolved isotopes may recombine and leave the bulks back into the gas. The corresponding dissolution and dissociation reactions of the molecules ${}^{i}\mathrm{H}{}^{j}\mathrm{H}$ from the gas phase into the different metals Me^{a} can be written as follows

$$ {}^{i}\mathrm{H}{}^{j}\mathrm{H}\ (\mathrm{gas}) \rightleftharpoons {}^{i}\mathrm{H} + {}^{j}\mathrm{H}\ (\mathrm{dissolved\ in\ Me}^{a}) \quad \text{if Me}^{a}\text{ shares interface with gas} \tag{2.5} $$

In this analysis, the system remains at an equal total pressure, an equal temperature and an equal number and chemical potential of the metal atoms. Then, equation (2.2) simplifies to

$$ \mathrm{d}G = \sum_{ij} \mu^{\mathrm{g}}_{ij} \mathrm{d}N^{\mathrm{g}}_{ij} + \sum_{a} \sum_{i} \mu^{a}_{i} \mathrm{d}N^{a}_{i} \,. \tag{2.6} $$

Here, it is assumed that the diatomic molecules ${}^{i}\mathrm{H}{}^{j}\mathrm{H}$ exist merely in the gas phase and the atomic hydrogen isotopes ${}^{i}\mathrm{H}$ are exclusively present in the metal phases Me^{a}. In equation (2.6), the quantities $\mu^{\text{subsystem}}_{\text{species}}$ and $N^{\text{subsystem}}_{\text{species}}$ label the chemical potential and number of the corresponding species inside of the respective subsystem. For the sake of clarity, several index abbreviations are introduced. The letter g stands for gas, the indexes a, b, etc. refer to the different metal species Me^{a} and the joined index ij replaces the symbol for the molecules ${}^{i}\mathrm{H}{}^{j}\mathrm{H}$. In this work, hydrogen isotope species are labeled with the letters i, j and k. The subscripts i and j stand for either different or the same isotopes ($i = j$ or $i \neq j$) and the index k refers to a hydrogen isotope different from those labeled with i or j ($k \neq i, j$). The spontaneous direction of reaction (2.5) is the one which leads to an overall reduction of the Gibbs free energy of the system, such that $\mathrm{d}G < 0$. According to equation (2.6), removing an infinitesimal number $\mathrm{d}N^{\mathrm{g}}_{ii} = -\mathrm{d}\xi$ of mono-isotopic molecules ${}^{i}\mathrm{H}_2$ from the gas phase while adding the conforming infinitesimal number $\mathrm{d}N^{a}_{i} = +2\mathrm{d}\xi$ of dissociated hydrogen isotopes ${}^{i}\mathrm{H}$ to one of the metal bulks Me^{a} would lead to the following change of the total Gibbs energy of the system

$$ \mathrm{d}G = \mu^{a}_{i} \frac{\partial N^{a}_{i}}{\partial \xi} \mathrm{d}\xi + \mu^{\mathrm{g}}_{ii} \frac{\partial N^{\mathrm{g}}_{ii}}{\partial \xi} \mathrm{d}\xi = \left(2\mu^{a}_{i} - \mu^{\mathrm{g}}_{ii}\right) \mathrm{d}\xi \tag{2.7} $$

As visible in figure 2.7 the different metals of the system may share part of their contact surfaces or completely surround another metal in their interior. Once dissolved into the metal, the isotopes may encounter a metal-metal interface and a further dissolution process of hydrogen isotopes migrating from one metal into the other needs to be considered:

$$^{i}\mathrm{H}\ (\text{dissolved in Me}^{a}) \rightleftharpoons {}^{i}\mathrm{H}\ (\text{dissolved in Me}^{b}) \quad \text{if Me}^{a}\ \text{has interface with Me}^{b} \tag{2.8}$$

The spontaneous direction ($\mathrm{d}G < 0$) of this reaction yields when calculating the change of the Gibbs energy for the example that an infinitesimal number of isotopes $\mathrm{d}N_i^a = -\mathrm{d}\xi$ migrates from the metal Me^a into the metal Me^b, where consequently $\mathrm{d}N_i^b = +\mathrm{d}\xi$:

$$\mathrm{d}G = \mu_i^a \frac{\partial N_i^a}{\partial \xi}\mathrm{d}\xi + \mu_i^b \frac{\partial N_i^b}{\partial \xi}\mathrm{d}\xi = \left(\mu_i^b - \mu_i^a\right)\mathrm{d}\xi \tag{2.9}$$

Moreover, it needs to be taken into account that between the six different diatomic hydrogen molecules in the gas six different isotope exchange reactions occur. They may be expressed by the following reaction equation

$$^{i}\mathrm{H}^{k}\mathrm{H} + {}^{j}\mathrm{H}^{k}\mathrm{H}\ (\mathrm{gas}) \rightleftharpoons {}^{i}\mathrm{H}^{j}\mathrm{H} + {}^{k}\mathrm{H}_2\ (\mathrm{gas})\,. \tag{2.10}$$

Removing an infinitesimal number of molecules $\mathrm{d}N_{ik}^{\mathrm{g}} = -\mathrm{d}\xi$ and $\mathrm{d}N_{jk}^{\mathrm{g}} = -\mathrm{d}\xi$ in a chemical reaction would cause the generation of an infinitesimal number of molecules $\mathrm{d}N_{ij}^{\mathrm{g}} = \mathrm{d}\xi$ and $\mathrm{d}N_{kk}^{\mathrm{g}} = \mathrm{d}\xi$. The Gibbs free energy would consequently change by

$$\mathrm{d}G = \mu_{ij}^{\mathrm{g}} \frac{\partial N_{ij}^{\mathrm{g}}}{\partial \xi}\mathrm{d}\xi + \mu_{kk}^{\mathrm{g}} \frac{\partial N_{kk}^{\mathrm{g}}}{\partial \xi}\mathrm{d}\xi + \mu_{ik}^{\mathrm{g}} \frac{\partial N_{ik}^{\mathrm{g}}}{\partial \xi}\mathrm{d}\xi + \mu_{jk}^{\mathrm{g}} \frac{\partial N_{jk}^{\mathrm{g}}}{\partial \xi}\mathrm{d}\xi = \left(\mu_{ij}^{\mathrm{g}} + \mu_{kk}^{\mathrm{g}} - \mu_{ik}^{\mathrm{g}} - \mu_{jk}^{\mathrm{g}}\right)\mathrm{d}\xi \tag{2.11}$$

2.1.1. Equilibrium conditions

At thermodynamic equilibrium, the total Gibbs energy of the system has reached a minimum value which implies that the variation of the Gibbs energy vanishes and $\mathrm{d}G = 0$. As a consequence, the equations (2.7), (2.9) and (2.11) yield the equilibrium conditions

$$\text{Equilibrium condition 1:} \qquad \mu_i^a = \frac{1}{2}\mu_{ii}^{\mathrm{g}} \tag{2.12}$$

$$\text{Equilibrium condition 2:} \qquad \mu_i^a = \mu_i^b \tag{2.13}$$

$$\text{Equilibrium condition 3:} \qquad \mu_{ik}^{\mathrm{g}} + \mu_{jk}^{\mathrm{g}} = \mu_{ij}^{\mathrm{g}} + \mu_{kk}^{\mathrm{g}} \tag{2.14}$$

They implicate that in equilibrium the reactions (2.5), (2.8) and (2.10) proceed with equal rates in both directions. In equilibrium, the conditions 1, 2 and 3 must be simultaneously fulfilled for every possible isotopic combination and at any gas-metal / metal-metal interface [119]. Therefore, equilibrium conditions 1 and 2 also apply among gas or metal phases that do not share part of their contact surfaces. This fact is known as the criterion

of phase equilibrium [120]. From now on, as long it is not necessary to explicitly differentiate between two metal-hydrogen systems of two different metal species, writing the superscripts a, b, etc. will be omitted.

The changes of enthalpy and entropy which would occur in the gas-metal system in equilibrium if one hydrogen isotope ${}^{i}\mathrm{H}$ is displaced from the gas into the metal are known as the so-called enthalpy of solution $\Delta\overline{H}$ and entropy of solution $\Delta\overline{S}$. According to equilibrium condition 1, they can be written as follows [see equations (2.3) and (2.12)] [114]

$$\Delta\overline{S}_i = \overline{S}_i - \frac{1}{2}\overline{S}^{\mathrm{g}}_{ii} \qquad \text{and} \qquad \Delta\overline{H}_i = \overline{H}_i - \frac{1}{2}\overline{H}^{\mathrm{g}}_{ii}\,. \tag{2.15}$$

To obtain more useful relations for the equilibrium conditions (2.12) - (2.14) the chemical potentials of an ideal diatomic hydrogen gas μ^{g}_{ij} and of hydrogen isotopes in a solid solution with a metal μ_i need to be expressed as a function of concentration, temperature and pressure. This is most accurately realized using the tools of statistical mechanics. Therefore, an alternative definition of the chemical potential of species s is used

$$\mu_s = \left(\frac{\partial F}{\partial N_s}\right)_{V,T,N'} \tag{2.16}$$

which is defined via the Helmholtz free energy $\mathfrak{F}$. The link between macroscopic thermodynamics and statistical mechanics is provided by expressing the Helmholtz free energy $\mathfrak{F}$ of the system with the canonical partition function Z

$$\mathfrak{F} = -k_{\mathrm{B}}T\ln(Z) = -k_{\mathrm{B}}T\ln\sum_n \exp\left(-\frac{E_n}{k_{\mathrm{B}}T}\right). \tag{2.17}$$

In this equation, E_n is the total energy of the system in a certain micro-state n and the sum is taken over all possible micro-states the system can take.

For temperatures $T > 400\,\mathrm{K}$ and pressures $p < 10\,\mathrm{MPa}$ a diatomic hydrogen gas of the same species can be considered as an ideal Boltzmann gas consisting of N^{g} indistinguishable molecules. In an ideal gas, the chance of finding two molecules in the same energy state is negligibly small. Hence, it can be assumed that in any possible state of the gas, the molecules of mass m occupy different energy states ϵ_q with $q = 1 \ldots N^{\mathrm{g}}$. The canonical partition function Z_q of a single diatomic molecule in the gas can be written as $Z_q = \sum_q^{N^{\mathrm{g}}} \exp(\epsilon_q/k_{\mathrm{B}}T)$, where the sum is taken over N^{g} different energy states the molecules can occupy [118]. The partition function of a system (the gas) made of an ensemble of N^{g} indistinguishable subsystems (each molecule) is given by $Z = 1/N^{\mathrm{g}}! \prod_q^{N^{\mathrm{g}}} Z_q$ [121]. The division by the factorial provokes that all possible permutations of the indistinguishable particles in the phase space are counted as a single state of the gas. Since Z_q is the same for each molecule the partition function of the gas yields $Z = 1/N^{\mathrm{g}}! \cdot (Z_q)^{N^{\mathrm{g}}}$. As a consequence, equation (2.17) transforms to

$$\mathfrak{F} = -k_{\mathrm{B}}T\ln\left\{\left[\sum_q \exp\left(\frac{-\epsilon_q}{k_{\mathrm{B}}T}\right)\right]^{N^{\mathrm{g}}} \frac{1}{N^{\mathrm{g}}!}\right\} = -k_{\mathrm{B}}TN^{\mathrm{g}}\ln\left[\frac{e}{N^{\mathrm{g}}}\sum_q \exp\left(\frac{-\epsilon_q}{k_{\mathrm{B}}T}\right)\right] \tag{2.18}$$

for which Stirling's formula is used. In classical statistical mechanics, the sum in equation (2.18) must be expressed by an integral over the entire phase space.

$$\mathfrak{F} = -k_\mathrm{B} T N^\mathrm{g} \ln\left[\frac{e}{N^\mathrm{g}(2\pi\hbar)^3}\int \exp\frac{-\epsilon\left(\vec{p},\vec{q}\right)}{k_\mathrm{B}T}\mathrm{d}\vec{p}\mathrm{d}\vec{q}\right], \text{with } \epsilon\left(\vec{p},\vec{q}\right) = \epsilon_\mathrm{b} + \frac{\vec{p}^{\,2}}{2m} + \frac{\vec{\mathfrak{M}}^2}{2\Theta} \tag{2.19}$$

where $\vec{p}$ and $\vec{q}$ are the phase space variables. Here, $\vec{\mathfrak{M}}$ labels the angular momentum, Θ the moment of inertia, and ϵ_b is the bond dissociation energy per molecule in the gas. Solving this integral finally leads to [121]

$$\mathfrak{F} = N\epsilon_\mathrm{b} - N^\mathrm{g} k_\mathrm{B} T \ln\left[V\frac{e}{N}\left(\frac{mk_\mathrm{B}T}{2\pi\hbar}\right)^{\frac{3}{2}}\right] - N^\mathrm{g} k_\mathrm{B} T \ln\left(\frac{k_\mathrm{B}T\Theta}{\hbar^2}\right). \tag{2.20}$$

Since in an ideal gas the molecules do not interact with each other the Helmholtz free energy of a gas mix of distinguishable molecular species ${}^i\mathrm{H}^j\mathrm{H}$ enclosed in the volume V is determined by $\mathfrak{F} = -k_\mathrm{B}T\ln\prod_{ij} Z_{ij} = \sum_{ij} -k_\mathrm{B}T\ln Z_{ij}$ where Z_{ij} labels the partition function of all molecules of the same species. Hence, the Helmholtz free energy of the entire system can be expressed as the sum of the individual Helmholtz free energies of each gas component ${}^i\mathrm{H}^j\mathrm{H}$, such that

$$\mathfrak{F} = \sum_{ij}\left\{N_{ij}^\mathrm{g}\epsilon_{\mathrm{b},ij} - N_{ij}^\mathrm{g} k_\mathrm{B} T \ln\left[V\frac{e}{N_{ij}^\mathrm{g}}\left(\frac{m_{ij}k_\mathrm{B}T}{2\pi\hbar}\right)^{\frac{3}{2}}\right] - N_{ij}^\mathrm{g} k_\mathrm{B} T \ln\left(\frac{k_\mathrm{B}T\Theta_{ij}}{\hbar^2}\right)\right\}. \tag{2.21}$$

To obtain the chemical potential of component ${}^i\mathrm{H}^j\mathrm{H}$ in the gas mixture, equation (2.16) is applied before inserting the ideal gas law $V = N_{ij}^\mathrm{g} k_\mathrm{B} T / p_{ij}$, resulting in [122]

$$\mu_{ij}^\mathrm{g} = \epsilon_{\mathrm{b},ij} + k_\mathrm{B}T\ln\left[\frac{p_{ij}}{p_{ij}^0(T)}\right], \quad \text{with} \quad p_{ij}^0(T) \equiv \frac{(k_\mathrm{B}T)^{7/2}\,\Theta_{ij} m_{ij}^{3/2}}{\hbar^5\,(2\pi)^{3/2}} \tag{2.22}$$

where p_{ij} is the partial pressure of component ${}^i\mathrm{H}^j\mathrm{H}$. By transformation, it may be expressed with respect to the standard state pressure $p^\circ = 101\,325\,\mathrm{Pa}$

$$\mu_{ij}^\mathrm{g} = \mu_{ij}^{\mathrm{g},\circ} + k_\mathrm{B}T\ln\left(\frac{p_{ij}}{p^\circ}\right), \quad \text{with} \quad \mu_{ij}^{\mathrm{g},\circ} = \epsilon_{\mathrm{b},ij} + k_\mathrm{B}T\ln\left[\frac{p^\circ}{p_{ij}^0(T)}\right] \tag{2.23}$$

where $\mu_{ij}^{\mathrm{g},\circ}$ is the standard state chemical potential of gas component ${}^i\mathrm{H}^j\mathrm{H}$. With the equations (2.3) it is possible to calculate the change of entropy and enthalpy of the diatomic hydrogen gas per removed or added molecule at a certain pressure [123]

$$\overline{S}_{ij}^\mathrm{g} = \overline{S}_{\mathrm{s},ij}^{\mathrm{g},\circ} + k_\mathrm{B}\ln\left(\frac{p_{ij}}{p^\circ}\right), \quad \text{with} \quad \overline{S}_{\mathrm{s},ij}^{\mathrm{g},\circ} = \frac{7}{2}k_\mathrm{B} + k_\mathrm{B}\ln\left[\frac{p^\circ}{p_{ij}^0(T)}\right] \tag{2.24}$$

$$\overline{H}_{ij}^\mathrm{g} = \overline{H}_{ij}^{\mathrm{g},\circ} = \epsilon_{\mathrm{b},ij} - \frac{7}{2}k_\mathrm{B}T \tag{2.25}$$

The quantities $\overline{S}_{ij}^{\mathrm{g},\circ}$ and $\overline{H}_{ij}^{\mathrm{g},\circ}$ are defined by the relations (2.3) when substituting the chemical potentials by the standard state chemical potentials of the gas, such that $\mu_{ij}^{\mathrm{g},\circ} =$

$\overline{H}^{\mathrm{g},\circ}_{ij} - T\overline{S}^{\mathrm{g},\circ}_{ij}$. This leads to the definitions of the standard state entropy and enthalpy of solution:

$$\Delta\overline{S}^{\circ}_{i} = \overline{S}_{i} - \frac{1}{2}\overline{S}^{\mathrm{g},\circ}_{ii} \qquad \text{and} \qquad \Delta\overline{H}^{\circ}_{i} = \overline{H}_{i} - \frac{1}{2}\overline{H}^{\mathrm{g},\circ}_{ii} \tag{2.26}$$

Having obtained the expression (2.23) for the chemical potential of multi-isotopic hydrogen gas enables rewriting equilibrium condition 3 [equation (2.14)] as follows [124]

$$\frac{p_{ik}p_{jk}}{p_{ij}p_{kk}} = \exp\left(\frac{\mu^{\mathrm{g},\circ}_{ij} + \mu^{\mathrm{g},\circ}_{kk} - \mu^{\mathrm{g},\circ}_{ik} - \mu^{\mathrm{g},\circ}_{jk}}{k_{\mathrm{B}}T}\right) \equiv K^{ik+jk}_{ij+kk} \tag{2.27}$$

where K^{ik+jk}_{ij+kk} is defined as the equilibrium constant for the different isotope exchange reactions (2.10) in the gas phase.

Even today, the exact physical mechanisms which determine the equilibrium state of hydrogen dissolved in metal are still far from fully understood. Great progress was made at the beginning of the 20th century when the methods of statistical mechanics combined with numerical analysis made it possible to develop first theoretical models with satisfying accuracy. Among the most successful is the mean-field theory of the lattice gas in which a metal-hydrogen solution is treated as a mono-atomic hydrogen gas made of N_i hydrogen isotopes ^{i}H [125]. The charge density distributions of the metal atoms lead to a potential energy landscape that exhibits periodically repeating potential energy minimums known as interstitial sites. In the lattice gas model, the hydrogen isotopes are considered to be confined in the volume occupied by the metal and randomly distributed over a total of N_{sites} interstitial sites.

Figure 2.2 illustrates three of the most common crystal structures of metals [body-centered cubic (BCC), hexagonal closed packed (HCP) and face-centered cubic (FCC)] and highlights the corresponding position of tetrahedral (T-sites) or octahedral (O-sites) interstitial sites which may be occupied by hydrogen isotopes. The figure is created by the author of this thesis using the computer-aided design (CAD) software CATIAv5.

According to the lattice gas model, every isotope of the same species ^{i}H dissolved in the metal possesses the same average energy $\epsilon_{\mathrm{s},i}$ [126]. Lacher *et al* [127] extended this picture by considering that the energy of a hydrogen isotope is influenced by the presence of close-by hydrogen isotopes in the metal. This effect is called H-H interactions. Amongst others, there is a repulsive electronic short-range and an attractive long-range elastic contribution to the interactive forces each dissolved hydrogen isotope exerts on the others [128]. The effect of H-H interaction on the hydrogen solution characteristics of metal becomes visible at elevated concentrations. Lacher *et al* used the approximation that the energy state of a hydrogen isotope is influenced only by the long-range elastic interaction of nearest neighbor hydrogen isotopes occupying adjacent interstitial sites. The elastic interaction arises from the fact that upon entering the metal, hydrogen isotopes expand the lattice structure. Thus, a dissolving isotope creates a long-range distortion field that makes surrounding interstitial sites more favorable for further hydrogen isotopes to occupy. Considering a random distribution of isotopes over the lattice, according to the

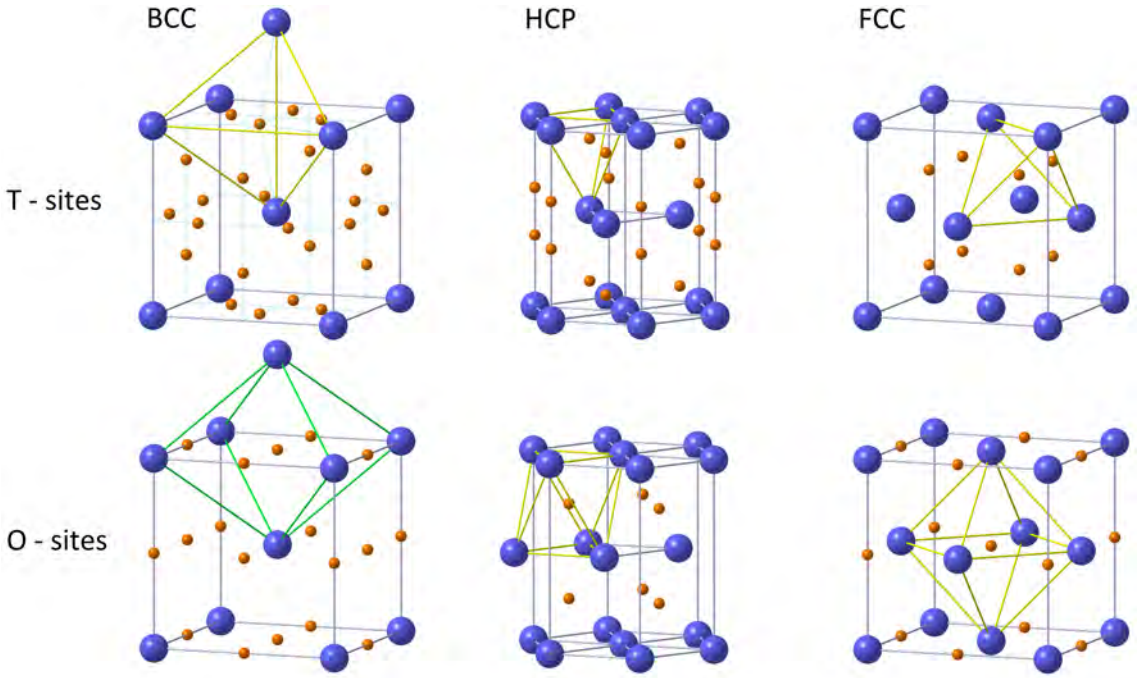

Fig. 2.2. Illustrated unit cells of the body-centered cubic (BCC), hexagonal closed packed (HCP) and face-centered cubic (FCC) crystal structures of metals. The orange spheres represent tetrahedral (T-sites) and octahedral (O-sites) interstitial sites which may be occupied by hydrogen isotopes, respectively.

Bragg and Williams approximation the probability for a hydrogen isotope to encounter another hydrogen isotope of any kind in an adjacent interstitial is approximately N_i/N_{sites} [129]. By assuming that an H-H interaction lowers the potential energy of both interacting isotopes by $\epsilon_{\text{HH}}/2 < 0$ the total energy of the lattice gas can be approximated by

$$E_{\text{LG}} \approx N_i \cdot \left(\epsilon_{\text{s},i} + N_{\text{adj}} \cdot \frac{N_i}{N_{\text{sites}}} \frac{\epsilon_{\text{HH}}}{2} \right), \qquad \epsilon_{\text{HH}} < 0 \quad \& \quad \epsilon_{\text{s},i} < 0\,. \tag{2.28}$$

Here, N_{adj} is the number of nearest neighbor interstitial sites surrounding each hydrogen isotope [130] (see figure 2.2). The Helmholtz free energy $\mathfrak{F}$ of the lattice gas constituting the isotope species ${}^{i}\text{H}$ is obtained using equation (2.17)

$$\mathfrak{F} = -k_{\text{B}} T \ln Z = -k_{\text{B}} T \ln \sum_n \exp\left(-\frac{E_{\text{LG},n}}{k_{\text{B}} T} \right). \tag{2.29}$$

Since every hydrogen isotope is assumed to have equal average energy $\epsilon_{\text{s},i}$, the total energy of any possible micro-state of the lattice gas is equal. For this reason, the sum in equation (2.29) can be replaced by a multiplication of the exponential term with the number of possible ways $\Omega = N_{\text{sites}}!/\left[N_i!\,[(N_{\text{sites}} - N_i)!\right]$ the isotopes can be configured over N_{sites} existing interstitial sites

$$\mathfrak{F} = -k_{\text{B}} T \ln \left\{ \Omega \cdot \exp\left[-\frac{1}{k_{\text{B}} T} \left(N_i \epsilon_{\text{s},i} + N_{\text{adj}} \cdot \frac{N_i^2}{N_{\text{sites}}} \frac{\epsilon_{\text{HH}}}{2} \right) \right] \right\}. \tag{2.30}$$

Transformation of this equation leads to

$$\mathfrak{F} = -k_{\text{B}} T \ln(\Omega) + N_i \epsilon_{\text{s},i} + \frac{N_{\text{adj}} \epsilon_{\text{HH}}}{2} \frac{N_i^2}{N_{\text{sites}}}. \tag{2.31}$$

By applying Stirling's formula and after introducing the bulk coverage as the fraction of occupied interstitial sites $\theta_{\mathrm{b},i} = N_i/N_{\mathrm{sites}} \leq 1$, equation (2.30) transforms to

$$\mathfrak{F} = N_{\mathrm{sites}} \left\{ k_{\mathrm{B}}T \left[\theta_{\mathrm{b},i} \ln\left(\theta_{\mathrm{b},i}\right) + \left(1-\theta_{\mathrm{b},i}\right) \ln\left(1-\theta_{\mathrm{b},i}\right) \right] + \epsilon_{\mathrm{s},i}\theta_{\mathrm{b},i} + \epsilon_{\mathrm{HH}} N_{\mathrm{adj}} \theta_{\mathrm{b},i}^2 \right\} \tag{2.32}$$

The approximated chemical potential of different isotopes ^{i}H dissolved in a metal is finally obtained using equation (2.16):

$$\mu_i \approx \frac{1}{N_{\mathrm{sites}}} \left(\frac{\partial F}{\partial \theta_{\mathrm{b},i}} \right)_{V,T} = k_{\mathrm{B}}T \ln\left(\frac{\theta_{\mathrm{b},i}}{1-\theta_{\mathrm{b},i}} \right) + \epsilon_{\mathrm{s},i} + \frac{\epsilon_{\mathrm{HH}} N_{\mathrm{adj}}}{2} \theta_{\mathrm{b},i} \tag{2.33}$$

Two definitions for the hydrogen concentration in a metal are introduced at this point:

$$x_i \approx \frac{N_i}{N_{\mathrm{Me}}} = x_{\mathrm{max}} \theta_{\mathrm{b},i} \qquad \text{and} \qquad c_i = \frac{N_i}{V N_{\mathrm{A}}} = \frac{\rho_{\mathrm{Me}}}{M_{\mathrm{Me}}} x_i = \frac{\rho_{\mathrm{Me}}}{M_{\mathrm{Me}}} x_{\mathrm{max}} \theta_{\mathrm{b},i} \tag{2.34}$$

Here, N_{Me} is the number of metal atoms, $x_{\mathrm{max}} = N_{\mathrm{sites}}/N_{\mathrm{Me}}$ the maximum possible concentration in the metal, N_{A} the Avogadro number, M_{Me} the molar mass and ρ_{Me} the density of the pure metal. The simple mean-field lattice gas model presented above neither takes into account the expansion of the metal volume during the dissolution process, nor the temperature-dependent occupation of vibrational energy states, nor further electronic contributions to the entropy [114]. A detailed discussion of how to consider these additional terms in the derivation of the chemical potential can be found in [114], [131]–[134]. For simplicity, in this work, they are taken into account in the form of a corrective excess term $\mu_{\mathrm{ex},i} = \overline{H}_{\mathrm{ex},i} - T\overline{S}_{\mathrm{ex},i}$ which is summed to equation (2.33), such that when considering the defined concentration x_i

$$\mu_i = k_{\mathrm{B}}T \ln\left(\frac{x_i}{x_{\mathrm{max}} - x_i} \right) + \epsilon_{\mathrm{s},i} + \epsilon_{\mathrm{HH}} N_{\mathrm{adj}} \cdot \frac{x_i}{x_{\mathrm{max}}} + \overline{H}_{\mathrm{ex},i} - T\overline{S}_{\mathrm{ex},i}\,. \tag{2.35}$$

The excess contributions to the entropy and enthalpy change per added or removed isotope $\overline{S}_{\mathrm{ex},i}$ and $\overline{H}_{\mathrm{ex},i}$ are here assumed to be constant [135]. For hydrogen isotopes dissolved in metal, equation (2.4) yields

$$\overline{S}_i = -k_{\mathrm{B}} \ln\left(\frac{x_i}{x_{\mathrm{max}} - x_i} \right) + \overline{S}_{\mathrm{ex},i} \qquad \text{and} \qquad \overline{H}_i \approx \epsilon_{\mathrm{s},i} + \epsilon_{\mathrm{HH}} N_{\mathrm{adj}} \cdot \frac{x_i}{x_{\mathrm{max}}} + \overline{H}_{\mathrm{ex},i}\,. \tag{2.36}$$

Inserting the derived chemical potentials (2.23) and (2.35) into equation (2.12) provides a more property-related expression of equilibrium condition 1 [equation (2.12)] if only one isotope species is involved in the dissolution process

$$\frac{p_{ii}}{p^\circ} = \left(\frac{x_i}{x_{\mathrm{max}} - x_i} \right)^2 \exp\left(\frac{2\epsilon_{\mathrm{s},i} + 2\epsilon_{\mathrm{HH}} N_{\mathrm{adj}} x_i/x_{\mathrm{max}} + 2\overline{H}_{\mathrm{ex},i} - 2T\overline{S}_{\mathrm{ex},i} - \mu_{ii}^{\mathrm{g},\circ}}{k_{\mathrm{B}}T} \right). \tag{2.37}$$

It relates the establishing equilibrium concentration x_i in the metal for a given partial pressure p_{ii} in the gas.

The entropy and enthalpy of solution at equilibrium are obtained by inserting the expressions (2.24), (2.25) and (2.36) into the definitions (2.15) and (2.26)

$$\Delta\overline{S}_i = -k_\mathrm{B}\ln\left(\frac{x_i}{x_\mathrm{max}-x_i}\right) + \overline{S}_{\mathrm{ex},i} - \frac{1}{2}\overline{S}^{\mathrm{g}}_{ii} \tag{2.38}$$

$$\Delta\overline{S}^{\circ}_i = -k_\mathrm{B}\ln\left(\frac{x_i}{x_\mathrm{max}-x_i}\right) + \overline{S}_{\mathrm{ex},i} - \frac{1}{2}\overline{S}^{\mathrm{g},\circ}_{ii} \tag{2.39}$$

$$\Delta\overline{H}_i = \epsilon_{\mathrm{s},i} + \epsilon_\mathrm{HH} N_\mathrm{adj}\cdot\frac{x_i}{x_\mathrm{max}} + \overline{H}_{\mathrm{ex},i} - \frac{1}{2}\overline{H}^{\mathrm{g}}_{ii} \tag{2.40}$$

$$\Delta\overline{H}^{\circ}_i = \epsilon_{\mathrm{s},i} + \epsilon_\mathrm{HH} N_\mathrm{adj}\cdot\frac{x_i}{x_\mathrm{max}} + \overline{H}_{\mathrm{ex},i} - \frac{1}{2}\overline{H}^{\mathrm{g},\circ}_{ii}\,. \tag{2.41}$$

Dependent on the metal, the enthalpy or heat of solution $\Delta\overline{H}_i$ at equilibrium is either positive or negative. It is found that alkali and alkaline-earth metals, titanium and vanadium subgroup metals, rare-earth metals, scandium, yttrium, palladium and actinide series metals are exothermic hydrogen absorbers with $\Delta\overline{H}_i < 0$ while e.g. cobalt, copper, nickel, silver, platinum, iron and iron alloys are endothermic absorbers and $\Delta\overline{H}_i > 0$ [136]. It should be noted that $\overline{H}^{\mathrm{g},\circ}_{ii} = \overline{H}^{\mathrm{g}}_{ii} \Rightarrow \Delta\overline{H}^{\circ}_i = \Delta\overline{H}_i$.

Equilibrium condition 2 [equation (2.13)] can be rewritten as well using the derived relations for the chemical potentials (2.23) and (2.35) by considering that in combination with equilibrium condition 1, it follows that $\mu^{\mathrm{g}}_{ii} = 2\mu^a_i = 2\mu^b_i$

$$\begin{aligned}\frac{p_{ii}}{p^\circ} &= \left(\frac{x^a_i}{x^a_\mathrm{max}-x^a_i}\right)^2 \exp\left(\frac{2\Delta\overline{H}^{a,\circ}_i - 2T\overline{S}^{a}_{\mathrm{ex},i} + T\overline{S}^{\mathrm{g},\circ}_{ii}}{k_\mathrm{B}T}\right)\\ &= \left(\frac{x^b_i}{x^b_\mathrm{max}-x^b_i}\right)^2 \exp\left(\frac{2\Delta\overline{H}^{b,\circ}_i - 2T\overline{S}^{b}_{\mathrm{ex},i} + T\overline{S}^{\mathrm{g},\circ}_{ii}}{k_\mathrm{B}T}\right).\end{aligned} \tag{2.42}$$

This condition states that once a gas phase containing the mono-isotopic molecules $^i\mathrm{H}_2$ is in thermodynamic equilibrium with isotopes $^i\mathrm{H}$ dissolved in two different metals, two distinct equilibrium concentrations x^a_i and x^b_i will establish in the metals, respectively. The enthalpies of solution $\Delta\overline{H}^{a,\circ}_i$ are those defined by the expression (2.41) considering the metal specific parameters $\epsilon^a_{\mathrm{s},i}$, ϵ^a_HH, n^a_adj, x^a_max and $\overline{H}^a_{\mathrm{ex},i}$ for each metal.

Thus, in a system without a gas phase in which a hydrogen-loaded metal Me^a is put into contact with a second metal Me^b the equilibrium condition determining the establishing equilibrium concentrations in the two metals is given by the right-hand equal sign of equation (2.42). Equation (2.42) holds for every isotope type in the metal, independently.

2.1.2. Dilute solutions and the Sieverts' law

In the limit of low concentrations ($x_i \to 0$) the influence of H-H interactions becomes negligible and equation (2.37) approaches the well-known Sieverts' law [137]

$$x_i = \exp\left[-\frac{\epsilon_{\mathrm{s},i} + \overline{H}_{\mathrm{ex},i} - \frac{1}{2}\overline{H}^{\mathrm{g},\circ}_{ii} - T\left(k_\mathrm{B}\ln x_\mathrm{max} + \overline{S}_{\mathrm{ex},i} - \frac{1}{2}\overline{S}^{\mathrm{g},\circ}_{ii}\right)}{k_\mathrm{B}T}\right]\sqrt{\frac{p_{ii}}{p^\circ}} \equiv k_{\mathrm{s},i}\sqrt{\frac{p_{ii}}{p^\circ}}\,. \tag{2.43}$$

It states that in the low-concentration limit and at constant temperature the equilibrium concentration of hydrogen isotopes dissolved in a metal is proportional to the square root of the equilibrium pressure in the surrounding gas. Its experimental reproducibility is an indicator for the fact that diatomic hydrogen molecules dissociate and enter the metal in atomic form. The metal and isotope specific proportionality constant $k_{\mathrm{s},i}$ is a measure for the affinity of a metal to absorb the hydrogen isotopes of species ${}^{i}\mathrm{H}$. It is called the Sieverts' constant. The first three summands in the exponential of equation (2.43) conform with the enthalpy of solution as defined in relation (2.41) considering the limit of low concentrations. Since $\Delta\overline{H}_i^{\circ} = \Delta\overline{H}_i$ it can be substituted by $\Delta\overline{H}_i$. For the sake of clarity, when expressed in the Sieverts' law the enthalpy of solution is subscripted with a lowercase s, such that $\Delta\overline{H}_i \equiv \Delta\overline{H}_{\mathrm{s},i}$. The term in parenthesis is similar but does not conform with the entropy of solution defined in (2.40). It is here referred to as the Sieverts' entropy of solution and labeled with $\Delta\overline{S}_{\mathrm{s},i}$

$$k_{\mathrm{s},i} = \exp\left(-\frac{\Delta\overline{H}_{\mathrm{s},i} - T\Delta\overline{S}_{\mathrm{s},i}}{k_{\mathrm{B}}T}\right) = \exp\left(\frac{\Delta\overline{S}_{\mathrm{s},i}}{k_{\mathrm{B}}}\right)\exp\left(-\frac{\Delta\overline{H}_{\mathrm{s},i}}{k_{\mathrm{B}}T}\right) = k_{\mathrm{s},i}^{0}\exp\left(-\frac{\Delta\overline{H}_{\mathrm{s},i}}{k_{\mathrm{B}}T}\right) \tag{2.44}$$

where $k_{\mathrm{s},i}^{0}$ is the pre-exponential factor of the Sieverts' constant. Since $\Delta\overline{H}_i$ and $\Delta\overline{S}_{\mathrm{s},i}$ are metal-specific parameters, so is the Sieverts' constant $k_{\mathrm{s},i}$. It can be seen that the Sieverts constant is also temperature dependent. In fact, for endothermic hydrogen absorbers, it increases with temperature and in the case of exothermic hydrogen absorbing metals it decreases with increasing temperature [136].

At thermodynamic equilibrium, equilibrium condition 1 [equation (2.37)] and equilibrium condition 3 [equation (2.27)] must be fulfilled simultaneously. This means, that at equilibrium the partial pressures of the different molecules in the gas establish strict relationships determined by equation (2.27). When considering the specific isotope exchange reaction $2\,{}^{i}\mathrm{H}\,{}^{k}\mathrm{H} \rightleftharpoons {}^{i}\mathrm{H}_2 + {}^{k}\mathrm{H}_2$, at equilibrium equation (2.27) yields

$$\frac{p_{ik}^2}{p_{ii}p_{kk}} = K_{ii+kk}^{ik+ik} \equiv K_{ik}^{\mathrm{ex}} \qquad \Leftrightarrow \qquad \frac{p_{ik}}{p^{\circ}} = \sqrt{K_{ik}^{\mathrm{ex}}}\sqrt{\frac{p_{ii}}{p^{\circ}}}\sqrt{\frac{p_{kk}}{p^{\circ}}} \tag{2.45}$$

where K_{ik}^{ex} is a shorter form of labeling the equilibrium constant of the isotope exchange reaction $2\,{}^{i}\mathrm{H}\,{}^{k}\mathrm{H} \rightleftharpoons {}^{i}\mathrm{H}_2 + {}^{k}\mathrm{H}_2$. Measuring the temperature dependence of the equilibrium constants K_{ik}^{ex} of the different isotope exchange reactions $2\,{}^{i}\mathrm{H}\,{}^{k}\mathrm{H} \rightleftharpoons {}^{i}\mathrm{H}_2 + {}^{k}\mathrm{H}_2$ has been the target of several experimental campaigns in the past [138], [139]. The following experimental relations are found in the literature [132]:

$$K_{12}^{\mathrm{ex}} = 4.241\frac{\left[1-\exp\left(-\frac{5986}{T}\right)\right]\left[1-\exp\left(-\frac{4307}{T}\right)\right]}{\left[1-\exp\left(-\frac{5225}{T}\right)\right]^2}\exp\left(-\frac{78.7}{T}\right) \tag{2.46}$$

$$K_{13}^{\mathrm{ex}} = 4.662\frac{\left[1-\exp\left(-\frac{5986}{T}\right)\right]\left[1-\exp\left(-\frac{3548}{T}\right)\right]}{\left[1-\exp\left(-\frac{4940}{T}\right)\right]^2}\exp\left(-\frac{176.3}{T}\right) \tag{2.47}$$

$$K_{23}^{\mathrm{ex}} = 4.083\frac{\left[1-\exp\left(-\frac{4307}{T}\right)\right]\left[1-\exp\left(-\frac{3548}{T}\right)\right]}{\left[1-\exp\left(-\frac{3948}{T}\right)\right]^2}\exp\left(-\frac{21.6}{T}\right) \tag{2.48}$$

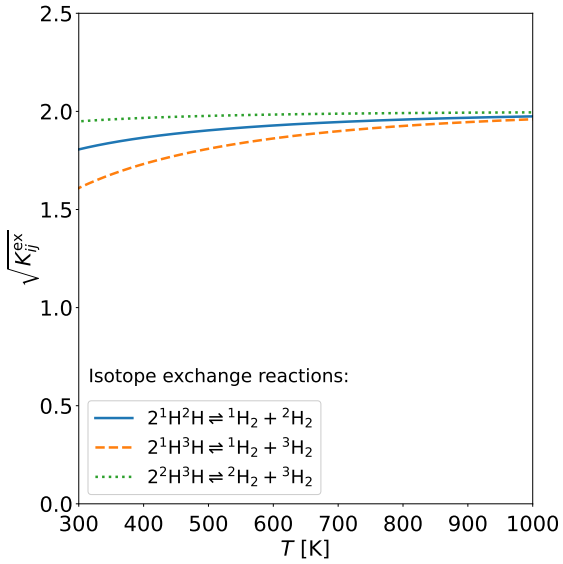

Fig. 2.3. Square root of measured equilibrium constants for three isotope exchange reactions in the temperature range relevant for this work using measured relations reported by [132].

Figure 2.3 shows the temperature dependence of the square root of the equilibrium constants as expressed in the formulas (2.46), (2.47) and (2.48) for the three isotope exchange reactions. It can be seen that with increasing temperature it converges against $\sqrt{K_{ij}^{\mathrm{ex}}} = 2$.

To find the Sieverts' law for the multi-isotopic case, the isotope-specific square roots in equation (2.45) are substituted with the corresponding versions of the mono-isotopic Sieverts' law (2.43)

$$x_i x_k = \frac{k_{\mathrm{s},i} k_{\mathrm{s},k}}{\sqrt{K_{ik}^{\mathrm{ex}}}} \cdot \frac{p_{ik}}{p^\circ} \,. \tag{2.49}$$

The Sieverts' constant as defined above is a unit-less parameter. When writing the Sieverts' law in terms of the molar concentration c_i the Sieverts' constant is usually reported as a parameter with the unit $[\mathrm{mol/m^3 Pa^{-1/2}}]$ and defined by

$$c_i = \frac{\rho_{\mathrm{Me}}}{M_{\mathrm{Me}} \sqrt{p^\circ}} \cdot k_{\mathrm{s},i} \sqrt{p_{ii}} \equiv K_{\mathrm{s},i} \sqrt{p_{ii}} \qquad \text{and} \qquad c_i c_k = \frac{K_{\mathrm{s},i} K_{\mathrm{s},k}}{\sqrt{K_{ik}^{\mathrm{ex}}}} \cdot p_{ik} \,. \tag{2.50}$$

The low-concentration approximation of equilibrium condition 2 [equation (2.42)] is obtain by equalizing the Sieverts' relations (2.43) for hydrogen isotopes in two different metals

$$\frac{x_i^a}{k_{\mathrm{s},i}^a} = \frac{x_i^b}{k_{\mathrm{s},i}^b} \quad \text{and} \quad \frac{c_i^a}{K_{\mathrm{s},i}^a} = \frac{c_i^b}{K_{\mathrm{s},i}^b} \quad \Leftrightarrow \quad c_i^b = K_{\mathrm{D},0,i}^{a-b} \cdot c_i^a \,, \quad \text{with} \quad K_{\mathrm{D},0,i}^{a-b} \equiv \frac{K_{\mathrm{s},i}^b}{K_{\mathrm{s},i}^a} \,. \tag{2.51}$$

The defined temperature-dependent parameter $K_{\mathrm{D},0,i}^{a-b}$ is called the low-concentration distribution coefficient of isotope species ${}^i\mathrm{H}$ dissolved in two different metals Me^a and Me^b, that either share part of their surface areas or are exposed to the same gas phase.

2.1.3. Metal hydride formation

The relationship between the partial pressure p_{ii} of a diatomic hydrogen gas and the establishing equilibrium concentration x_i at a fixed temperature in the metal is called pressure-

composition isotherm (PCI) and generally expressed by equation (2.37). It is unique for each metal and for each isotope species ^{i}H. The higher the establishing equilibrium concentration at a certain pressure, the higher the hydrogen isotope solubility of the metal. Even at very high temperatures and pressures p_{ii}, most endothermic hydrogen-absorbing metals exhibit very low equilibrium concentrations which implies a low hydrogen isotope solubility. Therefore, in almost all practical applications, endothermic metal-hydrogen solutions are sufficiently well described by the Sieverts' law. On the other hand, exothermic hydrogen-absorbing metals are associated with a high hydrogen isotope solubility. For many exothermic candidates, very low pressures p_{ii} correspond to equilibrium concentrations that are high enough that the effect of H-H interaction becomes important and the Sieverts' law starts to deviate from the true courses of the PCIs. To simplify the discussion, the occurring effects at higher hydrogen isotope concentrations are explained assuming a pure gas of only one type of mono-isotopic gas molecules.

Figure 2.4 shows PCIs for the palladium-protium (Pd-^{1}H) system (black dashed lines) at different temperatures which are calculated using equation (2.37). The used parameter values $\epsilon_{\mathrm{s}} = -2.33\,\mathrm{eV}$, $\epsilon_{\mathrm{HH}} N_{\mathrm{adj}} = -0.20\,\mathrm{eV}$, $\epsilon_{\mathrm{b},11} = -4.48\,\mathrm{eV}$, $x_{\mathrm{max}} = 0.59$ and $p_{11}^{0} = 4.07 \times 10^{9}\,\mathrm{Pa}$ are chosen according to fits against experimental data performed by Lacher *et al* [114], [122], [127]. For the calculation, the excess entropy and enthalpy appearing in equation (2.37) are neglected. To illustrate the influence of H-H interactions on the PCIs, the graph contains the course of the Sieverts' law for the highest plotted temperature $T = 586\,\mathrm{K}$. It can be seen how already at relatively low pressures and concentrations the calculated PCIs deviate from the Sieverts' law approximation. This means that with increasing pressure and concentration, H-H interaction leads to an increasing rise in hydrogen absorption capacity at a given pressure. It can be seen that within a certain pressure range, the calculated PCIs show three equilibrium concentrations where the hydrogen isotopes in the exothermic hydrogen-absorbing metal would have the same chemical potential as the gas phase at a fixed pressure. However, it is important to remember that the plotted PCI relations (2.37) are derived from the lattice gas model which assumes that the hydrogen isotopes are randomly distributed over the interstitial sites as a single metal-hydrogen phase with a unique concentration. Another aspect is that at the position of the intermediate of the three equilibrium concentrations corresponding to the same equilibrium pressure, the PCI and therefore the chemical potential of hydrogen dissolved in the metal have negative slopes. According to equation (2.3), a decreasing chemical potential with increasing particle number represents a maximum of the Gibbs free energy and hence does not describe a physically realistic equilibrium concentration. In fact, all of the concentration values between the two extreme points of the PCIs in figure 2.4 would correspond to unstable states and could not exist in equilibrium. However, contrary to this reasoning, experiments have shown that the total protium content in Pd can indeed take values corresponding to this critical concentration range [127].

An answer to these inconsistencies surrounding the two extreme points is illustrated in figure 2.5 and explained in the following. Below a critical pressure $p < p_{\mathrm{dec}}$ the metal-

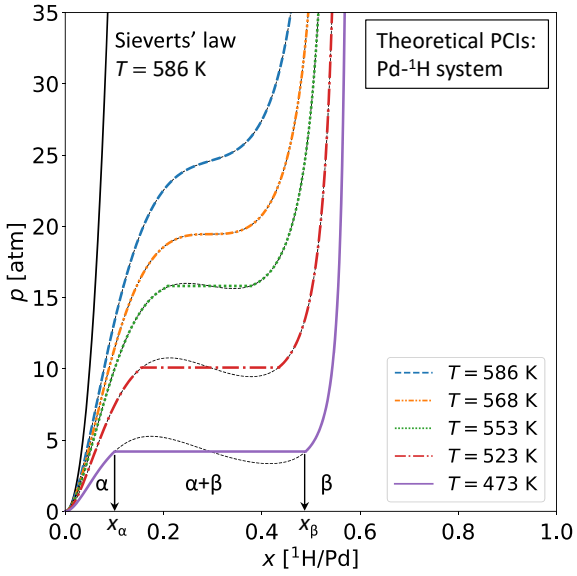

Fig. 2.4. Calculated pressure-composition isotherms (black dashed lines) of a simple exothermic metal-hydrogen system (Pd-^{1}H system) using equation (2.37) with parameters fitted by Lacher *et al* [127]. The flat plateau area arises assuming that two phases of equal chemical potentials but distinct concentrations x_α and x_β coexist in the range $x_\alpha < x < x_\beta$. For comparison, the plot shows the course of the Sieverts' law for $T = 586\,\mathrm{K}$.

hydrogen solution exists as a single phase (here called the α phase) where the hydrogen isotopes randomly distribute in the lattice and the equilibrium concentration increases with pressure. In the α phase, hydrogen is dissolved as an interstitial solute, which is why it is sometimes referred to as a solid solution (as long as the metal phase is solid). At $p = p_{\mathrm{dec}}$ the concentration of the α phase reaches a maximum value x_α, which is known as the terminal solubility [114]. Every additional hydrogen isotope added to the solution precipitates within a second hydride β phase that emerges at more and more locations in the lattice. These areas are characterized by a significantly higher concentration x_β and an ordered arrangement of the hydrogen isotopes over the lattice sites. The overall average concentration in the two-phase metal-hydrogen solution at $p = p_{\mathrm{dec}}$ can be written as

$$x = \theta^\alpha x_\alpha + \theta^\beta x_\beta\,, \quad \text{with} \quad \theta^\alpha + \theta^\beta = 1\,, \quad \text{if} \quad x_\alpha < x < x_\beta \tag{2.52}$$

In this expression θ^α stands for the fraction of hydrogen isotopes that are part of the α phase at the limit concentration x_α and θ^β labels the fraction of hydrogen isotopes constituting the hydride β phase which occurs with the fix concentration x_β. For pressures $p \geq p_{\mathrm{dec}}$, the alpha phase disappears in equilibrium ($\theta^\alpha = 0$). Furthermore, the equilibrium concentration is again pressure dependent with $x > x_\beta$ as described by equation (2.37). However, the existence of a second hydride phase in the two-phase region at equilibrium is bound to some conditions which ultimately determine the value of the critical concentrations x_α and x_β and the decomposition pressure p_{dec}.

According to equation (2.1), the Gibbs free energy of a mono-isotopic metal-hydrogen solution can be written as $G(x,T) = N_{\mathrm{Me}}\mu_{\mathrm{Me}}(x,T) + N\mu(x,T)$ with $\mu_{\mathrm{Me}}(x,T)$ and $\mu(x,T)$ being the chemical potentials of the metal atoms and the chemical potential of the hydrogen isotopes in the metal at a certain hydrogen concentration x. Dividing this equation by the total number of metal atoms N_{Me} and considering equation (2.2) yields

$$\frac{G(x,T)}{N_{\mathrm{Me}}} \equiv g(x,T) = \mu_{\mathrm{Me}}(x,T) + x\left[\frac{\partial g(x,T)}{\partial x}\right]_{p,T}, \quad \text{with} \quad \mu(x,T) = \left[\frac{\partial g(x,T)}{\partial x}\right]_{p,T} \tag{2.53}$$

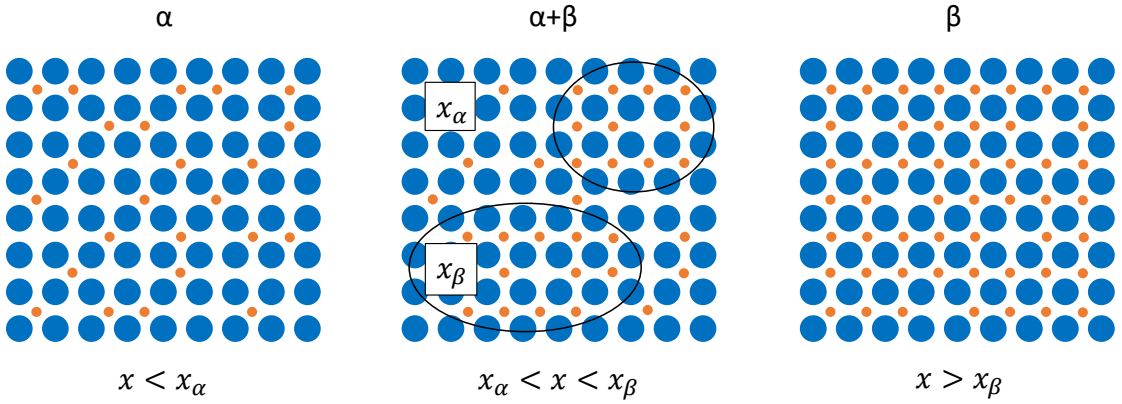

Fig. 2.5. Illustration of the distribution of hydrogen isotopes (orange dots) in the metal lattice (blue circles) for different concentration regimes. In the low-concentration α phase ($x < x_\alpha$) the isotopes are rather randomly distributed. While two phases coexist (α+β), the α phase has reached its fix maximum concentration x_α and the ordered hydride β phase precipitates at more and more locations with a fix concentration x_β [123].

By transformation, the chemical potential of the metal atoms writes

$$\mu_{\mathrm{Me}}(x,T) = g(x,T) - x\left(\frac{\partial g(x,T)}{\partial x}\right)_{p,T} \tag{2.54}$$

According to the criterion of phase equilibrium [120], the equilibrium chemical potentials of hydrogen isotopes dissolved in the two distinct phases $\mu^\alpha = \mu(x_\alpha, T)$ and $\mu^\beta = \mu(x_\beta, T)$ must be equal and fulfill equilibrium condition (2.12) with the gas phase. Moreover, thermodynamic equilibrium requires an equal chemical potential of the host metal atoms in both phases $\mu^\alpha_{\mathrm{Me}} = \mu_{\mathrm{Me}}(x_\alpha, T)$ and $\mu^\beta_{\mathrm{Me}} = \mu_{\mathrm{Me}}(x_\beta, T)$. Hence, the two-phase equilibrium conditions are

$$\mu^\alpha = \mu^\beta = \frac{1}{2}\mu^{\mathrm{g}} \qquad \text{with} \quad \mu^\alpha = \mu(x_\alpha, T) \qquad \text{and} \quad \mu^\beta = \mu(x_\beta, T) \tag{2.55}$$

$$\mu^\alpha_{\mathrm{Me}} = \mu^\beta_{\mathrm{Me}} \qquad \text{with} \quad \mu^\alpha_{\mathrm{Me}} = \mu_{\mathrm{Me}}(x_\alpha, T) \qquad \text{and} \quad \mu^\beta_{\mathrm{Me}} = \mu_{\mathrm{Me}}(x_\beta, T), . \tag{2.56}$$

Using relation (2.23), from condition (2.55) it follows that in the concentration range between x_α and x_β the famous Van't Hoff equation holds

$$\frac{1}{2}\ln\left(\frac{p_{\mathrm{dec}}}{p^\circ}\right) = \frac{\mu^\alpha - \frac{1}{2}\mu^{\mathrm{g},\circ}}{k_{\mathrm{B}}T} = \frac{\mu^\beta - \frac{1}{2}\mu^{\mathrm{g},\circ}}{k_{\mathrm{B}}T} \equiv \frac{\Delta\overline{H}^\circ_{\alpha\to\beta}}{k_{\mathrm{B}}T} - \frac{\Delta\overline{S}^\circ_{\alpha\to\beta}}{k_{\mathrm{B}}}. \tag{2.57}$$

The defined quantities $\Delta\overline{H}^\circ_{\alpha\to\beta}$ and $\Delta\overline{S}^\circ_{\alpha\to\beta}$ are the enthalpy and entropy of hydride formation, respectively.

Since in the entire two-phase region ($x_\alpha < x < x_\beta$) the chemical potential of the metal-hydrogen solution remains constant the two-phase equilibrium can exist at constant pressure, the decomposition pressure, which is only dependent on temperature. This is consistent with the Gibbs phase rule [136], which states that for a system of two components (hydrogen and metal) inheriting three phases (gas phase, α phase, β phase), the

number of degrees of freedom among the system variables p, T, x_α and x_β is one, the temperature. All other variables have to be fixed and are only dependent on temperature.

Inserting equation (2.54) into equilibrium condition (2.56) taking into account condition (2.55) leads to the general condition for the coexistence of two phases in equilibrium

$$\frac{g\,(x_\beta, T) - g\,(x_\alpha, T)}{x_\beta - x_\alpha} = \frac{1}{x_\beta - x_\alpha} \int_{x_\alpha}^{x_\beta} \mu(x, T)\ \mathrm{d}x = \mu\,(x^\alpha, T) = \mu\,(x_\beta, T)\,, \tag{2.58}$$

which is known as the Maxwell construction [114]. Its meaning becomes apparent when inserting the chemical potential $\mu\,(x, T)$ of hydrogen dissolved in metals (2.37) into equation (2.58). By neglecting excess contributions to the entropy and enthalpy of solution equation (2.58) reduced to

$$k_\mathrm{B} T \ln\left(\frac{x_\nu}{r - x_\nu}\right) + \epsilon_\mathrm{HH} N_\mathrm{adj} \left(\frac{x_\nu}{r} - \frac{1}{2}\right) = 0\,, \quad \text{for} \quad \nu = \alpha \text{ or } \nu = \beta\,. \tag{2.59}$$

Solving this equation for x^ν provides the corresponding critical concentrations x_α and x_β at a given temperature. The Van't Hoff relation for the plateau decomposition pressure is determined by inserting equation (2.59) into equation (2.37) (where excess contributions to the chemical potential are neglected) [122]

$$\frac{1}{2} \ln\left(\frac{p_\mathrm{dec}}{p^\circ}\right) = \frac{\epsilon_\mathrm{s} + \frac{1}{2}\epsilon_\mathrm{HH} N_\mathrm{adj} - \frac{1}{2}\mu^{\mathrm{g},\circ}}{k_\mathrm{B} T}\,. \tag{2.60}$$

Knowing both, the temperature dependency of the critical concentrations and the corresponding decomposition pressure enables correcting the plotted PCIs by considering a constant decomposition pressure p_dec for the entire concentration range $x_\alpha < x < x_\beta$ (see figure 2.4 for the example of the Pd-^{1}H system). It can be seen that the concentration range where two phases coexist narrows with temperature. Above a critical temperature $T_\mathrm{c} \approx -\epsilon_\mathrm{HH} N_\mathrm{adj}/(4k_\mathrm{B})$ the PCIs have a continuous positive slope and the coexistence of two separate phases becomes redundant [122]. Using the example of the Pd-^{1}H system, the theoretical temperature dependency of the critical concentrations x_α and x_β are plotted in a T-x phase diagram in figure 2.6 using equation (2.59). The right-hand graph of figure 2.6 contains the theoretically calculated Van't Hoff plot of the Pd-^{1}H system using equation (2.60). Its slope is proportional to the enthalpy or heat of hydride formation.

It is important to note that the presented lattice-gas model of metal-hydrogen solutions is the simplest approach to the theoretical explanation of PCIs, phase diagrams, and Van't Hoff plots. Moreover, the Pd-^{1}H system is one of the simplest metal-hydrogen systems and was therefore chosen as an example to explain the origin and effects of hydride formation in metals. Taking into account the ignored excess contributions to the enthalpy and entropy of solution would lead to a distortion of the PCIs and the phase diagram. Moreover, hydride formation is often accompanied by more complex side effects like the change of the lattice structure or the formation of lattice defects and stresses in the metal bulk. However, they require a more complex theoretical description to obtain accurate simulation results (for more details see the references [114], [136], [140]–[143]).

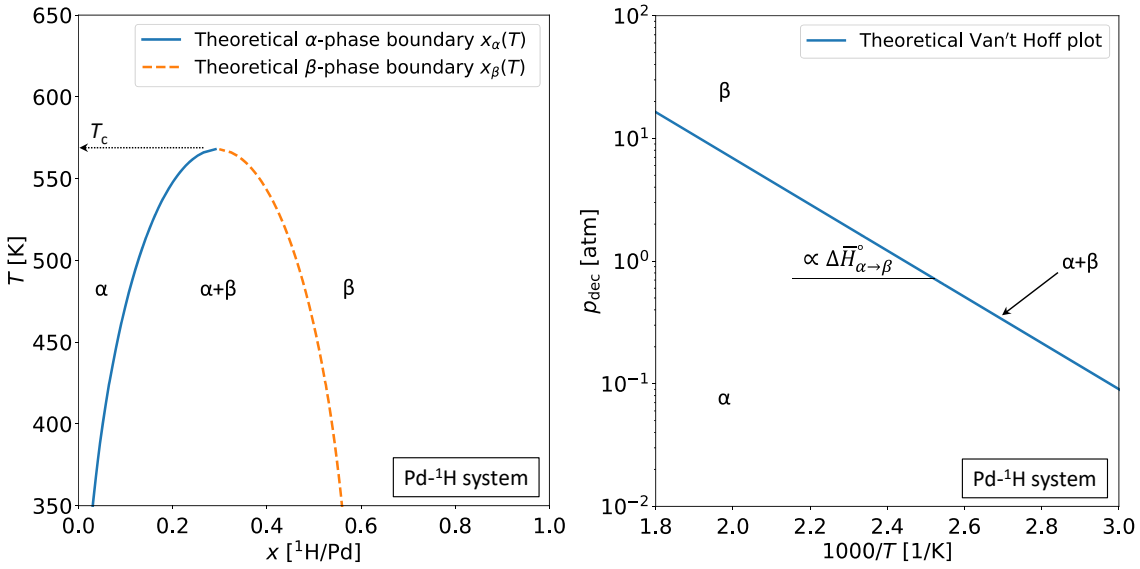

Fig. 2.6. [Left] Calculated T-x phase diagram of a simple exothermic metal-hydrogen system (Pd-^{1}H) using equation (2.59). [Right] Calculated Van't Hoff plot of a simple exothermic metal-hydrogen system (Pd-^{1}H) using equation (2.60).

For many metal-hydrogen systems, it is observed that an increase in the external hydrogen gas pressure leads to the formation of further hydride phases beyond the β phase. The PCIs of such metal-hydrogen solutions exhibit more than one plateau area where two phases coexist. Several theoretical multiplateau models have been developed in the past, giving insight into the underlying physical mechanisms. Significant progress in the development of multiplateau theories was made by the work of Rees and Kierstead [135], [144]–[146]. Kierstead extended Lachers single hydride model considering that metals showing PCIs with multiple plateaus contain several crystallographically different interstitial sites. Such groups of different interstitials may for example be octahedral and tetrahedral interstitial sites. The chemical potential of hydrogen isotopes occupying each group of interstitial sites is described by functions like equation (2.37) where each group of sites is characterized by different enthalpies and entropies of solution. Consequently, since at equilibrium, each group of sites must have an equal chemical potential, each group of sites is occupied with a different fractional concentration at a certain pressure. Moreover, each group experiences hydride formation at different decomposition pressures and in different concentration regimes. Therefore, each plateau area corresponds to hydride formation in a different group of sites. Furthermore, the model assumes that certain groups of sites may be created or annihilated when entering a new concentration regime, for example as a consequence of a change of the crystal structure during hydride formation in the same or in a different group. In multiplateau PCIs the plateau pressure is usually not perfectly constant but slightly sloped [128]. Examples of multipleatau metal-hydrogen systems are the Y-H system, the Zr-H system, the Ti-H system, as well as numerous metal hydrogen systems based on rare earth metals and specific alloys [136].

2.2. Transport processes

The previous section introduced the physical concepts which determine the absorption behavior of metals exposed to a multi-isotopic hydrogen gas in thermodynamic equilibrium. This section provides the tools for calculating the kinetics of hydrogen transport processes in thermodynamic non-equilibrium.

2.2.1. Diffusion

Hydrogen isotopes dissolved in the lattice of a metal bulk occupy interstitial potential energy wells where they take up different discrete vibrational energy states. The occupation distribution of these states is strongly temperature dependent. A migration of hydrogen isotopes through the metal occurs since under certain conditions it is possible for an isotope to jump into an adjacent interstitial site. The dominant physical mechanism which enables the transition into a neighboring site differs among temperature regimes. At low temperatures, this migration is dominated by tunneling processes and therefore a rather rare process. However, in the temperature range relevant to the applications discussed in this work ($300\,\mathrm{K} < T < 1000\,\mathrm{K}$), thermally activated over barrier jumps are energetically possible for a significant fraction of the isotopes. They occur at a relatively high rate. The energetic height of the potential energy barriers E_m which the oscillators have to overcome to reach adjacent interstitial sites is determined by the dimension and the bond strength of the lattice atoms. As long as the neighboring site is not occupied by another isotope the jump direction after each transition is completely random. This leads to an unpredictable random walk every hydrogen isotope performs through the crystal lattice, known as interstitial diffusion.

From the random walk model, it can be derived that when assuming an equal distance between interstitial sites α_int, the mean square distance a hydrogen isotope has passed after n jumps from its initial location is $\left\langle r_n^2 \right\rangle = n\alpha_\mathrm{int}^2$. Following the random walk approach in three dimensions[147], the probability for an interstitially dissolved isotope to have migrated from its origin at time $t = 0\,\mathrm{s}$ to a distance between r and $r + \mathrm{d}r$ after the time t can be expressed as

$$f_\mathrm{m}(r,t) = \frac{1}{(4\pi D t)^{\frac{3}{2}}} \exp\left(-\frac{r^2}{4Dt}\right). \tag{2.61}$$

As a consequence, the mean square distance $\left\langle r^2 \right\rangle$ is calculated with:

$$\left\langle r^2 \right\rangle = \int_{-\infty}^{\infty} r^2 f_\mathrm{m}(r,t)\,\mathrm{d}r = 6Dt = n\alpha_\mathrm{int}^2\,, \quad \text{with} \quad D = \frac{1}{6}\varpi\alpha_\mathrm{int}^2\,. \tag{2.62}$$

where $\varpi \equiv n/t$ is defined as the average jump frequency of the hydrogen atoms in any possible direction. Parameter D is known as the intrinsic diffusion coefficient or diffusivity [m^2/s]. In this work, it is interpreted as a measure for the velocity with which the random walk of interstitially dissolved solvent atoms in the metal proceeds. By expressing

the jump frequency of a hydrogen isotope towards one particular neighboring interstitial site as $\omega = \varpi / N_{\mathrm{adj}}$ and the probability that this interstitial site is not yet occupied by another hydrogen isotope with $(1 - \theta_{\mathrm{b,tot}})$, the diffusion coefficient defined in equation (2.62) transforms to

$$D = \gamma_{\mathrm{int}} a_0^2 (1 - \theta_{\mathrm{b,tot}}) \omega \,, \quad \text{with} \quad \gamma_{\mathrm{int}} \equiv \frac{1}{6} N_{\mathrm{adj}} \alpha_{\mathrm{int}}^2 / a_0^2 \,. \tag{2.63}$$

In this expression [148], a_0 is the cubic lattice parameter and γ_{int} a geometrical factor characteristic for the lattice geometry and the type of available interstitial sites (usually octahedral or tetrahedral sites). For simplicity, this explanation refers to cubic crystal structures. An extension to non-cubic lattices can be found in [149]. The used expression of the bulk coverage $\theta_{\mathrm{b,tot}} = \sum_i \theta_{\mathrm{b},i}$ refers to the total number of occupied interstitial sites including all involved hydrogen isotope species. Applying statistical mechanics it was found that the temperature dependency of the jump frequency ω follows an Arrhenius-type equation of the form

$$\omega = \nu_0 \exp\left(-\frac{\Delta G_{\mathrm{m}}}{k_{\mathrm{B}} T}\right) = \nu_0 \exp\left(\frac{\Delta S_{\mathrm{m}}}{k_{\mathrm{B}}}\right) \exp\left(-\frac{\Delta H_{\mathrm{m}}}{k_{\mathrm{B}} T}\right) \tag{2.64}$$

where ΔG_{m}, ΔH_{m} and ΔS_{m} are the Gibbs free energy, the enthalpy and entropy of migration, respectively. The work required to move a dilute atom from its interstitial position to the top of the saddle point of an adjacent potential energy barrier in an isothermal and reversible process is equal to the change of the Gibbs free energy ΔG_{m} of the nearby region of the lattice [147]. Hence, ν_0 can be understood as the attempt frequency with which the hydrogen isotopes oscillate towards a particular direction and the exponential factor represents the probability that a hydrogen isotope fulfills the energetic conditions to overcome the potential energy barrier. For a dilute metal-hydrogen solution ($\theta_{\mathrm{b}} \ll 1$), uniting the equations (2.63) and (2.64) leads to the known Arrhenius type temperature relation of the intrinsic interstitial diffusion coefficient for hydrogen in metals

$$D(T) = \gamma_{\mathrm{int}} a_0^2 \nu_0 \exp\left(\frac{\Delta S_{\mathrm{m}}}{k_{\mathrm{B}}}\right) \exp\left(-\frac{\Delta H_{\mathrm{m}}}{k_{\mathrm{B}} T}\right) = D^0 \exp\left(-\frac{E_{\mathrm{m}}}{k_{\mathrm{B}} T}\right). \tag{2.65}$$

In this expression, the enthalpy of migration is considered as the activation energy of diffusion $\Delta H_{\mathrm{m}} = E_{\mathrm{m}}$ and can be interpreted as the average heights of the potential hills between two interstitials as shown in the figure 2.7. The factor D_0 containing the entropy term is called the pre-exponential factor of the diffusion coefficient. In general, interstitial diffusion of heavier impurity atoms in metals like C, N or O is described by the same equations. However, due to the much lower activation energy of diffusion for hydrogen isotopes in metals, its diffusivity is many orders of magnitude faster [150]. It was found that diffusion in BCC lattices (Fe, V, Nb, Ta, etc.) is faster than in FCC crystal structures (Cu, Ni, Pd, etc), partially because there are no blocking metal atoms in the diffusion path to the adjacent interstitial sites and the distance between two sites is generally shorter (see figure 2.2). For these reasons, the potential energy barriers and thus the activation energy E_{m} in BCC lattices are smaller. In HCP lattices (Y, Ti, Zr, etc.) diffusion proceeds slightly slower than in FCC latices since the distance between interstitial sites in HCP lattices is usually a bit further [114].

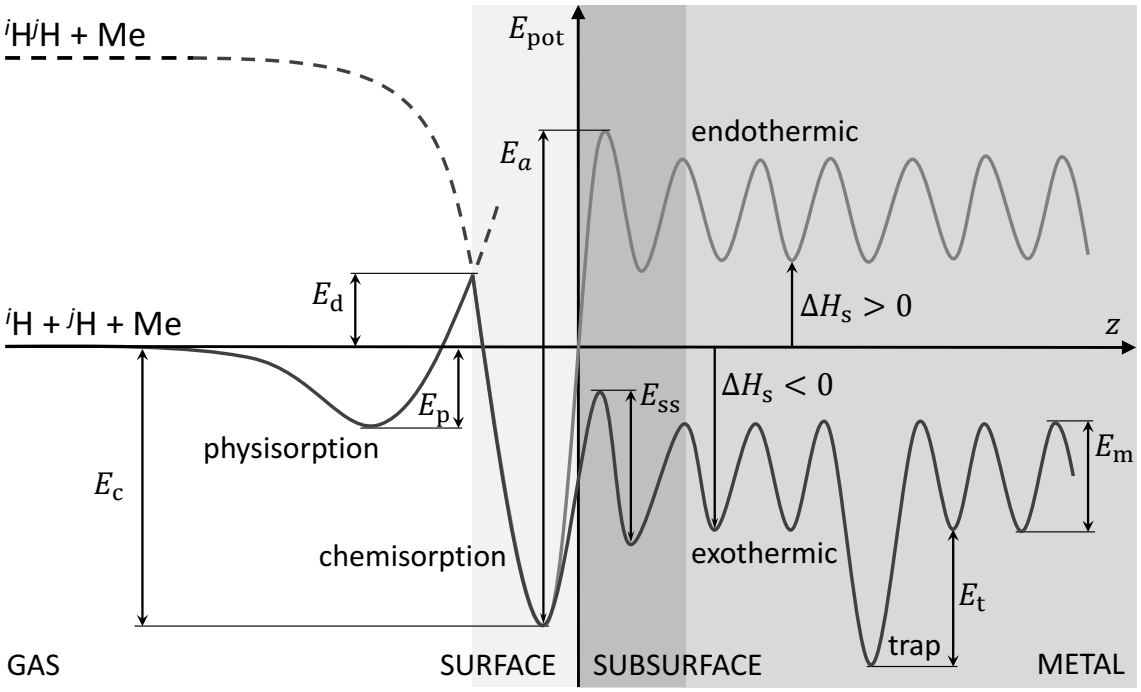

Fig. 2.7. One-dimensional qualitative potential energy curves for activated adsorption of hydrogen isotopes onto a metal surface and into the metal bulk forming an endothermic or exothermic metal-hydrogen solution. The image illustrates the potential energy landscape of interstitial sites in the metal lattices where hydrogen isotopes move by diffusion.

For the diffusion process of different hydrogen isotopes ^{i}H in the same metal it could be observed that $D_1(T) < D_2(T) < D_3(T)$. This inequality is known as the isotope effect of hydrogen diffusion in metals. It partially originates from non-classical effects related to the slightly different chemistry between different hydrogen isotopes and the metal. They are found to be responsible for the relationship $E_{m,1} < E_{m,2} < E_{m,3}$ [148]. An even stronger contribution to the isotope effect is that the attempt frequency ν_0 is strongly dependent on the mass of the oscillating diffuser, represented by the proportionality relation $\nu_{0,i} \propto 1/\sqrt{m_i}$. Estimating the variation of the diffusion coefficients among different hydrogen isotopes in the same metal by applying the relations

$$\frac{D_i}{D_j} = \sqrt{\frac{m_j}{m_i}} = \sqrt{M_j/M_i}\,. \tag{2.66}$$

turns out to be a relatively accurate method [150]. In this equation, M_i is the molar mass of the corresponding hydrogen isotope ^{i}H.

In the classical random motion model the intrinsic diffusion coefficient of a solvent in a metal lattice can be related to the mobility B of the diffusing particles by the Einstein relation $D = Bk_BT$. The mobility is defined through the equation $\vec{u}_m = B \cdot \vec{\mathcal{F}}_m$, where $\vec{u}$ is the establishing average drift velocity of the diffusing particles if they would be exposed to an external force $\vec{\mathcal{F}}_m$ [114]. According to equation (2.35) an inhomogeneous distribution of hydrogen isotopes ^{i}H inside of the metal lattice implies a spatial gradient of the chemical potential $\vec{\nabla}\mu_i$. As a consequence, a driving force $\vec{\mathcal{F}}_{m,i} = -\vec{\nabla}\mu_i$ arises which leads

to a net molar diffusion flux $\vec{J}_{\mathrm{dif},i}$ of the hydrogen isotopes ${}^{i}\mathrm{H}$ through the metal lattice expressed by Fick's first law of diffusion

$$\vec{J}_{\mathrm{dif},i} = c_i \vec{u}_{\mathrm{m},i} = -B_i c_i \vec{\nabla}\mu_i = -\frac{D_i c_i}{k_\mathrm{B} T}\frac{\partial \mu_i}{\partial c_i}\vec{\nabla} c_i = -\overline{D}_i \vec{\nabla} c_i \,. \tag{2.67}$$

A molar particle flux is defined as the mole number of particles $\varkappa_s = m_s/M_s$ of species s that pass per unit time through a unit area that is perpendicular to the direction of the flux vector. Here, m_s is the mass and M_s is the molar mass of the corresponding particles. Parameter $\overline{D}_i$ is called the chemical diffusion coefficient. In dilute solutions ($c_i \to 0$), the chemical potential of hydrogen in metals described by equation (2.35) can be approximated by the relation $\mu_i \approx \epsilon_{\mathrm{s},i} + k_\mathrm{B} T \ln c_i/c_{\max}$ which leads to the derivative $\partial\mu_i/\partial c_i \approx k_\mathrm{B} T/c_i$. Therefore, at low concentrations, the chemical diffusion coefficient approaches the intrinsic diffusion coefficient $\overline{D}_i \to D = B k_\mathrm{B} T$.

Usually, the net diffusion flux arising from the gradient of the chemical potential in non-equilibrium conditions changes the isotope distribution in the metal until all gradients have vanished and the system is in equilibrium. The time evolution of the isotope concentration at a certain position in the metal is described by the mass continuity equation

$$\frac{\partial c_i}{\partial t} = -\vec{\nabla}\vec{J}_i + \varsigma_i = -\vec{\nabla}\vec{J}_{\mathrm{dif},i} + \varsigma = \vec{\nabla}\left(\overline{D}_i \vec{\nabla} c_i\right) + \varsigma_i \tag{2.68}$$

By substituting the hydrogen isotope flux $\vec{J}_i$ in the first equation with the diffusion flux $\vec{J}_{\mathrm{dif},i}$ as defined in relation (2.67), the right-hand side of equation (2.68) takes the form of the famous diffusion equation or Fick's second law. The term ς_i represents a possible particle source or sink and has the units $[\mathrm{mol/m^3/s}]$. For example, this may be a chemical or nuclear reaction in which hydrogen isotopes are generated or annihilated at a certain rate.

Solute diffusion in liquified metal is a rather poorly understood physical mechanism for which several different theoretical models (Einstein relation model, density fluctuation model, modified hole theory, etc.) were developed in the past [151]–[155]. The models generally result in the definition of a diffusion coefficient that follows the same Arrhenius type temperature dependence (2.65) as found for solid metals [156].

2.2.2. Trapping

While migrating through the crystal lattice the hydrogen isotopes will come across microstructural imperfections such as impurities, internal interfaces, grain boundaries, voids, vacancies, and dislocations. Some of these imperfections significantly reduce the potential energy of an encountering hydrogen isotope. This implies a stronger bond between the imperfect lattice region compared to the surrounding interstitial sites. Lattice imperfections with such properties are referred to as trapping sites. The average energy value per isotope by which the binding energy $\epsilon_\mathrm{t} = \epsilon_\mathrm{s} - E_\mathrm{t}$ of a trapping site is lower than the binding energy of the regular interstitial sites $\epsilon_\mathrm{s} < 0$ is labeled with $E_\mathrm{t} > 0$ (see figure 2.7).

Certainly, the number of available trap sites per unit volume $\mathcal{N}^{\mathrm{T}}$ [mol/m^{-3}] is much lower than the concentration of lattice sites $\mathcal{N}^{\mathrm{L}}$ [mol/m^{-3}]. Despite this fact, if the solubility of the metal is low the molar concentration of hydrogen isotopes occupying trap sites c^{T} can exceed the molar concentration of hydrogen isotopes in lattice sites c^{L} [147]. This usually occurs for endothermic hydrogen-absorbing metals at low temperatures. Under such circumstances, trapping highly influences the solubility and diffusivity of hydrogen in metals which is discussed in the following. Since exothermic hydride-forming metals have a comparably high solubility which even increases towards lower temperatures the effect of trapping sites is found to have a negligible effect [147], [157].

For this reason, the quantitative treatment of the trapping phenomenon focuses on endothermic metal hydrogen systems which under the pressure and temperature conditions relevant to this work can be considered dilute solutions. Dilute solutions are characterized by a low ratio between occupied and available lattice sites ($\theta_{\mathrm{b}}^{\mathrm{L}} \ll 1$) where $c^{\mathrm{L}} = \mathcal{N}^{\mathrm{L}}\theta_{\mathrm{b}}^{\mathrm{L}}$. It is generally assumed that even in thermodynamic non-equilibrium hydrogen isotopes occupying the traps (T) and those in the regular lattice sites (L) are always in thermodynamic equilibrium. This implies an equality of their chemical potentials $\mu^{\mathrm{L}} = \mu^{\mathrm{T}}$ [158]. When ignoring the excess contributions to the enthalpy and entropy of solution, the chemical potentials of hydrogen occupying the lattice sites μ^{L} and hydrogen occupying the trap sites μ^{T} can be approximately described by equation (2.33). Since in the considered metal-hydrogen solution the concentration of occupied lattice sites is low ($\theta_{\mathrm{b}}^{\mathrm{L}} \ll 1$) it is assumed that $\theta_{\mathrm{b}}^{\mathrm{L}}/(1-\theta_{\mathrm{b}}^{\mathrm{L}}) \approx \theta_{\mathrm{b}}^{\mathrm{L}}$. In addition to that, even if $c^{\mathrm{T}} \gg c^{\mathrm{L}}$, because $\mathcal{N}^{\mathrm{T}} \ll \mathcal{N}^{\mathrm{L}}$, the overall concentration in the metal will remain low. This is why the H-H interaction terms in the expressions for the chemical potentials μ^{L} and μ^{T} can be neglected. With these assumptions the equilibrium condition between the concentration $\mu^{\mathrm{L}} = \mu^{\mathrm{T}}$ writes

$$\frac{1}{\theta_{\mathrm{b}}^{\mathrm{L}}}\left(\frac{\theta_{\mathrm{b}}^{\mathrm{T}}}{1-\theta_{\mathrm{b}}^{\mathrm{T}}}\right) \approx \exp\left(\frac{-E_{\mathrm{t}}}{k_{\mathrm{B}}T}\right). \tag{2.69}$$

Here, $\theta_{\mathrm{b}}^{\mathrm{T}}$ stands for the ratio between occupied trap sites and available trap sites. Inserting $c^{\mathrm{T}} = \mathcal{N}^{\mathrm{T}}\theta_{\mathrm{b}}^{\mathrm{T}}$ and $c^{\mathrm{L}} = \mathcal{N}^{\mathrm{L}}\theta_{\mathrm{b}}^{\mathrm{L}}$ into equation (2.69) provides a relation for the ratio between the concentration of occupied trap sites and occupied lattice sites

$$\frac{c^{\mathrm{T}}}{c^{\mathrm{L}}} \approx \frac{\mathcal{N}^{\mathrm{T}}}{\mathcal{N}^{\mathrm{L}}}\left(1-\theta_{\mathrm{b}}^{\mathrm{T}}\right)\exp\left(\frac{-E_{\mathrm{t}}}{k_{\mathrm{B}}T}\right) \tag{2.70}$$

The Sieverts' constant $K_{\mathrm{s},i}$ of an endothermic hydrogen-absorbing metal may be measured by experimentally determining the total amount of absorbed hydrogen isotopes ^{i}H in the metal sample after reaching equilibrium while maintaining a certain external partial pressure $\sqrt{p_{ii}}$ of a mono-isotopic hydrogen gas $^{i}\mathrm{H}_2$. Such a measurement would need to be repeated for different temperatures in order to obtain the temperature relation of the Sieverts' constant applying equation (2.50). It is evident that if part of the absorbed hydrogen isotopes occupy trapping sites the measured content of absorbed hydrogen isotopes will be different compared to a case in which the same metal sample was pure and free

from traps. The measured so-called effective Sieverts' constant $K_{s,i}^{\mathrm{eff}}$ would then fulfill the following relation with the real Sieverts' constant $K_{s,i} = c_i^{\mathrm{L}} / \sqrt{p_{ii}}$ of the pure metal lattice

$$K_{s,i}^{\mathrm{eff}} = \frac{c_i^{\mathrm{L}} + c_i^{\mathrm{T}}}{\sqrt{p_{ii}}} = K_{s,i} + \frac{c_i^{\mathrm{T}}}{\sqrt{p_{ii}}} = K_{s,i} + \frac{c_i^{\mathrm{T}}}{c_i^{\mathrm{L}}} K_{s,i} = K_{s,i} \left[1 + \frac{\mathcal{N}^{\mathrm{T}}}{\mathcal{N}^{\mathrm{L}}} \left(1 - \theta_{\mathrm{b}}^{\mathrm{T}} \right) \exp\left(\frac{-E_{\mathrm{t}}}{k_{\mathrm{B}} T} \right) \right] \quad (2.71)$$

In most experimental campaigns dedicated to the determination of hydrogen transport parameters in Fe-based alloys it is assumed that $\theta_{\mathrm{b}}^{\mathrm{T}} \ll 1$ which leads to the widely applied formula [159]–[161]

$$K_{s,i}^{\mathrm{eff}} = K_{s,i} \left[1 + \frac{\mathcal{N}^{\mathrm{T}}}{\mathcal{N}^{\mathrm{L}}} \left(1 - \theta_{\mathrm{b}}^{\mathrm{T}} \right) \exp\left(\frac{-E_{\mathrm{t}}}{k_{\mathrm{B}} T} \right) \right] \approx K_{s,i} \left[1 + \frac{\mathcal{N}^{\mathrm{T}}}{\mathcal{N}^{\mathrm{L}}} \exp\left(\frac{-E_{\mathrm{t}}}{k_{\mathrm{B}} T} \right) \right] . \quad (2.72)$$

It can be seen that $K_{s,i}^{\mathrm{eff}} > K_{s,i}$ which shows that the trapping increases the hydrogen solubility of a metal.

The diffusion coefficient is influenced by the presence of trapping sites as well. Therefore, in a measurement of the diffusion coefficient of hydrogen isotopes in a metal sample containing trapping sites the observed effective diffusion coefficient will differ from the real diffusion coefficient of the pure metal. This becomes apparent by observing the effect of trapping on Fick's second law assuming the presence of trapping sites and a homogeneous diffusion coefficient $\overline{D}_i$ [147], [162]. Due to the conservation of mass, the temporal evolution of the lattice concentration c_i^{L} is determined by the diffusion flow of hydrogen isotopes through the lattice sites and the conversion of lattice hydrogen isotopes into a trapped hydrogen isotopes. Mathematically, this can be considered as a particle sink occurring with the rate $\varsigma = -\partial c^{\mathrm{T}} / \partial t$. According to equation (2.68), this yields

$$\frac{\partial c_i^{\mathrm{L}}}{\partial t} = \vec{\nabla} \left(\overline{D}_i \vec{\nabla} c_i^{\mathrm{L}} \right) - \frac{\partial c_i^{\mathrm{T}}}{\partial t} = \overline{D}_i \Delta c_i^{\mathrm{L}} - \frac{\partial c_i^{\mathrm{T}}}{\partial c_i^{\mathrm{L}}} \frac{\partial c_i^{\mathrm{L}}}{\partial t} = \overline{D}_i \left(1 + \frac{\partial c_i^{\mathrm{T}}}{\partial c_i^{\mathrm{L}}} \right)^{-1} \Delta c_i^{\mathrm{L}} \equiv \overline{D}_{\mathrm{eff},i} \Delta c_i^{\mathrm{L}} \quad (2.73)$$

where $\overline{D}_{\mathrm{eff},i}$ is the effective chemical diffusion coefficient and Δ the Laplace operator. In endothermic hydrogen absorbers or dilute solutions $\overline{D}_{\mathrm{eff},i} \rightarrow D_{\mathrm{eff},i}$. Solving the derivative in parenthesis using equilibrium condition (2.70) leads to

$$\overline{D}_{\mathrm{eff},i} = \overline{D}_i \left[1 + \frac{\mathcal{N}^{\mathrm{T}}}{\mathcal{N}^{\mathrm{L}}} \left(1 - \theta_{\mathrm{b}}^{\mathrm{T}} \right) \exp\left(\frac{-E_{\mathrm{t}}}{k_{\mathrm{B}} T} \right) \right]^{-1} \approx \overline{D}_i \left[1 + \frac{\mathcal{N}^{\mathrm{T}}}{\mathcal{N}^{\mathrm{L}}} \exp\left(\frac{-E_{\mathrm{t}}}{k_{\mathrm{B}} T} \right) \right]^{-1} \quad (2.74)$$

2.2.3. Metal-metal interfaces

As discussed in section 2.2.1, the time evolution of the concentration profiles and fluxes of hydrogen isotopes in metal are described by Fick's first (2.67) and second (2.68) law of diffusion. If in chemical non-equilibrium two hydrogen-loaded metals Me^a and Me^b are put in contact with each other, a net diffusion flux of hydrogen isotopes occurs which is driven by the gradients of their chemical potentials in the two metals. However, boundary conditions apply at the metal-metal interface. It is reasonable to assume that even in chemical non-equilibrium, in an infinitesimal section crossing the interface (int), the

chemical potentials of the isotope ^{i}H in the two metals are continuous and therefore equal $\mu^{a}_{\mathrm{int},i} = \mu^{b}_{\mathrm{int},i}$. In this case, the relationship between the concentrations $c^{a}_{\mathrm{int},i}$ and $c^{b}_{\mathrm{int},i}$ at the interface is always determined by equilibrium condition (2.42) or its simpler expression for dilute solutions (2.51). In other words, at the interface, the concentration is a discontinuous function and experiences a jump. In addition to that, mass continuity across an interface enforces the continuity of the hydrogen isotope diffusion fluxes $J^{a}_{\mathrm{dif,int},i} = J^{b}_{\mathrm{dif,int},i}$. Using Fick's first (2.67) law this condition may be expressed by

$$-\overline{D}^{a}_{i} \nabla c^{a}_{\mathrm{int},i} = -\overline{D}^{b}_{i} \nabla c^{b}_{\mathrm{int},i} \tag{2.75}$$

Since the diffusion coefficients in the two metals are different, condition (2.75) is only fulfilled if the concentration gradients on both sides of the interface differ as well.

If instead, a solid metal (SM) is in contact with a liquid metal (LM) the same boundary conditions $J^{\mathrm{LM}}_{\mathrm{int},i} = J^{\mathrm{SM}}_{\mathrm{int},i}$ and $\mu^{\mathrm{LM}}_{\mathrm{int},i} = \mu^{\mathrm{SM}}_{\mathrm{int},i}$ apply. As long as the liquid metal is stationary it may be treated as a solid metal. However, if the liquid metal has a finite flow velocity $\vec{u} \neq 0$ the time evolution of the concentration profile in the liquid metal is described by a modified expression of Fick's second law. This is because the total flux of hydrogen isotopes through an infinitesimal volume in the liquid metal is now the sum of the diffusion flux and an advective flux term $\vec{J}_i = c_i \vec{u} + \vec{J}_{\mathrm{dif},i}$ [163]. Hence, the modified Fick's second law for liquid metal flows writes

$$\frac{\partial c_i}{\partial t} = -\vec{\nabla}\vec{J}_i + \varsigma_i = -\vec{\nabla}\left(c_i\vec{u} + \vec{J}_{\mathrm{dif},i}\right) + \varsigma_i = \vec{\nabla}\left(\overline{D}^{\mathrm{LM}}_{i} \cdot \vec{\nabla} c_i\right) - \vec{\nabla}\left(c_i\vec{u}\right) + \varsigma_i\,, \tag{2.76}$$

where $\overline{D}^{\mathrm{LM}}_{i}$ is the chemical diffusion coefficient of isotope species ^{i}H in the liquid metal. It can be seen that solving this equation for each position in the liquid requires knowing the exact velocity profile. Unfortunately, obtaining the velocity profile is often tricky and may only be calculated in extensive three-dimensional simulations by solving even further partial differential equations (Navier-Stokes equation, magneto-hydrodynamic (MHD) equations, etc.). Therefore, the transfer of hydrogen isotopes across a metal surface in contact with a laminar or turbulent liquid metal flow is approximately described assuming that close to the interface viscous forces prevail and the flow velocity at the interface approaches zero ($\vec{u}_{\mathrm{int}} \to 0$). The more turbulent the flow, the narrower the region where the main velocity drop occurs, and the flatter the time-averaged velocity profile of the core flow (CF) [164]. Hence, in stationary state and if $\varsigma_i = 0$, close to the interface equation (2.76) approaches $\partial c_i/\partial t = \vec{\nabla}(\overline{D}^{\mathrm{LM}}_{i} \cdot \vec{\nabla} c_i) = \vec{\nabla}\vec{J}_i$ [165]. Solving this equation for the stationary case ($\partial c_i/\partial t = 0$) reveals a linear concentration profile close to the interface in perpendicular direction to the metal surface. This is illustrated in figure 2.8. The more the time-averaged velocity increases with distance from the interface, the more the advection term of equation 2.76 determines the concentration profile in the core flow. As a consequence, the faster and more turbulent the flow conditions are, the flatter the concentration profile in the core flow will be.

In the boundary layer (BL) approximation it is assumed that the linear part of the concentration profile occurs in a thin layer of width d_{BL} at the interface and ranges from

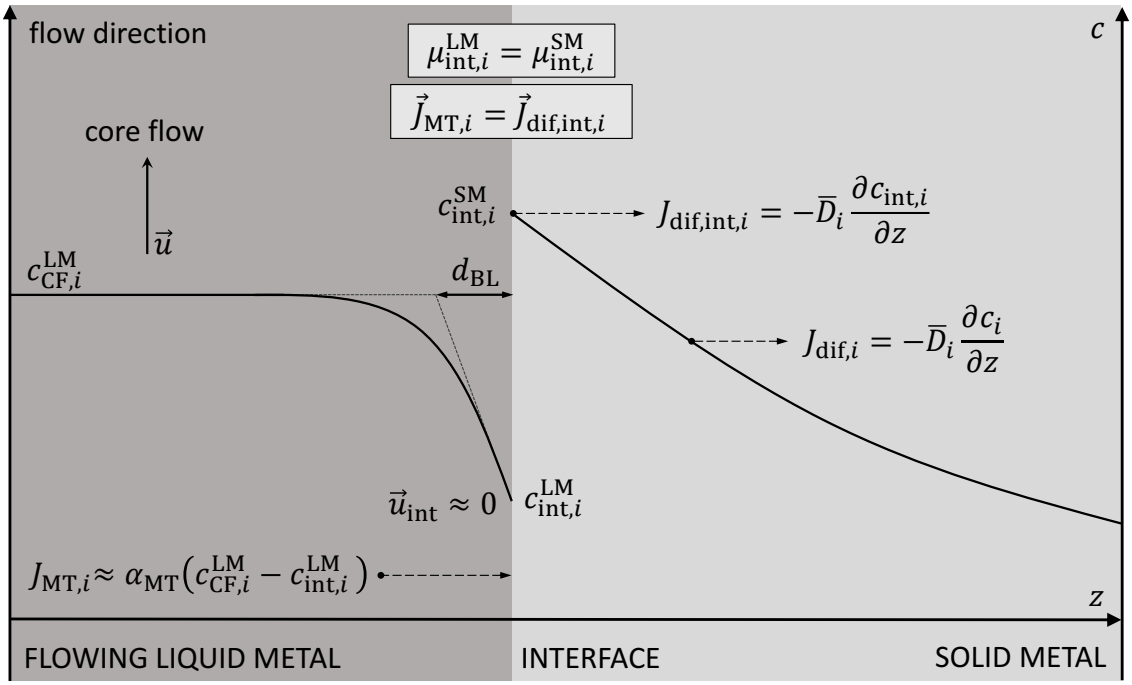

Fig. 2.8. Illustration of the concentration and flux distribution when a solid metal is put in contact with a hydrogen-loaded flowing liquid metal.

the concentration $c^{\mathrm{LM}}_{\mathrm{int},i}$ at the interface to the mean concentration $c^{\mathrm{LM}}_{\mathrm{CF},i}$ in the core flow (see figure 2.8). With these boundary conditions, the mass transfer flux $\vec{J}_{\mathrm{MT},i}$ in the boundary layer can be approximated by the solution of equation $\vec{\nabla}(\overline{D}^{\mathrm{LM}}_i \cdot \vec{\nabla} c_i) = \vec{\nabla}\vec{J}_{\mathrm{MT},i} = 0$. In one dimension, directed normal to the interface, it writes [165]–[167]

$$J_{\mathrm{MT},i} \approx \frac{\overline{D}^{\mathrm{LM}}_i}{d_{\mathrm{BL}}} \cdot \left(c^{\mathrm{LM}}_{\mathrm{int},i} - c^{\mathrm{LM}}_{\mathrm{CF},i}\right) = \alpha_{\mathrm{MT}} \left(c^{\mathrm{LM}}_{\mathrm{int},i} - c^{\mathrm{LM}}_{\mathrm{CF},i}\right) . \tag{2.77}$$

The defined parameter α_{MT} is the mass transfer coefficient. It depends on d_{BL} and hence on the distance from the interface where the advective flux contribution starts dominating the diffusion flux. It can be approximately described by the dimensionless Sherwood number Sh [166]

$$\mathrm{Sh} = \frac{\alpha_{\mathrm{MT}} L_{\mathrm{f}}}{\overline{D}^{\mathrm{LM}}} , \tag{2.78}$$

where L_{f} is the characteristic length of the flow environment. The dependence of the Sherwood number from the time-averaged flow velocity, the flow viscosity, the diffusion coefficient and the fluid density could be measured for many different flow conditions (pipe flow, pebble bed flow, etc.) [166], [168], [169]. Because of $\mu^{\mathrm{LM}}_{\mathrm{int},i} = \mu^{\mathrm{SM}}_{\mathrm{int},i}$, the interface concentration $c^{\mathrm{LM}}_{\mathrm{int},i}$ of the liquid metal flow is determined by equilibrium condition (2.51), and for dilute solutions by equilibrium condition (2.42). Moreover, at the interface, boundary condition $J^{\mathrm{LM}}_{\mathrm{int},i} = J^{\mathrm{SM}}_{\mathrm{int},i}$ transforms to

$$\alpha_{\mathrm{MT}} \left(c^{\mathrm{LM}}_{\mathrm{CF},i} - c^{\mathrm{LM}}_{\mathrm{int},i}\right) = J^{\mathrm{SM}}_{\mathrm{dif,int},i} . \tag{2.79}$$

2.2.4. Gas-metal interfaces

The adsorption/desorption process at a gas-metal interface is well understood by observing the qualitative potential energy curve of a hydrogen isotope ^{i}H as drawn in figure 2.7. The zero-state potential energy of the graph is assigned to a hydrogen isotope in the gas phase bound to a diatomic molecule far from the metal surface. Atomic unbound hydrogen isotopes in the gas phase would have a higher potential energy of about 2.238 eV which corresponds to half of the bond dissociation energy of the molecule [124], [170]. Upon entering the gas-metal interface region, the ^{i}H^{j}H molecule is noticeably attracted by van der Waals forces approximately described by the Lennard-Jones potential. It consists of an attractive term that decreases by a power of six with distance from the metal surface and a repulsive term that decreases by the power of twelve. As a result, at a distance of about half a molecular radius, the potential energy curve exhibits a minimum before it steeply increases. The resulting relatively weak binding of the molecule ^{i}H^{j}H to the metal surface is known as physisorption and is a spontaneous exothermic process [123], [171]. Closer to the metal, the increasing electron density of the surface atoms perturbs the internal potential energy curve of the diatomic gas molecules. This leads to an increase in the equilibrium distance between the bound nuclei of the diatomic molecule and a reduced bond dissociation energy [172].

At a certain distance, the potential energy of hydrogen in the atomic state falls below that of hydrogen in the molecular state and dissociation becomes energetically favorable. The energy barrier which a molecule has to overcome in order to reach the distance where the two potential energy curves intercept, is either above (activated dissociation) or below (non-activated dissociation) the zero energy line. In the latter case, the dissociation process is fast and occurs spontaneously. In contrast, overcoming the energy barrier of an activated dissociation process requires the vibrational and/or translational (kinetic) energy states of the gas molecule to be thermally excited to a certain energy state [172]. The probability for an incoming molecule to overcome the energy barrier for activated dissociation is represented by the unit-less sticking coefficient

$$\alpha_{\mathrm{s}} = \alpha_{\mathrm{s}}^{0} \cdot \exp\left(\frac{-2E_{\mathrm{d}}}{k_{\mathrm{B}}T}\right) \tag{2.80}$$

where $0 \leq \alpha_{\mathrm{s}}^{0} \leq 1$. It has been shown that the cleaner the metal surface the lower the activation energy E_{d} required for dissociation [173]. For very clean surfaces, $E_{\mathrm{d}} \approx 0$ and $\alpha_{\mathrm{s}}^{0} \approx 1$. On transition metals, dissociation is usually a non-activated process for which the sticking probability is $\alpha_{\mathrm{s}} \approx 1$ [174]. After a molecule is torn apart the hydrogen isotopes occupy ionic or covalent bonding states with the surface atoms [175]. The process of dissociation and subsequent bonding to the surface atoms is called chemisorption and is represented by a significantly lower potential minimum compared to the enthalpy of physisorption.

A crucial condition for a gas molecule to dissociate and reach the chemisorbed state in atomic form instead of being repelled back into the gas is that vacant interstitial sites

are available on the surface. The degree of superficial site occupation is described by the surface coverage $\theta_c = \sum_i \nu_i/\nu_s$ which is defined as the ratio between the sum of the areal molar densities of occupied sites ν_i [mol/m^2] of the three hydrogen isotopes and the areal molar density of existing surface sites ν_s [mol/m^2]. It should be mentioned that the sticking coefficient in equation (2.80) defines the probability for dissociation and chemisorption to occur in case $\theta_c \ll 1$ [170]. If the surface coverage is higher, the probability for dissociated hydrogen isotopes to find an empty site can be approximated by the product $\alpha_s \cdot (1-\theta_c)^2$. Hence, it is possible to express the absolute value of the molecular flux $j_{d,ij}$ of incoming dissociated and chemisorbed molecules ${}^i\mathrm{H}^j\mathrm{H}$ by

$$j_{d,ij} = \sigma\alpha_s(1-\theta_c)^2\Gamma_{ij} \tag{2.81}$$

where σ is the surface roughness factor defined as the ratio between the real and geometric surface area of the metal. If no other symbol is used to describe a particle flux, molecular fluxes are labeled with the lowercase letter j and atomic fluxes with the capital letter J. They are considered with the unit [mol m^{-2} s]. Unless otherwise noted, particle fluxes oriented into the metal are assumed to be positive and normal to the metal surface. Thus, vector notation is omitted. An expression for the total flux of impinging molecules onto the metal surface Γ_{ij} with the unit [mol m^{-2} s] is found by assuming that the considered surface is parallel to the xy-plane of a Cartesian coordinate system (plane normal to the z-axis in figure 2.7). The molar flux Γ_{ij} is then equal to the flux of molecules ${}^i\mathrm{H}^j\mathrm{H}$ which exhibit a positive velocity value in z-direction. It is derived from the normalized Maxwell-Boltzmann distribution function of velocity vectors $\vec{u} = (u_x, u_y, u_z)$ in an ideal gas

$$f_{ij}^{\vec{u}}\left(u_x, u_y, u_z\right) = \left(\frac{m_{ij}}{2\pi k_B T}\right)^{\frac{3}{2}} \exp\left[-\frac{m_{ij}(u_x^2+u_y^2+u_z^2)}{2k_B T}\right] \tag{2.82}$$

where m_{ij} is the mass of gas compound ${}^i\mathrm{H}^j\mathrm{H}$. The probability for a molecule to exhibit a positive velocity in z-direction in the range $[u_z, u_z + \mathrm{d}u_z]$ can be expressed by $f_{ij}(u_z)\,\mathrm{d}u_z$, with

$$f_{ij}(u_z) = \int_{-\infty}^{\infty}\int_{-\infty}^{\infty} f_{ij}^{\vec{u}}\left(u_x, u_y, u_z\right)\,\mathrm{d}u_x\mathrm{d}u_y\,. \tag{2.83}$$

As a consequence, the infinitesimal flux of molecules $\mathrm{d}\Gamma_{ij}(u_z)$ [mol m^{-2} s] impinging on the metal surface with velocities in z-direction in the range $[u_z, u_z + \mathrm{d}u_z]$ is given by

$$\mathrm{d}\Gamma_{ij} = c_{ij}u_z f_{ij}(u_z)\;\mathrm{d}u_z = c_{ij}u\cos(\theta)\,f_{ij}(u_z)\;\mathrm{d}u_z \tag{2.84}$$

where $u_z = u\cos(\theta)$ and $u = \sqrt{u_x^2+u_y^2+u_z^2}$ [176]. Variable c_{ij} labels the number of moles of molecules ${}^i\mathrm{H}^j\mathrm{H}$ per gas volume and θ is the angle between the velocity vector $\vec{u}$ and the z-axis [118]. To determine the flux of all molecules which possess a velocity component in the positive z-direction, $\mathrm{d}\Gamma_{ij}$ is integrated over u_z from zero to infinity

$$\Gamma_{ij} = \int_0^{\infty} c_{ij}u\cos(\theta)\,f_{ij}(u_z)\;\mathrm{d}u_z \tag{2.85}$$

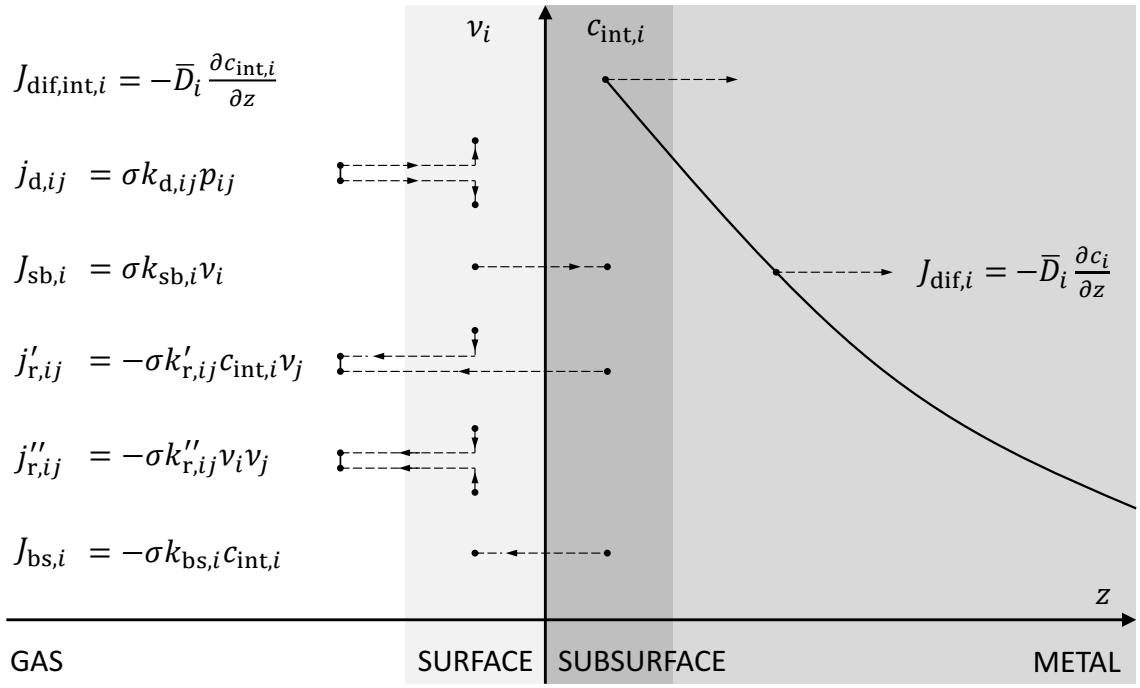

Fig. 2.9. Molecular and atomic hydrogen adsorption, absorption and desorption fluxes at a gas-metal interface.

Inserting the equations (2.82) and (2.83) as well as the infinitesimal velocity vector in spherical coordinates $\mathrm{d}u_\mathrm{x}\mathrm{d}u_\mathrm{y}\mathrm{d}u_\mathrm{z} = u^2 \sin(\theta)\ \mathrm{d}u\mathrm{d}\theta\mathrm{d}\varphi$ yields

$$\Gamma_{ij} = c_{ij} \left(\frac{m_{ij}}{2\pi k_\mathrm{B} T} \right)^{\frac{3}{2}} \int_0^\infty \int_0^{\frac{\pi}{2}} \int_0^{2\pi} u^3 \sin(\theta) \cos(\theta) \exp\left[-\frac{m_{ij}}{2 k_\mathrm{B} T} u^2 \right] \mathrm{d}\varphi \mathrm{d}\theta \mathrm{d}u \,, \tag{2.86}$$

where φ is the angle between the x-axis and the projection of the velocity vector $\vec{u}$ onto the xy-plane. The integrals are solved analytically [118]. After applying the ideal gas law $c_{ij} = p_{ij}/(k_\mathrm{B} N_\mathrm{A} T)$ equation (2.86) reduces to

$$\Gamma_{ij} = c_{ij} \cdot \sqrt{\frac{k_\mathrm{B} T}{2\pi m_{ij}}} = \frac{p_{ij}}{N_\mathrm{A} \sqrt{2\pi k_\mathrm{B} T m_{ij}}} \tag{2.87}$$

By inserting equation (2.87) into expression (2.81) the molecular dissociation flux writes

$$j_{\mathrm{d},ij} = \sigma k_{\mathrm{d},ij} p_{ij} \,, \tag{2.88}$$

where parameter $k_{\mathrm{d},ij}$ is defined as the metal-specific dissociation rate coefficient of molecular species ${}^i\mathrm{H}{}^j\mathrm{H}$ and expressed by

$$k_{\mathrm{d},ij}\,[\mathrm{mol\,m^{-2}\,s^{-1}\,Pa^{-1}}] = \frac{\alpha_\mathrm{s}(1-\theta_\mathrm{c})^2}{N_\mathrm{A} \sqrt{2\pi k_\mathrm{B} T m_{ij}}} \tag{2.89}$$

Once chemisorbed, the separated hydrogen isotopes oscillate around their equilibrium positions and diffuse along the metal surface. By annihilating or exciting substrate

phonons and electron-hole pairs of the metal atoms they dissipate a big part of their energy [171]. In this way, the isotopes thermalize with the surface atoms before being either exothermically or endothermically absorbed by the metal lattice [136].

The atomic flux $J_{\mathrm{sb},i}$ with which the chemisorbed isotopes enter the bulk is proportional to the areal molar density of occupied sites ν_i [mol/m^2] on the surface

$$J_{\mathrm{sb},i} = \sigma k_{\mathrm{sb},i} \nu_i \,, \quad \text{with} \quad k_{\mathrm{sb},i} \left[\mathrm{mol\,s^{-1}}\right] = k^0_{\mathrm{sb},i} \exp\left(-\frac{E_\mathrm{a}}{k_\mathrm{B} T}\right). \tag{2.90}$$

The pre-exponential factor k^0_{sb} [mol s^{-1}] of the rate coefficient $k_{\mathrm{sb},i}$ can be considered as the frequency at which each vibrating chemisorbed hydrogen isotope attempts to overcome the absorption energy barrier E_a of the surface atoms.

When hydrogen isotopes enter a metal lattice they occupy interstitial sites resulting in a slight increase in the lattice parameter. Since the metal surface is free to one side, the distances between the first two to three atom layers (known as the subsurface) are adjusted more easily and therefore require less work to be pushed apart by the entering hydrogen isotopes. This leads to the formation of additional subsurface sites and to a lowered enthalpy of solution in the subsurface. In figure 2.7 this is represented by the slightly different shape and depth E_ss of the potential wells in the subsurface compared to the layers located deeper in the bulk 2.7 [177], [178]. However, in this analysis, it is assumed that $E_\mathrm{ss} \approx E_\mathrm{m}$. The height of the surface-subsurface absorption energy barrier E_a mainly depends on the type of metal, its surface condition, and the surface coverage θ_c [136], [179].

After being absorbed by the bulk the hydrogen isotopes start their diffusive random walk through the metal lattice. For the hydrogen isotopes occupying subsurface sites, it is possible to jump back into the chemisorbed state at the surface. However, this requires that corresponding adjacent surfaces site are not already occupied by hydrogen isotopes. The flux of hydrogen isotopes from the subsurface back to the surface is therefore approximately proportional to the fraction of free surface sites $(1 - \theta_\mathrm{c})$, as well as to the areal concentration of hydrogen isotopes in the subsurface, such that

$$J_{\mathrm{bs},i} = -\sigma k_{\mathrm{bs},i} \delta_\mathrm{L} c_{\mathrm{int},i} \,, \quad \text{with} \quad k_{\mathrm{bs},i} \left[\mathrm{mol\,s^{-1}}\right] = (1-\theta_\mathrm{c}) k^0_{\mathrm{bs},i} \exp\left(-\frac{E_\mathrm{ss}}{k_\mathrm{B} T}\right). \tag{2.91}$$

To set up this equation, the areal concentration of hydrogen isotopes in the subsurface is estimated by $\delta_\mathrm{L} c_{\mathrm{int},i}$, where δ_L is a distance of the order of the lattice parameter [170], [174]. In equation (2.91), the parameter $c_{\mathrm{int},i}$ labels the volumetric concentration in the subsurface which is equivalent to the interface concentration in the metal. If the surface coverage is low ($\theta_\mathrm{c} \ll 1$) it may be hypothesized that even under the condition of chemical non-equilibrium, the surface and the subsurface are constantly in thermodynamic equilibrium. This implies [170]:

$$J_{\mathrm{bs},i} + J_{\mathrm{sb},i} \approx 0 \;\Rightarrow\; k_{\mathrm{sb},i} \nu_i \approx k_{\mathrm{bs},i} \delta_\mathrm{L} c_{\mathrm{int},i} \;\Leftrightarrow\; \nu_i \approx K_{\nu,i} c_{\mathrm{int},i} \,, \text{ with } K_{\nu,i} \equiv \frac{\delta_\mathrm{L} k_{\mathrm{bs},i}}{k_{\mathrm{sb},i}} \tag{2.92}$$

Despite supposing surface-subsurface equilibrium, since usually, $k_{\mathrm{sb},i} > k_{\mathrm{bs},i}$ the areal concentration at the surface ν_i is considerably higher than the concentration of hydrogen isotopes in the subsurface $\delta_{\mathrm{L}} c_{\mathrm{int},i}$. The equilibrium constant $K_{\nu,i}$ can be considered as some kind of Henry's constant for the surface-subsurface equilibrium [180].

It is generally regarded as probable that mainly two different processes determine the molecular desorption or recombination flux of molecules from the metal back into the gas. The first process considers the recombination between two chemisorbed isotopes ${}^{i}\mathrm{H}$ and ${}^{j}\mathrm{H}$ at the surface. Since the recombination rate is proportional to both areal concentrations ν_i and ν_j the contribution of this process to the molecular recombination flux is [170], [174]

$$j'_{\mathrm{r},ij} = -\sigma k'_{\mathrm{r},ij} \nu_i \nu_j \,, \quad \text{with} \quad k'_{\mathrm{r},ij} \left[\mathrm{m}^2/\mathrm{s}\right] = k'^{,0}_{\mathrm{r},ij} \exp\left[-\frac{2\,(E_{\mathrm{c}} + E_{\mathrm{d}})}{k_{\mathrm{B}} T}\right] . \tag{2.93}$$

Another possible desorption mechanism describes the recombination between a chemisorbed hydrogen isotope at the surface with an isotope emerging from the bulk to the surface [181]. The proportion of the recombination flux which results from the formation and desorption of molecules through this recombination process may be written as

$$j''_{\mathrm{r},ij} = -\sigma k''_{\mathrm{r},ij} \delta_{\mathrm{L}} c_{\mathrm{int},i} \nu_j \,. \tag{2.94}$$

Expressing the rate coefficient $k''_{\mathrm{r},ij}$ $[\mathrm{m}^2/\mathrm{s}]$ is rather complex and therefore not part of this discussion (for more details see [182], [183]). In any case, although the isotope emerging from the subsurface to the surface does not have to remain in a chemisorbed state before recombining with a surface isotope, parameter $k''_{\mathrm{r},ij}$ is expected to be dependent on the surface coverage. All discussed fluxes are illustrated in figure 2.9.

The total molecular recombination flux back into the gas is expressed as the sum of both recombination flux contributions $j_{\mathrm{r},ij} = j'_{\mathrm{r},ij} + j''_{\mathrm{r},ij}$, such that with equation (2.92)

$$j_{\mathrm{r},ij} = -\sigma \left(k'_{\mathrm{r},ij} \nu_i \nu_j + k''_{\mathrm{r},ij} \delta_{\mathrm{L}} c_{\mathrm{int},i} \nu_j\right) = -\sigma k_{\mathrm{r},ij} c_{\mathrm{int},i} c_{\mathrm{int},j} \,. \tag{2.95}$$

where the surface recombination rate coefficient is defined by

$$k_{\mathrm{r},ij} \left[\mathrm{m}^4\,\mathrm{mol}^{-1}\,\mathrm{s}^{-1}\right] \equiv k'_{\mathrm{r},ij} K_{\nu,i} K_{\nu,j} + k''_{\mathrm{r},ij} \delta_{\mathrm{L}} K_{\nu,j} \tag{2.96}$$

At this point, it is possible to provide an expression of the net flux of molecules whose atoms penetrate the metal bulk as a sum of the recombination flux (2.95) and the dissociation flux (2.88)

$$j_{\mathrm{net},ij} = j_{\mathrm{d},ij} + j_{\mathrm{r},ij} = \sigma k_{\mathrm{d},ij} p_{ij} - \sigma k_{\mathrm{r},ij} c_{\mathrm{int},i} c_{\mathrm{int},j} \tag{2.97}$$

Consequently, the net fluxes of penetrating hydrogen isotopes are given by

$$J_{\mathrm{net},k} = 2 j_{\mathrm{net},kk} + j_{\mathrm{net},ik} + j_{\mathrm{net},jk} = J_{\mathrm{dif,I},k} \qquad \text{with } i \neq j \tag{2.98}$$

Due to mass conservation across the interface J_{net} matches the diffusion flux $J_{\mathrm{dif,I}}$ in the subsurface of the metal bulk. At thermodynamic equilibrium, the net fluxes vanish, such that

$$j_{\mathrm{d},ij} + j_{\mathrm{r},ij} = 0 \qquad \Leftrightarrow \qquad c^2_{\mathrm{int},i} = \frac{k_{\mathrm{d},ii}}{k_{\mathrm{r},ii}} p_{ii} \quad \text{and} \quad c_{\mathrm{int},i} c_{\mathrm{int},k} = \frac{k_{\mathrm{d},ik}}{k_{\mathrm{r},ik}} p_{ik} \tag{2.99}$$

For dilute metal-hydrogen solutions, this equilibrium expression bears an analogy to the Sieverts' law (2.50) which yields the following formulas for the recombination rate constant

$$k_{\mathrm{r},ii} = \frac{k_{\mathrm{d},ii}}{K_{\mathrm{s},i}^2} \qquad \text{and} \qquad k_{\mathrm{r},ik} = \sqrt{K_{ik}^{\mathrm{ex}}}\,\frac{k_{\mathrm{d},ik}}{K_{\mathrm{s},i}K_{\mathrm{s},k}} \approx \frac{2k_{\mathrm{d},ik}}{K_{\mathrm{s},i}K_{\mathrm{s},k}}\,. \tag{2.100}$$

For the calculations performed in this work, it is assumed that $\sqrt{K_{ik}^{\mathrm{ex}}} \approx 2$ if the examined temperature is above $T = 550\,\mathrm{K}$ (see figure 2.3).

2.2.5. Isotope exchange kinetics

The ratio between the partial pressures of the molecules ${}^{i}\mathrm{H}^{j}\mathrm{H}$ in the gas phase which establishes at thermodynamic equilibrium is fully determined by equilibrium condition 3 [equation (2.27)] if the equilibrium constants K_{ij+kk}^{ik+jk} of all involved isotope exchange reactions ${}^{i}\mathrm{H}^{k}\mathrm{H} + {}^{j}\mathrm{H}^{k}\mathrm{H} \rightleftharpoons {}^{i}\mathrm{H}^{j}\mathrm{H} + {}^{k}\mathrm{H}_2$ are known. However, the equilibrium constant contains no information about the frequency with which the different isotope exchange reactions proceed. The reaction rates $r_{ik+jk}^{\mathrm{f,ex}}$ and $r_{ij+kk}^{\mathrm{b,ex}}$ of the forward reaction and backward reaction have the unit $[\mathrm{mol/m^3/s}]$ and may be expressed by second-order rate equations

$$r_{ik+jk}^{\mathrm{f,ex}} = k_{ik+jk}^{\mathrm{f,ex}} c_{ik} c_{jk} \qquad \text{and} \qquad r_{ij+kk}^{\mathrm{b,ex}} = k_{ij+kk}^{\mathrm{b,ex}} c_{ij} c_{kk} \tag{2.101}$$

The molar concentrations of the gas molecules c_{ij} are approximated by the ideal gas law $c_{ij} = p_{ij}/(RT)$, where $R = k_{\mathrm{B}} N_{\mathrm{A}}$ is the ideal gas constant. The rate coefficients $k_{ik+jk}^{\mathrm{f,ex}}$ and $k_{ij+kk}^{\mathrm{b,ex}}$ are strongly temperature dependent and have the unit $[\mathrm{m^3\,s^{-1}\,mol^{-1}}]$. At thermodynamic equilibrium, the forward and backward reaction of each isotope exchange reaction occurs with an equal rate ($r_{ik+jk}^{\mathrm{f,ex}} = r_{ij+kk}^{\mathrm{b,ex}}$). As a consequence, with equation (2.27), equation (2.101) and the ideal gas law it is found that

$$k_{ik+jk}^{\mathrm{f,ex}} c_{ik} c_{jk} = k_{ij+kk}^{\mathrm{b,ex}} c_{ij} c_{kk} \qquad \Leftrightarrow \qquad \frac{k_{ij+kk}^{\mathrm{b,ex}}}{k_{ik+jk}^{\mathrm{f,ex}}} = \frac{c_{ik} c_{jk}}{c_{ij} c_{kk}} = \frac{p_{ik} p_{jk}}{p_{ij} p_{kk}} = K_{ij+kk}^{ik+jk} \tag{2.102}$$

Hence, at all times the forward and backward rate coefficients are related to the equilibrium constant via the formula

$$k_{ij+kk}^{\mathrm{b,ex}} = K_{ij+kk}^{ik+jk} \cdot k_{ik+jk}^{\mathrm{f,ex}}\,. \tag{2.103}$$

Unfortunately, the exact temperature dependencies of the rate coefficients $k_{ik+jk}^{\mathrm{f,ex}}$ and $k_{ij+kk}^{\mathrm{b,ex}}$ could so far not be accurately measured. However, to estimate their order of magnitude one needs to be aware of the fact that, in reality, the considered isotope exchange reactions ${}^{i}\mathrm{H}^{j}\mathrm{H} + {}^{i}\mathrm{H}^{k}\mathrm{H} \rightleftharpoons {}^{i}\mathrm{H}_2 + {}^{j}\mathrm{H}^{k}\mathrm{H}$ are two-step free radical and ionic isotope exchange chain reactions of the form ${}^{k}\mathrm{H}^{\star} + {}^{i}\mathrm{H}^{k}\mathrm{H} \rightleftharpoons {}^{k}\mathrm{H}_2 + {}^{i}\mathrm{H}^{\star}$ and ${}^{i}\mathrm{H}^{\star} + {}^{j}\mathrm{H}^{k}\mathrm{H} \rightleftharpoons {}^{i}\mathrm{H}^{j}\mathrm{H} + {}^{k}\mathrm{H}^{\star}$ [124]. Ionic isotope exchange reactions happen between the diatomic gas molecules and triatomic hydrogen ions ${}^{i}\mathrm{H}^{\star} \in \{{}^{1}\mathrm{H}_2{}^{i}\mathrm{H}^{+}, {}^{2}\mathrm{H}_2{}^{i}\mathrm{H}^{+}, {}^{3}\mathrm{H}_2{}^{i}\mathrm{H}^{+}, {}^{1}\mathrm{H}^{2}\mathrm{H}{}^{i}\mathrm{H}^{+}, {}^{1}\mathrm{H}^{3}\mathrm{H}{}^{i}\mathrm{H}^{+}, {}^{2}\mathrm{H}^{3}\mathrm{H}{}^{i}\mathrm{H}^{+}\}$ [124], [184]. Free radical reactions occur between the diatomic gas molecules and atomic

radicals of the hydrogen isotopes ${}^{i}\mathrm{H}^{\star} \in \{{}^{1}\mathrm{H}^{\bullet}, {}^{2}\mathrm{H}^{\bullet}, {}^{3}\mathrm{H}^{\bullet}\}$ [184]. Both types of chain reactions are depended on an independent initiation step in which the ions or free radicals are formed by dissociating or ionizing a diatomic hydrogen gas molecule. This requires the presence of a catalyst, such as radiation, heat, a metal surface, or the β-radiation of tritium. It is found that the ionic isotope exchange reactions happen at a significantly higher rate than the free radical reactions [124]. The slowest among the free radical reactions are those involving the heavier hydrogen molecules. Their rate coefficients were calculated for temperatures between $300\,\mathrm{K} < T < 1000\,\mathrm{K}$ and found to be in the range $10\,\mathrm{m^3\,s^{-1}\,mol^{-1}} - 1 \times 10^5\,\mathrm{m^3\,s^{-1}\,mol^{-1}}$ [124], [185]. Therefore, it may be estimated that the reaction rate coefficients defined in equation (2.101) are greater than this range.

In this work, no calculation or experiment involves the simultaneous presence of all three hydrogen isotopes bound to diatomic molecules in a gas phase. Therefore, and to drastically simplify the notation, the further discussion considers the coexistence of a maximum of two different hydrogen isotopes (${}^{i}\mathrm{H}$ and ${}^{k}\mathrm{H}$) and three different diatomic hydrogen molecules (${}^{i}\mathrm{H}_2$, ${}^{i}\mathrm{H}{}^{k}\mathrm{H}$ and ${}^{k}\mathrm{H}_2$). Thus, the number of isotope exchange reactions between diatomic hydrogen molecules reduces from six to one ($2\,{}^{i}\mathrm{H}{}^{k}\mathrm{H} \rightleftharpoons {}^{i}\mathrm{H}_2 + {}^{k}\mathrm{H}_2$). According to the laws of chemical kinetics, in a closed system, at constant temperature and constant volume, the rates of formation $\varsigma_{ij}^{\mathrm{ex}}$ $[\mathrm{mol/m^3/s}]$ of the different molecules in the remaining isotope exchange reaction, are determined by the equations [120], [186]

$$\varsigma_{ii}^{\mathrm{ex}} = r_{ik+ik}^{\mathrm{f,ex}} - r_{ii+kk}^{\mathrm{b,ex}} \tag{2.104}$$

$$\varsigma_{kk}^{\mathrm{ex}} = r_{ik+ik}^{\mathrm{f,ex}} - r_{ii+kk}^{\mathrm{b,ex}} \tag{2.105}$$

$$\varsigma_{ik}^{\mathrm{ex}} = -2r_{ik+ik}^{\mathrm{f,ex}} + 2r_{ii+kk}^{\mathrm{b,ex}}\,. \tag{2.106}$$

2.2.6. Water-metal interfaces

To understand the kinetics of hydrogen transport across a water-metal interface, it is useful to imagine a system in which a gas phase of diatomic hydrogen molecules ${}^{i}\mathrm{H}{}^{j}\mathrm{H}$ is put in contact with a liquid water phase containing the molecules ${}^{1}\mathrm{H}_2\mathrm{O}$. The hydrogen molecules would dissolve into the water as diatomic molecules. Due to the criterion of phase equilibrium [120], at thermodynamic equilibrium, the chemical potential of hydrogen molecules ${}^{i}\mathrm{H}{}^{j}\mathrm{H}$ in the gas phase μ_{ij}^{g} equals the chemical potential of the molecules dissolved in the liquid water μ_{ij}^{w}. This condition ($\mu_{ij}^{\mathrm{w}} = \mu_{ij}^{\mathrm{g}}$) is called equilibrium condition 4. For dilute solutions it yields the Henry's law for hydrogen molecules ${}^{i}\mathrm{H}{}^{j}\mathrm{H}$ dissolved in water [118]

$$\mu_{ij}^{\mathrm{w}} = \mu_{ij}^{\mathrm{g}} \qquad \Rightarrow \qquad c_{ij}^{\mathrm{w}} = K_{\mathrm{H},ij} p_{ij}^{\mathrm{g}}\,. \tag{2.107}$$

The parameter $K_{\mathrm{H},ij}$ is the Henry's constant for the molecules ${}^{i}\mathrm{H}{}^{j}\mathrm{H}$ dissolved in water (${}^{1}\mathrm{H}_2\mathrm{O}$). It follows an Arrhenius-type temperature dependence. So far, only the Henry's constants for the molecules ${}^{1}\mathrm{H}_2$ and ${}^{2}\mathrm{H}_2$ dissolved in water (${}^{1}\mathrm{H}_2\mathrm{O}$) could be experimentally determined [187]. In contrast to the found data for ${}^{2}\mathrm{H}_2$, the Henry's constant for ${}^{1}\mathrm{H}_2$

could be verified in various experiments within a certain error range [187]

$$K_{\mathrm{H},11} \approx (7.7 \pm 0.2) \times 10^{-6} \, \frac{\mathrm{mol}}{\mathrm{m^3 Pa}} \cdot \exp\left[(500 \pm 50)\,\mathrm{K} \cdot \left(\frac{1}{T} - \frac{1}{298.15\,\mathrm{K}} \right) \right] . \tag{2.108}$$

The Henry's law provides the equilibrium concentration c_{ij}^{w} of the diatomic molecules ${}^{i}\mathrm{H}{}^{j}\mathrm{H}$ in the water which establishes at a certain partial pressure p_{ij}^{g} in the gas. If in addition to that the water is in contact with a metal, a further dissolution process needs to be taken into account in which part of the dissolved molecules ${}^{i}\mathrm{H}{}^{j}\mathrm{H}$ in the water dissociate at the metal surface and enter the metal bulk in atomic form. The net flux of hydrogen isotopes into the metal is zero once the hydrogen isotopes in the metal are in equilibrium with the hydrogen molecules in the water and in the gas phase. The mono-isotopic equilibrium condition for the three phase (gas-water-metal) system at low concentrations is therefore $\mu_{ii}^{\mathrm{w}} = \mu_{ii}^{\mathrm{g}} = 2\mu_i^a$. For dilute solutions in the metal, it may be rewritten using equation (2.100), equilibrium condition 1 [Sieverts' law: (2.50)] and equilibrium condition 4 [Henry's law: (2.107)], which leads to

$$\frac{c_{ii}^{\mathrm{w}}}{K_{\mathrm{H},ii}} = p_{ii}^{\mathrm{g}} = \frac{c_{\mathrm{int},i}^2}{K_{\mathrm{s},i}^2} = \frac{k_{\mathrm{r},ii}}{k_{\mathrm{d},ii}} . \tag{2.109}$$

The general water-metal equilibrium condition for the multi-isotopic case follows when combining the multi-isotopic Sieverts' law (2.50) with Henry's law (2.107)

$$\frac{c_{ik}^{\mathrm{w}}}{K_{\mathrm{H},ik}} = p_{ik}^{\mathrm{g}} = \frac{\sqrt{K_{ik}^{\mathrm{ex}}}}{K_{\mathrm{s},i} K_{\mathrm{s},k}} \cdot c_{\mathrm{int},i} c_{\mathrm{int},k} = \frac{k_{\mathrm{r},ik}}{k_{\mathrm{d},ik}} \cdot c_{\mathrm{int},i} c_{\mathrm{int},k} . \tag{2.110}$$

At equilibrium, the sum of the recombination and dissociation fluxes of hydrogen isotopes crossing the metal-water interface must be zero. Experiments suggest [188] that also water molecules ${}^{i}\mathrm{H}{}^{j}\mathrm{HO}$ may dissociate at the metal surface to ${}^{j}\mathrm{HO} + {}^{i}\mathrm{H}$. In this case, the dissociated hydrogen isotope would enter the metal bulk while the free radical ${}^{j}\mathrm{HO}$ recombines with a hydrogen isotope ${}^{i}\mathrm{H}$ at the metal surface and returns into the water as ${}^{i}\mathrm{H}{}^{j}\mathrm{HO}$. However, since not much is known about the kinetics of this absorption/desorption process, it will be ignored in the following discussion. Therefore, it may be assumed that the recombination flux is described by the same rate equation (2.95) as derived for the gas-metal interface. Hence, with the equations (2.95), (2.109) and (2.110), equilibrium condition $j_{\mathrm{d},ij} + j_{\mathrm{r},ij} = 0$ transforms to

$$j_{\mathrm{r},ij} = -\sigma k_{\mathrm{r},ij} c_{\mathrm{int},i} c_{\mathrm{int},j} = -\sigma \frac{k_{\mathrm{d},ij}}{K_{\mathrm{H},ij}} c_{ij}^{\mathrm{w}} = -j_{\mathrm{d},ij} , \quad \text{with} \quad j_{\mathrm{d},ij} = \sigma \frac{k_{\mathrm{d},ij}}{K_{\mathrm{H},ij}} c_{ij}^{\mathrm{w}} \tag{2.111}$$

Considering that the fluxes are positive when directed into the metal the molecular net flux crossing the metal-water interface in chemical non-equilibrium can be written as

$$j_{\mathrm{net},ij} = j_{\mathrm{d},ij} + j_{\mathrm{r},ij} = \sigma \frac{k_{\mathrm{d},ij}}{K_{\mathrm{H},ij}} c_{ij}^{\mathrm{w}} - \sigma k_{\mathrm{r},ij} c_{\mathrm{int},i} c_{\mathrm{int},j} \tag{2.112}$$

If the water occurs as a gas phase (steam) instead, hydrogen molecules entering the steam would mix with the water vapor as additional gas components. Since any chemical interaction between the water molecules and the metal is neglected, the transport of

hydrogen isotopes crossing a steam-metal interface can be described by the same rate equation (2.97) as derived for the gas-metal interface in section 2.2.4.

Furthermore, there are five different isotope exchange reactions that occur between water molecules ${}^{i}\mathrm{H}^{k}\mathrm{HO}$ and the diatomic hydrogen molecules ${}^{i}\mathrm{H}^{k}\mathrm{H}$ if only two different isotopes ${}^{i}\mathrm{H}$ and ${}^{k}\mathrm{H}$ are present [189]

$$\mathrm{I}: \quad {}^{i}\mathrm{H}^{k}\mathrm{HO} + {}^{i}\mathrm{H}^{k}\mathrm{H} \rightleftharpoons {}^{i}\mathrm{H}_2\mathrm{O} + {}^{k}\mathrm{H}_2 \quad \text{with} \quad K^{\mathrm{w}}_{\mathrm{I},ik} = \frac{c_{ik\mathrm{O}}c_{ik}}{c_{ii\mathrm{O}}c_{kk}} \tag{2.113}$$

$$\mathrm{II}: \quad {}^{i}\mathrm{H}^{k}\mathrm{HO} + {}^{i}\mathrm{H}^{k}\mathrm{H} \rightleftharpoons {}^{k}\mathrm{H}_2\mathrm{O} + {}^{i}\mathrm{H}_2 \quad \text{with} \quad K^{\mathrm{w}}_{\mathrm{II},ik} = \frac{c_{ik\mathrm{O}}c_{ik}}{c_{kk\mathrm{O}}c_{ii}} \tag{2.114}$$

$$\mathrm{III}: \quad {}^{i}\mathrm{H}^{k}\mathrm{HO} + {}^{i}\mathrm{H}_2 \rightleftharpoons {}^{i}\mathrm{H}_2\mathrm{O} + {}^{i}\mathrm{H}^{k}\mathrm{H} \quad \text{with} \quad K^{\mathrm{w}}_{\mathrm{III},ik} = \frac{c_{ik\mathrm{O}}c_{ii}}{c_{ii\mathrm{O}}c_{ik}} \tag{2.115}$$

$$\mathrm{IV}: \quad {}^{i}\mathrm{H}^{k}\mathrm{HO} + {}^{k}\mathrm{H}_2 \rightleftharpoons {}^{k}\mathrm{H}_2\mathrm{O} + {}^{i}\mathrm{H}^{k}\mathrm{H} \quad \text{with} \quad K^{\mathrm{w}}_{\mathrm{IV},ik} = \frac{c_{ik\mathrm{O}}c_{kk}}{c_{kk\mathrm{O}}c_{ik}} \tag{2.116}$$

$$\mathrm{V}: \quad 2\,{}^{i}\mathrm{H}^{k}\mathrm{HO} \rightleftharpoons {}^{i}\mathrm{H}_2\mathrm{O} + {}^{k}\mathrm{H}_2\mathrm{O} \quad \text{with} \quad K^{\mathrm{w}}_{\mathrm{V},ik} = \frac{c_{ik\mathrm{O}}c_{ik\mathrm{O}}}{c_{ii\mathrm{O}}c_{kk\mathrm{O}}}\,. \tag{2.117}$$

They occur in addition to the isotope exchange reactions between the molecules ${}^{i}\mathrm{H}^{j}\mathrm{H}$ discussed in the previous section. The defined parameters $K^{\mathrm{w}}_{\mathrm{I},ik}$ to $K^{\mathrm{w}}_{\mathrm{V},ik}$ are the temperature-depended equilibrium constants of the reactions I to V. They describe the concentration ratio between the different molecules ${}^{i}\mathrm{H}^{k}\mathrm{H}$ and ${}^{i}\mathrm{H}^{k}\mathrm{HO}$ which would establish at thermodynamic equilibrium in the water. Their expression is derived similarly to equilibrium condition 3 [see equations (2.11), (2.14) and (2.27)]. The forward and backward reaction rates of the reactions I to V can be expressed as follows

$$r^{\mathrm{f,w}}_{\mathrm{I},ik} = k^{\mathrm{f,w}}_{\mathrm{I},ik} c_{ik\mathrm{O}} c_{ik} \quad \text{and} \quad r^{\mathrm{b,w}}_{\mathrm{I},ik} = k^{\mathrm{b,w}}_{\mathrm{I},ik} c_{ii\mathrm{O}} c_{kk} \tag{2.118}$$

$$r^{\mathrm{f,w}}_{\mathrm{II},ik} = k^{\mathrm{f,w}}_{\mathrm{II},ik} c_{ik\mathrm{O}} c_{ik} \quad \text{and} \quad r^{\mathrm{b,w}}_{\mathrm{II},ik} = k^{\mathrm{b,w}}_{\mathrm{I},ik} c_{kk\mathrm{O}} c_{ii} \tag{2.119}$$

$$r^{\mathrm{f,w}}_{\mathrm{III},ik} = k^{\mathrm{f,w}}_{\mathrm{III},ik} c_{ik\mathrm{O}} c_{ii} \quad \text{and} \quad r^{\mathrm{b,w}}_{\mathrm{III},ik} = k^{\mathrm{b,w}}_{\mathrm{I},ik} c_{ii\mathrm{O}} c_{ik} \tag{2.120}$$

$$r^{\mathrm{f,w}}_{\mathrm{IV},ik} = k^{\mathrm{f,w}}_{\mathrm{IV},ik} c_{ik\mathrm{O}} c_{kk} \quad \text{and} \quad r^{\mathrm{b,w}}_{\mathrm{IV},ik} = k^{\mathrm{b,w}}_{\mathrm{I},ik} c_{kk\mathrm{O}} c_{ik} \tag{2.121}$$

$$r^{\mathrm{f,w}}_{\mathrm{V},ik} = k^{\mathrm{f,w}}_{\mathrm{V},ik} c^2_{ik\mathrm{O}} \quad \text{and} \quad r^{\mathrm{b,w}}_{\mathrm{V},ik} = k^{\mathrm{b,w}}_{\mathrm{I},ik} c_{ii\mathrm{O}} c_{kk\mathrm{O}}\,. \tag{2.122}$$

The rates of formation which are contributed to the isotope exchange reactions with water molecules are consequently given by [120], [186]

$$\varsigma^{\mathrm{w}}_{ii} = r^{\mathrm{f,w}}_{\mathrm{II},ik} - r^{\mathrm{b,w}}_{\mathrm{II},ik} - r^{\mathrm{f,w}}_{\mathrm{III},ik} + r^{\mathrm{b,w}}_{\mathrm{III},ik} \tag{2.123}$$

$$\varsigma^{\mathrm{w}}_{kk} = r^{\mathrm{f,w}}_{\mathrm{I},ik} - r^{\mathrm{b,w}}_{\mathrm{I},ik} - r^{\mathrm{f,w}}_{\mathrm{IV},ik} + r^{\mathrm{b,w}}_{\mathrm{IV},ik} \tag{2.124}$$

$$\varsigma^{\mathrm{w}}_{ik} = r^{\mathrm{f,w}}_{\mathrm{III},ik} - r^{\mathrm{b,w}}_{\mathrm{II},ik} + r^{\mathrm{f,w}}_{\mathrm{IV},ik} - r^{\mathrm{b,w}}_{\mathrm{IV},ik} \tag{2.125}$$

$$\varsigma^{\mathrm{w}}_{ii\mathrm{O}} = r^{\mathrm{f,w}}_{\mathrm{I},ik} - r^{\mathrm{b,w}}_{\mathrm{I},ik} + r^{\mathrm{f,w}}_{\mathrm{III},ik} - r^{\mathrm{b,w}}_{\mathrm{III},ik} + r^{\mathrm{f,w}}_{\mathrm{V},ik} - r^{\mathrm{b,w}}_{\mathrm{V},ik} \tag{2.126}$$

$$\varsigma^{\mathrm{w}}_{kk\mathrm{O}} = r^{\mathrm{f,w}}_{\mathrm{II},ik} - r^{\mathrm{b,w}}_{\mathrm{II},ik} + r^{\mathrm{f,w}}_{\mathrm{IV},ik} - r^{\mathrm{b,w}}_{\mathrm{IV},ik} + r^{\mathrm{f,w}}_{\mathrm{V},ik} - r^{\mathrm{b,w}}_{\mathrm{V},ik} \tag{2.127}$$

$$\varsigma^{\mathrm{w}}_{ik\mathrm{O}} = -2r^{\mathrm{f,w}}_{\mathrm{V},ik} + 2r^{\mathrm{b,w}}_{\mathrm{V},ik} - r^{\mathrm{f,w}}_{\mathrm{I},ik} + r^{\mathrm{b,w}}_{\mathrm{I},ik} - r^{\mathrm{f,w}}_{\mathrm{II},ik} + r^{\mathrm{b,w}}_{\mathrm{II},ik} - r^{\mathrm{f,w}}_{\mathrm{III},ik} + r^{\mathrm{b,w}}_{\mathrm{III},ik} - r^{\mathrm{f,w}}_{\mathrm{IV},ik} + r^{\mathrm{b,w}}_{\mathrm{IV},ik}\,. \tag{2.128}$$

Following the same argumentation used to derive relation (2.102) it is found that the rate coefficients for the forward and backward reactions of all five reactions $n = \mathrm{I}, \ldots, \mathrm{V}$ are related to the equilibrium constants by

$$k^{\mathrm{b,w}}_{n,ik} = K^{\mathrm{w}}_{n,ik} \cdot k^{\mathrm{f,w}}_{n,ik}\,. \tag{2.129}$$

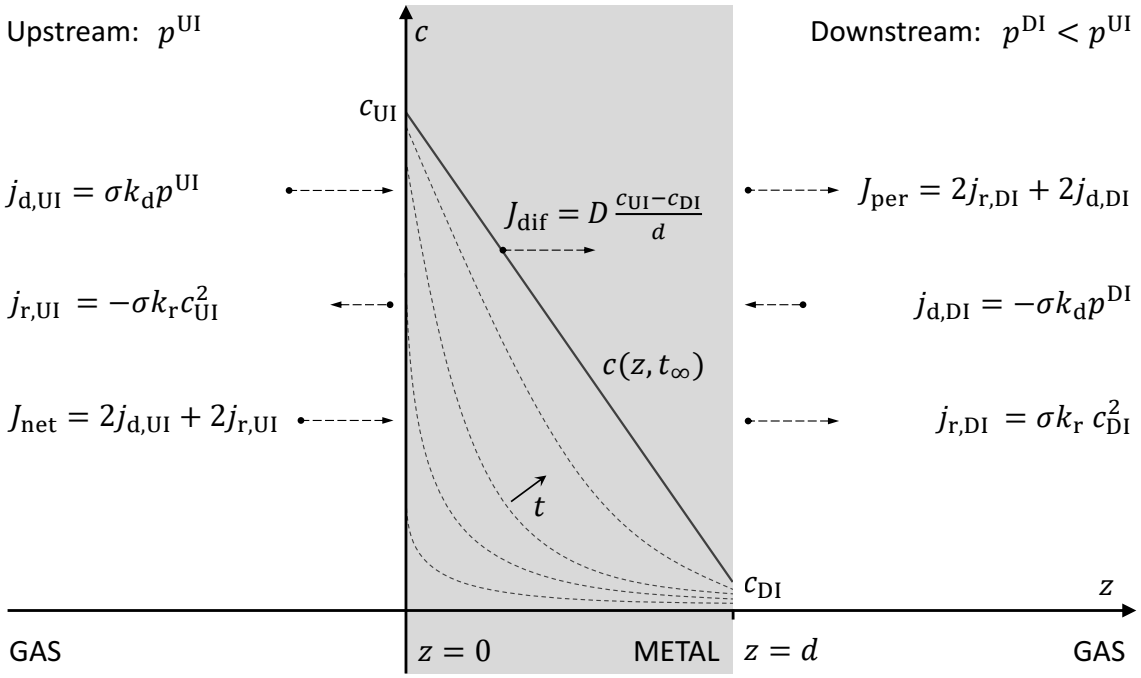

Fig. 2.10. Illustration of the occurring fluxes and the establishing concentration profile during steady state permeation of a mono-isotopic hydrogen gas from a high to a low-pressure side through a plane metal sheet [170], [190].

Until today, the rate coefficients of these reactions could never be experimentally determined.

2.3. Mono-isotopic permeation

A significant part of this thesis is devoted to the theoretical, numerical and experimental study of multi-isotopic hydrogen isotope permeation from one medium (solid metal, liquid metal, water, steam or hydrogen isotope gas) through a metal membrane into a second medium.

In order to deal with this rather complex problem, it is necessary to first introduce the basics of mono-isotopic permeation processes using the example of the simplest permeation scenario. This is the permeation of hydrogen isotopes ^{i}H from a mono-isotopic gas phase (upstream side) of constant pressure p_{ii}^{UI}, through a flat sheet of metal, into a second mono-isotopic gas phase (downstream side) of the same species and of constant pressure $p_{ii}^{\mathrm{DI}} < p_{ii}^{\mathrm{UI}}$. Due to the simplicity of this particular case, fundamental insights into permeation processes in general can be gained from its study. A sketch of the described permeation scenario is shown in figure 2.10. For the sake of clarity, since mono-isotopic permeation involves only a single isotope species, adding the self-evident indexes i (indicating ^{i}H) and ii (indicating ^{i}H$_2$) to the corresponding quantities is omitted. Furthermore, in this discussion, it is assumed that the occurring hydrogen isotope concentrations in the metal bulk are low enough so that the derived laws for dilute solutions are satisfied, which

implies that $\overline{D} = D$. Moreover, it is considered that no traps are present in the metal, meaning that $D_{\text{eff}} = D$ and $K_{\text{s}}^{\text{eff}} = K_{\text{s}}$.

Mono-isotopic permeation through a plane metal membrane can be mathematically treated in one dimension considering that the upstream interface (UI) of the bulk is located at a position $z = 0$ and the downstream interface (DI) at a position $z = d$. According to the equations (2.97), (2.98) and Fick's first law (2.67) in one dimension, the atomic net flux of isotopes ^{i}H from the upstream side into the metal bulk is described by

$$J_{\text{net,UI}} = -D\frac{\partial c_{\text{UI}}}{\partial z} = 2j_{\text{d,UI}} - 2j_{\text{r,UI}} = 2\sigma k_{\text{d}} p^{\text{UI}} - 2\sigma k_{\text{r}} c_{\text{UI}}^2 \qquad \text{(upstream)} \qquad (2.130)$$

Analogously, if the surface roughness σ is equal on both sides, the atomic net flux of isotopes ^{i}H from the bulk into the downstream side writes

$$J_{\text{net,DI}} = -D\frac{\partial c_{\text{DI}}}{\partial z} = -2j_{\text{d,DI}} + 2j_{\text{r,DI}} = 2\sigma k_{\text{r}} c_{\text{DI}}^2 - 2\sigma k_{\text{d}} p^{\text{DI}} \equiv J_{\text{per}} \quad \text{(downstream)} \quad (2.131)$$

The flux $J_{\text{net,DI}}$ is equivalent to the atomic permeation flux J_{per} into the downstream side.

Since the pressures on both the upstream and the downstream side are fixed it is evident that the establishing concentrations c_{UI} and c_{DI} will over time approach a constant value. Assuming that these constant concentrations are reached instantaneously at both interfaces and that the metal membrane is initially free of hydrogen isotopes ($c(z, t_0) = 0$), the one-dimensional expression of Fick's second law (2.68)

$$\frac{\partial c\,(z,t)}{\partial t} = \frac{\partial}{\partial z}\left[D\frac{\partial c(z,t)}{\partial z}\right] \qquad (2.132)$$

which describes the concentration profile in the membrane, has an analytical solution of the form [165]

$$c\,(z,t) = c_{\text{UI}} + (c_{\text{DI}} - c_{\text{UI}})\,\frac{z}{d} + \frac{2}{\pi}\sum_{n=1}^{\infty}\frac{c_{\text{DI}}\cos(n\pi) - c_{\text{UI}}}{n}\sin\left(\frac{n\pi z}{d}\right)\exp\left(\frac{-Dn^2\pi^2 t}{d^2}\right). \quad (2.133)$$

2.3.1. Steady state permeation

It can be seen that for $t \to \infty$ the concentration profile approaches a linear straight line (see figure 2.10)

$$\lim_{t\to\infty} c\,(z,t) = c_{\text{UI}} + (c_{\text{DI}} - c_{\text{UI}})\,\frac{z}{d}\,. \qquad (2.134)$$

According to Fick's first law, this implies the establishment of a homogeneous diffusion flux in the metal bulk over time, and consequently a steady state permeation flux $\overline{J}_{\text{per}}$ into the downstream side

$$\overline{J}_{\text{per}} = -D\frac{\partial c(z,t_\infty)}{\partial z} = D\frac{c_{\text{UI}} - c_{\text{DI}}}{d}\,, \qquad (2.135)$$

where $J_{\text{net,UI}} = J_{\text{net,DI}} = J_{\text{per}}$. By using the equations (2.130) and (2.131), the steady state condition (2.135) can be expressed by

$$\overline{J}_{\text{per}} = D\frac{c_{\text{UI}} - c_{\text{DI}}}{d} = 2\sigma k_{\text{d}} p^{\text{UI}} - 2\sigma k_{\text{r}} c_{\text{UI}}^2 = 2\sigma k_{\text{r}} c_{\text{DI}}^2 - 2\sigma k_{\text{d}} p^{\text{DI}}\,. \qquad (2.136)$$

In a hypothetical scenario, if during the permeation process, both the upstream and downstream gas phases were in thermodynamic equilibrium with their corresponding metal bulk interface regions (which is obviously not the case), the equilibrium concentrations at the respective interfaces, defined as $c_{\mathrm{UI,eq}}$ and $c_{\mathrm{DI,eq}}$, could be expressed by the Sieverts' law (2.99)

$$c_{\mathrm{UI,eq}} \equiv K_{\mathrm{s}} \sqrt{p^{\mathrm{UI}}} = \sqrt{\frac{k_{\mathrm{d}} p^{\mathrm{UI}}}{k_{\mathrm{r}}}} \qquad \text{and} \qquad c_{\mathrm{DI,eq}} \equiv K_{\mathrm{s}} \sqrt{p^{\mathrm{DI}}} = \sqrt{\frac{k_{\mathrm{d}} p^{\mathrm{DI}}}{k_{\mathrm{r}}}} \,. \tag{2.137}$$

Inserting the equations (2.137) into the equation (2.136) yields two expressions for the upstream and downstream concentrations during steady state permeation

$$c_{\mathrm{UI}}^2 = c_{\mathrm{UI,eq}}^2 - D\frac{c_{\mathrm{UI}} - c_{\mathrm{DI}}}{2\sigma k_{\mathrm{r}} d} = c_{\mathrm{UI,eq}}^2 \left(1 - D\frac{c_{\mathrm{UI}} - c_{\mathrm{DI}}}{2\sigma k_{\mathrm{d}} p^{\mathrm{UI}} d}\right) \tag{2.138}$$

$$c_{\mathrm{DI}}^2 = c_{\mathrm{DI,eq}}^2 + D\frac{c_{\mathrm{UI}} - c_{\mathrm{DI}}}{2\sigma k_{\mathrm{r}} d} = c_{\mathrm{DI,eq}}^2 \left(1 + D\frac{c_{\mathrm{UI}} - c_{\mathrm{DI}}}{2\sigma k_{\mathrm{d}} p^{\mathrm{DI}} d}\right) . \tag{2.139}$$

These relations demonstrate that $c_{\mathrm{UI}} < c_{\mathrm{UI,eq}}$ and $c_{\mathrm{DI}} > c_{\mathrm{DI,eq}}$. Adding up the equations (2.138) and (2.139) reveals that [170]

$$c_{\mathrm{UI}}^2 + c_{\mathrm{DI}}^2 = c_{\mathrm{UI,eq}}^2 + c_{\mathrm{DI,eq}}^2 \,. \tag{2.140}$$

2.3.2. Diffusion-limited regime

In case the surface is relatively clean (sticking coefficient $\alpha_{\mathrm{s}} \approx 1$) and the driving pressure p^{UI} is high, the atomic dissociation flux $2j_{\mathrm{d,UI}}$ on the upstream side is significantly higher than the diffusion flux J_{dif}. This means the transport process through the metal is mainly slowed down and determined by the velocity of the diffusion process inside the bulk material. In other words, diffusion becomes the rate-limiting step of the permeation process. At high driving pressures, the second term inside the bracket of equation (2.138) approaches zero and $c_{\mathrm{UI}} \to c_{\mathrm{UI,eq}}$. According to equation (2.140) this goes along with $c_{\mathrm{DI}} \to c_{\mathrm{DI,eq}}$, such that

$$c_{\mathrm{UI}} \approx K_{\mathrm{s}} \sqrt{p^{\mathrm{UI}}} \qquad \text{and} \qquad c_{\mathrm{DI}} \approx K_{\mathrm{s}} \sqrt{p^{\mathrm{DI}}} \,. \tag{2.141}$$

The parameter domain where this approximation can be applied is called the diffusion-limited (DL) permeation regime. Inserting the equations (2.141) into equation (2.135) yields the approximate steady state permeation flux in the diffusion-limited regime

$$\overline{J}_{\mathrm{per}}^{\mathrm{dl}} \approx K_{\mathrm{s}} D\frac{\sqrt{p^{\mathrm{UI}}} - \sqrt{p^{\mathrm{DI}}}}{d} \equiv \Phi\frac{\sqrt{p^{\mathrm{UI}}} - \sqrt{p^{\mathrm{DI}}}}{d} \approx \Phi\frac{\sqrt{p^{\mathrm{UI}}}}{d} \,. \tag{2.142}$$

It is found that if the permeation process is diffusion-limited and if $p^{\mathrm{UI}} \gg p^{\mathrm{DI}}$ the steady state permeation flux is approximately proportional to the square root of the gas pressure on the upstream side. The defined parameter Φ is the isotope and metal-specific hydrogen isotope permeability. In dilute metal hydrogen solutions, it is the product of the Sieverts'

constant [see equations (2.44) and (2.50)] and the intrinsic diffusion coefficient (2.65). Therefore, it has an Arrhenius-type temperature dependency [191]

$$\Phi(T) = K_\mathrm{s} D = K_\mathrm{s}^0 D^0 \exp\left(-\frac{\Delta\overline{H}_\mathrm{s} + E_\mathrm{m}}{k_\mathrm{B} T}\right). \tag{2.143}$$

with the unit $[\mathrm{mol/m/s/Pa^{\frac{1}{2}}}]$. The multiplication of the equations (2.72) and (2.74) confirms that $K_\mathrm{s}^\mathrm{eff} D^\mathrm{eff} = K_\mathrm{s} D$. Therefore, trapping effects, as considered in this work, do not influence the value of the permeability Φ.

2.3.3. Surface-limited regime

Another characteristic permeation regime establishes if the surface is not clean (sticking coefficient $\alpha_\mathrm{s} \ll 1$) or the driving pressure $p^\mathrm{UI} > p^\mathrm{DI}$ is low. According to the equations (2.138) and (2.139), under these conditions, the interface concentrations are considerably different from their equilibrium values (2.137) and [170]

$$c_\mathrm{UI} \approx c_\mathrm{DI} \approx \frac{c_\mathrm{UI,eq}}{\sqrt{2}}\,. \tag{2.144}$$

In such a scenario, transport across the membrane is mainly limited by the surface dissociation and recombination rates and is therefore referred to as the surface-limited (SL) regime. As a consequence, equation (2.140) may be expressed by

$$c_\mathrm{UI}^2 \approx c_\mathrm{DI}^2 \approx c_\mathrm{UI,eq}^2 + c_\mathrm{DI,eq}^2 \;\Leftrightarrow\; c_\mathrm{UI} \approx c_\mathrm{DI} \approx \sqrt{\frac{c_\mathrm{UI,eq}^2 + c_\mathrm{DI,eq}^2}{2}} = \sqrt{\frac{k_\mathrm{d}}{k_\mathrm{r}} \cdot \frac{p^\mathrm{UI} + p^\mathrm{DI}}{2}}\,. \tag{2.145}$$

for which the definitions (2.137) are used. Substituting the upstream or downstream concentration in equation (2.136) by their expressions derived in equation (2.145) allows writing an equation for the approximate permeation flux in the surface-limited regime

$$\overline{J}_\mathrm{per}^\mathrm{sl} \approx \sigma k_\mathrm{d} \left(p^\mathrm{UI} - p^\mathrm{DI}\right) \approx \sigma k_\mathrm{d} p^\mathrm{UI}\,. \tag{2.146}$$

The last equation holds if the downstream pressure is negligibly small.

2.3.4. Permeation number

To facilitate the characterization of permeation regimes, a dimensionless quantity, the permeation number W, is introduced. It is defined as the ratio between the upstream atomic dissociation flux and the expression for the steady state atomic permeation flux in the diffusion-limited regime (2.142)

$$W \equiv \frac{J_\mathrm{d,UI}}{\overline{J}_\mathrm{per}^\mathrm{dl}} = \frac{2\sigma k_\mathrm{d} p^\mathrm{UI}}{(\Phi/d)\sqrt{p^\mathrm{UI}}} = \frac{2\sigma k_\mathrm{d} d}{\Phi}\sqrt{p^\mathrm{UI}} = \frac{2\sigma d}{D} k_\mathrm{r} K_\mathrm{s} \sqrt{p^\mathrm{UI}}\,. \tag{2.147}$$

Since diffusion-limited permeation is characterized by a dissociation flux that is large in comparison with the diffusion flux in the bulk, the permeation number takes values

$W \to \infty$. In contrast, surface-limited permeation is represented by a permeation number $W \to 0$.

The usefulness of the permeation number becomes apparent when dividing the general definitions of the steady state permeation flux (2.136) by the derived diffusion-limited permeation flux $\overline{J}_{\mathrm{per}}^{\mathrm{dl}}$ assuming that $p^{\mathrm{DI}} \approx 0$

$$W\left(1-\lambda_{\mathrm{r}}^{2}\right)=\lambda_{\mathrm{r}}-\zeta_{\mathrm{r}} \quad \text{and} \quad W\zeta_{\mathrm{r}}^{2}=\lambda_{\mathrm{r}}-\zeta_{\mathrm{r}}\,. \tag{2.148}$$

Here, ζ_{r} and λ_{r} label the dimensionless reduced concentrations. They are defined by

$$\zeta_{\mathrm{r}} \equiv \frac{c_{\mathrm{DI}}}{c_{\mathrm{UI,eq}}} \qquad \text{and} \qquad \lambda_{\mathrm{r}} \equiv \frac{c_{\mathrm{UI}}}{c_{\mathrm{UI,eq}}} \tag{2.149}$$

where the equilibrium concentrations are those written in equation (2.137). Combining the two equations (2.148) leads to the general equation for steady state permeation

$$W^{2}\zeta_{\mathrm{r}}^{4}+2W\zeta_{\mathrm{r}}^{3}+2\zeta_{\mathrm{r}}^{2}=1\,. \tag{2.150}$$

This equation reveals that for $W \to \infty$ in the diffusion-limited regime $\zeta_{\mathrm{r}}^{2} \to 1/W$ and for $W \to 0$ in the surface-limited regime $\zeta_{\mathrm{r}}^{2} \to 1/2$. Inserting these limit values of the reduced concentration into equation (2.136) yields the expressions for $\overline{J}_{\mathrm{per}}^{\mathrm{dl}}$ [equation (2.142)] and $\overline{J}_{\mathrm{per}}^{\mathrm{sl}}$ [equation (2.146)], respectively.

A solution of the general equation for steady state permeation (2.150) of the form

$$\log\left(\zeta_{\mathrm{r}}^{2}\right)=\frac{\sum_{n=0}^{5} a_{n}\left[\ln\left(W^{2}\right)\right]^{n}}{\sum_{n=0}^{5} b_{n}\left[\ln\left(W^{2}\right)\right]^{n}} \tag{2.151}$$

was found by Serra *et al* [192]. They numerically determined the parameters $a_0 = 5.31 \times 10^{-1}$, $a_1 = -9.72 \times 10^{-2}$, $a_2 = -1.83 \times 10^{-2}$, $a_3 = -1.26 \times 10^{-2}$, $a_4 = -5.46 \times 10^{-5}$, $a_5 = -8.20 \times 10^{-7}$ and $b_0 = 1$, $b_1 = 1.10 \times 10^{-2}$, $b_2 = 1.13 \times 10^{-2}$, $b_3 = 1.74 \times 10^{-5}$, $b_4 = 8.98 \times 10^{-6}$, $b_5 = -4.67 \times 10^{-8}$. Substituting the obtained solution (2.151) into equation (2.148) provides the second reduced concentration λ_{r} as a function of W. Both reduced concentrations are plotted in figure 2.11 as a function of the permeation number W. Whenever in this work it is referred to Serra's solution of the general equation for steady state permeation, what is meant are the two plotted relationships between the reduced concentrations ζ_{r} and λ_{r} and the permeation number W determined by equation (2.151) with the above-reported coefficients.

Esteban *et al* evaluated that in a range of about $0.1 < W < 5.5$ the permeation numbers represent an intermediate permeation regime which can be assigned neither to the diffusion-limited nor to the surface-limited regime [190].

According to the equations (2.100), (2.137) and (2.149), if $p^{\mathrm{DI}} \approx 0$ the steady state permeation flux is given by

$$\overline{J}_{\mathrm{per}} = \zeta_{\mathrm{r}}^{2} \cdot 2\sigma k_{\mathrm{d}} p^{\mathrm{UI}}\,. \tag{2.152}$$

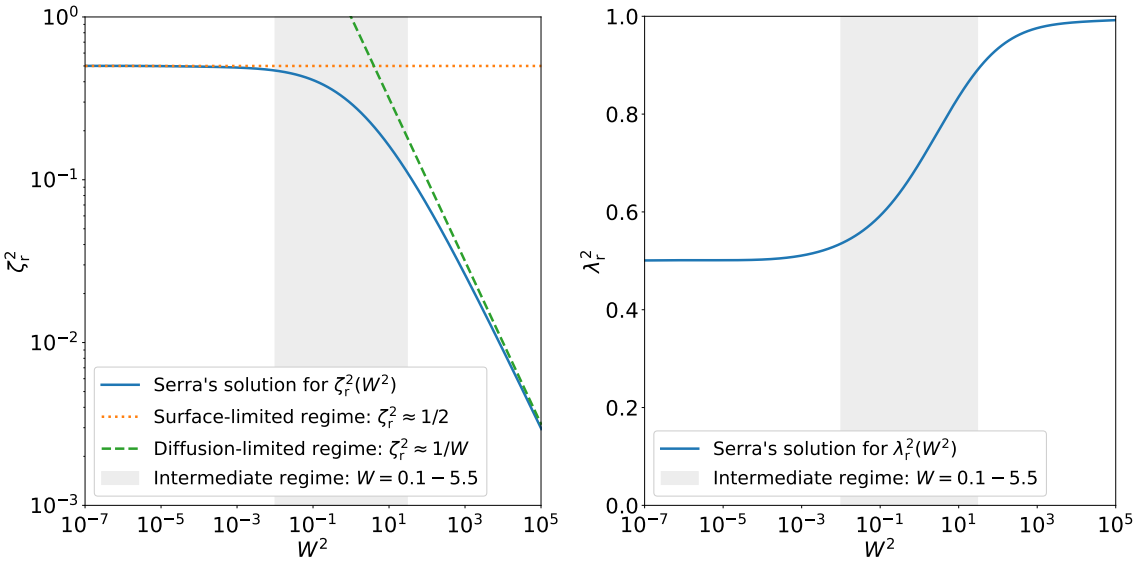

Fig. 2.11. [Left] Solution (2.151) of the general equation of steady state permeation (2.150) obtained by Serra *et al*. It is used to define the generally accepted zones of diffusion-limited and surface-limited permeation [193]. [Right] Relationship between λ_r and W determined from the numerically derived solution (2.151) and equation (2.149).

2.3.5. Permeation time-lag

The time evolution of the concentration profile derived from the analytical solution (2.133) of Fick's second law with the fixes interface concentrations c_{UI} and c_{DI} can be used to calculate the approximate atomic permeation flux into the downstream side by applying Fick's first law to $c(z = d, t)$. When additionally assuming that $c_{DI} = 0$, which for example would be approximately the case for diffusion-limited permeation into an evacuated downstream side, the permeation flux writes

$$J_{per}(t) = -D\frac{\partial c(z=d,t)}{\partial z} = \frac{Dc_{UI}}{d} + \frac{2Dc_{UI}}{d}\sum_{n=1}^{\infty}(-1)^n \exp\left(\frac{-Dn^2\pi^2 t}{d^2}\right). \tag{2.153}$$

The course of the permeation flux calculated with equation (2.153) for the example parameter set $D = 1 \times 10^{-8}\,\mathrm{m^2/s}$, $d = 1 \times 10^{-3}\,\mathrm{m}$ and $c_{UI} = 1\,\mathrm{mol/m^3}$ is plotted in the left-hand graph of figure 2.12. It can be seen how after a transient regime of increasing permeation flux, steady state permeation is established where the permeation flux becomes constant.

A subsequent integration over time provides the cumulative mole number of isotopes $\varkappa(t)$ which have passed through an area A_{per} of the downstream interface after the time t [165]

$$\frac{\varkappa(t)}{A_{per}} = \frac{Dc_{UI}t}{d} - \frac{c_{UI}d}{6} - \frac{2c_{UI}d}{\pi^2}\sum_{n=1}^{\infty}\frac{(-1)^n}{n^2}\exp\left(\frac{-Dn^2\pi^2 t}{d^2}\right). \tag{2.154}$$

It is plotted in the right-hand graph of figure 2.12 for $A_{per} = 1\,\mathrm{m}$. For $t \to \infty$ the total number of permeated isotopes $\varkappa(t)$ converges against a straight line (see figure 2.12)

$$\lim_{t\to\infty}\varkappa(t) = A_{per}\cdot\frac{Dc_{UI}}{d}\left(t - \frac{d^2}{6D}\right). \tag{2.155}$$

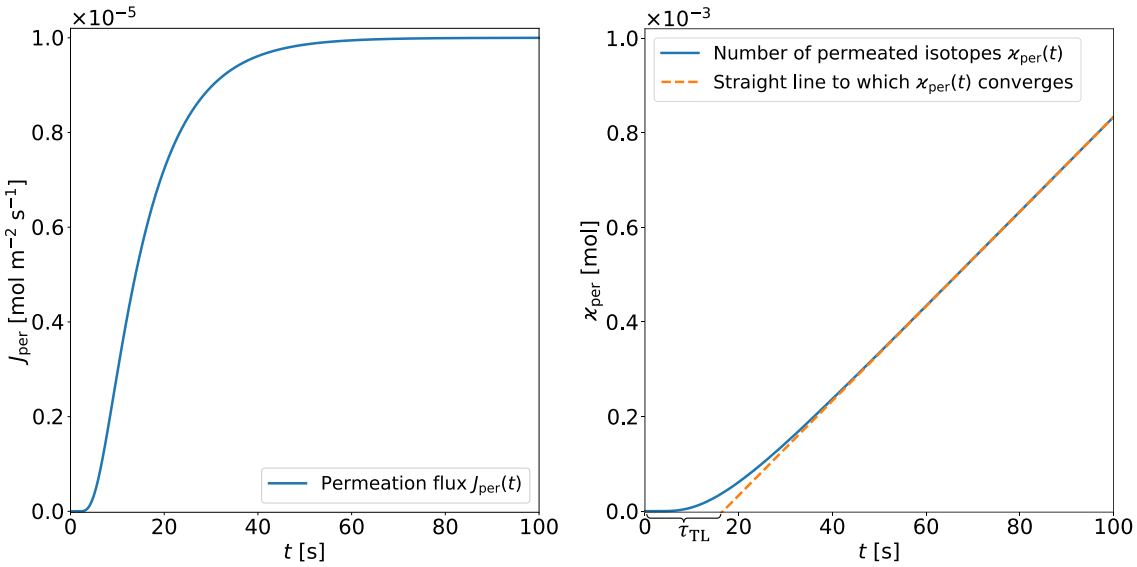

Fig. 2.12. [Left] Analytically calculated permeation flux using equation (2.153) with the parameter set $D = 1 \times 10^{-8}$ m^2/s, $d = 1 \times 10^{-3}$ m and $c_{UI} = 1$ mol/m^3. [Right] Cumulative mole number of permeated isotopes through a unit area $A_{per} = 1$ m calculated using equation (2.154). It converges against a straight line whose intercept with the t-axis is known as the permeation time-lag.

The intercept of the straight line with the t-axis τ is called the permeation time-lag and is related to the diffusion coefficient D as follows

$$\tau_{TL} \approx \frac{d^2}{6D} \,. \tag{2.156}$$

Thus, measuring the permeation time lags in a series of steady-state permeation flux measurements in the diffusion-limited regime is an experimental method for determining the diffusion coefficient of the sheet material. It should be noted, however, that if trapping effects are dominant, for example in endothermic hydrogen absorbing metals at low temperatures, the effective diffusion coefficient D^{eff} would be measured with this method instead.

2.3.6. Permeation through cylindrical wall

Steady state permeation through a plane metal sheet is characterized by equal atomic fluxes at both interfaces and a linear concentration profile. However, in a scenario where the two sides of the permeation membrane are the inner and outer surface of a cylindrical pipe the steady state concentration profile is no longer linear and the fluxes at the two interfaces differ.

For a cylindrical wall, Fick's second law and its steady state expression write

$$\frac{\partial c(r,t)}{\partial t} = \frac{1}{r}\frac{\partial}{\partial r}\left[rD\frac{\partial c(r,t)}{\partial r}\right] \quad \Rightarrow \quad 0 = \frac{\partial}{\partial r}\left[rD\frac{\partial c(r,t)}{\partial r}\right], \quad \text{if} \quad \frac{\partial c(r,t)}{\partial t} = 0 \tag{2.157}$$

If the concentration at the inner side of the cylindrical wall at the radial position r_{in} is kept at the constant concentration c_{in} and the outer side of the cylindrical wall at the radial

position r_{out} is maintained at the constant concentration c_{out}, the steady state diffusion equation has the solution [165]

$$c(r) = \frac{c_{\text{in}} \ln(r_{\text{out}}/r) + c_{\text{out}} \ln(r/r_{\text{in}})}{\ln(r_{\text{out}}/r_{\text{in}})}, \quad \text{with} \quad r_{\text{in}} \leq r \leq r_{\text{out}}. \tag{2.158}$$

Applying Fick's first law yields an expression for the steady state particle flux at the radial position r in the membrane. It takes the following form if it is defined as positive when oriented from the cylinder center towards its exterior space [194]

$$\overline{J}^{\circledcirc}(r) = \frac{D(c_{\text{in}} - c_{\text{out}})}{r \ln(r_{\text{out}}/r_{\text{in}})}. \tag{2.159}$$

General equation of steady state permeation through cylindrical membranes

While the information presented in the previous sections of this chapter is extracted from the literature, the theoretical formulation presented in the following last subsection of this chapter is a novel theoretical description developed within the scope of this thesis.

From equation (2.159) it follows that the particle flux at the interface of the inner radius of the cylindrical wall can be written as

$$\overline{J}^{\circledcirc}_{\text{in}} = f^{\text{c}}_{\text{in}} \cdot \frac{D(c_{\text{in}} - c_{\text{out}})}{d}, \quad \text{with} \quad f^{\text{c}}_{\text{in}} \equiv \frac{d}{r_{\text{in}} \ln(r_{\text{out}}/r_{\text{in}})}. \tag{2.160}$$

where the flux at the outer radius yields

$$\overline{J}^{\circledcirc}_{\text{out}} = f^{\text{c}}_{\text{out}} \cdot \frac{D(c_{\text{in}} - c_{\text{out}})}{d}, \quad \text{with} \quad f^{\text{c}}_{\text{out}} \equiv \frac{d}{r_{\text{out}} \ln(r_{\text{out}}/r_{\text{in}})}. \tag{2.161}$$

In these relations, $d = r_{\text{out}} - r_{\text{in}}$ is the thickness of the cylindrical wall. A relationship between the fluxes $\overline{J}^{\circledcirc}_{\text{in}}$ and $\overline{J}^{\circledcirc}_{\text{out}}$ yields when combining the equations (2.160) and (2.161)

$$\overline{J}^{\circledcirc}_{\text{out}} = \frac{f^{\text{c}}_{\text{out}}}{f^{\text{c}}_{\text{in}}} \cdot \overline{J}^{\circledcirc}_{\text{in}}. \tag{2.162}$$

Comparing the equations (2.160) and (2.161) with expression (2.135) of the particle flux through a parallel membrane $\overline{J}^{\parallel}$ reveals that for parallel membranes $f^{\text{c}}_{\text{in}} = f^{\text{c}}_{\text{out}} = 1$.

It is important to note that according to the steady state relation (2.162), for cylindrical membranes the two equations (2.130) and (2.131) are linked through the following expression, if it is assumed that $p^{\text{DI}} \approx 0$

$$\overline{J}^{\circledcirc}_{\text{net,DI}} = \frac{f^{\text{c}}_{\text{DI}}}{f^{\text{c}}_{\text{UI}}} \cdot \left(2\sigma k_{\text{d}} p^{\text{UI}} - 2\sigma k_{\text{r}} c^2_{\text{UI}}\right) = 2\sigma k_{\text{r}} c^2_{\text{DI}}. \tag{2.163}$$

The downstream atomic net flux is considered as the actual permeation flux through the cylindrical membrane and labeled with $\overline{J}_{\text{per}} \equiv \overline{J}^{\circledcirc}_{\text{net,DI}}$. If the inner cylinder surface is the upstream side then $f^{\text{c}}_{\text{UI}} = f^{\text{c}}_{\text{in}}$ and $f^{\text{c}}_{\text{DI}} = f^{\text{c}}_{\text{out}}$. Otherwise, the conversion factors follow the contrary relations $f^{\text{c}}_{\text{DI}} = f^{\text{c}}_{\text{in}}$ and $f^{\text{c}}_{\text{UI}} = f^{\text{c}}_{\text{out}}$.

Dividing equation (2.163) by the derived formula for the diffusion-limited permeation flux (2.142) for parallel membranes, and inserting the definitions of the permeation number (2.147) and the reduced concentrations (2.149), leads to the expressions

$$\frac{W}{f_{\mathrm{UI}}^{\mathrm{c}}}\left(1-\lambda_{\mathrm{r}}^{2}\right)=\lambda_{\mathrm{r}}-\zeta_{\mathrm{r}} \qquad \text{and} \qquad \frac{W}{f_{\mathrm{DI}}^{\mathrm{c}}}\zeta_{\mathrm{r}}^{2}=\lambda_{\mathrm{r}}-\zeta_{\mathrm{r}}\,. \tag{2.164}$$

Their combination yields the general equation for steady state permeation for cylindrical membranes

$$\left(\frac{W}{f_{\mathrm{DI}}^{\mathrm{c}}}\right)^{2}\zeta_{\mathrm{r}}^{4}+\frac{2W}{f_{\mathrm{DI}}^{\mathrm{c}}}\zeta_{\mathrm{r}}^{3}+\left(1+\frac{f_{\mathrm{UI}}^{\mathrm{c}}}{f_{\mathrm{DI}}^{\mathrm{c}}}\right)\zeta_{\mathrm{r}}^{2}=1\,. \tag{2.165}$$

From the equations (2.164) and (2.165) it can be seen that in the surface-limited regime where $W \ll 0$ the reduced concentrations approach the same relations

$$\lambda_{\mathrm{r}}^{2}\rightarrow\frac{1}{1+f_{\mathrm{UI}}^{\mathrm{c}}/f_{\mathrm{DI}}^{\mathrm{c}}} \qquad \text{and} \qquad \zeta_{\mathrm{r}}^{2}\rightarrow\frac{1}{1+f_{\mathrm{UI}}^{\mathrm{c}}/f_{\mathrm{DI}}^{\mathrm{c}}}\,. \tag{2.166}$$

Moreover, the equations (2.164) and (2.165) allow concluding that in the diffusion-limited permeation regime where the permeation number $W \gg 0$ is very high, the reduced concentrations in cylindrical membranes converge against

$$\lambda_{\mathrm{r}}^{2}\rightarrow 1 \qquad \text{and} \qquad \zeta_{\mathrm{r}}^{2}\rightarrow\frac{f_{\mathrm{DI}}^{\mathrm{c}}}{W}\,. \tag{2.167}$$

One needs to be aware of the fact that Serra's derived solution of the general equation for steady state permeation (2.151) in parallel membranes does not solve equation (2.165) for cylindrical membranes.

Eventually, inserting the determined limit values of ζ_{r}^{2} which are shown in the equations (2.166) and (2.167) into equation (2.152) provides expressions for the surface-limited and diffusion-limited mono-isotopic permeation flux at the downstream interface of a cylindrical membrane if $p^{\mathrm{DI}} \approx 0$.

$$\overline{J}_{\mathrm{per}}^{\mathrm{sl},\circledcirc}=\frac{1}{1+f_{\mathrm{UI}}^{\mathrm{c}}/f_{\mathrm{DI}}^{\mathrm{c}}}\cdot 2\sigma k_{\mathrm{d}}p^{\mathrm{UI}} \qquad \text{(surface-limited regime)} \tag{2.168}$$

$$\overline{J}_{\mathrm{per}}^{\mathrm{dl},\circledcirc}=f_{\mathrm{DI}}^{\mathrm{c}}\cdot\frac{\Phi}{d}\sqrt{p^{\mathrm{UI}}} \qquad \text{(diffusion-limited regime)} \tag{2.169}$$

3. MEASUREMENT TECHNIQUES AND COMPONENTS

This chapter presents the fundamentals of technical components, measuring devices, and techniques that are addressed or applied in this work. Introducing their characteristic features and working principles is important to justify the choice of technical devices and components which are used for the developed experimental designs presented in this thesis.

3.1. Vacuum technology

The experimental investigation of hydrogen in metals often demands an evacuation of air from the corresponding experimental chamber. This has multiple reasons ranging from the specific requirements of the measuring instrumentation to avoiding oxidation of the sample material. Depending on the applied experimental technique the air is usually replaced by either a hydrogen gas-inert gas mixture or by a high vacuum environment.

3.1.1. Vacuum fundamentals

The term vacuum refers to a gas mixture with a pressure below standard state atmospheric pressure $p^\circ < 101\,325\,\mathrm{Pa}$. The mean free path $\overline{\lambda}$ is defined as the average distance a particle travels before it collides with another particle. Applying the kinetic theory of gases the mean free path can be expressed by

$$\overline{\lambda} = \frac{RT}{\sqrt{2}\pi(2r)^2 p}\,, \tag{3.1}$$

where r is the radius of the gas particles [176]. The formula reveals that at constant temperature the product $\overline{\lambda} \cdot p = \text{const.}$ and merely depends on the particle sizes. For example, at an ambient temperature of $T = 293\,\mathrm{K}$ in a pure $^1H_2$ gas $\overline{\lambda} \cdot p = 1.2 \times 10^{-2}\,\mathrm{m\,Pa}$ and in air $\overline{\lambda} \cdot p = 6.67 \times 10^{-3}\,\mathrm{m\,Pa}$ [195]. The resulting average mean free paths for molecules in $^1H_2$ gas and in air as a function of the total pressure are plotted in the left-hand graph of figure 3.1. The movement of particles in a vacuum chamber (VC) with a characteristic wall distance L_{VC} has distinct characteristics depending on whether $\overline{\lambda} \gg L_{\mathrm{VC}}$, $\overline{\lambda} \approx L_{\mathrm{VC}}$ or $\overline{\lambda} \ll L_{\mathrm{VC}}$. Therefore, different vacuum regimes can be defined using a dimensionless number, the Knudsen number $\mathrm{Kn} \equiv \overline{\lambda}/L_{\mathrm{VC}}$.

It is generally accepted to speak of rough vacuum if $\mathrm{Kn} < 0.01$. In this regime, the motion of the gas particles is mainly driven by the interaction between particles as they collide with each other far more often than with the chamber wall. This results in a flow behavior known as viscous flow which is determined by the internal friction of the gas. It manifests in a collective laminar or turbulent particle motion driven by a pressure variation

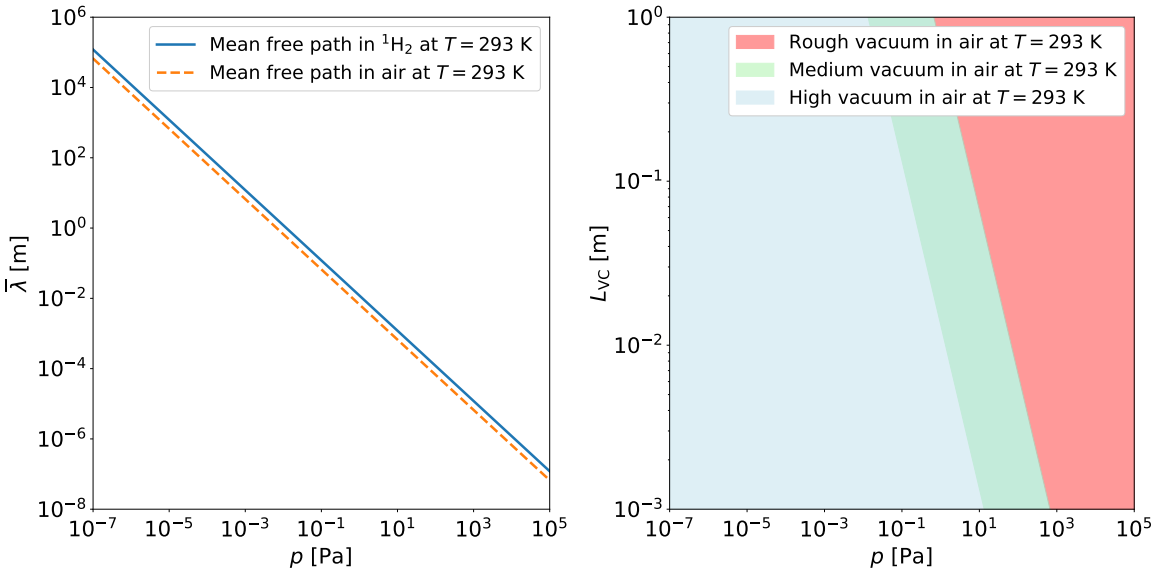

Fig. 3.1. [Left] Mean free path of molecules in $^1H_2$ and air at $T = 293$ K plotted against the total pressure. [Right] Pressure ranges of different vacuum regimes inside of a pipe as a function of the pipe diameter.

in the gas. The red shaded area in the right-hand plot of figure 3.1 represents the range of total pressure where air enclosed in a pipe with an inner radius r_{in} is considered to follow the characteristics of a rough vacuum at $T = 293$ K.

The lower the pressure the less the individual trajectories of the particles are influenced by collisions with other particles. At very low pressures where Kn > 0.5 a gas is generally considered to occur in the high vacuum regime where the particles collide far more frequently with the vessel wall than with other particles. Under such conditions, a collective particle motion can no longer be observed as the particles move almost freely through the vessel. They follow straight trajectories through the chamber and are randomly scattered towards arbitrary directions every time they collide with the vessel walls [196]. This results in a random bouncing motion of each particle through the vacuum chamber. Such a particle motion in gas is known as molecular flow. The pressure range of the high vacuum regime in which molecular flow occurs is represented by the blue shaded area in the right-hand graph of figure 3.1. Another property of the high vacuum regime is that the number of particles adsorbed to the chamber wall is considerably higher than the number of particles moving through the interior space of the chamber. The ultra-high-vacuum (UHV) regime is roughly defined for total pressures of approximately below $p < 1 \times 10^{-7}$ Pa. In this regime, the characteristic time required to form an entire monolayer of adsorbed particles at the wall lasts several minutes, in contrast to the high-vacuum regime where it lasts only a few seconds.

The transition regime between rough and high vacuum where $0.01 <$ Kn < 0.5 is called medium vacuum. Here, an intermediate flow regime determines the particle motion known as Knudsen flow. At higher temperatures or if the gas particles are smaller (like

in H_2 gas), the boundaries of the different vacuum regimes are slightly shifted towards higher pressures.

A method to quantify a net flow of gas molecules in a vacuum chamber is provided by the concept of the throughput q_{pV} defined through the ideal gas law

$$q_{\mathrm{pV}} \equiv \frac{\varkappa RT}{t} = \frac{pV}{t} \tag{3.2}$$

It is usually expressed with the units $[\mathrm{mbar} \cdot \mathrm{L/s}]$. Regardless of the vacuum regime the throughput from a zone of pressure p_1 towards an area of pressure $p_2 < p_1$ is proportional to the pressure difference $\Delta p = p_1 - p_2 > 0$, such that $q_{\mathrm{pV}} = \Delta p \cdot C_{\mathrm{sec}}$. In this equation, the proportionality factor C_{sec} is called the conductance of the observed section of the vacuum chamber.

In the viscous flow regime in rough vacuum, if the ratio of the two pressures p_1 and p_2 between which the flow occurs is greater than a critical value $p_1/p_2 > (p_1/p_2)_{\mathrm{chok}}$, the flow velocity reaches its maximum speed, the speed of sound, and the particle flow in the studied segment reaches a maximum throughput. Hence, above $\Delta p > \Delta p_{\mathrm{c}}$ the throughput remains constant which is known as choked flow. This occurs for example if the vessel is vented or in case of a leak between the vacuum chamber and the outer atmosphere.

For non-choked flows, the expression of the conductance depends on the geometrical shape of the flow segment (orifice, pipe, etc.) and on the vacuum regime. It can be derived [195] that in the laminar viscous flow regime in rough vacuum at $T = 293\,\mathrm{K}$, the conductance of a pipe of length l_{pipe} and inner diameter r_{in} approaches the expression

$$C_{\mathrm{pipe,vis}}\,[\mathrm{L/s}] = 1.35 \times 10^6 \cdot \frac{(2r_{\mathrm{in}})^4}{l_{\mathrm{pipe}}} \cdot \langle p \rangle \ , \tag{3.3}$$

It is a function of the average pressure $\langle p \rangle$ in the pipe section. In the molecular flow regime of air molecules, the conductance becomes pressure-independent and converges against

$$C_{\mathrm{pipe,mol}}\,[\mathrm{L/s}] = 1.21 \times 10^5 \cdot \frac{(2r_{\mathrm{in}})^3}{l_{\mathrm{pipe}}} \ . \tag{3.4}$$

The total conductance of a system of pipes $n = 1, \ldots, N$ connected in series is given by

$$\frac{1}{C_{\mathrm{tot}}} = \sum_{n=1}^{N} \frac{1}{C_{\mathrm{pipe},n}} \ . \tag{3.5}$$

Apart from the gas flow through the internal space of a chamber, it needs to be considered that in reality gas particles leave and enter the vacuum vessel through leakages, permeation, leak valves, and adsorption/desorption processes at the walls. The additional particle flows associated with each of these particle sinks and sources are quantified by individual flow rates as expressed in equation (3.2). Their sum is considered as the total additional particle flow $q_{\mathrm{pV}}^{\mathrm{add}} = q_{\mathrm{pV}}^{\mathrm{leak}} + q_{\mathrm{pV}}^{\mathrm{per}} + q_{\mathrm{pV}}^{\mathrm{degas}}$ due to particle sinks and sources into and out of the vacuum chamber.

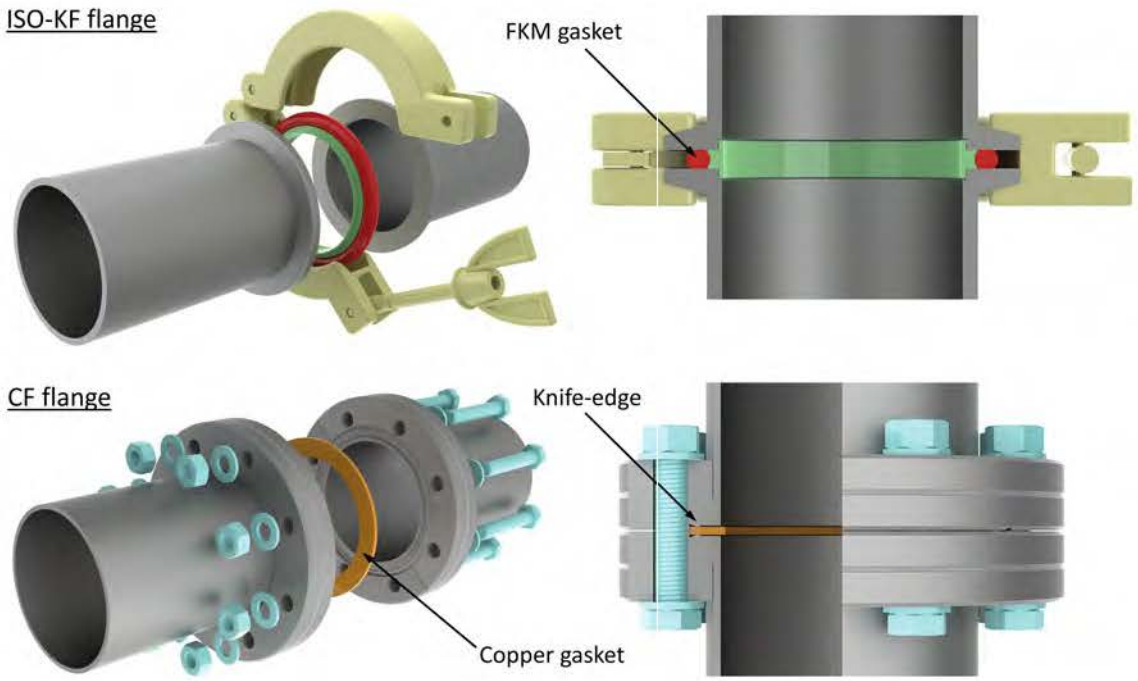

Fig. 3.2. [top] Image of an ISO-KF high-vacuum flange connection. It uses FKM gaskets for the seal and is fastened with a clamp. [bottom] Screwed CF ultra-high-vacuum flange connection. The seal is realized by circular knife edges cutting from both sides into a flat copper gasket [197].

3.1.2. Piping components

Most commercially available vacuum chamber components are made of 304L and 316L chromium-nickel austenitic stainless steel (SS). These alloys exhibit a relatively low permeability for atmospheric gases, good chemical compatibility with many harsh environments, and sufficiently high strength for flange connections [197]. The most common vacuum chamber components are pipes which come with different types of flanges or tube fittings. Each design has its individual advantages and disadvantages and is therefore chosen depending on the respective experimental conditions.

Flanges, fittings, and gaskets

For applications with maximum temperatures of approximately $T \approx 423\,\mathrm{K}$ in a pressure range $1 \times 10^{-7}\,\mathrm{Pa} < p < 1.5 \times 10^{5}\,\mathrm{Pa}$ it is convenient to use pipe components with commercially available ISO-KF flanges. A 3D image of a typical ISO-KF flange connection between two pipes is visualized at the top of figure 3.2 [197]. The image shows how two flat KF flanges are pressed from both sides against a fluoroelastomer (FKM) gasket surrounding a stainless steel spacer ring using a hand-fastened stainless steel clamp. There is no other type of vacuum flange that can be installed and disconnected as quickly and easily as ISO-KF flanges. However, there is the drawback that FKM gaskets have a lower temperature resistance compared to metallic gaskets. In addition, FKM gaskets exhibit a relatively high total gas permeation rate of the order of $q_{\mathrm{pV}} \approx 1 \times 10^{-6}\,\mathrm{mbar \cdot L/s}$ per

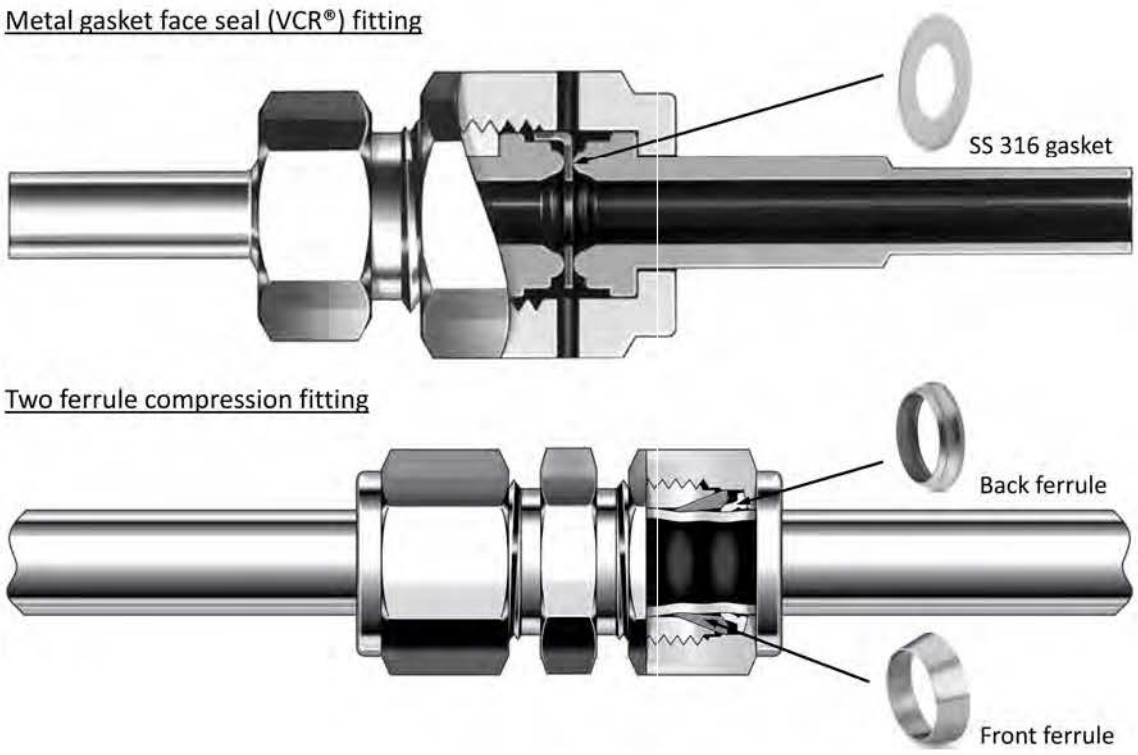

Fig. 3.3. Section cut through a typical commercially available [top] metal gasket face seal (VCR®) fitting [200] and a [bottom] two ferrule compression fitting [202] made entirely of 316 stainless steel.

gasket when the external atmosphere is air with a relative humidity of 75 % at $T = 293\,\mathrm{K}$ [198]. The gas component in air that has by far the highest permeation rate through FKM is ^1H_2O.

If lower pressures of $1 \times 10^{-10}\,\mathrm{Pa} < p < 1 \times 10^{5}\,\mathrm{Pa}$ are required for ultra-high-vacuum applications or if the seal is exposed to higher temperatures of $T < 723\,\mathrm{K}$ it is usually made use of commercially available CF flange connections. The principle of the CF seal is shown in figure 3.2 below [197]. A stainless steel knife edge surrounds the tube opening of each CF flange. The knife edges are pressed from both sides into a flat oxygen-free high conductivity (OFHC) copper gasket ring via a screwed flange connection. Thus, it is possible to reach helium leak rates of below $q_{\mathrm{pV}} \approx 1 \times 10^{-10}\,\mathrm{mbar \cdot L/s}$ per gasket [199]. For temperatures $473\,\mathrm{K} < T < 723\,\mathrm{K}$ it is required to use silver-plated OFHC copper gaskets.

In case even higher temperatures $T < 810\,\mathrm{K}$, higher pressures $1 \times 10^{-9}\,\mathrm{Pa} < p < 3.3 \times 10^{6}\,\mathrm{Pa}$ or corrosion resistance are needed, commercially available metal gasket face seal (VCR®) fittings can be used which are exclusively made of 316 stainless steel parts [197], [200], [201]. A section cut of such a fitting connecting two pipes with a VCR® flange is shown at the top of figure 3.3 [200]. VCR® flanges are characterized by a rounded bulge ring surrounding the pipe opening. The bulges of two flanges are pressed from both sides into a highly polished flat stainless steel gasket by screwing a single male nut from one side into a female nut on the other side. This relatively simple procedure

TABLE 3.1

INNER DIAMETERS OF STAINLESS STEEL TUBES/PIPES CONNECTED TO DIFFERENT TYPES AND SIZES OF COMMERCIALLY AVAILABLE VACUUM FITTINGS/FLANGES.

Fitting/flange	1/4 inch r_{in} [mm]	1/2 inch r_{in} [mm]	DN16 r_{in} [mm]	DN25 r_{in} [mm]	DN40 r_{in} [mm]	Ref.
ISO-KF	-	-	8	12	20.25	[197]
CF	-	-	8	12	18.75	[197]
VCR®	2.45	5.45	-	-	-	[200]
Double ferrule	2.45	5.45	-	-	-	[202]

allows the flanges to be connected and disconnected quickly and repeatedly.

An alternative to VCR® flanges are double ferrule compression fittings. They withstand even higher temperatures of $T < 921\,\mathrm{K}$ in a slightly narrower pressure range $1 \times 10^{-7}\,\mathrm{Pa} < p < 1.7 \times 10^{6}\,\mathrm{Pa}$ [197], [201], [202]. As the section cut at the bottom of figure 3.3 illustrates, double ferrule compression fittings allow connecting naked stainless steel pipes with no particular flange opening. Leak tightness is reached by pressing two cone-shaped stainless steel rings (back and front ferrule) from outside into each pipe wall using female nuts which are screwed to the corresponding ends of the fitting (see figure 3.3). A main advantage of VCR® and double ferrule compression fitting components is their outstanding chemical resistance against corrosive environments. Moreover, they can be used for both liquids and gases.

The inner diameters of several differently sized commercially available vacuum flanges and fittings of the presented types are listed in table 3.1 [197], [200], [202]. Of each of the introduced flange and fitting types, there exist nipples, elbows, tees, crosses, and flexible hoses.

Since commercially available flanges and fittings are bound to their fixed designs, finite gasket options, and limited temperature resistivities, some specific applications require custom-designed vacuum seals. Probably the most sophisticated vacuum sealing concept that can be adapted to a wide range of needs are spring-energized metal seals (Helicoflex®). They comprise a hollow helicoidal metal spring surrounded by an outer metallic lining as visible in the left-hand image in figure 3.4 [203], [204]. In the typical Helicoflex® design the metallic lining is open towards the high-pressure side. As the two images on the right-hand side of figure 3.4 show, a Helicoflex® seal is placed inside of a custom-designed metallic gasket bed. The vacuum seal is established by compressing the O-ring with a second metallic surface until metal-to-metal contact with the upper stage of the groove is attained. The cross-sectional diameter of a spring-energized gasket needs to be designed according to the depth of the gasket bed such that during compression it is contracted by a carefully specified amount which leads to plastic deformation of the outer

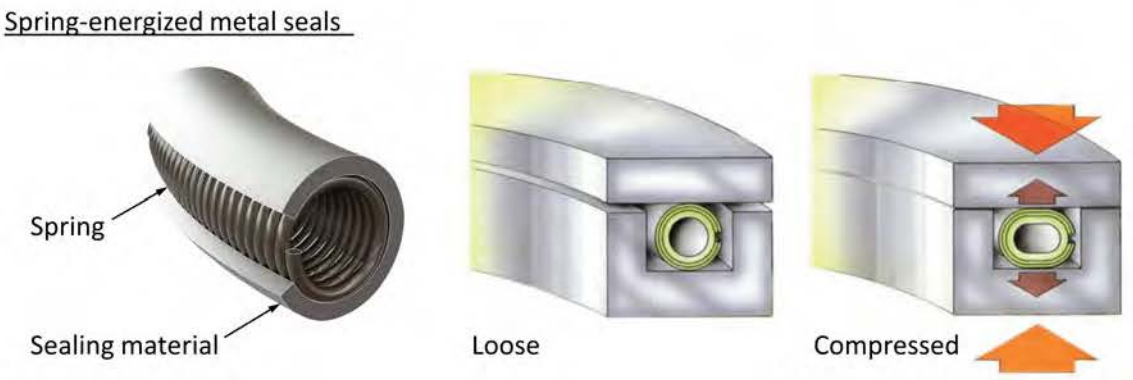

Fig. 3.4. Section-cut of a spring-energized vacuum seal and illustration of its sealing mechanism when placed into a custom-designed groove [203], [204].

lining without plastically deforming the flange material. The counter force of the seal is provided by the highly elastic interior spring which leads to an outstanding adaption of the outer lining material to irregularities of the groove surface. Dependent on the seal design this enables working at pressures between $1 \times 10^{-8}\,\mathrm{Pa} < p < 3 \times 10^{8}\,\mathrm{Pa}$ with leak rates down to $q_{\mathrm{pV}} < 1 \times 10^{-11}\,\mathrm{mbar \cdot L/s}$ [203]. The wide range of possible gasket materials is of specific interest when working with especially corrosive fluids like liquid alkali metals. Certain spring and outer lining materials allow maintaining ultra-high-vacuum conditions at temperatures of up to $T = 1073\,\mathrm{K}$.

Valves

Another crucial element of experimental vacuum or gas-filled chambers are valves. There are many different types of vacuum valves on the market that are used for different purposes. The following paragraphs introduce the type of valves installed in the developed experimental designs of this thesis.

Open/close valves are used to hermetically block one part of the vacuum chamber from another when closed. They can be opened to such an extent that the conductance of the chamber is nearly not affected by the valve's orifice. An image of a regular all-metal open/close angle valve together with its interior structure is presented on the left-hand side of figure 3.5 [205]. By rotating the valve's actuator a plate equipped with a metal gasket which is located at the end of a threaded rod moves down until it presses against the valve seat and thus closes one of the two exit pipes (see figure 3.5). The moving parts are hermetically separated from the valve interior by a welded non-rotating metal bellow. Thus, they have very low leak rates and can be used for ultra-high-vacuum applications [197]. This type of all-metal open/close valve withstands temperatures of up $T = 573\,\mathrm{K}$. They also exist equipped with FKM gaskets for lower temperature applications [206].

As discussed above, for higher pressures or temperatures $T > 573\,\mathrm{K}$ it is recommendable to design the experimental chamber with double ferrule compression fittings. One of the most chemically and thermally resistant compression fitting valve which simul-

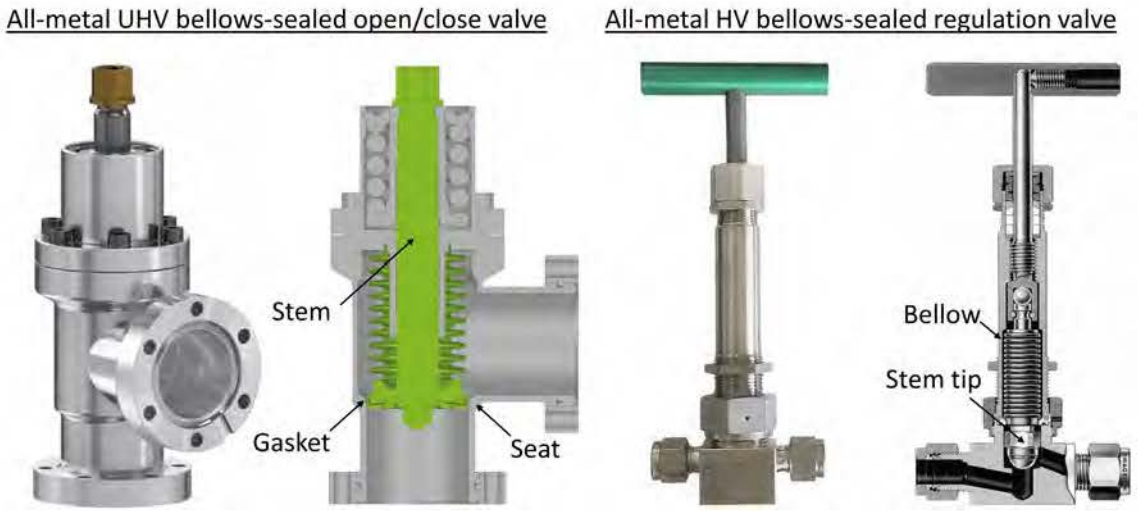

Fig. 3.5. [Left] Image and section cut of a closed all-metal ultra-high-vacuum open/close valve with CF flanges. Regular high-vacuum open/close valves have the same design but are sealed with FKM gaskets instead. [Right] Image and section cut of a high-vacuum bellows-sealed high-temperature regulating valve for double ferrule compression fitting connections [201], [205].

taneously allows working at very high pressures and temperatures of up to $T < 921\,\mathrm{K}$ is an all-metal bellows-sealed high vacuum valve of the Swagelok U-series whose inner structure can be seen on the right-hand side of figure 3.5 [201]. It exists as an open/close version with a spherical stem tip made of a cobalt-based alloy or as a regulating version with a needle-shaped stainless steel stem tip that allows linearly adjusting the flow rate between a fully open and totally closed position. Due to their unique properties under extreme conditions, all-metal bellows-sealed high-temperature compression fitting valves can be installed in pipe systems that contain highly corrosive interior fluids such as liquid alkali metals.

In some experimental vacuum applications, it may be necessary to introduce gas into a vacuum chamber and maintain it stable at a certain pressure value. This requires precisely controlling the gas flow rate into the chamber for which normal open/close or regulating valves would be far too coarse. Instead, for this purpose, it is made use of gas dosing or leak valves. The left images of figure 3.6 show a high vacuum gas dosing valve together with its inner workings [207]. Valves with this design work according to the principle of a needle valve. A needle-shaped stem tip is lowered into a thin orifice located at the valve flange connected to the low-pressure side. Thus, the valve opening and accordingly the gas flow rate is continuously reduced. In this way it is possible to create an artificial leak between the two flanges of the valve in a range $5 \times 10^{-6}\,\mathrm{mbar \cdot L/s} < q_{\mathrm{pV}} < 5 \times 10^{2}\,\mathrm{mbar \cdot L/s}$. To change the gas flow through the pipe from its minimum leak rate to its maximum value the hand wheel needs to be turned numerous times. Every gas dosing valve has a specific relationship between the number of turns and the flow rate. It typically follows a logarithmic relationship. A special feature of the valve depicted in figure 3.6 is that regardless of the currently adjusted position of the needle, a second exterior stem equipped with an FKM gasket can be lowered into the valve seat. This

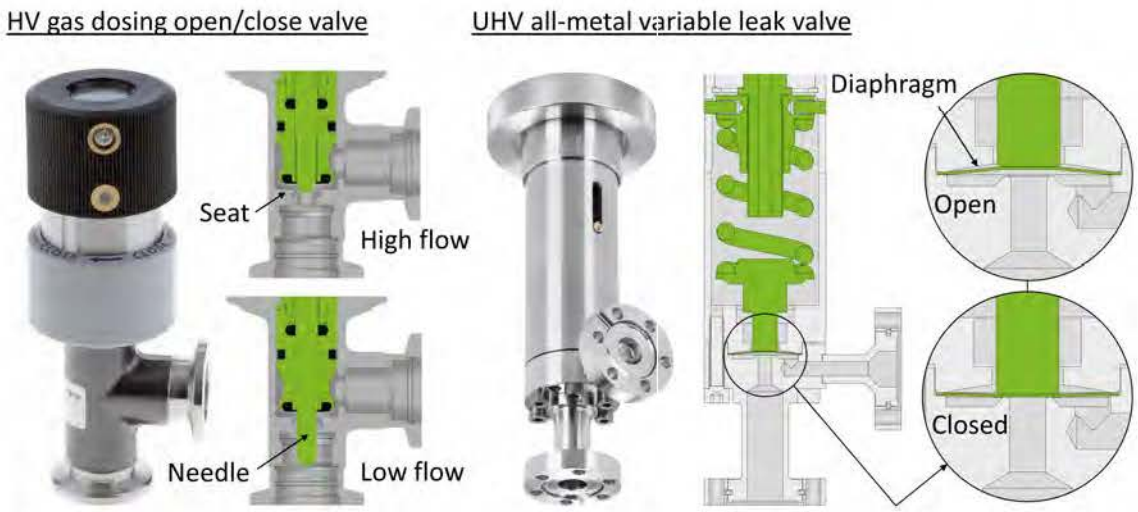

Fig. 3.6. Image and section cuts showing the partially opened and closed positions of a [Left] high-vacuum gas dosing open/close valve with ISO-KF flanges and an [Right] ultra-high-vacuum all-metal variable leak valve with CF flanges [207], [208].

allows closing and opening the valve without changing the adjusted flow rate in the open position. However, the gasket material limits the temperature resistance of this valve to relatively low temperatures of $T < 373\,\mathrm{K}$.

Higher temperatures of up to $T < 573\,\mathrm{K}$ can be withstood by all-metal variable leak valves like the one shown on the right-hand side of figure 3.6 [208]. As the picture reveals, the gas flow through the valve is controlled by varying the distance of a convex gold-plated diaphragm that sits above the valve seat. By turning the actuator a stem that is connected to a spring lowers the diaphragm and reduces the flow section. With this technique, the displayed ultra-high-vacuum valve enables controlling leak rates in a range of $1 \times 10^{-10}\,\mathrm{mbar \cdot L/s} < q_{\mathrm{pV}} < 5 \times 10^{2}\,\mathrm{mbar \cdot L/s}$.

3.1.3. Vacuum generation

To evacuate a gas vessel from atmospheric pressure down to the high vacuum regime it is necessary to connect the experimental chamber to a vacuum pumping system. A vacuum pump serves as a particle sink with a throughput $q_{\mathrm{pV}}^{\mathrm{pump}} = -p_{\mathrm{in}} \cdot S_{\mathrm{pump}} < 0$. Here, p_{in} is the intake pressure at the pump inlet, and $S_{\mathrm{pump}} = \mathrm{d}V/\mathrm{d}t$ the internal pumping speed of the vacuum pump. The pumping speed is equivalent to the net volume that leaves into the inlet of the pump per time and is given in $[\mathrm{L\,s^{-1}}]$.

However, vacuum pumps are usually attached to the vacuum chamber via a system of valves and pipes that impose resistance on the gas flow. As a consequence, the evacuation of the vacuum chamber takes place with a reduced pumping speed compared to that prevailing at the inlet flange of the pump. The reduced so-called effective pumping speed $S_{\mathrm{eff}} < S_{\mathrm{pump}}$ is a function of the internal pumping speed S_{pump} and the conductance of the

linking pipe system C_{tot} expressed by [195]

$$\frac{1}{S_{\text{eff}}} = \frac{1}{S_{\text{pump}}} + \frac{1}{C_{\text{tot}}}\,. \tag{3.6}$$

To ensure a maximum effective pumping speed for a given vacuum chamber the pump model should be chosen such that $S_{\text{pump}} > C_{\text{tot}}$. According to the continuity equation the gas throughputs at the pump inlet and in the vacuum chamber are equal, such that $p_{\text{VC}} = p_{\text{in}} \cdot S_{\text{pump}}/S_{\text{eff}}$. This implies that $p_{\text{VC}} > p_{\text{in}}$.

When assuming that the chamber volume V and the temperature T of the gas are constant, according to equation (3.2), the time derivative of the ideal gas law yields

$$V\frac{\mathrm{d}p_{\text{VC}}}{\mathrm{d}t} = \frac{\mathrm{d}\varkappa}{\mathrm{d}t}RT = -p_{\text{VC}} \cdot S_{\text{eff}} + q_{\text{pV}}^{\text{add}} \quad \Leftrightarrow \quad \frac{\mathrm{d}p_{\text{VC}}}{\mathrm{d}t} = \frac{1}{V} \cdot \left(q_{\text{pV}}^{\text{add}} - p_{\text{VC}} \cdot S_{\text{eff}}\right). \tag{3.7}$$

It describes the time evolution of the pressure in the vacuum chamber during the pump-down process. In this equation, it is taken into account that the total throughput in the vacuum chamber is the sum of the negative throughput induced by the pump and the throughput $q_{\text{pV}}^{\text{add}}$ that originates from molecules that leak, degas or permeate into or out of the chamber.

In the rough vacuum regime the particle flow $p_{\text{VC}} \cdot S_{\text{eff}}$ into the vacuum pump is high compared to the flow of leaking, permeating or degassing into or out of the chamber ($p_{\text{VC}} \cdot S_{\text{eff}} \gg q_{\text{pV}}^{\text{add}}$). This allows simplifying equation (3.7) and extracting an approximate expression for the pressure decrease during the pump-down process of a vacuum chamber if it is hypothetically assumed that S_{eff} remains constant

$$\int_{p^\circ}^{p_{\text{VC}}} \frac{1}{p'}\mathrm{d}p' = -\frac{S_{\text{eff}}}{V} \cdot t \quad \Leftrightarrow \quad p_{\text{VC}}(t) = p^\circ \exp\left(\frac{S_{\text{eff}}}{V} \cdot t\right). \tag{3.8}$$

Using this formula allows plotting the time required to lower the intake pressure from atmospheric pressure down to $p_{\text{VC}} = 1 \times 10^2\,\text{Pa}$ for different constant effective pumping speeds against the vessel volume. The graph is shown on the left-hand in figure 3.7.

Providing approximate formulas for the pump-down time in the high vacuum molecular flow regime is rather difficult since it depends on the total rate of permeating, leaking and degassing particles $q_{\text{pV}}^{\text{add}}$. Nevertheless, the ultimate pressure $p_{\text{VC}}^{\text{min}}$ in the vacuum chamber is reached once $\mathrm{d}p_{\text{VC}}/\mathrm{d}t = 0$ which according to equation (3.7) requires that $p_{\text{VC}} \cdot S_{\text{eff}} = q_{\text{pV}}^{\text{add}}$, such that

$$p_{\text{VC}}^{\text{min}} = \frac{1}{S_{\text{eff}}} \cdot q_{\text{pV}}^{\text{add}} = \frac{1}{S_{\text{eff}}} \cdot \left(q_{\text{pV}}^{\text{leak}} + q_{\text{pV}}^{\text{per}} + q_{\text{pV}}^{\text{degas}}\right). \tag{3.9}$$

In addition, equation (3.9) allows determining the ultimate pressure that adjusts right at the pump inlet by substituting S_{eff} for S_{pump}.

In the following, two different types of vacuum pumps are introduced, a dry scroll pump and a turbomolecular pump. They are both used for the experimental setups developed within the scope of this dissertation.

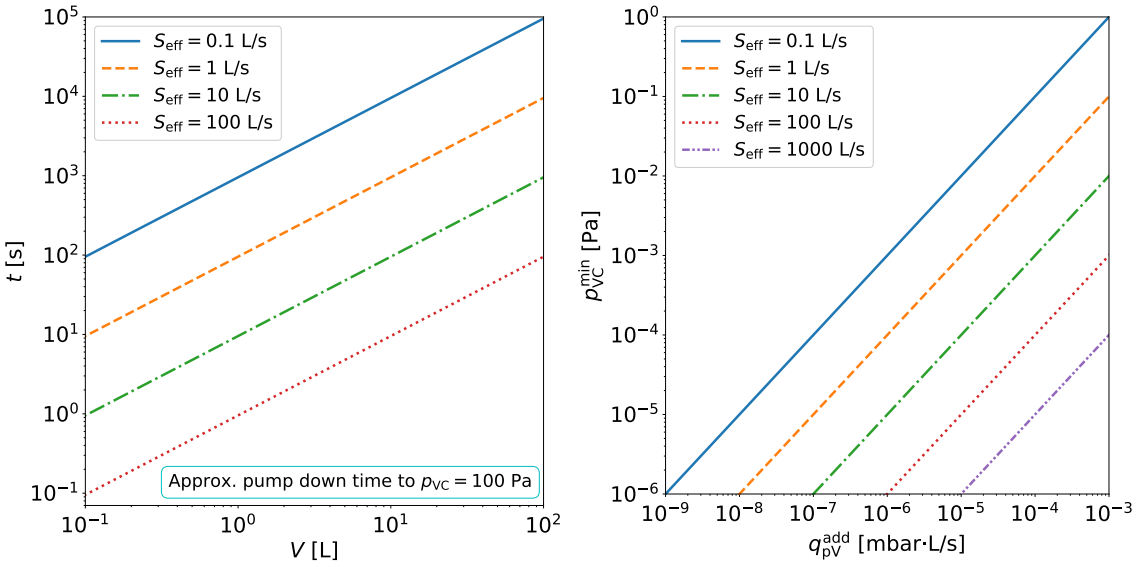

Fig. 3.7. [Left] Pump down time of a vacuum chamber from atmospheric pressure down to $p_{VC} = 1 \times 10^2$ Pa plotted against the volume of the vacuum chamber for different constant effective pumping speeds. [Right] Adjusting ultimate pressure in a vacuum chamber plotted against the rate of leaking, degassing or permeating particles into the vessel considering different effective pumping speeds.

Dry scroll vacuum pumps

Dry scroll vacuum pumps belong to the category of dry compression vacuum pumps and enable pumping down a vacuum chamber from atmospheric pressure to the edge of the high vacuum regime [195]. They are particularly efficient in a pressure range 1×10^2 Pa $< p < 1 \times 10^5$ Pa where their internal pumping speed remains roughly constant [196]. Below pressures of about $p < 1 \times 10^2$ Pa their internal pumping speed plunges. It reaches zero once the gas has entered the molecular flow regime in a range 1×10^{-1} Pa $< p < 1$ Pa which determines the minimum working pressure of a dry scroll vacuum pump. The interior structure and operating principle of a scroll vacuum pump are depicted on the left-hand side of figure 3.8. As the image illustrates, a scroll-shaped as an Archimedean spiral oscillates circularly around a crankshaft inside of a second stationary scroll without changing its orientation. Thus, pockets of gas are captured by the moving scroll and transported helically inwards. In this process, the gas is continuously compressed until it leaves through a hole in the center towards the exhaust of the pump. Dry scroll vacuum pumps ensure the creation of particularly clean vacuum environments as they are free of liquid lubricants.

Turbomolecular pumps

To further reduce the pressure and enter the high vacuum regime at $p < 1$ Pa a different type of pump has to be added to the pumping system, such as a turbomolecular vacuum

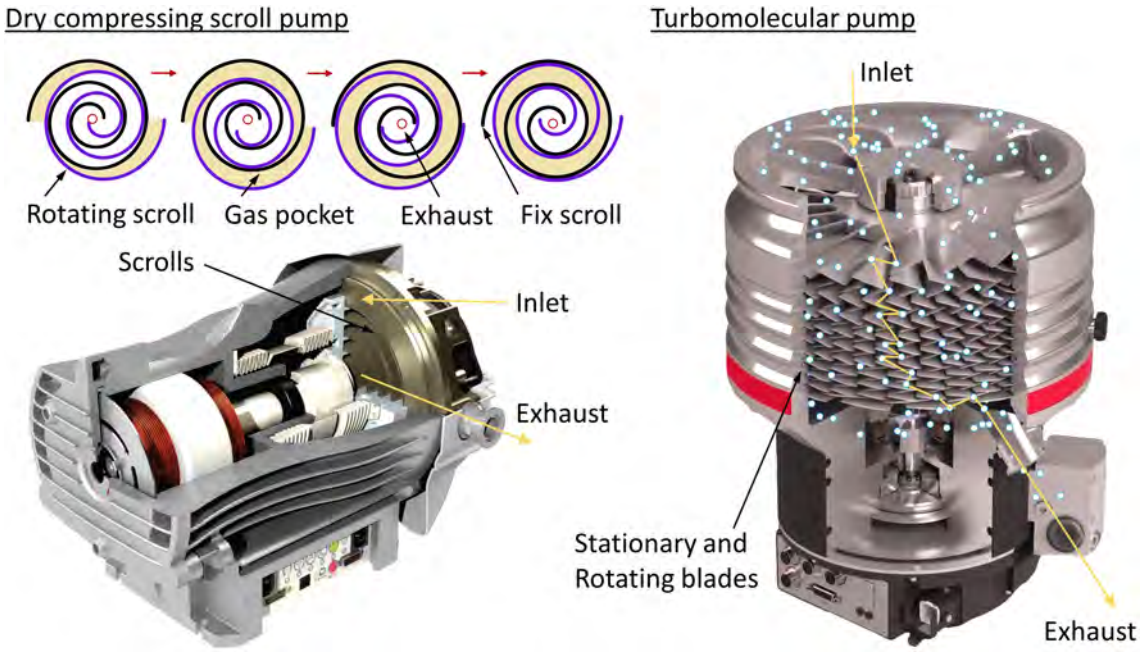

Fig. 3.8. [Left] Illustration of the working principle and image of the interior structure of a dry scroll vacuum pump [209]. [Right] Inner workings and particle trajectory inside of a turbomolecular vacuum pump [210].

pump. Turbomolecular vacuum pumps are designed to pump gas from a vacuum chamber in the molecular flow regime. Their principle of operation is based on the intention of removing any gas particle from the chamber that strikes the pump's open inlet flange while randomly bouncing through the vacuum system. For this purpose, a large number of stacked alternately fixed and rotating blades are axially arranged below the pump opening (see the right-hand picture in figure 3.8). A fraction of the incoming particles will hit a rotating blade, gaining additional momentum that pushes them through the layer of stationary blades below, before hitting another rotating blade in the layer below, and so on. This process repeats up to the lowest layer of rotor blades before the gas particles leave the pump through the exhaust. The internal pumping speed of a turbomolecular pump remains constant throughout the entire high vacuum regime [195]. Apart from the rotor blade velocity and the cross-sectional area of the inlet flange, the pumping speed is dependent on the type of pumped molecular species [197].

It is important that the pressure at the exhaust of the turbomolecular pump does not exceed a certain maximum outlet pressure, meaning that $p_{\mathrm{out}} < p_{\mathrm{out}}^{\mathrm{max}}$. Therefore, the exhaust must be connected to a second so-called backing pump which can cope with the throughput $q_{\mathrm{pV}}^{\mathrm{pump}} = p_{\mathrm{in}} \cdot S_{\mathrm{pump}}$ of the turbomolecular pump. This may be a dry scroll compression pump. The minimum required effective pumping speed $S_{\mathrm{BP}}^{\mathrm{min}}$ of the backing pump is that which allows maintaining the outlet pressure at a constant value of $p_{\mathrm{out}} = p_{\mathrm{out}}^{\mathrm{max}}$. According to the continuity equation, this requires that the throughputs of the turbomolecular pump and the backing pump are equal, meaning that

$$S_{\mathrm{BP}}^{\mathrm{min}} = \frac{p_{\mathrm{in}}}{p_{\mathrm{out}}^{\mathrm{max}}} \cdot S_{\mathrm{pump}} \,. \tag{3.10}$$

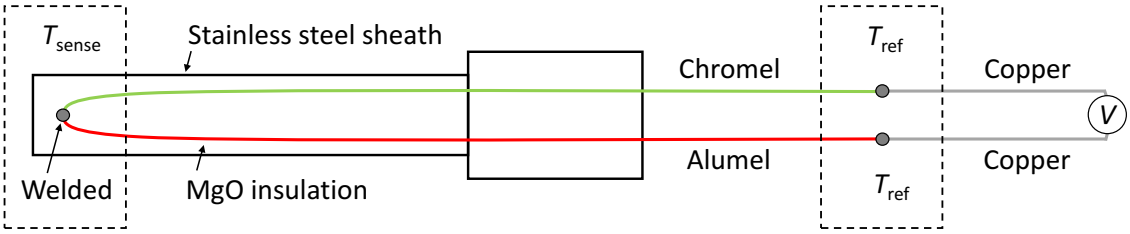

Fig. 3.9. Schema of a K-type thermocouple embedded in a stainless steel sheath and insulated with magnesium oxide powder [213].

During a pump-down process, the turbomolecular pump is started after the backing pump has pumped down the vacuum chamber to the molecular flow regime.

3.2. Measuring instrumentation

When hydrogen transport in material samples is experimentally studied inside a vacuum or gas chamber it is often required to obtain information about the sample temperature, total gas pressure, molecular partial pressures, and particle flows. Such is the case for the experimental setups developed within the scope of this work. The working principles of the measuring devices installed in the developed experiments are introduced below.

3.2.1. Thermocouples and feedthroughs

According to the Seebeck-effect [211], if the ends of an electric conductor have different temperatures the average thermal energy of the electrons at the hot end is higher compared to that at the cold end. As a consequence, more electrons diffuse from the hot to the cold end than vice verse and an electric field between the two ends establishes. In an open electric circuit, this leads to a measurable voltage U_V between the two ends which varies with the temperature difference ΔT. In a thermocouple, two conductors of different materials are welded together at one end which forms the tip of the temperature sensor while the other two ends are kept at a known reference temperature T_{ref}. Due to the difference in the temperature-dependency of the voltage drop $U_V(\Delta T)$ between the two conductor materials, it is possible to measure a voltage between the two open ends. It would be zero if the conductors were made of the same material. In a certain temperature range, the measured voltage is proportional to ΔT [212]. Hence, if the reference temperature and the characteristic temperature-dependencies of the voltage drop $U_V(\Delta T)$ of the two materials of the thermocouple are known, the temperature T_{sense} at the tip of the thermocouple can be determined.

In mineral-insulated K-type thermocouples the two dissimilar conductors are made of chromel (90 % nickel + 10 % chromium) and alumel (alloy: 95 % nickel, 2 % aluminum, 2 % manganese, and 1 % silicon), respectively [213]. The inner structure of a K-type thermocouple is visualized in figure 3.9. It consists of a thin cylindrical stainless steel

Fig. 3.10. Different types of electrical and thermocouple feedthroughs [197], [214].

sheath of arbitrary lengths containing the two conductors insulated by magnesium oxide powder [213]. Thus, it is specially designed for applications in high-temperature and corrosive environments and is protected against all kinds of damage. Moreover, the tip can be bent and twisted into any desired shape. The two conductors leave the metal sheath after a certain length where they are insulated by a polyvinyl acetate or fiberglass jacket that withstand temperatures of $T < 523\,\mathrm{K}$ and $T < 753\,\mathrm{K}$, respectively [213]. K-type thermocouples enable accurate temperature measurements in a temperature range between $T = 273\,\mathrm{K}$ and $T = 1373\,\mathrm{K}$ [213].

Commercially available thermocouple feedthroughs allow transferring the electric signal of a thermocouple through the wall of a sealed vacuum or gas chamber. A common thermocouple feedthrough is shown on the left-hand side of figure 3.10 [197], [214]. In this design, the two conductors of dissimilar metals which emerge from the stainless steel sheath of the thermocouple are screwed from inside of the vacuum chamber to the respective feedthrough electrode which is made of the same material as the connected conductor. The two electrodes of the feedthrough penetrate a closed CF or ISO-KF flange from which they are insulated with rigid aluminum oxide. Thus, such a feedthrough withstands temperatures of up to $T = 573\,\mathrm{K}$. A second type of thermocouple feedthrough is depicted in the center of figure 3.10 [214]. It can be used for vacuum pressures of minimum $p = 1 \times 10^{-4}\,\mathrm{Pa}$ and higher temperature applications of up to $T = 823\,\mathrm{K}$ where the jacket of the thermocouple cable would be damaged. For this reason, not the thermocouple cable but its stainless steel sheath penetrates the feedthrough and the cable leaves the thermocouple pin outside the chamber (see figure 3.9). As the section cut in figure 3.10 shows, the sheath passes through a round graphite block which serves as the sealant. The seal is realized by compressing the graphite block with a female nut. There are graphite blocks available that allow for the penetration of multiple thermocouples.

A typical vacuum feedthrough for electrical power connections is nearly identical to the presented ceramic insulated thermocouple feedthrough [197]. It can be seen on the right-hand side of figure 3.10. The electric power is transferred into the vacuum chamber via ceramic-insulated copper or stainless steel pins.

3.2.2. Pressure measurement

The total pressure in a gas chamber is measured with a pressure gauge. Depending on the applied measurement method, different types of pressure gauges cover specific pressure ranges. Some pressure gauges unite several measurement techniques in a single device and thus cover an extended pressure range [195].

Capacitance diaphragm gauges

Capacitance diaphragm gauges allow measuring the total pressure of a gas mix in a pressure range that covers three orders of magnitude within a wider range between $1 \times 10^{-1}\,\mathrm{Pa} < p < 1 \times 10^{5}\,\mathrm{Pa}$. They contain two disk-shaped electrodes that are connected to a voltage source and thus act as a capacitor. One of the two electrodes is a deformable membrane. Moreover, the space between the two electrodes is evacuated. The higher the pressure outside of the evacuated space, the more the deformable membrane bends inwards in the direction of the fixed electrode. This leads to a detectable increase in capacitance. The measurable pressure range of the gauge is set by the choice of membrane thickness. An advantage of using capacitance diaphragm gauges in the rough and medium vacuum regime is that the pressure measurement is independent of the molecular species.

Pirani gauges

Pirani gauges can be used to determine the pressure in a range of approximately $1 \times 10^{-2}\,\mathrm{Pa} < p < 100\,\mathrm{Pa}$ which corresponds to the medium vacuum and high vacuum regime [195]. In a Pirani gauge, a metal wire exposed to the interior of the vacuum chamber is heated to a constant temperature of $T \approx 400\,\mathrm{K}$ by an electric current. In contrast to the rough and ultra-high-vacuum regime, in the mentioned pressure range, the heat loss of the wire is a function of pressure which is determined by calibration. The heat loss and thus the pressure is obtained by measuring the electric power needed to maintain the wire at a constant temperature. However, the relationship between pressure and heat loss differs among different molecular species [195]. Therefore, measuring the pressure of a specific gas mix different from that used for calibration requires a multiplication of the displayed value with a conversion factor.

Cold cathode pressure gauges

Even lower pressures between $1 \times 10^{-7}\,\mathrm{Pa} < p < 1 \times 10^{1}\,\mathrm{Pa}$ can be measured with cold cathode pressure gauges [197]. They consist of a pin anode which is concentrically surrounded by a cylindrical cathode. A strong voltage is applied between the two elements causing the emission of electrons from the cathode. The arrangement is surrounded by a specifically shaped permanent magnet with a concentric magnetic field. Due to the

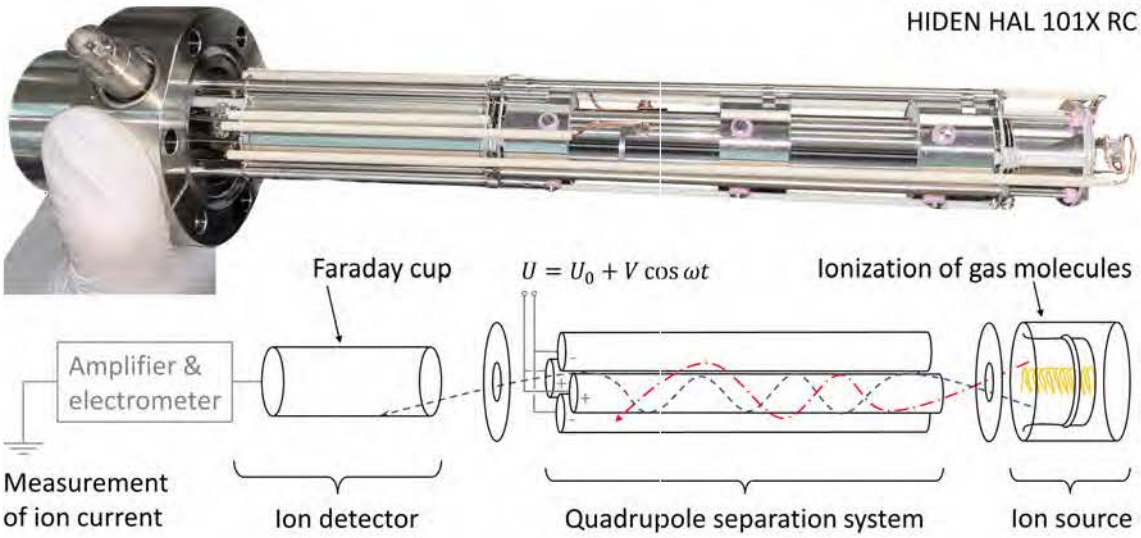

Fig. 3.11. Foto and illustration of the operating principle of a HIDEN HAL 101X RC quadrupole mass spectrometer [215].

Lorentz force the emitted electrons perform long spiral trajectories around the field lines before eventually reaching the anode. On their way, the electrons ionize gas molecules which leads to a measurable gas discharge. The discharge current is a function of the gas pressure. However, as with Pirani gauges, the relationship between the pressure and the measurable quantity (the discharge current) depends on the molecular species in the gas.

3.2.3. Quadrupole mass spectrometer

While the presented pressure gauges are limited to measuring the total pressure in a vacuum chamber, a quadrupole mass spectrometer (QMS) allows approximately determining the partial pressures of the individual gas components in a vacuum. It is therefore also referred to as a residual gas analyzer. Figure 3.1 shows a photo of a HAL 101X RC QMS from Hiden Analytical which is specially optimized for applications in fusion research [215]. Its interior structure is illustrated in the drawing below. The visible head of the QMS can be directly connected to a vacuum chamber via a DN40-CF flange.

Measuring principle

At the tip of the QMS head, there is an ion source which mainly consists of a hot cathode filament and an anode. Electrons that are emitted from the cathode accelerate toward the anode. On their way, they collide with neutral gas molecules that pass through the space between the anode and the cathode leading to the formation of positive ions. The electric current of ionized neutral gas molecules $I^+_{\mathrm{prod,tot},s}$ of species s is proportional to the corresponding partial pressure p_s in the gas

$$I^+_{\mathrm{prod,tot},s} = \gamma_s \cdot I^-_{\mathrm{IS}} \cdot p_s\,, \quad \text{with} \quad \gamma_s \equiv \sigma_s \cdot l_{\mathrm{e}}\,. \tag{3.11}$$

Here, γ_s is called the ion source constant of species s, parameter σ_s is the differential ionization effect cross-section of species s, parameter l_e the mean path length of an electron traveling to the anode and I_{IS}^- the electron current emitted from the ion source cathode [195]. The respective SI units of the introduced quantities are listed in table V. By defining $\sigma_s \equiv \mathrm{RIP}_s \cdot \sigma_{N_2}$, equation (3.11) transforms to

$$I_{prod,tot,s}^+ = \mathrm{RIP}_s \cdot \gamma_{N_2} \cdot I_{IS}^- \cdot p_s \,, \tag{3.12}$$

with RIP_s being the relative ionization probability. Since some molecular species can crack or lose multiple valence electrons from the collision, several different ions with distinct dimensionless mass-to-charge ratios κ may be formed from the same neutral parent molecule s. In this work, dimensionless mass-to-charge ratios are given in atomic mass number of the ion divided by its electric charge given as the number of elementary charges. It is evident that the generated current of ions with a certain value of κ that originate from a molecule of species s can be expressed by

$$I_{prod,\kappa,s}^+ = \mathrm{CF}_{\kappa,s} \cdot I_{prod,tot,s}^+ = \mathrm{RIP}_s \cdot \mathrm{CF}_{\kappa,s} \cdot \gamma_{N_2} \cdot I_{IS}^- \cdot p_s \tag{3.13}$$

where $0 \leq \mathrm{CF}_{\kappa,s} \leq 1$ is the cracking fraction of the corresponding ion.

Once formed the ions are diverted toward the quadrupole separation system by a negatively charged extractor aperture. Here, they enter the central interstitial space between four parallel metal rods (see figure 3.11). As visualized in figure (3.11), each of the two poles of a voltage source is connected in parallel to a pair of opposing rods. The application of an oscillating voltage of the form $U_V(t) = U_0 + V_{QMS} \cdot \cos(\omega_{QMS} t)$ with an angular frequency ω_{QMS} in the RF range leads to the generation of an electric field in the free circular space between the rods that imposes a spiral motion on the entering ions. By solving the equations of motion that result from the acting electrostatic force it is found that ions of a certain mass-to-charge ratio κ can only pass the interior tunnel of radius r_{QMS} between the four rods if for fixed values of ω_{QMS} and r_{QMS} the voltages V_{QMS} and U_0 are adjusted within certain κ-dependent stability ranges [196]. These stability ranges shift with changing mass-to-charge ratio. Therefore, varying the two voltages accordingly allows ions of an arbitrary mass-to-charge ratio to pass the rod system. All other ions either collide with a negatively charged rod or escape the electric field.

After leaving the rod system the ions of the chosen mass-to-charge ratio enter an ion detector. In a HIDEN 101X RC QMS this is a Faraday cup connected to an electrometer amplifier. However, even if the stability conditions for a certain mass-to-charge ratio are fulfilled, only a fraction of the ions with a suitable mass-to-charge ratio reaches the detector. This fraction is quantified with the transmission factor $\mathrm{TF}_{\kappa,s} < 1$ [195]. Hence, the electric current of ions with a mass-to-charge ratio κ originating from the parent molecular species s that eventually reach the detector surface can be written as

$$I_{cup,\kappa,s}^+ = \mathrm{TF}_{\kappa,s} \cdot I_{prod,\kappa,s}^+ = \mathrm{TF}_{\kappa,s} \cdot \mathrm{RIP}_s \cdot \mathrm{CF}_{\kappa,s} \cdot \gamma_{N_2} \cdot I_{IS}^- \cdot p_s \tag{3.14}$$

As soon as the ions hit the surface of the negatively charged cup, they pick up electrons and become neutral. This process induces a current $I_{meas,\kappa,s}^+$ in the Faraday cup circuit

which satisfies $I^+_{\mathrm{meas},\kappa,s} = I^+_{\mathrm{cup},\kappa,s}$. Eventually, the total current measured by the electrometer is the sum of the values of $I^+_{\mathrm{meas},\kappa,s}$ taken over all molecular species s that form ions with the same mass-to-charge ratio κ

$$I^+_{\mathrm{meas},\kappa} = \sum_s I^+_{\mathrm{meas},\kappa,s} = I^+_{\mathrm{meas},\kappa,s'} + \sum_{s \neq s'} I^+_{\mathrm{meas},\kappa,s} \tag{3.15}$$

Since $I^+_{\mathrm{meas},\kappa,s} = I^+_{\mathrm{cup},\kappa,s}$, inserting equation (3.14) into equation (3.15) yields an expression for the partial pressure of the neutral molecular species s'

$$p_{s'} = \frac{1}{\mathrm{TF}_{\kappa,s'} \cdot \mathrm{RIP}_{s'} \cdot \mathrm{CF}_{\kappa,s'} \cdot \gamma_{\mathrm{N_2}} \cdot I^-_{\mathrm{IS}}} \cdot I^+_{\mathrm{meas},\kappa} - \frac{\sum_{s \neq s'} I^+_{\mathrm{meas},\kappa,s}}{\mathrm{TF}_{\kappa,s'} \cdot \mathrm{RIP}_{s'} \cdot \mathrm{CF}_{\kappa,s'} \cdot \gamma_{\mathrm{N_2}} \cdot I^-_{\mathrm{IS}}} \tag{3.16}$$

The parameters $\mathrm{CF}_{\kappa,s}$, RIP_s, $\gamma_{\mathrm{N_2}}$ depend on the electron energy in the ion source while the transmission coefficient $\mathrm{TF}_{\kappa,s}$ is mainly determined by the respective ion mass [195]. The HIDEN 101X RC QMS system is equipped with a software that can access a data library containing pre-determined values of the variables $\mathrm{CF}_{\kappa,s}$, RIP_s, $\gamma_{\mathrm{N_2}}$, I^-_{IS} and $\mathrm{TF}_{\kappa,s}$. Equation (3.16) shows that if there are molecular species $s \neq s'$ in the gas that are ionized to ions with the same mass-to-charge ratio as ions originating from the molecular species s', it is not straightforward to calculate the partial pressure $p_{s'}$ from the measured current $I^+_{\mathrm{meas},\kappa}$. In this case, calculating $p_{s'}$ requires estimating the relative heights of the currents $I^+_{\mathrm{meas},\kappa,s}$ in comparison with the current $I^+_{\mathrm{meas},\kappa,s'}$. This is done in a critical analysis of the entire recorded κ - $I^+_{\mathrm{meas},\kappa}$ spectrum. In order for a QMS to provide precise measurement results it is of crucial importance that from the moment of being produced until hitting the Faraday cup the ions do not collide with each other. Therefore, a QMS must be operated in the molecular flow regime at total pressures of $p < 1 \times 10^{-2}$ Pa.

Calibration for particle flux measurements

Nonetheless, equation (3.16) indicates a linear relationship between $p_{s'}$ and the measured current $I^+_{\mathrm{meas},\kappa}$ by the QMS if the molecules s' can form ions with the corresponding mass-to-charge ratio κ. As illustrated in the left-hand process flow diagram (PFD) in figure 3.12, a QMS is often positioned very close to the inlet flange of a turbomolecular pump where the total pressure in the vacuum system is lowest. Thus, noise effects are reduced and the sensibility of the detector signal is increased. The symbols of the technical components that appear in the PFD are labeled in table XI. As equation (3.9) indicates, the adjusting minimum pressure at the pump inlet and in the nearby ion source of the QMS depends on the net flow $q^{\mathrm{add}}_{\mathrm{Vp}} = q^{\mathrm{leak}}_{\mathrm{Vp}} + q^{\mathrm{per}}_{\mathrm{Vp}} + q^{\mathrm{degas}}_{\mathrm{Vp}}$ of leaking, degassing and permeating particles entering the vacuum system. Of particular interest for this dissertation is the flow of permeating particles $q^{\mathrm{per}}_{\mathrm{Vp}}$ into the chamber. Transforming equation (3.9) it can be expressed by

$$q^{\mathrm{per}}_{\mathrm{pV}} = p^{\mathrm{min}}_{\mathrm{VC}} \cdot S_{\mathrm{eff}} - q^{\mathrm{leak}}_{\mathrm{pV}} - q^{\mathrm{degas}}_{\mathrm{pV}}. \tag{3.17}$$

Therefore, in case the total permeation flow $q^{\mathrm{per}}_{\mathrm{pV}}$ increases by the amount $\Delta q^{\mathrm{per}}_{\mathrm{pV}}$ while the flow of degassing and leaking particles remains equal, the minimum pressure at the QMS

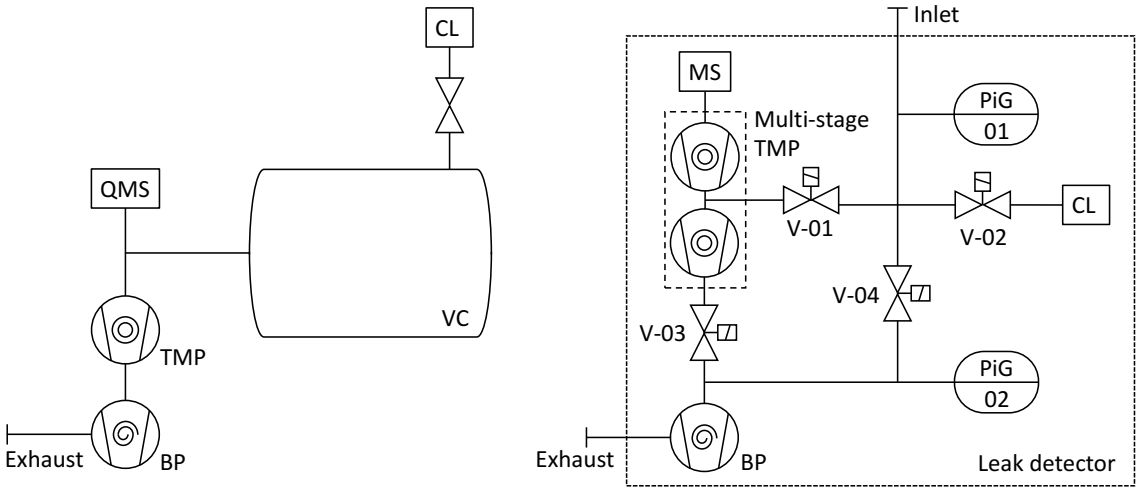

Fig. 3.12. [Left] Process flow diagram of a quadrupole mass spectrometer connected to a vacuum chamber and a test leak for calibration. [Right] Interior structure of a leak detector.

and the TMP inlet where $S_{\text{eff}} \approx S_{\text{pump}}$ experiences an increment by a certain value $\Delta p_{\text{pV}}^{\text{per}}$, according to

$$\Delta q_{\text{pV}}^{\text{per}} = S_{\text{pump}} \cdot \Delta p_{\text{pV}}^{\text{per}} \,. \tag{3.18}$$

It is evident that equation (3.18) remains valid when observing each molecular species separately, meaning that an increase in permeation flow of molecular species s' would result in an increment of the partial pressure of species s'

$$\Delta q_{\text{pV},s'}^{\text{per}} \approx S_{\text{pump}} \cdot \Delta p_{s'} \tag{3.19}$$

Moreover, equation (3.16) implies that if the partial pressure of species s' experiences an increment $\Delta p_{\text{pV},s'}^{\text{per}}$, the current $I_{\text{meas},\kappa}^{+}$ of the corresponding mass-to-charge ratio must increase as well. If during the partial pressure increase of species s' the partial pressures and hence the current fractions $I_{\text{meas},\kappa,s}^{+}$ of all other species $s \neq s'$ remain constant the following proportionality relationship arises

$$\Delta p_{s'} = \frac{1}{\text{TF}_{\kappa,s'} \cdot \text{RIP}_{s'} \cdot \text{CF}_{\kappa,s'} \cdot \gamma_{\text{N}_2} \cdot I_{\text{IS}}^{-}} \cdot \Delta I_{\text{meas},\kappa}^{+} \tag{3.20}$$

Inserting equation (3.19) into equation (3.20) finally leads to a relationship between the increment of the measured current in the QMS resulting from a certain increase in permeation flow

$$\Delta q_{\text{pV},s'}^{\text{per}} = f_{\kappa,s'}^{\text{cal}} \cdot \Delta I_{\text{meas},\kappa}^{+} \,, \quad \text{with} \quad f_{\kappa,s'}^{\text{cal}} \equiv \frac{S_{\text{pump}}}{\text{TF}_{\kappa,s'} \cdot \text{RIP}_{s'} \cdot \text{CF}_{\kappa,s'} \cdot \gamma_{\text{N}_2} \cdot I_{\text{IS}}^{-}} \,. \tag{3.21}$$

The defined factor $f_{\kappa,s'}^{\text{cal}}$ is labeled the calibration factor of the QMS and is unique for every molecular species and mass-to-charge ratio. It is evident that in order to be able to convert a measured increase in ion current $I_{\text{meas},\kappa}^{+}$ at a certain mass-to-charge ratio into the associated rise in permeation flow of species s', the value of the calibration factor $f_{\kappa,s'}^{\text{cal}}$ needs to be known.

The easiest way to determine $f^{\mathrm{cal}}_{\kappa,s'}$ is through a calibration measurement using a commercially available calibrated leak. A calibrated leak (CL) or test leak is a small gas cylinder filled with a gas of species s' that is attached to a flange of the vacuum chamber. The high-pressure side of the calibrated leak and the interior of the vacuum chamber are connected through an open capillary tube of very low conductance. As long as the pressure difference $\Delta p = p_{\mathrm{CL}} - p_{\mathrm{VC}}$ between the two sides of the tube is above a critical value the gas flow into the vacuum chamber occurs in the choked flow regime. This means that the gas particles leave the capillary tube into the vacuum chamber with the speed of sound at a constant throughput $q^{\mathrm{CL}}_{\mathrm{pV},s'}$ [195]. Before delivery, the manufacturer of the test leak determines its individual throughput in a calibration measurement.

To calibrate the QMS for particle flux measurements the test leak and the vacuum chamber are separated by an open/close valve. First, the valve is maintained closed and the underground current $I^{+}_{\mathrm{meas},\kappa}$ of a mass-to-charge ratio κ which corresponds to ions originating from molecular species s', is measured. Then, the valve of the calibrated leak is opened which causes the flow of species s' into the vacuum chamber to rise by $\Delta q^{\mathrm{CL}}_{\mathrm{pV},s'}$. Finally, the increase in current $\Delta I^{+}_{\mathrm{meas},\kappa}$ with respect to the underground measurement is recorded. Both the known value of $q^{\mathrm{CL}}_{\mathrm{pV},s'}$ and the measured value of $\Delta I^{+}_{\mathrm{meas},\kappa}$ are inserted into equation (3.21) which provides the experimentally determined value of $f^{\mathrm{cal}}_{\kappa,s'}$. After $f^{\mathrm{cal}}_{\kappa,s'}$ is determined, the QMS enables quantitatively measuring any increase in particle flow from outside into the vacuum chamber using equation (3.21).

Equation (3.2) allows converting the measured rise in permeation flow $\Delta q^{\mathrm{per}}_{\mathrm{pV},s'}$ into the corresponding rise in molecular permeation flux $\Delta j_{\mathrm{per},s'}$ of species s' into the chamber

$$\Delta j_{\mathrm{per},s'} = \frac{1}{A_{\mathrm{per}} R T_{\mathrm{QMS}}} \cdot \Delta q^{\mathrm{per}}_{\mathrm{pV},s'} \,. \tag{3.22}$$

Parameter A_{per} is the surface area through which the permeation process takes place and T_{QMS} is the gas temperature in the QMS.

3.2.4. Leak detector

A leak detector (LD) is a device that enables quantitatively measuring particle flows $q^{\mathrm{add}}_{\mathrm{pV}}$ of light gas components in a test vacuum chamber. Therefore, it applies a similar measuring principle as discussed in section 3.2.3, using a mass spectrometer calibrated with a test leak as a measuring device. The internal structure of a leak detector is shown in the PFD on the right-hand side of figure 3.12.

To make a measurement, the inlet flange of the leak detector is attached to the test chamber and the device is switched on. At this moment, valve V-03 is automatically opened and a backing pump evacuates the vacuum chamber up to the medium vacuum regime. The pressure is controlled by two internal Pirani gauges PiG-01 and PiG-02. In addition, the backing pump is connected to the exhaust of a TMP whose inlet is linked to the mass spectrometer of the leak detector. Once the pressure measured with PiG-02

at the inlet of the backing pump reaches a sufficiently low backing pressure the TMP is automatically started and valve V-03 is opened. The main difference between the particle flow measurement principle of a leak detector and that of a QMS as it was presented in section 3.2.3 is that in a leak detector, the mass spectrometer is not directly exposed to the atmosphere of the test chamber. Instead, the mass spectrometer of a leak detector merely sees the high vacuum environment which is generated in the space above the inlet of the TMP and therefore does not detect any heavy gas components from the test chamber (see figure 3.12). However, a fraction of very light gas particles, such as $^{1}H_2$, $^{1}H^{2}H$, $^{2}H_2$, ^{3}He and ^{4}He, that may originate from a leak or permeation source in the test chamber, are able to counter-flow from the exhaust of the TMP towards the mass spectrometer where they are ionized and detected. This measurement technique is called counter-flow mode. Nevertheless, a leak detector only allows detecting ions of only one particular mass-to-charge ratio $\kappa \in \{2, 3, 4\}$ at a time which must be selected prior to the measurement.

To increase the measurement sensitivity, leak detectors are often equipped with a TMP consisting of multiple stages [197] with intermediate inlet ports (see port connected to valve V-01 in figure 3.12). In this case, if the evacuation of the test chamber by the backing pump is capable of creating a sufficiently low pressure $p < 1 \times 10^2$ Pa, the leak detector automatically closes valve V-04 and opens valve V-01. This leads to a further evacuation of the test chamber through the lower stage of the TMP and thus to a further decrease in the pressure measured by PiG-01. Also in this operating mode, only light gas components can reach the mass spectrometer by passing through the upper stage of the TMP. In the following, this operating principle is referred to as the Twin-Flow™ mode [216].

One of the primary purposes of a leak detector is to detect and quantify a leakage occurring in a vacuum chamber. Therefore, certain areas of the test chamber, such as fittings, flanges, or valves, which are particularly susceptible to leaks, are sprayed from outside with ^{4}He gas. If ^{4}He is used as test gas, the detectable mass-to-charge ratio of the leak detector is set to $\kappa = 4$. The ^{4}He atoms enter the vacuum chamber at the location of a leak and make their way into the leak detector before they reach the ion source of the mass spectrometer. Here, the increased ^{4}He particle flow leads to an increment in measured ion current. By opening valve V-02 the leak detector measures the current rise resulting from the known ^{4}He flow of an internal calibrated test leak. By applying equation (3.21) the mass spectrometer is calibrated in the same manner as described in section 3.2.3 which enables the leak detector to convert any registered rise in ion current into a value of the occurring ^{4}He particle flow $q_{\mathrm{pV}}^{\mathrm{leak}}$ in the test chamber.

To quantitatively measure incoming particle flows of gas molecules like $^{1}H_2$ ($\kappa = 2$) or $^{2}H_2$ ($\kappa = 4$) with a leak detector, it needs to be calibrated with an external test leak of the corresponding gas component. The known throughput of the test leak can be specified in the device settings.

4. THEORETICAL STUDY OF MULTI-ISOTOPIC PERMEATION

This chapter presents a theoretical analysis of multi-isotopic permeation performed by the author of this thesis. Particular focus is placed on two distinct permeation scenarios which are relevant for permeation processes occurring in WCLL and HCPB breeding blankets. That is multi-isotopic hydrogen isotope permeation from gas to gas and from flowing liquid metal to water. For both permeation environments, new multi-isotope transport equations are theoretically derived.

4.1. Theoretical study of multi-isotopic permeation from gas to gas

The first observed scenario comprises a metal membrane whose upstream and downstream interfaces are exposed to a hydrogen isotope gas. Multi-isotopic permeation occurs once more than one isotope species is involved in the permeation process. In case only two different isotopes ${}^{i}\mathrm{H}$ and ${}^{k}\mathrm{H}$ are present, the upstream and downstream side of the membrane may contain the partial pressure configurations p_{ii}^{UI}, p_{ik}^{UI}, p_{kk}^{UI} (upstream side) and p_{ii}^{DI}, p_{ik}^{DI}, p_{kk}^{DI} (downstream side), respectively. As for the mono-isotopic case, if the partial pressures do not change over time it is evident that after some time constant steady state interface concentrations $c_{\mathrm{UI},i}$, $c_{\mathrm{DI},i}$ and $c_{\mathrm{UI},k}$, $c_{\mathrm{DI},k}$ will establish. For each isotope, this leads to an independent stationary concentration profile $c_i(z,t)$ and $c_k(z,t)$ and thus to steady state atomic permeation fluxes $\overline{J}_{\mathrm{per},i}$ and $\overline{J}_{\mathrm{per},k}$.

The following discussion analyzes multi-isotopic permeation in the general case of a cylindrical metal membrane that satisfies the geometry of a parallel membrane in the limit. To do so, it is made use of the conversion factors $f_{\mathrm{in}}^{\mathrm{c}}$ and $f_{\mathrm{out}}^{\mathrm{c}}$ which were defined by the author of this thesis in the equations (2.160) and (2.161). Depending on which side of the circular membrane is the upstream interface and which side is the downstream interface, either $f_{\mathrm{UI}}^{\mathrm{c}} = f_{\mathrm{in}}^{\mathrm{c}}$ or $f_{\mathrm{UI}}^{\mathrm{c}} = f_{\mathrm{out}}^{\mathrm{c}}$. According to the equations (2.98), (2.160) and (2.161), the steady state atomic net fluxes of isotope species ${}^{i}\mathrm{H}$ at the upstream and downstream interfaces can be expressed by

$$\overline{J}_{\mathrm{net,UI},i}^{\circledcirc} = 2\sigma k_{\mathrm{d},ii} p_{ii}^{\mathrm{UI}} - 2\sigma k_{\mathrm{r},ii} c_{\mathrm{UI},i}^2 + \sigma k_{\mathrm{d},ik} p_{ik}^{\mathrm{UI}} - \sigma k_{\mathrm{r},ik} c_{\mathrm{UI},i} c_{\mathrm{UI},k} = f_{\mathrm{UI}}^{\mathrm{c}} \cdot D_i \frac{c_{\mathrm{UI},i} - c_{\mathrm{DI},i}}{d} \tag{4.1}$$

$$\overline{J}_{\mathrm{net,DI},i}^{\circledcirc} = f_{\mathrm{DI}}^{\mathrm{c}} \cdot D_i \frac{c_{\mathrm{UI},i} - c_{\mathrm{DI},i}}{d} = 2\sigma k_{\mathrm{r},ii} c_{\mathrm{DI},i}^2 - 2\sigma k_{\mathrm{d},ii} p_{ii}^{\mathrm{DI}} + \sigma k_{\mathrm{r},ik} c_{\mathrm{DI},i} c_{\mathrm{DI},k} - \sigma k_{\mathrm{d},ik} p_{ik}^{\mathrm{DI}} \tag{4.2}$$

In the limit of a parallel membrane $f_{\mathrm{UI}}^{\mathrm{c}} = f_{\mathrm{DI}}^{\mathrm{c}} = 1$ which implies $\overline{J}_{\mathrm{net,UI},i}^{\circledcirc} = \overline{J}_{\mathrm{net,DI},i}^{\circledcirc}$. In contrast to the process of mono-isotopic permeation, the possibility of analytically exploring multi-isotopic permeation is rather limited. However, by sufficiently simplifying the studied permeation process it is possible to discover certain regularities which uncover the isotope effect of permeation. To facilitate the understanding of the multi-isotopic permeation process it is useful to consider ${}^{i}\mathrm{H}$ as tritium and ${}^{k}\mathrm{H}$ as protium. However, the

developed theory is valid for any isotope combination.

One may imagine a case in which the upstream side of a plane metal sheet contains the gas components ${}^{i}\mathrm{H}^{k}\mathrm{H}$ and ${}^{i}\mathrm{H}_2$ with the partial pressures $p_{ik}^{\mathrm{UI}} > 0$ and $p_{ii}^{\mathrm{UI}} > 0$ while on the downstream side $p_{ik}^{\mathrm{DI}} = p_{ii}^{\mathrm{UI}} = 0$. As equation (2.88) reveals, the dissociation coefficients of different molecular species ${}^{i}\mathrm{H}^{j}\mathrm{H}$ differ by their individual sticking coefficients α_{s} and a factor $1/\sqrt{m_{ij}}$ which contains the mass of the corresponding molecule. Hence, when assuming that the sticking coefficient α_{s} of each molecular species is equal, the dissociation coefficients of the molecules ${}^{i}\mathrm{H}^{k}\mathrm{H}$ and ${}^{i}\mathrm{H}_2$ can be related in the following manner

$$k_{\mathrm{d},ik} \approx k_{\mathrm{d},ii} \sqrt{\frac{m_{ii}}{m_{ik}}} \tag{4.3}$$

For the following analytic investigation it is considered that $K_{\mathrm{s}} \equiv K_{\mathrm{s},i} = K_{\mathrm{s},k}$. Therefore, from the equations (4.3) and (2.100) it follows that

$$k_{\mathrm{r},ik} \approx 2k_{\mathrm{r},ii} \sqrt{\frac{m_{ii}}{m_{ik}}} \tag{4.4}$$

As a consequence, applying the mentioned assumptions allows reducing the equations (4.1) and (4.2) to

$$\overline{J}_{\mathrm{net,UI},i}^{\circledcirc} = 2\sigma k_{\mathrm{d},ii} p_{ii}^{\mathrm{UI}} + \sigma k_{\mathrm{d},ik} p_{ik}^{\mathrm{UI}} - 2\sigma k_{\mathrm{r},ii} \left(c_{\mathrm{UI},i}^2 + \sqrt{\frac{m_{ii}}{m_{ik}}} c_{\mathrm{UI},i} c_{\mathrm{UI},k} \right) = f_{\mathrm{UI}}^{\mathrm{c}} \cdot D_i \frac{c_{\mathrm{UI},i} - c_{\mathrm{DI},i}}{d} \tag{4.5}$$

$$\overline{J}_{\mathrm{net,DI},i}^{\circledcirc} = f_{\mathrm{DI}}^{\mathrm{c}} \cdot D_i \frac{c_{\mathrm{UI},i} - c_{\mathrm{DI},i}}{d} = 2\sigma k_{\mathrm{r},ii} \left(c_{\mathrm{DI},i}^2 + \sqrt{\frac{m_{ii}}{m_{ik}}} c_{\mathrm{DI},i} c_{\mathrm{DI},k} \right) . \tag{4.6}$$

At first, it is taken a closer look at a non-equilibrium scenario in which additionally $p_{kk}^{\mathrm{UI}} = p_{kk}^{\mathrm{DI}} = 0$. Based on the expressions in equation (2.99), the following upstream equilibrium concentrations are defined

$$c_{\mathrm{UI,eq},i}^2 \equiv \frac{k_{\mathrm{d},ii}}{k_{\mathrm{r},ii}} p_{ii}^{\mathrm{UI}} \quad \text{and} \quad c_{\mathrm{UI,eq},i} c_{\mathrm{UI,eq},k} \equiv \frac{k_{\mathrm{d},ik}}{k_{\mathrm{r},ik}} p_{ik}^{\mathrm{UI}} \tag{4.7}$$

A substitution of the equilibrium concentrations (4.7) into the two equations (4.5) and (4.6) yields

$$c_{\mathrm{UI},i}^2 + \sqrt{\frac{m_{ii}}{m_{ik}}} c_{\mathrm{UI},i} c_{\mathrm{UI},k} = \left(c_{\mathrm{UI,eq},i}^2 + \sqrt{\frac{m_{ii}}{m_{ik}}} c_{\mathrm{UI,eq},i} c_{\mathrm{UI,eq},k} \right) \cdot \left(1 - f_{\mathrm{UI}}^{\mathrm{c}} D_i \cdot \frac{c_{\mathrm{UI},i} - c_{\mathrm{DI},i}}{2\sigma k_{\mathrm{d},ii} p_{\mathrm{eff},i}^{\mathrm{UI}} d} \right) \tag{4.8}$$

$$c_{\mathrm{DI},i}^2 + \sqrt{\frac{m_{ii}}{m_{ik}}} c_{\mathrm{DI},i} c_{\mathrm{DI},k} = f_{\mathrm{DI}}^{\mathrm{c}} D_i \cdot \frac{c_{\mathrm{UI},i} - c_{\mathrm{DI},i}}{2\sigma k_{\mathrm{d},ii} d} . \tag{4.9}$$

For the expression of equation (4.8), a new quantity is introduced, the effective pressure $p_{\mathrm{eff},i}$ of isotope species ${}^{i}\mathrm{H}$

$$p_{\mathrm{eff},i} \equiv p_{ii} + \frac{1}{2} \sqrt{\frac{m_{ii}}{m_{ik}}} p_{ik} \tag{4.10}$$

Variable $p^{\mathrm{UI}}_{\mathrm{eff},i}$ is the effective pressure at the upstream side of the membrane. Combining the equations (4.8) and (4.9) yields

$$c^2_{\mathrm{UI,eq},i} + \sqrt{\frac{m_{ii}}{m_{ik}}} c_{\mathrm{UI,eq},i} c_{\mathrm{UI,eq},k} = \left(c^2_{\mathrm{UI},i} + \sqrt{\frac{m_{ii}}{m_{ik}}} c_{\mathrm{UI},i} c_{\mathrm{UI},k} \right) + \frac{f^{\mathrm{c}}_{\mathrm{UI}}}{f^{\mathrm{c}}_{\mathrm{DI}}} \cdot \left(c^2_{\mathrm{DI},i} + \sqrt{\frac{m_{ii}}{m_{ik}}} c_{\mathrm{DI},i} c_{\mathrm{DI},k} \right) \quad (4.11)$$

In section 2.3, it was demonstrated that at very low driving pressures, a mono-isotopic permeation process occurs in the surface-limited regime where $c_{\mathrm{UI}} \approx c_{\mathrm{DI}}$. Therefore, in a permeation process in which the effective pressure $p^{\mathrm{UI}}_{\mathrm{eff},i}$ is very small and $p^{\mathrm{UI}}_{kk} = p^{\mathrm{DI}}_{kk} = 0$ there must be a surface-limited regime in which $c_{\mathrm{UI},i} \approx c_{\mathrm{DI},i}$ and $c_{\mathrm{UI},k} \approx c_{\mathrm{DI},k}$. Thus, by applying the equations (4.3), (4.4) and (4.7), in a surface-limited scenario, equation (4.11) transforms to

$$\begin{aligned} c^2_{\mathrm{DI},i} + \sqrt{\frac{m_{ii}}{m_{ik}}} c_{\mathrm{DI},i} c_{\mathrm{DI},k} \approx c^2_{\mathrm{UI},i} + \sqrt{\frac{m_{ii}}{m_{ik}}} c_{\mathrm{UI},i} c_{\mathrm{UI},k} \approx \frac{1}{1 + f^{\mathrm{c}}_{\mathrm{UI}}/f^{\mathrm{c}}_{\mathrm{DI}}} \cdot \left(c^2_{\mathrm{UI,eq},i} + \sqrt{\frac{m_{ii}}{m_{ik}}} c_{\mathrm{UI,eq},i} c_{\mathrm{UI,eq},k} \right) \\ = \frac{1}{1 + f^{\mathrm{c}}_{\mathrm{UI}}/f^{\mathrm{c}}_{\mathrm{DI}}} \cdot \left(\frac{k_{\mathrm{d},ii}}{k_{\mathrm{r},ii}} p^{\mathrm{UI}}_{ii} + \sqrt{\frac{m_{ii}}{m_{ik}}} \frac{k_{\mathrm{d},ik}}{k_{\mathrm{r},ik}} p^{\mathrm{UI}}_{ik} \right) = \frac{1}{1 + f^{\mathrm{c}}_{\mathrm{UI}}/f^{\mathrm{c}}_{\mathrm{DI}}} \cdot \frac{k_{\mathrm{d},ii}}{k_{\mathrm{r},ii}} p^{\mathrm{UI}}_{\mathrm{eff},i} \quad (4.12) \end{aligned}$$

Eventually, inserting equation (4.12) into equation (4.6) provides an expression for the permeation flux $\overline{J}_{\mathrm{per},i} \equiv \overline{J}^{\circledcirc}_{\mathrm{net,DI},i}$ of isotope species ^{i}H in the surface-limited permeation regime where the effective upstream pressure $p^{\mathrm{UI}}_{\mathrm{eff},i}$ is very low and $p^{\mathrm{UI}}_{kk} = p^{\mathrm{DI}}_{kk} = 0$

$$\overline{J}_{\mathrm{per},i} = \frac{1}{1 + f^{\mathrm{c}}_{\mathrm{UI}}/f^{\mathrm{c}}_{\mathrm{DI}}} \cdot 2\sigma k_{\mathrm{d},ii} p^{\mathrm{UI}}_{\mathrm{eff},i} \quad (4.13)$$

Apparently, equation (4.13) has an identical shape as equation (2.168) of the pure mono-isotopic case, with the difference that now the effective pressure $p^{\mathrm{UI}}_{\mathrm{eff},i}$ is the driving pressure. Equation (4.13) is derived in this dissertation for the first time. It is consistent with experimental results performed by Kizu *et al* [91]. The first factor on the right-hand side of equation (4.13) may be considered as the reduced concentration ζ_r^2 in equation (2.152). The left-hand plot in figure 2.11 illustrates that it is constant in the surface-limited regime and described by equation (2.166). However, once the permeation process enters the intermediate permeation regime at higher effective pressures, parameter ζ_r^2 or the first factor on the right-hand side of equation (4.13) is no longer constant and decreases towards a diffusion-limited regime. However, at higher effective pressures, in this multi-isotopic case, the permeation flux no longer depends only on the effective pressure $p^{\mathrm{UI}}_{\mathrm{eff},i}$ but rather on the values of the individual partial pressures p^{UI}_{ii} and p^{UI}_{ik}.

To continue the theoretical analysis, it is now considered that in addition, either the upstream or the downstream side contains the gas component $^k\mathrm{H}_2$ with a partial pressure p_{kk}. The following treatment is based on the assumption that the partial pressures p^{UI}_{ik} and p^{UI}_{ii} are considerably smaller than the partial pressure of the gas component $^k\mathrm{H}_2$, so that $p_{kk} \gg p^{\mathrm{UI}}_{\mathrm{eff},i}$. This condition leads to a situation in which the interface concentrations satisfy $c_{\mathrm{UI},i} \ll c_{\mathrm{UI},k}$ and $c_{\mathrm{DI},i} \ll c_{\mathrm{DI},k}$. The less abundant isotope species ^{i}H is denoted the primary species and the more abundant isotope ^{k}H is labeled the secondary species. Under such circumstances, at a metal interface, a ^{i}H atom is much more likely to recombine

with a ${}^{k}\mathrm{H}$ atom to form ${}^{i}\mathrm{H}{}^{k}\mathrm{H}$ than with another ${}^{i}\mathrm{H}$ atom to form ${}^{i}\mathrm{H}_2$ [see equation (2.95)]. Therefore, it is reasonable to neglect the formation of ${}^{i}\mathrm{H}_2$ molecules. As a consequence, the expressions (4.5) and (4.6) reduce to

$$\overline{J}^{\circledcirc}_{\mathrm{net,UI},i} = 2\sigma k_{\mathrm{d},ii} p^{\mathrm{UI}}_{ii} + \sigma k_{\mathrm{d},ik} p^{\mathrm{UI}}_{ik} - \sigma k_{\mathrm{r},ik} c_{\mathrm{UI},i} c_{\mathrm{UI},k} = f^{\mathrm{c}}_{\mathrm{UI}} \cdot D_i \frac{c_{\mathrm{UI},i} - c_{\mathrm{DI},i}}{d} \tag{4.14}$$

$$\overline{J}^{\circledcirc}_{\mathrm{net,DI},i} = f^{\mathrm{c}}_{\mathrm{DI}} \cdot D_i \frac{c_{\mathrm{UI},i} - c_{\mathrm{DI},i}}{d} = \sigma k_{\mathrm{r},ik} c_{\mathrm{DI},i} c_{\mathrm{DI},k} \tag{4.15}$$

with $\overline{J}^{\circledcirc}_{\mathrm{net,DI},i} \equiv \overline{J}_{\mathrm{per},i}$. Combining the equations (4.14) and (4.15) and applying the expressions (4.3) and (4.10) yields the following formula for the downstream permeation flux of isotope species ${}^{i}\mathrm{H}$

$$\overline{J}_{\mathrm{per},i} = \frac{f^{\mathrm{c}}_{\mathrm{DI}}}{f^{\mathrm{c}}_{\mathrm{UI}}} \cdot \left(2\sigma k_{\mathrm{d},ii} p^{\mathrm{UI}}_{\mathrm{eff},i} - \sigma k_{\mathrm{r},ik} c_{\mathrm{UI},i} c_{\mathrm{UI},k}\right) = \sigma k_{\mathrm{r},ik} c_{\mathrm{DI},i} c_{\mathrm{DI},k} \,. \tag{4.16}$$

By taking into account that $\overline{J}_{\mathrm{per},i} = \sigma k_{\mathrm{r},ik} c_{\mathrm{DI},i} c_{\mathrm{DI},k}$, a division of equation (4.16) by $\overline{J}_{\mathrm{per},i}$ leads to

$$\overline{J}_{\mathrm{per},i} = 2\sigma k_{\mathrm{d},ii} p^{\mathrm{UI}}_{\mathrm{eff},i} \cdot \left(\frac{c_{\mathrm{UI},i}}{c_{\mathrm{DI},i}} \cdot \frac{c_{\mathrm{UI},k}}{c_{\mathrm{DI},k}} + \frac{f^{\mathrm{c}}_{\mathrm{UI}}}{f^{\mathrm{c}}_{\mathrm{DI}}}\right)^{-1} \,. \tag{4.17}$$

From the equations (4.15) and (2.100) it follows that

$$\frac{c_{\mathrm{UI},i}}{c_{\mathrm{DI},i}} \cdot \frac{c_{\mathrm{UI},k}}{c_{\mathrm{DI},k}} = \frac{1}{f^{\mathrm{c}}_{\mathrm{DI}}} \frac{\sigma k_{\mathrm{r},ik} d}{D_i} c_{\mathrm{UI},k} + \frac{c_{\mathrm{UI},k}}{c_{\mathrm{DI},k}} = \frac{1}{f^{\mathrm{c}}_{\mathrm{DI}}} \frac{2\sigma k_{\mathrm{d},ik} d}{K_{\mathrm{s}}^2 D_i} c_{\mathrm{UI},k} + \frac{c_{\mathrm{UI},k}}{c_{\mathrm{DI},k}} \,. \tag{4.18}$$

Another consequence of the assumption $p_{kk} \gg p^{\mathrm{UI}}_{\mathrm{eff},i}$ is that the permeation process of the isotopes ${}^{k}\mathrm{H}$ can be considered unaffected by the presence of the gas components ${}^{i}\mathrm{H}{}^{k}\mathrm{H}$ and ${}^{i}\mathrm{H}_2$. Therefore, the permeation of the isotopes ${}^{k}\mathrm{H}$ is determined by the general equations of mono-isotopic steady state permeation (2.164). Hence, the permeation regime of the species ${}^{k}\mathrm{H}$ can be assessed with its permeation number W_k. Its definition (2.147) may be rewritten as follows

$$W_k = \frac{2\sigma k_{\mathrm{r},kk} d}{D_k} K_{\mathrm{s}} \sqrt{p_{kk}} = \frac{2\sigma k_{\mathrm{d},kk} d}{K_{\mathrm{s}}^2 D_k} c_{\mathrm{eq},k} = \sqrt{\frac{m_{ik} m_k}{m_{kk} m_i}} \frac{2\sigma k_{\mathrm{d},ik} d}{K_{\mathrm{s}}^2 D_i} c_{\mathrm{eq},k} \tag{4.19}$$

To set up this expression, the same approximated molecular mass relationship between different dissociation coefficients is applied as used in equation (4.3). Moreover, it is applied that $D_k \approx D_i \sqrt{m_i/m_k}$ [see equation (2.66)]. Eventually, inserting equation (4.19) into equation (4.18) yields

$$\frac{c_{\mathrm{UI},i}}{c_{\mathrm{DI},i}} \cdot \frac{c_{\mathrm{UI},k}}{c_{\mathrm{DI},k}} = \frac{W_k}{f^{\mathrm{c}}_{\mathrm{DI}}} \sqrt{\frac{m_{kk} m_i}{m_{ik} m_k}} \cdot \frac{c_{\mathrm{UI},k}}{c_{\mathrm{eq},k}} + \frac{c_{\mathrm{UI},k}}{c_{\mathrm{DI},k}} \,. \tag{4.20}$$

Both the permeation number W_k and the equilibrium concentration $c_{\mathrm{eq},k} = K_{\mathrm{s}} \sqrt{p_{kk}}$ refer to the upstream or downstream side where the partial pressure of ${}^{k}\mathrm{H}_2$ is high. Substituting this expression into equation (4.17) and using that $m_{ij} = m_i + m_j$ provides an alternative expression of the atomic permeation flux of isotope species ${}^{i}\mathrm{H}$

$$\overline{J}_{\mathrm{per},i} = 2\sigma k_{\mathrm{d},ii} p^{\mathrm{UI}}_{\mathrm{eff},i} \cdot \left(\frac{W_k}{f^{\mathrm{c}}_{\mathrm{DI}}} \sqrt{\frac{2m_i}{m_{ik}}} \cdot \frac{c_{\mathrm{UI},k}}{c_{\mathrm{eq},k}} + \frac{c_{\mathrm{UI},k}}{c_{\mathrm{DI},k}} + \frac{f^{\mathrm{c}}_{\mathrm{UI}}}{f^{\mathrm{c}}_{\mathrm{DI}}}\right)^{-1} \,. \tag{4.21}$$

At this point, a new quantity is defined, that is the multi-isotopic permeation flux factor

$$\Psi_{ik} \equiv \frac{\overline{J}_{\mathrm{per},i}}{2\sigma k_{\mathrm{d},ii} p_{\mathrm{eff},i}^{\mathrm{UI}}} = \left(\frac{W_k}{f_{\mathrm{DI}}^{\mathrm{c}}} \sqrt{\frac{2m_i}{m_{ik}}} \cdot \frac{c_{\mathrm{UI},k}}{c_{\mathrm{eq},k}} + \frac{c_{\mathrm{UI},k}}{c_{\mathrm{DI},k}} + \frac{f_{\mathrm{UI}}^{\mathrm{c}}}{f_{\mathrm{DI}}^{\mathrm{c}}} \right)^{-1} . \tag{4.22}$$

It describes the dependency of the permeation flux of species ^{i}H on the concentration profile of species ^{k}H in the bulk, and hence on the partial pressure of the molecules $^{k}H_2$. According to equation (4.22), the multi-isotopic permeation flux factor is independent of the effective pressure $p_{\mathrm{eff},i}^{\mathrm{UI}}$. Substituting Ψ_{ik} with the corresponding terms in equation (4.21) yields

$$\overline{J}_{\mathrm{per},i} = \Psi_{ik} \cdot 2\sigma k_{\mathrm{d},ii} p_{\mathrm{eff},i}^{\mathrm{UI}} . \tag{4.23}$$

Combining the two equations (4.16) and (4.23) leads to the following relationship

$$\Psi_{ik} = \frac{f_{\mathrm{DI}}^{\mathrm{c}}}{f_{\mathrm{UI}}^{\mathrm{c}}} \cdot \left(1 - \frac{k_{\mathrm{r},ik} c_{\mathrm{UI},i} c_{\mathrm{UI},k}}{2k_{\mathrm{d},ii} p_{\mathrm{eff},i}^{\mathrm{UI}}} \right) . \tag{4.24}$$

Inserting the relations (2.100) and (4.3) into equation (4.24) yields an expression for the upstream interface concentration of species ^{i}H

$$c_{\mathrm{UI},i} = \left(1 - \frac{f_{\mathrm{UI}}^{\mathrm{c}}}{f_{\mathrm{DI}}^{\mathrm{c}}} \cdot \Psi_{ik} \right) \cdot \sqrt{\frac{m_{ik}}{2m_i}} \cdot \frac{p_{\mathrm{eff},i}^{\mathrm{UI}}}{c_{\mathrm{UI},k}} K_{\mathrm{s}}^2 . \tag{4.25}$$

Moreover, from the equations (4.15) and (4.23) it follows that

$$c_{\mathrm{DI},i} = \frac{\overline{J}_{\mathrm{per},i}}{\sigma k_{\mathrm{r},ik} c_{\mathrm{DI},k}} = \Psi_{ik} \cdot \sqrt{\frac{m_{ik}}{2m_i}} \cdot \frac{p_{\mathrm{eff},i}^{\mathrm{UI}}}{c_{\mathrm{DI},k}} K_{\mathrm{s}}^2 . \tag{4.26}$$

Since an increase in partial pressure of the gas component $^{k}H_2$ on any of the two sides causes a rise in both $c_{\mathrm{UI},k}$ and $c_{\mathrm{DI},k}$ [see equation (2.149) and figure 2.11)], the interface concentrations $c_{\mathrm{UI},i}$ and $c_{\mathrm{DI},i}$ must reduce and the overall content of the isotopes ^{i}H in the bulk decreases [see equations (4.25) and (4.26)].

In the following, it is examined how the permeation regime of the undisturbed permeation process of isotope species ^{k}H influences the permeation flux of the isotopes ^{i}H from the upstream to the downstream side. Therefore, a new quantity is defined. It is called the normalized multi-isotopic permeation flux factor Λ_{ik} and defined by

$$\Lambda_{ik} = \Psi_{ik} \cdot \left(1 + \frac{f_{\mathrm{UI}}^{\mathrm{c}}}{f_{\mathrm{DI}}^{\mathrm{c}}} \right) \tag{4.27}$$

It describes the factor $0 < \Lambda_{\mathrm{ik}} \leq 1$ by which the permeation flux of isotopes ^{i}H in the presence of isotope species ^{k}H differs from a case where no isotopes ^{k}H are present in the system. For parallel membranes, equation (4.29) simplifies to $\Lambda_{ik} = 2\Psi_{ik}$. Alternatively the permeation flux of isotopes ^{i}H given by equation (4.23) can be expressed by

$$\overline{J}_{\mathrm{per},i} = \frac{\Lambda_{ik}}{1 + f_{\mathrm{UI}}^{\mathrm{c}} / f_{\mathrm{DI}}^{\mathrm{c}}} \cdot 2\sigma k_{\mathrm{d},ii} p_{\mathrm{eff},i}^{\mathrm{UI}} . \tag{4.28}$$

4.1.1. Surface-limited multi-isotopic permeation from gas to gas

The surface-limited regime of the considered multi-isotopic permeation process occurs for permeation numbers $W_k \ll 1$, meaning when either the metal surface is not clean or the partial pressure p_{kk} on the ${}^{k}H_2$ containing side is low. According to equation (2.166), in the surface-limited permeation regime of parallel and cylindrical membranes $c_{\mathrm{UI},k} \approx c_{\mathrm{DI},k}$. Considering both limit conditions, equation (4.21) reduces to

$$\overline{J}_{\mathrm{per},i} = \Psi_{ik} \cdot 2\sigma k_{\mathrm{d},ii} p_{\mathrm{eff},i}^{\mathrm{UI}}, \quad \text{with} \quad \Psi_{ik} = \frac{1}{1 + f_{\mathrm{UI}}^{\mathrm{c}}/f_{\mathrm{DI}}^{\mathrm{c}}}. \tag{4.29}$$

Equation (4.29) reveals that in the surface-limited multi-isotopic permeation regime the permeation flux of the isotopes ${}^{i}H$ into the downstream side depends neither on the partial pressure nor on the permeation direction of the dominant gas component ${}^{k}H_2$. For parallel membranes where $f_{\mathrm{UI}}^{\mathrm{c}} = f_{\mathrm{DI}}^{\mathrm{c}} = 1$, in the surface-limited multi-isotopic permeation regime the permeation flux factor approaches $\Psi = 1/2$. Moreover, from equation (4.27) it follows that the normalized multi-isotopic permeation flux factor approaches unity in the surface-limited multi-isotopic permeation regime so that $\Lambda_{ik} = 1$.

It is important to note that equation (4.29) is identical to equation (4.13). This result indicates that equation (4.29) holds even if the condition $p_{kk} \gg p_{\mathrm{eff},i}^{\mathrm{UI}}$ is not satisfied, as long as the effective pressure $p_{\mathrm{eff},i}^{\mathrm{UI}}$ is low enough so that in a case where $p_{kk} = 0$ the permeation process of the isotopes ${}^{i}H$ would occur in the surface-limited regime.

At higher effective pressures $p_{\mathrm{eff},i}^{\mathrm{UI}}$ where the permeation process of the isotopes ${}^{i}H$ is no longer surface-limited, the conditions $p_{kk} \gg p_{\mathrm{eff},i}^{\mathrm{UI}}$ need to be simultaneously satisfied in order for equation (4.29) to be valid. If in a situation where $W_k \ll 1$ the condition $p_{kk} \gg p_{\mathrm{eff},i}^{\mathrm{UI}}$ is not satisfied and the effective pressure $p_{\mathrm{eff},i}^{\mathrm{UI}}$ is relatively high so that the permeation process of the isotopes ${}^{i}H$ is no longer surface-limited regime, the permeation flux of isotope species ${}^{i}H$ would approach a value smaller than given by equation (4.13).

In the surface-limited regime of the undisturbed permeation process of species ${}^{k}H$, the interface concentrations $c_{\mathrm{UI},k}$ and $c_{\mathrm{DI},k}$ yield from the equations (2.166), (2.149) and (2.137)

$$c_{\mathrm{UI},k} \approx c_{\mathrm{DI},k} \approx \sqrt{\frac{1}{1 + f_{\mathrm{UI}}^{\mathrm{c}}/f_{\mathrm{DI}}^{\mathrm{c}}}} \cdot K_{\mathrm{s}} \cdot \sqrt{p_{kk}}. \tag{4.30}$$

By inserting them into the equations (4.25) and (4.26), it is found that in the surface-limited multi-isotopic permeation regime ($W_k \ll 1$) the concentrations of isotope species ${}^{i}H$ at the two interfaces follow the relations

$$c_{\mathrm{DI},i} \approx c_{\mathrm{UI},i} \approx \sqrt{\frac{1}{1 + f_{\mathrm{UI}}^{\mathrm{c}}/f_{\mathrm{DI}}^{\mathrm{c}}}} \cdot K_{\mathrm{s}} \cdot p_{\mathrm{eff},i}^{\mathrm{UI}} \cdot p_{kk}^{-\frac{1}{2}} \tag{4.31}$$

The partial pressure p_{kk} refers to the either p_{kk}^{UI} or p_{kk}^{DI}, depending which of the two sides contains the ${}^{k}H_2$ gas. The equations (4.30) and (4.31) well demonstrate that in the surface-limited multi-isotopic permeation regime the concentration profiles of both isotopes in the

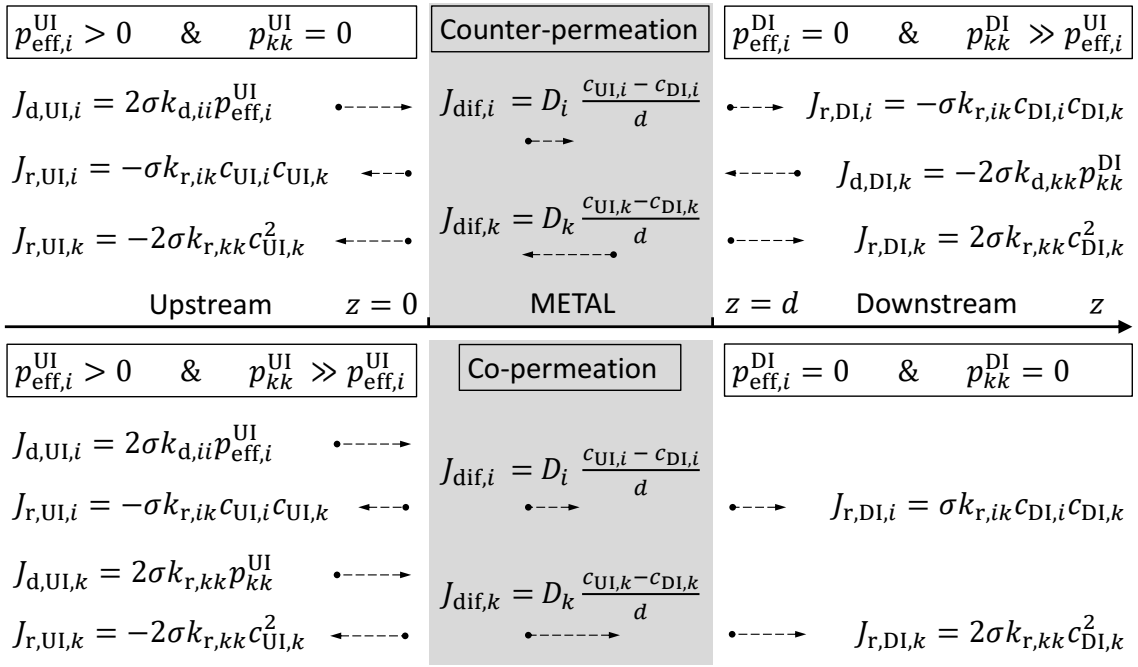

Fig. 4.1. Illustration of the molecular flux contributions in a multi-isotopic co- and counter-permeation scenario as considered in the presented theoretical study where it is assumed that isotope species ^{k}H is much more abundant in the system than isotope species ^{i}H. The image shows the case of a parallel membrane where $f^{\mathrm{c}}_{\mathrm{UI}} = f^{\mathrm{c}}_{\mathrm{DI}} = 1$.

bulk are flat. Moreover, it is found that the interface concentrations $c_{\mathrm{DI},i}$ and $c_{\mathrm{UI},i}$ decrease with increasing partial pressure p_{kk}.

4.1.2. Counter-permeation from gas to gas

Pure gas-to-gas counter-permeation refers to a scenario in which $p^{\mathrm{DI}}_{kk} \gg p^{\mathrm{UI}}_{\mathrm{eff},i}$ and $p^{\mathrm{UI}}_{kk} = 0$. Therefore, hydrogen isotopes ^{k}H are permeating from the downstream side into the upstream side, in the opposite direction to the diffusion flow of isotopes ^{i}H which permeate from the upstream side into the downstream side. The upper part of figure 4.1 shows the flux and partial pressure settings that define a case of pure gas-to-gas counter-permeation in the case of a parallel membrane, where the concentration profiles in the bulk are linear and $f^{\mathrm{c}}_{\mathrm{UI}} = f^{\mathrm{c}}_{\mathrm{DI}} = 1$. Since it is assumed that the permeation of ^{k}H isotopes occurs undisturbed, equation (4.21) can be expressed in terms of the defined reduced concentrations $\zeta_{\mathrm{r},k} = c_{\mathrm{UI},k}/c_{\mathrm{eq,DI},k}$ and $\lambda_{\mathrm{r},k} = c_{\mathrm{DI},k}/c_{\mathrm{eq,DI},k}$

$$\overline{J}_{\mathrm{per},i} = \Psi_{ik} \cdot 2\sigma k_{\mathrm{d},ii} p^{\mathrm{UI}}_{\mathrm{eff},i}\,, \quad \text{with} \quad \Psi_{ik} = \left(\sqrt{\frac{2m_i}{m_{ik}}} \frac{W_k}{f^{\mathrm{c}}_{\mathrm{DI}}} \zeta_{\mathrm{r},k} + \frac{\zeta_{\mathrm{r},k}}{\lambda_{\mathrm{r},k}} + \frac{f^{\mathrm{c}}_{\mathrm{UI}}}{f^{\mathrm{c}}_{\mathrm{DI}}} \right)^{-1} . \tag{4.32}$$

In this chapter, the labels UI and DI refer to the upstream and downstream interfaces of the primary species ^{i}H. The difference between the definitions of the reduced concentrations of species ^{k}H in this section in comparison with their definitions in equation (2.149) is due to the fact that in a counter-permeation scenario the label DI refers to the upstream

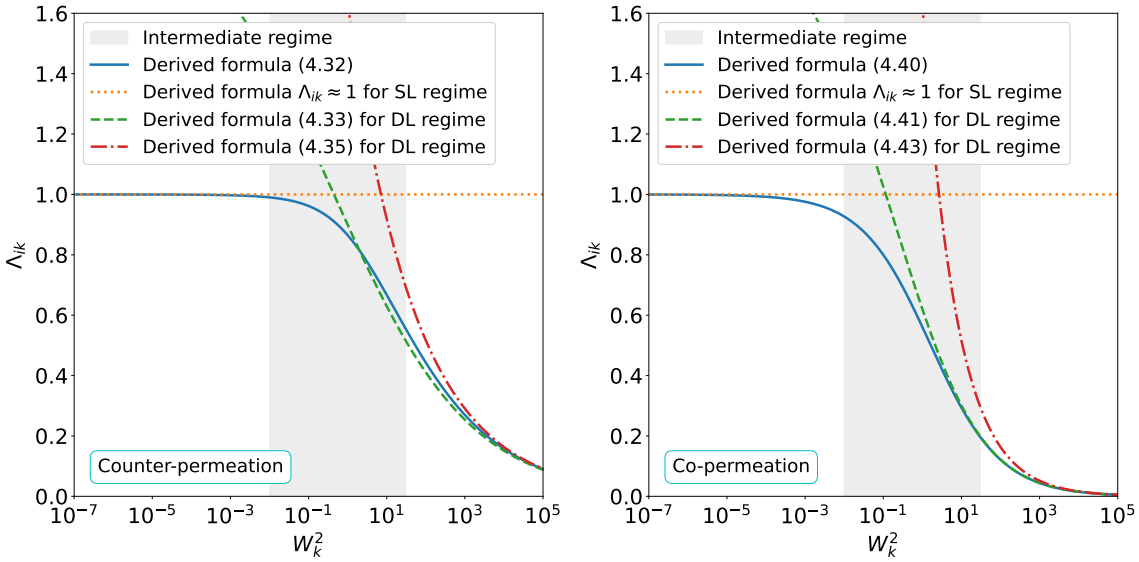

Fig. 4.2. Normalized multi-isotopic permeation flux factor Λ_{ik} for a parallel membrane if isotope species ${}^{k}\mathrm{H}$ is much more abundant in the system than isotope species ${}^{i}\mathrm{H}$. The plotted curves represent different algebraic formulas derived in this work that approximately describe the value of Λ_{ik}. [Left] Pure counter-permeation scenario. [Right] Pure co-permeation scenario.

interface of the permeation process of isotope species ${}^{k}\mathrm{H}$ which permeates in opposite direction to the primary species ${}^{i}\mathrm{H}$.

Serra *et al* [192] solved the general equation for steady state permeation (2.150), and thus found the dependency of the reduced concentration ζ_r on the permeation number in parallel membranes (2.151) plotted on the left in figure 2.11. Inserting the solution for ζ_r into equation (2.148) reveals the dependency of λ_r on the permeation number, which is plotted on the right in figure 2.11. Considering these dependencies for the reduced concentrations $\zeta_{\mathrm{r},k}(W_k)$ and $\lambda_{\mathrm{r},k}(W_k)$ of the secondary species ${}^{k}\mathrm{H}$ allows uncovering the relationship between the multi-isotopic permeation flux factor and the permeation number W_k in parallel membranes, by inserting both reduced concentrations into equation (4.32). It is plotted in the left graph in figure 4.2 with a solid blue line after being normalized according to $\Lambda_{\mathrm{ik}} = 2\Psi_{ik}$ [see equation (4.27)]. The plot reveals that, as predicted by equation (4.29), in the surface-limited regime $\Lambda_{ik} \approx 1$ or $\Psi_{ik} \approx 1/2$. However, it turns out that in the intermediate regime, the multi-isotopic permeation flux factor declines with increasing permeation number and approaches zero when $W_k \to \infty$ in the diffusion-limited regime.

A similar relationship between the multi-isotopic permeation flux factor and the permeation number is expected for cylindrical membranes. However, since the general equation of steady state permeation for cylindrical membranes (2.165) has not yet been solved, only its limit behavior in the diffusion-limited permeation regime of the counter-permeating species ${}^{k}\mathrm{H}$ is discussed at this point.

In the diffusion-limited counter-permeation regime where $W_k \gg 1$, the reduced con-

centrations $\zeta_{\mathrm{r},k}$ and $\lambda_{\mathrm{r},k}$ converge against $\zeta_{\mathrm{r},k} \rightarrow \sqrt{f_{\mathrm{UI}}^{\mathrm{c}}/W_k}$ and $\lambda_{\mathrm{r},k} \rightarrow 1$ [see equation (2.167)]. Once again, it is important to remember that in a counter-permeation scenario, the interface labeled UI is the downstream interface of the counter-permeating isotopes ${}^{k}\mathrm{H}$. Substituting the limit expressions of the reduced concentrations into the expression (4.32) results in

$$\overline{J}_{\mathrm{per},i} = \Psi_{ik} \cdot 2\sigma k_{\mathrm{d},ii} p_{\mathrm{eff},i}^{\mathrm{UI}}, \quad \text{with} \quad \Psi_{ik} = \left(\sqrt{\frac{2m_i}{m_{ik}}} \frac{\sqrt{f_{\mathrm{UI}}^{\mathrm{c}} W_k}}{f_{\mathrm{DI}}^{\mathrm{c}}} + \frac{f_{\mathrm{UI}}^{\mathrm{c}}}{f_{\mathrm{DI}}^{\mathrm{c}}} \right)^{-1} . \tag{4.33}$$

For $W \rightarrow \infty$ the second term in the brackets can be neglected. Considering this and inserting the definition of the permeation number (4.19) gives the dependency of the permeation flux $\overline{J}_{\mathrm{per},i}$ on the partial pressure p_{kk}^{DI} in the diffusion-limited counter-permeation regime

$$\overline{J}_{\mathrm{per},i} = \sqrt{\frac{m_{ik}}{2m_i}} \frac{f_{\mathrm{DI}}^{\mathrm{c}}}{\sqrt{f_{\mathrm{UI}}^{\mathrm{c}} W_k}} \cdot 2\sigma k_{\mathrm{d},ii} p_{\mathrm{eff},i}^{\mathrm{UI}} = \frac{f_{\mathrm{DI}}^{\mathrm{c}}}{\sqrt{f_{\mathrm{UI}}^{\mathrm{c}}}} \cdot \frac{\sqrt{m_{ik} m_k}}{m_i} \sqrt{\frac{\sigma k_{\mathrm{d},kk} \Phi_k}{d}} \cdot p_{\mathrm{eff},i}^{\mathrm{UI}} \cdot \left(p_{kk}^{\mathrm{DI}} \right)^{-\frac{1}{4}} . \tag{4.34}$$

Here, it is used that $k_{\mathrm{d},ii} \approx k_{\mathrm{d},kk} \sqrt{m_{kk}/m_{ii}}$. Hence, in the diffusion-limited counter-permeation regime, the multi-isotopic permeation flux factor converges against

$$\Psi_{ik} = \sqrt{\frac{m_{ik}}{2m_i}} \frac{f_{\mathrm{DI}}^{\mathrm{c}}}{\sqrt{f_{\mathrm{UI}}^{\mathrm{c}} W_k}} . \tag{4.35}$$

It is important to note that the permeation number (4.19) depends not only on the pressure p_{kk}^{DI} but also on the bulk thickness and the values of the temperature-dependent coefficients K_{s} and $k_{\mathrm{d},kk}$. For this reason, at a fix value of p_{kk}^{DI}, the permeation flux reduction factor Ψ_{ik} varies with temperature and wall thickness. After normalization with $\Lambda_{\mathrm{ik}} = 2\Psi_{ik}$, the two derived diffusion-limited expressions of the multi-isotopic permeation flux factor (4.33) and (4.35) are plotted in the left graph of figure 4.2 considering a parallel membrane. The graph reveals that both diffusion-limited expressions converge against the general solution (solid blue line) derived from Serra's solution of the general equation for steady state permeation. Equation (4.33) describes the course of the permeation flux factor more accurately than equation (4.35).

According to equation (2.167), in the diffusion-limited counter-permeation regime where of the undisturbed permeation process of isotope species ${}^{k}\mathrm{H}$ from the downstream into the upstream side where $W \rightarrow \infty$ the interface concentrations of species ${}^{k}\mathrm{H}$ approach $c_{\mathrm{DI},k} \rightarrow c_{\mathrm{eq,DI},k}$ and $c_{\mathrm{UI},k} \rightarrow c_{\mathrm{eq,DI},k} \cdot \sqrt{f_{\mathrm{UI}}^{\mathrm{c}}/W_k}$. Inserting the equations (2.137) and (4.19) leads to the expressions

$$c_{\mathrm{UI},k} = \sqrt{\frac{f_{\mathrm{UI}}^{\mathrm{c}} \cdot \Phi_k}{2\sigma k_{\mathrm{d},kk} d}} \cdot K_{\mathrm{s}} \left(p_{kk}^{\mathrm{DI}} \right)^{\frac{1}{4}} \qquad \text{and} \qquad c_{\mathrm{DI},k} = K_{\mathrm{s}} \sqrt{p_{kk}^{\mathrm{DI}}} . \tag{4.36}$$

Furthermore, substituting the equation (4.35) and (4.36) into the equations (4.25) and (4.26) yields the approximate upstream and downstream interface concentrations of the

isotopes ^{i}H in the diffusion-limited counter-permeation regime.

$$c_{\mathrm{UI},i} = \sqrt{\frac{m_{ik}}{2m_i}} \cdot K_\mathrm{s} p_{\mathrm{eff},i}^{\mathrm{UI}} \cdot \left(p_{kk}^{\mathrm{DI}}\right)^{-\frac{1}{2}} \cdot \left[\sqrt{\frac{2\sigma k_{\mathrm{d},kk} d}{f_{\mathrm{UI}}^{\mathrm{c}} \cdot \Phi_k}} \left(p_{kk}^{\mathrm{DI}}\right)^{\frac{1}{4}} - \sqrt{\frac{m_{ik}}{2m_i}} \right] \tag{4.37}$$

$$c_{\mathrm{DI},i} = \frac{m_{ik}}{2m_i} \sqrt{\frac{f_{\mathrm{UI}}^{\mathrm{c}} \cdot \Phi_k}{2\sigma k_{\mathrm{d},kk} d}} \cdot K_\mathrm{s} p_{\mathrm{eff},i}^{\mathrm{UI}} \cdot \left(p_{kk}^{\mathrm{DI}}\right)^{-\frac{3}{4}} . \tag{4.38}$$

The equations show that in the diffusion-limited regime, the downstream concentration $c_{\mathrm{DI},i}$ is described by a stronger decreasing function $c_{\mathrm{DI},i} \propto \left(p_{kk}^{\mathrm{DI}}\right)^{-3/4}$ with increasing value of p_{kk}^{DI} than in the surface-limited regime where $c_{\mathrm{DI},i} \propto \left(p_{kk}^{\mathrm{DI}}\right)^{-1/2}$ [see equation (4.31)]. In contrast, the increase in upstream concentration $c_{\mathrm{UI},i}$ occurs at a lower rate compared to the surface-limited regime [see equation (4.30)].

A useful quantity to explain the permeation mitigating effect of counter-permeation is the product of the upstream interface concentrations of both species in the diffusion-limited counter-permeation regime where $W \to \infty$

$$c_{\mathrm{UI},k} c_{\mathrm{UI},i} = \sqrt{\frac{m_{ik}}{2m_i}} \cdot K_\mathrm{s}^2 p_{\mathrm{eff},i}^{\mathrm{UI}} - \frac{m_{ik}}{2m_i} \sqrt{\frac{f_{\mathrm{UI}}^{\mathrm{c}} \cdot \Phi_k}{2\sigma k_{\mathrm{d},kk} d}} \cdot K_\mathrm{s}^2 p_{\mathrm{eff},i}^{\mathrm{UI}} \cdot \left(p_{kk}^{\mathrm{DI}}\right)^{-\frac{1}{4}} . \tag{4.39}$$

It shows that with increasing pressure p_{kk}^{DI} the recombination flux $J_{\mathrm{UI,r},i} = -\sigma k_{\mathrm{r},ik} c_{\mathrm{UI},i} c_{\mathrm{UI},k}$ of the isotopes ^{i}H back into the upstream chamber increases. This occurs even if the atomic dissociation flux $J_{\mathrm{UI,d},i} = 2\sigma k_{\mathrm{d},ii} p_{\mathrm{eff},i}^{\mathrm{UI}}$ remains constant. According to equation (4.14), an increased upstream recombination flux at constant effective pressure $p_{\mathrm{eff},i}^{\mathrm{UI}}$ causes the permeation flux to decrease. This explains the permeation mitigating effect of counter-permeation.

4.1.3. Co-permeation from gas to gas

In contrast, pure co-permeation occurs if $p_{kk}^{\mathrm{UI}} \gg p_{\mathrm{eff},i}^{\mathrm{UI}}$ and $p_{kk}^{\mathrm{DI}} = 0$. As a consequence, the net diffusion direction of both isotopes is from the upstream into the downstream side. They co-permeate side-by-side through the metal bulk. The flux configuration occurring in a pure co-permeation scenario is showcased at the bottom in figure 4.1. In a co-permeation scenario, the reduced concentrations of the permeation process of isotope species ^{k}H are defined by $\zeta_{\mathrm{r},k} = c_{\mathrm{DI},k}/c_{\mathrm{eq,UI},k}$ and $\lambda_{\mathrm{r},k} = c_{\mathrm{UI},k}/c_{\mathrm{eq,UI},k}$. In a co-permeation scenario, the reduced concentrations of isotope species ^{k}H differ from those in a counter-permeation scenario since the label UI now refers to the upstream interface of both species. Substituting these definitions into equation (4.21) allows it to be rewritten as follows

$$\overline{J}_{\mathrm{per},i} \approx \Psi_{ik} \cdot 2\sigma k_{\mathrm{d},ii} p_{\mathrm{eff},i}^{\mathrm{UI}} , \quad \text{with} \quad \Psi_{ik} = \left(\sqrt{\frac{2m_i}{m_{ik}}} \frac{W_k}{f_{\mathrm{DI}}^{\mathrm{c}}} \lambda_{\mathrm{r},k} + \frac{\lambda_{\mathrm{r},k}}{\zeta_{\mathrm{r},k}} + \frac{f_{\mathrm{UI}}^{\mathrm{c}}}{f_{\mathrm{DI}}^{\mathrm{c}}} \right)^{-1} . \tag{4.40}$$

Once again, for the specific case of parallel membranes, the theoretical solutions for the reduced concentrations $\zeta_{\mathrm{r},k}(W_k)$ and $\lambda_{\mathrm{r},k}(W_k)$ displayed in figure 2.11 are inserted into

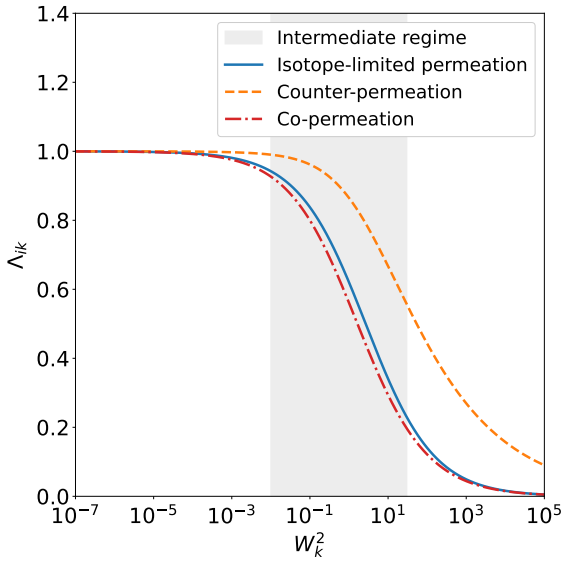

Fig. 4.3. Normalized multi-isotopic permeation flux factors of parallel membranes for a co- and counter-permeation scenario calculated by inserting the theoretical solutions of the reduced concentrations $\zeta_{\mathrm{r},k}(W_k)$ and $\lambda_{\mathrm{r},k}(W_k)$ displayed in figure 2.11 into the derived algebraic formulas (4.40) and (4.32), respectively. Moreover, the plot contains a curve representing an isotope-limited permeation scenario which is calculated with the derived equation (4.48).

equation (4.21) which reveals the relationship between the multi-isotopic permeation flux factor of co-permeation and the permeation number W_k. It is plotted in the right-hand graph of figure 4.2 with a solid blue line after being normalized. A comparison of the solid blue lines in the two plots in figure 4.2 shows that the relationships between the multi-isotope permeation flux factor and the permeation number W_k are very similar in a counter- and co-permeation scenario. However, in a co-permeation scenario the value of Ψ_{ik} starts decreasing at lower permeation numbers and with a steeper negative slope at the inflection point. This means that at a certain permeation number outside of the surface-limited regime, the permeation flux factor reduces to much smaller values in a co-permeation process compared to in a counter-permeation process. This becomes apparent in figure 4.3 which compares the courses of the normalized permeation flux factors of both permeation processes in the case of parallel membranes.

In the diffusion-limited co-permeation regime ($W_k \gg 1$), where both isotope species share the same downstream interface, the reduced concentration $\zeta_{\mathrm{r},k}$ approaches $\zeta_{\mathrm{r},k} \to f_{\mathrm{DI}}^{\mathrm{c}}/\sqrt{W_k}$ and $\lambda_{\mathrm{r},k} \to 1$ [see equation (2.167)]. For this reason, in the diffusion-limited co-permeation regime equation (4.40) simplifies to

$$\overline{J}_{\mathrm{per},i} = \Psi_{ik} \cdot 2\sigma k_{\mathrm{d},ii} p_{\mathrm{eff},i}^{\mathrm{UI}}\,, \quad \text{with} \quad \Psi_{ik} = \left(\sqrt{\frac{2m_i}{m_{ik}}} \frac{W_k}{f_{\mathrm{DI}}^{\mathrm{c}}} + \sqrt{\frac{W_k}{f_{\mathrm{DI}}^{\mathrm{c}}}} + \frac{f_{\mathrm{UI}}^{\mathrm{c}}}{f_{\mathrm{DI}}^{\mathrm{c}}} \right)^{-1} . \tag{4.41}$$

For $W \to \infty$ the second and third terms in parenthesis become increasingly unimportant and can be neglected. Eventually, substituting the permeation number with its definition in equation (4.19) leads to

$$\overline{J}_{\mathrm{per},i} \approx 2\sigma k_{\mathrm{d},ii} p_{\mathrm{eff},i}^{\mathrm{UI}} \sqrt{\frac{m_{ik}}{2m_i}} \cdot \frac{f_{\mathrm{DI}}^{\mathrm{c}}}{W_k} = f_{\mathrm{DI}}^{\mathrm{c}} \cdot \frac{\Phi_k}{d} \sqrt{\frac{m_{ik} m_k}{2m_i^2}} \cdot p_{\mathrm{eff},i}^{\mathrm{UI}} \cdot \left(p_{kk}^{\mathrm{DI}}\right)^{-\frac{1}{2}} . \tag{4.42}$$

In this approximation, the multi-isotopic permeation flux factor converges against

$$\Psi_{ik} \approx \sqrt{\frac{m_{ik}}{2m_i}} \cdot \frac{f_{\mathrm{DI}}^{\mathrm{c}}}{W_k} . \tag{4.43}$$

Both diffusion-limited relations of the permeation flux factor (4.41) and (4.43) are plotted in the right-hand graph in figure 4.2 after applying the normalization procedure for parallel membranes ($\Lambda_{ik} = 2\Psi_{\mathrm{ik}}$). While expression (4.41) describes almost perfectly the theoretical course of Λ_{ik} above permeation numbers $W_k^2 > 10$, equation (4.41) is in good agreement with the theoretical solution only when $W_k^2 > 1000$.

By comparing the derived algebraic permeation flux relations (4.34) and (4.42) for the co- and counter-permeation regimes, it is found that in a diffusion-limited counter-permeation scenario the steady state permeation flux of isotope species ^{i}H is proportional to $\overline{J}_{\mathrm{per},i} \propto \left(p_{kk}^{\mathrm{UI}}\right)^{-1/2}$ while diffusion-limited co-permeation is characterized by $\overline{J}_{\mathrm{per},i} \propto \left(p_{kk}^{\mathrm{UI}}\right)^{-1/4}$. Hence, co-permeating isotopes ^{k}H reduce the permeation flux of isotope species ^{i}H more efficiently than counter-permeating isotopes ^{k}H.

In contrast to a counter-permeation scenario, due to the reverse permeation direction of species ^{k}H, in the diffusion-limited co-permeation regime the upstream and downstream interface concentrations of species ^{k}H converge against the expressions $c_{\mathrm{UI},k} \rightarrow c_{\mathrm{eq,UI},k}$ and $c_{\mathrm{DI},k} \rightarrow c_{\mathrm{eq,UI},k} \cdot \sqrt{f_{\mathrm{DI}}^{\mathrm{c}}/W_k}$. With the equations (2.137) and (4.19) this yields

$$c_{\mathrm{UI},k} = K_{\mathrm{s}} \sqrt{p_{kk}^{\mathrm{UI}}} \qquad \text{and} \qquad c_{\mathrm{DI},k} = \sqrt{f_{\mathrm{DI}}^{\mathrm{c}} \cdot \frac{\Phi_k}{2\sigma k_{\mathrm{d},kk} d}} \cdot K_{\mathrm{s}} \left(p_{kk}^{\mathrm{UI}}\right)^{\frac{1}{4}} . \tag{4.44}$$

Analogously to the equations (4.37) and (4.38), one obtains the interface concentrations of isotope species ^{i}H for the diffusion-limited regime of co-permeation by inserting the expressions (4.43) and (4.44) into the equations (4.25) and (4.26)

$$c_{\mathrm{UI},i} = \sqrt{\frac{m_{ik}}{2m_i}} \cdot K_{\mathrm{s}} p_{\mathrm{eff},i}^{\mathrm{UI}} \cdot \left(p_{kk}^{\mathrm{UI}}\right)^{-\frac{1}{2}} \cdot \left[1 - \sqrt{\frac{m_{ik}}{2m_i}} \frac{f_{\mathrm{UI}}^{\mathrm{c}} \cdot \Phi_k}{2\sigma k_{\mathrm{d},kk} d} \cdot \left(p_{kk}^{\mathrm{UI}}\right)^{-\frac{1}{2}}\right] \tag{4.45}$$

$$c_{\mathrm{DI},i} = \frac{m_{ik}}{2m_i} \sqrt{\frac{f_{\mathrm{DI}}^{\mathrm{c}} \cdot \Phi_k}{2k_{\mathrm{d},kk} d}} \cdot K_{\mathrm{s}} p_{\mathrm{eff},i}^{\mathrm{UI}} \cdot \left(p_{kk}^{\mathrm{UI}}\right)^{-\frac{3}{4}} . \tag{4.46}$$

A comparison of the equations (4.38) and (4.46) shows that in the co- and the counter-permeation diffusion-limited regimes, the downstream interface concentrations of the isotopes ^{i}H are described by the same p_{kk}^{UI} dependent function. It can be seen that both the upstream and downstream interface concentrations of the isotopes ^{i}H decrease at a slower rate with increasing partial pressure p_{kk}^{UI} than in the surface-limited regime.

Consequently, the product of both upstream concentrations yields

$$c_{\mathrm{UI},k} c_{\mathrm{UI},i} = \sqrt{\frac{m_{ik}}{2m_i}} \cdot K_{\mathrm{s}}^2 p_{\mathrm{eff},i}^{\mathrm{UI}} - \frac{m_{ik}}{4m_i} \frac{f_{\mathrm{UI}}^{\mathrm{c}} \cdot \Phi_k}{\sigma k_{\mathrm{d},kk} d} \cdot K_{\mathrm{s}}^2 p_{\mathrm{eff},i}^{\mathrm{UI}} \cdot \left(p_{kk}^{\mathrm{UI}}\right)^{-\frac{1}{2}} . \tag{4.47}$$

As it is the case for diffusion-limited counter-permeation, the product of the two concentrations $c_{\mathrm{UI},k} c_{\mathrm{UI},i}$, and thus the probability for a recently dissociated isotope ^{i}H to recombine with an isotope ^{k}H and return back into the upstream interface, rises with climbing partial pressure p_{kk}^{DI}. For this reason, the upstream atomic recombination flux into the upstream side $J_{\mathrm{UI,r},i} = -\sigma k_{\mathrm{r},ik} c_{\mathrm{UI},i} c_{\mathrm{UI},k}$ increases. At constant pressure $p_{\mathrm{eff},i}^{\mathrm{UI}}$, this

causes the permeation flux of the isotopes ^{i}H to decrease which explains the permeation flux-reducing effect of co-permeation [see equation (4.14)]. However, in contrast to the counter-permeation scenario, in the diffusion-limited co-permeation regime the upstream concentration of isotope species ^{i}H increases stronger with rising pressure p_{kk}^{UI} than in the surface-limited regime. Therefore, also the recombination flux into the upstream side increases at a higher rate with increasing partial pressure p_{kk}^{UI}. This is why co-permeation exhibits a more intense permeation flux mitigating effect than counter-permeation.

Three important algebraic equations (4.29), (4.33) and (4.41) could be derived within the scope of this work that describe the permeation flux of the primary species ^{i}H as a function of the partial pressure p_{kk} of the secondary species for the surface-limited regime and for the diffusion-limited co- and counter-permeation regimes. Strongly reduced versions of these equations were formulated in a previous theoretical assessment performed by Waelbroeck *et al* [170]. In contrast to the previous study, the algebraic equations of gas-to-gas multi-isotopic permeation derived in this work include several new terms and are based on much less simplifying assumptions. The new equations are generalized for cylindrical permeation membranes and take into account the mass difference between different isotopes. Moreover, by introducing the concept of the effective pressure in this work, the derived equations are applicable to systems containing a mix of all three molecules ^{i}H, ^{i}H^{k}H and ^{k}H while the much more simplified model by Waelbroeck *et al* is only valid in systems involving merely the two molecular species ^{i}H^{k}H and ^{k}H. The performed modifications in this work are of significant importance since in any realistic multi-isotopic scenario isotope exchange reactions lead to the coexistence of all three molecular species. The derived algebraic equations (4.29), (4.33) and (4.41) will be validated in section 5.3.

Furthermore, for the first time in this work, the solution (2.151) of the general equation of steady state permeation calculated by Sierra *et al* has been applied to an analytical multi-isotopic permeation model. Thus, it was possible to derive and plot the theoretical relationships (4.32) and (4.40) between the permeation flux of the isotopes ^{i}H and the permeation number of the co- or counter-permeating isotopes ^{k}H for the case of parallel membranes which are plotted in figure 4.2.

4.1.4. Isotope-limited permeation from gas to gas

Given that $p_{kk} \gg p_{\mathrm{eff},i}^{\mathrm{UI}}$, there is a special case of multi-isotopic gas-to-gas permeation, that allows deriving an algebraic formula for the permeation flux of species ^{i}H which is valid in the entire partial pressure range of the molecular species ^{k}H. It is here referred to as isotope-limited permeation which is theoretically studied for the first time in this thesis.

In an isotope-limited permeation scenario, the partial pressure of the gas component ^{k}H$_2$ is equal on both sides of the membrane, such that $p_{kk} \equiv p_{kk}^{\mathrm{UI}} = p_{kk}^{\mathrm{DI}}$. Consequently, the isotopes ^{k}H dissolved in the metal bulk must be in chemical equilibrium with the gaseous upstream and downstream sides. According to the Sieverts' law, this implies that

$c_{\mathrm{eq,UI},k} = c_{\mathrm{eq,DI},k} = c_{\mathrm{UI},k} = c_{\mathrm{DI},k} = K_\mathrm{s}\sqrt{p_{kk}}$. Consequently, equation (4.21) transforms to

$$\overline{J}_{\mathrm{per},i} = \Psi_{ik} \cdot 2\sigma k_{\mathrm{d},ii} p_{\mathrm{eff},i}^{\mathrm{UI}}\,, \quad \text{with} \quad \Psi_{ik} = \left(\frac{1}{f_{\mathrm{DI}}^{\mathrm{c}}} \sqrt{\frac{8m_i}{m_{ik}}} \frac{\sigma k_{\mathrm{d},kk} d}{\Phi_k} \sqrt{p_{kk}} + 1 + \frac{f_{\mathrm{UI}}^{\mathrm{c}}}{f_{\mathrm{DI}}^{\mathrm{c}}} \right)^{-1} . \quad (4.48)$$

It can be seen that the permeation flux of the primary species reduces with increasing partial pressure p_{kk}. Furthermore, it is found that with increasing partial pressure p_{kk} the equation (4.48) converges against relation (4.41) of diffusion-limited co-permeation.

The example of isotope-limited permeation demonstrates that the flux-reducing effect of multi-isotopic gas-to-gas permeation originates from the sheer presence of the secondary species ^{k}H in the system. A higher concentration $c_{\mathrm{UI},k}$ in the subsurface of the upstream interface increases the recombination flux $J_{\mathrm{UI,r},i} = -\sigma k_{\mathrm{r},ik} c_{\mathrm{UI},i} c_{\mathrm{UI},k}$ of isotopes ^{i}H back into the upstream side. According to equation (4.14), it thus lowers the concentration and the permeation flux of species ^{i}H into the downstream side. A concentration gradient of the secondary species ^{k}H, as it is present in the co- and counter-permeation case, merely reduces or increases this effect. The left-hand graph in figure (4.3) contains a plot showing the relationship between the normalized multi-isotopic permeation flux factor of isotope-limited permeation in parallel membranes ($\Lambda_{ik} = 2\Psi_{\mathrm{ik}}$) and the permeation number W_k, which is obtained by inserting the definition of the permeation number (4.19) into equation (4.48). The plot shows that the permeation flux-reducing effect of isotope-limited permeation is stronger than that of diffusion-limited counter-permeation but slightly weaker than that of diffusion-limited co-permeation (see figure 4.3). However, the curves of the multi-isotopic permeation flux factor of the co-permeation and isotope-limited scenarios follow a very similar path. Hence, equation (4.48) may be used as a formula to algebraically estimate the occurring permeation flux reduction in a co-permeation process for any permeation number W_k. The physical mechanisms of multi-isotopic gas-to-gas permeation are further discussed in section 5.3.

Figure 4.4 compares the courses of the normalized multi-isotopic permeation flux factor of a parallel membrane with those of cylindrical membranes of different ratios $r_{\mathrm{out}}/r_{\mathrm{in}} = 1.5$ and $r_{\mathrm{out}}/r_{\mathrm{in}} = 3$. It can be seen that even if the thickness of the membrane is as much as half of the inner radius ($r_{\mathrm{out}}/r_{\mathrm{in}} = 1.5$), the relationship between Λ_{ik} and W_k is almost identical to that of a parallel membrane. Therefore, it is to expect that also in a co- or counter-permeation scenario, the relationships between Λ_{ik} and W_k of cylindrical membranes do not differ much from the known theoretical courses of $\Lambda_{ik}(W_k)$ of parallel membranes shown in figure 4.2. However, if the ratio $r_{\mathrm{out}}/r_{\mathrm{in}}$ is even higher a noticeable difference from the case of a parallel membrane can be observed (see the plot for $r_{\mathrm{out}}/r_{\mathrm{in}} = 3$ in figure 4.4).

4.1.5. Multi-isotopic permeation at elevated concentrations

Another effect of multi-isotopic permeation arises if the total bulk concentration $c_{\mathrm{tot}} = \sum_i c_i$ of the isotopes involved in the permeation process is well above the range of validity

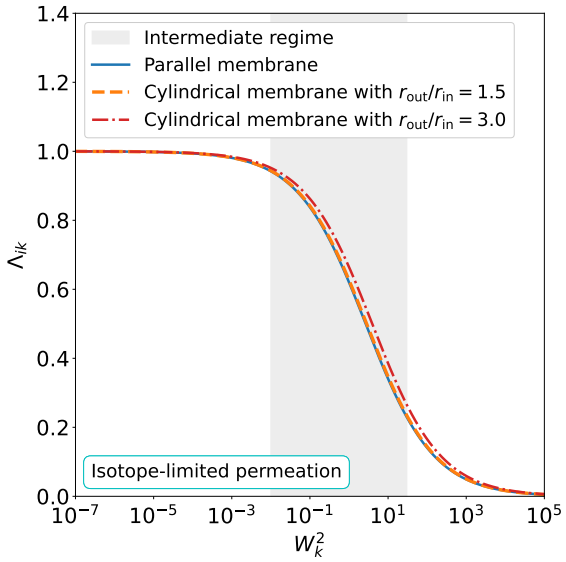

Fig. 4.4. Normalized multi-isotopic permeation flux factor for the case of isotope-limited permeation calculated using the derived algebraic equation (4.48). The different curves represent a parallel membrane and different cylindrical membranes.

of the Sieverts' law. One might imagine a case in which isotopes of species ^{i}H permeate from the upstream into the downstream side at a low driving pressure $p^{\mathrm{UI}}_{\mathrm{eff},i}$ and with a low bulk concentration profile $c_i(z)$. In addition, one or both sides of the membrane are exposed to a very high partial pressure p_{kk} of the gas component $^{k}H_2$ leading to a bulk concentration profile $c_k(z)$ high enough to noticeably reduce the number of available interstitial sites the permeating isotopes ^{i}H can jump into. Equation (2.63) reveals that if the total bulk coverage $\theta_{\mathrm{b,tot}} = \sum_i \theta_{\mathrm{b},i}$ [see definition in equation (2.34)] is sufficiently high, the factor $(1 - \theta_{\mathrm{b,tot}})$ appearing in the expression of the intrinsic diffusion coefficient [147] is considerably smaller than unity and therefore not negligible. According to Fick's first law (2.67), the diffusion flux of the isotopes ^{i}H is proportional to the diffusion coefficient and likewise to the factor $(1 - \theta_{\mathrm{b,tot}})$. Hence, even if c_i is small, the permeation flux of the isotopes ^{k}H might be strongly reduced if the concentration c_k in the bulk is high.

Furthermore, a high total bulk concentration of isotope species ^{k}H is accompanied by an even greater areal surface concentration ν_k. Equation (2.88) reveals that a high surface coverage θ_{c} reduces the dissociation flux of the isotopes ^{i}H on the upstream side by a factor $(1 - \theta_{\mathrm{c}})^2$. Both the decrease in diffusion flux and the decrease in dissociation flux result in a reduced permeation flux of the isotopes ^{i}H into the downstream chamber [see equation (4.14)]. Since the surface concentration of interstitial solutes in metals is usually much higher than the bulk concentration [180], it is reasonable to assume that the blocking of surface sites by the isotopes ^{k}H reveals its permeation mitigating effect at considerably lower partial pressures p_{kk} than the blocking of interstitial sites in the bulk.

Nevertheless, the permeation phenomena studied in this work involve merely endothermic iron-based hydrogen absorbers with a very low hydrogen solubility. In these materials, the studied pressure conditions are not high enough to cause bulk concentrations which would lead to the discussed high-concentration isotope effects. These effects would however play a significant role in multi-isotopic gas-to-gas permeation scenarios through exothermic hydrogen absorbing metals such as yttrium, palladium or vanadium.

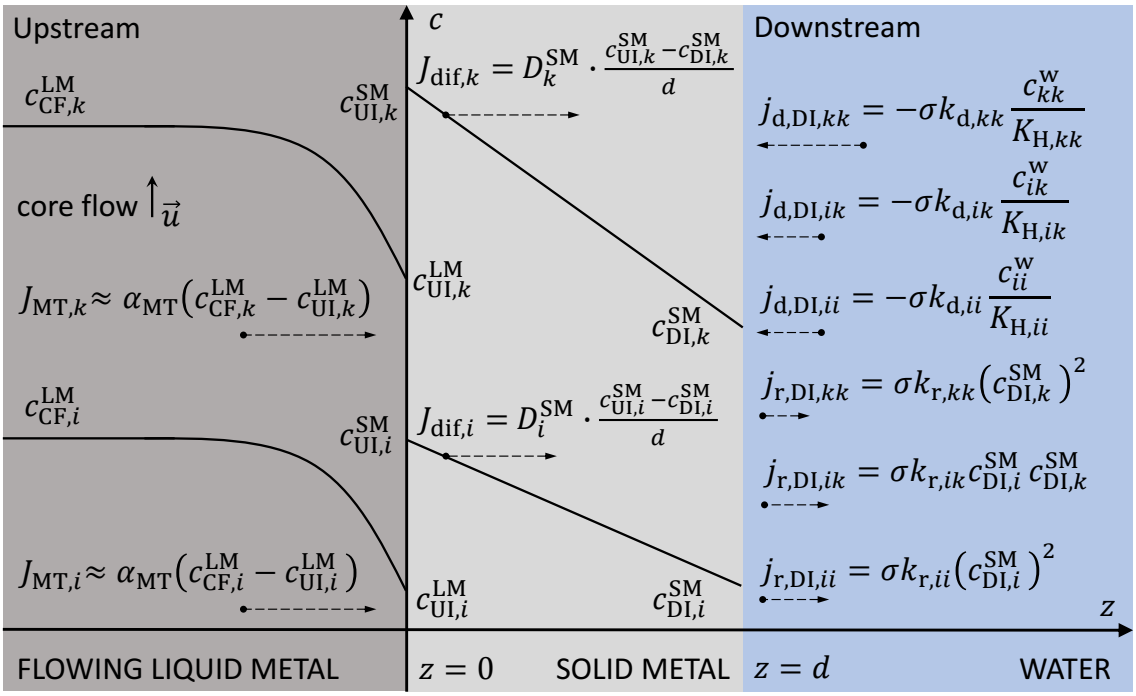

Fig. 4.5. Simplified flux contributions in a multi-isotopic permeation scenario from flowing liquid metal through a plane metal bulk into water.

4.2. Theoretical study of multi-isotopic permeation from liquid metal to water

Another multi-isotopic permeation scenario examined in this theoretical study is the permeation of isotope species ^{i}H from flowing liquid metal through a metal membrane into water. Again, it is assumed that a secondary isotope species ^{k}H is present in the system. The steady state flux configuration and permeation profile of such a permeation process is presented in figure 4.5 for the case of a parallel membrane.

Similar to the discussed multi-isotopic gas-to-gas permeation scenario, steady state permeation is characterized by the establishment of constant interface concentrations of the two isotopes in the bulk, as long as the mass transfer coefficient of the liquid metal flow, the hydrogen isotope concentrations in the liquid metal and the concentrations of hydrogen isotope containing molecules in the water remain constant. As is the case for multi-isotopic gas-to-gas permeation, the establishing steady state concentration profiles of both isotopes follow straight lines described by equation (2.134) if the membrane is parallel and non-straight lines described by equation (2.158) if the membrane is cylindrical. Applying the laws of hydrogen transport across metal-metal interfaces derived in section 2.2.3 and respecting mass continuity across interfaces leads to the following expressions

$$\overline{J}^{\circledcirc}_{\mathrm{net,UI},i} = \alpha_{\mathrm{MT}}\left(c^{\mathrm{LM}}_{\mathrm{CF},i} - c^{\mathrm{LM}}_{\mathrm{UI},i}\right) = \alpha_{\mathrm{MT}}\left(c^{\mathrm{LM}}_{\mathrm{CF},i} - c^{\mathrm{SM}}_{\mathrm{UI},i} K^{\mathrm{SM-LM}}_{\mathrm{D},0,i}\right) = f^{\mathrm{c}}_{\mathrm{UI}} D^{\mathrm{SM}}_{i} \frac{c^{\mathrm{SM}}_{\mathrm{UI},i} - c^{\mathrm{SM}}_{\mathrm{DI},i}}{d} \tag{4.49}$$

$$\overline{J}^{\circledcirc}_{\mathrm{net,DI},i} = f^{\mathrm{c}}_{\mathrm{DI}} D^{\mathrm{SM}}_{i} \frac{c^{\mathrm{SM}}_{\mathrm{UI},i} - c^{\mathrm{SM}}_{\mathrm{DI},i}}{d} = \sigma \cdot \left[2k_{\mathrm{r},ii}\left(c^{\mathrm{SM}}_{\mathrm{DI},i}\right)^2 + k_{\mathrm{r},ik} c^{\mathrm{SM}}_{\mathrm{DI},i} c^{\mathrm{SM}}_{\mathrm{DI},k} - 2\frac{k_{\mathrm{d},ii} c^{\mathrm{w}}_{ii}}{K_{\mathrm{H},ii}} - \frac{k_{\mathrm{d},ik} c^{\mathrm{w}}_{ik}}{K_{\mathrm{H},ik}} \right] \tag{4.50}$$

where D_i^{SM} is the diffusion coefficient of isotope species ^{i}H in the solid metal membrane. The two equations describe the steady state atomic net flux of isotope species ^{i}H in the presence of isotope species ^{k}H at both interfaces of a cylindrical membrane. To set up these equations, it is considered that boundary condition (2.51) is satisfied in an infinitesimal segment crossing the liquid-solid metal interface (see section 2.2.3). Moreover, the dissociation fluxes (2.88) at the water-metal interface are expressed with regards to the molecular concentrations in the water by making use of the Henry's constant [see equation (2.109)]. The nature of the cylindrical geometry of the membrane is represented by the conversion factors $f_{\mathrm{UI}}^{\mathrm{c}}$ and $f_{\mathrm{DI}}^{\mathrm{c}}$ according to the equations (2.160) and (2.161). In the limit of parallel membranes $f_{\mathrm{UI}}^{\mathrm{c}} = f_{\mathrm{DI}}^{\mathrm{c}} = 1$ and $\overline{J}_{\mathrm{net,UI},i}^{\circledcirc} = \overline{J}_{\mathrm{net,DI},i}^{\circledcirc}$. Again, the following discussion uses the notation $\overline{J}_{\mathrm{per},i} \equiv \overline{J}_{\mathrm{per},i}^{\mathrm{DI}}$.

The following theoretical study is built on the single assumption that $c_{ii}^{\mathrm{w}} = c_{ik}^{\mathrm{w}} = 0$. For the sake of lucidity, the following equations are expressed by means of an effective concentration, defined by

$$c_{\mathrm{eff}} \equiv c_{\mathrm{DI},i}^{\mathrm{SM}} + \sqrt{\frac{m_{ii}}{m_{ik}}} c_{\mathrm{DI},k}^{\mathrm{SM}} \tag{4.51}$$

Consequently, taking into account the relations (2.100), (2.162), (4.3) and the definition $\overline{J}_{\mathrm{per},i} \equiv \overline{J}_{\mathrm{net,DI},i}^{\circledcirc}$, a combination of the equations (4.49) and (4.50) results in the following approximated expression for the permeation flux into the downstream water side.

$$\overline{J}_{\mathrm{per},i} = f_{\mathrm{DI}}^{\mathrm{c}} \cdot D_i^{\mathrm{SM}} \frac{c_{\mathrm{UI},i}^{\mathrm{SM}} - c_{\mathrm{DI},i}^{\mathrm{SM}}}{d} = \frac{f_{\mathrm{DI}}^{\mathrm{c}}}{f_{\mathrm{UI}}^{\mathrm{c}}} \cdot \left(\alpha_{\mathrm{MT}} \cdot c_{\mathrm{CF},i}^{\mathrm{LM}} - \alpha_{\mathrm{MT}} c_{\mathrm{UI},i}^{\mathrm{SM}} K_{\mathrm{D},0,i}^{\mathrm{SM-LM}} \right) \approx 2\sigma k_{\mathrm{r},ii} c_{\mathrm{DI},i}^{\mathrm{SM}} c_{\mathrm{eff}} \tag{4.52}$$

It can be seen that when assuming $c_{ii}^{\mathrm{w}} = c_{ik}^{\mathrm{w}} \approx 0$, the permeation flux is equal to the atomic recombination flux of species ^{i}H at the water-metal interface. It is represented by the term on the right-hand side of the last equal sign in equation (4.52).

According to equation (4.51), an increase in the concentration $c_{\mathrm{DI},k}^{\mathrm{SM}}$ leads to a rise in effective concentration c_{eff}. Since $\overline{J}_{\mathrm{per},i} = 2\sigma k_{\mathrm{r},ii} c_{\mathrm{DI},i}^{\mathrm{SM}} c_{\mathrm{eff}}$, a rise in the value of $c_{\mathrm{DI},k}^{\mathrm{SM}}$ causes an increase in permeation flux of species ^{i}H into the water. A useful mathematical observation of this effect suggests expressing the permeation flux of species ^{i}H as a direct function of the concentrations $c_{\mathrm{CF},i}^{\mathrm{LM}}$, $c_{\mathrm{CF},k}^{\mathrm{LM}}$ and c_{kk}^{w}. This is possible for certain limit conditions and the objective of this theoretical investigation. A division of relation (4.52) by $\overline{J}_{\mathrm{per},i} = 2\sigma k_{\mathrm{r},ii} c_{\mathrm{DI},i}^{\mathrm{SM}} c_{\mathrm{eff}}$ yields

$$\overline{J}_{\mathrm{per},i} = c_{\mathrm{CF},i}^{\mathrm{LM}} \cdot \left[\frac{f_{\mathrm{DI}}^{\mathrm{c}}}{f_{\mathrm{UI}}^{\mathrm{c}}} \cdot \frac{1}{\alpha_{\mathrm{MT}}} + \frac{K_{\mathrm{D},0,i}^{\mathrm{SM-LM}}}{2\sigma k_{\mathrm{r},ii}} \cdot \frac{c_{\mathrm{UI},i}^{\mathrm{SM}}}{c_{\mathrm{DI},i}^{\mathrm{SM}} \cdot c_{\mathrm{eff}}} \right]^{-1} . \tag{4.53}$$

Moreover, a transformation of the right equation (4.52) leads to

$$\frac{c_{\mathrm{UI},i}^{\mathrm{SM}}}{c_{\mathrm{DI},i}^{\mathrm{SM}} \cdot c_{\mathrm{eff}}} = \frac{1}{f_{\mathrm{DI}}^{\mathrm{c}}} \frac{2\sigma k_{\mathrm{r},ii} d}{D_i^{\mathrm{SM}}} + \frac{1}{c_{\mathrm{eff}}} . \tag{4.54}$$

Finally, substituting equation (4.54) into equation (4.53) allows writing an expression for $\overline{J}_{\mathrm{per},i}$ as a function of the effective concentration in the solid metal at the water-metal

interface.

$$\overline{J}_{\mathrm{per},i} = c^{\mathrm{LM}}_{\mathrm{CF},i} \cdot \left[\frac{f^{\mathrm{c}}_{\mathrm{DI}}}{f^{\mathrm{c}}_{\mathrm{UI}}} \cdot \frac{1}{\alpha_{\mathrm{MT}}} + \frac{K^{\mathrm{SM-LM}}_{\mathrm{D},0,i}}{2\sigma k_{\mathrm{r},ii}} \cdot \left(\frac{1}{f^{\mathrm{c}}_{\mathrm{DI}}} \frac{2\sigma k_{\mathrm{r},ii} d}{D^{\mathrm{SM}}_i} + \frac{1}{c_{\mathrm{eff}}} \right) \right]^{-1} . \tag{4.55}$$

4.2.1. Mono-isotopic permeation from liquid metal to water

In case no isotope species ^{k}H is present in the system $c^{\mathrm{SM}}_{\mathrm{DI},k} = 0$ and $c_{\mathrm{eff}} = c^{\mathrm{SM}}_{\mathrm{DI},i}$. Then, the last equal sign in equation (4.52) reduces to

$$\overline{J}_{\mathrm{per},i} = 2\sigma k_{\mathrm{r},ii} \left(c^{\mathrm{SM}}_{\mathrm{DI},i} \right)^2 . \tag{4.56}$$

An expression for the downstream interface concentration $c^{\mathrm{SM}}_{\mathrm{DI},i}$ as a function of the concentration $c^{\mathrm{LM}}_{\mathrm{CF},i}$ in the core of the liquid metal flow is obtained by combining equation (4.55) and equation (4.56)

$$c^{\mathrm{SM}}_{\mathrm{DI},i} = \frac{f^{\mathrm{c}}_{\mathrm{DI}}}{4\sigma k_{\mathrm{r},ii}} \left(\frac{f^{\mathrm{c}}_{\mathrm{UI}}}{\alpha_{\mathrm{MT}}} + \frac{K^{\mathrm{SM-LM}}_{\mathrm{D},0,i} d}{D^{\mathrm{SM}}_i} \right)^{-1} \cdot \left[\sqrt{\frac{8\sigma k_{\mathrm{r},ii}}{f^{\mathrm{c}}_{\mathrm{DI}}} \left(\frac{f^{\mathrm{c}}_{\mathrm{UI}}}{\alpha_{\mathrm{MT}}} + \frac{K^{\mathrm{SM-LM}}_{\mathrm{D},0,i} d}{D^{\mathrm{SM}}_i} \right) c^{\mathrm{LM}}_{\mathrm{CF},i} + \left(K^{\mathrm{SM-LM}}_{\mathrm{D},0,i} \right)^2} - K^{\mathrm{SM-LM}}_{\mathrm{D},0,i} \right] \tag{4.57}$$

Substituting this expression into equation (4.56) yields the following algebraic formula for the mono-isotopic permeation flux of species ^{i}H from flowing liquid metal into the water considering that $c^{\mathrm{w}}_{ii} = c^{\mathrm{w}}_{ik} \approx 0$.

$$\overline{J}_{\mathrm{per},i} = \frac{\left(f^{\mathrm{c}}_{\mathrm{DI}} \right)^2}{8\sigma k_{\mathrm{r},ii}} \left(\frac{f^{\mathrm{c}}_{\mathrm{UI}}}{\alpha_{\mathrm{MT}}} + \frac{K^{\mathrm{SM-LM}}_{\mathrm{D},0,i} d}{D^{\mathrm{SM}}_i} \right)^{-2} \cdot \left[\sqrt{\frac{8\sigma k_{\mathrm{r},ii}}{f^{\mathrm{c}}_{\mathrm{DI}}} \left(\frac{f^{\mathrm{c}}_{\mathrm{UI}}}{\alpha_{\mathrm{MT}}} + \frac{K^{\mathrm{SM-LM}}_{\mathrm{D},0,i} d}{D^{\mathrm{SM}}_i} \right) c^{\mathrm{LM}}_{\mathrm{CF},i} + \left(K^{\mathrm{SM-LM}}_{\mathrm{D},0,i} \right)^2} - K^{\mathrm{SM-LM}}_{\mathrm{D},0,i} \right]^2 \tag{4.58}$$

It is important to note that this algebraic formula for the steady state mono-isotopic permeation flux is also valid for a permeation process from flowing liquid metal to vacuum. Therefore, it should be considered an important formula for the development of tritium extraction systems or hydrogen isotope concentration sensors based on the permeation to vacuum technology [101], [217].

4.2.2. Counter-permeation from liquid metal to water

As it is the case for multi-isotopic gas-to-gas permeation, the presence of isotope species ^{k}H noticeably affects the permeation process of isotope species ^{i}H from liquid metal to water. This influence of multi-isotopic transport is especially strong when the mole number of isotope species ^{k}H in the system is considerably higher than that of isotope species

^{i}H, meaning that $c^{\mathrm{SM}}_{\mathrm{DI},k} \gg c^{\mathrm{SM}}_{\mathrm{DI},i}$. In such a case, $c_{\mathrm{eff}} \approx c^{\mathrm{SM}}_{\mathrm{DI},k}$ and equation (4.55) can be approximated by

$$\overline{J}_{\mathrm{per},i} = c^{\mathrm{LM}}_{\mathrm{CF},i} \cdot \left[\frac{f^{\mathrm{c}}_{\mathrm{DI}}}{f^{\mathrm{c}}_{\mathrm{UI}}} \cdot \frac{1}{\alpha_{\mathrm{MT}}} + \frac{K^{\mathrm{SM-LM}}_{\mathrm{D},0,i}}{2\sigma k_{\mathrm{r},ii}} \cdot \left(\frac{1}{f^{\mathrm{c}}_{\mathrm{DI}}} \frac{2\sigma k_{\mathrm{r},ii} d}{D^{\mathrm{SM}}_{i}} + \sqrt{\frac{m_{ii}}{m_{ik}}} \frac{1}{c^{\mathrm{SM}}_{\mathrm{DI},k}} \right) \right]^{-1} . \tag{4.59}$$

As expected, with increasing concentration $c^{\mathrm{SM}}_{\mathrm{DI},k}$ the permeation flux $\overline{J}_{\mathrm{per},i}$ climbs and converges against the relation

$$\overline{J}_{\mathrm{per},i} = c^{\mathrm{LM}}_{\mathrm{CF},i} \cdot \left(\frac{f^{\mathrm{c}}_{\mathrm{DI}}}{f^{\mathrm{c}}_{\mathrm{UI}}} \cdot \frac{1}{\alpha_{\mathrm{MT}}} + K^{\mathrm{SM-LM}}_{\mathrm{D},0,i} \cdot \frac{d}{f^{\mathrm{c}}_{\mathrm{DI}} D^{\mathrm{SM}}_{i}} \right)^{-1} . \tag{4.60}$$

Since increasing any of the two concentrations $c^{\mathrm{LM}}_{\mathrm{CF},k}$ and c^{w}_{kk} increases the interface concentration $c^{\mathrm{SM}}_{\mathrm{DI},k}$, both a co- and a counter-permeation process of isotope species ^{k}H would lead to a rise in the permeation flux of species ^{i}H.

First, it is assumed that isotope species ^{k}H is counter-permeating from the water into the liquid metal, contrary to the primary permeation direction of the isotopes ^{i}H. A pure counter-permeation scenario occurs if $c^{\mathrm{LM}}_{\mathrm{CF},i} > 0$, $c^{\mathrm{w}}_{kk} > 0$ and $c^{\mathrm{LM}}_{\mathrm{CF},k} = 0$. Moreover, it is considered that c^{w}_{kk} is sufficiently high such that the establishing bulk concentrations satisfy $c^{\mathrm{SM}}_{\mathrm{DI},k} \gg c^{\mathrm{SM}}_{\mathrm{DI},i}$. Consequently and according to equation (4.50), the flux balance for isotope species ^{k}H at the water-metal downstream interface takes the reduced form (assuming that $c^{\mathrm{w}}_{ik} \approx 0$)

$$f^{\mathrm{c}}_{\mathrm{DI}} \cdot D^{\mathrm{SM}}_{k} \frac{c^{\mathrm{SM}}_{\mathrm{UI},k} - c^{\mathrm{SM}}_{\mathrm{DI},k}}{d} = 2\sigma k_{\mathrm{r},kk} \left(c^{\mathrm{SM}}_{\mathrm{DI},k} \right)^{2} - 2\sigma k_{\mathrm{d},kk} \frac{c^{\mathrm{w}}_{\mathrm{kk}}}{K_{\mathrm{H},kk}} . \tag{4.61}$$

By applying the equations (2.109) and (2.137) the equilibrium concentration at the water-metal interface may be written as

$$c^{\mathrm{SM}}_{\mathrm{DI,eq},k} = K_{\mathrm{s},kk} \sqrt{\frac{c^{\mathrm{w}}_{kk}}{K_{\mathrm{H},kk}}} , \tag{4.62}$$

By inserting the equilibrium concentration into equation (4.61), a similar relationship can be found as expressed in equation (2.138)

$$\left(c^{\mathrm{SM}}_{\mathrm{DI},k} \right)^{2} \approx \left(c^{\mathrm{SM}}_{\mathrm{DI,eq},k} \right)^{2} \cdot \left(1 - f^{\mathrm{c}}_{\mathrm{DI}} \cdot D^{\mathrm{SM}}_{k} K_{\mathrm{H},kk} \cdot \frac{c^{\mathrm{SM}}_{\mathrm{DI},k} - c^{\mathrm{SM}}_{\mathrm{UI},k}}{2\sigma k_{\mathrm{d},kk} c^{\mathrm{w}}_{kk} d} \right) . \tag{4.63}$$

Since counter-permeation is characterized by the condition $c^{\mathrm{SM}}_{\mathrm{DI},k} > c^{\mathrm{SM}}_{\mathrm{UI},k}$, it follows from equation (4.63) that $c^{\mathrm{SM}}_{\mathrm{DI},k} < c^{\mathrm{SM}}_{\mathrm{DI,eq},k}$. With equation (4.62) this further implies that for high values of c^{w}_{kk} the second term in the parenthesis of equation (4.63) approaches zero and $c^{\mathrm{SM}}_{\mathrm{DI},k}$ converges against $c^{\mathrm{SM}}_{\mathrm{DI,eq},k}$. Hence, in a counter-permeation scenario in which c^{w}_{kk} is sufficiently high, the permeation flux of isotope species ^{i}H into the water (4.59) can be approximated by the algebraic equation

$$\overline{J}_{\mathrm{per},i} \approx c^{\mathrm{LM}}_{\mathrm{CF},i} \cdot \left[\frac{f^{\mathrm{c}}_{\mathrm{DI}}}{f^{\mathrm{c}}_{\mathrm{UI}}} \cdot \frac{1}{\alpha_{\mathrm{MT}}} + \frac{K^{\mathrm{SM-LM}}_{\mathrm{D},0,i}}{2\sigma k_{\mathrm{r},ii}} \cdot \left(\frac{1}{f^{\mathrm{c}}_{\mathrm{DI}}} \frac{2\sigma k_{\mathrm{r},ii} d}{D^{\mathrm{SM}}_{i}} + \frac{1}{K_{\mathrm{s},kk}} \sqrt{\frac{m_{ii}}{m_{ik}} \frac{K_{\mathrm{H},kk}}{c^{\mathrm{w}}_{kk}}} \right) \right]^{-1} . \tag{4.64}$$

4.2.3. Co-permeation from liquid metal to water

Pure co-permeation of both isotope species from flowing liquid metal into water is defined through the conditions $c^{\mathrm{LM}}_{\mathrm{CF},i} > 0$, $c^{\mathrm{LM}}_{\mathrm{CF},k} > 0$ and $c^{\mathrm{w}}_{kk} = 0$. If in such a situation $c^{\mathrm{LM}}_{\mathrm{CF},k} \gg c^{\mathrm{LM}}_{\mathrm{CF},i}$ the permeation process of isotopes ^{k}H into the water proceeds practically undisturbed by the presence of isotopes ^{i}H. Then, the permeation of species ^{k}H can be treated as a mono-isotopic permeation process and the downstream interface concentration $c^{\mathrm{SM}}_{\mathrm{DI},k}$ can be expressed with equation (4.57), substituting index k for the index i. Hence, if $c^{\mathrm{LM}}_{\mathrm{CF},k} \gg c^{\mathrm{LM}}_{\mathrm{CF},i}$ the permeation flux of isotope species ^{i}H into the water can be approximated with equation (4.59) by inserting relation (4.57) as an expression for $c^{\mathrm{SM}}_{\mathrm{DI},k}$.

$$\overline{J}_{\mathrm{per},i} \approx c^{\mathrm{LM}}_{\mathrm{CF},i} \cdot \left\{ \frac{f^{\mathrm{c}}_{\mathrm{DI}}}{f^{\mathrm{c}}_{\mathrm{UI}}} \cdot \frac{1}{\alpha_{\mathrm{MT}}} + \frac{K^{\mathrm{SM-LM}}_{\mathrm{D},0,i}}{2\sigma k_{\mathrm{r},ii}} \cdot \left[\frac{1}{f^{\mathrm{c}}_{\mathrm{DI}}} \frac{2\sigma k_{\mathrm{r},ii} d}{D^{\mathrm{SM}}_{i}} + \sqrt{\frac{m_{ii}}{m_{ik}}} \frac{4\sigma k_{\mathrm{r},kk}}{f^{\mathrm{c}}_{\mathrm{DI}}} \left(\frac{f^{\mathrm{c}}_{\mathrm{UI}}}{\alpha_{\mathrm{MT}}} + \frac{K^{\mathrm{SM-LM}}_{\mathrm{D},0,k} d}{D^{\mathrm{SM}}_{k}} \right) \cdot \right. \right.$$
$$\left. \left. \cdot \left(\sqrt{\frac{8\sigma k_{\mathrm{r},kk}}{f^{\mathrm{c}}_{\mathrm{DI}}} \left\langle \frac{f^{\mathrm{c}}_{\mathrm{UI}}}{\alpha_{\mathrm{MT}}} + \frac{K^{\mathrm{SM-LM}}_{\mathrm{D},0,k} d}{D^{\mathrm{SM}}_{k}} \right\rangle c^{\mathrm{LM}}_{\mathrm{CF},k} + \left\langle K^{\mathrm{SM-LM}}_{\mathrm{D},0,k} \right\rangle^{2}} - K^{\mathrm{SM-LM}}_{\mathrm{D},0,k} \right)^{-1} \right] \right\}^{-1} . \quad (4.65)$$

It can be seen that with increasing concentration $c^{\mathrm{LM}}_{\mathrm{CF},k}$, this algebraic formula of the permeation flux of the isotopes ^{i}H in a co-permeation from liquid metal to water when $c^{\mathrm{LM}}_{\mathrm{CF},k} \gg c^{\mathrm{LM}}_{\mathrm{CF},i}$ converges against the maximum permeation flux expressed by equation (4.60).

The same algebraic co-permeation formula is valid to approximate the permeation flux of isotope species ^{i}H from liquid metal to vacuum when $c^{\mathrm{LM}}_{\mathrm{CF},k} \gg c^{\mathrm{LM}}_{\mathrm{CF},i}$.

5. MODELING OF MULTI-ISOTOPIC PERMEATION IN DEMO

The theoretical study of multi-isotopic permeation through a metal membrane in chapter 4 suggests that co- and counter-permeating protium would have a significant effect on the escape of tritium from the breeder into the coolant of an HCPB (gas-to-gas permeation) or WCLL (liquid metal-to-water permeation) breeding blanket. Nonetheless, the relationships obtained in chapter 4 are the result of several simplifying assumptions and therefore do not provide sufficient information to evaluate the consequences of different protium concentrations in the corresponding breeder fluid and coolant flow. This requires a more in-depth focus on the geometry, material and application-specific conditions of both WCLL and HCPB blanket designs.

5.1. EcosimPro© hydrogen transport simulation tool

The example of mono-isotopic gas-to-gas permeation through a flat sheet presented in section 2.3 demonstrates, that even the simplest permeation environment exceeds the maximum level of complexity that would allow the calculation of the time-evolving hydrogen permeation flux in the non-steady state to be performed analytically. This is in part due to the fact that Fick's differential diffusion equation (2.68) has analytical solutions only under very specific geometric and predetermined boundary conditions [165]. Hydrogen transport in breeding blanket environments occurs in a system of multiple interconnected solid and liquid media with different geometries, temperatures, and material-specific transport coefficients where chemical reactions take place. A system of coupled partial differential equations must be solved to simulate the temporal evolution of the concentration profiles and isotope fluxes in such environments, making an analytical approach impossible. For this reason, obtaining information about multi-isotopic transport effects in WCLL and HCPB breeding blankets relies on the development of numerical finite-difference hydrogen transport models.

For this purpose, the simulation tool EcosimPro© is used in this thesis [218]. It is an object-oriented programming software capable of solving large systems of linear/non-linear algebraic and coupled differential equations. To do this, EcosimPro© uses the DASSL algorithm [219], which employs the Newton-Raphson method combined with the Backward Differentiation Formula (BDF). When working with EcosimPro©, the internal BDF method is used to solve the time evolution of a physical quantity by repeatedly integrating the corresponding time derivative of the differential equation that describes it. Therefore, the time is discretized with a user-defined time step Δt. For the numerical treatment of multivariable partial differential equations such as Fick's second law (2.68), it is necessary to manually define the finite difference method of the second discretized variable. As the diffusion equation suggests, in this thesis the manually discretized variable is

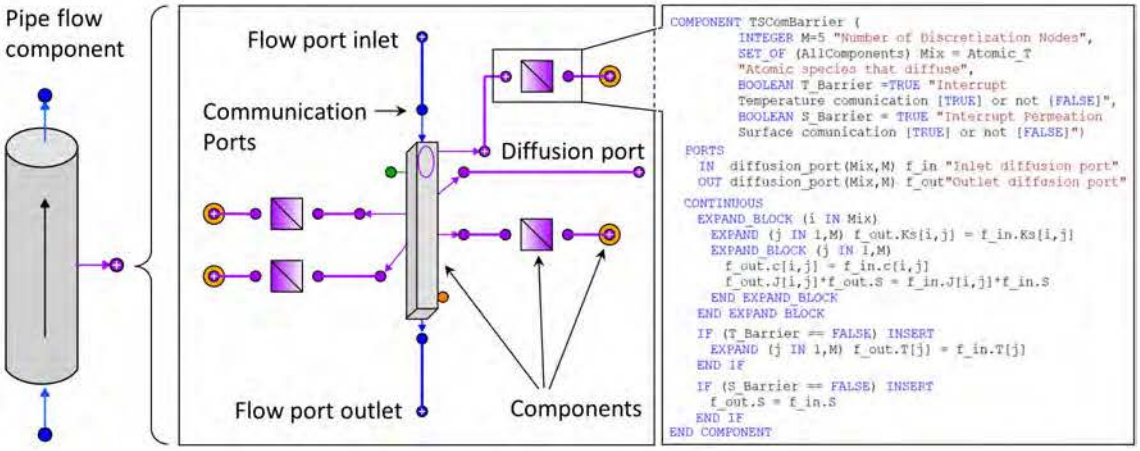

Fig. 5.1. Layer structure of components in EcosimPro©. Each component is described by a code containing a set of equations describing its physics. Linked components can be grouped to form higher-level components represented by an individual symbol. This picture shows the component structure of the created higher-level pipe flow component.

the location. EcosimPro© permits the user to group sets of equations into separate components, each of them describing the physics of a separate subsystem with an individual source code (see figure 5.1). The developed components are graphically represented by a symbol. Input and output ports allow components to communicate dynamically, meaning that each component shares values of certain variables with directly coupled components, where they are treated as input values. The set of shared variables is determined by the type of port used for transmission. To simplify the creation of larger systems, clusters of components can be grouped and represented by higher-level parent components with their own input and output ports. This makes it possible to create flowcharts of macroscopic physical systems such as experiments or chemical plants. The hierarchical component layer structure of EcosimPro© is shown in figure 5.1.

The symbols of the components used for the hydrogen transport simulations presented in this chapter are shown in figure 5.2. They have been developed in the past by the tritium modeling group of Ciemat in collaboration with the company Empresarios Agrupados and are based on previously developed codes of the EcosimPro© tritium transport library [113]. EcosimPro© simulations performed with earlier versions of these components have been experimentally validated in the LIBRETTO experimental captain [220].

More recently, the hydrogen transport equations used in the developed components have been extended to the simultaneous transport of multiple isotopes [78]. The consequences of this extension are therefore still little explored numerically. In general, the presented components contain the physical equations of hydrogen transport in dilute metal-hydrogen solutions introduced in chapter 2 of this thesis expressed in finite difference form. They are described in the following.

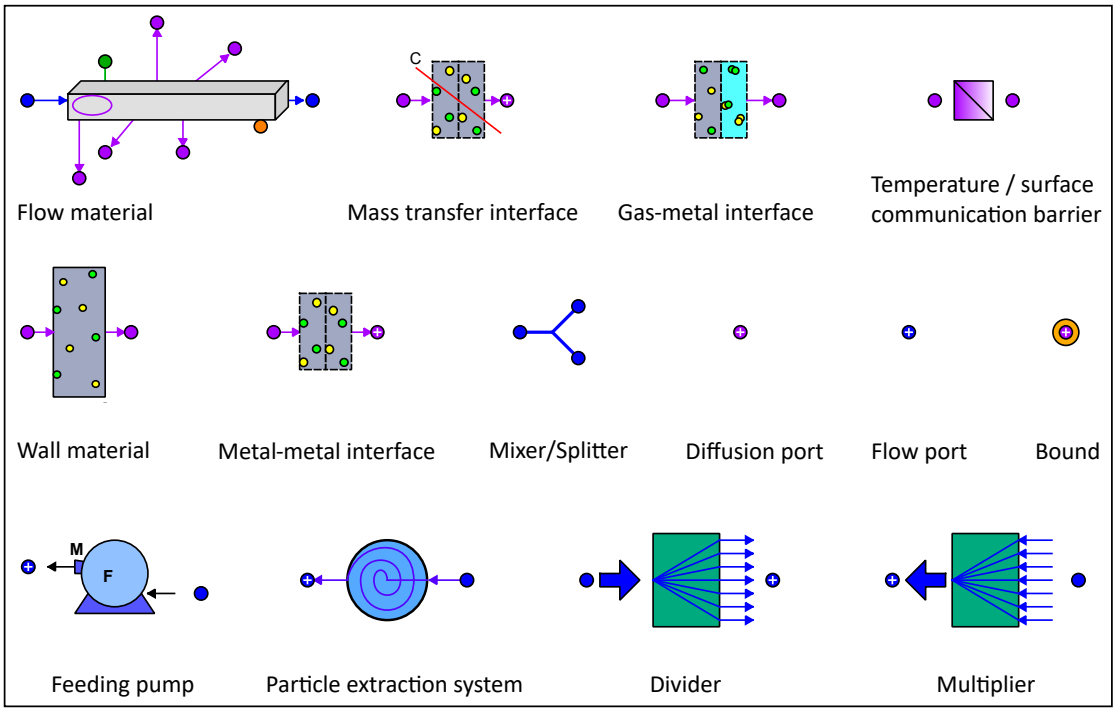

Fig. 5.2. Graphical representation of different EcosimPro© components.

Ports

Two types of ports are used to transmit variable values between the inputs and outputs of connected components (see symbols in figure 5.2). The flow port (blue circle) forwards the variables c_s, T, p, $\dot{m}$ and the diffusion port (purple circle) the variables c_i, $K_{s,i}$, T, J_s, A. Of these variables, $\dot{m}$ labels the mass flow rate of a fluid and A the surface area through which the particle fluxes J_s occur. In the following, the input and output variables of the flow and diffusion ports are referred to by the indexes f.IN, f.OUT and d.IN, d.OUT, respectively.

Flow material component

The flow material component shown in the top left-hand corner of figure 5.2 describes the transport of hydrogen isotopes in flowing liquid metal, water, steam, or gas. In this work, it is assumed that in fluid media the concentration of isotopes and molecules is homogeneous in the perpendicular direction to the flow velocity (except in the boundary layer of a liquid metal flow which is treated as a separate component). Hence, it is sufficient to calculate the temporal and spatial variation of the concentration of each species in one dimension, that is in the direction of the fluid flow, the y-axis. Therefore, the flow component is discretized into $\mathcal{M}$ segments, with Δy being the discretization length and $l_{\text{flow}} = \mathcal{M}\Delta y$ the length of the entire flow section. The method of discretization along the y-axis is illustrated in figure 5.3. The variation of the different concentrations in any of the considered fluids is described by the mass continuity equation (2.76). Considering

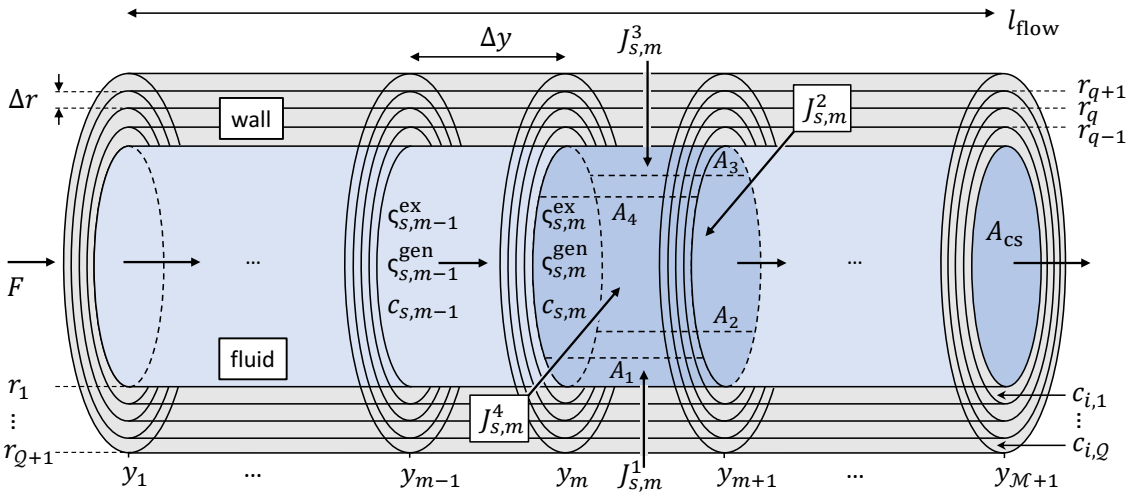

Fig. 5.3. Illustration of the discretization in a cylindrical flow component along the direction of the fluid motion. In addition, the image shows the discretization of a surrounding material wall component in the perpendicular direction to the fluid flow.

that there is no concentration gradient perpendicularly to the flow direction, it reduces to

$$\frac{\partial c_s(t,y)}{\partial t} = -\vec{\nabla}\left[c_s(t,y)\cdot\vec{u}(y)\right] + \varsigma_s = -\frac{\partial\left[c_s(t,y)\cdot u(y)\right]}{\partial y} + \varsigma_s\,. \tag{5.1}$$

In the flow component, this equation is represented by its numerical finite-difference form

$$\frac{\partial c_s(t,y_m)}{\partial t} = -F\cdot\frac{c_s(t,y_{m-1}) - c_s(t,y_m)}{A_{\text{cs}}\Delta y} + \sum_{n=1}^{4}\frac{J_s^n(t,y_m)\,A_n}{A_{\text{cs}}\Delta y} + \\ + \varsigma_s^{\text{ex}}(t,y_m) + \varsigma_s^{\text{w}}(t,y_m) + \varsigma_s^{\text{gen}}(t,y_m)\,. \tag{5.2}$$

As mentioned above, solving the temporal part of this differential equation is executed internally by EcosimPro© while the spatial discretization is performed manually and solved in a forward loop after each time step. For the treatment of the first trap segment the concentration $c_s(t,y_{m-1})$ is replaced by the input concentration $c_s^{\text{f.IN}}(t)$. The concentration at the outlet port is defined as $c_s(t,y_{\mathcal{M}}) = c_s^{\text{f.OUT}}(t)$. Parameter $F = uA_{\text{cs}}$ is the volume flow rate and A_{cs} the cross section of the fluid flow. The volumetric flow rate is related to the mass flow rate by $\dot{m} = F\rho_{\text{fluid}}$. In this work, it is assumed that the flow rate is constant in each flow component.

For the numerical expression of equation (5.1), the source term ς_s is substituted by four terms. The first describes outlet particle fluxes $J_s^n(t,y_m) = J_s^{\text{d.OUT},n}(t,y_m)$ of species s which causes growth or reduction in the number of particles in the corresponding flow segment. The created component offers the possibility to describe four different particle fluxes $J_s^n(t,y_m)$ crossing four default surface areas A_n per trap segment. The fluxes are treated as particle sources or sinks since they are assumed to be perpendicular to the surface of the fluid flow. To convert the fluxes into a rate of entering or leaving particles per trap segment they are multiplied with the corresponding surface area A_n before being divided by the volume of a flow segment. The flow component describes an axis-symmetric fluid flow with a homogeneous cross-section A_{cs}.

The second and third source terms describe the rates of formation $\varsigma_s^{\mathrm{ex}}(t, y_m)$ and $\varsigma_s^{\mathrm{w}}(t, y_m)$ of species s. For isotope exchange reactions between diatomic hydrogen gas molecules, the source terms are described by the equations (2.104)-(2.106) and for those between hydrogen molecules and water molecules by the equations (2.123)-(2.128). The last term represents an arbitrary generation rate $\varsigma_s^{\mathrm{gen}}$ which represents hydrogen isotope generation in a liquid metal flow. As visible in figure 5.3, the flow component has an input flow port, an output flow port, and five diffusion ports. In fact, the diffusion ports consist of $\mathcal{M}$ ports, one for each discretized segment in the y-direction. While the flow ports can be connected to a mixer, a splitter, or other flow components, four of the diffusion ports may be linked to components that determine the fluxes J_s^n crossing the surfaces A_n. The fifth diffusion port is used to describe an internal particle source or sink. The concentrations $c_s(t, y_m)$ are equal to the output concentrations $c_s^{\mathrm{d.OUT}}(t, y_m)$ at the five diffusion ports.

Splitter and Mixer components

A splitter component enables separating a fluid flow described by a flow component into two separate flows with different mass flow rates. In order to not violate mass conservation the inlet mass flow rate and the two outlet mass flow rates fulfill the relations $\dot{m}_{\mathrm{f.OUT1}} = f_{\mathrm{sp}} \cdot m_{\mathrm{f.IN}}$ and $\dot{m}_{\mathrm{f.OUT2}} = (1 - f_{\mathrm{sp}}) \cdot \dot{m}_{\mathrm{IN}}$. Parameter $0 \leq f_{\mathrm{sp}} \leq 1$ describes the mass flow fraction each outlet receives. All other flow port variables do not change between the inlet and outlet ports of the splitter. The mixer component unites two inlet flows into a single outlet flow. Mass continuity requires $\dot{m}_{\mathrm{f.IN1}} + \dot{m}_{\mathrm{f.IN2}} = \dot{m}_{\mathrm{OUT}}$. The mixed outlet concentration is calculated according to

$$c_s^{\mathrm{f.OUT}}(t) = \frac{\rho_{\mathrm{fluid}}\left(T^{\mathrm{f.OUT}}, p^{\mathrm{f.OUT}}\right)}{\dot{m}^{\mathrm{f.OUT}}} \cdot \left[\frac{c_s^{\mathrm{f.IN1}}(t) \cdot \dot{m}^{\mathrm{f.IN1}}}{\rho_{\mathrm{fluid}}\left(T^{\mathrm{f.IN1}}, p^{\mathrm{f.IN1}}\right)} + \frac{c_s^{\mathrm{f.IN2}}(t) \cdot \dot{m}^{\mathrm{f.IN2}}}{\rho_{\mathrm{fluid}}\left(T^{\mathrm{f.IN2}}, p^{\mathrm{f.IN2}}\right)}\right]. \tag{5.3}$$

Assuming equal heat capacities the temperature of the mixed fluids is determined through

$$T^{\mathrm{f.OUT}} = \frac{T^{\mathrm{f.IN1}}\dot{m}^{\mathrm{f.IN1}} + T^{\mathrm{f.IN2}}\dot{m}^{\mathrm{f.IN2}}}{\dot{m}^{\mathrm{f.OUT}}}. \tag{5.4}$$

Divider and Multiplier components

Divider components are used to split a fluid flow component into N_{split} flows with the same mass flow rate. It changes the mass flow rate of the output port according to the relation $\dot{m}^{\mathrm{f.OUT}} = \dot{m}^{\mathrm{f.IN}}/N_{\mathrm{split}}$. The multiplier component unites N_{split} equal flows to one flow such that $\dot{m}^{\mathrm{f.OUT}} = N_{\mathrm{split}} \cdot \dot{m}^{\mathrm{f.IN}}$. Both components maintain all other flow port variables equal.

Particle extraction system component

This component lowers the input concentration of any of the flowing hydrogen isotope-containing molecules by an arbitrary factor which determines the extraction efficiency

$\eta_{\mathrm{TES},s}$ of species s by $c_s^{\mathrm{f.OUT}} = (1 - \eta_{\mathrm{TES},s}) \cdot c_s^{\mathrm{f.IN}}$. All other flow variables remain the same.

Feeding pump component

With the feeding pump component, it is possible to fix a certain mass flow rate and pressure of a flow system at the position of the pump output. Furthermore, it allows setting the output concentration of any species s to a certain value independent of its input concentration. Those species whose concentrations are not supposed to be changed by this component can be left untouched.

Mass transfer interface component

The mass transfer interface component contains the physics of the boundary layer in a liquid metal flow described in subsection 2.2.3. It is connected to the diffusion output ports of a flow material component in case it describes a liquid metal flow. The diffusion port input variables of a mass transfer interface component are equal to those at the output port. Nevertheless, it imposes the following additional condition for the atomic hydrogen isotope fluxes and concentrations at both ports

$$J_i^{\mathrm{d.IN}}(t, y_m) = J_i^{\mathrm{d.OUT}}(t, y_m) = \alpha_{\mathrm{MT}}(y_m) \left[c_i^{\mathrm{d.OUT}}(t, y_m) - c_i^{\mathrm{d.IN}}(t, y_m) \right] . \tag{5.5}$$

Metal-metal interface component

The boundary conditions at the interface between two metals are introduced by the metal-metal interface component. This can be two solid metals or a liquid metal flowing past a solid metal wall. As explained in subsection 2.2.3, in addition to mass conservation across an interface which is represented by $J_i^{\mathrm{d.IN}}(t, y_m) = J_i^{\mathrm{d.OUT}}(t, y_m)$ the assumption of continuous thermodynamic equilibrium inside of an infinitesimal layer across a metal-metal interface implies

$$c_i^{\mathrm{d.IN}}(t, y_m) = \frac{K_{\mathrm{s},i}^{\mathrm{d.IN}} \left[T^{\mathrm{d.IN}}(y_m) \right]}{K_{\mathrm{s},i}^{\mathrm{d.OUT}} \left[T^{\mathrm{d.OUT}}(y_m) \right]} \cdot c_i^{\mathrm{d.OUT}}(t, y_m) . \tag{5.6}$$

All other variables remain unchanged.

Wall material component

In this work, the wall material component represents a metal bulk of thickness d. It has an inlet and an outlet diffusion port and contains the physical laws which describe the temporal evolution of the hydrogen isotope concentration profile in the perpendicular direction to the metal surface. A boolean switch embedded in the component algorithm offers the user to choose between a parallel wall or a cylindrical wall. For parallel walls,

the diffusion axis perpendicular to the metal surface is the Cartesian z-axis and for cylindrical walls the radial r-axis. Figure 5.3 illustrates the discretization of a cylindrical wall material around a flow material into $\mathfrak{Q}$ segments with $\mathfrak{Q}+1$ spatial nodes. Depending on the wall geometry the length of the discretization step is either $\Delta z = d/\mathfrak{Q}$ or $\Delta r = d/\mathfrak{Q}$. It becomes apparent that each of the segments of the flow material arranged in y-direction represents a separate channel for diffusing isotopes in r or z-direction. To some extent, this allows describing the transport of hydrogen isotopes in two dimensions. However, the two-dimensional transport description is limited since the model does not consider the diffusion of hydrogen isotopes in y-direction inside of the bulk material.

As explained in section 2.2.1, the temporal evolution of the isotope concentration profile in metal is described by Fick's second law (2.68). Since the nabla operator $\vec{\nabla}$ in Cartesian coordinates differs from its definition in cylindrical coordinates, two different finite-difference expressions of Fick's second law are used

$$\frac{\partial c_i\left(t, y_m, z_q\right)}{\partial t} = -\frac{J_i\left(t, y_m, z_{q+1}\right) - J_i\left(t, y_m, z_q\right)}{\Delta z} + \varsigma_s\left(t, z_q\right) \qquad \text{(Cartesian)} \tag{5.7}$$

$$\frac{\partial c_i\left(t, y_m, r_q\right)}{\partial t} = -\frac{r_q J_i\left(t, y_m, r_{q+1}\right) - r_q J_i\left(t, y_m, r_q\right)}{r_q \Delta r} + \varsigma_s\left(t, z_q\right) \qquad \text{(cylindrical)}\,. \tag{5.8}$$

In the drawing of figure 5.3 it can be seen that $c_i(t, y_m, r_q)$ is defined as the hydrogen isotope concentration present between two nodes r_q and r_{q+1} and $J_i(t, y_m, r_q)$ stands for the hydrogen isotope flux crossing the node r_q. The atomic fluxes across the surfaces of the metal wall are equal to the input and output fluxes $J_i(t, y_m, r_1) = J_i^{\mathrm{d.IN}}(t, y_m)$ and $J_i(t, y_m, r_{\mathfrak{Q}+1}) = J_i^{\mathrm{d.OUT}}(t, y_m)$. The same applies to the z-direction of a wall material component in Cartesian coordinates. Parameter $\varsigma_s\left(t, z_q\right)$ has the unit [mol m^{-3} s^{-1}] and serves as a sink or source term for hydrogen isotopes within the material bulk. Unless otherwise noted, it is assumed to be zero for the simulations in this work.

There is the possibility that the input and output surfaces of each segment of the wall material in y-direction are kept at different temperatures $T^{\mathrm{d.IN}}(y_m)$ and $T^{\mathrm{d.OUT}}(y_m)$. Regardless of the geometry of the component, the temperatures of the segments within the wall material are approximated by a linear straight line

$$T\left(y_m, z_q\right) = T\left(y_m, r_q\right) = T^{\mathrm{d.IN}} + \frac{q-1}{\mathfrak{Q}}\left[T^{\mathrm{d.OUT}}(y_m) - T^{\mathrm{d.IN}}(y_m)\right]. \tag{5.9}$$

Fick's first law (2.67) relates the flux values to the concentration gradients in the bulk. For dilute solutions ($D \approx \overline{D}$) the finite difference expression of Fick's first law writes

$$J_i\left(t, y_m, z_q\right) = -D_i\left(y_m, z_{q+1}\right) \cdot \frac{c_i\left(t, y_m, z_{q+1}\right) - c_i\left(t, y_m, z_q\right)}{\Delta z} \qquad \text{(Cartesian)} \tag{5.10}$$

$$J_i\left(t, y_m, r_q\right) = -D_i\left(y_m, r_{q+1}\right) \cdot \frac{c_i\left(t, y_m, r_{q+1}\right) - c_i\left(t, y_m, r_q\right)}{\Delta r} \qquad \text{(cylindrical)}\,. \tag{5.11}$$

The spatial variation of the diffusion coefficient takes into account a possible variation of the temperature in $r-$ or z-direction. The definitions of the inlet and outlet concentrations

in the wall material component depend on whether the corresponding diffusion port is connected to a gas-metal or metal-metal interface component

$$c_i^{\mathrm{d.IN}}(t, y_m) = c_i(t, y_m, r_1) \qquad \text{(gas-metal interface)} \tag{5.12}$$

$$c_i^{\mathrm{d.IN}}(t, y_m) = c_i(t, y_m, r_1) + \Delta r \cdot \frac{J_i^{\mathrm{d.IN}}(t, y_m)}{D_i(y_m, r_{\mathrm{Q}+1})} \qquad \text{(metal-metal interface)} \tag{5.13}$$

$$c_i^{\mathrm{d.OUT}}(t, y_m) = c_i(t, y_m, r_{\mathrm{Q}}) \qquad \text{(gas-metal interface)} \tag{5.14}$$

$$c_i^{\mathrm{d.OUT}}(t, y_m) = c_i(t, y_m, r_{\mathrm{Q}}) - \Delta r \cdot \frac{J_i^{\mathrm{d.OUT}}(t, y_m)}{D_i(y_m, r_{\mathrm{Q}+1})} \qquad \text{(metal-metal interface)}\,. \tag{5.15}$$

These relations are analogous for the Cartesian coordinate z.

The surface areas transmitted by the input and output diffusion ports of the material wall component are related through $A^{\mathrm{d.IN}} = A^{\mathrm{d.OUT}}$ for Cartesian coordinates and through $A^{\mathrm{d.IN}}/r_1 = A^{\mathrm{d.OUT}}/r_{\mathrm{Q}+1}$ for cylindrical coordinates.

Gas-metal interface component

A gas-metal interface component is placed between a wall material component and a flow material component if the fluid medium is either water, steam, or hydrogen gas. It contains the physical laws of dissociation and recombination processes discussed in subsection 2.2.3. Thus, it converts the concentrations of molecular species ${}^{i}\mathrm{H}^{j}\mathrm{H}$ at the diffusion port of a connected flow material component into concentrations and atomic fluxes of isotopes ${}^{i}\mathrm{H}$ at the diffusion port of a connected wall material components.

The molecular net fluxes of isotopes ${}^{i}\mathrm{H}^{j}\mathrm{H}$ entering the metal bulk are determined by equation (2.97) and have the finite difference form

$$j_{ij}^{\mathrm{d.IN}}(t, y_m) = \sigma k_{\mathrm{d},ij}(y_m) p_{ij}(t, y_m) - \sigma k_{\mathrm{r},ij}(y_m) c_i^{\mathrm{d.OUT}}(t, y_m)\, c_j^{\mathrm{d.OUT}}(t, y_m) \tag{5.16}$$

The dependency of the dissociation and recombination coefficients on the y-direction accounts for a possible temperature profile in the fluid along the flow direction. In EcosimPro©, the recombination coefficient is calculated from equation (2.100) using experimentally determined expressions for the dissociation coefficient and the Sieverts' constant $K_{\mathrm{s},i}^{\mathrm{d.IN}}(y_m) = K_{\mathrm{s},i}^{\mathrm{d.OUT}}(y_m)$ of the connected wall material component.

The pressure $p_{ij}(t, y_m)$ is determined from the concentrations of molecules ${}^{i}\mathrm{H}^{j}\mathrm{H}$ in each segment of the flow material component. If the fluid flow consists of hydrogen gas or steam the applied conversion relation is the ideal gas law $p_{ij}(t, y_m) = c_{ij}^{\mathrm{d.IN}}(t, y_m)\, RT^{\mathrm{d.IN}}$. In the case of water as the fluid medium, Henry's law $p_{ij}(t, y_m) = K_{\mathrm{H},ij}^{\mathrm{w}}(T^{\mathrm{d.IN}})/c_{ij}^{\mathrm{d.IN}}(t, y_m)$ is applied instead (see subsection 2.2.6).

The output atomic fluxes of isotope species ${}^{k}\mathrm{H}$ entering the metal bulk are determined by equation (2.98)

$$J_k^{\mathrm{d.OUT}}(t, y_m) = 2 j_{kk}^{\mathrm{d.IN}}(t, y_m) + j_{ik}^{\mathrm{d.IN}}(t, y_m) + j_{jk}^{\mathrm{d.IN}}(t, y_m) \qquad \text{with } i \neq j \tag{5.17}$$

Communication barrier and bound components

With a bound component, it is possible to impose an arbitrary particle flux at a diffusion port of a wall material or flow material component. In this work, it is mostly used to block a diffusion port by setting the permeation flux crossing the corresponding diffusion port zero (see the symbol in figure 5.2).

The communication barrier component (see the symbol in figure 5.2) linked to a diffusion port of an arbitrary component enables avoiding the output temperature or surface variable of that component being shared with a component connected to it. To block a diffusion port with a bound component, it is necessary to interrupt the transmission of temperature information to the bound component by interposing a communication barrier (see figure 5.1).

5.2. Hydrogen isotopes in Eurofer'97

In this work, the examination of multi-isotopic hydrogen transport in HCPB and WCLL breeding blankets focuses on the occurring co- and counter-permeation processes happening in the breeder modules where the breeder and coolant fluid are merely separated by a thin metal wall. In both breeding blankets, the wall material is mainly made of the reduced activation martensitic steel Eurofer'97 (E97).

Hydrogen isotopes dissolved in Eurofer'97 occupy preferably tetrahedral sites of its BCC crystal structure [161]. The left-hand graph in figure 5.4 shows temperature relations of the Sievert's constant of protium [159], [161] and deuterium [221], [222] in Eurofer'97 plotted against temperature which were measured in four different experimental campaigns. Although it is expected that because of its bigger atomic size the Sievert's constant of deuterium is slightly lower than that of protium, no clear separation between the measured relations of different isotopes can be identified. It turns out that in comparison to deviations that could be observed between measured Sieverts' relations of other metal-hydrogen systems, the four relations agree fairly well [82]. They differ by at most a factor of three. Figure 5.4 shows that the plotted Sieverts' relations rise with temperature. This uncovers Eurofer'97 as an endothermic hydrogen absorber with relatively low solubility. In the four measurement campaigns the Sieverts' relations were obtained in permeation experiments as the quotient of measured permeability and diffusivity relations of protium [159], [161] and deuterium [221], [222] [see equation (2.143)]. To better compare the measured diffusion coefficients, those reported for deuterium are converted to relations applicable to protium using equation (2.66). All four diffusivity relations of protium in Eurofer'97 are plotted in the right-hand graph in figure 5.4.

Since Eurofer'97-hydrogen solutions are endothermic, trapping effects highly influence the measured diffusivities. However, at temperatures of approximately $T > 600\,\mathrm{K}$ their influence on the hydrogen transport properties is found to significantly reduce [159],

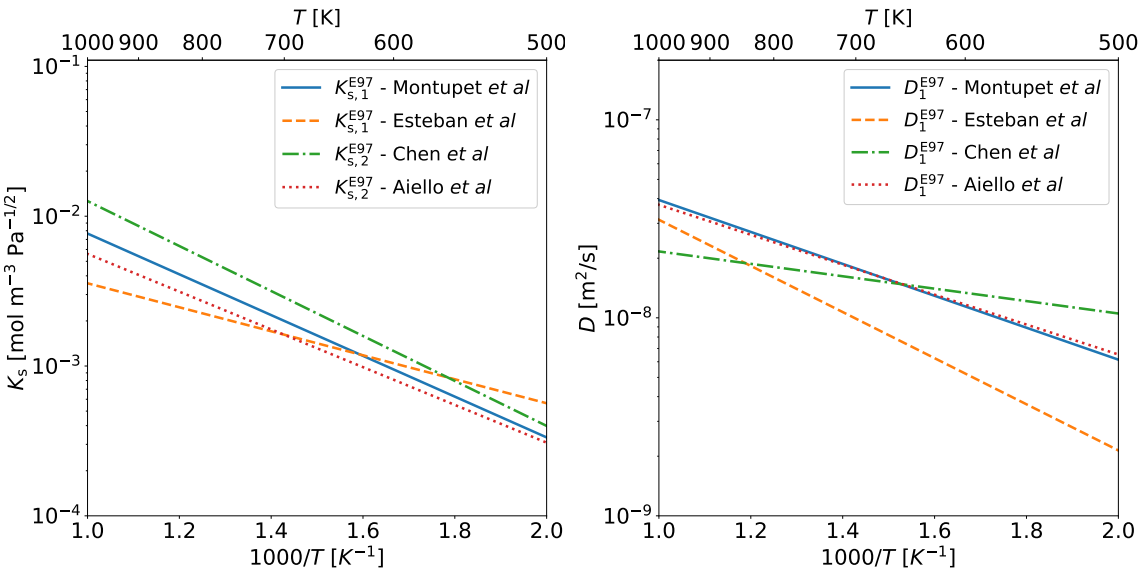

Fig. 5.4. [Left] Experimentally determined temperature dependency of the Sieverts' constant of hydrogen isotopes in Eurofer'97 [159], [161], [221], [222]. [Right] Temperature dependency of the diffusion coefficient of protium in Eurofer'97 based on experimental data by Montupet *et al* [161], Esteban *et al* [159], Chen *et al* [221] and Aiello *et al* [222].

[161], [221], [222]. Since the operating temperatures of the breeder units of both breeding blanket concepts are expected to be above this temperature, the hydrogen transport models discussed in the following sections are developed without taking into account trapping effects. In other words, it is assumed that in the relevant temperature range $D_{\mathrm{eff},i}^{\mathrm{E97}} \approx D_i^{\mathrm{E97}}$ and $K_{\mathrm{s},i}^{\mathrm{eff,E97}} \approx K_{\mathrm{s},i}^{\mathrm{E97}}$.

At $T > 600\,\mathrm{K}$, the measured diffusion relations differ at most by a factor of two (see the right-hand plot in figure 5.4). A striking agreement is observed between the diffusion coefficients of Aiello *et al* and Montupet *et al*. This increases trust in the correctness of both their measurements. The Sieverts' constants and diffusion coefficients measured by Montupet *et al* are relatively high compared to the other relations. According to equation (2.142), this implies a higher permeability Φ and consequently higher permeation fluxes under equal conditions. This is beneficial for obtaining conservative simulation results which result in rather too-high than too-low tritium permeation fluxes. For these reasons, the experimental data by Montupet *et al* is chosen for the following simulations. The pre-exponential factors and activation energies of the utilized Sieverts' constant [see equations (2.44) and (2.50)] and diffusion coefficient (2.65) are listed in table 5.1. Due to the lack of experimental data for the tritium solubility in Eurofer'97, it has been decided to use the Sieverts' constant of protium for all three hydrogen isotopes. The diffusivity relations for deuterium and tritium are determined from the measured coefficient of protium by taking into account the isotope effect of diffusion which is represented by equation (2.66).

To date, neither the dissociation rate coefficient (2.89) nor the recombination rate coefficient (2.96) of any hydrogen isotope species in Eurofer'97 could be measured. However, the rate coefficients of a similar reduced activation martensitic steel called OPTIFER-IVb

TABLE 5.1

PRE-EXPONENTIAL FACTORS AND ACTIVATION ENERGIES OF THE SIEVERTS' CONSTANTS AND DIFFUSION COEFFICIENTS OF PROTIUM IN EUROFER'97, α-IRON AND PBLI USED FOR THE SIMULATIONS IN THIS CHAPTER.

Quantity	Eurofer'97	Ref.	α-iron	Ref.	PbLi	Ref.
$K^0_{s,1}\ \left[\frac{\text{mol}}{\text{m}^3\sqrt{Pa}}\right]$	1.76×10^{-1}	[161]	6.90×10^{-1}	[223]	$\frac{\rho_{\text{PbLi}}}{M_{\text{PbLi}}}\cdot 2.44\times10^{-8}$	[224]
$\Delta\overline{H}_{s,1}\ \left[\frac{\text{kJ}}{\text{mol}}\right]$	26.05	[161]	24.30	[223]	1.35	[224]
$D^0_1\ \left[\frac{\text{m}^2}{\text{s}}\right]$	2.52×10^{-7}	[159]	4.43×10^{-8}	[225]	4.03×10^{-8}	[224]
$E_{m,1}\ \left[\frac{\text{kJ}}{\text{mol}}\right]$	15.4	[159]	5.31	[225]	19.50	[224]

have been experimentally determined by Esteban *et al* [190]. They determined the following Arrhenius-type temperature dependence of the dissociation rate coefficient for $^2H_2$

$$\sigma k^{\text{E97}}_{\text{d},22} = 2.99\times10^{-8}\,\frac{\text{mol}}{\text{m}^2\text{sPa}}\cdot\exp\left(\frac{-29\,230\,\text{J mol}^{-1}}{RT}\right). \tag{5.18}$$

Due to the similarity of both materials, the dissociation rate coefficient of $^2H_2$ in Eurofer'97 is approximated with relation (5.18). The recombination rate coefficient on the other hand is obtained with equation (2.100) using the considered Sieverts' constant of protium in Eurofer'97 listed in table 5.1. Following the same reasoning as for setting up equation (4.3), the dissociation coefficients of all remaining molecular species $^iH^jH$ in Eurofer'97 are determined with the relation

$$\sigma k_{\text{d},ij} = \sigma k_{\text{d},22}\sqrt{\frac{m_{22}}{m_{ij}}}\,. \tag{5.19}$$

5.3. Modeling of multi-isotopic permeation in an HCPB breeding blanket

As described in detail in section 1.2.3, in an HCPB breeding blanket, tritium is bred in fuel-breeder pins located in breeder modules that are arranged around the toroidally-shaped fusion plasma. The current DEMO design counts a total number 1×10^5 fuel pins (FP) distributed over the 16 segments of the vacuum vessel [71]. In each fuel pin tritium generation happens in a pebble bed made of the lithium-containing ceramic material KALOS (see section 1.2.3) [73], [74]. The diameters and wall thicknesses given in [mm] of the different cylindrical structures of a fuel pin are presented in the lower right-hand corner of figure 5.5 [71].

An illustration of a pebble bed cladding sitting inside of the cylindrical envelope of a fuel pin is shown in figure 5.5. Depending on the poloidal position of the breeder module in the fusion reactor and the position of the fuel pin in the corresponding breeder module, the length of the pebble bed claddings varies slightly around a value of $l_{\text{FP}} = 0.5\,\text{m}$. As figure 5.5 shows, the heat generated in the tritium breeding and neutron multiplying

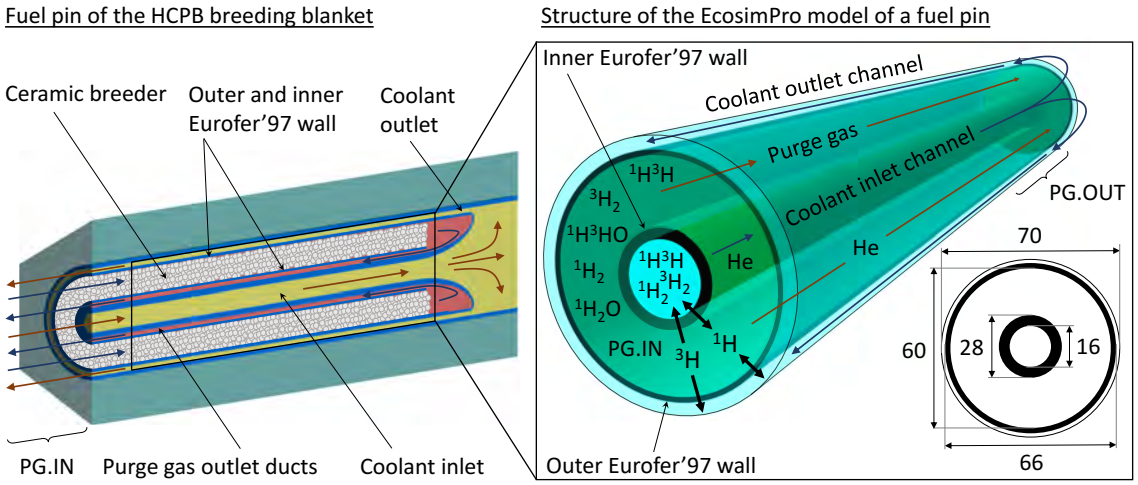

Fig. 5.5. Illustration of the studied permeation environment in a fuel pin of an HCPB breeding blanket [71], [226].

reactions is dissipated by the helium coolant gas. With a total pressure of $p_{CG} = 8\times10^{6}$ Pa it enters each fuel pin through a 16×10^{-3} m wide tunnel which is surrounded by the pebble bed cladding [71]. This tunnel is referred to as the coolant inlet channel (CIC). From here, the gas moves towards the back plate of the first wall. At the back plate it expands, reverses its flow direction and flows back to the coolant outlet through a 2×10^{-3} m thick cylindrical gap between the fuel pin envelope and the pebble bad cladding (see figure 5.5). In the following, this gap will be referred to as the coolant outlet channel (COC). While flowing through the fuel pins the coolant gas temperature increases from approximately $T \approx 623$ K to $T \approx 793$ K. The mass flow rate of the coolant gas through a fuel pin is estimated to be approximately $\dot{m}_{CG} = 2\times10^{-2}$ kg s^{-1} [227].

Via transmutation reactions between the lithium in the ceramic pebbles and the impelling neutrons coming from the fusion plasma or the neutron multiplier, tritium is bred in atomic form. Subsequently, it diffuses along the grain boundaries of the pebbles towards the pebble surfaces where they emerge as $^{3}H^{+}$ [76]. As indicated by the arrows in figure 5.5, a helium purge gas rinses the pebble bed with a total pressure of $p_{PG} = 2\times10^{5}$ Pa [71]. The current HCPB design envisages adding a small amount of $^{1}H_2$ to the purge gas [73]. When colliding with the ceramic pebbles part of the $^{1}H_2$ molecules in the purge gas dissociate before being chemisorbed by the pebble surfaces. Here, they form bonds with oxygen (O $^{1}H^{-}$) or lithium atoms (Li^{+} $^{1}H^{-}$ Li^{+}) of the ceramic material [76]. As a consequence, chemical reactions

$$\mathrm{O}\,{}^{1}\mathrm{H}^{-}\,(\text{chemisorbed}) + {}^{3}\mathrm{H}^{+}\,(\text{pebble}) \rightleftharpoons {}^{1}\mathrm{H}{}^{3}\mathrm{HO}\,(\text{gas}) + \mathrm{V_0}\quad(\text{pebble}) \tag{5.20}$$

$$\mathrm{Li}^{+}\,{}^{1}\mathrm{H}^{-}\,\mathrm{Li}^{+}\,(\text{chemisorbed}) + {}^{3}\mathrm{H}^{+}\,(\text{pebble}) \rightleftharpoons {}^{1}\mathrm{H}{}^{3}\mathrm{H}\quad(\text{gas}) + 2\mathrm{Li}^{+}\,(\text{pebble}) \tag{5.21}$$

lead to a release of tritium, in the form of $^{1}H^{3}H$ and $^{1}H^{3}HO$ molecules into the purge gas [75], [78], [228]. Further reactions occur between the pebble surface and the purge gas which cause an additional release of $^{3}H_2$ and $^{3}H_2O$ molecules [77]. However, these reactions are expected to occur at a drastically lower rate compared to the reactions (5.20)

and (5.21). Therefore, they are neglected in this analysis. DEMO requires a total tritium generation rate of about 3.20×10^{-1} kg/day in order to achieve tritium self-sufficiency. This corresponds to a molar tritium generation rate of $\dot{\varkappa}^{\mathrm{FP}}_{3,\mathrm{gen}} = 1.23 \times 10^{-8}\,\mathrm{mol\,s^{-1}}$ per fuel pin. Due to the pulsed operating mode of DEMO the generation rate experiences oscillations in time [229]. Nevertheless, integrated over time the amount of generated tritium approaches the amount of tritium released into the purge gas, so on average the release rates of $^1H^3HO$ and $^1H^3H$ molecules per fuel pin can be estimated with $\dot{\varkappa}^{\mathrm{FP}}_{3,\mathrm{gen}} \approx \dot{\varkappa}^{\mathrm{FP}}_{13\mathrm{O}} + \dot{\varkappa}^{\mathrm{FP}}_{13}$. Studies suggest [75], that by far the majority of the generated tritium is released in the form of $^1H^3H$ [78]. For the calculations in this work, it is assumed that

$$\dot{\varkappa}^{\mathrm{FP}}_{13} \approx 0.8 \cdot \left(\dot{\varkappa}^{\mathrm{FP}}_{13} + \dot{\varkappa}^{\mathrm{FP}}_{13\mathrm{O}}\right) \qquad \text{and} \qquad \dot{\varkappa}^{\mathrm{FP}}_{13\mathrm{O}} \approx 0.2 \cdot \left(\dot{\varkappa}^{\mathrm{FP}}_{13} + \dot{\varkappa}^{\mathrm{FP}}_{13\mathrm{O}}\right). \tag{5.22}$$

Further isotope exchange reactions between the released molecules from the ceramic breeder and the $^1H_2$ of the purge gas cause an additional generation of ^1H_2O and $^3H_2$. Since in an HCPB breeding blanket, the $^1H_2$ concentration in both the coolant and the breeder fluid is usually significantly higher than that of the other molecular species (except of He), the four reactions (2.113) - (2.115) and (2.117) occur with a much lower reaction rate than the reactions (2.10) and (2.116). Therefore, this model merely takes into account the two isotope exchange reactions (2.10) and (2.116) which with $i = 3$ and $k = 1$ can be expressed as

$$2\,^1H^3H \rightleftharpoons {}^1H_2 + {}^3H_2 \tag{5.23}$$

$$^1H^3HO + {}^1H_2 \rightleftharpoons {}^1H_2O + {}^1H^3H\,. \tag{5.24}$$

Following the explanation given in section 2.2.5, the forward reaction rate coefficients of these reactions [see equations (2.102) and (2.121)] are estimated to be of the order of $k^{\mathrm{f,ex}}_{13+13} \approx 1\times10^5\,\mathrm{m^3\,s^{-1}\,mol^{-1}}$ and $k^{\mathrm{f,w}}_{\mathrm{IV},31} \approx 1\times10^5\,\mathrm{m^3\,s^{-1}\,mol^{-1}}$, respectively. The backward reaction rate coefficients are calculated with the equations (2.103) and (2.129). Equation (2.47) provides the experimental relation to determine the equilibrium constant of reaction (5.23). The temperature dependency of the equilibrium constant of reaction (5.24) could be theoretically determined by Libby *et al* as [189], [230]

$$\log K^{\mathrm{w}}_{\mathrm{IV},31} = 0.292 \log T + \frac{336.5}{T} - 1.055 \tag{5.25}$$

This relation was experimentally validated by Black *et al* [231].

During tritium breeding operation part of the pebble beds in the fuel pins reach temperatures of up to $T = 1200\,\mathrm{K}$ [74]. While trespassing through the pebble beds the purge gas heats up from its inlet temperature of approximately $T = 573\,\mathrm{K}$ to a maximum upper limit temperature of $T = 823\,\mathrm{K}$. The gas is maintained below this maximum temperature to prevent the Eurofer'97 material from experiencing a decrease in creep strength. After emerging from the pebble bed, the purge gas, now enriched with tritiated molecules, enters two thin ducts in the inner wall (IW) between the pebble bed and the coolant inlet channel and flows back towards the outlet.

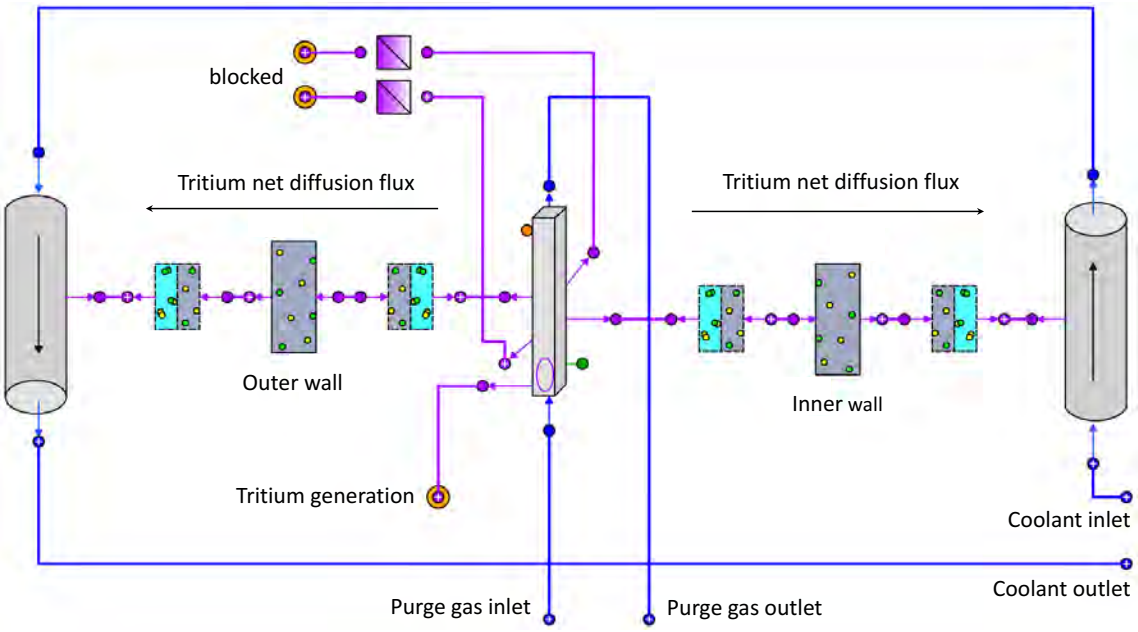

Fig. 5.6. EcosimPro© component structure of a fuel pin in an HCPB breeding blanket.

Within the scope of this work, a hydrogen transport model of the fuel pin is developed in EcosimPro© using the components presented in section 5.1. The numerically reproduced geometric structure of the fuel pin considered in the model is illustrated on the right-hand side in figure 5.5. The EcosimPro© component flow chart of the fuel pin model is shown in figure 5.6. It considers the purge gas as a cylindrical flow component linked to two cylindrical wall material components which represent the inner and outer cylindrical Eurofer'97 walls of the pebble bed case. Via gas-metal interface components, each wall material component is connected with a flow component representing the inlet and outlet coolant channels. For the sake of lucidity, the coolant flow components with four blocked diffusion ports are grouped into a single so-called pipe flow component whose set-up and symbol are depicted in figure 5.1. The output flow port of the flow component representing the coolant inlet channel is connected to the input flow port of the flow component representing the coolant outlet channel. This makes it possible to model the flow reversal of the coolant gas at the front of the fuel pins. The chosen thicknesses and contact surfaces of the considered $l_{\mathrm{FP}} = 0.5\,\mathrm{m}$ long cylindrical flow and wall material components are taken from the drawing in the lower right-hand corner of figure 5.5. The intrinsic diffusion port of the purge gas component is linked to a bound component. In a simplified manner, it reproduces the physics of the ceramic breeder by acting as a particle source imposing the formation of $^{1}\mathrm{H}^{3}\mathrm{HO}$ and $^{3}\mathrm{H}_{2}$ molecules. The rates of formation per flow segment are set to $\dot{\varkappa}^{\mathrm{FP}}_{13\mathrm{O}}/\mathcal{M}$ and $\dot{\varkappa}^{\mathrm{FP}}_{33}/\mathcal{M}$, respectively. By introducing a void fraction of the ceramic breeder pebble bed of $\varepsilon = 0.5$ the volume of the purge gas flow reduces by a factor of two. The coolant gas mass flow rate is chosen as specified above.

The purge gas inlet concentrations of the different molecular species in a fuel pin are determined by the temporal evolutions of their concentrations in the entire purge gas loop system. Therefore, in addition to the numerical representation of a fuel pin, a simplified

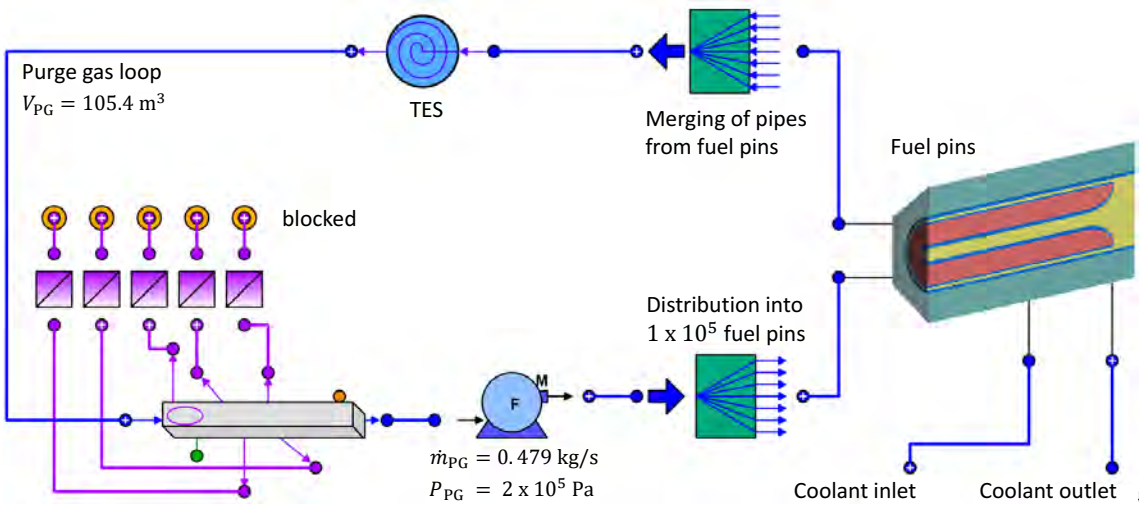

Fig. 5.7. EcosimPro© component structure of the purge gas loop system of an HCPB breeding blanket.

model of the purge gas loop system of DEMO is developed in EcosimPro©. Its component structure is shown in figure 5.7. Here, the model of the fuel pin of figure 5.7 appears as a grouped higher-level component. Outside of the fuel pins, the purge gas flow is described as a single flow component. In the HCPB breeding blanket designed of DEMO the total mass flow rate of the purge gas loop system is specified to approximately $\dot{m}_{PG} = 5 \times 10^{-1}\,\mathrm{kg\,s^{-1}}$ with the total purge gas volume being $V_{PG} = 105.4\,\mathrm{m^3}$. These properties are introduced by the feeding pump component. Moreover, the pump component serves as a purge gas recycling unit where the $^1H_2$ partial pressure in the purge gas coming from the fuel pins can be set back to a desired value before passing again through the fuel pins. In this model, the $^1H_2$ partial pressure specified in the feeding pump conforms with its partial pressure at the purge gas inlet of a fuel pin (PG.IN). A divider component splits the single main stream of the purge gas into $N_{split} = 1 \times 10^5$ flows, each connected to a fuel pin. Consequently, in the model, the purge gas mass flow rate through each fuel pin is about $\dot{m}_{PG}^{FP} = 5 \times 10^{-6}\,\mathrm{kg\,s^{-1}}$ [71]. After leaving the fuel pins, the purge gas outlet streams unite again before passing through a particle extraction component which shall simulate the tritium extraction system (TES). This model considers an efficiency of $\eta_{TES} = 0.8$ for every hydrogen isotope-containing molecule.

The coolant gas loop of DEMO which is part of the PHTS will contain a coolant purification system (CPS) that removes most of the tritium that permeated from the purge gas into the coolant. The CPS is envisaged to achieve a tritium removal efficiency of about $\eta_{CPS} = 0.9$. However, to obtain conservative simulation results which lead to the highest possible tritium permeation fluxes from the purge gas into the coolant, this analysis assumes a CPS efficiency of $\eta_{CPS} = 100\,\%$, meaning that the $^1H^3H$ and $^3H_2$ partial pressures at the coolant gas inlet of the fuel pins are zero.

It should be noted that the model of the purge gas loop does not describe its exact geometry. Neither does it take into account permeation processes happening through the

purge gas pipe walls outside of the fuel pins. Moreover, the pulsed tritium breeding operation and the detailed kinetics of tritium generation, diffusion, and desorption in the ceramic pebbles are also neglected. For these reasons, the developed model should be exclusively regarded as a tool to study the co- and counter-permeation process between the purge gas and the coolant inside of fuel pins in an HCPB breeding blanket. The applied simplifications are chosen on purpose to reduce external influences on the simulation results. This enables a more undisturbed investigation of the ongoing multi-isotopic permeation effects.

The numerical calculations in this section are executed with a discretization of each material component into $\mathcal{Q} = 30$ segments in the diffusion direction and $\mathcal{M} = 10$ segments in the flow direction. For the temperature of both gases and the Eurofer'97 wall in the fuel pins the simulation assumes a homogeneous relatively high average temperature of $T = 773\,\mathrm{K}$. Choosing an equal temperature for the different components causes the tritium transport coefficients to be homogeneous throughout the system. This provides a clearer view of the pure multi-isotopic transport effects occurring between the purge gas and the coolant gas.

To start with the evaluation of multi-isotopic permeation effects occurring in the fuel pins of an HCPB breeding blanket it is important to determine general characteristics of the inner and outer Eurofer'97 walls of the pebble bed cladding as permeation membranes. As the sketch in the lower right corner of figure 5.5 shows, their thicknesses are $d_{\mathrm{IW}} = 6 \times 10^{-3}\,\mathrm{m}$ and $d_{\mathrm{OW}} = 3 \times 10^{-3}\,\mathrm{m}$, respectively. For this analysis, the EcosimPro© model of the fuel pin is used to simulate the steady state tritium permeation flux from the purge gas into an evacuated coolant that would occur if either only $^1\mathrm{H}^3\mathrm{H}$ or only $^3\mathrm{H}_2$ molecules were present in the purge gas. For the simulation, it is considered that neither generation nor isotope exchange reactions occur in the system such that the partial pressures of any other molecular species are kept zero. Figure 5.8 shows the simulated tritium permeation flux as a function of the effective tritium pressure $p^{\mathrm{PG}}_{\mathrm{eff},3}$ in the purge gas flow of a fuel pin if either $p^{\mathrm{PG}}_{13} = 0\,\mathrm{Pa}$ and $p^{\mathrm{PG}}_{\mathrm{eff},3} = p^{\mathrm{PG}}_{33}$ (dashed line) or $p^{\mathrm{PG}}_{33} = 0\,\mathrm{Pa}$ and $p^{\mathrm{PG}}_{\mathrm{eff},3} = 1/2 \cdot \sqrt{m_{33}/m_{13}} \cdot p^{\mathrm{PG}}_{13}$ (dotted line). The left-hand plot shows the permeation flux through the inner Eurofer'97 membrane into the coolant inlet channel and the right-hand graph the permeation flux through the outer Eurofer'97 membrane into the coolant outlet channel. It can be seen that as mathematically derived in section 4.1, at very low effective tritium pressures the tritium permeation flux approaches equation (4.13). The corresponding correction factors $f^{\mathrm{c}}_{\mathrm{UI}}$ and $f^{\mathrm{c}}_{\mathrm{DI}}$ of each membrane are calculated from the geometry data shown in figure 5.5. At higher effective tritium pressures where the tritium permeation process is no longer purely surface-limited, the two curves that describe the permeation fluxes for the cases in which either only $^3\mathrm{H}_2$ molecules or only $^1\mathrm{H}^3\mathrm{H}$ molecules are present in the purge gas are no longer identical. They progressively separate with increasing effective tritium pressure. As predicted in the paragraph below equation (4.13), with growing effective tritium pressure both simulated curves show ever smaller permeation flux values than those given by the surface-limited equation (4.13). It is evident that if

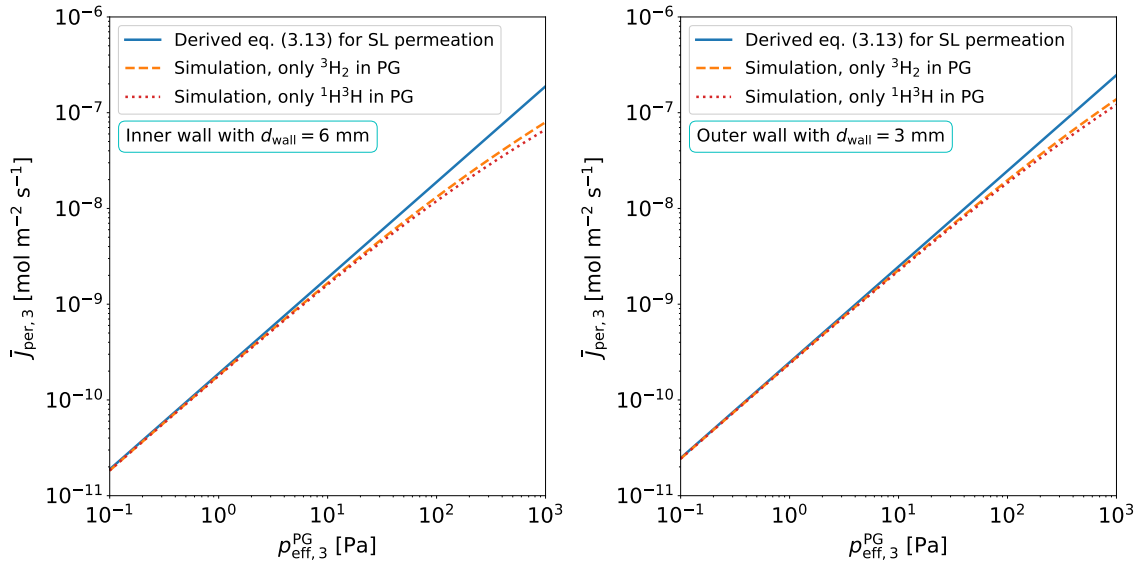

Fig. 5.8. Simulated steady state tritium permeation flux [Left] through the inner Eurofer'97 membrane into the coolant inlet channel, and [Right] through the outer Eurofer'97 membrane into the coolant outlet channel, as a function of the effective tritium pressure in the purge gas flow of an HCPB fuel pin if either only $^3H_2$ or only $^1H^3H$ molecules were present in the purge gas while the partial pressures of all other molecular species are maintained zero. Both graphs contain a plot of the derived equation (4.13).

both molecular species $^1H^3H$ and $^3H_2$ are present in the purge gas the curve of the resulting tritium permeation flux would run somewhere between the dashed and the dotted curves. Since the inner wall of the fuel pin pebble bed cladding is thicker the permeation process leaves the surface-limited regime at smaller effective tritium pressures than the permeation process through the outer wall. For this reason, at a fixed effective tritium pressure, the curves belonging to the inner membrane are more separated than those belonging to the outer membrane.

5.3.1. Counter-permeation in an HCPB breeding blanket

The first analysis focuses on a situation that represents a pure counter-permeation scenario in a fuel pin by adding $^1H_2$ to the coolant. To enable an isolated examination of counter-permeation effects on the tritium escape into the coolant, any overlapping co-permeation effects are reduced as much as possible. Therefore, it is considered that no additional $^1H_2$ gas is fed to the purge gas by the feeding pump component. Although in reality, this would greatly suppress the release of tritium into the purge gas, it is assumed for now that the tritium release will still occur with a total ^3H release rate of 1.23×10^{-8} mol s^{-1} per fuel pin satisfying the condition (5.22). As soon as the simulation is launched, it starts calculating the temporal evolution of the occurring partial pressures, concentrations, and fluxes of all involved species in the entire system after each time step. Although in this first simulation, the purge gas is initially free from hydrogen isotope-containing

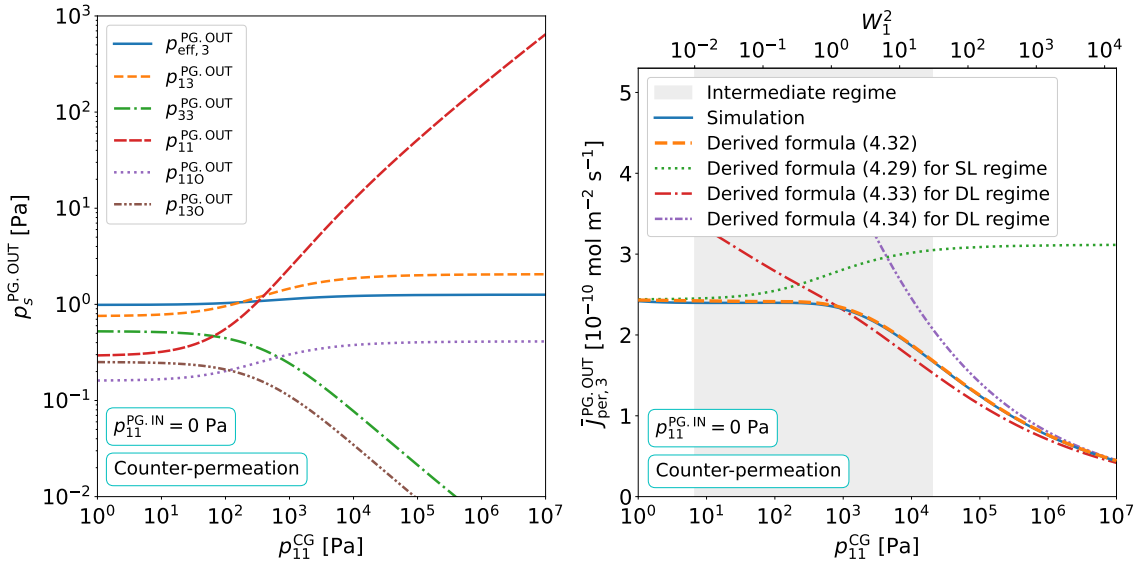

Fig. 5.9. [Left] Simulated partial pressures of hydrogen isotope containing molecules in the last purge gas segment of an HCPB fuel pin for the case for a counter-permeation scenario in which $p_{11}^{\mathrm{PG.IN}} = 0\,\mathrm{Pa}$, plotted against the $^1H_2$ partial pressure in the coolant. [Right] Steady state atomic tritium permeation flux from the last purge gas segment of an HCPB fuel pin into the coolant outlet channel for a counter-permeation scenario in which $p_{11}^{\mathrm{PG.IN}} = 0\,\mathrm{Pa}$, plotted against the $^1H_2$ partial pressure in the coolant. The plot shows a simulation as well as curves that are calculated using algebraical formulas derived in section 4.1.

molecules, the ongoing release of $^1H^3H$ and $^1H^3HO$ molecules from the ceramic breeder leads to a gradual rise in their partial pressures. In addition, the liberated molecules undergo the chemical reactions (5.23) and (5.24) leading to the formation of $^1H_2$, $^3H_2$ and ^1H_2O, which additionally accumulate in the purge gas flow. By passing through the tritium extraction system, the increasing partial pressures of all hydrogen isotope-containing molecules are continuously reduced. After some time this causes the partial pressure increase in the loop to come to a hold and a steady state establishes. As the purge gas passes through the tritium-releasing pebble beds, the time-constant partial pressures of the different molecular species increase along the length of the fuel pins. This means that the steady state partial pressures in the purge gas outlet segments of the fuel pins (PG.OUT) are higher than at the purge gas inlets (PG.IN). Since in addition to that $^1H_2$ gas is added to the coolant, the permeation of protium from the coolant into the purge gas flow further influences the partial pressure configuration that sets up in the fuel pins.

The left-hand plot in figure 5.9 presents simulation results of the adjusting steady state partial pressures in the last segment of the purge gas flow through the fuel pins for a broad range of different $^1H_2$ partial pressure in the coolant. The observed slight increase in $^1H_2$ partial pressure in the purge gas with increasing $^1H_2$ partial pressure in the coolant is due to an elevated protium permeation flux from the coolant into the purge gas. Especially at low $^1H_2$ partial pressures in the coolant, the $^1H_2$ partial pressure in the purge gas remains so low that co-permeation effects may be ignored. Since the assumed rate coefficients

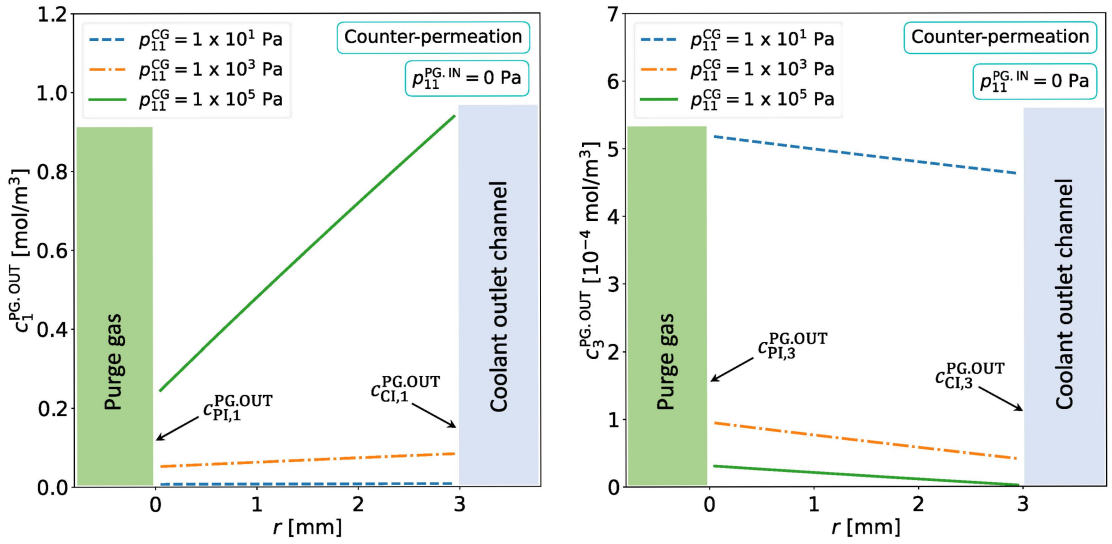

Fig. 5.10. [Left] Simulated protium concentration profiles and [Right] simulated tritium concentration profiles in the OW of the last purge gas segment of an HCPB fuel pin for the case in which $p_{11}^{PG.IN} = 0$ Pa. The plotted profiles correspond to three different $^1H_2$ partial pressures present in the coolant.

$k_{13+13}^{f,ex} = k_{IV,31}^{f,w} = 1 \times 10^5\,m^3\,s^{-1}\,mol^{-1}$ of the reactions (5.23) and (5.24) are relatively high, a significant fraction of the released $^1H^3H$ molecules react and form $^1H_2$ and $^3H_2$ molecules before reaching the purge gas outlet. Moreover, on their way to the purge gas outlet, part of the formed $^1H_2$ molecules react with released $^1H^3HO$ molecules from the ceramic breeder which leads to the generation of additional $^1H^3H$ molecules. The rise in $^1H_2$ partial pressure in the purge gas with growing partial pressure in the coolant shifts the equilibrium state of reaction (5.24) towards the $^1H^3H$ side. Therefore, with increasing $^1H_2$ partial pressure in the coolant the $^1H^3H$ partial pressure in the purge gas experiences an increment and the amount of $^3H_2$ plunges (see the left-hand plot in figure 5.9).

While moving through the pebble bed, part of the tritium bound to the $^1H^3H$ and $^3H_2$ molecules in the purge gas permeates into the coolant. The right-hand graph in figure 5.9 presents the simulated steady state atomic tritium permeation flux from the last purge gas segment (see figure 5.5) through the outer cylindrical Eurofer'97 wall (OW) into the coolant outlet channel. It is plotted as a function of the $^1H_2$ partial pressure in the coolant. To support the analysis of this plot, figure 5.10 displays the steady state protium (left-hand graph) and tritium (right-hand graph) concentration profiles that adjust in the outer Eurofer'97 wall. The graphs reveal that for $^1H_2$ partial pressures $p_{11}^{CG} > 10$ Pa in the coolant, the tritium concentrations at the purge gas interface (PI) and the coolant gas interface (CI) are significantly lower than the corresponding protium concentrations. Equation (2.95) implies that in this case, it is reasonable to assume that the recombination fluxes of $^3H_2$ molecules into the purge gas and the coolant are negligibly small compared to the recombination fluxes of $^1H^3H$ molecules. Therefore, the simulated permeation scenario well satisfies the conditions on which the theoretical study of multi-isotopic permeation in section 4.1 is based. Consequently, with $i = 3$ (tritium) and $k = 1$ (protium), and

by considering the purge gas interface of the Eurofer'97 wall as the upstream interface and the coolant gas interface as the downstream interface, the simulated tritium permeation process should behave according to the analytic study of multi-isotopic permeation presented in section 4.1.

One of the main conclusions from the theoretical study in section 4.1 is that the influence of counter-permeating protium on the tritium permeation flux depends on the protium permeation regime. This can be evaluated by calculating the permeation number (2.148) of the protium counter-permeation process which is indicated in the right-hand plot in figure 5.9 by the second x-axis. The graph reveals that for $^1H_2$ partial pressures in the coolant below approximately $p_{11}^{CG} < 10\,\text{Pa}$, the protium counter-permeation process occurs in the surface-limited regime. The derived algebraic expression for the tritium permeation flux in the surface-limited regime (4.29) is plotted in the right-hand graph in figure 5.9. It can be seen that the lower the $^1H_2$ partial pressure in the coolant, the smaller the permeation number and the more the simulated tritium permeation flux converges against the algebraic relation (4.29) of the pure surface-limited regime. It is important to note that for a case in which $p_{11}^{CG} = 0\,\text{Pa}$, the right-hand graph in figure 5.8 shows that at the simulated effective tritium pressure in the purge gas of only about $p_{\text{eff},3}^{PG} \approx 1\,\text{Pa}$ the tritium permeation flux is almost perfectly described by equation (4.13). Since the equations (4.29) and (4.13) are identical it can be concluded that in the surface-limited protium permeation regime of the observed permeation scenario, the tritium permeation flux is described by equation (4.29), even for pressures $p_{11}^{CG} < p_{\text{eff},3}^{PG}$

One must be aware of the fact that the variation of the simulated tritium permeation flux with increasing value of p_{11}^{CG} is a superposition of counter-permeation effects and the fact that the effective tritium pressure in the purge gas also slightly increases with p_{11}^{CG} (see left-hand plot in figure 5.9). An isolated view on the contribution of counter-permeation on the tritium permeation flux can hence only be obtained by examining the normalized multi-isotopic permeation flux factor (4.27) of the simulated counter-permeation process. It is shown in the left-hand graph in figure 5.11 as a function of p_{11}^{CG} after being calculated from the simulated permeation flux shown in the right-hand plot in figure 5.9 by applying equation (4.28). The plot confirms that in the specified surface-limited protium permeation regime the permeation flux factor is very close to $\Lambda_{13}^{PG.OUT} = 1$. The simulated values of the protium and tritium interface concentrations at the outer Eurofer'97 wall are plotted in the right-hand graph in figure 5.11. As the equations (4.30) and (4.31) predict, in the surface-limited regime, both tritium interface concentrations $c_{PI,3}^{PG.OUT} > c_{CI,3}^{CG.OUT}$ plunge with increasing partial pressure p_{11}^{CG} and the protium interface concentrations increase.

For $p_{11}^{CG} > 10\,\text{Pa}$, the protium counter-permeation process occurs in the intermediate regime. Here, the tritium permeation flux and the multi-isotopic permeation flux factor decrease with growing $^1H_2$ partial pressure in the coolant (see the right-hand plot in figure 5.9 and left-hand plot in figure 5.11). The right-hand graph in figure 5.11 visualizes how, outside of the surface-limited regime, the dependencies of the two protium interface concentrations on the $^1H_2$ partial pressure transform from relation (4.30) to the

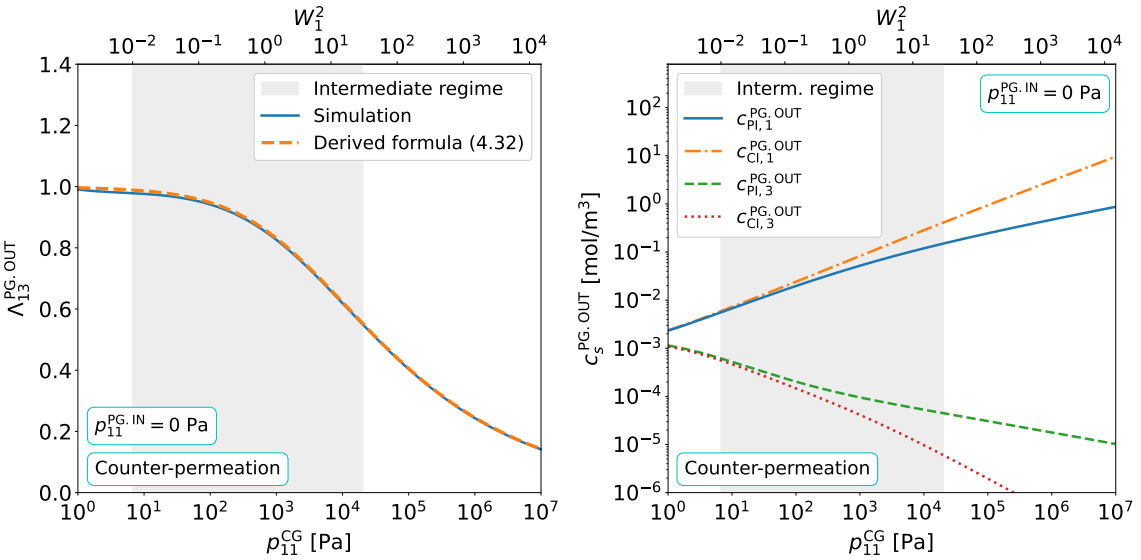

Fig. 5.11. [Left] Normalized multi-isotopic permeation flux factor in the last purge gas segment of an HCPB fuel pin plotted against the partial pressure p_{11}^{CG} for a counter-permeation scenario in which $p_{11}^{PG.IN} = 0\,Pa$. One curve is simulated using the numerical model and the other curve is calculated with the derived equation (4.32). [Right] Simulated protium and tritium concentrations at the purge gas interface (PI) and the coolant gas interface (CI) of the outer Eurofer'97 wall in the last purge gas segment of an HCPB fuel pin plotted against the partial pressure p_{11}^{CG} for a counter-permeation scenario in which $p_{11}^{PG.IN} = 0\,Pa$.

relations (4.36). Moreover, the expressions of the tritium interface concentrations change from equation (4.31) to the equations (4.37) and (4.38). According to equation (4.39), the product of the protium and tritium purge gas interface concentrations and hence the tritium recombination flux into the purge gas increase when moving from the intermediate towards the diffusion-limited regime. In the right-hand graph in figure 5.11 this can be confirmed by the fact that with increasing partial pressure p_{11}^{CG} the value of $c_{PI,1}^{PG.OUT}$ increases with a higher rate than the value of $c_{PI,3}^{PG.OUT}$ decreases. As revealed in section 4.1, the increase in tritium recombination flux into the purge gas with increasing partial pressure p_{11}^{CG} explains the permeation flux-reducing effect of multi-isotopic permeation.

Above protium partial pressures in the coolant of about $p_{11}^{CG} > 2 \times 10^4\,Pa$ the protium permeation process enters the diffusion-limited domain. This is confirmed by the left plot in figure 5.10, which shows a steep protium concentration gradient at such high pressures. The right-hand graph in figure 5.9 shows how with growing permeation number the simulated tritium permeation flux is approached by the derived algebraic formulas (4.33) and (4.34) that approximately describe the tritium permeation flux in a diffusion-limited counter-permeation scenario. Furthermore, the dashed line shows the theoretically determined tritium permeation flux as a function of p_{11}^{CG} using the derived equation (4.32). It is calculated by inserting the reduced concentrations $\zeta_{r,1}(W_1)$ and $\lambda_{r,1}(W_1)$ for parallel membranes which are plotted in figure 2.11 into equation (4.32). Moreover, the dashed line in the left-hand plot in figure 5.11 presents the theoretically calculated normalized per-

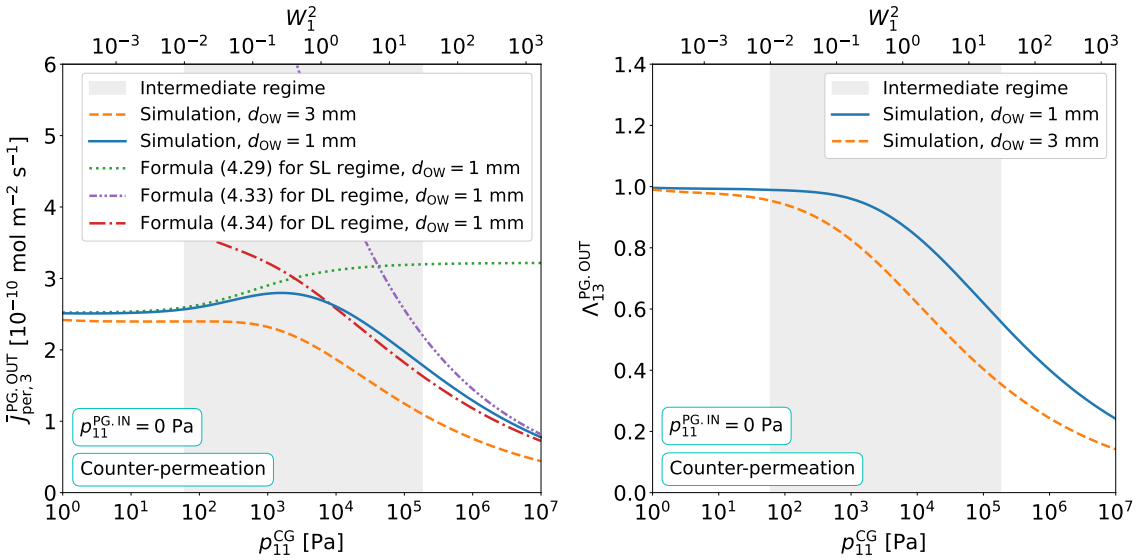

Fig. 5.12. [Left] Steady state atomic tritium permeation flux from the last purge gas segment of an HCPB fuel pin into the coolant outlet channel plotted against the $^1H_2$ partial pressure in the coolant for two different outer wall thicknesses for a counter-permeation scenario in which $p_{11}^{PG.IN} = 0\,Pa$. The plot shows simulation results as well as curves that are calculated using algebraical formulas derived in section 4.1. [Right] Simulated normalized multi-isotopic permeation flux factors occurring in the last purge gas segment of an HCPB fuel pin for two different outer wall thicknesses in a counter-permeation scenario in which $p_{11}^{PG.IN} = 0\,Pa$.

meation flux factor which is obtained in the same way by inserting the calculated reduced concentrations shown in figure 2.11 into equation (4.32) before applying equation (4.27). Even though the theoretically obtained reduced concentrations are only valid for parallel membranes (see section 2.3.4), the theoretical and simulated values agree extremely well. This was expected since the ratio of the inner and outer radii $r_{out}/r_{in} = 1.1$ of the outer Eurofer'97 wall is relatively small. In conclusion, equation (4.32) and the algebraic formulas (4.29), (4.33), (4.34) which are derived in section 4.1.2 are in very good agreement with the simulation results and are thus numerically validated.

As the tritium permeation mitigating effect of a protium counter-flow in a fuel pin is revealed, the same simulation is performed assuming a thinner cylindrical outer Eurofer'97 wall with a width of $d_{OW} = 1 \times 10^{-3}$ m but an unchanged inner diameter of 6×10^{-2} m (see figure 5.5). In the left-hand plot in figure 5.12, the resulting steady state tritium permeation flux from the last purge gas segment into the coolant outlet channel is plotted against the $^1H_2$ partial pressure in the coolant. As is the case for the thicker membrane, at low $^1H_2$ partial pressures in the coolant the tritium permeation flux converges against the relation (4.29) which is independent of the membrane thickness. However, a reduced thickness means that the same number of particles entering the inner purge gas interface now leave through a smaller surface area at the coolant interface compared to the thicker wall. This explains the observed slight increment of the simulated surface-limited permeation flux (see the left-hand plot in figure 5.12). Since the permeation number (2.147) of the protium

counter diffusion is proportional to the membrane thickness, the surface-limited regime of the thinner membrane lasts up to a higher $^1H_2$ partial pressure in the coolant of almost $p_{11}^{CG} \approx 1 \times 10^2$ Pa. The left-hand graph in figure 5.12 confirms that due to the displaced range of the permeation number the derived algebraic formula (4.29) describes the tritium permeation flux up to higher pressures compared to the thicker membrane. Consequently, the reduction in tritium permeation flux due to counter-permeation phenomena happening in the intermediate permeation regime occurs at higher $^1H_2$ partial pressures in the coolant. For the thinner membrane, the pure diffusion-limited counter-permeation regime starts at pressures of approximately $p_{11}^{CG} > 2 \times 10^5$ Pa. As expected, in this regime the tritium permeation flux starts converging against the plotted curves of the derived algebraic formulas (4.33) and (4.34). Furthermore, the right-hand graph in figure 5.12 shows the simulated normalized multi-isotopic permeation flux factors in the case of both membrane thicknesses. It is observed that as a result of the shift in permeation number, the tritium permeation flux reduction sets in at higher $^1H_2$ partial pressures in the coolant. Therefore, it can be concluded that the reducing effect of counter-permeating protium on the tritium permeation flux is more efficient the thicker the wall thickness of the Eurofer'97 walls.

5.3.2. Co-permeation in an HCPB breeding blanket

At this point, the focus of the investigation is pointed towards a more realistic scenario encountered in an HCPB breeding blanket in which $^1H_2$ gas is added to the purge gas to trigger the release of tritiated molecules from the ceramic breeder [226].

The amount of $^1H_2$ gas added to the purge gas is a critical parameter that to some extent determines the tritium release rate from the pebbles into the purge gas. Therefore, in DEMO it will likely be controlled by some kind of purge gas recovery system. In the model, the $^1H_2$ partial pressure is controlled by the feeding pump component at the inlet ports of the fuel pins (see figures 5.2 and 5.7) where it is set back to a chosen value of $p_{11}^{PG.IN}$.

Because in this model the coolant is considered as a perfectly purified system, if no additional $^1H_2$ gas is added to the coolant ($p_{11}^{CG} = 0$ Pa) the partial pressures of all hydrogen isotope containing molecules at the coolant inlet of the fuel pins are zero. In this case, the occurring hydrogen isotope permeation processes represent a pure co-permeation scenario in which protium and tritium isotopes are permeating side-by-side from the purge gas into the coolant. The left-hand plot in figure 5.13 shows how the addition of $^1H_2$ gas to the purge gas changes the establishing steady state partial pressures in the purge gas outlet segment. The increased partial pressure of $^1H_2$ molecules in the purge gas provokes reaction (5.24) to proceed faster compared to the previous simulation. This causes the $^1H^3HO$ and $^3H_2$ contents to diminish and the partial pressures of the ^1H_2O and $^1H^3H$ molecules to increase.

In the right-hand graph in figure 5.13 the tritium permeation flux from the last purge gas segment into the coolant outlet channel is plotted against the partial pressure of added

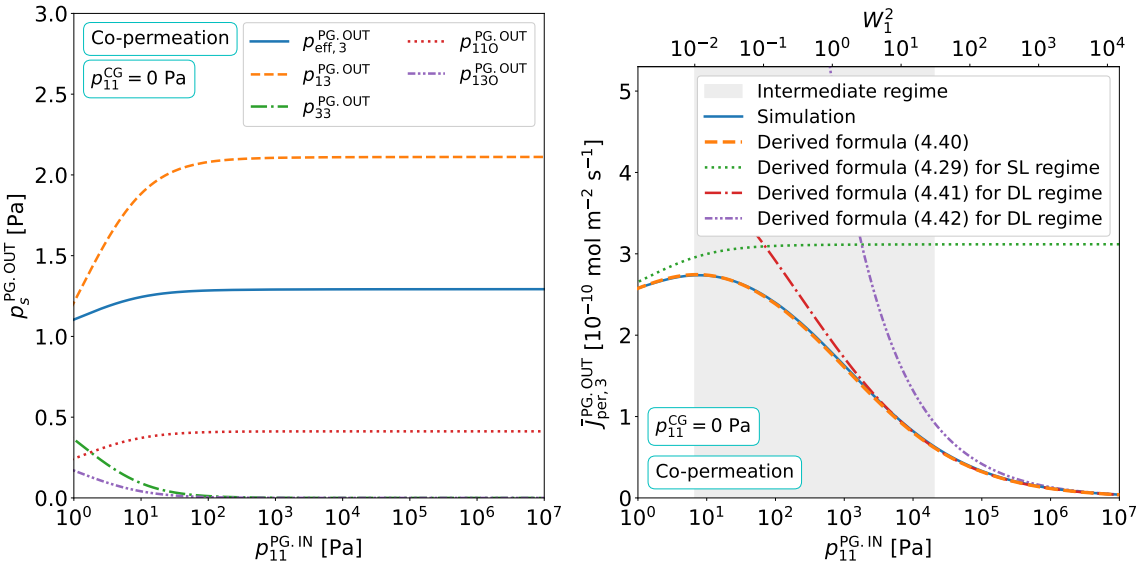

Fig. 5.13. [Left] Simulated partial pressures of hydrogen isotope containing molecules in the last purge gas segment of an HCPB fuel pin plotted against the partial pressure $p_{11}^{PG.IN}$ for a co-permeation scenario in which $p_{11}^{CG} = 0\,Pa$. [Right] Steady state atomic tritium permeation flux from the last purge gas segment of an HCPB fuel pin into the coolant outlet channel plotted against the $p_{11}^{PG.IN}$ for a co-permeation scenario in which $p_{11}^{CG} = 0\,Pa$. The plot shows a numerical simulation as well as curves that are calculated using algebraic formulas derived in section 4.1.

$^1H_2$ gas to the purge gas. Moreover, the upper graphs of figure 5.14 show the establishing protium and tritium concentration profiles in the outer Eurofer'97 wall of the last purge gas segment during the co-permeation process. This time, the protium concentration gradient is tilted in the same direction as the tritium concentration profile. It is found that for partial pressures in the purge gas of above approximately $p_{11}^{PG.IN} > 1\,Pa$ the condition $p_{11}^{PG.IN} \gg p_{eff,3}^{PG.OUT}$ is sufficiently well fulfilled which is why the theoretical model presented in section 4.1 should once again serve as a valid approximation for the simulation results.

As indicated by equation (4.28), the tritium permeation flux is proportional to the effective tritium pressure. Since in the range $p_{11}^{PG.IN} < 200\,Pa$ the effective tritium pressure in the purge gas rises, the simulated tritium permeation flux increases as well (see the right-hand plot in figure 5.13). Nevertheless, the right-hand graph in figure 5.13 shows that despite this finding, in the surface-limited regime, the simulated tritium permeation flux converges against the plotted relation (4.29). Again, since the effective tritium pressure in the purge gas is sufficiently low, the equations (4.29) and (4.13) describe the tritium permeation flux even for pressures $p_{11}^{PG.IN} < p_{eff,3}^{PG.OUT}$ (see right graph in figure 5.8).

An isolated insight into the pure co-permeation effects on the tritium permeation flux is provided by the left-hand graph in figure 5.15 which displays the simulated normalized multi-isotopic permeation flux factor. As expected, in the surface-limited regime it approaches $\Lambda_{13}^{PG.OUT} = 1$. However, compared to the previously analyzed counter-permeation scenario the permeation flux factor decreases to a visibly lower value before entering the intermediate permeation regime. This is compatible with the findings illus-

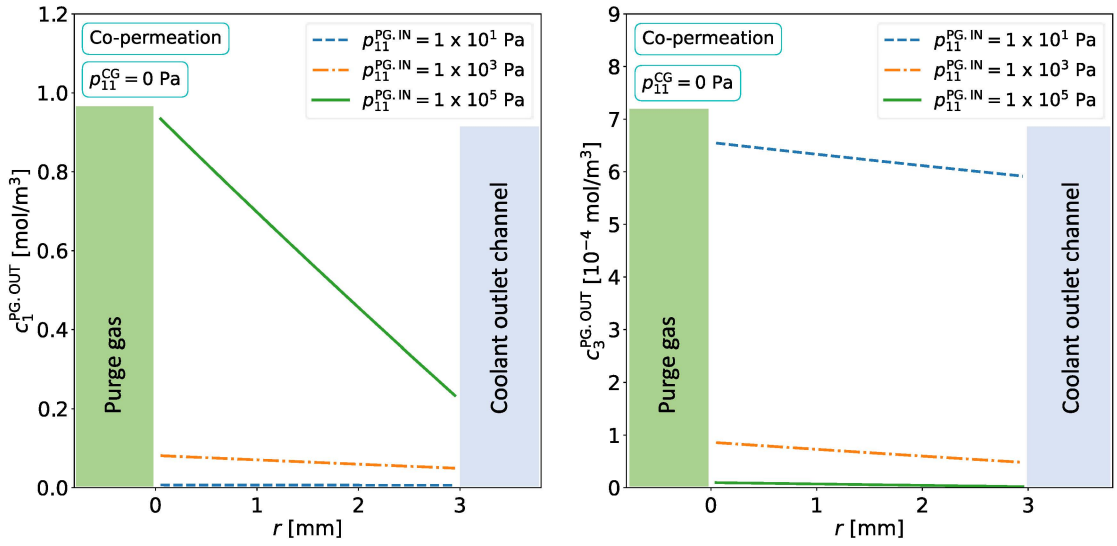

Fig. 5.14. [Left] Simulated protium concentration profiles and [Right] simulated tritium concentration profiles in the OW of the last purge gas segment of an HCPB fuel pin for the case in which $p_{11}^{CG} = 0\,\text{Pa}$. The plotted profiles correspond to three different $^1H_2$ partial pressures at the purge gas inlet.

trated in figure 4.3. The permeation flux reduces once the reduction in $\Lambda_{13}^{PG.OUT}$ exceeds the observed increase in effective tritium pressure [see equation (4.27)].

As predicted in section 4.1 by the equations (4.25) and (4.26), also in a co-permeation scenario the tritium interface concentrations decrease with increasing value of $p_{11}^{PG.IN}$ while the protium interface concentrations increase. The simulated protium and tritium interface concentrations in the outer Eurofer'97 wall of the last purge gas segment are plotted in the right-hand graph in figure 5.15. The plot visualizes that, as discussed in section 4.1, in the surface-limited regime both tritium interface concentrations $c_{PI,3}^{PG.OUT}$ and $c_{CI,3}^{PG.OUT}$ are described by an approximately equal relation (4.31) and separate into the different relations (4.45) and (4.46) in the diffusion-limited permeation regime. Comparing the right-hand plot in figure 5.11 and the right-hand plot in figure 5.15 reveals that in the intermediate and diffusion-limited permeation regimes, the tritium upstream interface concentrations decline more intensely in a co-permeation than in counter-permeation scenario. Furthermore, in the transition from the surface-limited to the diffusion-limited regime, the plot shows that the expressions of the protium interface concentrations transform from an equal relation (4.30) in the surface-limited regime into the two different relations (4.44) in the diffusion-limited regime. The right-hand graph in figure 5.15 confirms the statement made in section 4.1 that in a co-permeation scenario, as $p_{11}^{PG.IN}$ increases, the concentration $c_{PI,1}^{PG.OUT}$ grows with a higher rate than the concentration $c_{PI,3}^{PG.OUT}$ decreases. For this reason, the product of the protium and tritium purge gas interface concentrations and thus the tritium recombination flux back into the purge gas increases with growing pressure $p_{11}^{PG.IN}$. According to equation (4.14) an increasing recombination flux at the upstream purge gas interface causes the tritium permeation flux into the coolant to decrease which explains the permeation flux reducing effect of co-permeation.

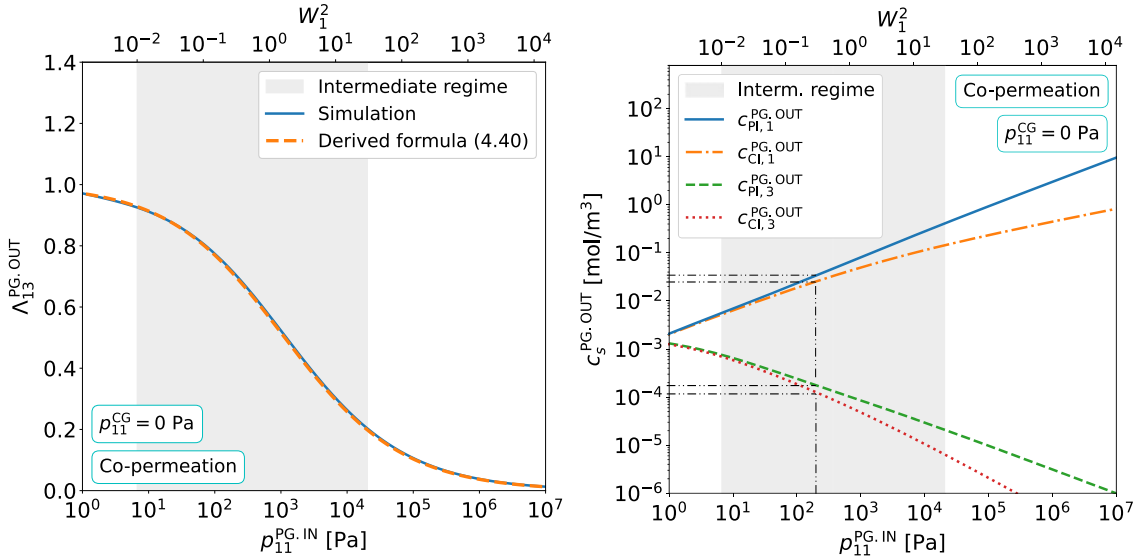

Fig. 5.15. [Left] Normalized multi-isotopic permeation flux factor in the last purge gas segment of an HCPB fuel pin plotted against the partial pressure $p_{11}^{PG.IN}$ for a co-permeation scenario in which $p_{11}^{CG} = 0\,\text{Pa}$. One curve is simulated using the numerical model and the other curve is calculated using the derived algebraic equation (4.40). [Right] Simulated protium and tritium concentrations at the purge gas interface (PI) and the coolant gas interface (CI) of the outer Eurofer'97 wall in the last purge gas segment of an HCPB fuel pin plotted against the partial pressure $p_{11}^{PG.IN}$ for a co-permeation scenario in which $p_{11}^{CG} = 0\,\text{Pa}$.

The right-hand plot in figure 5.13 visualizes the two derived algebraic formulas (4.41) and (4.42). They approximately describe the tritium permeation flux in a co-permeation diffusion-limited regime. The plot confirms that the derived equations approach the simulated curve of the tritium permeation flux when moving toward higher permeation numbers. As expected, equation (4.41) matches the simulation results very well already at much lower permeation numbers than the equation (4.42). Furthermore, the right-hand plot in figure 5.13 and the left-hand plot in figure 5.15 display the curves of the theoretical dependency of the tritium permeation flux and the normalized multi-isotopic permeation flux factor on the $^1H_2$ partial pressure in the purge gas. They are calculated by inserting the reduced concentrations $\zeta_{r,1}(W_1)$ and $\lambda_{r,1}(W_1)$ for parallel membranes which are plotted in figure 2.11 into equation (4.40). Despite the cylindrical geometry of the fuel pin walls, both theoretically determined curves are almost identical to the corresponding simulated curves. To conclude, equation (4.40) and the algebraic expressions (4.29), (4.41), (4.42) derived in section 4.1.3 agree very well with the simulation results and are therefore numerically verified.

5.3.3. Isotope-limited permeation in an HCPB breeding blanket

The left-hand plot in figure 5.16 shows the simulated steady state tritium permeation flux from the last purge gas segment through the outer Eurofer'97 wall into the coolant gas

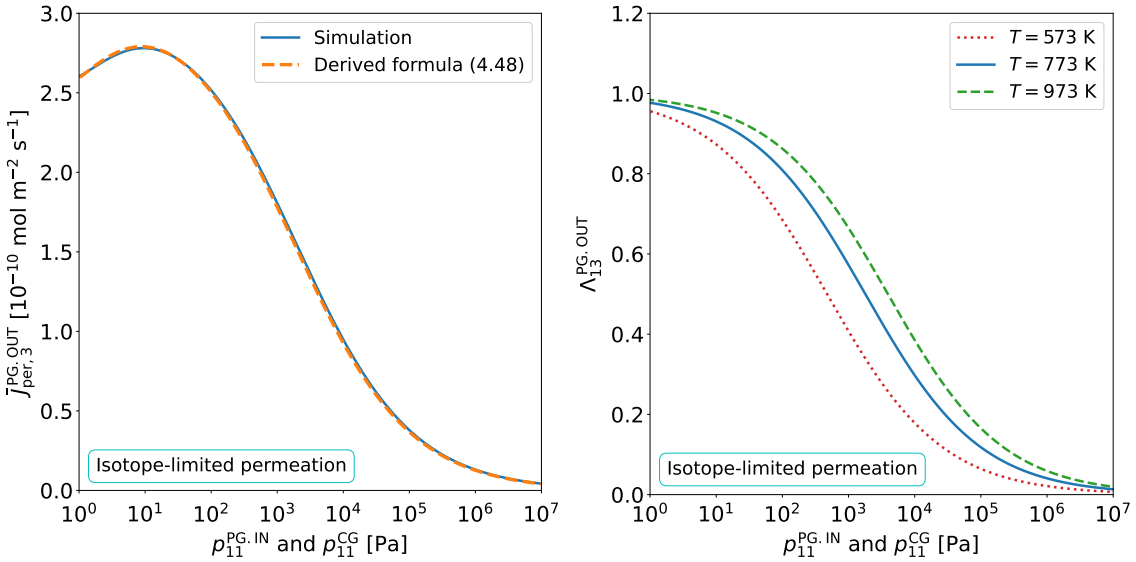

Fig. 5.16. [Left] Simulated steady state tritium permeation flux from the last purge gas segment into the outer coolant channel of an HCPB fuel pin for an isotope-limited permeation scenario in which the $^1H_2$ partial pressure at the purge gas and the coolant gas inlets are equal. The graph includes a simulated curve using the numerical model and a calculated curve using the derived algebraic formula (4.48). [Right] Normalized multi-isotopic permeation flux factor of the isotope-limited permeation scenario in which the $^1H_2$ partial pressure in the purge gas and the coolant gas inlets are equal. The curves are calculated for different temperatures using the derived algebraic formula (4.48).

assuming that the partial pressures of added $^1H_2$ gas at the purge gas and the coolant gas inlets are equal. In section 4.1, such a multi-isotopic permeation scenario is labeled with the term isotope-limited permeation. It turns out that in the observed isotope-limited case the adjusting partial pressures in the purge gas outlet segment follow identical curves as those of the analyzed co-permeation scenario which is visualized in the left-hand plot in figure 5.13. The change in simulated tritium permeation flux with rising $^1H_2$ partial pressure in the isotope-limited scenario has a very similar shape as in the examined co-permeation scenario shown in the right-hand graph in figure 5.13. This finding conforms with the plot in figure 4.3. In addition to the simulation, the permeation fluxes are calculated using the derived algebraic formula (4.48). It is plotted in the left-hand plot in figure 5.16 using an orange dashed line. Both the simulated and the theoretically calculated permeation flux values of the isotope-limited scenario are in very good agreement which numerically validates the derived algebraic formula (4.48).

The multi-isotopic permeation flux factor of the isotope-limited case calculated with equation (4.48) is shown in the right-hand plot in figure 5.16 after normalization using equation (4.27) (see solid blue line for $T = 773\,\mathrm{K}$). In addition, the graph contains the calculated courses of Λ_{13} for different temperatures. It can be seen that the lower the temperature, the smaller the normalized multi-isotopic permeation flux factor as well as the tritium permeation flux at a certain value of p_{11}. This is a result of the fact that the hydro-

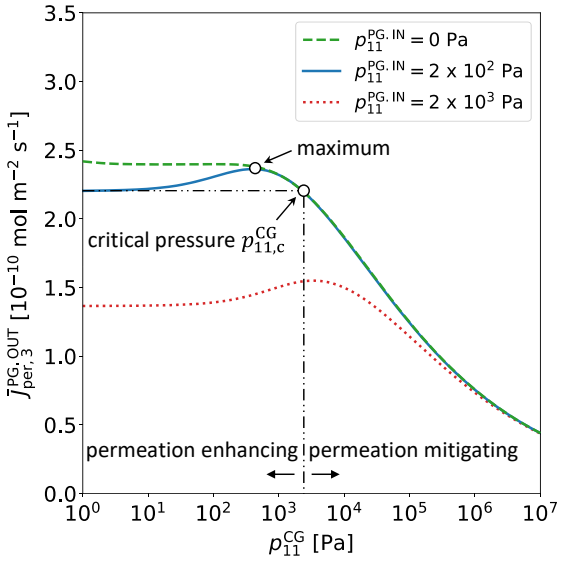

Fig. 5.17. Simulated steady state tritium permeation flux from the last purge gas segment of an HCPB fuel pin into the coolant outlet channel for different $^1H_2$ partial pressures at the purge gas inlet plotted against the partial pressure of $^1H_2$ gas added to the coolant. The plot indicates the $^1H_2$ partial pressure in the coolant which results in the maximum tritium permeation flux and the critical $^1H_2$ partial pressure in the coolant above which the permeation flux is effectively reduced.

gen transport parameters and therefore the protium permeation number are temperature dependent. Hence, it can be said the permeation flux mitigating effect of multi-isotopic permeation in endothermic hydrogen absorbing metals decreases with increasing temperature. This is not only true for isotope-limited permeation but for a co- and counter-permeation scenario.

5.3.4. Evaluation of co-/counter-permeation for tritium control in an HCPB BB

In the current design of the HCPB breeding blanket, it is planned that about 0.1 wt% of the total purge gas pressure will consist of $^1H_2$ gas, which corresponds to a partial pressure of about $p_{11}^{PG.IN} = 2 \times 10^2$ Pa [73]. The right-hand plot in figure 5.13 indicates that if no extra $^1H_2$ gas is added to coolant, the $^1H_2$ gas in the purge gas leads to a reduction in tritium permeation flux if the $^1H_2$ partial pressure in the purge gas satisfies the approximate condition $p_{11}^{PG.IN} > 1 \times 10^2$ Pa. This tendency can also be observed in figure 5.17 which shows the simulated tritium permeation flux from the last purge gas segment into the coolant outlet channel for different $^1H_2$ partial pressures in the purge gas plotted against the $^1H_2$ partial pressure in the coolant. The dashed curve is identical to the studied case of pure counter-permeation shown in the right-hand graph in figure 5.9. As expected from the co-permeation simulations presented in figure 5.13, figure 5.17 shows that at $p_{11}^{CG} = 1$ Pa, above values of $p_{11}^{PG.IN} > 1 \times 10^2$ Pa, the tritium permeation flux decreases with increasing $^1H_2$ partial pressure in the purge gas (compare solid blue line and red dotted line).

However, the purpose of the addition of $^1H_2$ gas to the purge gas is to trigger the release of tritiated molecules from the ceramic pebbles rather than to reduce the tritium permeation flux through co-permeation effects [78]. Hence, the $^1H_2$ partial pressure in the purge gas is a carefully chosen value that might have a relatively low degree of design freedom. For this reason, the further analysis considers the value $p_{11}^{PG.IN} = 2 \times 10^2$ Pa as the design pressure and focuses in particular on the consequences that an additional injection

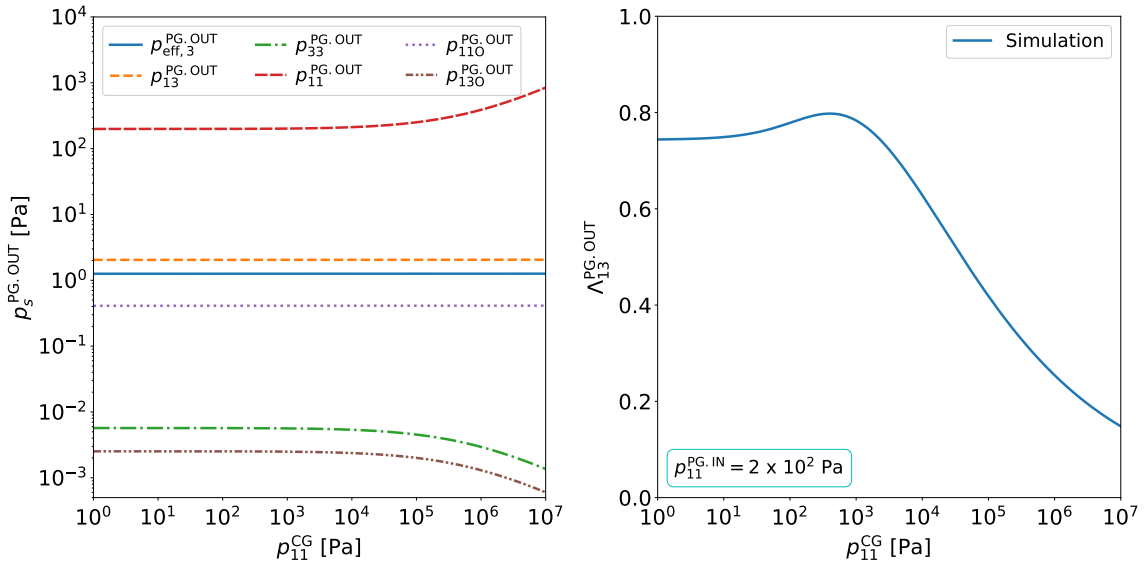

Fig. 5.18. [Left] Simulated partial pressures of different molecules that adjust in the purge gas outlet segment of the purge gas in a fuel pin plotted against the $^1H_2$ partial pressure in the coolant if $^1H_2$ gas with a partial pressure of $p_{11}^{\mathrm{PG.IN}} = 200\,\mathrm{Pa}$ is added to the purge gas. [Right] Simulated normalized multi-isotopic permeation flux factor plotted against the $^1H_2$ partial pressure in the coolant if $^1H_2$ gas with a partial pressure of $p_{11}^{\mathrm{PG.IN}} = 200\,\mathrm{Pa}$ is added to the purge gas.

of $^1H_2$ gas to the coolant has on the tritium permeation flux.

The simulation in figure 5.17 reveals that if $p_{11}^{\mathrm{PG.IN}} > 0\,\mathrm{Pa}$, adding $^1H_2$ gas to the coolant may have an enhancing or mitigating effect on the tritium permeation flux. When following the continuous curve in figure 5.17 towards higher $^1H_2$ partial pressures in the coolant the tritium permeation flux first increases. However, at a certain pressure, the tritium permeation flux exhibits a maximum before it decreases. As visible in figure 5.17, there is a critical value $p_{11,\mathrm{c}}^{\mathrm{CG}}$ above which the tritium permeation flux is reduced compared to a scenario in which the coolant is free from $^1H_2$ gas. In other words, for $p_{11}^{\mathrm{CG}} < p_{11,\mathrm{c}}^{\mathrm{CG}}$, an addition of $^1H_2$ gas to the coolant has a tritium permeation flux enhancing effect and for $p_{11}^{\mathrm{CG}} > p_{11,\mathrm{c}}^{\mathrm{CG}}$, it has a tritium permeation flux reducing effect.

The left-hand plot in figure 5.18 shows the simulated partial pressures that adjust in the last purge gas segment in steady state if $p_{11}^{\mathrm{PG.IN}} = 2 \times 10^2\,\mathrm{Pa}$. It can be seen that the effective tritium pressure in the purge gas shows no noticeable variation as the value of p_{11}^{CG} increases. For this reason, the particular shape of the tritium permeation flux for $p_{11}^{\mathrm{PG.IN}} = 2 \times 10^2\,\mathrm{Pa}$ can be exclusively traced back to multi-isotopic transport effects and not to a variation in effective tritium pressure [see equation (4.28)]. This finding is confirmed by the fact that the simulated curve of the multi-isotopic permeation flux factor $\Lambda_{13}^{\mathrm{PG.OUT}}$, which is plotted in the right-hand graph in figure 5.18, has an identical shape as the tritium permeation flux shown in figure 5.17.

The left-hand graph in figure 5.19 shows the dissociation and the recombination fluxes at the purge gas interface of the outer Eurofer'97 wall plotted against the $^1H_2$ partial

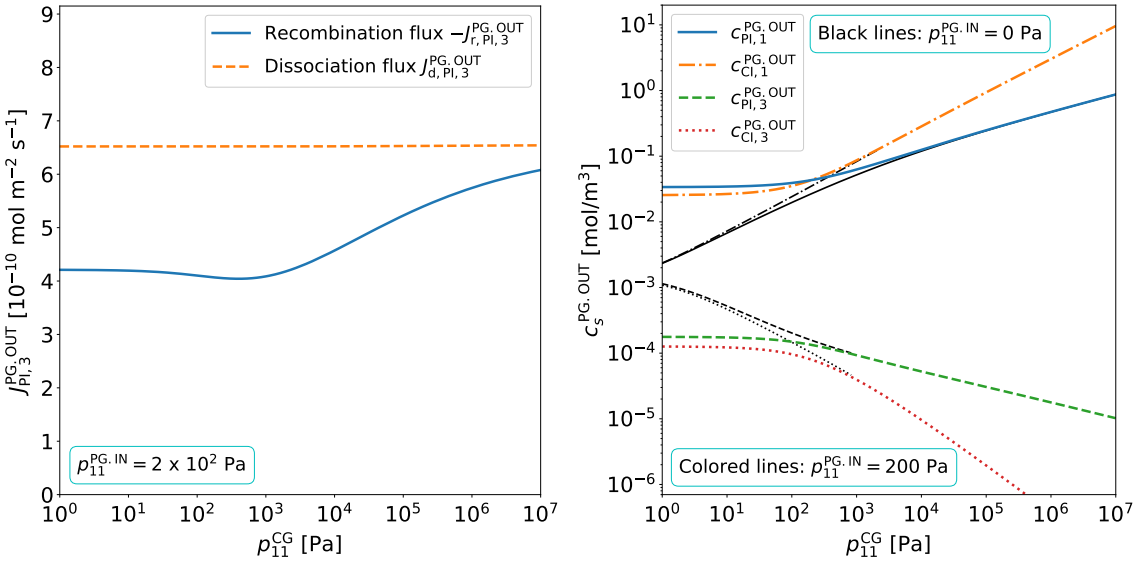

Fig. 5.19. [Left] Simulated tritium recombination flux and dissociation flux at the purge gas interface of the outer wall in the last purge gas segment of an HCPB fuel pin plotted against the $^1H_2$ partial pressure in the coolant for a case in which $^1H_2$ gas with a partial pressure of $p_{11}^{PG.IN} = 2{\times}10^2$ Pa is added to the purge gas. [Right] Simulated protium and tritium concentrations at the purge gas interface and the coolant gas interface in the outer Eurofer'97 wall of the last purge gas segment of an HCPB fuel pin plotted against the $^1H_2$ partial pressure in the coolant. The colored thick lines refer to a case in which $p_{11}^{PG.IN} = 2 \times 10^2$ Pa. For comparison, the black lines represent the pure counter-permeation case of the right-hand plot in figure 5.11 where $p_{11}^{PG.IN} = 0$ Pa.

pressure in the coolant. Since the effective tritium pressure in the purge gas is unchanged throughout the entire visualized pressure range of p_{11}^{CG}, the dissociation flux $J_{d,PI,3}^{PG.OUT} = 2\sigma k_{d,33} p_{eff,3}^{PG.OUT}$ at the purge gas interface remains constant. Consequently, according to the equations (4.16) and (4.24) the courses of the multi-isotopic permeation flux factor and the tritium permeation flux are fully determined by the tritium recombination flux into the purge gas $J_{r,PI,3}^{PG.OUT} \approx -\sigma k_{r,13} c_{PI,1}^{PG.OUT} c_{PI,3}^{PG.OUT}$ or more precisely by the product of the protium and tritium concentrations at the purge gas interface.

The right-hand graph in figure 5.19 depicts the protium and tritium purge gas and coolant gas interface concentrations plotted against the $^1H_2$ partial pressure in the coolant. It reveals that in a case where $p_{11}^{PG.IN} = 2 \times 10^2$ Pa, the tritium interface concentrations at $p_{11}^{CG} = 1$ Pa are significantly lower compared to a pure counter-permeation scenario (shown by the thin black lines). This is due to the fact that at very low $^1H_2$ partial pressures in the coolant, the existence of $^1H_2$ gas in the purge gas creates an almost pure co-permeation scenario. Hence, the observed tritium interface concentrations at $p_{11}^{CG} = 1$ Pa in the right-hand graph in figure 5.19 are consistent with the observed decrease in the interface concentration $c_{PI,3}^{PG.OUT}$ shown in the right-hand plot in figure 5.15 at $p_{11}^{PG.IN} = 2{\times}10^2$ Pa (see dash-dot-dotted lines). Nevertheless, the right-hand graph in figure 5.19 reveals that eventually, with growing p_{11}^{CG}, the tritium interface concentrations reduce. At higher values of p_{11}^{CG} they converge against the corresponding curves of the pure counter-permeation

case which are drawn in figure 5.19 with black thin lines.

In contrast, the protium purge gas and coolant interface concentrations increase with p_{11}^{CG}. Due to the presence of $^1H_2$ gas in the purge gas, at $p_{11}^{\mathrm{CG}} = 1\,\mathrm{Pa}$ the protium interface concentrations are significantly higher compared to a case of pure counter-permeation and are equal to those indicated by the dash-dot-dotted lines in the right-hand graph in figure 5.15. The protium purge gas interface concentrations continuously increase. At $p_{11}^{\mathrm{CG}} = p_{11}^{\mathrm{PG.IN}}$ both concentrations intercept and match the equilibrium concentration $c_{\mathrm{PI},1}^{\mathrm{PG.OUT}} = c_{\mathrm{CI},1}^{\mathrm{PG.OUT}} = c_{\mathrm{eq},1}^{\mathrm{PG.OUT}}$. Here, the protium isotopes are in thermodynamic equilibrium with the metal bulk and the gas phases. At higher pressures $p_{11}^{\mathrm{CG}} > p_{11}^{\mathrm{PG.IN}}$ the values of $c_{\mathrm{PI},1}^{\mathrm{PG.OUT}}$ and $c_{\mathrm{CI},1}^{\mathrm{PG.OUT}}$ converge against their corresponding curves in the case of a pure counter-permeation scenario (see thin black lines).

It is found that at partial pressures p_{11}^{CG} below a certain value, the decrease in $c_{\mathrm{PI},3}^{\mathrm{PG.OUT}}$ occurs at a higher rate than the increase in $c_{\mathrm{PI},1}^{\mathrm{PG.OUT}}$. This is why at lower $^1H_2$ partial pressures in the coolant the product of the protium and tritium purge gas interface concentrations, and hence the tritium recombination flux into the purge gas decreases. However, at partial pressures p_{11}^{CG} above a certain value, the increase in $c_{\mathrm{PI},1}^{\mathrm{PG.OUT}}$ prevails and the product of the protium and tritium purge gas interface concentrations increases. For this reason, the simulated tritium recombination flux at the purge gas interface forms a minimum at a pressure where the tritium permeation flux in figure 5.17 exhibits a maximum. It is important to note that the maximum of the tritium permeation flux occurs at a $^1H_2$ partial pressure in the coolant which satisfies the condition $p_{11}^{\mathrm{CG}} > p_{11}^{\mathrm{PG.IN}}$, but certainly not the condition $p_{11}^{\mathrm{CG}} = p_{11}^{\mathrm{PG.IN}}$.

Figure 5.17 reveals that if the $^1H_2$ partial pressure in the purge gas is increased from $p_{11}^{\mathrm{PG.IN}} = 2\times10^2\,\mathrm{Pa}$ to $p_{11}^{\mathrm{PG.IN}} = 2\times10^3\,\mathrm{Pa}$ the observed maximum of the tritium permeation flux shifts to higher $^1H_2$ partial pressures in the coolant. This implies that in comparison with the situation in which $p_{11}^{\mathrm{PG.IN}} = 2\times10^2\,\mathrm{Pa}$ it would require adding more $^1H_2$ gas to the coolant to achieve a tritium mitigating effect through counter-permeation effects. Nevertheless, when examining figure 5.17, it can be seen that above $p_{11}^{\mathrm{PG.IN}} > 1\times10^2\,\mathrm{Pa}$, an increase of the partial pressure of $^1H_2$ in the purge gas leads to a much more effective reduction of the tritium permeation flux due to co-permeation effects than an addition of $^1H_2$ gas to the coolant would have due to counter-permeation effects.

By analyzing multi-isotopic permeation in the last purge gas segment of an HCPB fuel pin it was possible to validate the findings and derived algebraic formulas for co-, counter-, and isotope-limited permeation presented in section 4.1. In addition, the reason why a situation where $^1H_2$ gas is simultaneously present in the purge gas and the coolant flow can lead to either an increase or a decrease in the tritium permeation flux has been uncovered. At this point, the focus of is directed to the evaluation of multi-isotopic permeation as a potential tritium mitigation method in an HCPB breeding blanket. Therefore, a parametric study is performed in which the $^1H_2$ partial pressures in the coolant and the purge gas are varied considering two different purge gas mass flow rates.

Case A: Purge gas mass flow rate of 0.5 kg/s

At first, like in the previous simulations, the purge gas mass flow rate is assumed to be $\dot{m}_{\mathrm{PG}} = 5 \times 10^{-1}\,\mathrm{kg\,s^{-1}}$ which is the current HCPB mass flow rate design value [71]. The simulated average effective tritium pressures $\langle p \rangle_{\mathrm{eff},3}^{\mathrm{PG}}$ that adjusts in the purge gas flow through the fuel pins plotted against the $^1H_2$ partial pressure in the coolant is presented in the top left-hand plot in figure 5.20. The curves shown refer to different partial pressures of added $^1H_2$ gas to the purge gas inlet. It can be seen that except for a case in which $p_{11}^{\mathrm{PG.IN}} = 1\,\mathrm{Pa}$ the adjusting effective tritium pressures are very close to $p_{\mathrm{eff},3}^{\mathrm{PG}} \approx 1\,\mathrm{Pa}$. This value conforms with the simulations performed in [232].

At this point, the focus is no longer just on the permeation process happening in the outer wall of the last purge gas segment in a fuel pin, but on the permeation process occurring in a fuel pin as a whole. Therefore, the investigation now concentrates on the average tritium permeation flux $\left\langle \overline{J} \right\rangle_{\mathrm{per},3}$ in a fuel pin from the purge gas into the coolant gas, averaged along the lengths of the inner and outer Eurofer'97 walls. In the right-hand plot in figure 5.17, the simulated average tritium permeation flux from the purge gas into the coolant is plotted in a three-dimensional graph against the partial pressure of the added $^1H_2$ gas to the purge gas inlet (x-axis) and the coolant gas (y-axis).

It is important to note that the plotted average tritium permeation flux values are based on the assumption of a continuous release of $^1H^3H$ and $^1H^3HO$ molecules from the ceramic pebble beds with a total ^3H release rate of $1.23 \times 10^{-8}\,\mathrm{mol\,s^{-1}}$ per fuel pin ($3.20 \times 10^{-1}\,\mathrm{kg/day}$ in the whole breeding blanket). In the model, this value is assumed to be the same, regardless of the $^1H_2$ partial pressure in the purge gas. It is to expect that at very low $^1H_2$ partial pressures in the purge gas the chemical reactions (5.20) and (5.21) would be suppressed leading to a reduced ^3H release rate from the pebble surfaces. This would go along with lower effective tritium pressures in the fuel pins and hence a decreased tritium permeation flux to the coolant. Nevertheless, assuming the maximum possible ^3H release rate from the pebbles (the ^3H generation rate) independent of the value of $p_{11}^{\mathrm{PG.IN}}$ allows obtaining rather conservative simulation results.

In the presented three-dimensional plot in figure 5.20 the average tritium permeation flux values, which belong to the purest co- and counter-permeation scenarios, are those lines in the plotted flux surface which are colored in yellow and red, respectively. The corresponding flux values are slightly lower than those calculated for a permeation process from the last purge gas segment into the coolant outlet channel shown in the figures 5.9 and 5.13. This is because the thicknesses of the inner and outer Eufofer'97 walls differ. Furthermore, due to the spatial expansion of the pebble bed along the purge gas flow in a fuel pin, the effective tritium pressure is lower in purge gas segments closer to the purge gas inlet.

It can be seen that regardless of the chosen $^1H_2$ partial pressure in the coolant, increasing the $^1H_2$ partial pressure in the purge gas leads to a reduction in the average tritium permeation flux into the coolant. The graph reveals that in a range $p_{11}^{\mathrm{CG}} < 1{\times}10^3\,\mathrm{Pa}$ increasing

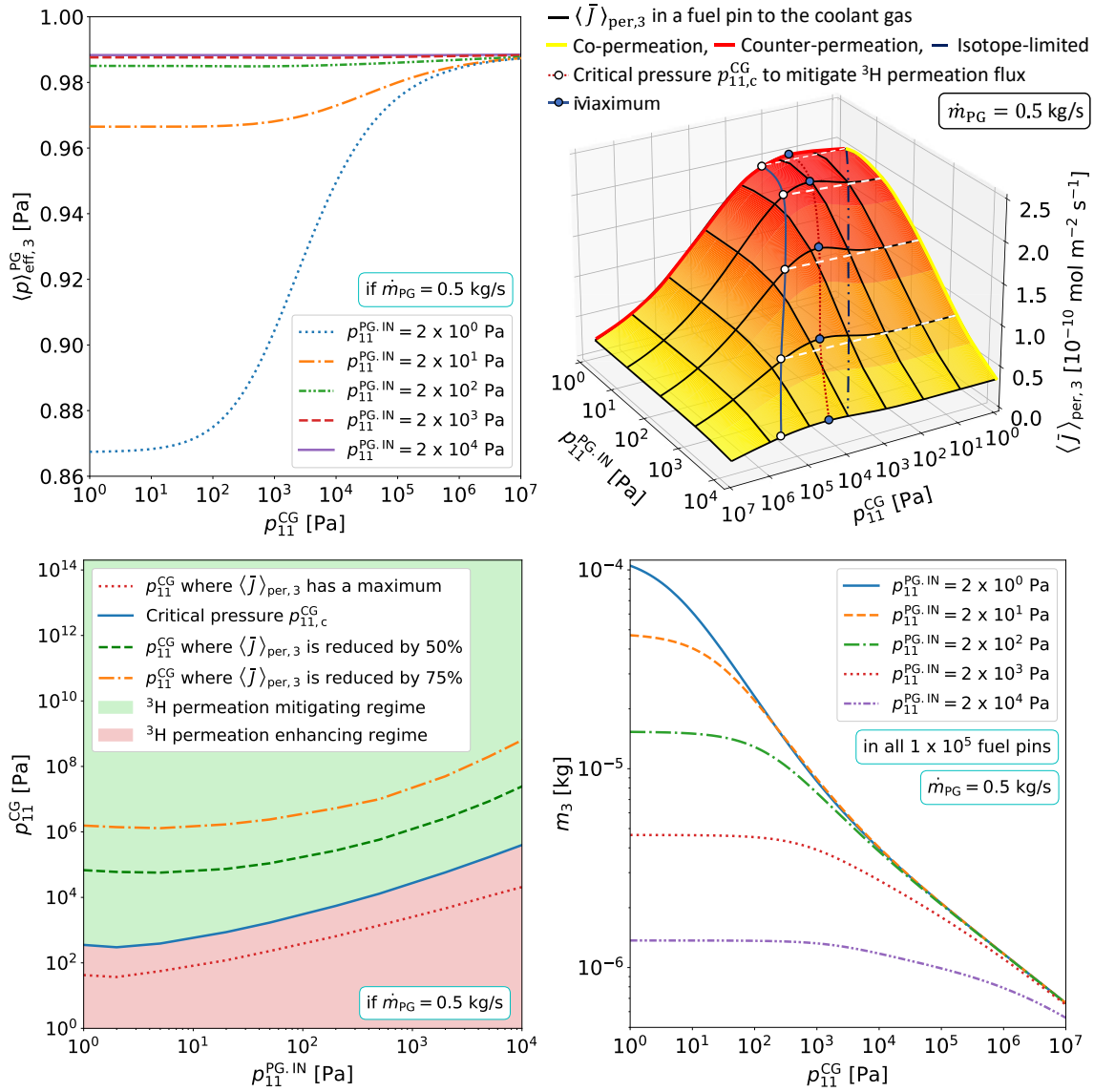

Fig. 5.20. [Top left] Simulated effective tritium pressure in the purge gas flow of an HCPB fuel pin averaged along the length of a fuel pin for different partial pressures of added $^1H_2$ gas to the purge gas. It is plotted against the partial pressure of added $^1H_2$ gas to the coolant. [Top right] Simulated average steady state tritium permeation flux from the purge gas into the coolant in an HCPB fuel pin plotted against the partial pressure of added $^1H_2$ gas to the purge gas and the coolant gas. [Lower left] Simulated critical $^1H_2$ gas pressures in the coolant with different consequences for the tritium permeation flux into the coolant of an HCPB fuel pin. It is plotted against the $^1H_2$ partial pressure in the purge gas. [Lower right] Simulated total mass of tritium absorbed in the inner and outer Eurofer'97 walls of all 1×10^5 fuel pins of an HCPB breeding blanket. The simulations are performed assuming that $\dot{m}_{PG} = 5 \times 10^{-1}$ kg s^{-1}.

the $^1H_2$ partial pressure in the purge gas from $p_{11}^{PG.IN} = 1$ Pa to $p_{11}^{PG.IN} = 1 \times 10^2$ Pa reduces the tritium permeation flux by approximately 25 %. An injection of $p_{11}^{PG.IN} = 1 \times 10^3$ Pa to the purge gas leads to a reduction of about 60 % and if $p_{11}^{PG.IN} = 1 \times 10^4$ Pa the permeation flux mitigation even reaches 85 %. Due to this finding, it can be said that, as long as it is technically feasible, increasing the $^1H_2$ partial pressure in the purge gas from the planned

$p_{11}^{\mathrm{PG.IN}} = 2 \times 10^2$ Pa to $p_{11}^{\mathrm{PG.IN}} = 1 \times 10^3$ Pa or higher would be a recommendable design change and could effectively mitigate the tritium permeation flux to the coolant. Therefore, this numerical investigation identifies an addition of $^1H_2$ gas to the purge gas as a reasonable tritium permeation mitigation method for HCPB breeding blankets.

The dash-dot-dotted dark-blue line in the three-dimensional plot indicates the path of the tritium permeation flux in an isotope-limited scenario in which the $^1H_2$ partial pressures at the purge gas inlet and in the coolant are equal. It can be seen that the curve of the isotope-limited case runs over a slightly elevated part of the plotted permeation flux surface in comparison with the yellow line of the co-permeation curve. This fact and its inclination relative to the yellow co-permeation curve explain the similar but less effective permeation flux-reducing effect of an isotope-limited case in comparison with a pure co-permeation scenario, as it was predicted in the right-hand plot in figure 4.3.

As expected from the analysis of figure 5.17, by observing the change in tritium permeation flux in the direction of the p_{11}^{CG}-axis it is found that for elevated $^1H_2$ partial pressure in the purge gas, the tritium permeation flux first rises, runs through a maximum before it decreases. The formation of the maximum has the same explanation as the maximum observed in figure 5.17, which was discussed above. The position of the maximum is marked with blue circles and a red dotted line in the top right-hand plot in figure 5.20. The same red dotted line is drawn in the lower left-hand graph in figure 5.20 which is a projection of the three-dimensional plot onto the pressure plane. This line stands for the $^1H_2$ partial pressure in the coolant that causes the highest possible tritium permeation flux for a fixed value of $p_{11}^{\mathrm{PG.IN}}$. It is evident that for a safe operation of an HCPB breeding blanket, the $^1H_2$ partial pressure configuration in the purge gas and the coolant indicated by the red dotted line should be avoided under all circumstances. The critical pressure $p_{11,\mathrm{c}}^{\mathrm{CG}}$ in the coolant above which the tritium permeation flux sinks below its value at $p_{11,\mathrm{c}}^{\mathrm{CG}} = 0$ Pa (see figure 5.17) is marked in the top right-hand and lower left-hand graph in figure 5.20 with a solid blue line. It can be said that for a fixed $^1H_2$ partial pressure in the purge gas, an injection of $^1H_2$ gas to the coolant only has a permeation mitigating effect if its partial pressure lays in the green shaded area shown in the lower left-hand graph in figure 5.20. Only then would an injection of $^1H_2$ to the coolant lead to a further reduction in tritium permeation flux on top of the already achieved mitigation due to the presence of $^1H_2$ gas in the purge gas. As the lower left-hand graph reveals, if the chosen $^1H_2$ partial pressure in the purge gas is $p_{11}^{\mathrm{PG.IN}} = 2 \times 10^2$ Pa, a 50 % reduction in tritium permeation flux caused by the injection of $^1H_2$ gas into the coolant would require at least a partial pressure of about $p_{11}^{\mathrm{CG}} \approx 1 \times 10^5$ Pa. The risks and technological challenges connected to such a high $^1H_2$ partial pressure might overweight the benefits. Especially since the same reduction in permeation flux could be achieved at $p_{11}^{\mathrm{CG}} = 0$ Pa by increasing the $^1H_2$ partial pressure in the purge gas from $p_{11}^{\mathrm{PG.IN}} = 2 \times 10^2$ Pa to merely $p_{11}^{\mathrm{PG.IN}} \approx 2 \times 10^3$ Pa instead (see top right-hand plot in figure 5.20).

The lower right-hand graph shows the total mass of tritium dissolved in the inner and outer Eurofer'97 walls in all 1×10^5 fuel pins of the HCPB breeding blanket plotted

against the $^1H_2$ partial pressure in the coolant. The mass of dissolved tritium is simulated and plotted for different $^1H_2$ partial pressures in the purge gas. The decrease in tritium mass dissolved in the Eurofer'97 walls with increasing $^1H_2$ partial pressures in the purge gas or the coolant is due to the predicted decrease in tritium concentration in the presence of protium which was discussed in section 4.1. It is found that injecting $^1H_2$ gas to the purge gas leads to a stronger reduction in tritium content than an injection of the same partial pressure of $^1H_2$ gas to the coolant. This is attributed to the fact that according to the right-hand plot in figure 5.11 and the right-hand graph in figure 5.15 the tritium purge gas interface concentration declines stronger in a co-permeation process than in a counter-permeation process while the decrease in coolant interface concentration is approximately equal. Therefore, in addition to a reduction in coolant contamination by tritium, increasing the $^1H_2$ partial pressure in the coolant or the purge gas could be considered as a method to reduce the exposure of the metal lattice of the Eurofer'97 structural material to the beta radiation of dissolved tritium and thus to reduce radiation damage. In addition, a smaller tritium content in the structural material lowers the amount of tritium-containing material which would escape into the environment in case of an accident.

Case B: Purge gas mass flow rate of 0.05 kg/s

To continue the parameter study it is now analyzed how the effect of multi-isotopic transport on the tritium permeation flux in a fuel pin changes when moving to higher effective tritium pressures in the purge gas. This is important in case it is planned to reduce the purge gas mass flow rate. The top left-hand plot in figure 5.21 shows the simulated average steady state effective tritium pressure adjusting in the purge gas flow through a fuel pin if the design purge gas mass flow rate was reduced by a factor ten to $\dot{m}_{\mathrm{PG}} = 5\times10^{-2}\,\mathrm{kg\,s^{-1}}$. It is found that at elevated $^1H_2$ partial pressures in the purge gas the simulated effective tritium pressures are about ten times higher compared to those visible in figure 5.20. At lower $^1H_2$ partial pressures in the purge gas of $p_{11}^{\mathrm{PG}} \approx 2\,\mathrm{Pa}$ and $p_{11}^{\mathrm{PG}} \approx 2\times10^{1}\,\mathrm{Pa}$, the increase in adjusting effective tritium pressure is merely eight and nine-fold, respectively. The three-dimensional plot in figure 5.21 shows an increment in simulated tritium permeation flux values which almost exactly matches the increase in effective tritium pressure compared to figure 5.20. This partially explains the difference in shape between the plateau areas of the plotted flux surfaces in the figures 5.20 and 5.21.

In addition to that, it is observed that in contrast to the 3D plot in figure 5.20 even at very low $^1H_2$ partial pressures of $p_{11}^{\mathrm{PG.IN}} \approx 1\,\mathrm{Pa}$ the permeation flux runs through a pronounced maximum when increasing the $^1H_2$ partial pressure in the coolant. This is explained by the fact that according to figure 5.8, at a higher effective tritium pressure of about $p_{\mathrm{eff},3}^{\mathrm{PG}} \approx 10\,\mathrm{Pa}$, for pressures $p_{kk}^{\mathrm{PG}} \approx p_{kk}^{\mathrm{CG}} \approx 0\,\mathrm{Pa}$ the tritium permeation processes through both the inner and outer Eurofer'97 walls are no longer surface-limited and therefore the permeation fluxes approach smaller values than those given by the equations (4.29) and (4.13). The formation of the maximum at $p_{11}^{\mathrm{PG.IN}} \approx 1\,\mathrm{Pa}$ can be explained

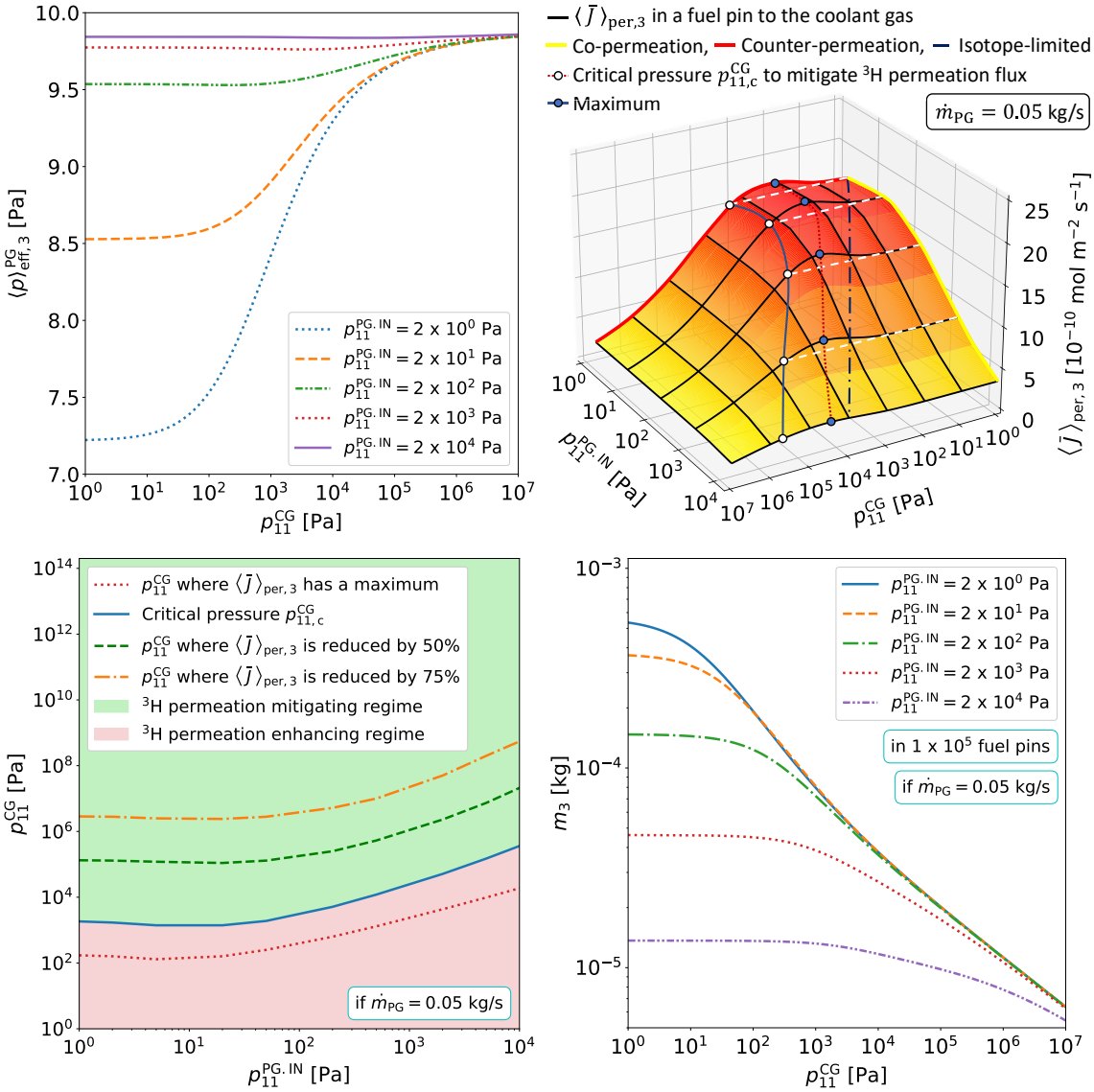

Fig. 5.21. [Top left] Simulated effective tritium pressure in the purge gas flow of an HCPB fuel pin averaged along the length of a fuel pin for different partial pressures of added $^1H_2$ gas to the purge gas. It is plotted against the partial pressure of added $^1H_2$ gas to the coolant. [Top right] Simulated average steady state tritium permeation flux from the purge gas into the coolant gas of an HCPB fuel pin plotted against the partial pressure of added $^1H_2$ gas to the purge gas and to the coolant gas. [Lower left] Simulated critical $^1H_2$ gas pressures in the coolant with different consequences for the tritium permeation flux into the coolant of an HCPB fuel pin. It is plotted against the $^1H_2$ partial pressure in the purge gas. [Lower right] Simulated total mass of tritium absorbed in the inner and outer Eurofer'97 walls of all 1×10^5 fuel pins of an HCPB breeding blanket. The simulations are performed assuming that $\dot{m}_{PG} = 5 \times 10^{-2}\,\mathrm{kg\,s^{-1}}$.

by the fact that when moving from higher to lower $^1H_2$ partial pressures in the coolant, the permeation flux first approaches the equations (4.29) and (4.13) as long as the condition $c_{PI,k} \gg c_{PI,i}$ is satisfied before it declines towards its lower value at $p_{kk}^{CG} = 0\,\mathrm{Pa}$ corresponding the non-surface-limited tritium permeation regime (see figure 5.8).

Next, the plotted graphs in the lower left corners of the figures 5.20 and 5.21 are compared. It can be seen that at a slower purge gas mass flow rate, and thus at a higher adjusting effective tritium pressure, both the maximum of the plotted tritium permeation flux surface and the critical $^1H_2$ partial pressure, above which an addition of $^1H_2$ into the coolant mitigates the tritium permeation flux, shift to slightly higher values of p_{11}^{CG}. This finding can be explained by the fact that at higher effective tritium pressures higher $^1H_2$ partial pressures are required to satisfy the condition $c_{PI,k} \gg c_{PI,i}$. This condition must be met such that the presence of protium considerably increases the tritium recombination flux back into the purge gas and thus decreases the permeation flux into the coolant [see equation (4.1)].

Furthermore, it is found that at a slower purge gas mass flow rate, the simulated masses of dissolved tritium in the Eurofer'97 walls of all fuel pins are increased by approximately the same factors as the effective tritium pressures (see lower right plot in figure 5.21).

In summary, the same conclusions regarding the effectiveness of co- and counter-permeation as a tritium permeation flux mitigation method apply even when the purge gas mass flow rate is reduced and the setting effective tritium pressures are significantly higher than those that could be drawn for the analyzed higher purge gas mass flow rate in case A.

Case C: Addition of steam to the purge gas

Finally, the tritium permeation mitigating effect of co- and counter-permeation is compared with the consequences of an additional injection of steam (^1H_2O) to the purge gas. Therefore, the average steady state tritium permeation flux into the coolant flow of a fuel pin is plotted as a function of the partial pressure of ^1H_2O gas at the purge gas inlet. It is shown in the left-hand graph in figure 5.22. This simulation again considers the design value of the purge gas mass flow rate of $\dot{m}_{PG} = 5 \times 10^{-1}\,\mathrm{kg\,s^{-1}}$ and is executed for three different partial pressures of added $^1H_2$ gas at the purge gas inlet. The plot reveals that the tritium permeation flux drastically decreases with growing ^1H_2O partial pressure in the purge gas. When comparing the observed decline in tritium permeation flux with the three-dimensional plot in figure 5.20 one can say that according to the simulation, an increase in ^1H_2O partial pressure in the purge gas has an even stronger tritium mitigating effect than an addition of $^1H_2$ gas to the purge gas or the coolant.

To reveal the origin of this effect it is looked at the right-hand plot in figure 5.22 which depicts the adjusting average partial pressures of the different hydrogen isotope-containing molecules in the purge gas flow of the fuel pins plotted against the partial pressure of steam at the purge gas inlet for the case in which $p_{11}^{PG.IN} = 1 \times 10^2\,\mathrm{Pa}$ (see solid blue line). It can be seen that with a growing value of $p_{11O}^{PG.IN}$ the $^1H^3HO$ partial pressure increases while the $^3H_2$ and $^1H^3H$ partial pressures plunge. The reason for this to happen is that due to an increased concentration of ^1H_2O molecules in the purge gas the chemical reaction (5.24) occurs at a higher rate. As a result, the consumption of $^1H^3H$

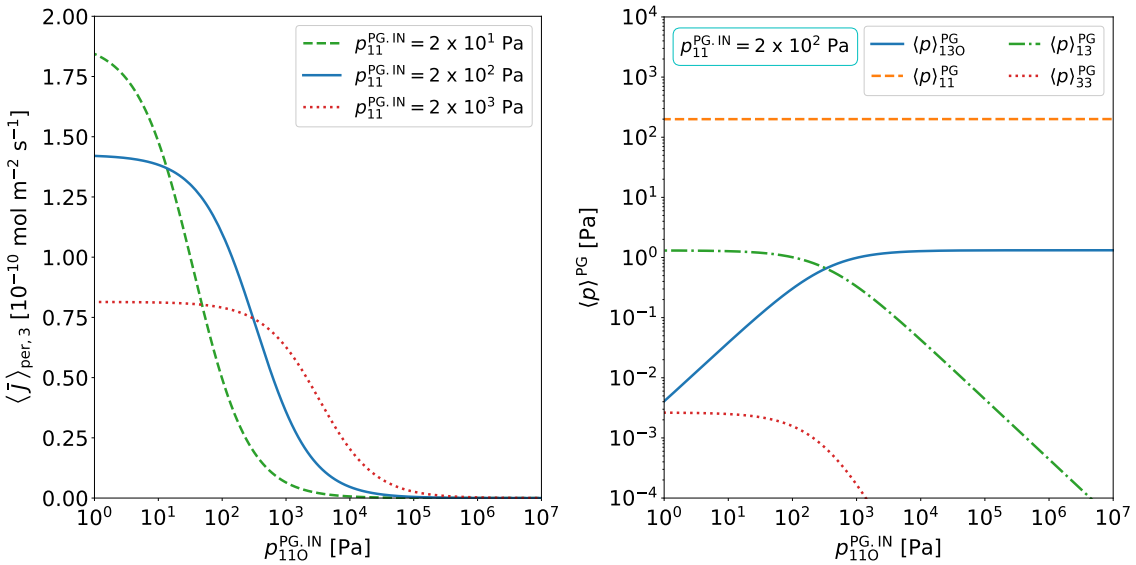

Fig. 5.22. [Left] Simulated average steady state atomic tritium permeation flux from the purge gas into the coolant of an HCPB fuel pin plotted against the partial pressure of ^1H_2O steam added to the purge gas. The simulations are performed for different partial pressures of $^1H_2$ gas that is additionally added to the purge gas. [Right] Simulated average partial pressures of the different hydrogen isotope-containing molecules in an HCPB fuel pin plotted against the partial pressure of added ^1H_2O steam, if the partial pressure of additionally added $^1H_2$ gas to the purge gas is $p_{11}^{PG.IN} = 1 \times 10^2$ Pa. The simulations assume that $\dot{m}_{PG} = 5 \times 10^{-1}$ kg s^{-1}.

molecules and the formation $^1H^3HO$ and $^1H_2$ molecules increases. The reduced number of $^1H^3H$ molecules suppresses reaction (5.23) which leads to the formation of less $^3H_2$. Eventually, the tritium mitigating effect of an ^1H_2O injection to the purge gas arises from the observed intense reduction in effective tritium pressure in the purge gas.

If the $^1H_2$ partial pressure in the purge gas is higher, as it is the case for the red dotted curve in the left-hand plot in figure 5.22, the intensified co-permeation effect leads to an overall reduction in tritium permeation flux. For the same reason, if the $^1H_2$ partial pressure in the purge gas is lower, the tritium permeation flux is higher, as shown by the orange dashed line. However, it is also observed that an increased $^1H_2$ partial pressure in the purge gas reduces the tritium permeation flux-reducing effect of steam addition to the purge gas. This is because increasing the concentration of $^1H_2$ molecules in the purge gas leads to an increased formation of $^1H^3H$ molecules through the chemical reaction (5.24) which increases the tritium effective pressure and thus the tritium permeation flux.

5.4. Modeling of multi-isotopic permeation in a WCLL breeding blanket

As described in section 1.2.3, the water-cooled pebble bed (WCLL) breeding blanket is characterized by a liquid PbLi fluid flow as the tritium breeding material. Figure 5.23 shows a close-up section-cut of a three-dimensional CAD model of the breeding zone in an elementary WCLL cell. It is shown from a different angle in figure 1.12. The

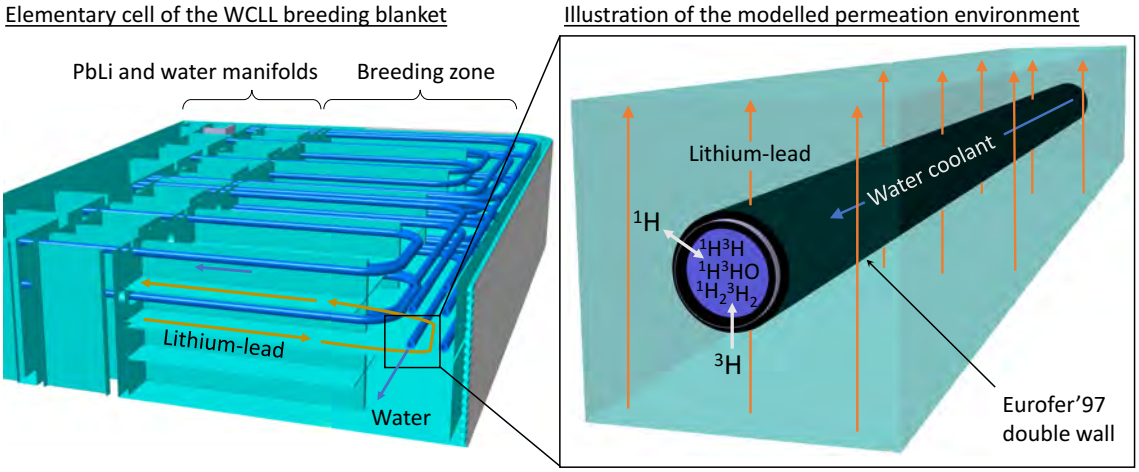

Fig. 5.23. [Left] Section cut of the breeder zone in an outboard elementary cell of the WCLL breeding blanket. [Right] Illustration of a water cooling pipe in the breeder zone, overflown by the liquid PbLi flow.

inboard and outboard segments of the 16 toroidally arranged blanket sectors of the WCLL breeding blanket are made of a large number of stacked elementary cells surrounding the plasma. Hot liquid PbLi enters the breeding zone from the inlet PbLi manifold. It flows through radially arranged rectangular channels towards the plasma-facing first wall where it rises and reverses its flow direction back into the PbLi outlet manifold (see orange arrows). Despite the occurring exothermic lithium spallation reactions, it is expected that the PbLi flow in the breeding zone remains approximately isothermal at roughly $T = 600\,\mathrm{K}$ [233]. As shown in the 3D drawing, the PbLi flow is penetrated by U-shaped coolant water pipes. The water temperature ranges from approximately $T = 570\,\mathrm{K}$ at the water inlet to $T = 600\,\mathrm{K}$ at the water outlet of the breeding zone [234]. The current WCLL design envisages water pipes with an inner radius of $r_{\mathrm{in}} = 8 \times 10^{-3}\,\mathrm{m}$. The water is separated from the PbLi stream by a Eurofer'97 double wall with a welded $1 \times 10^{-4}\,\mathrm{m}$ thick α-iron (α-Fe) layer in between (see the right-hand image in figure 5.23). At both sides of the interlayer, the Eurofer'97 walls have a designed thickness of $1.33 \times 10^{-3}\,\mathrm{m}$. This results in a total pipe wall thickness of $d_{\mathrm{pipe}} = 2.75 \times 10^{-3}\,\mathrm{m}$ with the outer radius being $r_{\mathrm{out}} = 1.08 \times 10^{-2}\,\mathrm{m}$.

In recent years, the Ciemat tritium modeling group has developed an EcosimPro© tritium transport model of the WCLL breeding blanket for DEMO at system level, taking into account many details of its complexity [235]. This includes the specific geometry of the breeder and coolant fluid cycles as well as the tritium extraction and coolant purification systems. The model enables calculating the accumulation of generated tritium in the PbLi, dependent on the distance from the first wall and the duration of the plasma pulses of the tokamak. Some model outcomes based on different parameter sets are presented in [232]. It was found that by assuming an efficiency of the tritium extraction system of 80 % the adjusting steady state tritium concentration in the breeding zone oscillates around a value of approximately $c_{\mathrm{CF,3}}^{\mathrm{PbLi}} \approx 1.4 \times 10^{-2}\,\mathrm{mol\,m^{-3}}$ in the PbLi core flow.

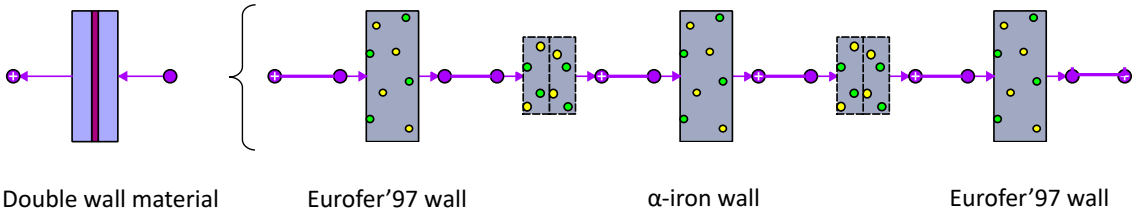

Fig. 5.24. EcosimPro© inner component structure of the double wall material component used to simulate the water pipe wall in a WCLL elementary cell.

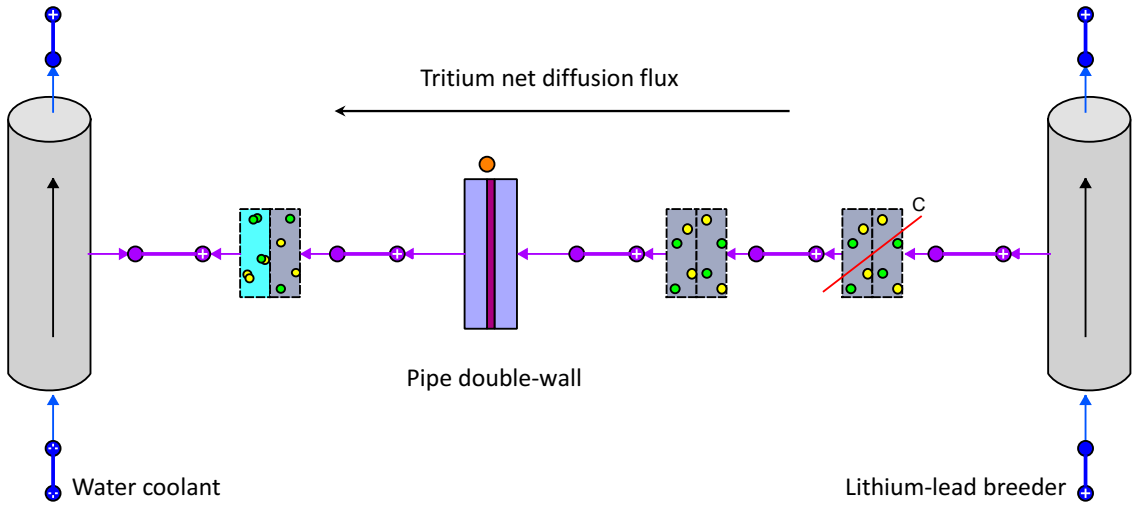

Fig. 5.25. EcosimPro© component flow chart of the examined permeation environment which represents a section of a water cooling pipe inside of the breeder unit in an elementary cell of a WCLL breeding blanket.

For the analysis of multi-isotopic transport effects on tritium permeation into the water coolant, this study focuses on a one-meter-long section of a cooling pipe at the reversal point of the PbLi flow, near the first wall. As visible in figure 5.23, the cylinder axis of the considered pipe section is oriented perpendicular to the PbLi flow direction (see figure 5.23). An EcosimPro© model of the considered permeation environment is developed within the scope of this work. In the model, the Eurofer'97-iron-Eurofer'97 double wall is represented by a higher-order component shown in figure 5.24. It comprises three cylindrical wall material components whose diffusion ports are linked by metal-metal interface components. Via a gas-metal interface component, the double wall material component is connected to a cylindrical pipe flow component which represents the water flow through the pipe. The EcosimPro© component structure of the entire pipe section sitting inside of the PbLi flow is presented in figure 5.25. It can be seen that the PbLi flow around the pipe is described by another pipe flow component. Its free diffusion port is linked to a mass transfer interface component and a metal-metal interface component which together contain the physics of the PbLi boundary layer at the PbLi-Eurofer'97 interface. In contrast to the rather complex model developed for the analysis of the HCPB breeding blanket in section 5.3, the permeation process into the water pipe is modeled with only a single discretization node ($\mathcal{M} = 1$) in the directions of the water and the PbLi

flows. Moreover, in this model, the three wall material components of the double wall in figure 5.24 are each discretized into $\Omega = 30$ segments in diffusion direction.

Although in reality there will be a temperature gradient between the inlet and outlet port of a water coolant pipe in the breeder zone, the simulations in this work assume constant and equal temperatures of the PbLi and the water pipe of $T = 600\,\mathrm{K}$. As indicated by simulations in [81], the water mass flow rate in the cooling pipes will be of the order of $u_{\mathrm{water}} \approx 1\,\mathrm{m\,s^{-1}}$.

To calculate the forward and backward reaction rates (2.121) of reaction (5.24) proceeding in the water coolant the model requires information about the concentration of water molecules as an input value. It is calculated from steam tables [236] which, at the designed WCLL water coolant pressure of $p_{\mathrm{water}} = 1.55 \times 10^7\,\mathrm{Pa}$, report a water density of about $\rho^{\mathrm{w}}_{11\mathrm{O}} = 6.8 \times 10^2\,\mathrm{kg\,m^{-3}}$. It corresponds to an approximate concentration of water molecules of $c^{\mathrm{w}}_{11\mathrm{O}} = \rho^{\mathrm{w}}_{11\mathrm{O}}/M_{11\mathrm{O}} = 3.8 \times 10^4\,\mathrm{mol\,m^{-3}}$ where $M_{11\mathrm{O}} = 18.02 \times 10^{-3}\,\mathrm{kg\,mol^{-1}}$ is the molar mass of a water molecule. The reaction rate coefficients of both isotope exchange reactions (5.23) and (5.24) in the water are set to $k^{\mathrm{f,ex}}_{13+13} = k^{\mathrm{f,w}}_{\mathrm{IV},31} = 1 \times 10^5\,\mathrm{m^3\,s^{-1}\,mol^{-1}}$.

The considered velocity of the PbLi core flow around the water cooling pipes is taken from a fluid dynamic simulation performed by Urgorri *et al* in [237]. They found that the core velocity is highest close to the pipe walls where it takes values of approximately $u_{\mathrm{PbLi}} \approx 3 \times 10^{-3}\,\mathrm{m\,s^{-1}}$. Knowing the fluid velocities of the PbLi flow and the water flow enables calculating the volume flow rates F_{PbLi} and F_{w} which are necessary input values of the model to solve equation (5.2).

Another input quantity of the model is the mass transfer coefficient α_{MT} which appears in equation (5.5) as part of the mass transfer interface component. Al-Enezi *et al* experimentally determined the following relation for the mass transfer coefficient of a fluid flow around a single cylinder for Reynolds numbers $\mathrm{Re} < 500$ [238], [239].

$$\alpha_{\mathrm{MT}} = 1.71 \cdot u_{\mathrm{PbLi}} \mathrm{Re}^{-0.672} \mathrm{Sc}^{-0.67} \quad \left[\mathrm{m\,s^{-1}}\right] \tag{5.26}$$

Their data is in good agreement with the results of another experimental campaign which creates confidence to use their experimental relation for the simulations in this work. The Reynolds number Re and Schmidt number Sc of the PbLi flow around the pipe is calculated using the equations [238]

$$\mathrm{Re} = 2r_{\mathrm{out}} \cdot \frac{\rho_{\mathrm{PbLi}} u_{\mathrm{PbLi}}}{\varrho_{\mathrm{PbLi}}} \qquad \text{and} \qquad \mathrm{Sc} = \frac{\varrho_{\mathrm{PbLi}}}{\rho_{\mathrm{PbLi}} D_3^{\mathrm{PbLi}}}\,. \tag{5.27}$$

Here, D_3^{PbLi} is the diffusion coefficient of tritium in PbLi and ρ_{PbLi} the temperature-dependent density of eutectic liquid lithium lead. It can be estimated through relation [240]

$$\rho_{\mathrm{PbLi}} = 10.52 \times 10^3 \cdot \left(1 - 1.13 \times 10^{-4} \cdot T\right) \quad \left[\mathrm{kg\,m^{-3}}\right]. \tag{5.28}$$

In addition, the dimensionless numbers (5.27) are dependent on the dynamic viscosity

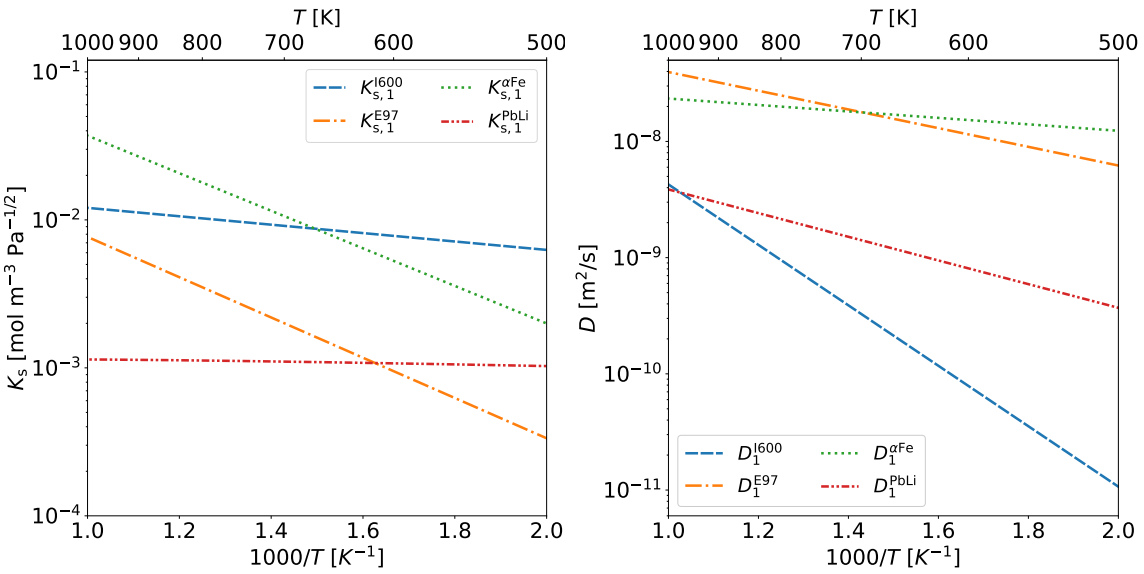

Fig. 5.26. [Left] Temperature dependencies of the Sieverts' constants of protium in different endothermic hydrogen-absorbing metals reported in the references [161], [223], [224]. [Right] Temperature dependencies of the diffusivities of protium in different endothermic hydrogen-absorbing metals reported in the references [161], [224], [225].

ϱ_{PbLi} which according to [241] may be calculated with the expression

$$\varrho_{\mathrm{PbLi}} = 1.87 \times 10^{-4}\,\mathrm{Pa\,s} \cdot \exp\left(\frac{11\,640\,\mathrm{J\,mol^{-1}}}{RT}\right). \tag{5.29}$$

5.4.1. Hydrogen isotopes in α-iron

Like in Eurofer'97, hydrogen isotopes are endothermically dissolved in the bcc lattice of α-iron. Therefore, its hydrogen absorption behavior is well described by the Sieverts' law. Eichenauer *et al* measured the Sieverts'constant of protium in α-iron [223], [242]. The experimental coefficients are shown in table 5.1. Since no specific solubility measurements of deuterium and tritium were performed, in this study the same Sieverts' constant of protium is assumed for all three hydrogen isotopes.

Furthermore, several experimental campaigns could measure the diffusion coefficient $D_1^{\alpha\mathrm{Fe}}$ of protium in α-iron [140], [225], [243]–[245]. As shown in [225], the measured results differ merely within the same order of magnitude. Since the measurements performed by Tahara *et al* cover exactly the temperature range relevant for breeding blanket applications $500\,\mathrm{K} < T < 1000\,\mathrm{K}$ it is decided to use their data for the calculations in this work [225], [242]. The corresponding Arrhenius coefficients are shown in table 5.1. Equation (2.66) is used to extrapolate the diffusion coefficients of the other hydrogen isotopes.

Figure 5.26 presents the considered relations of $D_1^{\alpha\mathrm{Fe}}(T)$ and $K_{s,1}^{\alpha\mathrm{Fe}}(T)$ plotted against temperature. For comparison, the graphs contain the corresponding plots of the Eurofer'97-

hydrogen system based on the coefficients listed in table 5.1. The fact that the Sieverts' constants of both metals increase with temperature is an indication of their endothermic hydrogen-absorbing nature. The plots reveal that hydrogen isotopes have a higher solubility in α-iron than in Eurofer'97, but a very similar diffusivity. Therefore, the permeability of hydrogen isotopes in α-iron is higher than in Eurofer'97 [see equation (2.143)].

5.4.2. Hydrogen isotopes in PbLi

In eutectic lead lithium a slight variation of the lithium content seems to have a great influence on its hydrogen transport and absorption characteristics [82]. This may be traced back to the strong exothermic nature of lithium as a hydrogen isotope absorber and is a possible explanation for why the Sieverts' constants that could be measured for PbLi scatter over several orders of magnitude [82]. However, because of the large fraction of lead in the eutectic alloy, it is found that PbLi rather behaves like an endothermic hydrogen-absorbing metal in which the relevant part of the PCIs can be well described with the Sieverts' law [246]. Among all measured Sieverts' constants that can be found in literature, the relation measured by Reiter *et al* in a temperature range $508\,\mathrm{K} < T < 700\,\mathrm{K}$ is the lowest and therefore yields the smallest low-concentration distribution coefficient $K_{\mathrm{D},0}^{\mathrm{E97-PbLi}}$ between PbLi and Eurofer'97 [224]. Since according to equation (4.55), a lower distribution coefficient results in a higher permeation flux, considering Reiters Sievert's coefficient provides the most conservative simulation results from the safety point of view. For this reason, for the simulations in this work, the Sieverts' constant of protium in PbLi measured by Reiter *et al* is considered for all three hydrogen isotopes.

In contrast to the Sieverts' constant, the measured diffusion relations which can be found in the literature differ considerably less. To stay consistent, the diffusion relation which was measured by Reiter *et al* in a temperature range $573\,\mathrm{K} < T < 773\,\mathrm{K}$ is chosen for the calculations in this work [224]. They concluded that the same diffusivity relations approximately apply to all three hydrogen isotopes.

The used experimental Arrhenius coefficients of both the Sieverts' constant and the diffusivity of protium in PbLi are listed in table 5.1. In addition, both quantities are plotted in the two graphs of figure 5.26. It is interesting to note that especially in the temperature range relevant for WCLL breeding blankets the solubility of hydrogen isotopes in PbLi is of the same order of magnitude as the plotted solubilities in the two iron alloys. However, compared to the other two metals the Sieverts' constant of PbLi increases only very little with temperature. Moreover, it can be seen that the diffusivity of hydrogen isotopes in PbLi is at least an order of magnitude lower than in Eurofer'97 and α-iron.

5.4.3. Counter-permeation in a WCLL breeding blanket

The first simulations target the validation of the algebraic expressions for mono- and multi-isotopic permeation from flowing liquid metal to water (4.58), (4.60), (4.64) and

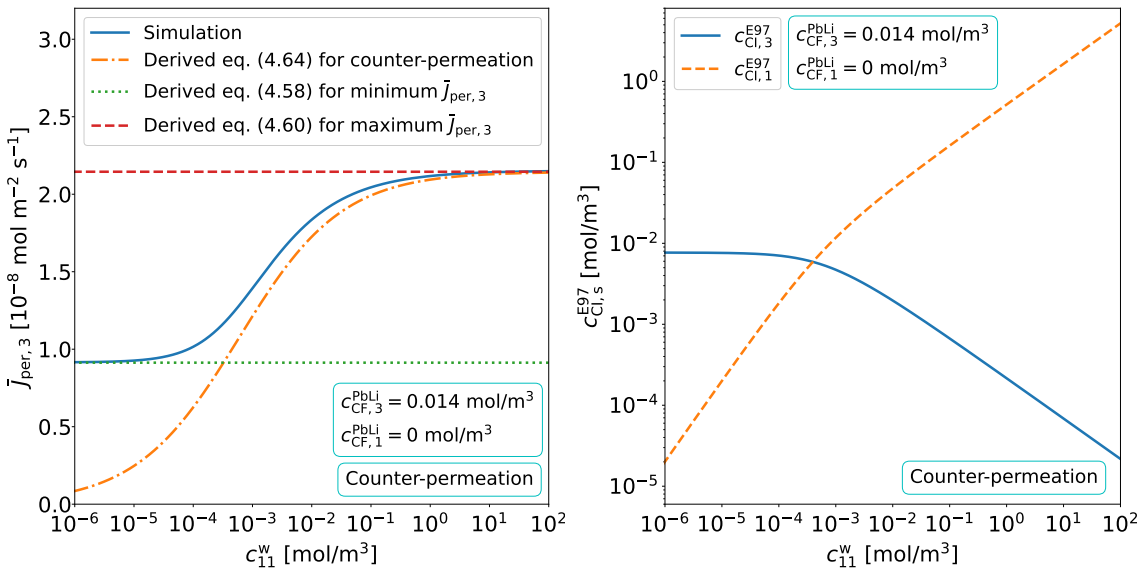

Fig. 5.27. [Left] Tritium permeation flux from the PbLi breeder flow into the water coolant of a WCLL breeding blanket in a counter-permeation scenario where $^1H_2$ gas is added to the water coolant assuming the pipe wall is exclusively made of Eurofer'97. The graph shows a simulated curve as well as curves that are calculated using algebraic formulas derived in section 4.2. [Right] Simulated protium and tritium concentrations at the coolant downstream interface of the water pipe wall of a WCLL breeding blanket in a counter-permeation scenario where $^1H_2$ gas is added to the water coolant assuming the pipe wall is exclusively made of Eurofer'97.

(4.65) which are derived in the theoretical analysis in section 4.2. Since these formulas are only applicable to a membrane made of a single material the following preliminary simulations consider a hypothetical case in which the interlayer of the pipe wall (central material component in figure 5.24) is made of Eurofer'97 as well, instead of α-iron.

The tritium concentration at the inlet of the liquid PbLi pipe flow component assumed in the simulations is taken from the mentioned calculations performed in [232] and is set to $c^{\mathrm{PbLi}}_{\mathrm{CF},3} \approx 1.4 \times 10^{-2}\,\mathrm{mol\,m^{-3}}$. Furthermore, it is assumed that the concentrations of the tritium containing molecules $^1H^3HO$, $^1H^3H$ and $^3H_2$ at the inlet of the water pipe component are zero. This ensures obtaining conservative simulation results.

Initially, a pure counter-permeation scenario is simulated in which $^1H_2$ gas is added to the coolant while the protium concentration at the inlet of the PbLi flow component is maintained at zero. The blue continuous curve in the left-hand plot in figure 5.27 shows the resulting simulated tritium permeation flux from the PbLi flow into the water flow plotted against the $^1H_2$ concentration in the water. The graph confirms that if the $^1H_2$ concentration in the water is close to zero the permeation flux approaches a finite minimum value which is calculated by the derived algebraic formula (4.58) for mono-isotopic permeation from liquid metal to water (see dotted line). As the $^1H_2$ concentration in the water grows the tritium permeation flux increases. The simulated protium and tritium concentrations in the pipe wall at the coolant downstream interface (CI) are visualized in the right-hand graph. When the protium coolant interface concentration $c^{\mathrm{E97}}_{\mathrm{CI},1}$ is of the

same order as the tritium coolant interface concentration $c_{\mathrm{CI},3}^{\mathrm{E97}}$ or higher, a steep rise in tritium permeation flux can be observed. For $c_{11}^{\mathrm{w}} \to \infty$, the tritium permeation flux approaches a finite maximum value. As derived in section 4.2, equation (4.60) provides an algebraic formula for this maximum permeation flux. It is validated through its graphical representation with the dashed line in the left-hand graph in figure 5.27. At concentrations in the water above approximately $c_{11}^{\mathrm{w}} > 1 \times 10^{-2}\,\mathrm{mol\,m^{-3}}$ the coolant interface concentrations satisfy $c_{\mathrm{CI},1}^{\mathrm{E97}} \gg c_{\mathrm{CI},3}^{\mathrm{E97}}$. In section 4.2 it is derived that for such high concentrations in the water, the tritium permeation flux of a counter-permeation scenario is approximately described by the derived algebraic formula (4.64). To validate this claim the expression is plotted into the left-hand graph in figure 5.27 (see dash-dotted line) after inserting the same input parameters as used for the simulation. It can be seen that the higher the concentration c_{11}^{w} in the water, the better describes the relation (4.64) the simulated curve.

5.4.4. Co-permeation in a WCLL breeding blanket

To continue the numerical validation the same simulation is repeated, this time considering that the $^1H_2$ concentration at the inlet of the water flow component is kept zero while additional protium is added to the inlet of the PbLi flow component. Such a configuration allows numerically observing a pure co-permeation process from the PbLi flow into the modeled water coolant. A plot of the simulated tritium permeation flux into the coolant as a function of the concentration of added protium into the breeder flow component is presented in the left-hand graph in figure 5.28. It is immediately noticeable that in a co-permeation scenario, the dependence of the permeation flux on the protium concentration in the PbLi flow has an almost identically shape as the dependency on the c_{11}^{w} in a counter-permeation process. If the protium concentration in the PbLi is vanishingly small the permeation flux is practically equal to its minimum mono-isotopic permeation flux value which is plotted with a dotted line using the derived algebraic equation (4.58).

The right-hand plot in figure 5.28 shows the simulated coolant interface concentrations of the two isotopes in the pipe wall. It is found that the tritium permeation flux, plotted in the left-hand graph, increases when $c_{\mathrm{CI},1}^{\mathrm{E97}}$ is of the order of $c_{\mathrm{CI},3}^{\mathrm{E97}}$ or higher. At very high protium concentrations in the PbLi, the tritium permeation flux converges against the plotted maximum permeation flux given by the derived algebraic equation (4.60). The plot also contains a graphical representation of the derived algebraic formula (4.65) for the tritium permeation flux as a function of the protium and tritium concentration in the PbLi flow. The two graphs in figure 5.28 confirm that the stronger the condition $c_{\mathrm{CI},1}^{\mathrm{E97}} \gg c_{\mathrm{CI},3}^{\mathrm{E97}}$ is fulfilled, the better the derived formula describes the permeation flux in a co-permeation scenario from liquid PbLi to water.

After analyzing the influence of co- and counter-permeating protium on the tritium permeation flux from liquid PbLi to water it can be concluded that from a safety point of view, it should be intended to avoid any protium in the system to obtain the minimum tritium permeation flux given by equation (4.58). Nevertheless, the two left-hand graphs

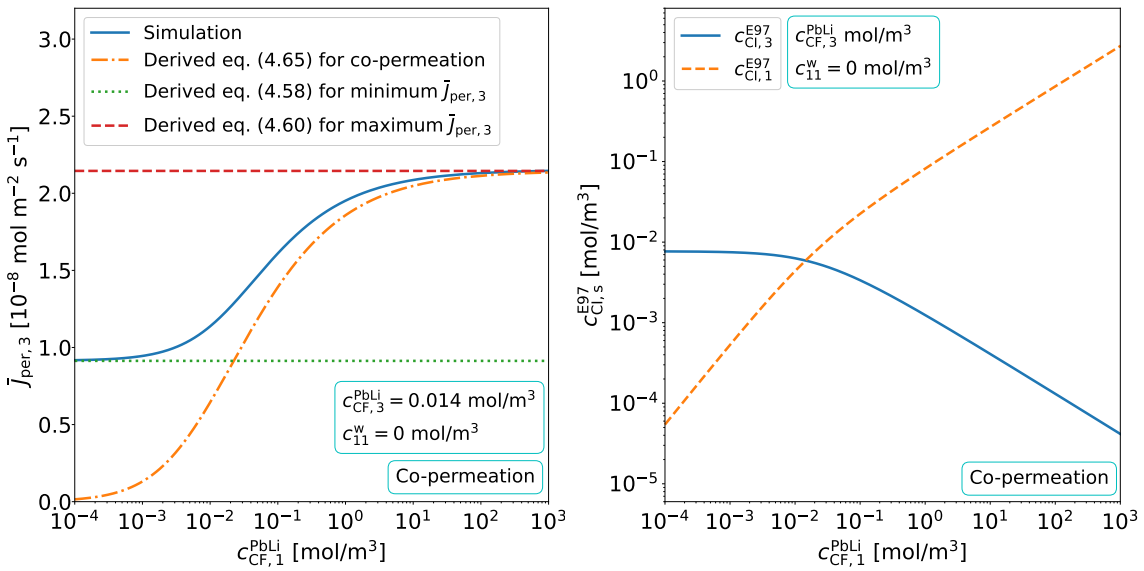

Fig. 5.28. [Left] Tritium permeation flux from the PbLi breeder flow into the water coolant of a WCLL breeding blanket in a co-permeation scenario where protium is added to the PbLi flow assuming the pipe wall is exclusively made of Eurofer'97. The graph shows a simulated curve as well as curves that are calculated using algebraic formulas derived in section 4.2. [Right] Simulated protium and tritium concentrations at the coolant downstream interface of the water pipe wall of a WCLL breeding blanket in a co-permeation scenario where protium is added to the PbLi flow assuming the pipe wall is exclusively made of Eurofer'97.

of the figures 5.27 and 5.28 give the impression that in a worst-case scenario, in which a high amount of protium is present in the system, the tritium permeation flux could be merely doubled. However, it is found that the difference between the minimum and the maximum permeation flux is highly dependent on the tritium concentration in the PbLi.

The left-hand graph in figure 5.29 shows a plot of the simulated minimum and maximum permeation flux as a function of $c^{\mathrm{PbLi}}_{\mathrm{CF},3}$. In addition, the graph contains the curves of the derived algebraic formulas (4.58) and (4.60). The correctness of the two equations is confirmed since they perfectly match the simulation. It is found that if the tritium concentration in the liquid PbLi is small an addition of protium to the system can increase the permeation flux by a much higher factor than if the tritium concentration is high. The plot reveals that as $c^{\mathrm{PbLi}}_{\mathrm{CF},3}$ grows, the minimum permeation flux (4.58) approaches the maximum permeation flux (4.60). Therefore, at very high values of $c^{\mathrm{PbLi}}_{\mathrm{CF},3}$, the influence an addition of protium to the system has on the tritium permeation flux becomes negligible as the minimum and maximum value of the tritium permeation flux are almost identical. This is an important finding since its cause is directly connected to the origin of the permeation-enhancing effect of co- and counter-permeation from liquid metal to water.

To comprehend this, it is looked at the right-hand graph in figure 5.29. It shows the simulated tritium concentrations at the coolant interface and the PbLi breeder interface (BI) for different tritium concentrations in the liquid PbLi assuming that no protium is present in the entire system. The derived algebraic formula (4.57) for the tritium down-

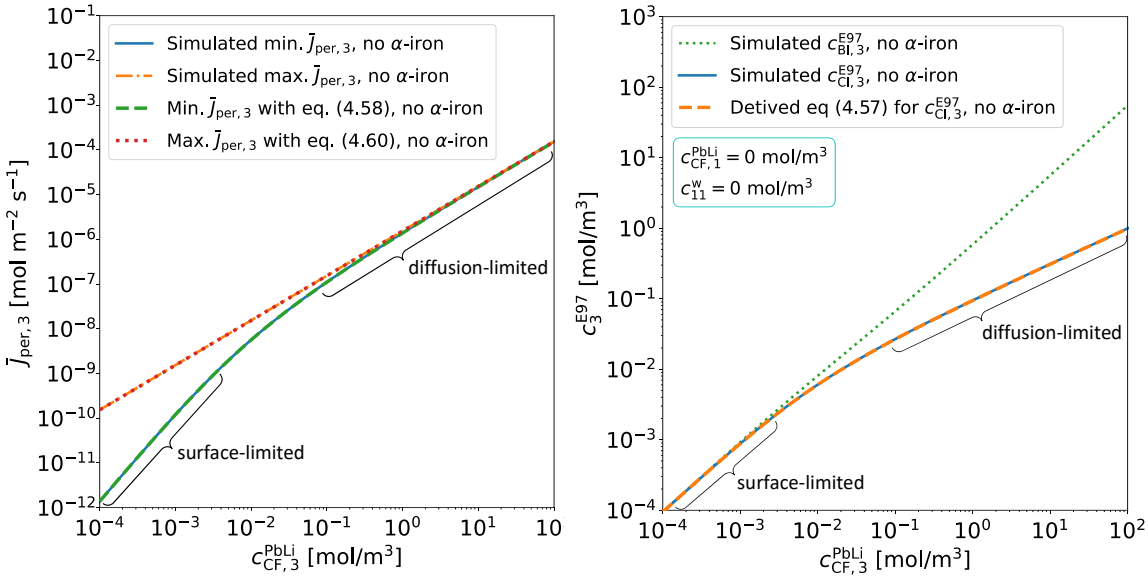

Fig. 5.29. [Left] Minimum steady state tritium permeation flux from the PbLi flow into the water coolant of a WCLL breeding blanket that establishes if there is no protium in the system plotted against the tritium concentration in the PbLi flow. It is shown together with the maximum permeation flux that adjusts if there is much more protium than tritium in the system. The curves are simulated and calculated using the algebraic equations (4.58) and (4.60) derived in section 4.2. [Right] Tritium concentrations at the breeder interface (BI) and coolant interface (CI) in the pipe wall if it consists exclusively of Eurofer'97, plotted against the tritium concentration in the PbLi flow if no protium is present in the system.

stream interface concentration in a mono-isotopic permeation scenario from liquid metal to water is plotted in the graph as well. The simulated and algebraically calculated curves match perfectly which validates the correctness of the derived formula. It can be seen that at low tritium concentrations in the PbLi flow, the breeder and coolant interface concentrations are almost equal. This implies a flat concentration profile in the bulk. In contrast, above approximately $c^{\mathrm{PbLi}}_{\mathrm{CF},3} > 1 \times 10^{-2}\,\mathrm{mol\,m^{-3}}$ the downstream coolant interface concentrations become increasingly separated from the upstream breeder interface concentration, meaning that the slope of the concentration profile in the bulk rises with increasing value of $c^{\mathrm{PbLi}}_{\mathrm{CF},3}$. This behavior is well known from the permeation from gas to gas and suggests that also for a permeation process from liquid metal to water there exists a surface-limited and diffusion-limited mono-isotopic permeation regime. The two regimes are indeed recognizable in the left-hand graph in figure 5.29. At very low and very high tritium concentrations in the liquid metal, the minimum mono-isotopic tritium permeation flux (blue continuous and orange dashed lines) exhibits two distinct straight slopes (in a logarithmic scale representation). The brackets in the two graphs indicate the approximate concentration ranges of the surface-limited ($c^{\mathrm{PbLi}}_{\mathrm{CF},3} < 3 \times 10^{-3}\,\mathrm{mol\,m^{-3}}$) and diffusion-limited ($c^{\mathrm{PbLi}}_{\mathrm{CF},3} > 1 \times 10^{-1}\,\mathrm{mol\,m^{-3}}$) mono-isotopic permeation regimes.

By looking at the left-hand graph it is found that an addition of protium to the system only has a permeation-enhancing effect if, in a protium-free system, the mono-isotopic

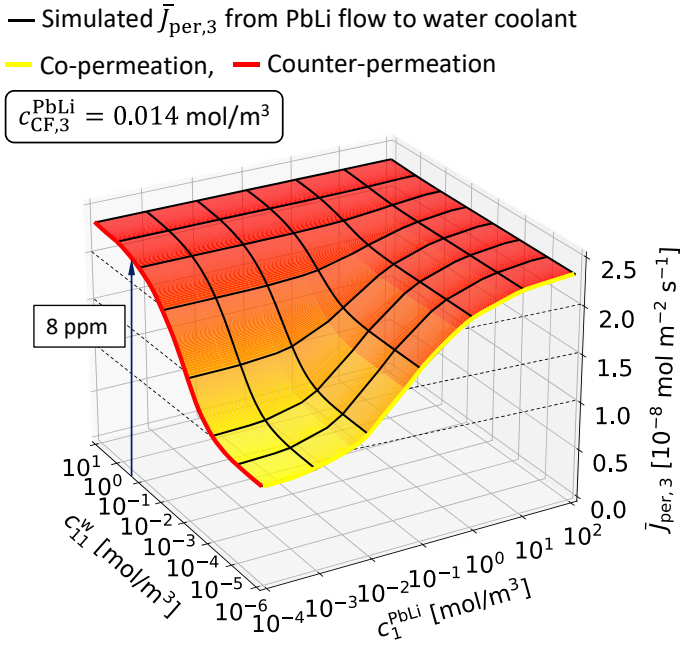

Fig. 5.30. Steady state tritium permeation flux from the PbLi flow into the water coolant of a WCLL breeding blanket plotted against the concentration of added $^1H_2$ to coolant and the concentration of added ^1H to the PbLi flow if $c_{\mathrm{CF},3}^{\mathrm{PbLi}} \approx 1.4 \times 10^{-2}$ mol m^{-3}. The plot indicates the concentration of $^1H_2$ in the water equal to $x_{11}^{\mathrm{w}} = 8$ ppm.

tritium permeation process would occur in the surface-limited regime. In this regime, a high concentration of protium at the coolant downstream interface considerably increases the tritium surface recombination rate. Thus, it takes the tritium permeation process out of the surface-limited and towards the diffusion-limited regime where the tritium concentration profile in the bulk is steep. This is the reason why at low tritium concentrations in the PbLi flow a high protium content in the system increases the permeation flux to a maximum value which seems to have the same dependency on the tritium concentration in the PbLi as the mono-isotopic tritium permeation flux in the diffusion-limited regime. If the tritium concentration in the PbLi flow is high enough that in a protium-free system, tritium permeation would occur in the diffusion-limited regime, an addition of protium could not further increase the permeation flux since it is already limited by diffusion processes.

5.4.5. Evaluation of co-/counter-permeation for tritium control in a WCLL BB

At this point, it is focused on a real WCLL-relevant multi-isotopic permeation scenario in which protium may be simultaneously present in the PbLi breeder and the water coolant. Moreover, now as the calculations are exclusively performed using the EcosimPro© model, it is possible to consider that in reality, the interlayer material of the pipe wall is α-iron. Again, this simulation assumes a tritium concentration in the PbLi core flow of $c_{\mathrm{CF},3}^{\mathrm{PbLi}} \approx 1.4 \times 10^{-2}$ mol m^{-3}.

Figure 5.30 shows the simulated steady state tritium permeation flux from the PbLi flow into the water coolant for different concentrations of added protium to the PbLi flow and of added $^1H_2$ to the coolant. It can be seen that in a pure counter-permeation scenario (thick red line) and a pure co-permeation scenario (thick yellow line) the permeation flux rises with increasing protium concentration in the corresponding system. It is found that

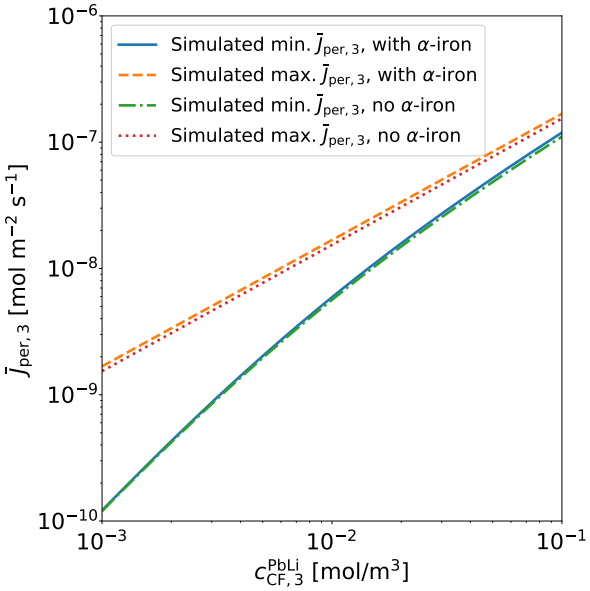

Fig. 5.31. Minimum steady state tritium permeation flux from the PbLi flow into the water coolant of a WCLL breeding blanket if there is no protium in the system plotted against the tritium concentration in the PbLi flow. It is shown together with the maximum permeation flux that adjusts if there is much more protium than tritium in the system. The plot contains the simulated curves for a pipe wall which exclusively consists of Eurofer'97 and a pipe wall with an α-iron interlayer. Both walls have the same thicknesses.

when an α-iron interlayer is present in the bulk, the curves of both limit scenarios also rise from a certain minimum value at low protium concentrations to a finite maximum flux at high protium concentrations. In addition, figure 5.30 shows the resulting tritium permeation flux for any possible configuration of the concentrations $c^{\mathrm{PbLi}}_{\mathrm{CF},1}$ and c^{w}_{11}. It is found that only if both protium concentrations in the PbLi and the water are very small, the condition $c^{\mathrm{E97}}_{\mathrm{CI},1} \ll c^{\mathrm{E97}}_{\mathrm{CI},3}$ is satisfied and the permeation flux takes its minimum value.

Figure 5.31 shows the simulated minimum (blue continuous line) and maximum (orange dashed line) tritium permeation flux values that occur if either no protium or a lot of protium is present in the system, this time taking into account the α-iron interlayer. The curves are presented together with those previously shown in the left-hand diagram of figure 5.29, which represent a scenario without the α-iron interlayer (green dash-dotted and red dotted lines), but with the same total wall thickness. It is found that in a protium-free permeation environment, where the mono-isotopic tritium permeation flux is minimal, and at low tritium concentrations in the PbLi stream, where the tritium permeation process occurs in the surface-limited regime, the presence of the α-iron interlayer has a negligible effect on the permeation flux. This is because, in the surface-limited regime, the permeation process is mainly slowed down by the surface recombination kinetics rather than by diffusion processes. The higher the tritium concentration in the PbLi, the more the mono-isotopic permeation process shifts towards the diffusion-limited regime, where the surface recombination rate is higher and the diffusivity of the tube wall material rather determines the permeation flux. This explains the increasing separation of the blue solid and the green dash-dotted curve at higher tritium concentrations. In a system where a lot of protium is present, the surface recombination reactions are fast even if the tritium concentration in the PbLi is very low. Therefore, when the protium content is high, the permeation flux is mainly determined by the speed of the diffusion process. This explains why, regardless of the tritium concentration in the PbLi stream, the presence of an α-iron interlayer leads to an increased maximum tritium permeation flux.

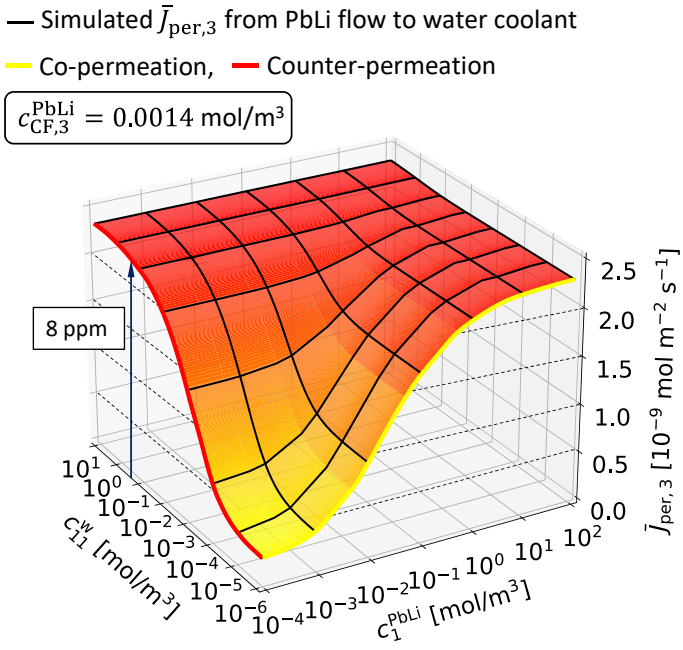

Fig. 5.32. Steady state tritium permeation flux from the PbLi flow into the water coolant of a WCLL breeding blanket plotted against the concentration of added $^1H_2$ to coolant and the concentration of added ^1H to the PbLi flow if $c_{\mathrm{CF},3}^{\mathrm{PbLi}} \approx 1.4 \times 10^{-3}$ mol m^{-3}. The plot indicates the concentration of $^1H_2$ in the water equal to $x_{11}^{\mathrm{w}} = 8$ ppm.

Figure 5.32 presents another three-dimensional plot of the tritium permeation flux for a wide range of possible configurations of protium concentrations in the PbLi and the water. In contrast to figure 5.30, it represents a simulation in which all parameters are equal but the tritium concentration in the PbLi is ten times smaller. As can already be seen from figure 5.31, the plot well visualizes how, at lower tritium concentrations in the PbLi, an injection of protium into the system causes the tritium permeation flux to increase by a much higher factor compared to the situation in figure 5.30.

In conclusion, from a radiation safety point of view, to achieve a minimum tritium permeation flux into the coolant, the concentration of protium in both the PbLi and the water coolant of a WCLL breeding blanket should be maintained as low as possible.

However, to counteract the generation of corrosion-enhancing O_2 by radiolysis reactions in the water, it might be considered to keep the $^1H_2$ concentration in the coolant at a relatively high level of about $x_{11}^{\mathrm{w}} \approx 8$ ppm or $c_{11}^{\mathrm{w}} \approx x_{11}^{\mathrm{w}} \cdot \rho_{11\mathrm{O}}^{\mathrm{w}} / M_{11\mathrm{O}} \approx 0.3$ mol m^{-3}. In this way, the O_2 concentration in the water can be significantly reduced. This technique is typically employed in pressurized water fission reactors [247]. The arrows in the figures 5.30 and 5.32 indicate the tritium permeation flux into the coolant for a counter-permeation scenario that would establish assuming that $x_{11}^{\mathrm{w}} = 8$ ppm. It is found that the counter-permeation effect of such a high $^1H_2$ concentration in the coolant would lead to the maximum possible increase in tritium permeation flux. Hence, if the tritium content in the PbLi flow will have the expected average concentration of $c_{\mathrm{CF},3}^{\mathrm{PbLi}} \approx 1.4 \times 10^{-2}$ mol m^{-3} an addition of $x_{11}^{\mathrm{w}} = 8$ ppm of $^1H_2$ to the water double the tritium permeation flux into the coolant. However, if eventually, the tritium concentration will be rather of the order of $c_{\mathrm{CF},3}^{\mathrm{PbLi}} \approx 1.4 \times 10^{-3}$ mol m^{-3}, a $^1H_2$ concentration of $x_{11}^{\mathrm{w}} = 8$ ppm would increase the tritium permeation flux by a factor ten compared to a scenario without protium. It would therefore have a far more unfortunate impact on the plant's radiation safety.

5.5. Experimental validation of gas-to-gas counter-permeation model

Both the theory developed in section 4.1 and the numerical simulations performed in section 5.3 discovered a permeation flux-reducing effect of gas-to-gas co- and counter-permeation. However, theoretical and numerical predictions of this effect are not sufficient to verify its existence. Indeed, experimental validation of the permeation flux-reducing mechanism of multi-isotope gas-to-gas permeation is indispensable.

In the past, the effect of co- and counter-permeation was experimentally observed for sample membranes made of palladium and nickel by Kizu *et al* [88], [89], [91]. Unfortunately, in their experimental campaign, Kizu *et al* only addressed the investigation of multi-isotopic effects in the surface-limited pressure regime of the co- and counter-permeating species. However, as it is demonstrated in the developed analytical model in section 4.1 and shown in figure 4.2, the strong permeation mitigating effect of multi-isotopic permeation is expected to occur in the intermediate and diffusion-limited high-pressure regime of the co- or counter-permeating species.

Indeed, a counter-permeation process in the diffusion-limited pressure regime was experimentally explored by Takeda *et al* [90]. They experimentally demonstrated that the permeation flux of deuterium from the inside of an Inconel®600 (I600) tube to the outside is significantly reduced when protium counter-permeates in the diffusion-limited regime by injecting relatively high partial pressures of $^1H_2$ gas into the outer space of the tube. This finding is consistent with the theory of counter-permeation developed in section 4.1, the implications of which are visualized in the left plot of figure 4.2. Fortunately, the simple geometric structure of Tekeda's permeation chamber allows the reproduction of their experimental results using the derived algebraic formulas (4.33) and (4.34) for gas-to-gas counter-permeation and a numerical model using the EcosimPro© components presented in section 5.1. Thus, it is possible to experimentally validate the physical theory of multi-isotopic hydrogen transport presented in section 2, which is used as a basis for the theoretical and numerical studies performed in sections 4.1 and 5.3.

The experimental chamber of Takeda's counter-permeation device is a test tube made of Inconel®600, with a length of 2.25 m. The inner and outer radii of the pipe are $r_{in} = 3.5\times10^{-3}$ m and $r_{out} = 4.7\times10^{-3}$ m, respectively. It is bent to fit into the interior of a wider closed cylinder case with a length of 1 m and an inner diameter of 5×10^{-2} m. The test pipe enters the wider cylinder case at its top end and exits at its bottom end. At both ends, the wider cylinder case is equipped with additional gas inlet and outlet tubes (see sketch in [90]). For the counter-permeation flux measurements, a gas mixture of $^2H_2$ + Ar was injected into the inlet of the test tube interior at a volume flow rate of $F = 5\times10^{-4}\,m^3\,s^{-1}$. The test tube interior represents the upstream side of the deuterium permeation process, while the downstream side is the space between the outer wall of the test tube and the inner wall of the wider cylinder housing. The downstream side was fed with a $^1H_2$ + Ar gas mixture at the same volume flow rate of $F = 5 \times 10^{-4}\,m^3\,s^{-1}$. Regardless of the adjusted $^1H_2$ and $^2H_2$ partial pressures in the gas mixtures, the total pressures of the two

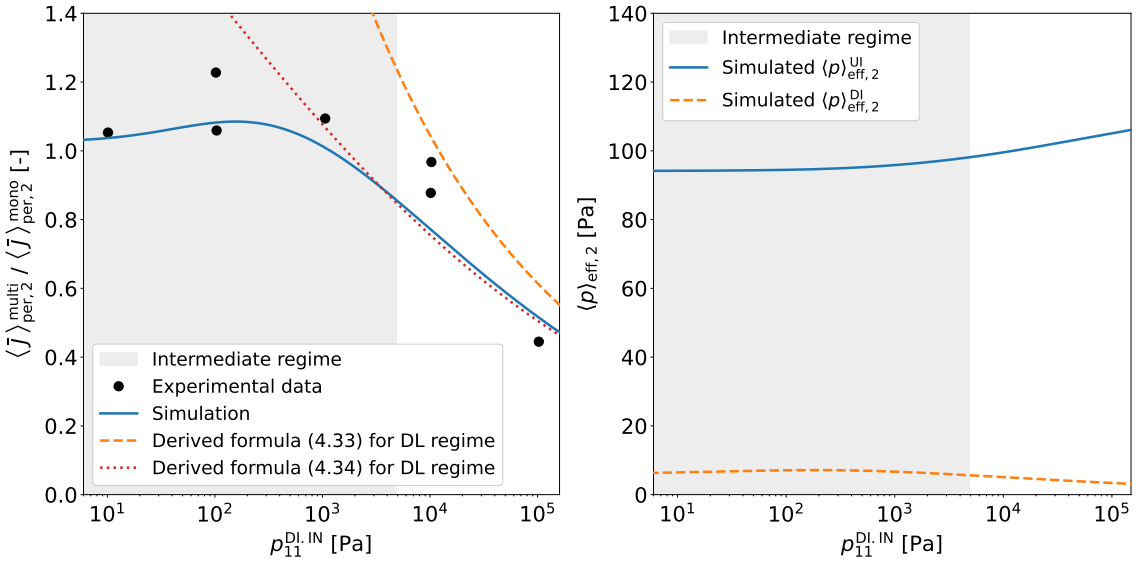

Fig. 5.33. [Left] Average ^{2}H permeation flux from the interior $^2H_2$+Ar gas flow of the test pipe of Takeda's counter-permeation chamber through its Inconel®600 pipe wall into an $^1H_2$+Ar gas mix flowing through the wider cylinder case of the experimental setup. The graph contains experimental data points [90], a simulated curve, and two calculated curves using algebraic equations determined in section 4.1. The permeation flux is shown relative to the simulated flux which occurs if no ^{1}H is present at the downstream side. It is plotted against the $^1H_2$ partial pressure injected into the inlet of the downstream side. The considered $^2H_2$ partial pressure at the test pipe inlet is $p_{22}^{\mathrm{UI.IN}} = 102\,\mathrm{Pa}$. [Right] Simulated average effective deuterium pressures inside (upstream) and outside (downstream) of the test pipe of Takeda's counter-permeation experiment. They are plotted against the $^1H_2$ partial pressure injected into the inlet of the downstream side.

gas streams were kept at atmospheric pressure by adding appropriate amounts of Ar gas.

For one of their experiments, Takeda *et al* kept the $^2H_2$ partial pressure at the inlet of the test tube at $p_{22}^{\mathrm{UI.IN}} = 102\,\mathrm{Pa}$. The temperature of the test tube was set to $T = 1092\,\mathrm{K}$. Takeda *et al* measured the partial pressure configuration of the gas components $^1H_2$, $^1H^2H$ and $^2H_2$ at the outlet of the upstream and downstream gas flow using a QMS. They made these measurements for different partial pressures $p_{11}^{\mathrm{DI.IN}}$ of injected $^1H_2$ gas at the gas inlet of the wider cylinder case. By knowing the volumetric flow rates of the two gas streams, Takeda *et al* were able to calculate the amounts of permeated deuterium atoms into the wider cylinder case (the downstream side) during a given time period for each of the observed values of $p_{11}^{\mathrm{DI.IN}}$. To extract the effect of the $^1H_2$ counter-flow on the deuterium permeation flux, Takeda *et al* divided the obtained values by the amounts of permeated deuterium atoms measured when no $^1H_2$ gas was added to the downstream side. It is evident that the ratios obtained are equal to the ratios between the average deuterium permeation fluxes through the tube wall in the presence of a $^1H_2$ counter-flow and the permeation flux occurring in the absence of $^1H_2$ gas. Their experimental results are shown in the left graph of figure 5.33 as black round markers [90].

To numerically represent their experimental results, a model of Takeda's experiment

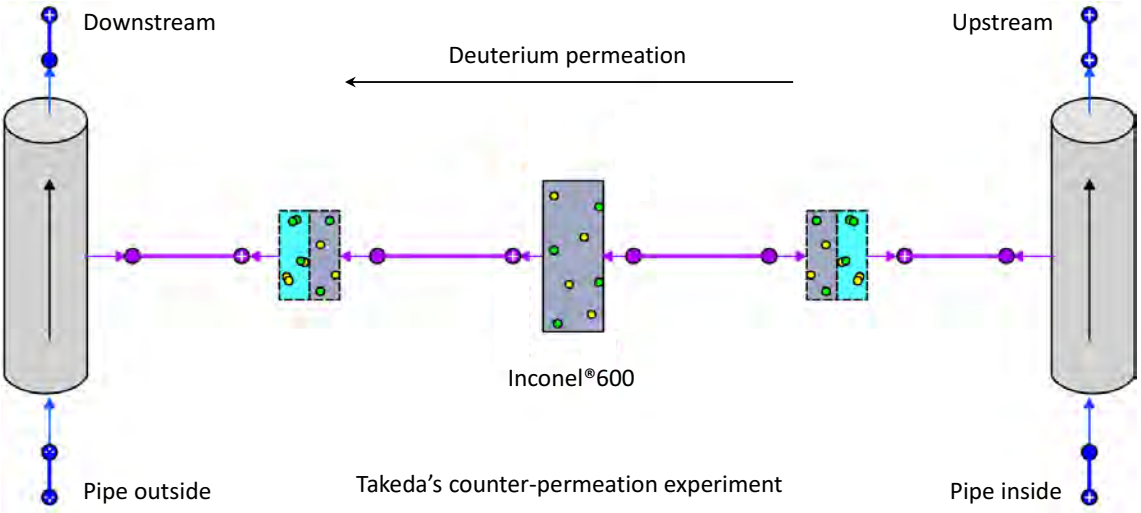

Fig. 5.34. Develloped EcosimPro© component flow chart of the counter-permeation experiment executed by Takeda *et al* [90].

is developed within the scope of this work using EcosimPro©. The created component flow structure is shown in figure 5.34. Both the gas flow through the thin test pipe and the gas flow through the wider cylinder case are modeled with pipe flow components (see figure 5.1) discretized into $\mathcal{M} = 10$ segments. In the model, equation (2.46) is used to calculate the equilibrium constant for the occurring isotope exchange reactions $2\,{}^1\mathrm{H}{}^2\mathrm{H} \rightleftharpoons {}^1\mathrm{H}_2 + {}^2\mathrm{H}_2$ between the protium and deuterium containing gas molecules. Like in the previous simulations, the forward reaction rate of this reaction can only be estimated. For the calculation it is set to $k_{12+12}^{\mathrm{f,ex}} \approx 1 \times 10^5\,\mathrm{m^3\,s^{-1}\,mol^{-1}}$. The considered lengths of the two pipe flow components and their volume flow rates are those specified above in the description of Takeda's experimental set-up. A wall material component between the two flow components represents the Inconel®600 pipe wall connected to gas-metal interface components on each side. It has a thickness of $d_{\mathrm{pipe}} = 1.2 \times 10^{-3}\,\mathrm{m}$ and is discretized into $\mathcal{Q} = 30$ segments.

Inconel®600 is a nickel alloy with chromium and iron as main secondary elements. The diffusion coefficients D_i^{I600} and Sieverts' constants $K_{\mathrm{s},i}^{\mathrm{I600}}$ of protium in Inconel®600 which are used in the model were measured by Rota *et al* in a temperature range between $T = 423\,\mathrm{K}$ and $T = 673\,\mathrm{K}$ [248]. While the diffusion coefficient of deuterium is extrapolated from that of protium using equation (2.66) the Sieverts' constant of deuterium is considered equal to that of protium. The measured Arrhenius coefficients of both physical quantities are shown in table 5.2. Figure 5.26 visualizes the temperature dependency of the two quantities $K_{\mathrm{s},1}^{\mathrm{I600}}$ and D_1^{I600} of protium in Inconel®600. The temperature relationship of the dissociation coefficient of ${}^2\mathrm{H}_2$ at an Inconel®600 surface could also be measured by Rota *et al*. [248]. They determined the relationship

$$\sigma k_{\mathrm{d},22}^{\mathrm{I600}} = 3.32 \times 10^{-7}\,\frac{\mathrm{mol}}{\mathrm{m^2 sPa}}\,\exp\left(\frac{-46\,000\,\mathrm{J\,mol^{-1}}}{RT}\right). \tag{5.30}$$

In the model, the values of $k_{\mathrm{d},ij}^{\mathrm{I600}}$ of all other hydrogen-containing molecules are deter-

TABLE 5.2

MEASURED PRE-EXPONENTIAL FACTORS AND ACTIVATION ENERGIES OF THE SIEVERTS' CONSTANTS AND DIFFUSION COEFFICIENTS OF PROTIUM IN INCONEL®600 USED FOR THE NUMERICAL REPRESENTATION OF TAKEDA'S COUNTER-PERMEATION EXPERIMENT [248].

Sievert's constant	Inconel®600	Diffusion coefficient	Inconel®600	Ref.
$K^0_{\mathrm{s},1}$ [mol m^{-3} Pa$^{-\frac{1}{2}}$]	2.32×10^{-2}	D^0_1 [m^2 s^{-1}]	1.7×10^{-6}	[248]
$\Delta\overline{H}_{\mathrm{s},1}$ [kJ mol^{-1}]	5.44	$E_{\mathrm{m},1}$ [kJ mol^{-1}]	49.80	[248]

mined using equation (5.19) and the values of $\sigma k^{\mathrm{I600}}_{\mathrm{r},ij}$ are obtained with equation (2.100).

In addition to Takeda's experimental results, the left-hand graph in figure 5.33 shows the ratio (blue curve) between the simulated average steady state deuterium permeation flux $\left\langle \overline{J} \right\rangle^{\mathrm{multi}}_{\mathrm{per},2}$ into the wider cylinder case in the presence of a protium counter-flow and the simulated permeation flux $\left\langle \overline{J} \right\rangle^{\mathrm{mono}}_{\mathrm{per},2}$ which occurs if $p^{\mathrm{DI.IN}}_{11} = 0\,\mathrm{Pa}$. The simulated permeation fluxes shown are averaged over the discretized segments of the pipe flow components in flow direction and plotted against the $^1H_2$ partial pressure at the downstream gas inlet of the outer cylinder case. Considering that the experimental data points scatter relatively strongly, the simulated curve is in good accordance with the general course of the experimental results. The gray shaded area in the plot shows the approximate pressure range of the intermediate protium permeation regime calculated with equation (2.147) as a function of $p^{\mathrm{DI.IN}}_{11}$. The diffusion-limited regime is adjacent to its right. As expected from the analysis performed in section 4.1, the left-hand graph in figure 5.33 shows that in the diffusion-limited regime of the protium counter-permeation process, the experimentally measured and numerically simulated deuterium permeation fluxes decrease with increasing $^1H_2$ partial pressure.

In section 4.1 it was derived that at high permeation numbers, the permeation flux is approximately described by the derived algebraic formulas (4.33) and (4.34) provided that the downstream effective deuterium pressure is negligibly small. Both algebraic equations (4.33) and (4.34) are plotted in the left-hand graph in figure 5.33 after inserting the average upstream effective deuterium pressure $\langle p \rangle^{\mathrm{DI}}_{\mathrm{eff},2}$. The simulated upstream and downstream effective deuterium pressures averaged over the discretized segments of the pipe flow components are plotted in the right-hand graph in figure 5.33. The simulations reveal that the relatively small volume flow rate of the gas through the wider cylinder case leads to a non-negligible effective deuterium pressure in the gas flow of the downstream side (see the right-hand graph in figure 5.33). This finding is consistent with experimental data reported in [90]. Nevertheless, both algebraic formulas (4.33) and (4.34) describe the measured and simulated decrease in deuterium permeation flux very well and approach the simulated curve with increasing permeation number.

6. DEVELOPMENT OF THE COOPER EXPERIMENT

[1] While the decreasing effect of counter-permeating protium on the deuterium permeation flux could be experimentally observed by Takeda *et al*, the mitigating effect of co-permeating protium on the deuterium permeation flux in the diffusion-limited regime has not been measured yet. To complete the experimental validation of the theoretical findings presented in section 4.1, its experimental validation is urgently needed. In addition, the experimental validation of both co- and counter-permeation effects must be performed with different sample membrane materials than those used in previous experimental campaigns. Of particular interest for HCPB applications is the experimental validation of multi-isotopic permeation effects using Eurofer'97 as the membrane material. Due to the different hydrogen transport properties of the already investigated materials palladium, nickel, and Inconel®600 compared to Eurofer'97, the previously developed experimental setups [88]–[91] were designed for sample membrane shapes, pressure, and temperature regimes that would not be suitable for observation of multi-isotopic transport effects in Eurofer'97. An experimental setup that enables studying these effects in Eurofer'97 would need to be fully adapted to its characteristic hydrogen transport parameters.

For these reasons, a new multi-isotopic hydrogen permeation experiment has been designed from scratch and constructed within the scope of this dissertation. It is called COOPER (CO- and cOunter PERmeation) experiment [249]. This chapter presents the conceptual design, construction, and commissioning of the newly developed experimental facility COOPER.

6.1. Design input parameters

The heart of the COOPER experiment is a sample permeation membrane through which the permeation process under investigation takes place. Each side of the membrane is exposed to a single gas chamber. One of the cavities is defined as the upstream chamber, called permeation cell A (PC-A), and the other as the downstream chamber, called permeation cell B (PC-B).

Although the purge gas and coolant gas of an HCPB breeding blanket contain the two hydrogen isotopes protium and tritium, the COOPER experiment is designed to experimentally explore co- and counter-permeation with an isotope combination of protium and deuterium. The use of deuterium as a substitute for radioactive tritium greatly simplifies

[1] This chapter contains material and text that is contained in the following published article. The author of this dissertation is the first author of this article:

- S.J. Hendricks *et al*, "Design of a multi-isotopic hydrogen co- and counter-permeation experiment for HCPB related tritium mitigation studies," *Fusion Eng. Des.*, vol. 175, p. 112991, 2022.

the experimental setup, since no radiation protection measures need to be taken. Another advantage of using deuterium is that it is much cheaper and more readily available than tritium.

As shown theoretically in section 4.1 and observed in Takeda's experiment, the measurable influence of co- or counter-permeating protium on the permeation flux of deuterium has different characteristics in the surface-limited and diffusion-limited regime of the protium permeation process (see figure 4.2). Therefore, a critical requirement for the COOPER experiment is the ability to measure permeation processes for permeation numbers ranging from the surface-limited to the diffusion-limited regime. Furthermore, the ability to perform experiments in different permeation regimes extends the range of possible permeation experiments with COOPER. It allows the measurement of material-specific deuterium transport parameters of the sample material, such as its dissociation coefficient in the surface-limited regime and the diffusion coefficient and Sieverts' constant in the diffusion-limited regime.

The definition of the permeation number (2.147) shows that the regime of the permeation process depends on the membrane thickness, the driving pressure, and the temperature-sensitive material-specific hydrogen transport properties. Therefore, to cover all three permeation regimes with the COOPER experiment, its range of adjustable operating temperatures, membrane thicknesses, and controllable hydrogen gas pressures must be carefully defined.

The first design parameter, the operating temperature, is chosen to range from ambient temperature to $T = 823\,\mathrm{K}$. This upper limit is identical to the maximum allowable temperature of Eurofer'97 in breeding blankets. Thus, it is possible to measure co- and counter-permeation effects as well as temperature relationships of hydrogen isotope-specific parameters over the entire temperature range relevant to breeding blanket applications. The maximum design temperature of the experimental device is set to a slightly higher value of $T = 873\,\mathrm{K}$. As discussed in detail in section 3.1.2, even higher temperatures would severely limit design freedom, since the choice of suitable vacuum seals and heating methods decreases sharply with temperature.

The left-hand plot of figure 6.1 shows the deuterium permeation flux (blue continuous line) from the upstream side of a sample membrane with a thickness of $d_{\mathrm{disk}} = 1 \times 10^{-3}\,\mathrm{m}$ into an evacuated downstream side at $T = 573\,\mathrm{K}$ which would occur in a mono-isotopic permeation scenario. It is plotted against the value of the $^2H_2$ driving pressure p_{22}^{UI} at the upstream side. The permeation flux is calculated by inserting the definition of the permeation number (2.147) and the solution of the general equation for steady state permeation (2.151) into equation (2.152) [192]. This analytical calculation assumes the same experimental hydrogen transport parameters for Eurofer'97 as those given in table 5.1 and equation (5.18), the same which are used for the simulations in chapter 5. It can be seen that, according to this calculation, the use of a permeation membrane of $d_{\mathrm{disk}} = 1 \times 10^{-3}\,\mathrm{m}$ at $T = 573\,\mathrm{K}$ would allow measurements in the pure mono-isotopic

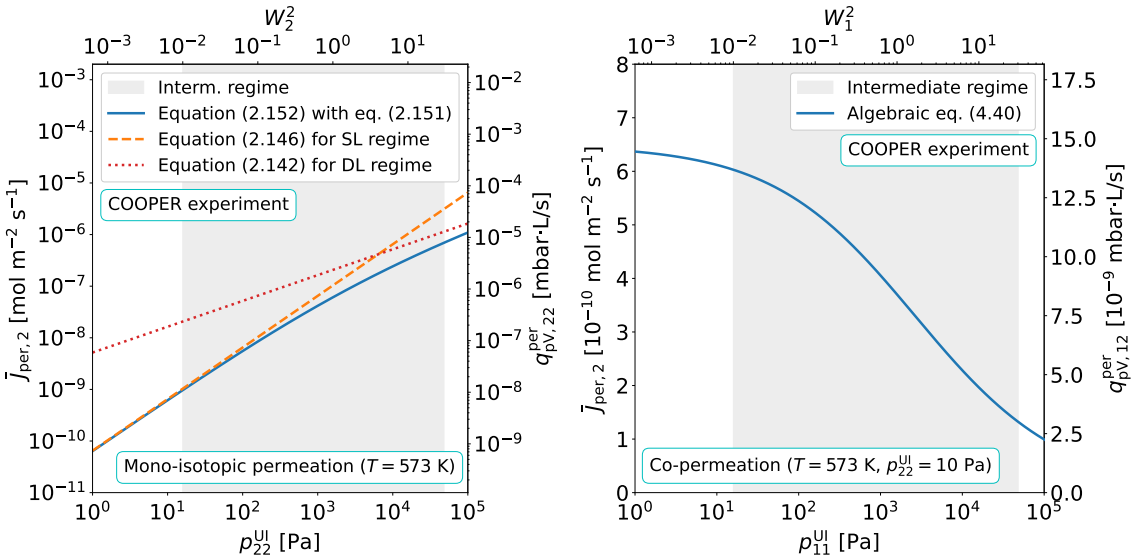

Fig. 6.1. [Left] Theoretically calculated steady state deuterium permeation flux from an upstream gas chamber through a $d_{\mathrm{disk}} = 1 \times 10^{-3}$ m thick and plane Eurofer'97 membrane into vacuum at $T = 573$ K plotted against the $^2H_2$ partial pressure in the upstream chamber. [Right] Theoretically calculated deuterium permeation flux from an upstream chamber with $p^{\mathrm{UI}}_{22} = 10$ Pa through a $d_{\mathrm{disk}} = 1 \times 10^{-3}$ m thick and plane Eurofer'97 membrane into vacuum in a co-permeation scenario at $T = 573$ K plotted as a function of the $^1H_2$ gas partial pressure p^{DI}_{11} in the upstream chamber.

surface-limited regime at driving pressures of up to about $p^{\mathrm{UI}}_{22} \approx 20$ Pa and in the diffusion-limited regime at pressures above $p^{\mathrm{UI}}_{22} \approx 500$ Pa. Based on this calculation, in order to cover all three permeation regimes experimentally, the COOPER measurement system must be able to detect deuterium fluxes resulting from $^2H_2$ driving pressures in the pressure range 1 Pa $< p_{22} < 1 \times 10^5$ Pa. Working with total pressures higher than $p = 1 \times 10^5$ Pa in the permeation cells could lead to leakage at the flanges of installed vacuum piping components (see section 3.1.2). This must be avoided at all costs because of the risk of an oxyhydrogen explosion.

According to equation (2.147), the use of thinner permeation membranes shifts the intermediate permeation regime towards higher pressures and the use of thicker membranes towards lower pressures. Nevertheless, to avoid breakage or deformation of the sample membrane during clamping with high-temperature vacuum seals, it was decided to design the COOPER experiment for Eurofer'97 membranes with a thickness greater than $d_{\mathrm{disk}} \geq 1$ mm. In any case, the design of the COOPER experiment presented in the following sections refers to a reference membrane thickness of $d_{\mathrm{disk}} = 1$ mm.

The left-hand plot of figure 6.1 has a second y-axis which indicates the number of permeated $^2H_2$ molecules per second expressed as a molecular permeation flow $q^{\mathrm{per}}_{\mathrm{pV},22}$. The atomic permeation flux $\bar{J}_{\mathrm{per}}$ is converted into the molecular permeation flow $q^{\mathrm{per}}_{\mathrm{pV},22}$ using equation (3.22) and taking into account that $^2H_2$ contains two deuterium isotopes. The effective surface area of a sample permeation membrane installed in the COOPER experiment has a design value of $A_{\mathrm{per}} = 9.1 \times 10^{-4}$ m^2. It denotes the area of the membrane

that is directly exposed to the atmosphere inside the permeation cells. The plot shows that for $A_{\mathrm{per}} = 9.1 \times 10^{-4}\,\mathrm{m}^2$ and $T = 573\,\mathrm{K}$, the ability to measure permeation fluxes resulting from $^2H_2$ upstream driving pressures in the range of $1\,\mathrm{Pa} < p_{22} < 1 \times 10^5\,\mathrm{Pa}$ requires the installation of a measurement system sufficiently sensitive to resolve permeation flows in a range of $1 \times 10^{-9}\,\mathrm{mbar \cdot L/s} < q^{\mathrm{per}}_{\mathrm{pV},s} < 1 \times 10^{-5}\,\mathrm{mbar\,L/s}$. It is found that when the operating temperature is increased from $T = 573\,\mathrm{K}$ to $T = 823\,\mathrm{K}$, the permeation flux resulting from a given $^2H_2$ upstream driving pressure increases by about a factor of ten. Therefore, the employed flux measurement system should be able to handle even higher molecular flows of up to about $q^{\mathrm{per}}_{\mathrm{pV},s} = 1 \times 10^{-4}\,\mathrm{mbar\,L/s}$.

As mentioned in section 3.2.3, a QMS is a device that allows quantitative measurement of the partial pressures of different gas molecules in a vacuum chamber. They can resolve partial pressures in a range of about $1 \times 10^{-9}\,\mathrm{Pa} < p_s < 1 \times 10^{-2}\,\mathrm{Pa}$ [195].

Transformation of equation (3.18) yields

$$S_{\mathrm{pump}}[\mathrm{L\,s^{-1}}] = \frac{\Delta q^{\mathrm{per}}_{\mathrm{pV},s}\,[\mathrm{mbar \cdot L/s}]}{\Delta p_s\,[\mathrm{mbar}]}\,. \tag{6.1}$$

This equation provides the required gas-specific pumping speed S_{pump} of a turbomolecular pump positioned near a QMS so that a given increment in permeation flow $\Delta q^{\mathrm{per}}_{\mathrm{pV},s}$ into a vacuum system results in a certain increment in partial pressure Δp_s. For the COOPER experiment, it is aimed that the minimum expected molecular permeation flow of $q^{\mathrm{per}}_{\mathrm{pV},s} = 1 \times 10^{-9}\,\mathrm{mbar \cdot L/s}$ into the measurement system leads to a partial pressure increase in the QMS of the observed deuterium-containing hydrogen gas of at least $\Delta p_s = 1 \times 10^{-9}\,\mathrm{Pa}$. According to equation (6.1), to achieve this, it is required to install a turbomolecular pump with a pumping speed of approximately $S_{\mathrm{pump}} \approx 100\,\mathrm{L\,s^{-1}}$. Of course, a lower pumping speed would theoretically result in a higher Δp_s and thus in a higher detector signal. However, the increased vacuum base pressure resulting from a reduced pumping speed would at the same time increase the noise in the QMS detector. The right-hand plot in figure 3.7 indicates that a pumping speed of the turbomolecular pump of $S_{\mathrm{pump}} \approx 100\,\mathrm{L\,s^{-1}}$ would maintain the total pressure in the QMS below $p = 1 \times 10^{-4}\,\mathrm{Pa}$ even if the highest expected permeation flow of $q^{\mathrm{per}}_{\mathrm{pV},s} = 1 \times 10^{-4}\,\mathrm{mbar\,L/s}$ occurs in the system. Therefore, designing the experimental system with such a high pumping speed prevents the QMS from being damaged by too high pressures of $p > 1 \times 10^{-2}\,\mathrm{Pa}$.

In addition, the COOPER experiment will use a leak detector as a backup flux measurement device. As explained in section 3.2.4, leak detectors can only measure the permeation flow of one mass-to-charge ratio at a time. However, due to the different operating principle of a leak detector compared to a QMS (explained in section 3.2.4), they can measure particle flows with often higher sensitivity, allowing them to resolve particle flows as low as $q^{\mathrm{per}}_{\mathrm{pV},s} = 1 \times 10^{-12}\,\mathrm{mbar \cdot L/s}$ [195].

Due to the relatively large experimental setup, it is decided to use ISO-KF flange connections for the cold piping components that connect the permeation cells to the measurement system. These connections are presented in section 3.1.2. The primary vacuum

TABLE 6.1
ESTABLISHED INPUT DESIGN PARAMETERS OF THE COOPER EXPERIMENT.

Design parameter	Parameter range
Operating temperature	$T \leq 823\,\mathrm{K}$
Membrane thickness	$d_{\mathrm{disk}} \geq 1 \times 10^{-3}\,\mathrm{m}$
Explorable $^2H_2$ driving pressures	$1\,\mathrm{Pa} < p_{22} < 1 \times 10^{5}\,\mathrm{Pa}$
Measurable permeation flux range	$1 \times 10^{-9} < q^{\mathrm{per}}_{\mathrm{pV},s} < 1 \times 10^{-4}$ [mbar · L/s]
Effective permeation surface area	$A_{\mathrm{per}} = 9.1 \times 10^{-4}\,\mathrm{m}^2$
Target pumping speed of TMP	$S_{\mathrm{pump}} \approx 100\,\mathrm{L\,s^{-1}}$
Target vacuum level at QMS	$p < 1 \times 10^{-4}\,\mathrm{Pa}$
Target S_{eff} in permeation cells	$S_{\mathrm{eff}} > 1\,\mathrm{L\,s^{-1}}$

level in the permeation cells prior to hydrogen gas injection is aimed at $p < 1 \times 10^{-3}$ Pa. This ensures a sufficiently low partial pressure of O_2 in the system to prevent oxidation of the permeation membrane while it is hot. As explained in section 3.1.2, the leak rate of ISO-KF flanges is of the order of $q^{\mathrm{add}}_{\mathrm{pV}} \approx 1 \times 10^{-6}\,\mathrm{mbar \cdot L/s}$. According to the right-hand graph in figure 3.7 and considering that the number of installed ISO-KF flanges is relatively high, maintaining a vacuum pressure of $p < 1 \times 10^{-3}$ Pa requires an effective pumping speed within the permeation cells of about $S_{\mathrm{eff}} \approx 1\,\mathrm{L/s}$. Moreover, the right-hand graph in figure 3.7 shows that even if the molecular permeation flux into the downstream chamber was as high as $q^{\mathrm{per}}_{\mathrm{pV},s} \approx 1 \times 10^{-4}\,\mathrm{mbar \cdot L/s}$, an effective pumping speed of $S_{\mathrm{eff}} \approx 1\,\mathrm{L/s}$ would result in a vacuum level in the downstream permeation cell of at most $p \approx 1 \times 10^{-2}$ Pa. Therefore, an effective pumping speed of $S_{\mathrm{eff}} \approx 1\,\mathrm{L/s}$ in the permeation cells is considered a reasonable input parameter for the COOPER design. All design input parameters of the COOPER experiment defined in this section are listed in table 6.1.

The right-hand plot in figure 6.1 shows the theoretically calculated steady state deuterium permeation flux as a function of the partial pressure of $^1H_2$ gas injected into the upstream chamber that would occur in a co-permeation measurement at $T = 573\,\mathrm{K}$ with the COOPER experiment. For the calculation, it is assumed that the $^2H_2$ partial pressure in the upstream chamber is maintained at $p^{\mathrm{UI}}_{22} = 10\,\mathrm{Pa}$. The plot is calculated by inserting the reduced concentrations $\zeta_{\mathrm{r},1}(W_1)$ and $\lambda_{\mathrm{r},1}(W_1)$ for parallel membranes which are plotted in figure 2.11 into equation (4.40). The plot shows that the above-defined input parameters of the COOPER experiment would allow covering all three permeation regimes of the co-permeating protium isotopes. Therefore, the COOPER experiment is designed to allow the investigation of co-permeation from the surface-limited to the diffusion-limited co-permeation regime. According to the plotted theoretical calculation, the COOPER experiment would allow measuring a reduction in the deuterium permeation flux due to co-permeation effects by a factor of about six if $^1H_2$ gas with a pressure

of $p_{11}^{\mathrm{UI}} \approx 500\,\mathrm{Pa}$ was injected into the upstream chamber. Since the COOPER experiment covers the diffusion-limited regime of co-permeating protium isotopes, it would allow the experimental validation of the derived algebraic formulas for co-permeation (4.41) and (4.42).

It is important to note that the presented design input parameters are based on the experimental hydrogen transport parameters of Eurofer'97 listed in table 5.1 and equation (5.18). Therefore, whether the permeation processes occur as theoretically predicted in figure 6.1 depends to some extent on the approximate correctness of these values.

It should also be noted that the design input parameters of COOPER are optimized for co-permeation measurements. However, as will be shown later, the COOER experiment should also allow performing counter-permeation measurements and thus the validation of the derived algebraic formulas for counter-permeation (4.33) and (4.34).

6.2. Engineering design and construction

Figure 6.2 shows the process flow diagram of the entire COOPER experiment. The meanings of the symbols used in the PFD are listed in table XI. The heart of the COOPER facility is the so-called permeation tube in which the multi-isotopic permeation processes investigated take place. It denotes the bolted connection of PC-A and PC-B separated by the sample permeation membrane, which can be seen on the right-hand side in figure 6.2. The design of the permeation tube has been developed from scratch using the CAD software CATIAv5. It allows the creation of three-dimensional drawings of any shape and their translation into manufacturing plans. A sectional view of a CAD drawing of the permeation tube consisting of both permeation cells is shown in figure 6.3.

Both permeation cells consist of identical square, thick-walled stainless steel chambers with cylindrical internal cavities. Their flat back walls are welded to DN16CF flanges sealed with high-temperature silver-plated copper gaskets. While the flange of the downstream chamber PC-B is closed with a blank flange, the flange of the upstream chamber PC-A is connected to a thermocouple feedthrough. A graphite-sealed thermocouple feedthrough of the type shown in the middle panel of figure 3.10 is used for this purpose. This type of feedthrough is chosen because it is suitable for vacuum pressures as low as $p \approx 5 \times 10^{-4}\,\mathrm{Pa}$ at temperatures up to $T = 823\,\mathrm{K}$ [214]. Three mineral-insulated K-type thermocouples (see description in section 3.2.1) called TC-02, TC-03, and TC-04 are inserted through the graphite seal of the feedthrough into PC-A (see figure 6.3). They measure the temperature of the disk center (TC-02), the disk border (TC-03), and the temperature of the injected gas in PC-A (TC-04), respectively.

As can be seen in the center of figure 6.3, each permeation cell ends in a wide open flange that allows the two chambers to be bolted together with the sample membrane between them. A photo of the fabricated permeation tube is shown in the left photo in figure 6.4. Gas can enter and exit each permeation cell through a narrow gas inlet tube and

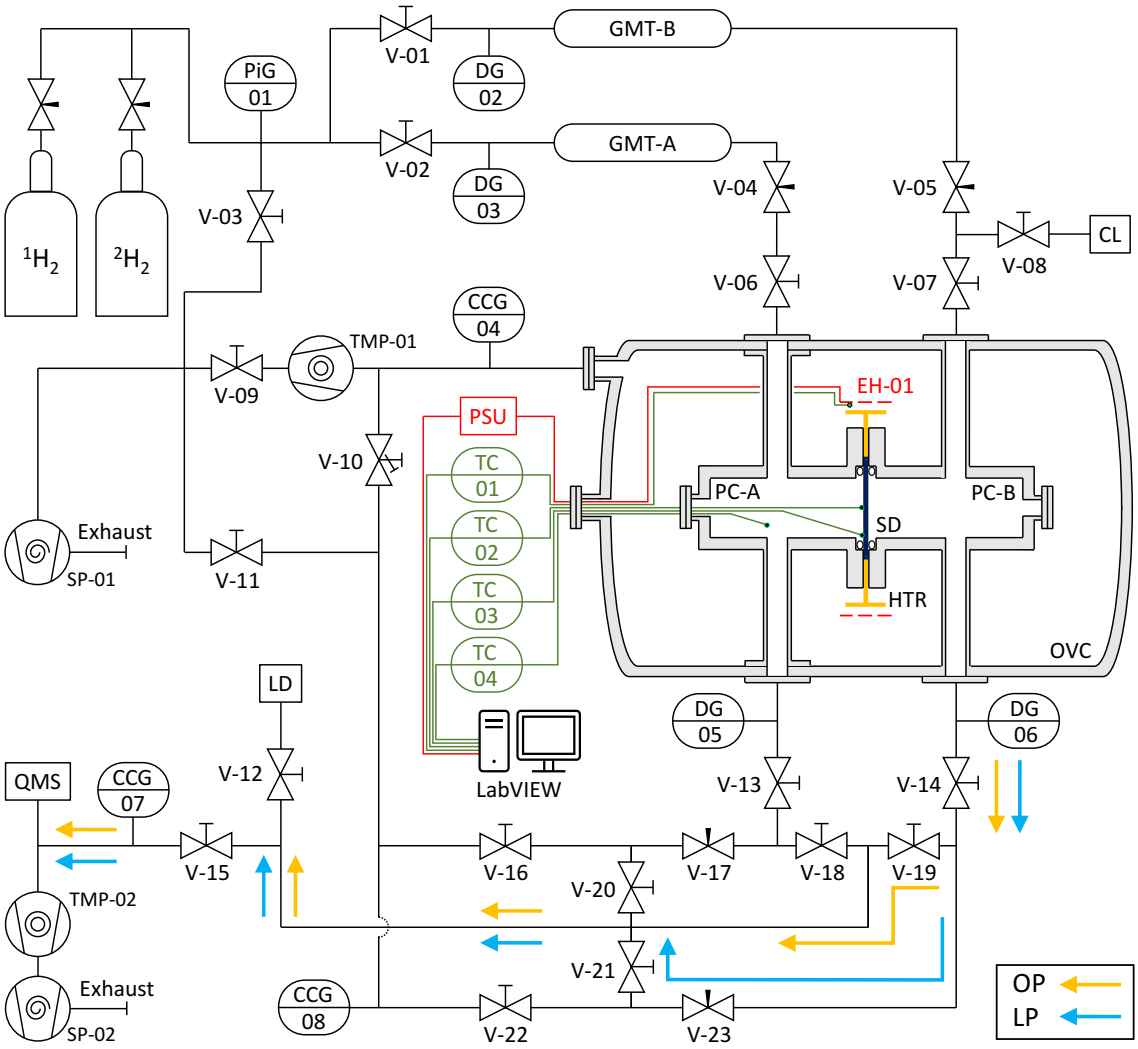

Fig. 6.2. Process flow diagram of the experimental setup of the COOPER facility.

a wider outlet tube. They penetrate the two vertical walls of an outer vacuum chamber (OVC) that surrounds the permeation tube (see the left photo in figure 6.4). A picture of the fabricated outer OVC is shown in the right-hand photo in figure 6.4. It is a cubic vessel made of 316 stainless steel. The front and rear planes of the OVC are open and form flanges with embedded Viton® seals. They are closed by bolted rectangular cover plates. The front cover plate has a large viewport that allows the condition of the permeation tube to be observed during operation. The outer vacuum chamber is also designed using CATIAv5. The created manufacturing plan showing the dimensions of the OVC can be seen in figure 6.5.

The rear cover plate of the OVC is connected to ceramic sealed thermocouple and power feedthroughs of the same type as those described in section 3.2.1 and shown at left and right in figure 3.10. The cables that leave the metal sheaths of the thermocouples outside of PC-A are connected to the thermocouple feedthroughs at the rear plate of the OVC. To protect the cables from the intense thermal radiation of the hot permeation tube, their raw metal wires are insulated by ceramic tubes and additionally surrounded by pure

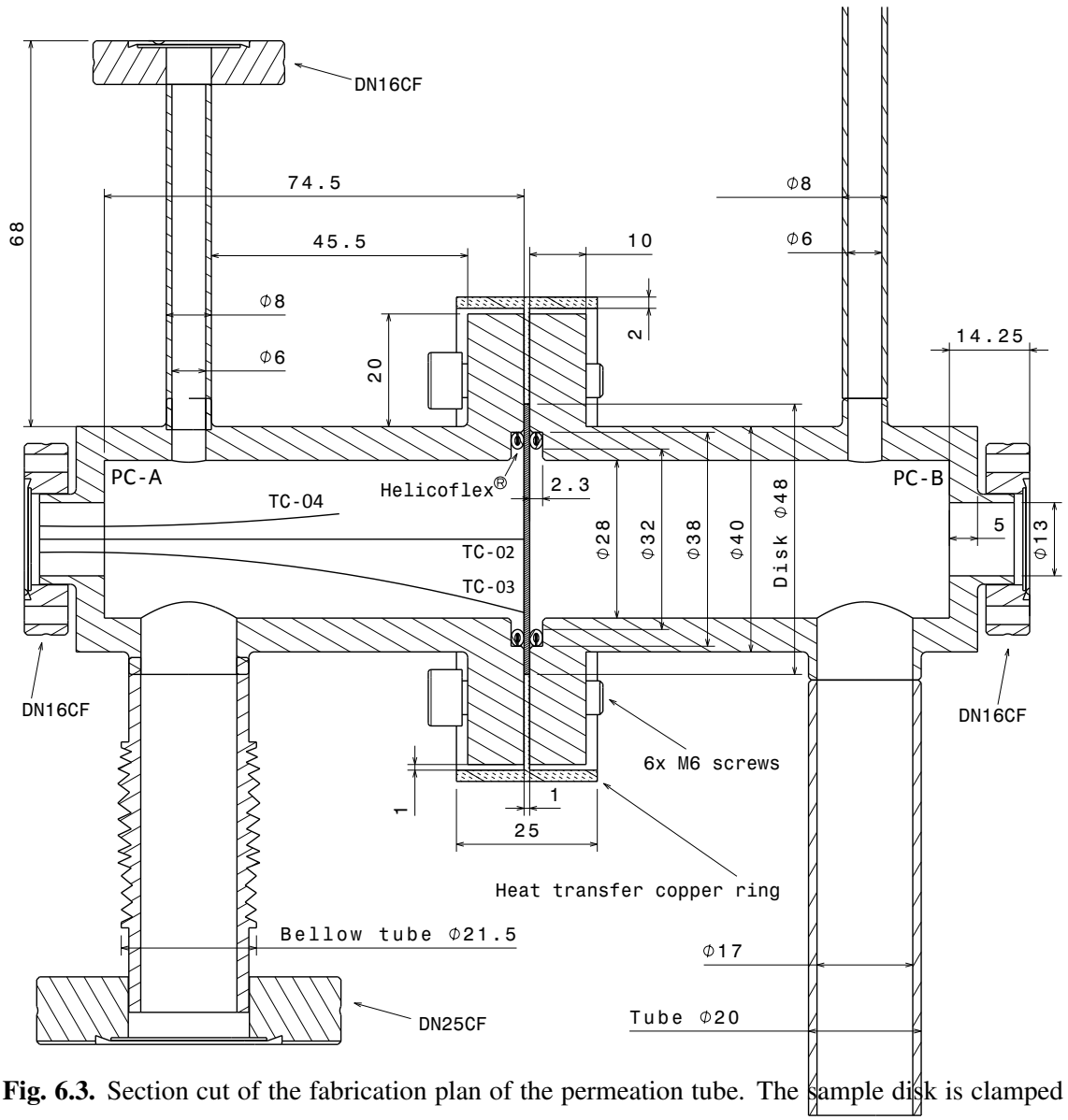

Fig. 6.3. Section cut of the fabrication plan of the permeation tube. The sample disk is clamped between the two permeation cells.

fiberglass tape. Using standard high-temperature thermocouple cable insulation made of polyvinyl acetate or wax-impregnated fiberglass would not be suitable for the OVC environment because the low pressure and high temperature would cause the insulation to vaporize.

While the tubes exiting PC-B are welded from the inside against the inner walls of the OVC, the tubes exiting PC-A are bolted through internal CF flanges using silver-plated copper gaskets. This design allows PC-A to be disconnected and removed from the system while PC-B remains in its fixed position. This reduces the possibility of leakage at the flanged joints. Installing the copper gaskets and tightening the CF flange bolts of PC-A requires some longitudinal and lateral clearance of at least one of the gas tubes. For this reason, the PC-A gas outlet tube is designed as a welded flexible bellows tube. Outside the OVC, the inlet and outlet connections of the permeation tube terminate in welded DN16CF flanges. A sectional view of the permeation tube connected to the internal ports

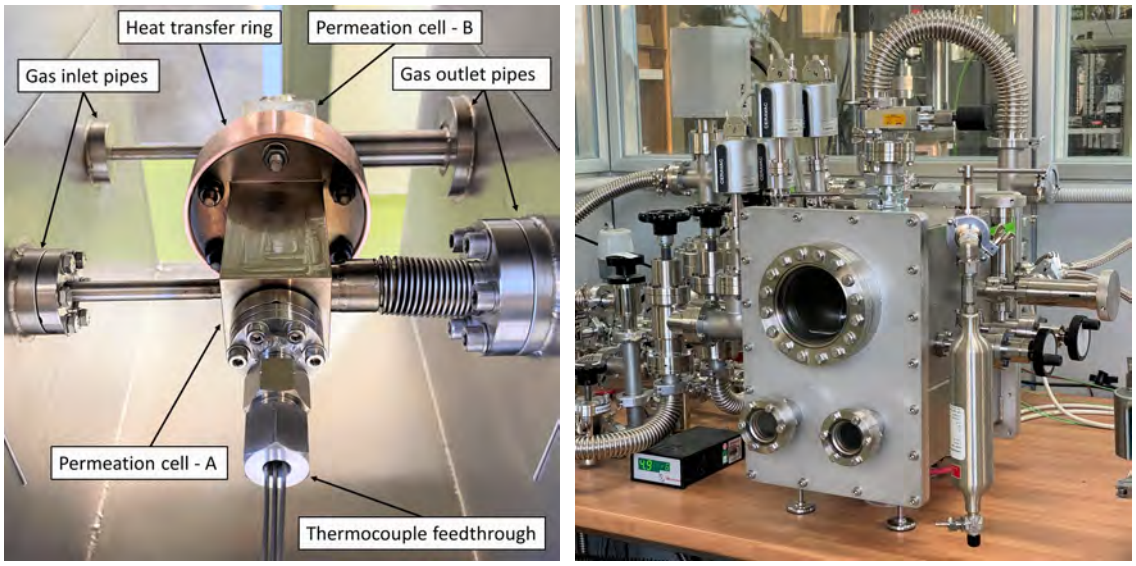

Fig. 6.4. [Left] Photo of the permeation tube connected to the outlet ports of the outer vacuum chamber. [Right] Exterior view of the outer vacuum chamber containing the permeation tube.

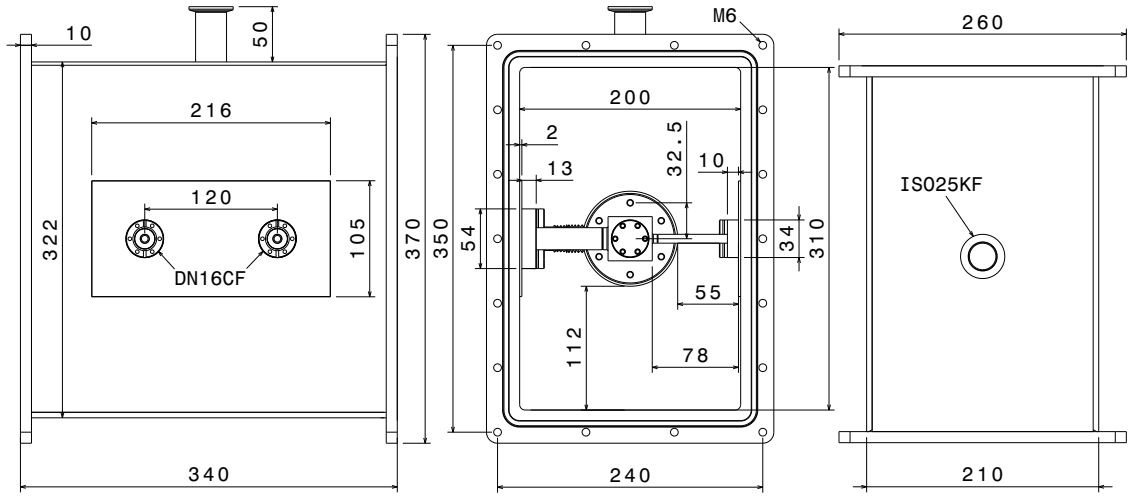

Fig. 6.5. Fabrication plan of the designed outer vacuum chamber without the cover plates which contains the permeation tube.

of the OVC is shown in figure 6.6. It provides insight into permeation cells and net deuterium permeation direction from PC-A to PC-B.

The sample disk (SD) with a radius of $r_{\text{disk}} = 24 \times 10^{-3}$ m is clamped between the two inner custom flanges of the permeation cells using six M6 high-temperature stainless steel bolts made of Incoloy Alloy® A-286. This high-temperature alloy maintains an approximately constant yield strength of 600 MPa up to a temperature of $T = 873$ K [250]. This prevents the flange joint from weakening during the heat-up and cool-down phases of the test campaigns. Very good sealing between the permeation cells and the sample disk is essential for accurate measurements. Although the permeation measurements are performed at temperatures of at most $T = 823$ K, the design temperature of COOPER is higher, at $T = 873$ K. To ensure good sealing under such extreme conditions, specially de-

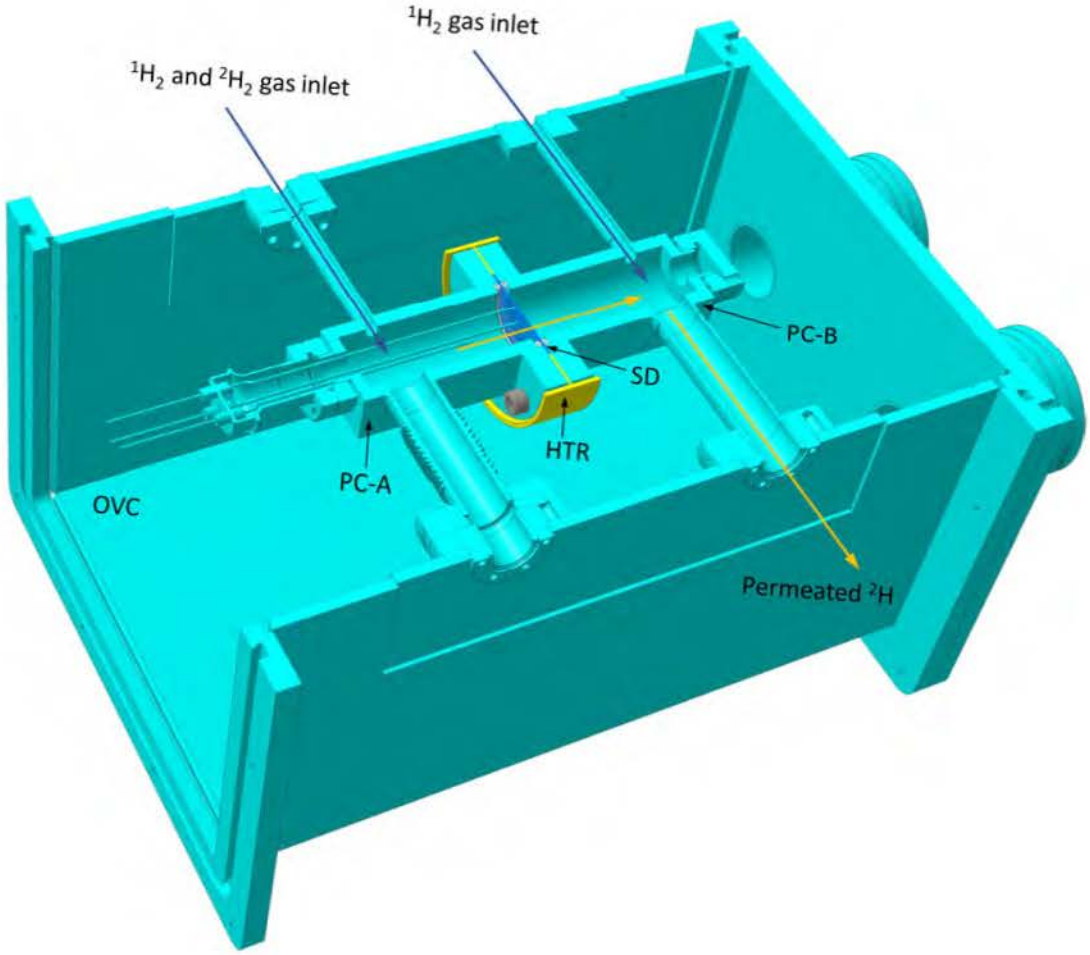

Fig. 6.6. Sectional view through the outer chamber and the inner permeation cells which are separated by the sample disk and a heat transfer copper ring.

signed Helicoflex® O-rings are employed. Their working principle is described in section 3.1.2. The spring energized seals selected consist of a silver plated Inconel®600 lining surrounding an internal Nimonic90 spring from Technetics. They provide sufficient leak tightness for the required vacuum conditions up to a temperature of $T = 923\,\mathrm{K}$.

The top left photo of figure 6.7 shows the open flange of permeation cell A. It is equipped with a gasket bed that surrounds the internal gas cavity. The flange of permeation cell B has an identical shape. A Helicoflex® O-ring placed inside the gasket bed is shown in the upper right photo. Note that the designed depth of the bed is equal to the thickness of a Helicoflex® gasket in the compressed state, which provides maximum tightness. In the lower left photo in figure 6.7 it can be seen how the sample disk is positioned on top of the gasket. The sample disk is surrounded by a copper disk that merges into a wide copper cylinder surrounding the flanges of the permeation cells. It is called the heat transfer ring (HTR). The assembly of the permeation tube is shown in the lower right photo in figure 6.7. To thermally connect the two thermocouples TC-02 and TC-03 to the sample disk, they are inserted into cylindrical thermocouples sockets made of 316 stainless steel that are previously welded to the disk surface.

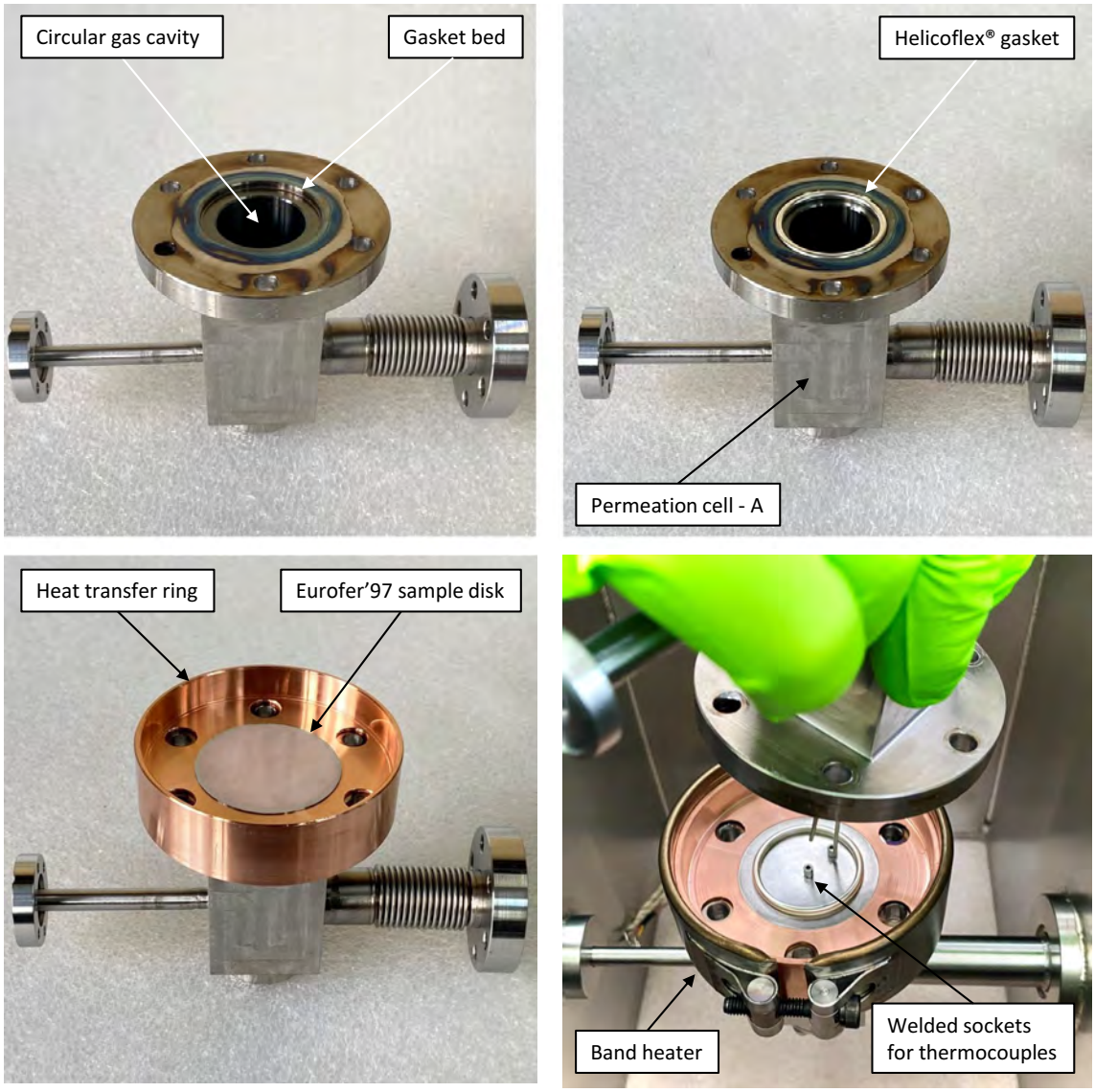

Fig. 6.7. Photos showing the assembly of the permeation tube.

The sample disk is heated to the mentioned temperature range by a cylindrical mineral-insulated band heater with a power of 600 W clamped around the HTR. The inner mineral insulation surrounding the heating wires of the band heater transfers heat by thermal contact and is therefore suitable for vacuum applications. It can be operated up to a temperature of $T = 1033\,\mathrm{K}$ [251]. There is an engineered gap of one millimeter between the HTR cylinder and the permeation cell flanges. This allows both parts, which are made of different materials, to thermally expand and contract independently during heating cycles. The contact force between the HTR and the sample disk is increased by tightening the band heater clamping screw. To ensure continuous thermal contact between the two during thermal expansion and contraction, the heater is secured around the HTR with a spring-loaded high-temperature bolt.

The power supply of the band heater is controlled by a LabVIEW program. It allows the user to set an arbitrary target temperature of maximum $T = 1013\,\mathrm{K}$ for the heater

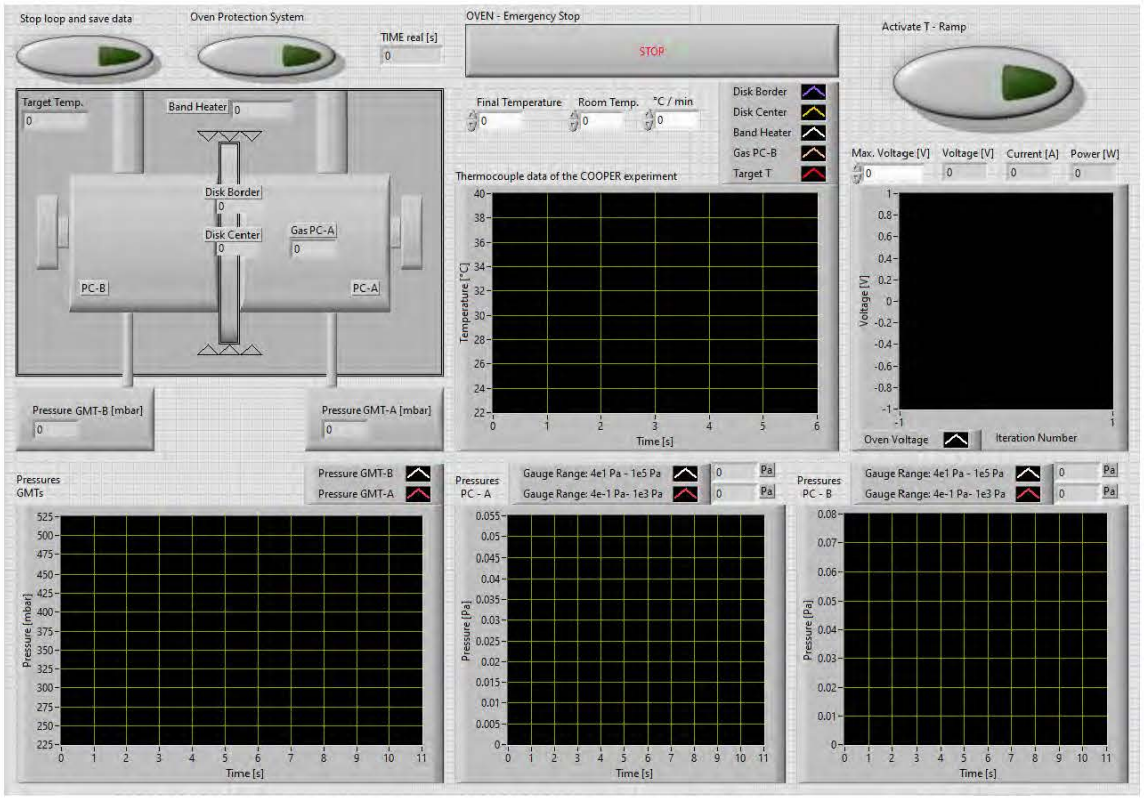

Fig. 6.8. Developed LabVIEW program to control the power supply of the band heater and to monitor the temperatures and pressures measured at different locations in the experimental setup of the COOPER facility.

and the desired rate of increase or decrease of the temperature ramp. Figure 6.8 shows the control panel of the created LabVIEW program. A PID controller is built into the LabVIEW program. It uses the momentary temperature of the heater as an input to control the voltage applied to the band heater (see the upper plot on the right in figure 6.8). The momentary temperature of the heater is measured by a thermocouple called TC-01, which is integrated into its internal mineral structure. The control panel monitors the temperature data measured by all four thermocouples TC-01, TC-02, TC-03, and TC-04 (see the upper central graph in figure 6.8).

When the band heater is turned on, heat quickly diffuses into the HTR disk between the permeation cells before entering the sample disk. Since the HTR is in close contact with the permeation cell flanges, they will heat up as well. The heat enters the sample disk through the contact surface between the HTR and the sample disk, as well as through the contact surface between the permeation cell flanges and the sample disk. An advantage of this custom-designed external heating system is that any degassing contaminants from the heater do not enter the permeation cells and thus the measurement system during operation. This is an important requirement for accurate permeation measurements.

The design of the heating system is based on a simulation of the temperature profile that establishes in steady state inside the heat transfer ring and the sample disk. Therefore, the designed 3D model of the permeation tube attached to the OVC is imported into the

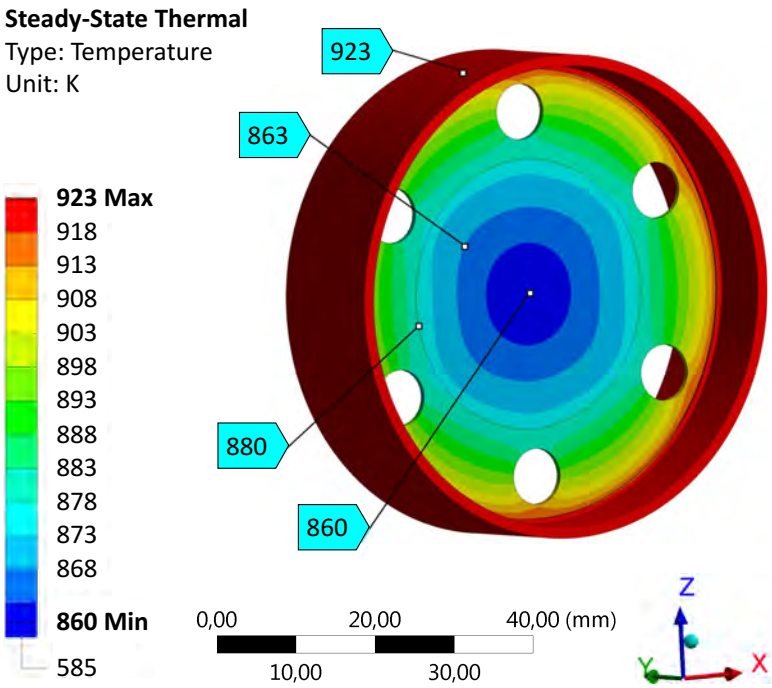

Fig. 6.9. Simulated steady state temperature profile which establishes throughout the heat transfer ring surrounding an Eurofer'97 sample disk in its center considering that the outer cylinder surface of the HTR is kept at a temperature of 650 K.

finite element software ANSYS. The simulation is performed assuming that the contact surface between the band heater and the HTR is kept at a temperature of $T = 923$ K. The simulation assumes that the interior cavities of the permeation cells and the OVC are free of gas. Therefore, the model considers that all components inside the OVC experience heat transfer only by radiation and thermal conduction. Only the outer walls of the OVC are assumed to have additional heat removal by air convection. The calculated steady state temperature profile established throughout the HTR attached to the sample disk is shown in Figure 6.9. It shows that at steady state, according to the simulation, the temperature of the HTR drops from $T = 923$ K at the HTR jacket to $T = 880$ K at the contact surface of HTR and sample disk. Thermocouple TC-03 which is attached to the disk border near the Helicoflex® gasket would therefore indicate a temperature of approximately $T = 868$ K. Thermocouple TC-02 located in the center of the sample disk would measure a temperature of $T = 860$ K. Therefore, the simulation suggests that the designed heating system placed inside of the OVC would result in a relatively small radial temperature gradient established within the sample disk of only about $\Delta T = 10\,^{\circ}$C. Ensuring a relatively flat radial temperature profile of the sample disk is essential for meaningful and precise experimental results.

The simulated steady state temperature profile that would adjust over the entire outer surface of the permeation tube is shown in figure 6.10. It can be seen that the temperature decreases rapidly as one moves away from the permeation cell flanges toward the DN16CF flanges at the back walls of the permeation cells. In fact, according to the finite element simulation performed, the square bodies of the permeation cells would be on average about $\Delta T = 150$ K - $\Delta T = 220$ K colder than the HTR. The temperatures of the tube walls connecting the permeation cells to the OVC decrease linearly from about $T = 673$ K at the permeation tube walls to $T = 373$ K at the OVC walls. The simulation shows that

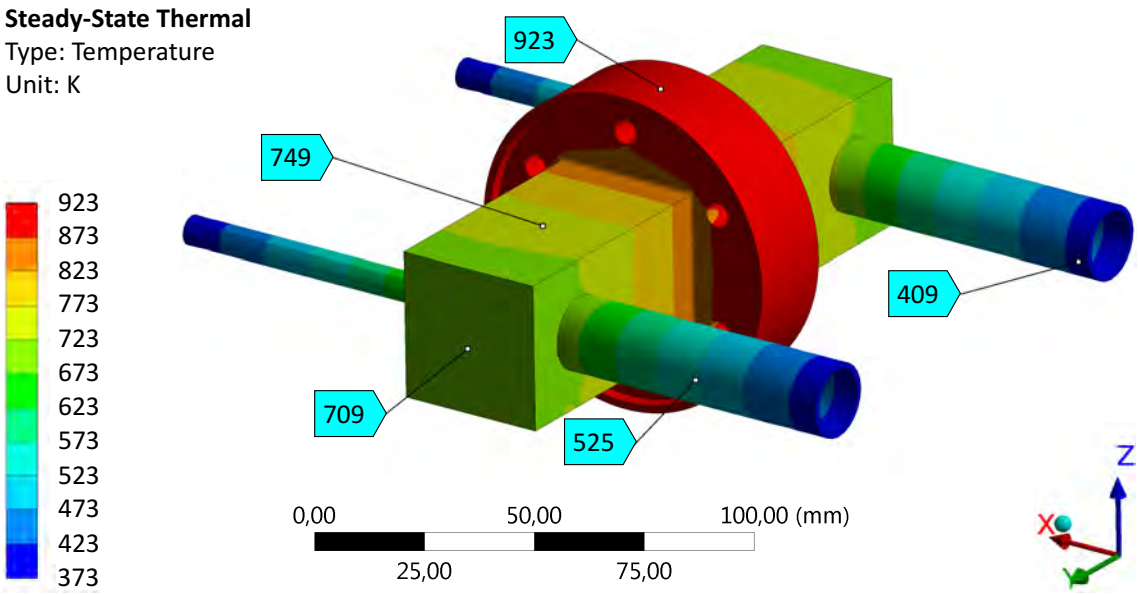

Fig. 6.10. Simulated steady state temperature profile which establishes throughout the permeation tube surface considering that the outer cylinder surface of the HTR is kept at a temperature of 650 K.

even if the band heater is set to a temperature as high as $T = 923$ K, the outer walls of the OVC facing the atmosphere of the laboratory would have an average temperature of only $T \approx 350$ K, a temperature that poses no immediate danger to the user or the surrounding equipment.

The vacuum inside the OVC has the advantage of eliminating leakage or permeation of atmospheric gases into the interior of the permeation cells. This helps to eliminate difficult-to-estimate uncertainty factors in the measurement results. Thus, it provides a much cleaner environment compared to previous experiments where the permeation tubes are located in air [88], [190]. In addition, the vacuum of the OVC enables efficient degassing of the permeation cell walls after each permeation flux measurement.

A photograph of the fully assembled setup of the COOPER experiment is depicted in figure 6.11. Upon exiting the OVC, the two external DN16CF flanges linked to the inlet gas pipes of the permeation tube are connected to all-metal UHV open/close valves (V-06 and V-07) of the same type as shown on the left in figure 3.5. The downstream permeation cell B has an additional connection to a calibrated $^2H_2$ leak with the purpose of calibrating the QMS and the LD for $^2H_2$ permeation flux measurements.

Furthermore, the gas inlet pipes of the permeation tube are linked to a gas preparation and injection system which is shown in figure 6.12. It allows the introduction of an arbitrary partial pressure configuration of $^1H_2$ and $^2H_2$ into each permeation cell via UHV all-metal leak valves of the same type as shown on the right in figure 3.6 (V-04 and V-05). It should be noted that to avoid contamination of the downstream chamber, the injection of $^2H_2$ gas into permeation cell B must be avoided at all costs. Both gas inlet valves are connected by flexible stainless steel tubing to custom-made gas mixing tanks

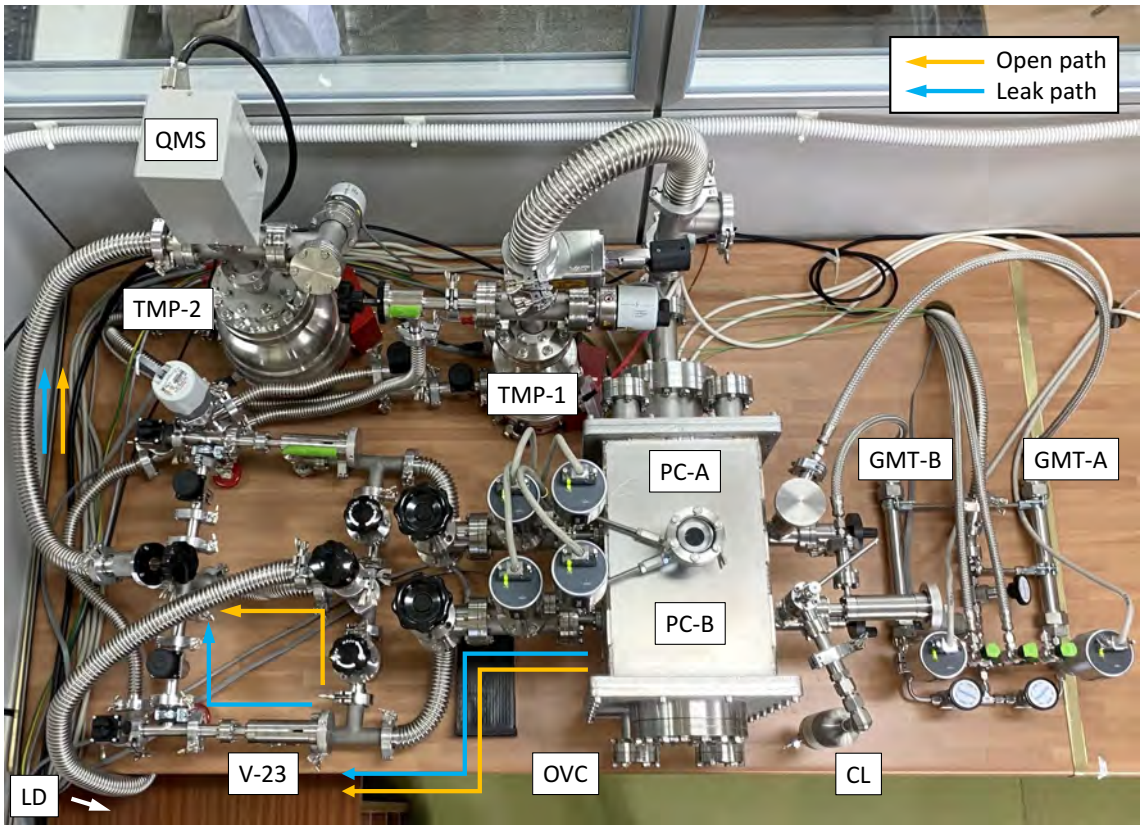

Fig. 6.11. Photo of the mounted COOPER experiment. The outer vacuum chamber which houses the permeation tube is visible in the center. On the right, there is the gas mixing and gas injection system. On the left, the leak paths and open paths are linked to the QMS, leak detector, and vacuum system.

(GMT-A and GMT-B) with a volume of about 100 mL each. As visible in figure 6.12, the gas piping system is constructed using double ferrule compression fittings. Unlike conventional vacuum components, double ferrule compression fittings are sufficiently tight to withstand gas pressures of $p > 1 \times 10^5$ Pa (see section 3.1.2). The gas mixing tanks serve as individual gas reservoirs for the two permeation cells. In each tank, an arbitrary partial pressure configuration of $^1H_2$ and $^2H_2$ can be premixed prior to gas injection. The gas pressures inside of the two GMTs are controlled by the two capacitance diaphragm pressure gauges DG-02 and DG-03 with measuring ranges of 1.3×10^1 Pa $< p < 1.3 \times 10^5$ Pa (see description in section 3.2.2). Two bellows-sealed high-temperature valves (V-01 and V-02), with characteristics similar to the valves shown on the right in figure 3.5, are placed directly behind the pressure sensors and serve as open/close gates for the GMTs. These two valves are connected to a manifold that connects to a $^1H_2$ and a $^2H_2$ gas cylinder. Each is equipped with a pressure regulator and a fine flow needle valve similar to those shown on the left-hand side in figure 3.6. Through valve V-03, the manifold is connected to a dry scroll vacuum pump (SP-01) of the type described in section 3.1.3 and a Pirani gauge (PiG-01) which is calibrated for hydrogen gas pressure measurements.

After an initial evacuation of the entire gas line system, both GMTs can be successively filled with individual gas mixtures of arbitrary partial pressure compositions. Given

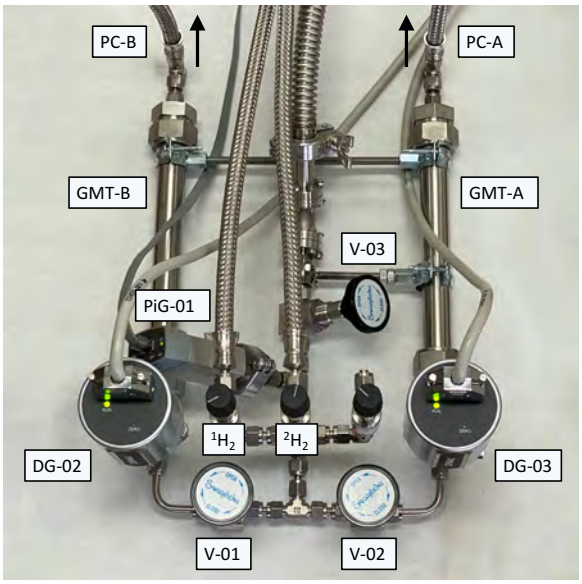

Fig. 6.12. Photo of gas preparation and injection system of the COOPER experiment involving the two gas mixing tanks GMT-A and GMT-B.

that the valves V-01 to V-08 are initially closed, the procedure for preparing individual gas mixtures in the two GMTs is as follows. First, the gas preparation and injection system is evacuated via SP-01 by opening the valves V-01, V-02, and V-03 until PiG-01 indicates a total pressure that is sufficiently low to continue the mixing process. Then, valve V-01 and valve V-03 are closed while valve V-02 is maintained open. The needle valve of the first gas component is carefully manipulated until the desired partial pressure in GMT-A is reached, which is measured by DG-03. Subsequently, the needle valve of the second gas component is opened until the target partial pressure of the second gas component is reached. It is equal to the momentary pressure measured by DG-03 minus the partial pressure of the first gas component which was injected previously. When GMT-A contains the desired gas composition, valve V-02 is closed. To fill GMT-B, valve V-02 is opened and the gas-filling procedure is repeated.

The two exit ports of the outlet gas pipes of the OVC are each connected to two capacitance diaphragm pressure gauges, one for a measurement range of 1.3×10^{-1} Pa $< p < 1.3 \times 10^{3}$ Pa and the other with a range of 1.3×10^{1} Pa $< p < 1.3 \times 10^{5}$ Pa. The signals of all four pressure gauges are read out, monitored and stored by the developed LabVIEW program (see the lower middle and lower right-hand plots in figure 6.8). In this way, it is possible to precisely control the pressures of the gas injected into the permeation cells. While the two pressure gauges connected to PC-A share the name DG-05, the two gauges linked to PC-B are labeled DG-06.

As visible in the PFD in figure 6.2, both permeation cells can expose their internal atmospheres to a HAL 101X RC QMS from Hiden Analytical (see section 3.2.3) and a high-vacuum pumping system. Alternatively, both permeation cells can be linked to a HLT 570 SmartTest leak detector from Pfeiffer Vacuum with an integrated Twin-Flow™ mode (see section 3.2.4) [216]. The connecting system of valves and piping is made of ISO-25KF flange components with inner radii as specified in table 3.1. Depending on whether a permeation flux measurement is performed with the QMS or the LD, either

valve V-12 or valve V-15 is opened while the other remains closed.

During a permeation measurement with the COOPER experiment, only the downstream permeation cell B is connected to the measurement system. Valves V-18 and V-20 are therefore only opened during the initial evacuation of the whole pipe system or during degassing of both permeation cells. The unique design of the COOPER experiment is based on the ability to connect the downstream permeation cell B to the vacuum and measurement system in two different ways.

The *open path* (OP) is defined as a route from PC-B to the QMS or LD via the open/close valves V-14 and V-19, keeping the valves V-21 and V-23 closed (see orange arrows in the figures 6.2 and 6.11). This path is used, for example, in a mono-isotopic or co-permeation measurement where the downstream permeation cell B is kept at a high vacuum by connecting it directly to the QMS and vacuum system.

In contrast, the *leak path* (LP) describes a route from PC-B to the QMS or LD via the open/close valves V-14 and V-21, passing the leak valve V-23, while keeping the open/close valve V-19 closed (see blue arrows in the figures 6.2 and 6.11). Hence, while the *open path* is a pipe connection with only open/close valves of high conductance, the *leak path* is interrupted by a UHV all-metal leak valve V-23 with a variable flow rate. The selected leak valve is of the same type as that shown on the right in figure 3.6. It is highlighted in figure 6.11. Manipulation of the leak valves allows controlling the gas leak rate from the corresponding permeation cell to the measuring system in a wide range of $1 \times 10^{-10}\,\mathrm{mbar \cdot L/s} < q_{\mathrm{pV}}^{\mathrm{leak}} < 5 \times 10^{2}\,\mathrm{mbar \cdot L/s}$ (see description of all-metal leak valves in section 3.1.2). This path is needed, for example, for counter-permeation measurements where the downstream permeation cell B is filled with $^{1}H_2$ gas. The leak path allows the gas flow from a gas-filled permeation cell to the QMS and vacuum system to be controlled so that the operating pressure requirement $p < 1 \times 10^{-2}\,\mathrm{Pa}$ of the QMS is met.

The QMS is directly connected to the inlet of a HiPace® 700 turbomolecular pump from Pfeiffer Vacuum with an internal pumping speed for $^{1}H_2$ gas of $S_{\mathrm{pump}}^{\mathrm{TMP-02}} = 550\,\mathrm{L\,s^{-1}}$, called TMP-02 [252]. Its pumping speed is slightly higher than the design value given in table 6.1, but of the same order of magnitude. Therefore, it should meet the requirements. This pump model requires the backing pressure of the fore-vacuum at the pump outlet to be at most $p_{\mathrm{out}}^{\mathrm{max}} = 1.1 \times 10^{3}\,\mathrm{Pa}$. Considering that the TMP is switched on below a pressure of about $p \approx 10\,\mathrm{Pa}$, it follows from equation (3.10) that a backing pump with a pumping speed of at least $S_{\mathrm{out}}^{\mathrm{min}} \approx 5\,\mathrm{L\,s^{-1}}$ in the pressure range of the fore-vacuum should be connected to the outlet of TMP-02. Therefore, in the COOPER experimental setup, a nXDS15i dry scroll pump from Edwards Vacuum is selected as the backing pump for the TMP-02 and labeled SP-02. It has a pumping speed of $S_{\mathrm{pump}}^{\mathrm{SP-02}} \approx 15\,\mathrm{L\,s^{-1}}$ in the required fore-vacuum pressure regime [209].

The *open path* connecting the interior of a permeation cell to the inlet of TMP-02 has a length of about $l_{\mathrm{pipe}} = 1.5\,\mathrm{m}$ and an average inner radius of about $r_{\mathrm{in}} = 1.2 \times 10^{-2}\,\mathrm{m}$ (see ISO-25KF specifications in table 3.1). Taking this into account, it follows from the

formulas (3.4) and (3.5) that the conductance of the *open path* is about $C_{\mathrm{OP}} \approx 1\,\mathrm{L\,s^{-1}}$. Inserting C_{OP} and the internal pumping speed of TMP-02 into equation (3.6) yields that the effective pumping speed inside a permeation cell connected to the vacuum system via the open path is approximately $S_{\mathrm{eff}}^{\mathrm{OP}} \approx 1\,\mathrm{L\,s^{-1}}$. This agrees with the design input parameter shown in table 6.1.

According to equation (3.3) and considering that TMP-02 is connected to SP-02 via an ISO-16KF bellows tube with a length of $l_{\mathrm{pipe}} = 1\,\mathrm{m}$, at $p = 100\,\mathrm{Pa}$ the conductance of the piping system which connects the permeation cells with SP-02 is estimated to be at least $C_{\mathrm{OP}} \approx 6\,\mathrm{L\,s^{-1}}$. Since the pumping speed of SP-02 is about $S_{\mathrm{pump}}^{\mathrm{SP-02}} \approx 15\,\mathrm{L\,s^{-1}}$, it follows from equation (3.6) that the lowest effective pumping speed during pump-down is approximately $S_{\mathrm{eff}}^{\mathrm{OP}} \approx 4\,\mathrm{L\,s^{-1}}$. Consequently, by estimating that the volume of the entire piping system between the two permeation cells and the vacuum system is approximately $V = 5 \times 10^{-3}\,\mathrm{m^3}$, the left-hand graph in figure 3.7 yields that the pump-down time during evacuation will be at most three minutes before reaching $p < 100\,\mathrm{Pa}$.

The OVC is connected to an independent system of turbomolecular pump and dry scroll backing pump. They are named TMP-01 and SP-01. While the selected dry scroll pump model is the same model as that of SP-02, the turbomolecular pump connected to the OVC is a HiPace® 300 from Pfeiffer Vacuum with a pumping speed of $S_{\mathrm{pump}}^{\mathrm{TMP-02}} = 250\,\mathrm{L\,s^{-1}}$ for air molecules. During COOPER operation, the hot band heater degasses particles at a rate significantly higher than the degassing and permeation rate occurring inside the permeation cell chambers. To handle such high degassing rates, a higher effective pumping speed is required inside the OVC. Therefore, the OVC and the TMP-01 are connected by a combination of DN40CF and ISO-40KF piping components with an approximate length of $l_{\mathrm{pipe}} \approx 1\,\mathrm{m}$ and an average inner radius of $r_{\mathrm{in}} \approx 2 \times 10^{-2}\,\mathrm{m}$ (see table 3.1). According to the formulas (3.4), (3.5) and (3.6) this implies that in the molecular flow regime $C_{\mathrm{OVC}} \approx S_{\mathrm{eff}}^{\mathrm{OVC}} \approx 8\,\mathrm{L\,s^{-1}}$. By performing an equivalent calculation as above, it is concluded that the minimum effective pumping speed during initial pump-down of the OVC is about $S_{\mathrm{eff}}^{\mathrm{OVC}} \approx 5\,\mathrm{L\,s^{-1}}$. Therefore, and because the interior volume of the OVC is approximately $V = 5 \times 10^{-2}\,\mathrm{m^3}$, from the right-hand plot in figure 3.7, it can be derived that the highest expected pump-down time of the OVC is about 10 min.

Each permeation cell can be evacuated after a measurement without destroying the vacuum created by TMP-02 and SP-02. This is done by slowly opening the valves V-13, V-16 and V-17 (if PC-A is evacuated) or V-14, V-22 and V-23 (if PC-B is evacuated) while keeping the valves V-18 and V-20 (if PC-A is evacuated) or V-19 and V-21 (if PC-B is evacuated) closed. Evacuation is performed using TMP-01 and SP-01. Therefore, first, valve V-11 is opened which enables reducing the pressure in the corresponding permeation cell to the backing pressure provided by SP-01. Then, valve V-11 is closed and needle valve V-10 is slowly opened to further reduce the pressure in the permeation cell using the turbomolecular pump TMP-1. Evacuating the permeation cell with TMP-01 and SP-01 instead of TMP-02 and SP-02 prevents the QMS from being exposed to high loads of hydrogen gas and the piping system from being contaminated.

Continuous total vacuum pressure measurements in the pipe systems of the COOPER experiment are performed by the cold cathode pressure transmitters CCG-04, CCG-07 and CCG-08 (see figure 6.2). When a temperature or pressure value is given below, an index corresponding to the sensor name is added to the physical quantity.

6.3. Commissioning

This section presents the results obtained during the various steps of the commissioning of the COOPER experiment that has been carried out in the past.

The commissioning phase is initiated by turning on the two dry scroll vacuum pumps SP-01 and SP-02. Therefore, the valves V-06, V-07, V-16 and V-22 are closed while all other valves of the gas system connecting both permeation cells with the QMS and the vacuum system are opened. It is found that, as predicted during the engineering phase, it takes only a few minutes for both vacuum systems to reach sufficiently low pressures of $p_{\mathrm{CCG-04}} \approx 100\,\mathrm{Pa}$ and $p_{\mathrm{CCG-08}} \approx 100\,\mathrm{Pa}$, so that the turbomolecular pumps TMP-01 and TMP-02 can be switched on safely. From that moment on, it takes a few hours for both vacuum systems to reach stable ultimate vacuum pressures of below $p < 1 \times 10^{-5}\,\mathrm{Pa}$ with the band heater switched off. Considering that $S_{\mathrm{pump}}^{\mathrm{TMP-02}} = 550\,\mathrm{L\,s^{-1}}$, the right-hand plot in figure 3.7 suggests that the total rate of particles entering the vacuum system through leaks, permeation and degassing is of the order of $q_{\mathrm{pV}}^{\mathrm{add}} = 5 \times 10^{-5}\,\mathrm{mbar \cdot L/s}$. This was to expect due to the fact that about a hundred ISO-KF flanges are used for the construction of the gas line system that each have a permeation rate of the order of $q_{\mathrm{pV}}^{\mathrm{per}} \approx 1 \times 10^{-6}\,\mathrm{mbar \cdot L/s}$.

6.3.1. Vacuum analysis and leak tightness

A first scan of the vacuum atmosphere in the gas line system that connects the permeation cells with the measuring system is made using the QMS while the system is cold. Therefore, the partial pressures of molecules corresponding to the mass-to-charge ratios $0 < \kappa < 50$ are recorded. The recorded spectrum can be seen in figure 6.13. The plot is supported by table 6.2 which shows the possible ion species that may be responsible for the formation of the peaks. In addition, for each mass-to-charge ratio and corresponding possible ion species, the table lists the parent molecules from which the ions formed in the QMS ion source originate. See section 3.2.3 for a more detailed explanation of how a QMS spectrum is generated.

The partial pressures indicated by the spectrum are the sum of the individual partial pressures of the possible parent molecules listed in table 6.2 associated with the different mass-to-charge ratios κ. The QMS calculates the recorded pressures shown in the spectrum from the measured ion current $I_{\mathrm{cup},\kappa,s}^{+}$ in its Faraday detector. It converts the measured currents into a partial pressure by applying equation (3.14), assuming that only one type

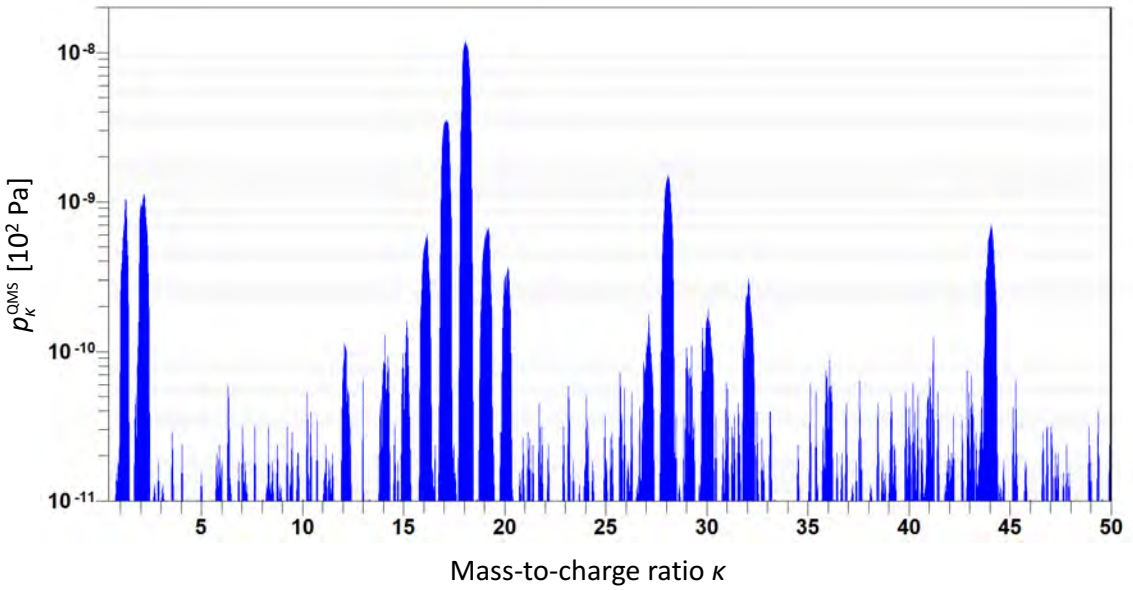

Fig. 6.13. Partial pressure spectrum of the vacuum atmosphere that establishes in the gas line system connecting the permeation cells of the COOPER experiment with the QMS once the ultimate pressure in the system is reached. It is recorded for mass-to-charge ratios in a range of $0 < \kappa < 50$ using a QMS.

TABLE 6.2

ION SPECIES THAT MAY BE ASSOCIATED WITH A PEAK IN A QMS SPECTRUM AT A CERTAIN MASS-TO-CHARGE RATIO κ AND POSSIBLE PARENT MOLECULES FROM WHICH THE FORMED IONS IN THE QMS ORIGINATED.

κ	Ion species in QMS detector	Possible parent molecules
1	$^1H^+$	$^1H_2$, ^1H_2O, $^1H^2HO$
2	$^1H_2^+$, $^2H^+$	$^1H_2$, $^1H^2H$, $^2H_2$, ^1H_2O, $^1H^2HO$, ^2H_2O
3	$^1H^2H^+$	$^1H^2H$, $^1H^2HO$
4	$^2H_2^+$,He^+	$^2H_2$, ^2H_2O, ^4He
12	C^+	CO, CO_2
14	N^+	N_2
16	O^+	O_2, CO, CO_2, ^1H_2O, $^1H^2HO$, ^2H_2O
17	$^1HO^+$	^1H_2O, $^1H^2HO$
18	$^1H_2O^+$, $^2HO^+$	^1H_2O, $^1H^2HO$, ^2H_2O
19	$^1H^2HO^+$, $^1H_3O^+$	^1H_2O, $^1H^2HO$
20	$^2H_2O^+$, Ar^{++}, Ne^+	^2H_2O, Ar, Ne
28	N^+, CO^+	N_2, CO, CO_2
32	O_2^+	O_2
40	Ar^+	Ar
44	CO_2^+	CO_2

of molecular species s is responsible for the ion current. For the conversion, the QMS software applies pre-determined values of the transmission coefficient $\mathrm{TF}_{\kappa,s}$, the cracking fraction $\mathrm{CF}_{\kappa,s}$, the relative ionization probability RIP_s and the ion source constant $\gamma_{\mathrm{N_2}}$ that belong to the molecular species that is likely most responsible for the peak.

It can be seen that according to the table, no other molecular species than N_2 and O_2 are responsible for the formation of the peaks at $\kappa = 14$ and $\kappa = 32$, respectively. The fact that the ratio between the measured partial pressures of N_2 and O_2 does not correspond to their ratio in air suggests that the system is leak tight and that the source of incoming particles is rather the result of permeation through the ISO-KF flanges and degassing from the tube walls. The highest peaks shown in the spectrum are those associated with ions originating from ^1H_2O molecules. These originate mainly from permeation through the FKM seals (see FKM properties discussed in section 3.1.2). Water molecules degassing from the walls also contribute significantly to the relatively high ^1H_2O particle flux in the system. As the table shows, the other prominent peaks in the spectrum are mainly made up of residual air molecules such as Ar, N_2, O_2, CO_2, CO and $^1H_2$. It is found that the measured partial pressures of molecules associated with the mass-to-charge ratio $\kappa = 4$ are vanishing small. Therefore, contamination of helium-4 in the system can be excluded. Any future partial pressure measured at $\kappa = 4$ can hence be assigned exclusively to $^2H_2$ gas.

6.3.2. Commissioning of heating system

The highest temperature of the band heater reached during the commissioning of the heating system is $T_{\mathrm{TC-1}} = 923\,\mathrm{K}$. As expected from the simulations shown in the figures 6.10, such a heater temperature indeed results in a temperature of the sample disk of about $T_{\mathrm{TC-2}} = 873\,\mathrm{K}$. It is observed that the smoothest way to heat and cool the permeation tube is by setting the temperature ramp of the band heater to $\Delta T = 2\,\mathrm{K\,min^{-1}}$. This allows the sample disk and permeation tube walls to heat up and cool down at approximately the same rate as the heater.

During the commissioning phase, it is found that the increased degassing of molecules from the permeation cell walls into their inner cavities does not cause a noticeable increase in the vacuum pressure monitored by CCG-07. This is beneficial for precise QMS measurements at elevated temperatures. However, it turns out that the intense degassing of the band heater during heating causes the vacuum pressure in the OVC to increase from $p_{\mathrm{CCG-04}} \approx 1 \times 10^{-5}\,\mathrm{Pa}$ when cold to $p_{\mathrm{CCG-04}} \approx 1 \times 10^{-2}\,\mathrm{Pa}$ when heated. Since $S_{\mathrm{eff}}^{\mathrm{OVC}} \approx 8\,\mathrm{L\,s^{-1}}$, this result suggests that the band heater degassing rate is of the order of $q_{\mathrm{pV}}^{\mathrm{degas}} = 1 \times 10^{-3}\,\mathrm{mbar \cdot L/s}$. According to the right plot in figure 3.1, a pressure of $p_{\mathrm{CCG-04}} \approx 1 \times 10^{-2}\,\mathrm{Pa}$ is associated with the high vacuum molecular flow regime, which is still low enough that the thermal insulation provided by the vacuum in the OVP prevents the heat from the band heater from being dissipated by gas molecules.

However, once the temperature of the band heater reaches its target temperature and

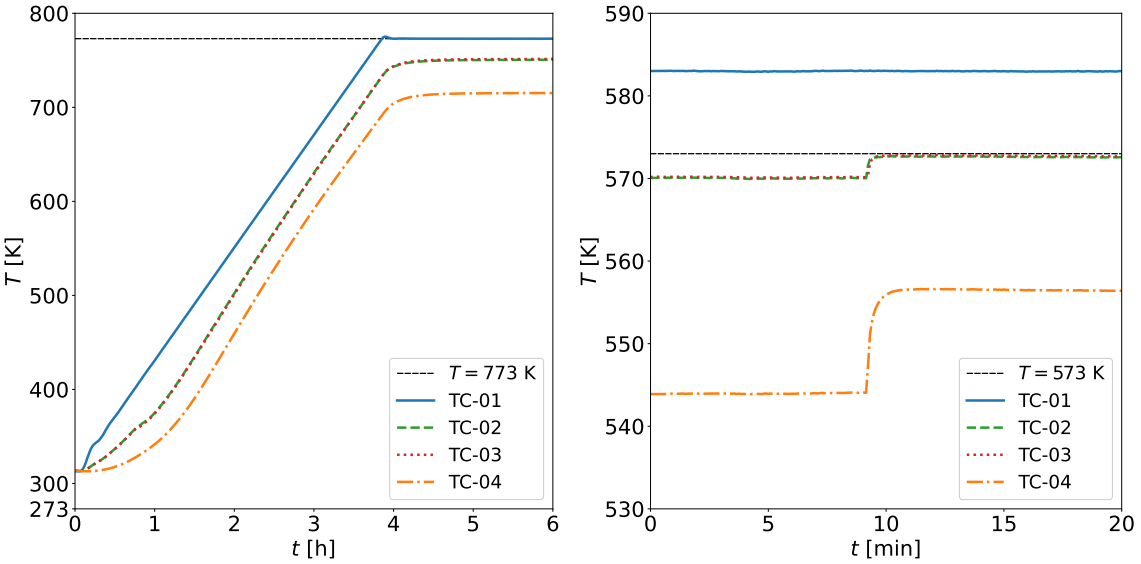

Fig. 6.14. [Left] Temperatures measured by the different thermocouples installed in the COOPER experiment during a typical heating phase in which the band heater is heated to $T_{\mathrm{TC-1}} = 773\,\mathrm{K}$ with an adjusted temperature ramp of $\Delta T = 2\,\mathrm{K\,min^{-1}}$. [Right] Temperatures measured by the different thermocouples installed in the COOPER experiment during thermal steady state at the moment a $^2H_2$ partial pressure of $p_{22}^{\mathrm{UI}} = 2{\times}10^4\,\mathrm{Pa}$ is abruptly injected into the upstream permeation cell PC-A.

thermal steady state establishes in the permeation tube, the voltage required to power the heater drops significantly and so does the degassing rate of the band heater, causing the pressure in the OVC to return to its previous value of $p_{\mathrm{CCG-04}} < 1 \times 10^{-5}\,\mathrm{Pa}$.

The upper left-hand plot in figure 6.14 shows the temperature measured by the thermocouples TC-02, TC-03, and TC-04 during a typical heating phase if the band heater target temperature is set to $T_{\mathrm{TC-1}} = 773\,\mathrm{K}$. As shown in the graph, it takes approximately one hour for the disk temperature to rise at the same rate as the band heater temperature. Once the band heater has reached its target temperature, it takes about an additional hour for the various components of the permeation tube to reach a constant temperature in thermal steady state. To perform accurate permeation flux measurement, it is essential that the permeation tube temperature has stopped rising before the flux is recorded. This is because the slightest increase in temperature has a significant effect on the permeation flux. It is observed that at a target temperature of the band heater of $T_{\mathrm{TC-1}} = 773\,\mathrm{K}$ the temperature difference between the band heater and the center of the sample disk $\Delta T = T_{\mathrm{TC-1}} - T_{\mathrm{TC-2}}$ is only $\Delta T = 23\,\mathrm{K}$. Obviously, this difference would be even smaller at lower heater temperatures. This result confirms good thermal contact between the band heater and the sample disk and shows that the designed heating system works very well.

The temperature difference between the disk border and the disk center is found to be negligibly small (only about $\Delta T = 1\,\mathrm{K}$). This fact is very advantageous for precise permeation measurements, especially for the determination of the temperature relations of hydrogen transport parameters. These require a homogeneous temperature distribu-

tion over the whole surface of the disk through which the permeation takes place. The measured small temperature difference between the disk center and the disk border is consistent with the simulation shown in figure 6.9, which was performed assuming even higher temperatures. It should be noted that thermocouple TC-03 measures the temperature of the disk border within the Helicoflex® gasket, at a distance of about 13×10^{-3} m from the center of the disk. This position does not correspond to the real edge of the sample disk which is outside the Helicoflex® gaskets at a radius of $r_{\mathrm{disk}} = 24 \times 10^{-3}$ m.

Temperature measurements during commissioning have shown that at a band heater temperature of $T_{\mathrm{TC-1}} = 773\,\mathrm{K}$ the outer walls of the OVC reach temperatures of about $T = 343\,\mathrm{K}$, while the outer flange connections of the gas inlet and outlet tubes reach a temperature of up to $T = 373\,\mathrm{K}$. As already anticipated by the presented finite element calculations, such temperatures pose no direct harm to the user. The airflow outside the OVC cools the tubes connected to the gas inlet and outlet flanges. Even if gas is present in the permeation cells, the exterior gas pipes reach room temperature within a few centimeters distance from the OVC. Therefore, damage of the capacitance diaphragm gauges DG-05 and DG-06 can be excluded.

The right-hand graph in figure 6.14 shows a time frame of a temperature measurement with the COOPER experiment where the target temperature of the band heater has been set to $T_{\mathrm{TC-1}} = 583\,\mathrm{K}$ and the system has reached thermal steady state, i.e. the temperatures of all four thermocouples are constant in time. This measurement is performed to test the temperature response of the various components of the permeation tube at the moment of gas injection, as will be done during a permeation flux measurement. With the valve V-13 maintained closed, at $t = 9\,\mathrm{min}$ of the presented time frame, a $^2H_2$ partial pressure of $p_{22}^{\mathrm{UI}} = 2 \times 10^4\,\mathrm{Pa}$ is abruptly injected into the upstream permeation cell PC-A. The gas injection procedure is explained in more detail in section 6.4. It is found that the injected cold gas does not lead to a decrease in temperature of the sample disk but rather to an increase in temperature of a few K. Therefore, in order to perform a permeation flux measurement at a specific desired temperature of the sample disk, the thermocouples TC-02 and TC-03 must indicate steady state temperatures prior to gas injection that are slightly below the temperature at which the actual measurement is to be performed. For example, if a permeation flux measurement is to be made at $T_{\mathrm{TC-2}} = 573\,\mathrm{K}$, the thermocouple TC-02 should indicate a temperature of only about $T_{\mathrm{TC-2}} = 570\,\mathrm{K}$ before the gas is introduced (see right-hand graph in figure 6.14). The rise in temperature of the thermocouples during gas injection is probably due to the following reason. While permeation cell A is under vacuum, the thermocouple tips connected to the sample disk are heated by the hot disk surface primarily by heat conduction at their contact surfaces with the disk and by ambient heat radiation. When gas is present in the permeation cell, they are additionally heated by conduction and convection of the surrounding gas. Due to the reduced heat transfer between the disk surface and the thermocouple tips in vacuum, the measured temperature of the thermocouples is probably lower than the real temperature of the sample disk. It is reasonable to assume that before the gas is injected, the sample disk is already at

the temperature that the thermocouples indicate after the gas is injected. Moreover, the plot reveals that also the measured temperature of TC-04 that is located in free space in the center of the PC-A cavity increases during gas injection. The temperature of the thermocouple increases because the heat from the disk and the walls of the permeation tube, which in a vacuum is transferred to the thermocouple only by thermal radiation, is additionally transferred by gas conduction and convection after the gas is injected.

6.3.3. Controllable pressure range of injected gas

With the purpose of exploring the range of controllable gas pressures injected into the permeation cells, $^2H_2$ gas with different partial pressures in the range $0.1\,\text{Pa} < p_{22}^{\text{UI}} < 5 \times 10^4\,\text{Pa}$ are injected into PC-A while maintaining valve V-13 closed. It is found that regardless of the permeation tube temperature, if gas with a pressure satisfying $p_{22}^{\text{UI}} > 1 \times 10^1\,\text{Pa}$ is injected into PC-A, degassing or absorption of the surrounding permeation cell walls does not lead to a measurable change in pressure over time. However, if $p_{22}^{\text{UI}} < 1 \times 10^1\,\text{Pa}$ the degassing or absorption rate causes a visible pressure change. Therefore, maintaining a low-pressure stable requires constantly injecting and relieving gas into PC-A through the leak valves V-04 and V-17. Therefore, valves V-02, V-06, V-13, V-16, and V-11 are opened and the gas flow is controlled by manipulating both leak valves simultaneously. In fact, performing a permeation measurement with a $^2H_2$ gas flow through PC-A much more closely mimics the scenario of a purge gas flowing through a fuel pin of an HCPB breeding blanket.

6.3.4. Sensitivity test of QMS detector

Finally, the sensitivity of the QMS detector is tested. For this purpose, different partial pressures of $^2H_2$ gas are injected into PC-A and the increase in signal height in the QMS detector caused by the permeating deuterium atoms into PC-B is measured. The increase in detector signal for the mass-to-charge ratio $\kappa = 4$ is of particular interest. The reason for this is that in this mono-isotopic permeation measurement, most of the permeated deuterium atoms will recombine with another deuterium atom at the downstream interface to form $^2H_2$ molecules. According to the fragmentation patterns in [253], the vast majority of $^2H_2$ molecules ionize to $^2H_2^+$ in the QMS ion source with $\kappa = 4$. For the conversion of the measured ion current at $\kappa = 4$ into a partial pressure of $^2H_2$, the fraction of $^2H_2$ molecules ionized to $^2H_2^+$ is estimated to be equal to the known value $\text{CF} \approx 0.9$, which holds for ionization of $^1H_2$ molecules to $^1H_2^+$ ions [253]. In addition, the relative ionization probability $\text{RIP} \approx 0.35$ of $^2H_2$ molecules is taken from the reference [195]. Both values are manually added to the QMS software database.

Figure 6.15 shows the $^2H_2$ partial pressure increment in PC-B at a sample disk temperature of $T_{\text{TC}-2} = 823\,\text{K}$ measured by the QMS via the *open path* resulting from an injection of $^2H_2$ gas into PC-A with the partial pressures $p_{22}^{\text{UI}} = 50\,\text{Pa}$ (solid blue line)

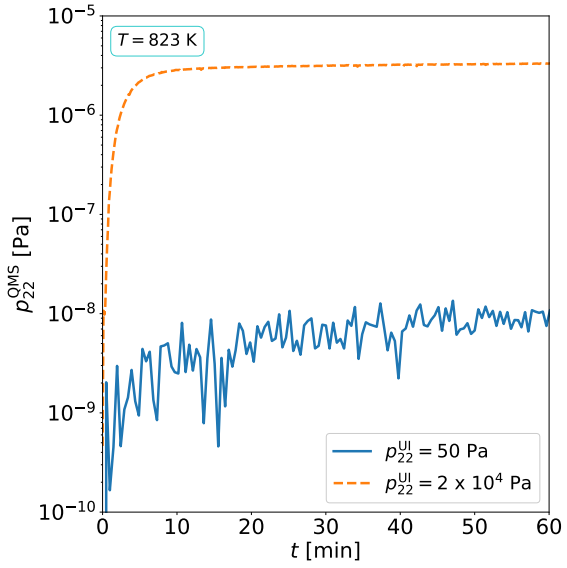

Fig. 6.15. Time evolution of the $^2H_2$ partial pressure in PC-B at $T_{TC-2} = 823\,K$ measured by the QMS via the *open path* after an injection of $^2H_2$ gas with the partial pressures $p_{22}^{UI} = 50\,Pa$ (solid blue line) and $p_{22}^{UI} = 2 \times 10^4\,Pa$ (dashed orange line) into PC-A.

and $p_{22}^{UI} = 2 \times 10^4\,Pa$ (dashed orange line), respectively. The plot reveals that in case of high upstream pressures, the QMS shows an excellent detector signal. However, at upstream pressures $p_{22}^{UI} < 50\,Pa$ the QMS approaches its lower resolution limit. Therefore, for permeation flux measurements with the COOPER experiment at upstream pressures $p_{22}^{UI} < 50\,Pa$, permeation flux measurements will be performed using the leak detector instead. The $^2H_2$ gas used for all measurements discussed in this chapter has a purity of 99.8 %.

6.4. Procedure for mono- and multi-isotopic permeation measurements

The following sections present measurement procedures for mono- and multi-isotopic deuterium permeation flux measurements using the COOPER experiment, which are established within the scope of this dissertation. A preliminary permeation experiment is presented to demonstrate the calibration and measurement procedure for mono-isotopic permeation measurements. A standard scheme for obtaining characteristic hydrogen transport parameters in a mono-isotopic permeation experiment such as the permeability, the diffusion coefficient and the Sieverts' constant is presented. Finally, the planned experimental procedure for co- and counter-permeation measurements is described.

6.4.1. Sample material characterization

Prior to any permeation experiment, the composition of the sample disk material must be characterized. This is important in order to be able to interpret the experimental results of performed permeation flux measurements with those obtained in previous experimental campaigns that might have used sample material with the same name but slightly different composition.

The presented mono-isotopic permeation experiment is executed with a sample disk

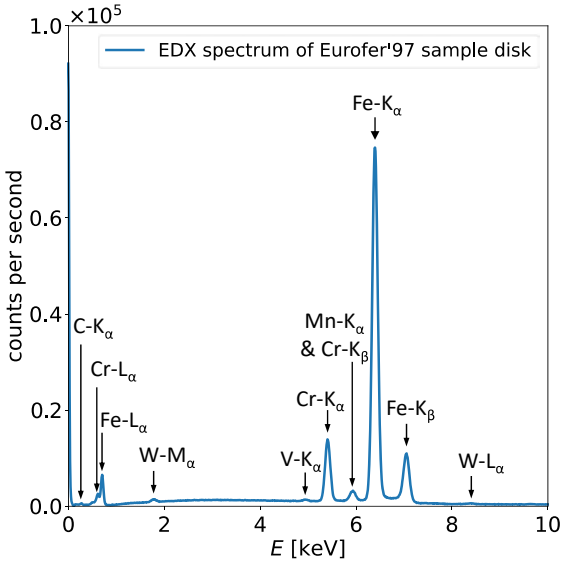

Fig. 6.16. Measured EDX spectrum of the Eurofer'97 material used to manufacture the sample disk installed in the COOPER experiment.

TABLE 6.3

MATERIAL COMPOSITION OF THE EUROFER'97 MATERIAL GIVEN IN [WT %] WHICH IS USED TO MANUFACTURE THE SAMPLE DISK INSTALLED IN THE COOPER EXPERIMENT. THE COMPOSITION IS MEASURED USING EDX.

Fe	Cr	C	Mn	V	W	Ta
85.55	10.93	1.38	0.52	0.20	1.33	0.10

made of Eurofer'97 supplied by Atmostat (patch 3, lot 1615, normalized at 1253 K for 11 min in air, tempering at 1033 K for 65 min in air).

The composition of the obtained Eurofer'97 material is determined by applying the technique EDX (Energy-Dispersive X-ray Spectroscopy) inside of a SEM (Scanning Electron Microscope). In this experimental technique, atoms on the sample surface are irradiated with X-rays, which excite electrons in the lower atomic shells (K, L, M, etc.), causing them to be ejected from the atom. An electron from a higher energy level occupies the now available electron hole in the lower energy shell, releasing energy in the form of a photon that can be captured by a detector. The released photon energies are characteristic of the atomic species. The energy level of the atomic shell from which the electron falls back into the lower shell (K, L, M, etc.) determines the name of the characteristic photon energy line (K_α, K_β, L_α, M_β, etc.). The number of detected photons per second of a specific energy line is a measure of the concentration of the corresponding atomic species. More information about the EDX technique can be found in the reference [254]. The recorded spectrum with the indicated energy lines associated with different elements on the observed Eurofer'97 sample surface can be seen in figure 6.16. From the relative heights of the peaks, the used EDX software obtains a material composition which is shown in table 6.2. A comparison of the measured composition with table 1.1 suggests that the obtained sample material has a Cr content that is outside the range of the specified composition requirements for Eurofer'97. Also, the Cr content of the sample material

appears to be slightly higher than the Eurofer'97 material specifications.

The average thickness of the installed sample disk is measured to be approximately $d_{\mathrm{disk}} = (1.00 \pm 0.05) \times 10^{-3}\,\mathrm{m}$ and the sample disk surface exposed to the gas chamber cavities within the gaskets is estimated to be $A_{\mathrm{per}} = (9.1 \pm 0.5) \times 10^{-4}\,\mathrm{m}^2$. Prior to its installation, the disk is roughly polished with emery paper. To mimic a surface roughness more similar to the Eurofer'97 surface conditions expected in a real breeding blanket, further polishing is omitted.

6.4.2. Mono-isotopic permeation measurements in the diffusion-limited regime

The execution of permeation flux measurements using the QMS begins with an evacuation of all pipe lines of the experimental setup. Therefore, all valves except V-04, V-05, V-08, V-10, V-11 and V-12 are opened and the two vacuum systems are turned on. It is waited until both systems reach an ultimate minimum vacuum pressure of $p < 1 \times 10^{-5}\,\mathrm{Pa}$.

Then, the valves V-03, V-06, V-07, V-13, V-17, V-18, V-20, V-21, V-23 are closed and the valves V-04 and V-11 are opened. In this configuration of open and closed valves, the downstream permeation cell B is connected with the QMS via the *open path* which is required for a mono-isotopic permeation measurement into vacuum. The experimental procedure described in the following suppose that the permeation cells are already degassed which is done at the end of every set of permeation measurements.

The deuterium permeation flux measurements presented in this work are all performed with the same $^2H_2$ upstream pressure of $p_{22}^{\mathrm{UI}} = 2 \times 10^4\,\mathrm{Pa}$ at five different sample disk temperatures $T_{\mathrm{TC-2}} = [573\,\mathrm{K}, 623\,\mathrm{K}, 673\,\mathrm{K}, 723\,\mathrm{K}, 773\,\mathrm{K}]$. According to the left plot in figure 6.1 at $T_{\mathrm{TC-2}} = 573\,\mathrm{K}$ such a high upstream pressure corresponds to the edge of the intermediate and the beginning of the diffusion-limited permeation regime. In a previous mono-isotopic permeation experiment performed by Montupet-Leblond *et al*, who also used Eurofer'97 permeation membranes of approximately the same thickness, a $^2H_2$ upstream pressure of $p_{22}^{\mathrm{UI}} = 2 \times 10^4\,\mathrm{Pa}$ could be assigned to the diffusion-limited permeation regime [161]. Experimental confirmation of the upstream pressure range for surface-limited and diffusion-limited permeation flux measurements with the COOPER experiment remains to be performed. However, for the time being, it is assumed that the permeation flux measurements described below correspond to the diffusion-limited regime.

During the commissioning phase, it is learned that heating the permeation tube system from a lower temperature to a higher constant target temperature allows thermal steady state of the permeation tube to be reached more quickly than if the system is cooled from a higher temperature to a lower temperature. In addition, heating the system brings the resulting equilibrium temperature of the sample disk closer to the set constant target temperature of the band heater than if the target temperature is reached by cooling. The left plot in figure 6.17 shows the temperatures measured by the various thermocouples throughout

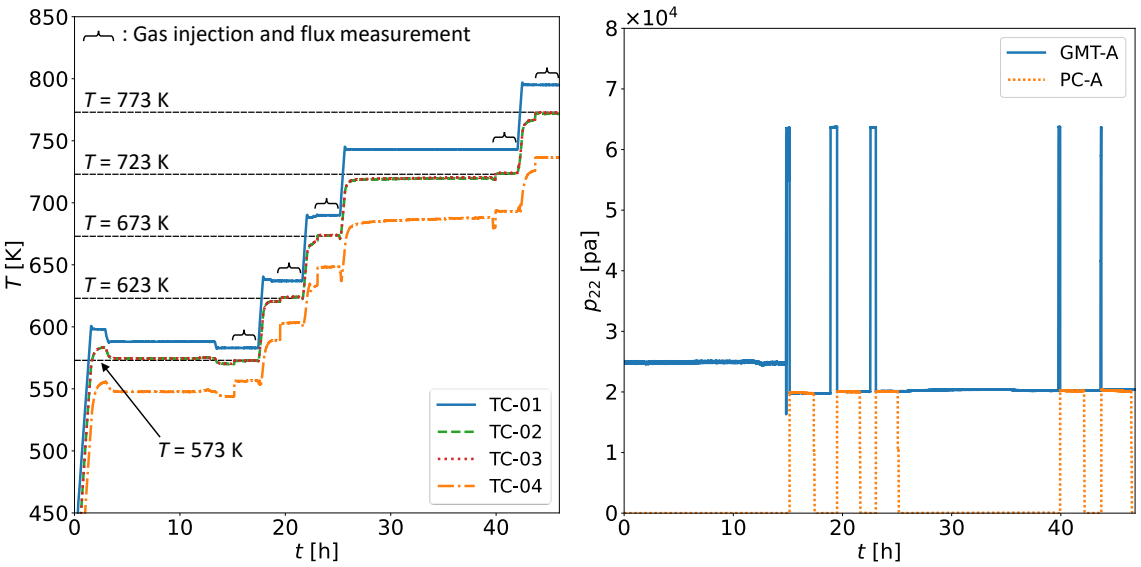

Fig. 6.17. [Left] Temperatures measured by the different thermocouples installed in the COOPER experiment during the performed mono-isotopic permeation measurements. [Right] Pressures of $^2H_2$ gas in GMT-A and PC-A measured by DG-03 and DG-05 during the performed mono-isotopic permeation measurements.

the period during which the mono-isotopic permeation measurements discussed in this section are being performed. It is started with the lowest disk temperature of the test matrix of $T_{\mathrm{TC}-2} = 573\,\mathrm{K}$. As the right plot in figure 6.14 shows, this requires the band heater to be kept at a constant target temperature of $T_{\mathrm{TC}-2} = 583\,\mathrm{K}$. It is reached at about $t = 14\,\mathrm{h}$ of the time frame shown in the left-hand plot in figure 6.17. From this moment, it is waited for about one hour until the temperatures of the components of the permeation tube have reached their steady state values. For the reasons explained above, the measured sample disk temperature will increase by some kelvin during the gas injection. Therefore, it is aimed that the displayed temperature of the thermocouple TC-02 levels out a few Kelvin below the sample disk target temperature.

Prior to the injection of $^2H_2$ gas into the upstream chamber, the QMS is calibrated to allow for permeation flux measurements as described in section 3.2.3. For the calibration, a $^2H_2$ test leak with a calibrated throughput of $q^{\mathrm{CL}}_{\mathrm{pV},22} = 2.04 \times 10^{-7}\,\mathrm{mbar \cdot L/s}$ is used. It is connected to the gas inlet port of PC-B outside the OVC via valve V-08 (see the figures 6.2 and 6.11). As soon as the valves V-07 and V-08 are opened the test leak releases its calibrated $^2H_2$ flux into the *open path*. Here, it is detected by the QMS in the form of an increase in ion current $\Delta I^+_{\mathrm{meas},\kappa}$ of mainly the mass-to-charge ratio $\kappa = 4$ since the $^2H_2$ molecules ionize primarily to $^2H_2^+$ ions in the QMS ion source [253]. The increment in ion current $\Delta I^+_{\mathrm{meas},4}$ resulting from the increase in particle flow in the open path $q^{\mathrm{CL}}_{\mathrm{pV},22}$ is measured by the QMS. According to equation (3.21), the calibration factor of the QMS is obtained with

$$f^{\mathrm{cal}}_{\kappa,22} = \frac{q^{\mathrm{CL}}_{\mathrm{pV},22}}{\Delta I^+_{\mathrm{meas},4}} \tag{6.2}$$

Having obtained $f_{\kappa,22}^{\mathrm{cal}}$ allows conversion of the ion current increment $\Delta I_{\mathrm{meas},4}^{+}$ measured during a permeation flux measurements into a deuterium permeation flow using equation (3.21) and into a deuterium permeation flux applying relation (3.22). Once the calibration factor is determined the valves V-07 and V-08 are closed again. This calibration procedure is repeated at every new temperature step.

In a mono-isotopic permeation experiment, a deuterium isotope that has permeated into PC-B will most likely recombine with another deuterium atom to form $^{2}H_2$, which then enters the vacuum of PC-B before making its way to the QMS detector. However, since $^{1}H_2$ gas is relatively abundant in air and the used $^{2}H_2$ gas cylinder contains $^{1}H^{2}H$ impurities, there will be a low concentration of dissolved protium in the sample disk material. Therefore, it is important to consider that some of the permeating deuterium atoms will recombine with protium to form $^{1}H^{2}H$. In addition, subsequent isotope exchange reactions with water molecules at the disk and the wall surfaces of PC-B lead to the formation of $^{1}H^{2}HO$ and $^{2}H_2O$ molecules. Consequently, the total flux of permeated deuterium isotopes can only be measured by recording the molecular fluxes of all deuterium-containing molecules, i.e. $^{1}H^{2}H$, $^{2}H_2$, $^{1}H^{2}HO$, $^{2}H_2O$. Table 6.2 shows that in the ion source of the QMS these four molecular species fragment into ions corresponding to the set of mass-to-charge ratios $\kappa \in \{1, 2, 3, 4, 16, 17, 18, 19, 20\}$. Hence, to measure the exact deuterium permeation flux, the increments in ion current of all these mass-to-charge ratios would have to be measured. However, it is found that due to the high partial pressure of $^{2}H_2O$ molecules in the system, the ion current signals in the QMS detector of the mass-to-charge ratios $\kappa \in \{1, 2, 16, 17, 18, 19, 19\}$ are so high that any increment associated with an increase in deuterium-containing molecules is lost in the detector noise. For this reason, permeation flux measurements with the COOPER experiment merely take into account the ion current increments measured at the mass-to-charge ratios $\kappa \in \{3, 4, 20\}$. The mass-to-charge ratio $\kappa = 3$ represents ions that are formed from the molecules $^{1}H^{2}H$, $^{1}H^{2}HO$, $\kappa = 4$ is associated with the molecules $^{2}H_2$, $^{2}H_2O$ and $\kappa = 20$ with the molecule $^{2}H_2O$. Since calibrated leaks of $^{1}H^{2}H$, $^{1}H^{2}HO$ and $^{2}H_2O$ gas do not exist the conversion of the measured ion current increments into permeation fluxes is done using the same QMS calibration factor as that measured for $^{2}H_2$ gas.

Consequently, the total atomic deuterium permeation flux is calculated from the measured increments in ion currents $\Delta I_{\mathrm{meas},\kappa}^{+}$ that correspond to the three recorded mass-to-charge ratios $\kappa \in \{3, 4, 20\}$, according to

$$J_{\mathrm{per},2} = j_{\mathrm{per}}^{\kappa=3} + 2j_{\mathrm{per}}^{\kappa=4} + 2j_{\mathrm{per}}^{\kappa=20} = \frac{f_{\kappa,22}^{\mathrm{cal}}}{A_{\mathrm{per}} R T_{\mathrm{QMS}}} \cdot \left(\Delta I_{\mathrm{meas},3}^{+} + 2\Delta I_{\mathrm{meas},4}^{+} + 2\Delta I_{\mathrm{meas},20}^{+} \right) . \quad (6.3)$$

To set up this equation it is made use of the equation (3.21) and (3.22) and it is taken into account that the deuterium-containing molecules that correspond to the mass-to-charge ratios $\kappa \in \{3, 4, 20\}$ contain one or two deuterium isotopes (see table 6.2).

After the QMS is calibrated, $^{2}H_2$ gas with a partial pressure of $p_{22}^{\mathrm{UI}} = 2 \times 10^{4}\,\mathrm{Pa}$ is injected into PC-A. In order to enable a precise measurement of the diffusion coefficient with the time-lag method described in section 2.3.5, the gas injection must occur as

quickly as possible. Therefore, GMT-A is filled with a specific partial pressure $p_{\mathrm{init},22}^{\mathrm{GMT-A}}$ of $^2H_2$ gas, which implies the establishment of a final overall pressure of $p_{\mathrm{inj},22}^{\mathrm{PC-A}} = 2 \times 10^4\,\mathrm{Pa}$ in both PC-A and GMT-A at the moment when valve V-06 is opened and the gas enters the vacuum of PC-A. The initial pressure in GMT-A that is required to inject a given value of p_{22}^{UI} into the previously evacuated PC-A is determined by the ideal gas law and given by

$$p_{\mathrm{init},22}^{\mathrm{GMT-A}} = \alpha_{\mathrm{inj}} \cdot p_{\mathrm{inj},22}^{\mathrm{PC-A}} = , \quad \text{with} \quad \alpha_{\mathrm{inj}} = \frac{V_{\mathrm{GMT-A}} + V_{\mathrm{PC-A}}}{V_{\mathrm{GMT-A}}} \cdot \frac{T_{\mathrm{room}}^{\mathrm{gas}}}{T_{\mathrm{aver}}^{\mathrm{gas}}} . \tag{6.4}$$

In this expression, $V_{\mathrm{GMT-A}}$ describes the volume of GMT-A between the valves V-02 and V-06, and $V_{\mathrm{PC-A}}$ specifies the volume of PC-A between the valves V-06 and V-13. Moreover, variable $T_{\mathrm{room}}^{\mathrm{gas}}$ is the gas temperature in GMT-A and $T_{\mathrm{aver}}^{\mathrm{gas}}$ is the average temperature of the gas in both GMT-A and PC-A after gas injection. During commissioning it could be experimentally determined that $\alpha_{\mathrm{inj}} = 3.17$ at $T_{\mathrm{TC-2}} = 573\,\mathrm{K}$ and $\alpha_{\mathrm{inj}} = 3.2$ at $T_{\mathrm{TC-2}} = 773\,\mathrm{K}$. Following this calculation, at the first temperature step of the performed permeation flux measurements, GMT-A is pre-filled with a $^2H_2$ pressure of $p_{22}^{\mathrm{GMT-A}} = 6.38 \times 10^4\,\mathrm{Pa}$. The pressures in GMT-A and PC-A measured by DG-03 and DG-05 during the performed mono-isotopic permeation measurements are shown in the left-hand graph in figure 6.17. The periods in which the GMT-A is pre-filled and subsequently emptied into PC-A are clearly visible.

The deuterium permeation process is initiated at the moment when valve V-06 is opened, resulting in a rapid injection of exactly $p_{22}^{\mathrm{UI}} = 2 \times 10^4\,\mathrm{Pa}$ into PC-A (see right-hand plot in figure 6.17). Then valve V-06 is closed again and the deuterium permeation flux into PC-B is recorded for about two hours. The measurement is completed by removing the gas from PC-A. To do this, valve V-13 is opened and the leak rate through valve V-17 is carefully increased so that the $^2H_2$ gas slowly escapes into the dry scroll pump SP-01. As soon as DG-05 monitors a pressure of $p < 10\,\mathrm{Pa}$, valve V-11 is closed and needle valve V-10 is slowly opened to reduce the pressure in PC-A to the high vacuum range with the help of TMP-01. The evacuation processes after each permeation measurement can be seen in the right-hand graph of figure 6.2 as well (see orange dotted line). Then, the next higher target temperature is set in the LabVIEW program. Once all thermocouples confirm the establishment of thermal steady state, the calibration, gas injection, permeation flux measurement and evacuation procedures are repeated.

The left-hand graph in figure 6.18 presents the recorded deuterium permeation fluxes at five different temperatures, converted from the measured ion currents of the three mass-to-charge ratios using equation (6.3). In the plot, $t = 0\,\mathrm{min}$ corresponds to the moment of gas injection. It can be seen that for all observed temperatures it takes more than 30 min for the permeation flux to reach thermal steady state permeation. The right-hand plot in figure 6.18 shows the measured molecular permeation fluxes

$$j_{\mathrm{per}}^{\kappa} = \frac{1}{A_{\mathrm{per}} R T_{\mathrm{QMS}}} \cdot f_{\kappa,22}^{\mathrm{cal}} \cdot \Delta I_{\mathrm{meas},\kappa}^{+} \tag{6.5}$$

at the last temperature step $T_{\mathrm{TC-2}} = 773\,\mathrm{K}$, that are associated with molecules whose ions

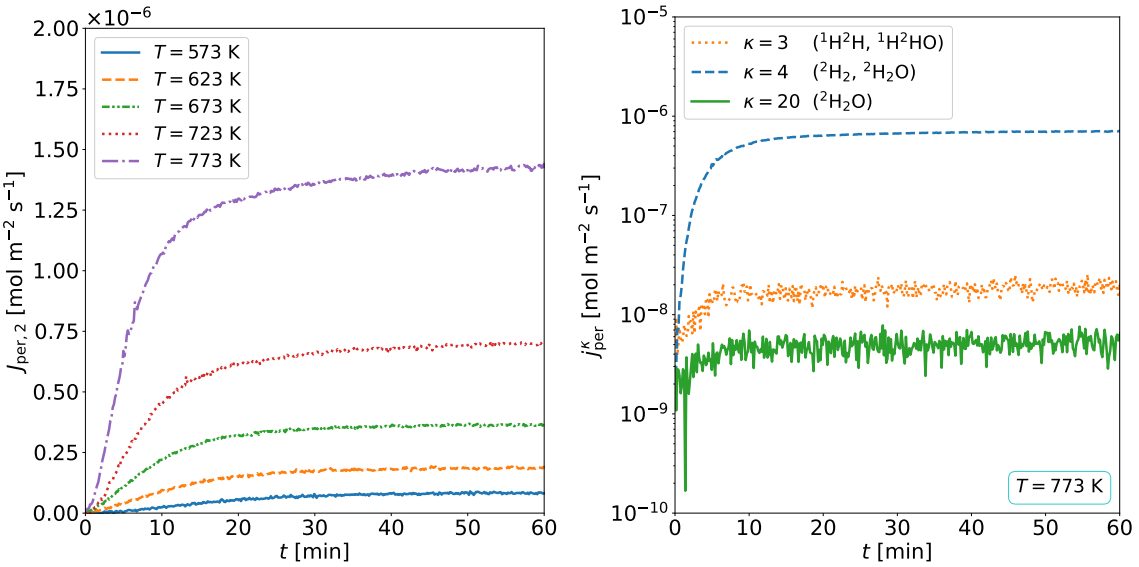

Fig. 6.18. [Left] Measured deuterium permeation flux into PC-B resulting from an injection of $^2H_2$ gas into PC-A with a partial pressure of $p_{22}^{\mathrm{UI}} = 2 \times 10^4$ Pa. The measurements are performed at five different sample disk temperatures. [Right] Molecular permeation fluxes associated to molecules that are ionized by the QMS into fragments with the mass-to-charge ratios $\kappa = 3$, $\kappa = 4$ and $\kappa = 20$ that result from an injection of $^2H_2$ gas into PC-A with a partial pressure of $p_{22}^{\mathrm{UI}} = 2 \times 10^4$ Pa at $T_{\mathrm{TC-2}} = 773$ K.

have the mass-to-charge ratios $\kappa = 3$, $\kappa = 4$ and $\kappa = 20$ (see legend in the right-hand plot in figure 6.18). These molecular fluxes are inserted into equation (6.3) to obtain the total atomic deuterium flux. It can be seen that the height of the steady state permeation flux measured for $\kappa = 4$ is approximately two orders of magnitude higher than the permeation fluxes that correspond to the other two mass-to-charge ratios.

Figure 6.19 shows the values of the measured steady state deuterium permeation fluxes. They are obtained by determining the mean value of the permeation fluxes which are measured during the last ten minutes of the shown time frame in the left-hand plot in figure 6.18. The error of the temperature measurement of the sample disk is estimated to be $\Delta T = 3$ K. This error takes into account the fact that the sample disk is slightly colder at the border than at the center. The error bars of the permeation flux measurement are derived from the equations (6.2) and (6.3) using error propagation, according to

$$\Delta J_{\mathrm{per},2} = J_{\mathrm{per},2} \cdot \sqrt{\left(\frac{\Delta q_{\mathrm{pV},22}^{\mathrm{CL}}}{q_{\mathrm{pV},22}^{\mathrm{CL}}}\right)^2 + \left(\frac{\Delta A_{\mathrm{per}}}{A_{\mathrm{per}}}\right)^2 + \left(\frac{\Delta T_{\mathrm{QMS}}}{T_{\mathrm{QMS}}}\right)^2}. \tag{6.6}$$

Here, it is assumed that the relative errors of the ion currents measured by the QMS are negligible since they are small in comparison with the relative errors of the other quantities that occur in equation (6.6). The relative error of the test leak rate $\Delta q_{\mathrm{pV},22}^{\mathrm{CL}}$ is assumed to be $\Delta q_{\mathrm{pV},22}^{\mathrm{CL}} = 0.2 \cdot q_{\mathrm{pV},22}^{\mathrm{CL}}$. It is estimated that the gas temperature in the QMS is at room temperature $T_{\mathrm{QMS}} = (293 \pm 5)$ K. This value is given with a relatively large error. This is due to the difficult-to-estimate effect of the thermal radiation from the QMS filament on

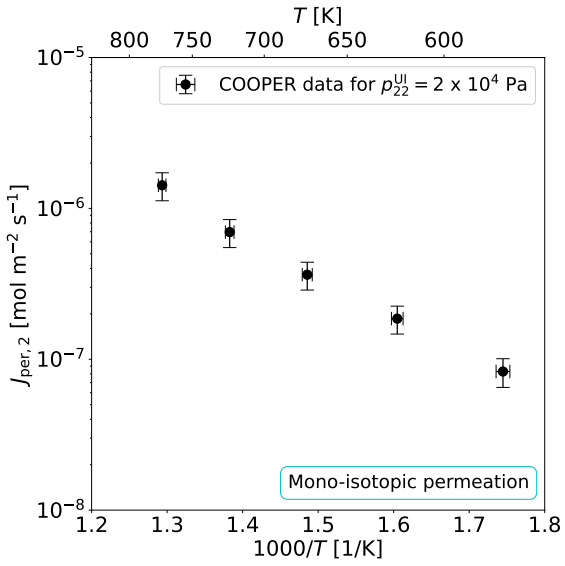

Fig. 6.19. Measured steady state deuterium permeation fluxes into PC-B resulting from an injection of $^2H_2$ gas into PC-A with a partial pressure of $p_{22}^{UI} = 2 \times 10^4$ Pa. The measurements are performed at five different sample disk temperatures.

the gas temperature.

At the end of the last permeation measurement, PC-A is evacuated as described above. This is followed by the degassing process. Therefore, after evacuation, the valves V-17, V-16 and V-10 are closed again and valve V-18 is opened. As a result, both permeation cells are now connected to the QMS and TMP-02. At this stage, the temperature of the band heater is raised to $T_{TC-01} = 873$ K and the ion currents of the mass-to-charge ratios $\kappa \in \{3, 4, 20\}$ are recorded. The heater is held at the degassing temperature until the recorded ion currents disappear in the detector noise. It was found that this is the case after about 24 h.

6.4.3. Measurement of the deuterium permeability in Eurofer'97

Considering that the presented mono-isotopic permeation flux measurements are performed in the diffusion-limited regime, it is possible to determine the permeability of deuterium in Eurofer'97 from the steady state permeation fluxes plotted in the left-hand plot in figure 6.19. Therefore, it is made use of equation (2.142) which is transformed to

$$\Phi_2^{E97} = \frac{d_{disk}}{\overline{J}_{per,2} \cdot \sqrt{p_{22}^{UI}}}, \quad \text{with} \quad \Delta\Phi_2^{E97} = \Phi_2^{E97} \cdot \sqrt{\left(\frac{\Delta d_{disk}}{d_{disk}}\right)^2 + \left(\frac{\Delta J_{per,2}}{J_{per,2}}\right)^2 + \left(\frac{\Delta p_{22}^{UI}}{2 p_{22}^{UI}}\right)^2}. \quad (6.7)$$

It yields the deuterium permeabilities which are shown in figure 6.20. The error of the permeabilities is determined by error propagation as reported in equation (6.7). Therefore, it is estimated that the error of the injected upstream pressure is $\Delta p_{22}^{UI} = 5 \times 10^2$ Pa. Because of the Arrhenius-type temperature dependence of the permeability given in equation (2.143), its temperature relationship is determined by a linear fit to the natural logarithm of the permeability values obtained. The error of the slope of the fitted line and the error of its intercept with the y-axis are estimated such that the error lines would diagonally

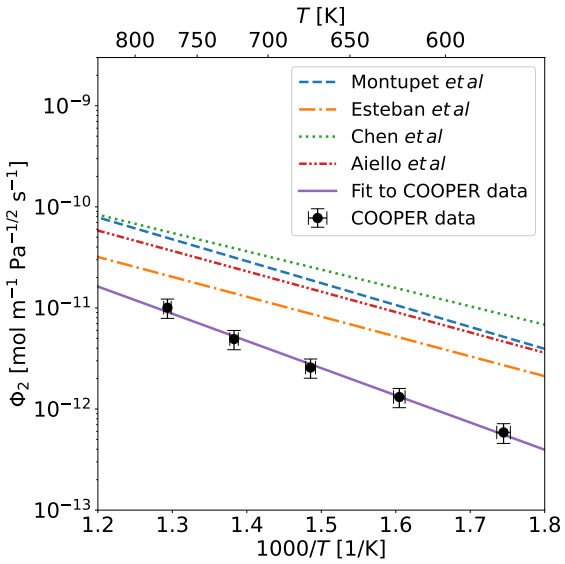

Fig. 6.20. Measured permeability of deuterium in Eurofer'97 as a function of the sample temperature. The diagram contains experimental deuterium permeability relations obtained from the literature [159], [161], [221], [222].

connect the extreme ends of the error bars of the highest and lowest temperature. Thus, the following permeability relation for deuterium in Eurofer'97 is obtained.

$$\Phi_2^{\mathrm{E97}}(T) = (3.0 \pm 0.5) \times 10^{-8}\,\mathrm{mol/m/s/Pa^{\frac{1}{2}}} \cdot \exp\left[-\frac{(51.5 \pm 0.5)\,\mathrm{kJ\,mol^{-1}}}{RT}\right]. \tag{6.8}$$

Expression (6.8) is plotted in figure 6.20 together with permeability relations obtained from the literature [159], [161], [221], [222]. While the permeability relations reported by Chen *et al* [221] and Aiello *et al* [222] were measured for deuterium, Montupet-Leblond *et al* and Esteban *et al* measured the permeability relation for protium. As the equations (2.143) and (2.66) suggest, when assuming an approximately equal Sieverts' constant for protium and deuterium the measured protium permeabilities in the references [159], [161] can be converted to deuterium permeabilities considering that $\Phi_2 \approx \Phi_1 \sqrt{M_1/M_2}$. This conversion is applied before plotting the relations in figure 6.20.

It can be seen that the permeability relation measured with the COOPER experiment is slightly lower than the literature data. There could be two reasons for this. The first reason could be that the installed sample disk has oxidized during the experimental phase. An oxidation layer behaves like a permeation barrier coating and drastically reduces the surface recombination coefficient. According to equation (2.147), this would imply a reduced permeation number and thus mean that the measurements may actually have been made in the intermediate and not the diffusion-limited permeation regime. According to the left-hand plot in figure 6.1, in the intermediate regime, the steady state permeation flux is not sufficiently well described by equation (2.142) that is used for the determination of the permeability. Therefore, measuring the permeation flux in the intermediate permeation regime implies an underestimation of the permeability obtained with equation (2.142).

Another reason for the discrepancy could be the fact that the determined composition of the Eurofer'97 sample disk shown in table 6.3 differs considerably from the compositions of the Eurofer'97 samples shown in the references [161], [221], [222]. In fact, the

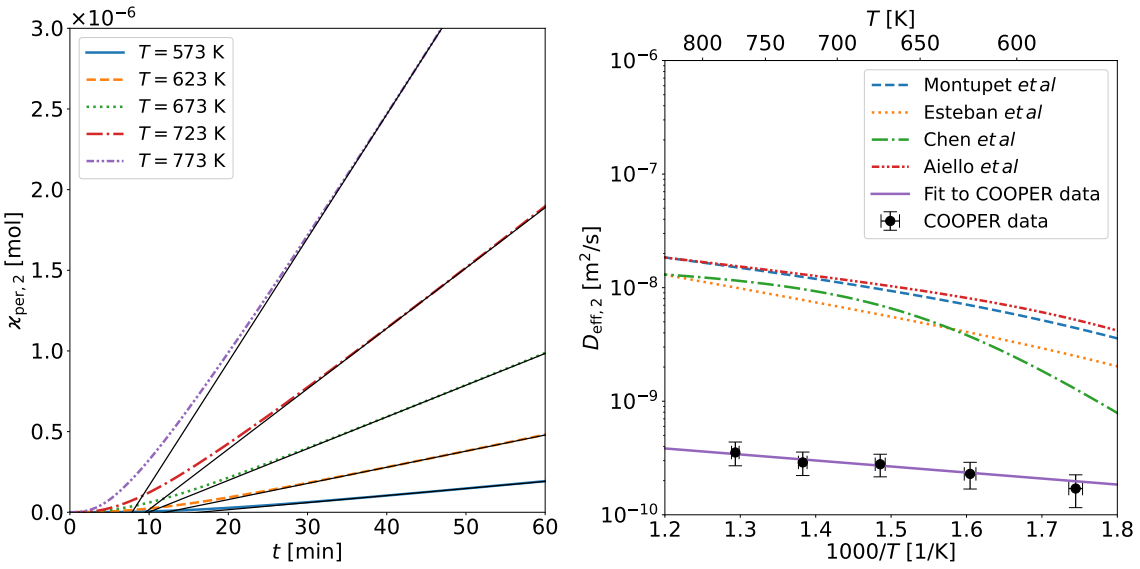

Fig. 6.21. [Left] Cumulative number of permeated deuterium atoms at different disk temperatures plotted against time. The plots approach straight lines, which are approximated by linear fits. The intercepts of the fits provide the permeation time-lags used to obtain the effective deuterium diffusion coefficients at the observed temperatures. [Right] Effective diffusivities of deuterium in Eurofer'97 measured with the COOPER experiment compared with literature values [159], [161], [221], [222]. The solid blue line is the determined temperature relation of the diffusivity which is assumed to be valid for temperatures $T > 673\,\mathrm{K}$ where $D_{\mathrm{eff},2} \approx D_2$.

sample material installed in the COOPER experiment has significantly higher Cr and C contents than the samples observed in the mentioned references.

6.4.4. Measurement of the deuterium diffusivity in Eurofer'97

In addition, the COOPER device enables measuring the temperature-dependent effective diffusion coefficient of the sample disk material by applying the time-lag method that is introduced in section 2.3.5. The concept of the effective diffusivity is addressed in section 2.2.2. From equation (2.156) it follows that

$$D_{\mathrm{eff},2}^{\mathrm{E97}} = \frac{d_{\mathrm{disk}}^2}{6 \cdot \tau_{\mathrm{TL}}}\,, \quad \text{with} \quad \Delta D_{\mathrm{eff},2}^{\mathrm{E97}} = D_{\mathrm{eff},2} \cdot \sqrt{\left(\frac{\Delta d_{\mathrm{disk}}}{d_{\mathrm{disk}}}\right)^2 + \left(2 \cdot \frac{\Delta \tau_{\mathrm{TL}}}{\tau_{\mathrm{TL}}}\right)^2}\,. \tag{6.9}$$

In order to obtain the permeation time-lags τ_{TL} of the measurements at each temperature step, the cumulative number of permeated isotopes $\varkappa_{\mathrm{per},2}$ is calculated as a function of time. Therefore, the measured permeation fluxes visualized in the left-hand plot in figure 6.18 are inserted into the equation

$$\varkappa_{\mathrm{per},2}\,(t) = A_{\mathrm{per}} \cdot \int_0^t J_{\mathrm{per},2}\,(t')\;\mathrm{d}t'\,. \tag{6.10}$$

The result is plotted in the left-hand graph in figure 6.21.

Straight lines are fitted to the linear sections of the curves corresponding to the time interval $30\,\mathrm{min} < t < 60\,\mathrm{min}$. The intercepts τ_{TL} of the linear fits with the t-axis are determined. These intercepts are independent of the area A_{per}. Therefore, the error of A_{per} has no influence on the obtained values of τ_{TL}. Nevertheless, the inaccuracy in the determination of the time-lags rather results from an incorrect choice of the time interval boundaries used for the linear fits. For this reason, the error of τ_{TL} is estimated by varying the lower time boundary of the fit interval by a reasonable time range.

Inserting the determined time-lags into equation (6.9) yields the effective diffusion coefficients of deuterium in Eurofer'97 measured with the COOPER experiment. The measured data points are shown in the right graph of figure 6.21, together with the effective diffusivity relations in Eurofer'97 reported in the references [159], [161], [221], [222]. Before plotting the curves, the diffusivity relations measured in [159], [161] for protium in Eurofer'97 are converted to relations for deuterium using equation (2.66). It can be seen that above a temperature of about $T = 673\,\mathrm{K}$, the effective diffusivities measured with the COOPER experiment and reported in the mentioned references show an Arrhenius-type temperature dependence, i.e. they increase linearly with the inverse temperature when plotted on a logarithmic scale. Below this critical temperature, trapping mechanisms significantly affect the diffusivity and cause a deviation from the Arrhenius-type behavior. To determine the intrinsic interstitial diffusivity D_2^{E97} of deuterium in Eurofer'97, it is assumed that $D_{\mathrm{eff},2}^{\mathrm{E97}} \approx D_2^{\mathrm{E97}}$ at temperatures of $T > 673\,\mathrm{K}$. The Arrhenius relation (2.65) is then fitted to the diffusion coefficients determined at the temperature steps $T_{\mathrm{TC-2}} = [673\,\mathrm{K},\ 723\,\mathrm{K},\ 773\,\mathrm{K}]$. The error of the fits is determined in the same way as for the permeability relation. Consequently, the intrinsic interstitial diffusion relation for deuterium in Eurofer'97 measured with the COOPER experiment is

$$D_2^{\mathrm{E97}}(T) = (1.7 \pm 0.3) \times 10^{-9}\,\mathrm{m^2\,s^{-1}} \cdot \exp\left[-\frac{(10.1 \pm 0.1)\,\mathrm{kJ\,mol^{-1}}}{RT}\right]. \tag{6.11}$$

It is found that the measured diffusivities are significantly smaller than the literature data. This may be for the same reasons as those suggested for the observed discrepancy in the measured permeability relation. That is an unclean or oxidized disk surface may have led to slower surface recombination and dissociation kinetics, and thus to a shift into the intermediate permeation regime. If the measured permeation processes occurred in the intermediate rather than the diffusion-limited regime, the time-lag method would have underestimated the true deuterium diffusivity. This is because, in the intermediate regime, it takes longer to reach steady state permeation.

In future measurements of the effective diffusivity relation with the COOPER experiment, more experimental data points will be recorded at lower temperatures and the entire expression (2.74) will be fitted against the measured values using the parameters D_2^0, E_{m}, $\mathcal{N}^{\mathrm{T}}$ and E_{t} as free fitting coefficients, as was done in [161].

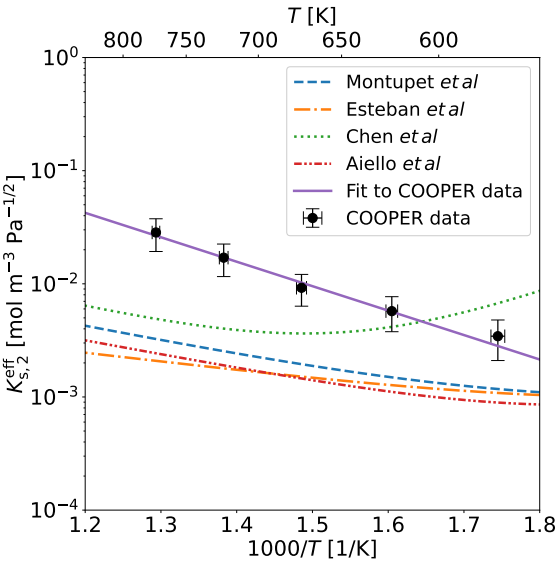

Fig. 6.22. Effective Sieverts' constant of deuterium in Eurofer'97 measured with the COOPER experiment as a function of temperature compared with literature values [159], [161], [221], [222]. The solid blue line is the obtained temperature relation of the interstitial Sieverts' constant which is assumed to be valid for temperatures $T > 673\,\mathrm{K}$ where $D_{\mathrm{eff},2} \approx D_2$.

6.4.5. Measurement of the deuterium Sieverts' constant in Eurofer'97

According to equation (2.143), the effective Sieverts' constants $K_{\mathrm{s},2}^{\mathrm{eff,E97}}$ at the five observed temperature steps are obtained by dividing the data points of the measured permeabilities Φ_2 shown in figure 6.20 by the obtained data points of the effective diffusivities $D_{\mathrm{eff},2}$ plotted in the right-hand graph in figure 6.21, such that

$$K_{\mathrm{s},2}^{\mathrm{eff,E97}} = \frac{\Phi_2^{\mathrm{E97}}}{D_{\mathrm{eff},2}^{\mathrm{E97}}}, \quad \text{with} \quad \Delta K_{\mathrm{s},2}^{\mathrm{eff,E97}} = K_{\mathrm{s},2}^{\mathrm{eff,E97}} \cdot \sqrt{\left(\frac{\Delta\Phi_2^{\mathrm{E97}}}{\Phi_2^{\mathrm{E97}}}\right)^2 + \left(\frac{\Delta D_{\mathrm{eff},2}^{\mathrm{E97}}}{D_{\mathrm{eff},2}^{\mathrm{E97}}}\right)^2}. \tag{6.12}$$

The resulting data points and their error limits are shown in figure 6.22. They are plotted together with the effective Sieverts' relations reported by the references [159], [161], [221], [222]. Indeed, the discrepancies in the measured Sieverts' constants arise from the discrepancies of the measured permeabilities and diffusivities. The temperature relation of the real Sievert's constant is obtained for temperatures of approximately $T > 673\,\mathrm{K}$ by dividing the determined relation (6.8) by relation (6.11), so that

$$K^{\mathrm{E97}_{\mathrm{s},2}}(T) = (55.9 \pm 4.5)\,\mathrm{mol/m^3{\cdot}Pa^{-\frac{1}{2}}} \cdot \exp\left[-\frac{(48.7 \pm 1.0)\,\mathrm{kJ\,mol^{-1}}}{RT}\right]. \tag{6.13}$$

The previous sections show that the design of the COOPER experiment allows the measurement of the permeability, the diffusion coefficient and the Sieverts' constant of deuterium in Eurofer'97. For future measurements, however, a prior characterization of the permeation regime is essential. To ensure measurement in the diffusion-limited regime, the deuterium upstream pressure could be increased, which according to equation (2.147), would lead to an increased permeation number.

6.4.6. Mono-isotopic permeation measurements in the surface-limited regime

The left plot in figure 6.1 suggests that performing measurements in the surface-limited regime requires $^2H_2$ upstream pressures of $p < 20\,\mathrm{Pa}$. These are best performed using the

leak detector to measure the permeation flux because such low upstream pressures result in permeation fluxes that are difficult for the QMS to resolve (see figure 6.15).

Measurements in the surface-limited regime are executed by applying the same experimental procedure as for the described measurements in the diffusion-limited regime. However, since no time-lag method is applied, the $^2H_2$ gas can be injected slowly into PC-A using the leak valve V-04. To ensure a stable $^2H_2$ pressure in PC-A, a continuous $^2H_2$ gas flow through PC-A may be created by simultaneously manipulating the leak valves V-04 and V-17.

In the surface-limited regime, the steady state permeation flux and the upstream pressure are related by equation (2.146). Therefore, performing permeation flux measurements at different temperatures in this regime would allow the determination of the dissociation coefficient $k_{d,22}$ of $^2H_2$ molecules. The recombination coefficient $k_{r,22}$ would then be obtained by inserting the obtained value $k_{d,22}$ into equation (2.100).

6.4.7. Multi-isotopic co-permeation measurements

The experimental procedure for co-permeation measurements with the COOPER experiment starts in the same way as the mono-isotopic permeation measurements described above. After the evacuation of the whole system, the downstream chamber PC-B is connected to the QMS and the vacuum system via the *open path*. Therefore, the configuration of open and closed valves during the heating and measuring phases is identical to that described for the mono-isotopic permeation experiments. Since no temperature-dependent hydrogen transport parameters are measured in a co-permeation measurement, it is in principle sufficient to execute the experiment at a fixed temperature. Nevertheless, measuring at a higher temperature has the advantage that the detected permeation fluxes are higher, and thus noise effects are reduced.

A co-permeation measurement is initiated once the band heater has reached the target temperature and the permeation tube has reached thermal steady state. For a co-permeation measurement, it is not necessary to inject the gas quickly. This is because the analysis of co-permeation effects focuses merely on the influence of multi-isotopic transport on the height of the establishing steady state deuterium permeation flux and not on the period of transient permeation at the beginning of a permeation process. The objective of the co-permeation measurements is to observe whether at a fixed $^2H_2$ upstream pressure p_{22}^{PC-A} an additional injection of $^1H_2$ gas to the same side changes the steady state deuterium permeation flux into the evacuated PC-B. In the previous chapter, it was theoretically derived that co-permeation significantly reduces the steady state permeation flux of the primary isotope species when the permeation of the co-permeating secondary isotope species occurs in the diffusion-limited permeation regime (see right-hand plot in figure 6.1). To test this theoretical claim, two different co-permeation measurement schemes are planned.

The first involves measuring the flux-reducing effect of co-permeation in separate successive permeation flux measurements. In each measurement, the upstream partial pressure $p_{22}^{\mathrm{PC-A}}$ of the injected $^2H_2$ gas is held constant while the partial pressure $p_{11}^{\mathrm{PC-A}}$ of the injected $^1H_2$ gas is incrementally increased. First, a mono-isotopic permeation flux measurement is performed by injecting only $^2H_2$ gas with a pressure of $p_{22}^{\mathrm{PC-A}}$ into PC-A. The resulting permeation flux is measured until steady state permeation occurs. Then, PC-A is evacuated. The next measurement involves the injection of a $^1H_2$ + $^2H_2$ gas mix into PC-A. Before gas injection, the gas mixture is prepared in GMT-A. To guarantee the injection of a certain partial pressure $p_{11}^{\mathrm{PC-A}}$ of $^1H_2$ together with the fixed partial pressure $p_{22}^{\mathrm{PC-A}}$ of $^2H_2$, the ratio of the partial pressures in the premixed gas $p_{11}^{\mathrm{GMT-A}}/p_{22}^{\mathrm{GMT-A}}$ must satisfy

$$\frac{p_{11}^{\mathrm{GMT-A}}}{p_{22}^{\mathrm{GMT-A}}} = \frac{p_{11}^{\mathrm{PC-A}}}{p_{22}^{\mathrm{PC-A}}} \,. \tag{6.14}$$

The total pressure of the injected gas mix into PC-A is controlled by DG-05. The fixed partial pressure $p_{22}^{\mathrm{PC-A}}$ of $^2H_2$ gas is reached as soon as the total pressure reaches the value

$$p^{\mathrm{PC-A}} = \left(\frac{p_{11}^{\mathrm{GMT-A}}}{p_{22}^{\mathrm{GMT-A}}} + 1 \right) \cdot p_{22}^{\mathrm{PC-A}} \,. \tag{6.15}$$

After gas injection, the steady state deuterium permeation flux is recorded again until steady state permeation is reached. The described gas mix injection and measurement procedure is repeated several times. With each new permeation flux measurement, the partial pressure $p_{11}^{\mathrm{PC-A}}$ is increased while $p_{22}^{\mathrm{PC-A}}$ is held equal. It is observed whether the measured steady state permeation fluxes change with every new measurement. According to the right graph in figure 6.1, it is expected that in a measurement where a high partial pressure $p_{11}^{\mathrm{PC-A}}$ of $^1H_2$ gas is injected into PC-A, the deuterium permeation flux should be significantly reduced compared to a measurement where $p_{11}^{\mathrm{PC-A}} = 0\,\mathrm{Pa}$.

The second planned experimental scheme for co-permeation measurements makes use of the physical concept of a choked flow that was explained in section 3.1.1. It says that if the ratio between the total pressures in GMT-A and PC-A exceeds a critical value $p^{\mathrm{GMT-A}}/p^{\mathrm{PC-A}} > (p^{\mathrm{GMT-A}}/p^{\mathrm{PC-A}})_{\mathrm{chok}}$ the flow of gas particles through the leak valve V-04 reaches the speed of sound and therefore occurs only in one direction, from GMT-A to PC-A. For $^1H_2$ gas this critical pressure ratio is found to be [255]

$$\left(\frac{p^{\mathrm{GMT-A}}}{p^{\mathrm{PC-A}}} \right)_{\mathrm{chok}} = 1.89 \,. \tag{6.16}$$

For this reason, a co-permeation measurement with the COOPER experiment can also be performed in the following way. A fixed partial pressure $p_{22}^{\mathrm{PC-A}}$ of $^2H_2$ gas is injected into PC-A, the leak valve V-04 is closed and the permeation flux measurement is started. At this point, GMT-A is evacuated and then filled with pure $^1H_2$ gas from the gas cylinder, which must satisfy the condition $p_{11}^{\mathrm{GMT-A}} > 1.899 \cdot p^{\mathrm{PC-A}}$ at all times during the following measurement period. Once the deuterium permeation flux has reached steady state permeation, the leak valve V-04 is carefully opened and $^1H_2$ gas is continuously injected into

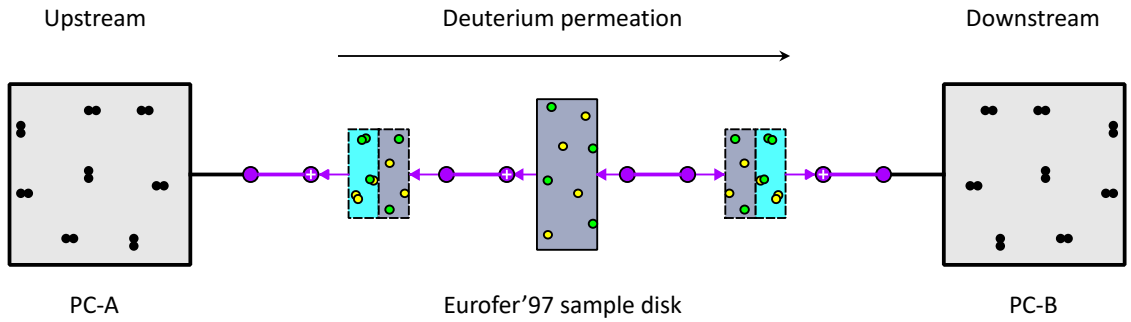

Fig. 6.23. Flow structure of the developed numerical model of the COOPER experiment using EcosimPro©.

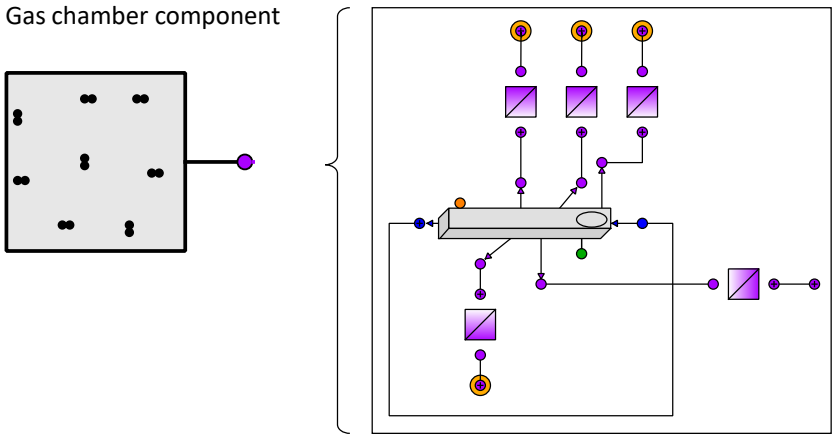

Fig. 6.24. Flow structure of the developed numerical model of a gas chamber component using EcosimPro©.

PC-A. The gas injection must be slow enough to allow the protium permeation process to remain in a steady state. As long as the condition $p_{11}^{\mathrm{GMT-A}} > 1.899 \cdot p^{\mathrm{PC-A}}$ is satisfied, there is no risk that the previously injected $^2H_2$ gas will flow back into GMT-A. To ensure this, fresh $^1H_2$ gas must be added to GMT-A several times during the experiment. The continuous gas injection is stopped when $p^{\mathrm{PC-A}} = 1 \times 10^5$ Pa. The predicted effect of co-permeating protium on the deuterium permeation flux should be directly visible in a changing QMS signal during continuous $^1H_2$ gas injection.

Within the scope of this thesis, a numerical model of the COOPER experiment is developed using the software EcosimPro©. Therefore, it is made use of the components described in section 5.1, whose symbols are shown in figure 5.2. Figure 6.23 presents the component flow structure of the developed model in which a wall material component is connected to two gas chamber components on each side, with gas-metal interface components in between. The gas chamber component is a higher-level component created as part of this work. Its inner structure is shown in figure 6.24. It consists of a flow material component with a fluid mass-flow rate of zero and a single discretization segment whose flow ports are connected in a closed loop. It has only one diffusion port while all other diffusion ports are blocked (see figure 6.24). The considered permeation surface of the parallel wall material component is $A_{\mathrm{per}} = 9.1 \times 10^{-4}\,\mathrm{m}^2$. Moreover, the gas volume of the upstream gas chamber component is assumed to be $V_{\mathrm{PC-A}} = 5 \times 10^{-4}\,\mathrm{m}^3$ which approximately corresponds to the volume enclosed between the valves V-06 and V-13.

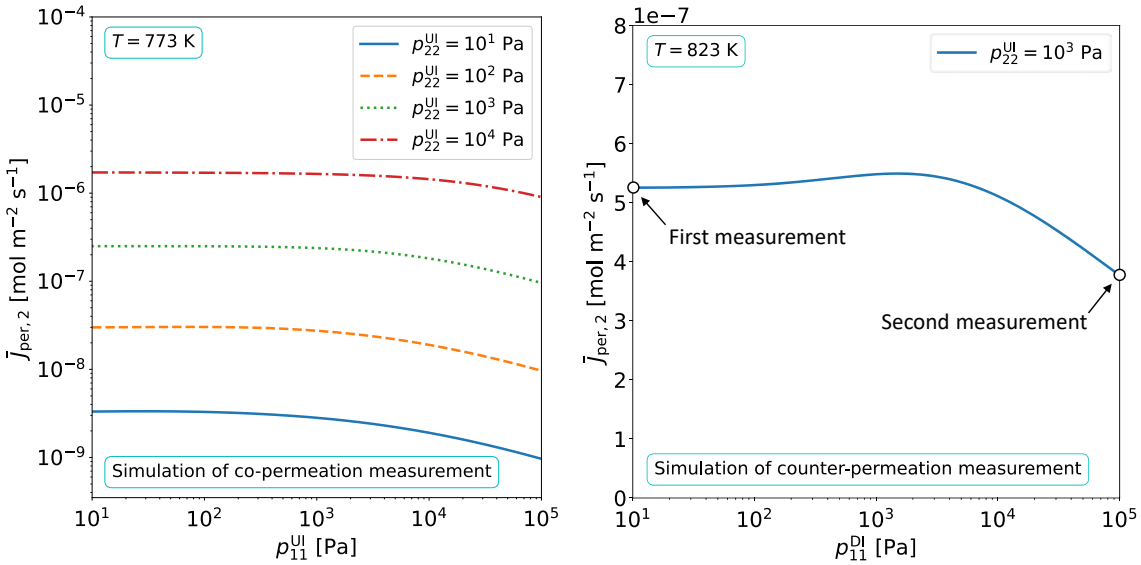

Fig. 6.25. [Left] Simulated steady state deuterium permeation flux into PC-B as a function of the $^1H_2$ upstream partial pressures in PC-A, which would result in a co-permeation measurement with the COOPER experiment at $T = 773\,\mathrm{K}$ considering four different $^2H_2$ upstream partial pressures in PC-A. [Right] Simulated steady state deuterium permeation flux as a function of the $^1H_2$ downstream partial pressures, which would result in a counter-permeation measurement with the COOPER experiment at $T = 773\,\mathrm{K}$ if the injected $^2H_2$ upstream partial pressures is $p_{22}^{PC-A} = 1 \times 10^3\,\mathrm{Pa}$.

To simulate co-permeation measurements into vacuum, the gas volume assigned to the downstream gas chamber is not important since the pressure in the *open path* of PC-B is bound to $p^{PC-B} = 0\,\mathrm{Pa}$. The hydrogen transport properties used in the model are the same as those given in table 5.1 and equation (5.18). It should be reminded that the model does take into account the isotope exchange reaction $2\,^1H^2H \rightleftharpoons {}^1H_2 + {}^2H_2$ to occur in the gas mixture. According to the justification given in section 2.2.5, a forward reaction rate coefficient of $k_{12+12}^{f,ex} \approx 1 \times 10^5\,\mathrm{m^3\,s^{-1}\,mol^{-1}}$ is considered for the reaction. This chosen relatively fast reaction rate coefficient basically means that the model assumes that the isotope exchange reaction reaches equilibrium almost immediately. The backward reaction rate coefficient is obtained with equation (2.103), considering equation (2.47) as the experimental relation for the equilibrium constant of the reaction.

The left-hand plot in figure 6.25 presents the simulated steady state deuterium permeation flux as a function of the $^1H_2$ upstream partial pressure that would theoretically occur in a co-permeation measurement for four different constant $^2H_2$ partial pressures if the measurements were performed at a sample disk temperature of $T = 773\,\mathrm{K}$. It can be seen that, according to the simulations, at all four $^2H_2$ upstream pressures, the presence of $^1H_2$ gas in PC-A should significantly reduce the deuterium permeation flux if the $^1H_2$ partial pressure is high. The higher the fixed $^2H_2$ upstream pressure, the higher the injected $^1H_2$ partial pressure must be for the permeation flux reduction effect to be noticeable.

6.4.8. Multi-isotopic counter-permeation measurements

Performing a counter-permeation measurement is considerably more complex than a mono-isotopic or co-permeation measurement, and the results are more prone to error. This is because the downstream chamber PC-B is not in vacuum but filled with $^1H_2$ gas of pressures up to $p_{11}^{\mathrm{PC-B}} \approx 1 \times 10^5$ Pa. Since the QMS does not work in a hydrogen gas environment at pressures of $p > 1 \times 10^{-2}$ Pa the permeation flux in a counter-permeation experiment can not be directly measured. To overcome this problem, the COOPER experimental setup is equipped with the *leak path* connection between PC-B and the QMS described in section 6.2.

A counter-permeation experiment begins like a mono-isotopic and co-permeation experiment, with an evacuation of the entire pipe system in which all valves except V-04, V-05, V-08, V-10, V-11 and V-12 are opened and the band heater is heated to the desired target temperature. In order to increase the accuracy of the measurement as much as possible, a counter-permeation experiment is performed at conditions where the deuterium permeation flux is highest, i.e. at the highest operating temperature of $T_{\mathrm{TC-01}} = 823$ K. Once the permeation tube has reached thermal steady state, the valves V-03, V-13, V-17, V-18, V-19, V-20, V-22 and V-23 are closed, and the valves V-04 and V-11 are opened.

A counter-permeation experiment is performed to verify the theoretical findings of section 4.1.2. These predict that the deuterium permeation flux from PC-A to PC-B is reduced when the permeation process of the counter-permeating protium isotopes occurs in the intermediate or diffusion-limited regime. In order to plan a series of appropriate counter-permeation measurements, it is helpful to simulate in advance the deuterium permeation flux that will occur during the measurement as a function of the partial pressure of the injected $^1H_2$-gas in PC-B. Therefore, it is made use of the developed numerical model of the COOPER experiment. The input values of the model are the same as those considered for the simulation of the co-permeation measurement. However, this time it is important to take into account that the gas volume in PC-B which is enclosed by the sample disk and the valves V-07, V-19 and V-23 is approximately $V_{\mathrm{PC-B}} \approx (764 \pm 5) \times 10^{-6}$ m^3. This value is determined using the developed CAD model of the COOPER experiment. The right-hand plot in figure 6.24 shows the simulated deuterium permeation flux at a sample disk temperature of $T = 823$ K and a $^2H_2$ upstream pressure of $p_{22}^{\mathrm{PC-A}} = 1 \times 10^3$ Pa as a function of the partial pressure of injected $^1H_2$ gas into PC-B.

It can be seen that with increasing $^1H_2$ partial pressure in PC-B the permeation flux first runs through a maximum before reducing considerably below the value that is expected in a mono-isotopic permeation measurement. The formation of the maximum is due to the fact that at a pressure of $p_{22}^{\mathrm{UI}} = 10^3$ Pa and $p_{11}^{\mathrm{DI}} = 0$ Pa, the deuterium permeation process is not surface-limited. Therefore, at $p_{11}^{\mathrm{DI}} = 0$ Pa, where $p_{11}^{\mathrm{DI}} \ll p_{22}^{\mathrm{UI}}$, the deuterium permeation flux is described by a lower value than that given by equation (4.29). With increasing value of p_{11}^{DI} the condition for equation (4.29) to be valid $p_{11}^{\mathrm{DI}} \gg p_{22}^{\mathrm{UI}}$ is approached more and more, which leads to an increase of the tritium permeation flux with increas-

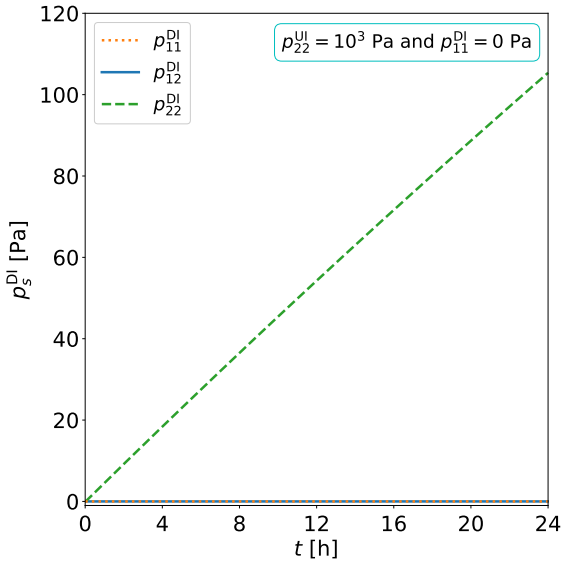

Fig. 6.26. Simulated $^1H_2$, $^1H^2H$ and $^2H_2$ partial pressures in a closed PC-B during a mono-isotopic permeation measurement performed with the COOPER experiment at a sample disk temperature of $T = 823\,\mathrm{K}$ and a $^2H_2$ upstream partial pressure of $p_{22}^{PC-A} = 1 \times 10^3\,\mathrm{Pa}$.

ing value of p_{11}^{DI}. However, as soon as in the diffusion-limited counter-permeation regime the deuterium permeation flux reducing effect of the counter-permeating protium prevails, the deuterium permeation flux decreases and a maximum is formed. No maximum would have formed if the considered $^2H_2$ upstream pressure had been lower so that at $p_{11}^{DI} = 0\,\mathrm{Pa}$ the deuterium permeation process would have occurred in the surface-limited regime.

In order to experimentally verify the simulation results, two measurements are planned with the specification highlighted by circles in the right-hand plot in figure 6.25.

The first measurement is a mono-isotopic permeation experiment in which $^2H_2$ gas with an upstream pressure of $p_{22}^{PC-A} = 1 \times 10^3\,\mathrm{Pa}$ is injected through the leak valve V-04 into PC-A. As a result, the permeated $^2H_2$ molecules will accumulate in the enclosed volume of PC-B, causing the $^2H_2$ partial pressure in PC-B to increase over time. The pressure increase predicted for the first measurement is simulated and plotted in figure 6.26. Note that the simulation does not take into account the presence of protium impurities, nor isotope exchange reactions between permeated $^2H_2$ molecules and residual water molecules. Therefore, the simulated partial pressures of $^1H_2$ and $^1H^2H$ remain zero. In fact, an outgassing of the residual molecules from the walls of the permeation cell chamber or absorption of the permeated $^2H_2$ into the wall will lead to a systematic deviation of the real pressure measurement from the simulation. In order to keep the relative systematic error $\Delta p^{PC-B}/p^{PC-B}$ of the total pressure increase caused by the permeated $^2H_2$ molecules from PC-A to PC-B as small as possible, the mono-isotopic permeation measurement is carried out for as long as practically possible. The plotted simulation shows that after a measurement period of $t = 24\,\mathrm{h}$ the pressure in PC-B will have increased to about $p^{PC-B} = 105\,\mathrm{Pa}$. Such a value is well measurable with the installed capacitance diaphragm gauges DG-06. Since in a real mono-isotopic permeation experiment, it is expected that residual protium-containing molecules are present in the system, the total pressure p^{PC-B} will not be equal to the $^2H_2$ partial pressure p_{22}^{PC-B} in PC-B. To determine the partial pressure configuration of deuterium-containing molecules in PC-B after the measurement ends, the total

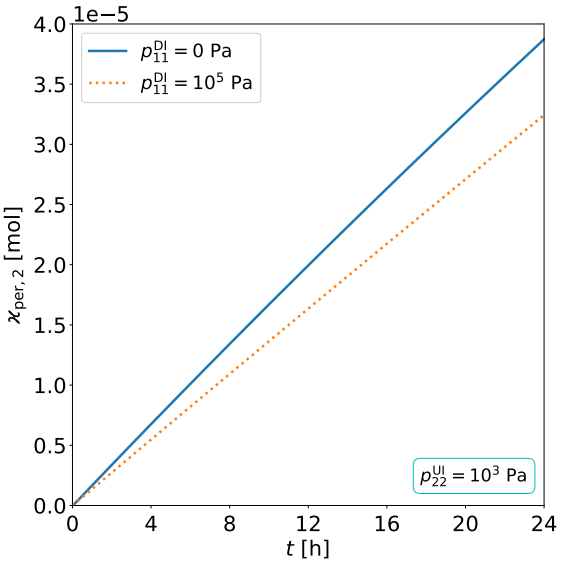

Fig. 6.27. Simulated cumulative number of permeated deuterium atoms into a close PC-B at a sample disk temperature of $T = 823\,\mathrm{K}$ and a $^2H_2$ upstream partial pressure of $p_{22}^{\mathrm{PC-A}} = 1 \times 10^3\,\mathrm{Pa}$ considering that either no $^1H_2$ gas is present in PC-B or a partial pressure of $p_{11}^{\mathrm{PC-B}} = 1 \times 10^5\,\mathrm{Pa}$.

pressure measurement is supported by a gas composition measurement using the QMS. Therefore, the leak valve V-23 is carefully opened and the resulting increments in the detector signals $\Delta I^+_{\mathrm{meas},\kappa}$ of the mass-to-charge ratios $\kappa \in \{1, 2, 3, 4, 16, 17, 18, 19, 20\}$ related to hydrogen isotope containing molecules are measured. The partial pressures related to the mass-to-charge ratios $\kappa' \in \{3, 4, 20\}$ are then obtained with the formula

$$p_{\kappa'}^{\mathrm{PC-B}} = \frac{\Delta I^+_{\mathrm{meas},\kappa'}}{\sum_\kappa \Delta I^+_{\mathrm{meas},\kappa}} \cdot p^{\mathrm{PC-B}}\,, \tag{6.17}$$

where the sum must be taken over the increases in ion current of all mass-to-charge ratios $\kappa \in \{1, 2, 3, 4, 16, 17, 18, 19, 20\}$. The cumulative number of permeated deuterium isotopes can then be calculated with the ideal gas law

$$\varkappa_{\mathrm{per,2}} = \frac{V_{\mathrm{PC-B}}}{RT} \cdot \left(p_{\kappa=3}^{\mathrm{PC-B}} + 2p_{\kappa=4}^{\mathrm{PC-B}} + 2p_{\kappa=20}^{\mathrm{PC-B}}\right)\,, \tag{6.18}$$

The simulated cumulative number of permeated deuterium isotopes into PC-B as a function of time is represented by the blue solid line in figure 6.27. Once the value of $\varkappa_{\mathrm{per,2}}$ at the end of the performed experiment at time t_{end} is experimentally determined, the average deuterium permeation flux that must have governed during the time of the experiment can be estimated, considering that $\overline{J}_{\mathrm{per,2}} \approx \varkappa_{\mathrm{per,2}}\left(t_{\mathrm{end}}\right)/t_{\mathrm{end}}$.

The second measurement is identical to the first, with the only difference that this time the injection of $^2H_2$ gas with a partial pressure of $p_{22}^{\mathrm{PC-A}} = 1 \times 10^3\,\mathrm{Pa}$ into PC-A is followed by an injection of $^1H_2$ gas with a partial pressure of $p_{11}^{\mathrm{PC-B}} = 1 \times 10^5\,\mathrm{Pa}$ into PC-B. Again, the total pressure and the partial pressure configuration that establish at the end of the measurement period are measured using DG-06 and the QMS, in the same way as in the first measurement. The simulated development of the partial pressures in PC-B is shown in figure 6.28. The slight decrease in the $^1H_2$ partial pressure over time is related to the $^1H_2$ molecules lost in the counter-permeation process into PC-A. Due to the high abundance of $^1H_2$ molecules in PC-B, most of the permeated deuterium isotopes

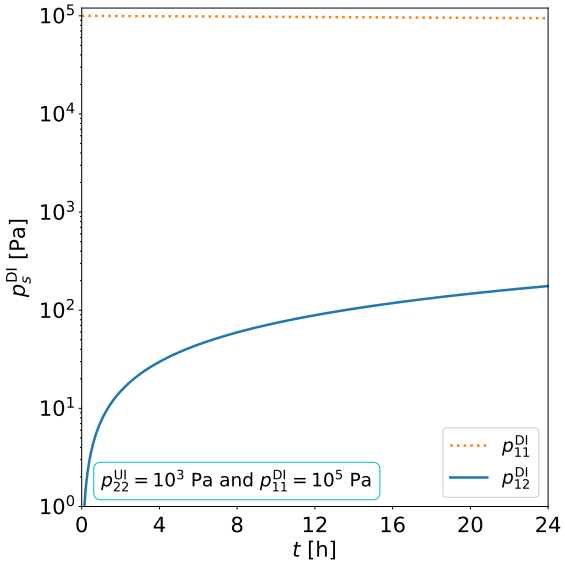

Fig. 6.28. Simulated $^1H_2$ and $^1H^2H$ partial pressures in a closed PC-B during counter-permeation measurements with the COOPER experiment at a sample disk temperature of $T = 823\,\mathrm{K}$, a $^2H_2$ upstream partial pressure of $p_{22}^{\mathrm{PC-A}} = 1 \times 10^3\,\mathrm{Pa}$ and a $^1H_2$ downstream pressure of $p_{11}^{\mathrm{PC-B}} = 1 \times 10^5\,\mathrm{Pa}$.

recombine with protium upon entering PC-B. Moreover, the isotope exchange reactions between $^1H_2$ and $^2H_2$ result in a vanishing partial pressure of $^2H_2$ molecules. Therefore, almost all deuterium isotopes in PC-B are bound in $^1H^2H$ molecules. It can be seen that after $t = 24\,\mathrm{h}$ the partial pressure ratio between $^1H_2$ and $^1H^2H$ molecules in PC-B is expected to be of the order of $p_{22}^{\mathrm{PC-B}}/p_{11}^{\mathrm{PC-B}} \approx 1/500$. Resolving a 500-fold difference in detector signal between the $\kappa = 3$ mass-to-charge ratio signal associated with $^1H^2H$ molecules and that of $\kappa = 2$ associated mainly with $^1H_2$ molecules is not an issue for a QMS. The expected cumulative number of permeated deuterium isotopes in the second measurement is represented by the dotted orange line in figure 6.27. It can be seen that according to the simulation, due to the reduced permeation flux caused by the high $^1H_2$ pressure in PC-B, less deuterium will permeate into PC-B over time compared to the first mono-isotopic permeation measurement. This implies that the average permeation flux estimated by $\overline{J}_{\mathrm{per},2} \approx \varkappa_{\mathrm{per},2}\,(t_{\mathrm{end}})\,/t_{\mathrm{end}}$ must have been smaller.

If the predicted difference in the cumulative number of deuterium isotopes permeated can be experimentally demonstrated, the permeation flux-reducing effect of counter-permeation in Eurofer'97 would be confirmed.

7. MODELING OF YTTRIUM-BASED HYDROGEN CAPTURE IN DONES

[2]In this chapter, the focus of the dissertation is turned to the numerical investigation of hydrogen isotope capture in the DONES lithium loop with yttrium metal as the getter material. For this purpose, a numerical tool is developed from scratch capable of simulating the transport of hydrogen isotopes from the DONES liquid lithium system into a hydride-forming yttrium-based getter trap. After an in-depth theoretical study of the physical mechanisms involved, the tool is used to simulate the hydrogen isotope transport occurring in the DONES lithium loop during a proposed initial purification run and during the DONES experimental phase. Furthermore, conditions for the optimal pebble bed mass and suitable operating modes to meet the tritium safety requirements during the different phases of DONES are derived from the underlying theoretical model. Finally, experimental validation of the simulation tool is performed by reproducing measurement data from a previous deuterium retention experiment [112].

To simulate the process of hydrogen isotope retention by an yttrium getter trap in the liquid lithium loop of DONES, a numerical model of the lithium circuit is developed using the EcosimPro© software [113]. In the model, absorption and permeation processes of hydrogen isotopes in loop components other than the getter trap are neglected. Therefore, it is sufficient to model hydrogen transport in the DONES lithium loop with a simplified layout compared to the full piping and instrumentation diagram shown in [256]. All material characteristic properties of lithium mentioned in the following refer to natural lithium containing 7.42 % of ^{6}Li and 92.58 % of ^{7}Li.

7.1. Hydrogen transport in the DONES lithium loop

A component flow chart of the created loop model is presented on the right-hand side in figure 7.1. It consists of a main loop with a volume flow rate F_{main} and a purification side loop connected in parallel. For this configuration, the model makes use of the EcosimPro© splitter and mixer components which are defined in section 5.1 (see figure 5.2). In this model, the purification side loop merely contains an yttrium getter trap which is exposed to a lithium flow rate of F_{trap}. The total volume of liquid lithium in the loop system is denoted by V_{Li}.

The temporal and spatial evolution of the concentrations $c^{\text{Li}}_{i,\text{main}}(y', t)$ of hydrogen iso-

[2]This chapter contains material and text that is contained in the following published article. The author of this dissertation is the first author of this article:

- S.J. Hendricks *et al*, "Impact of yttrium hydride formation on multi-isotopic hydrogen retention by a getter trap for the DONES lithium loop," *Nuclear Fusion*, vol. 63, p. 056012, 2023.

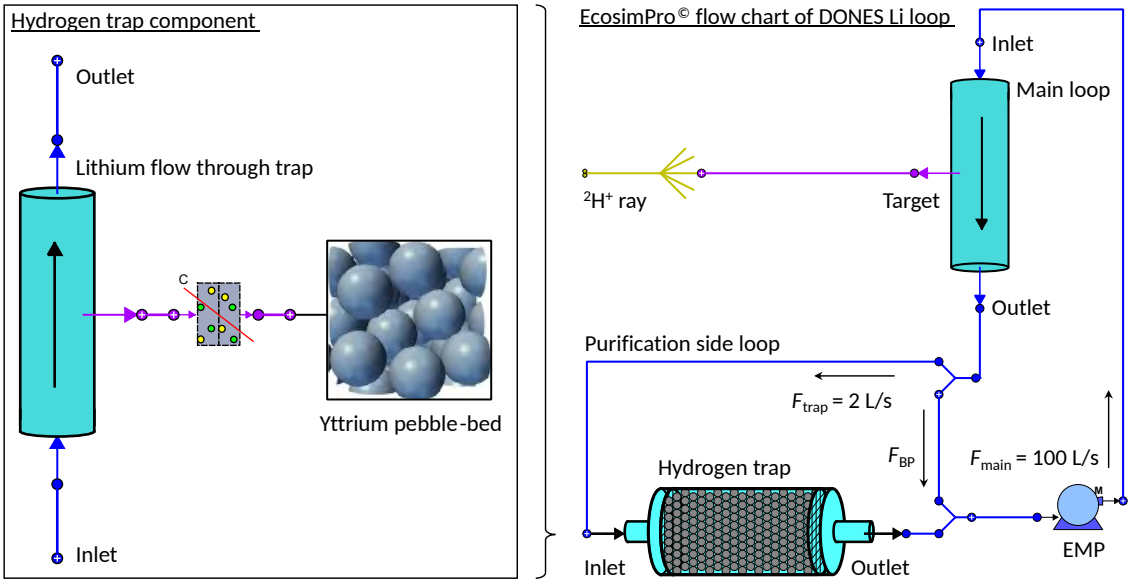

Fig. 7.1. [Left] Internal component structure of the hydrogen trap component developed using the software EcosimPro© [113]. [Right] Flow diagram of the numerical model of the DONES lithium loop using EcosimPro© [113].

tope species ^{i}H in the main loop are represented by an EcosimPro© pipe flow component (see figure 5.1) and described by the finite difference mass continuity equation (5.2). It is discretized along its longitudinal axis y' axis into U spatial segments $y'_n = y'_1, \ldots, y'_U$. The generation of hydrogen isotopes originating from the impelling deuterons into the lithium target is quantified by a generation rate $\dot{\varkappa}_{i,\mathrm{gen}}$ with the unit [mol s^{-1}] and considered to happen in the first segment y'_1 of the main loop pipe. Here, it is treated as a particle source with $\varsigma_i^{\mathrm{gen}}(y'_1, t) = \dot{\varkappa}_{i,\mathrm{gen}} \cdot U / V_{\mathrm{Li,main}}$. This allows equation (5.2) to be adapted to the situation occurring in the lithium target, which is expressed by the following finite-difference form (5.2)

$$\frac{\partial c_{i,\mathrm{main}}^{\mathrm{Li}}(y'_1, t)}{\partial t} = \frac{U}{V_{\mathrm{Li,main}}} \cdot \dot{\varkappa}_{i,\mathrm{gen}} - \frac{F_{\mathrm{main}} \cdot U}{V_{\mathrm{Li,main}}} \cdot \left[c_{i,\mathrm{main}}^{\mathrm{Li}}(y'_1, t) - c_{i,\mathrm{main}}^{\mathrm{Li,f.IN}}(t) \right], \tag{7.1}$$

where $c_{i,\mathrm{main}}^{\mathrm{Li,f.IN}}(t)$ is the concentration at the inlet flow port of the main loop pipe flow component (see figure 7.1). The parameter $V_{\mathrm{Li,main}} = V_{\mathrm{Li}} - V_{\mathrm{Li,trap}}$ is the volume of lithium flowing through the main loop. Neither particle sinks nor sources are assumed to occur in the remaining main loop sections $y'_n = y'_2, \ldots, y'_U$. This reduces the finite difference expression of the mass continuity equation in these segments to

$$\frac{\partial c_{i,\mathrm{main}}^{\mathrm{Li}}(y'_n, t)}{\partial t} = -\frac{F_{\mathrm{main}} \cdot U}{V_{\mathrm{Li,main}}} \cdot \left[c_{i,\mathrm{main}}^{\mathrm{Li}}(y'_n, t) - c_{i,\mathrm{main}}^{\mathrm{Li}}(y'_{n-1}, t) \right]. \tag{7.2}$$

The hydrogen hot trap is considered to be a cylindrical tube of diameter d_{trap}. It is densely filled with N_{peb} round yttrium pebbles of radius r_{peb}, diameter d_{peb} and individual surface area $A_{\mathrm{peb}} = 4\pi r_{\mathrm{peb}}^2$. Consequently, the total yttrium surface area yields $A_{\mathrm{Y}} = N_{\mathrm{peb}} A_{\mathrm{peb}}$. The length l_{trap} and the internal volume V_{trap} of the trap container are determined by the relations $l_{\mathrm{trap}} = 4V_{\mathrm{trap}}/(\pi d_{\mathrm{trap}}^2)$ and $V_{\mathrm{trap}} = V_{\mathrm{Y}}/(1-\varepsilon)$. Here, ε is the void fraction

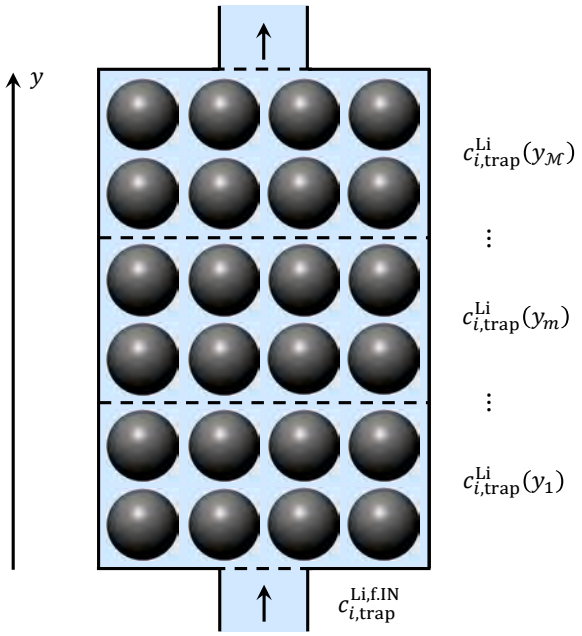

Fig. 7.2. Numerical discretization of the trap container which contains the yttrium pebble bed as considered in the numerical model.

of the yttrium pebble bed. The volume and mass of the yttrium pebble bed are given by $V_{\mathrm{Y}} = 4/3 \cdot N_{\mathrm{peb}} \pi r^3_{\mathrm{peb}}$ and $m_{\mathrm{Y}} = \rho_{\mathrm{Y}} V_{\mathrm{Y}}$, respectively. Parameter $\rho_{\mathrm{Y}} = 4469\,\mathrm{kg\,m^{-3}}$ is the density of pure yttrium. The volume of liquid lithium filling the interstitials of the pebble bed is determined by $V_{\mathrm{Li,trap}} = V_{\mathrm{trap}} - V_{\mathrm{Y}}$.

Again, equation (5.2) is used to calculate the concentrations $c^{\mathrm{Li}}_{i,\mathrm{trap}}$ in the lithium core flow through the interstitial spaces of the pebble bed. This is done by considering the retention of hydrogen isotopes into the yttrium pebbles as a particle sink. It is quantified by an isotope-specific retention flux $J_{\mathrm{ret},i}(y,t)$ which is assumed negative for fluxes directed towards the pebble centers and varies along the y-direction of the trap. For its numerical treatment, the lithium flow through the trap container is described by a pipe flow component discretized into $\mathcal{M}$ segments $y_m = y_1, \ldots, y_{\mathcal{M}}$, with $\Delta y = l_{\mathrm{trap}}/\mathcal{M}$ (see left-hand image in figure 7.1). A sketch of the applied discretization is shown in figure 7.2. The retention flux into the pebbles occurs in each trap segment and is equivalent to the diffusion flux $J^{\mathrm{d.OUT}}_i(y,t)$ at the $\mathcal{M}$ diffusion ports of the pipe flow component describing the trap. Since no isotopic exchange reactions take place in the lithium and permeation losses are neglected, equation (5.2) is transformed into the following finite difference form to describe the lithium flow through the trap

$$\frac{\partial c^{\mathrm{Li}}_{i,\mathrm{trap}}(y_m,t)}{\partial t} = \frac{A_{\mathrm{Y}}}{V_{\mathrm{Li,trap}}} \cdot J_{\mathrm{ret},i}(y_m,t) - \frac{F_{\mathrm{trap}} \cdot \mathcal{M}}{V_{\mathrm{Li,trap}}} \cdot \left[c^{\mathrm{Li}}_{i,\mathrm{trap}}(y_m,t) - c^{\mathrm{Li}}_{i,\mathrm{trap}}(y_{m-1},t) \right] . \tag{7.3}$$

For $m = 1$, the term $c^{\mathrm{Li}}_{i,\mathrm{trap}}(y_{m-1},t)$ in equation (7.3) is replaced by $c^{\mathrm{Li,f.IN}}_{i,\mathrm{trap}}(t)$. The parameters $c^{\mathrm{Li,f.IN}}_{i,\mathrm{trap}}(t)$ and $c^{\mathrm{Li,f.OUT}}_{i,\mathrm{trap}}(t) \equiv c^{\mathrm{Li}}_{i,\mathrm{trap}}(y_{\mathcal{M}},t)$ label the concentrations at the inlet and outlet of the pipe flow component of the trap. The isotope specific retention rate $\dot{\varkappa}^{\mathrm{Y}}_i(t)$ of the yttrium pebble bed is defined by

$$\dot{\varkappa}^{\mathrm{Y}}_i(t) \equiv A_{\mathrm{Y}} \cdot \sum_m^{\mathcal{M}} \frac{J_{\mathrm{ret},i}(y_m,t)}{\mathcal{M}} = \frac{3 m_{\mathrm{Y}}}{r_{\mathrm{peb}} \rho_{\mathrm{Y}}} \cdot \sum_m^{\mathcal{M}} \frac{J_{\mathrm{ret},i}(y_m,t)}{\mathcal{M}} . \tag{7.4}$$

The total retention rate is determined by $\dot{\varkappa}^{\mathrm{Y}}(t) = \sum_i \dot{\varkappa}_i^{\mathrm{Y}}(t)$.

In this model, the lithium density is calculated by $\rho_{\mathrm{Li}}(T) = 562 - 0.1 \cdot T[\mathrm{K}]$ [257]. Both the temperature and the lithium density are assumed to be constant throughout the loop. Consequently, mass continuity requires $F_{\mathrm{main}} = F_{\mathrm{BP}} + F_{\mathrm{trap}}$, where F_{BP} designates the volume flow through the bypass parallel to the purification side loop (see figure 7.1). As a result, equation (5.3), which describes the physics of the mixer component employed for the parallel connection of the purification side loop, reduces to

$$c_{i,\mathrm{main}}^{\mathrm{Li,f.IN}}(t) = \frac{1}{F_{\mathrm{main}}} \cdot \left[c_{i,\mathrm{main}}^{\mathrm{Li,f.OUT}}(t) \cdot F_{\mathrm{BP}} + c_{i,\mathrm{trap}}^{\mathrm{Li,f.OUT}}(t) \cdot F_{\mathrm{trap}} \right] . \tag{7.5}$$

The average concentration in the whole lithium system is calculated with

$$\left\langle c_i^{\mathrm{Li}} \right\rangle (t) = \frac{V_{\mathrm{Li,main}}}{U V_{\mathrm{Li}}} \sum_{n=1}^{U} c_{i,\mathrm{main}}^{\mathrm{Li,f.IN}}(y_n', t) + \frac{V_{\mathrm{Li,trap}}}{\mathcal{M} V_{\mathrm{Li}}} \sum_{m=1}^{\mathcal{M}} c_{i,\mathrm{trap}}^{\mathrm{Li,f.IN}}(y_m, t) . \tag{7.6}$$

7.2. Hydrogen transport from lithium into an yttrium getter bed

The diffusive hydrogen isotope transport from the liquid lithium core flow through the interstitial sites of the pebble bed into the yttrium pebbles is numerically described by the EcosimPro© mass transfer component described in section 5.1. It mainly represents the boundary layer approximation which describes the hydrogen isotope retention flux $J_{\mathrm{ret},i}$ in lithium at the Li-Y interfaces as a mass transfer flux expressed by equation (5.5)

$$J_{\mathrm{ret},i}(y_m, t) = \alpha_{\mathrm{MT}} \cdot [c_{\mathrm{int},i}^{\mathrm{Li}}(y_m, t) - c_{i,\mathrm{trap}}^{\mathrm{Li}}(y_m, t)] . \tag{7.7}$$

The mass transfer between liquids and spheres in packed beds has been studied by E. J. Wilson and C. J. Geankoplis [168]. Their experimental results allow writing the following two expressions for the mass transfer coefficient, which are valid in two different Reynolds number regimes [105], [166]

$$\alpha_{\mathrm{MT}} = 1.09 \cdot \frac{D^{\mathrm{Li}}}{\varepsilon \cdot d_{\mathrm{peb}}} \cdot \mathrm{Re}^{1/3} \mathrm{Sc}^{1/3} , \qquad 0.0016 < \mathrm{Re} < 55 \tag{7.8}$$

$$\alpha_{\mathrm{MT}} = 0.25 \cdot \frac{D^{\mathrm{Li}}}{\varepsilon \cdot d_{\mathrm{peb}}} \cdot \mathrm{Re}^{0.69} \mathrm{Sc}^{1/3} , \qquad 55 < \mathrm{Re} < 1500 . \tag{7.9}$$

This thesis considers expressions for the Reynolds number Re and the Schmidt number Sc of a fluid flow through a pebble bed, as reported in [166], [168].

$$\mathrm{Re} = \frac{u_{\mathrm{int}} d_{\mathrm{peb}} \rho_{\mathrm{Li}}}{\varrho_{\mathrm{Li}}} \qquad \& \qquad \mathrm{Sc} = \frac{\varrho_{\mathrm{Li}}}{\rho_{\mathrm{Li}} D^{\mathrm{Li}}} . \tag{7.10}$$

where the interfacial velocity around the pebbles in the packed bed is calculated with [258]:

$$u_{\mathrm{int}} = \frac{\varepsilon l_{\mathrm{trap}} F_{\mathrm{Li}}}{V_{\mathrm{Li,trap}}} \tag{7.11}$$

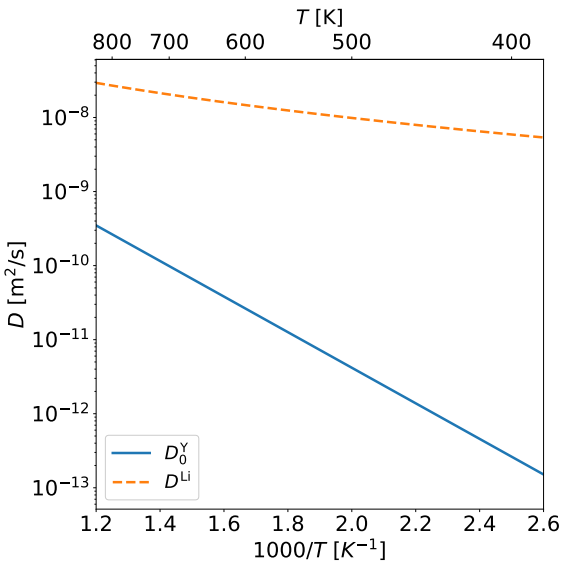

Fig. 7.3. Temperature dependency of the diffusivity relations of deuterium in liquid lithium and in the α-Y phase of yttrium obtained from experimental values reported in [259] and [154]. In this model, these relations are considered for all three hydrogen isotopes.

The temperature-dependent parameter ϱ_{Li} is the dynamic viscosity of liquid lithium, which is given by [257]

$$\log \varrho_{\mathrm{Li}}\,(\pm 19\,\%) = -3.08 + \frac{58}{T} - 5.2 \times 10^{-4} \cdot T\,. \tag{7.12}$$

The parameter D^{Li} is the diffusivity of hydrogen isotopes in lithium. This model uses the diffusivity relation of deuterium in lithium for all three hydrogen isotopes. It is determined from the tritium diffusivity measured in [259] by taking into account the isotope effect of hydrogen diffusion in metals, expressed by equation (2.66)

$$\log D^{\mathrm{Li}} = 1.737 \log T - \frac{110}{T} - 8.562 + \log \sqrt{\frac{M_3}{M_2}}\,, \tag{7.13}$$

Here M_2 and M_3 denote the molar masses of deuterium and tritium [154], [260]. This particular diffusivity relation for liquid lithium is chosen because it was measured at the lowest temperature range of $640\,\mathrm{K} < T < 1000\,\mathrm{K}$ among the experimental data found in the literature [154], [259], [261], [262]. A critical analysis of the different literature values can be found in [105]. Relation (7.13) is plotted in figure 7.3.

The physical laws describing the hydrogen isotope transport across the lithium-yttrium interface and inside the pebbles are included in an EcosimPro© component which is developed from scratch by the author of this thesis. It is called yttrium pebble bed component (see figure 7.1). Transmitted by the connected mass transfer interface component which mainly contains equation (7.7), the inlet concentration and inlet particle flux of the yttrium pebble bed component are $c^{\mathrm{Li}}_{\mathrm{int},i}(y_m, t)$ and $J_{\mathrm{ret},i}(y_m, t)$, respectively.

In this model, the yttrium pebbles are regarded as spheres. Each sphere consists of $\mathcal{Q} + 2$ spherical shells q. Figure 7.4 illustrates the discretized shell structure under consideration. The pebble center forms the first shell and is described as a sphere with radius $r_1 = \delta$. The last shell is considered as a spherical layer of thickness δ with an inner radius of $r_{\mathcal{Q}+2} = r_{\mathrm{peb}} - \delta$ and an outer radius of $r_{\mathcal{Q}+3} = r_{\mathrm{peb}}$. The defined radial positions of the

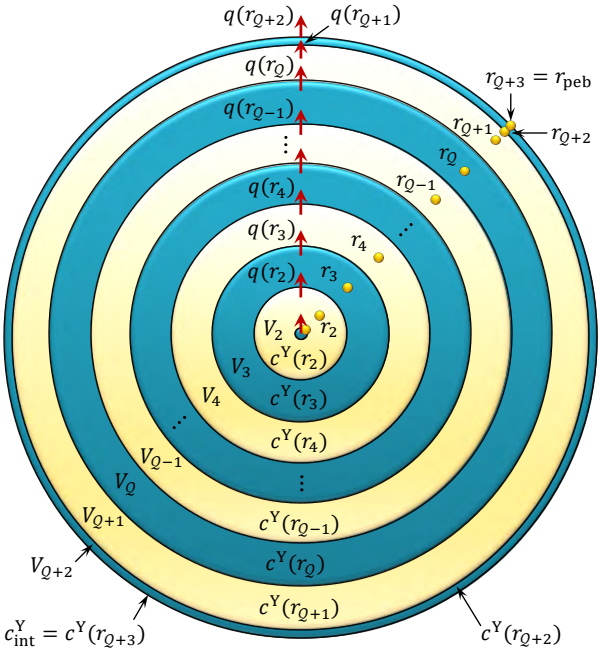

Fig. 7.4. Discretized shell structure considered for the finite difference description of hydrogen transport inside of each yttrium pebble.

remaining shells $r_q = (q - 3/2) \cdot \Delta r$ with $\Delta r = r_{\mathrm{peb}}/\mathrm{Q} \gg \delta$ are in the middle between their inner and outer spherical surface planes. Consequently, the volumes V_q of the spherical shells q can be expressed by

$$V_q = \begin{cases} \frac{4}{3}\pi\delta^3 & \text{if } q = 1 \\ \frac{4}{3}\pi\left(\Delta r^3 - \delta^3\right) & \text{if } q = 2 \\ \frac{4}{3}\pi\left(\left[(q-1)\,\Delta r\right]^3 - \left[(q-2)\,\Delta r\right]^3\right) & \text{if } 2 < q \leq \mathrm{Q} \\ \frac{4}{3}\pi\left(r_{\mathrm{Q}+2}^3 - \left[r_{\mathrm{Q}+3} - \Delta r\right]^3\right) & \text{if } q = \mathrm{Q}+1 \\ \frac{4}{3}\pi\left(r_{\mathrm{Q}+3}^3 - r_{\mathrm{Q}+2}^3\right) & \text{if } q = \mathrm{Q}+2\,. \end{cases} \tag{7.14}$$

By using Fick's first law of diffusion (2.67), the number of isotopes $\dot{\varkappa}_i^{\mathrm{shell}}$ of species ${}^i\mathrm{H}$ that cross a spherical plane of an yttrium pebble at radius r per time yields

$$\dot{\varkappa}_i^{\mathrm{shell}}(r, y, t) = -4\pi r^2 \overline{D}^{\mathrm{Y}}(r, y, t) \cdot \frac{\partial c_i^{\mathrm{Y}}(r, y, t)}{\partial r}\,. \tag{7.15}$$

Integrating this equation on both sides from one radial discretization node to the next, and assuming the chemical diffusion coefficient $\overline{D}^{\mathrm{Y}}(r_q, y_m, t)$ of hydrogen isotopes in yttrium to be isotropic inside of a single shell q, allows defining the following two finite difference relations [263]

$$\dot{\varkappa}_i^{\mathrm{shell}}(r_q, y_m, t) = \frac{4\pi\overline{D}^{\mathrm{Y}}(r_q, y_m, t) \cdot \left[c_i^{\mathrm{Y}}(r_q, y_m, t) - c_i^{\mathrm{Y}}(r_{q+1}, y_m, t)\right]}{1/r_q - 1/r_{q+1}} \tag{7.16}$$

and

$$\frac{\partial c_i^{\mathrm{Y}}(r_q, y_m, t)}{\partial t} = \frac{\dot{\varkappa}_i^{\mathrm{shell}}(r_{q-1}, y_m, t) - \dot{\varkappa}_i^{\mathrm{shell}}(r_q, y_m, t)}{V_q}\,. \tag{7.17}$$

They approximately describe the time-evolving fluxes and concentrations of each hydrogen isotope ${}^i\mathrm{H}$ at the nodes q in the pebbles. The concentration of hydrogen isotopes in yttrium at the Li-Y interface is defined by $c_{\mathrm{int},i}^{\mathrm{Y}}(y_m, t) \equiv c_i^{\mathrm{Y}}(r_{\mathrm{Q}+3}, y_m, t)$.

As has been observed in the past, the diffusivity of hydrogen isotopes in yttrium is concentration-dependent [68]. Hence, above a certain hydrogen concentration in the yttrium $\overline{D}^{\mathrm{Y}} \neq D^{\mathrm{Y}}$ which. Therefore, the calculations in this chapter must consider the chemical diffusion coefficient of hydrogen isotopes in yttrium instead of the intrinsic diffusivity (see section 2.2.1 for more details). Obtaining an expression for $\overline{D}^{\mathrm{Y}}(r_q, y_m, t)$ requires a previous theoretical analysis of the thermodynamics of the yttrium-hydrogen system which is carried out in section 7.3.2. The final expression for $\overline{D}^{\mathrm{Y}}(r_q, y_m, t)$ is derived in section 7.5.

7.3. Determination of the lithium-yttrium boundary condition

Two boundary conditions are required to complete the set of hydrogen transport equations contained in the yttrium pebble bed component. The first condition follows from the principle of mass conservation across an interface

$$J_{\mathrm{ret},i}(y_m, t) \equiv \dot{\varkappa}_i^{\mathrm{shell}}(r_{\mathrm{Q}+2}, y_m, t)/A_{\mathrm{peb}} \,. \tag{7.18}$$

This condition means that the hydrogen retention flux in the boundary layer on the lithium side of the interface is equal to the hydrogen diffusion flux crossing the outer layer of an yttrium pebble.

The second boundary condition is the relation between the hydrogen isotope concentrations $c_{\mathrm{int},i}^{\mathrm{Li}}$ and $c_{\mathrm{int},i}^{\mathrm{Y}}$ at the Li-Y interface. It will be seen that this boundary condition mainly determines the hydrogen isotope absorption dynamics of the yttrium pebble bed and describes the process of hydride formation (HyF) in the getter material.

From now on, the term hydrogen (H) will be considered as a unified expression for all three hydrogen isotopes, leading to the definitions $c^{\mathrm{Me}} \equiv \sum_i c_i^{\mathrm{Me}}$ and $J^{\mathrm{Me}} \equiv \sum_i J_i^{\mathrm{Me}}$. In general, when in this chapter a quantity is not assigned to a specific hydrogen isotope by the index i, it refers to the sum of all hydrogen isotopes. Here the symbol Me stands for either yttrium or lithium. Furthermore, in the following, it is not necessary to relate each quantity to the corresponding longitudinal position in the trap, since the boundary conditions apply to each trap segment.

According to equilibrium condition 1 [relation (2.12)] derived in section 2.1.1, hydrogen isotopes are absorbed from the lithium flow by the yttrium pebbles until the concentration and temperature-dependent chemical potential of hydrogen dissolved in lithium $\mu_{\mathrm{H}}^{\mathrm{Li}}(c^{\mathrm{Li}}, T)$ is equal to the chemical potential of hydrogen dissolved in yttrium $\mu_{\mathrm{H}}^{\mathrm{Y}}(c^{\mathrm{Y}}, T)$. At this moment, all concentration gradients and diffusion fluxes disappear and thermodynamic equilibrium is reached. Here, $\mu_{\mathrm{H}}^{\mathrm{Me}} = \sum_i \mu_i^{\mathrm{Me}}$ refers to the summed chemical potential of all hydrogen isotopes dissolved in a metal. The thermodynamic equilibrium between the two metal-hydrogen systems Li-H and Y-H is described mathematically by the defined equilibrium condition 2 which is expressed by the equations (2.13) and (2.42). According to condition (2.42), in thermodynamic equilibrium, the equality of the

chemical potentials between the Li-H and Y-H systems can be represented by an equality of their temperature- and concentration-dependent equilibrium pressures $p^{\mathrm{Li}}_{\mathrm{H_2}}\left(c^{\mathrm{Li}}, T\right)$ and $p^{\mathrm{Y}}_{\mathrm{H_2}}\left(c^{\mathrm{Y}}, T\right)$. The model assumes that within an infinitesimal layer crossing the Li-Y interface, the chemical potentials in both materials are always at equilibrium. This leads to the definition of the second boundary condition

$$p^{\mathrm{Li}}_{\mathrm{H_2}}\left(c^{\mathrm{Li}}_{\mathrm{int}}, T\right) = p^{\mathrm{Y}}_{\mathrm{H_2}}\left(c^{\mathrm{Y}}_{\mathrm{int}}, T\right) , \tag{7.19}$$

where the variables $c^{\mathrm{Li}}_{\mathrm{int}}$ and $c^{\mathrm{Y}}_{\mathrm{int}}$ refer to the concentrations in the corresponding metal at the Li-Y interface. It should be mentioned that in this model, boundary condition (7.19) refers to the summed concentration $c^{\mathrm{Me}}_{\mathrm{int}} = \sum_i c^{\mathrm{Me}}_{\mathrm{int},i}$ in the respective metals. The concentrations $c^{\mathrm{Y}}_{\mathrm{int},i}$ of the individual hydrogen isotopes in yttrium at the Li-Y interface are here determined through the relation

$$c^{\mathrm{Y}}_{\mathrm{int},i} = \frac{c^{\mathrm{Li}}_{i,\mathrm{trap}}}{c^{\mathrm{Li}}_{\mathrm{trap}}} \cdot c^{\mathrm{Y}}_{\mathrm{int}} . \tag{7.20}$$

Boundary condition (7.19) states that the concentrations $c^{\mathrm{Li}}_{\mathrm{int}}$ and $c^{\mathrm{Y}}_{\mathrm{int}}$ in the two metals at the Li-Y interface are those assigned to the same equilibrium pressure given by the pressure-composition isotherms of the two metal-hydrogen solutions. In section 2.1.2 it is deduced that at very low concentrations the PCIs of a metal-hydrogen system can be approximately described by Sieverts' law (2.50). Consequently, when the concentrations in both metals are low, boundary condition (7.19) reduces to equation (2.51), so that

$$c^{\mathrm{Y}}_{\mathrm{int}} = c^{\mathrm{Li}}_{\mathrm{int}} \cdot \frac{K^{\mathrm{Y}}_{\mathrm{s}}}{K^{\mathrm{Li}}_{\mathrm{s}}} = c^{\mathrm{Li}}_{\mathrm{int}} \cdot K^{\mathrm{Li-Y}}_{\mathrm{D},0} . \tag{7.21}$$

At higher concentrations, the Sieverts' law as well as boundary condition (7.21) are no longer valid. As explained in section 2.1.3, beyond the Sieverts' regime, H-H interaction and the formation of metal hydrides dictate the courses of the PCIs of the Li-H and Y-H systems. Indeed, it turns out that hydride formation has a particularly strong influence on the absorption characteristics of an yttrium getter trap exposed to flowing liquid lithium. In order to find a generalized expression of boundary condition (7.19), the relations which approximately describe the courses of the PCIs of the Li-H and the Y-H systems at higher concentrations are derived in the following.

7.3.1. Construction of pressure-composition isotherms of the Li-H system

In the past, PCIs covering the entire concentration range of the Li-H binary system could be measured for temperatures $973\,\mathrm{K} < T < 1173\,\mathrm{K}$ [119], [264]. However, it is not possible to determine them experimentally in the temperature range relevant for DONES ($473\,\mathrm{K} < T < 673\,\mathrm{K}$), since the equilibrium pressures are too small to be measured.

In the low-concentration liquid α-Li phase, hydrogen is dissolved as a solute. As mentioned above, the PCIs in this regime are described by Sieverts' law (2.50). This

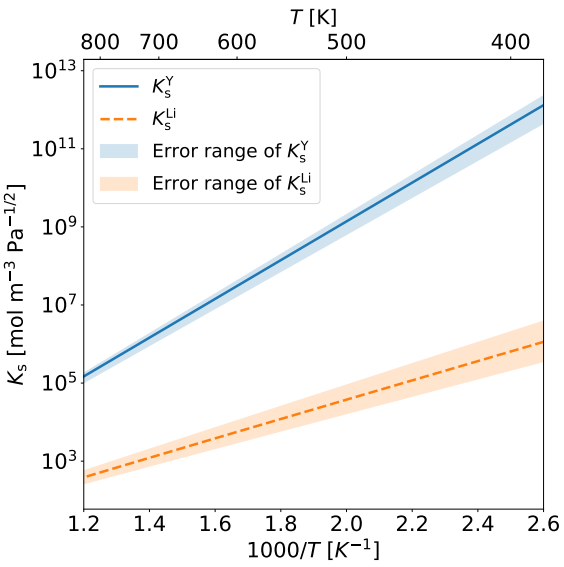

Fig. 7.5. Temperature dependency of the Sieverts' constants of deuterium in the α-Li phase and the α-Y phase together with their defined error ranges obtained from experimental values reported in [119] and [268]. In this model, these relations are considered for all three hydrogen isotopes.

model considers the same Sieverts' constant for all three hydrogen isotopes. Namely, the Sieverts' constant of deuterium in lithium, determined by Smith *et al* [119]

$$K_s^{Li} = \left(9.2 \times 10^{-4} \cdot \rho_{Li}\right) \mathrm{mol/m^3 \cdot Pa^{-\frac{1}{2}}} \cdot \exp\left(\frac{46.9\,\mathrm{kJ\,mol^{-1}}}{RT}\right). \tag{7.22}$$

The Sieverts' constants of the Li-H system have been measured in several experimental campaigns [119], [264]–[267]. They differ within a narrower zone than the range limited by the Sieverts' relations of ^{1}H and ^{3}H measured by Smith *et al.* [119]. Thus, the model considers

$$\Delta^+ K_s^{Li} \approx \left|K_{s,1}^{Li} - K_{s,2}^{Li}\right| \tag{7.23}$$

$$\Delta^- K_s^{Li} \approx \left|K_{s,3}^{Li} - K_{s,2}^{Li}\right| \tag{7.24}$$

as the upper and lower error limits of K_s^{Li}. The Sieverts' relation (7.22) of the Li-H system, together with its defined error range is plotted in figure 7.5. It can be seen that because the enthalpy of solution of hydrogen in lithium satisfies $\Delta\overline{H}_s < 0$, the Sieverts' constant decreases with increasing temperature (see section 2.1.2). This is an indication that lithium is an exothermic hydride-forming hydrogen absorber (see section 2.1.1).

In fact, at elevated hydrogen concentrations a hydride phase, the β-LiH phase, precipitates within the solid solution α-Li phase. As in the example of the Pd-H system discussed in section 2.1.3, the PCIs of the Li-H system exhibit a single plateau [264]. The physical mechanism of hydride formation in a Li-H solution which causes the formation of the flat plateau is described in section 2.1.3. Certainly, it may be possible to theoretically calculate the exact shape of the PCIs of the Li-H system with the equations (2.37), (2.59) and (2.60) as demonstrated for the Pd-H system in section 2.1.3. However, the thermodynamic parameters of the Li-H system required for such a calculation are not sufficiently well measured to allow for an accurate calculation. Therefore, the PCIs of the Li-H system are constructed mathematically based on experimentally confirmed data from the literature.

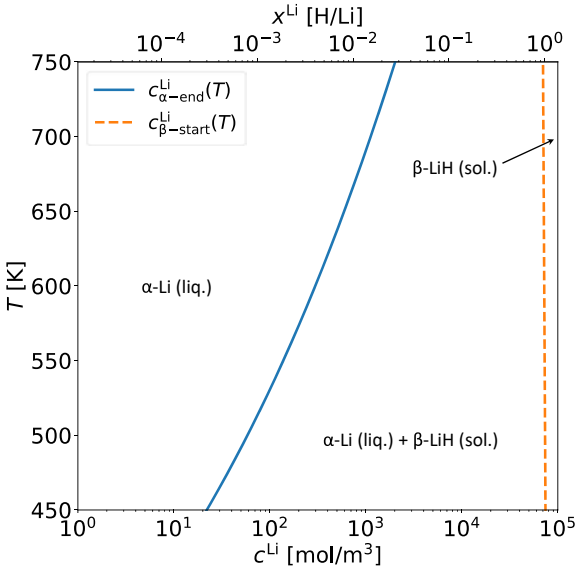

Fig. 7.6. Temperature-concentration phase diagram of the Li-H system as considered in the model [272].

The maximum concentration $c^{\mathrm{Li}}_{\alpha\text{-end}}$ of the pure solid solution α-Li phase could be measured in the experimental campaigns [269]–[271] for ^{1}H and ^{2}H between 523 K and 773 K. Yakimovich *et al* evaluated their data for deuterium dissolved in lithium and derived the expression

$$\ln c^{\mathrm{Li}}_{\alpha\text{-end}} = -1.52 - 1197\left(\frac{1}{T} - \frac{1}{T_{\mathrm{M}}}\right) + 6.83 \ln \frac{T}{T_{\mathrm{M}}}\,, \tag{7.25}$$

with $[\mathrm{mol_H}/(\mathrm{mol_H} + \mathrm{mol_{Li}})]$ as the unit of $c^{\mathrm{Li}}_{\alpha\text{-end}}$ [272]. All other equations in this work consider $[\mathrm{mol\,m^{-3}}]$ as the unit of the concentration. In equation (7.25), $T_{\mathrm{M}} \approx 963$ K is the monotectic temperature of the Li-H system [272]. The reported mean square error of the coefficients in equation (7.25) is 1.9 %. It defines an error range of $c^{\mathrm{Li}}_{\alpha\text{-end}}$. The position of the phase boundary for protium dissolved in lithium given in [272] is located within this error range. Figure 7.6 presents the calculated phase boundary $c^{\mathrm{Li}}_{\alpha\text{-end}}$ plotted in the T-c binary phase diagram of the Li-H system. The corresponding equilibrium pressure $p^{\mathrm{Li}}_{\alpha\text{-end}}$ at the end of the pure α-Li phase is estimated by inserting relation (7.25) into the Sieverts' law (2.50)

$$p^{\mathrm{Li}}_{\alpha\text{-end}} = \left(\frac{c^{\mathrm{Li}}_{\alpha\text{-end}}}{K^{\mathrm{Li}}_{\mathrm{s}}}\right)^2 . \tag{7.26}$$

Thus, this model estimates the height of the $\alpha \rightarrow \beta$ decomposition pressure of the Li-H system (see section 2.1.3). As shown by the example of the Pd-H system in figure 2.4, the decomposition pressure of the Li-H system increases with temperature. At the decomposition pressure, a very small increase in equilibrium pressure implies the precipitation of solid lithium hydride compounds (β-LiH). The decomposition regime where the two hydride phases α-Li (liq.) and β-LiH (sol.) coexist is called the $\alpha \rightarrow \beta$ phase transition of the Li-H system.

As illustrated by figure 2.5, while the concentration in the precipitating solid β-LiH compounds is $c^{\mathrm{Li}}_{\beta\text{-start}}$ the concentration in the coexisting liquid α-Li phase remains at $c^{\mathrm{Li}}_{\alpha\text{-end}}$. Nevertheless, if in this model it is referred to a concentration c^{Me}, what is meant is the

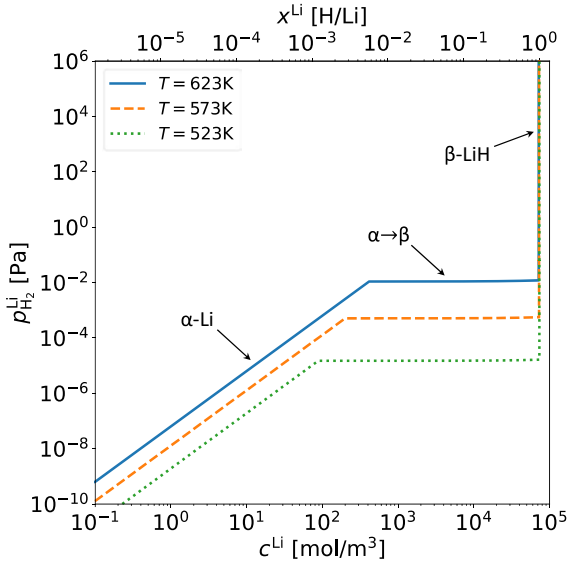

Fig. 7.7. Theoretically approximated pressure-composition isotherms of the Li-H system at three temperatures relevant for the DONES lithium loop.

concentration averaged over the distinct concentrations occurring in coexisting metal-hydrogen phases as expressed by equation (2.52).

Once the entire Li-H solution has transformed to solid β-LiH, the pure β-LiH phase is reached. The concentration in the pure β-LiH phase is here approximated by $c^{\mathrm{Li}}_{\beta\text{-start}} = \rho_{\mathrm{Li}}/M_{\mathrm{Li}}$. In this expression, M_{Li} is the molar mass of lithium. The calculated phase boundary of pure β-LiH is plotted in the phase diagram of figure 7.6. For the model, it is assumed that when passing through the $\alpha \rightarrow \beta$ phase transition the equilibrium pressure increases by about 1 %, such that $p^{\mathrm{Li}}_{\beta\text{-start}} = f^{\alpha\beta}_{\mathrm{Li}} \cdot p^{\mathrm{Li}}_{\alpha\text{-end}}$, with $f^{\alpha\beta}_{\mathrm{Li}} \approx 1.01$. The assumed slight slope of the plateau region is necessary for the model to work and agrees with previously measured PCIs of the Li-H system [119], [264]. In the $\alpha \rightarrow \beta$ phase transition regime as well as in the β-LiH phase, this model describes the PCIs by linear straight lines. For the reproduction of an almost infinite slope of the equilibrium pressure in the β-LiH phase the hypothetical values $p^{\mathrm{Li}}_{\beta\text{-end}} = 10^{10}$Pa and $c^{\mathrm{Li}}_{\beta\text{-end}} = 1.01 \cdot c^{\mathrm{Li}}_{\beta\text{-start}}$ are assumed in the model.

Finally, the complete mathematically constructed relation describing PCIs of the Li-H system can be expressed by

$$p^{\mathrm{Li}}_{\mathrm{H_2}} \approx \begin{cases} \left(c^{\mathrm{Li}}/K^{\mathrm{Li}}_{\mathrm{s}}\right)^2 & \text{if} \quad c^{\mathrm{Li}} < c^{\mathrm{Li}}_{\alpha\text{-end}} \\ s^{\mathrm{Li}}_{\alpha\beta} \cdot \left(c^{\mathrm{Li}} - c^{\mathrm{Li}}_{\alpha\text{-end}}\right) + p^{\mathrm{Li}}_{\alpha\text{-end}} & \text{if} \quad c^{\mathrm{Li}}_{\alpha\text{-end}} \leq c^{\mathrm{Li}} < c^{\mathrm{Li}}_{\beta\text{-start}} \\ s^{\mathrm{Li}}_{\beta\beta} \cdot \left(c^{\mathrm{Li}} - c^{\mathrm{Li}}_{\beta\text{-start}}\right) + p^{\mathrm{Li}}_{\beta\text{-start}} & \text{if} \quad c^{\mathrm{Li}}_{\beta\text{-start}} \leq c^{\mathrm{Li}}, \end{cases} \tag{7.27}$$

where the slopes s^{Li} of the straight lines are defined by

$$s^{\mathrm{Li}}_{\alpha\beta} = \left(p^{\mathrm{Li}}_{\beta\text{-start}} - p^{\mathrm{Li}}_{\alpha\text{-end}}\right) / \left(c^{\mathrm{Li}}_{\beta\text{-start}} - c^{\mathrm{Li}}_{\alpha\text{-end}}\right) \tag{7.28}$$

$$s^{\mathrm{Li}}_{\beta\beta} = \left(p^{\mathrm{Li}}_{\beta\text{-end}} - p^{\mathrm{Li}}_{\beta\text{-start}}\right) / \left(c^{\mathrm{Li}}_{\beta\text{-end}} - c^{\mathrm{Li}}_{\beta\text{-start}}\right). \tag{7.29}$$

Figure 7.7 presents three PCIs of the Li-H system belonging to the temperatures $T = 523$ K, $T = 573$ K and $T = 623$ K. They are plotted using equation (7.27).

7.3.2. Construction of pressure-composition isotherms of the Y-H system

In the relevant temperature range 473 K $< T <$ 673 K, PCIs of the Y-H system could only be measured for equilibrium pressures $p^{\mathrm{Y}}_{\mathrm{H_2}} > 100\,\mathrm{Pa}$ which led to very high equilibrium concentrations [115], [273]. In contrast, the T-c phase diagram of the Y-H system could be experimentally explored in a much greater concentration and temperature range [67], [115], [268], [274], [275]. It reveals the ability of yttrium to absorb up to three hydrogen atoms per yttrium atom. Besides the solid solution α-Y phase, two hydride phases (δ-$YH_{2\pm x}$ and ε-YH_{3-y}) exist for the Y-H system. Consequently, the Y-H system is described by multiplateau PCIs, the physics of which is discussed in the last paragraph of section 2.1.3. In fact, the PCIs of the Y-H system exhibit two phase transition plateaus. The approximate shape of the PCIs of the Y-H system is constructed mathematically using data from the literature, as was done for the Li-H system.

In the low-concentration α-Y phase, hydrogen is interstitially dissolved in yttrium where it occupies tetrahedral sites without changing the HCP lattice structure (see figure 2.2) of the pure metal [136]. To describe the PCIs of the Y-H system in this regime, the model considers the same Sieverts' constant of deuterium in yttrium for each hydrogen isotope. Therefore, it is made use of the experimentally determined Sieverts' relation which was measured by Begun *et al* in a high temperatures measurement [268]

$$K^{\mathrm{Y}}_{\mathrm{s}} = 16.4 \times 10^{-2}\,\mathrm{mol/m^3{\cdot}Pa^{-\frac{1}{2}}} \cdot \exp\left(\frac{95.0\,\mathrm{kJ\,mol^{-1}}}{RT}\right). \tag{7.30}$$

Indeed, the Sieverts' relation of the Y-H system was measured in several experimental campaigns in the past [268], [273], [276]. However, since Begun's experimental results are in agreement with a low-temperature measurement of the Sieverts' constant performed for the Y-^{3}H system by Clinton *et al* [276], equation (7.30) should be valid in a wider temperature range of 523 K - 1273 K. Like for the Li-H system, it is found that the difference between the Sieverts' relations measured for different hydrogen isotopes by Begun *et al* is greater than the disagreement among the Sieverts' relations measured in different experimental campaigns. Therefore, the upper and lower error limits of the Sieverts' constant are estimated by.

$$\Delta^{+}K^{\mathrm{Y}}_{\mathrm{s}} \approx \left|K^{\mathrm{Y}}_{\mathrm{s},1} - K^{\mathrm{Y}}_{\mathrm{s},2}\right| \tag{7.31}$$

$$\Delta^{-}K^{\mathrm{Y}}_{\mathrm{s}} \approx \left|K^{\mathrm{Y}}_{\mathrm{s},3} - K^{\mathrm{Y}}_{\mathrm{s},2}\right|. \tag{7.32}$$

Relation (7.30) and the defined error range is plotted in figure 7.5. Like for the Li-H system, the enthalpy of solution of the Y-H system satisfies $\Delta\overline{H}_{\mathrm{s}} < 0$. Therefore, the Sieverts' constant decreases with increasing temperature, which is characteristic of an exothermic hydrogen-absorbing hydride-forming metal.

Figure 7.5 reveals that the Sieverts' constant of hydrogen in yttrium is several orders of magnitude higher than of hydrogen in lithium. This implies that the affinity of yttrium to absorb hydrogen isotopes is much higher than that of lithium.

TABLE 7.1

FITTING COEFFICIENTS OF THE POLYNOMIAL $c^{\mathrm{Y}}(T) = a_1 \cdot T^5 + a_2 \cdot T^4 + a_3 \cdot T^3 + a_4 \cdot T^2 + a_5 \cdot T + a_6$ WHICH IS USED TO DESCRIBE THE TEMPERATURE-DEPENDENT CONCENTRATIONS $c^{\mathrm{Y}}_{\alpha\text{-end}}$, $c^{\mathrm{Y}}_{\delta\text{-start}}$, $c^{\mathrm{Y}}_{\delta\text{-end}}$ AND $c^{\mathrm{Y}}_{\varepsilon\text{-start}}$ THAT MARK THE PHASE BOUNDARIES IN THE T-c DIAGRAM OF THE Y-H SYSTEM.

$\left[\frac{\mathrm{mol}}{\mathrm{m}^3}\right]$	$a_1 \left[\frac{\mathrm{mol}}{\mathrm{m}^3\mathrm{K}^5}\right]$	$a_2 \left[\frac{\mathrm{mol}}{\mathrm{m}^3\mathrm{K}^4}\right]$	$a_3 \left[\frac{\mathrm{mol}}{\mathrm{m}^3\mathrm{K}^3}\right]$	$a_4 \left[\frac{\mathrm{mol}}{\mathrm{m}^3\mathrm{K}^2}\right]$	$a_5 \left[\frac{\mathrm{mol}}{\mathrm{m}^3\mathrm{K}}\right]$	$a_6 \left[\frac{\mathrm{mol}}{\mathrm{m}^3}\right]$
$c^{\mathrm{Y}}_{\alpha\text{-end}}$	1.4×10^{-11}	-6.3×10^{-8}	1.0×10^{-4}	-7.2×10^{-2}	4.0×10^{1}	6.6×10^{3}
$c^{\mathrm{Y}}_{\delta\text{-start}}$	1.0×10^{-10}	-5.6×10^{-7}	1.2×10^{-3}	-1.1	3.8×10^{2}	5.6×10^{4}
$c^{\mathrm{Y}}_{\delta\text{-end}}$	4.4×10^{-12}	-2.2×10^{-8}	4.2×10^{-5}	-3.8×10^{-2}	1.6×10^{1}	9.8×10^{4}
$c^{\mathrm{Y}}_{\varepsilon\text{-start}}$	4.6×10^{-11}	-2.1×10^{-7}	3.5×10^{-4}	-2.4×10^{-1}	5.3×10^{1}	1.4×10^{5}

Peng *et al* performed a thermodynamic study in which the entire T-c phase diagram of the Y-H system was theoretically calculated [116]. Their calculation is based on an improved thermodynamic description compared to the previously determined phase diagram by Fu *et al* [115]. For this reason, it is chosen to use Peng's theoretical results as the basis for the mathematical reconstruction of the PCIs in this model. The temperature-dependent concentration $c^{\mathrm{Y}}_{\alpha\text{-end}}$ which marks the end of the pure α-Y phase is determined by fitting the fifth order polynomial

$$c(T) = a_1 \cdot T^5 + a_2 \cdot T^4 + a_3 \cdot T^3 + a_4 \cdot T^2 + a_5 \cdot T + a_6 \tag{7.33}$$

against the theoretically calculated phase boundary. Table 7.1 presents the obtained fitting coefficients. The phase boundary $c^{\mathrm{Y}}_{\alpha\text{-end}}$ which is calculated in the fitting procedure is plotted in the Y-H phase diagram in figure 7.8. By comparing the obtained expression for $c^{\mathrm{Y}}_{\alpha\text{-end}}$ with a relation derived by Beaudry *et al*, it is estimated that in the range $473\,\mathrm{K} < T < 673\,\mathrm{K}$ the uncertainty of the determined expression for $c^{\mathrm{Y}}_{\alpha\text{-end}}$ is approximately [274]

$$\Delta c^{\mathrm{Y}}_{\alpha\text{-end}} \approx 2 \times 10^{3}\,\mathrm{mol/m^3}\,. \tag{7.34}$$

The corresponding decomposition plateau pressure at the end of the pure α-Y phase is determined by inserting the obtained relation $c^{\mathrm{Y}}_{\alpha\text{-end}}$ into the Sieverts' law (2.50), such that

$$p^{\mathrm{Y}}_{\alpha\text{-end}} = \left(\frac{c^{\mathrm{Y}}_{\alpha\text{-end}}}{K^{\mathrm{Y}}_{\mathrm{s}}}\right)^2 . \tag{7.35}$$

In the $\alpha \rightarrow \delta$ phase transition regime, yttrium dihydride (YH_2) precipitates within the lattice. This goes along with a change of the HCP crystal structure into an FCC structure (see figure 2.2) in which all tetrahedral sites are occupied by hydrogen isotopes [136].

When most of the lattice has transformed to yttrium dihydride, the solution enters the δ-$YH_{2\pm x}$ phase. The increase in equilibrium pressure during the $\alpha \rightarrow \delta$ phase transition is estimated from measured PCIs by Fu *et al* to be roughly 10 %, such that

$$p^{\mathrm{Y}}_{\delta\text{-start}} = f^{\alpha\delta}_{\mathrm{Y}} \cdot p^{\mathrm{Y}}_{\alpha\text{-end}}\,, \quad \text{with} \quad f^{\alpha\delta}_{\mathrm{Y}} \approx 1.1 \pm 0.1\,. \tag{7.36}$$

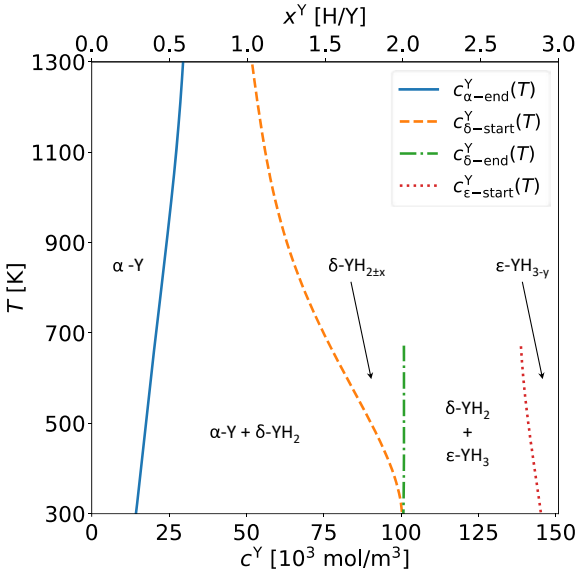

Fig. 7.8. Temperature-concentration phase diagram of the Y-H system determined by fitting against theoretically calculated phase boundaries in [116].

Using equation (7.35), the error of $p^{\mathrm{Y}}_{\delta\text{-start}}$ yields

$$\Delta^{\pm} p^{\mathrm{Y}}_{\delta\text{-start}} = p^{\mathrm{Y}}_{\delta\text{-start}} \cdot \sqrt{\left(2\frac{\Delta^{\pm} K^{\mathrm{Y}}_{\mathrm{s}}}{K^{\mathrm{Y}}_{\mathrm{s}}}\right)^2 + \left(2\frac{\Delta c^{\mathrm{Y}}_{\alpha\text{-end}}}{c^{\mathrm{Y}}_{\alpha\text{-end}}}\right)^2 + \left(\frac{\Delta f^{\alpha\delta}_{\mathrm{Y}}}{f^{\alpha\delta}_{\mathrm{Y}}}\right)^2}\,. \tag{7.37}$$

Fitting the polynomial (7.33) against the lower phase boundary of the δ-YH$_{2\pm x}$ phase, which was theoretically calculated in [116], enables defining a relation for $c^{\mathrm{Y}}_{\delta\text{-start}}$. It is plotted in figure 7.8 using the corresponding fitting parameters listed in table 7.1.

In the δ-YH$_{2\pm x}$ phase, further hydrogen isotopes occupy octahedral sites of the FCC structure, which demands a relatively large amount of energy. Here, significantly rising the concentration in the bulk requires increasing the equilibrium pressure by several orders of magnitude. At some point, a second plateau area is reached, which is characterized by the precipitation of HCP yttrium trihydride (YH$_3$). A relation for the height of the $\delta \rightarrow \varepsilon$ decomposition pressure $p^{\mathrm{Y}}_{\delta\text{-end}}$ is estimated by applying a linear regression against the corresponding Van't Hoff plot which was measured by Peng *et al* [116] in the relevant temperature range.

$$p^{\mathrm{Y}}_{\delta\text{-end}} \approx 1.45 \times 10^{11}\,\mathrm{Pa} \cdot \exp\left(-\frac{76.14\,\mathrm{kJ\,mol^{-1}}}{RT}\right). \tag{7.38}$$

The physical background on the meaning of Van't Hoff plots is given in section 2.1.3. By comparing relation (7.38) with the Van't Hoff relation which yields from a fit to the equilibrium pressures $p^{\mathrm{Y}}_{\delta\text{-end}}$ measured by Fu *et al* a relative uncertainty of $\Delta p^{\mathrm{Y}}_{\delta\text{-end}} \approx 0.6 \cdot p^{\mathrm{Y}}_{\delta\text{-end}}$ is determined.

Based on experimental data by Fu *et al* [115], the equilibrium pressure assigned to the end of the $\delta \rightarrow \varepsilon$ transition regime and beginning of the δ-YH$_{2\pm x}$ phase is here approximated by $p^{\mathrm{Y}}_{\varepsilon\text{-start}} \approx f^{\delta\varepsilon}_{\mathrm{Y}} \cdot p^{\mathrm{Y}}_{\delta\text{-end}}$, with $f^{\delta\varepsilon}_{\mathrm{Y}} \approx 1.1$. The obtained fitting coefficients, which provide the concentrations $c^{\mathrm{Y}}_{\delta\text{-end}}$ and $c^{\mathrm{Y}}_{\varepsilon\text{-start}}$, are shown in table 7.1. From the observed discrepancies between the phase diagrams calculated by Peng *et al* and Fu *et al*, it

is estimated that the errors of the calculated phase boundaries are approximately

$$\Delta c^{\mathrm{Y}}_{\delta\text{-start}} \approx 7 \times 10^3\,\mathrm{mol/m^3} \tag{7.39}$$

$$\Delta c^{\mathrm{Y}}_{\delta\text{-end}} \approx 2 \times 10^3\,\mathrm{mol/m^3} \tag{7.40}$$

$$\Delta c^{\mathrm{Y}}_{\varepsilon\text{-start}} \approx 5 \times 10^3\,\mathrm{mol/m^3}\,. \tag{7.41}$$

In this model, the courses of the PCIs in the $\alpha \rightarrow \delta$ and $\delta \rightarrow \varepsilon$ phase transition regimes as well as in the δ-$YH_{2\pm x}$ and ε-YH_{3-y} phases are described by linear straight lines linking the defined characteristic points $p^{\mathrm{Y}}_{\mathrm{H_2}}(c^{\mathrm{Y}})$. They mark the start and end points of the different hydride phases. This leads to the following definition of the PCIs of the Y-H system

$$p^{\mathrm{Y}}_{\mathrm{H_2}} \approx \begin{cases} \left(c^{\mathrm{Y}}/K^{\mathrm{Y}}_{\mathrm{s}}\right)^2 & \text{if} \quad c^{\mathrm{Y}} < c^{\mathrm{Y}}_{\alpha\text{-end}} \\ s^{\mathrm{Y}}_{\alpha\delta} \cdot \left(c^{\mathrm{Y}} - c^{\mathrm{Y}}_{\alpha\text{-end}}\right) + p^{\mathrm{Y}}_{\alpha\text{-end}} & \text{if} \quad c^{\mathrm{Y}}_{\alpha\text{-end}} \leq c^{\mathrm{Y}} < c^{\mathrm{Y}}_{\delta\text{-start}} \\ s^{\mathrm{Y}}_{\delta\delta} \cdot \left(c^{\mathrm{Y}} - c^{\mathrm{Y}}_{\delta\text{-start}}\right) + p^{\mathrm{Y}}_{\delta\text{-start}} & \text{if} \quad c^{\mathrm{Y}}_{\delta\text{-start}} \leq c^{\mathrm{Y}} < c^{\mathrm{Y}}_{\delta\text{-end}} \\ s^{\mathrm{Y}}_{\delta\varepsilon} \cdot \left(c^{\mathrm{Y}} - c^{\mathrm{Y}}_{\delta\text{-end}}\right) + p^{\mathrm{Y}}_{\delta\text{-end}} & \text{if} \quad c^{\mathrm{Y}}_{\delta\text{-end}} \leq c^{\mathrm{Y}} < c^{\mathrm{Y}}_{\varepsilon\text{-start}} \\ s^{\mathrm{Y}}_{\varepsilon\epsilon} \cdot \left(c^{\mathrm{Y}} - c^{\mathrm{Y}}_{\varepsilon\text{-start}}\right) + p^{\mathrm{Y}}_{\varepsilon\text{-start}} & \text{if} \quad c^{\mathrm{Y}}_{\varepsilon\text{-start}} \leq c^{\mathrm{Y}}\,, \end{cases} \tag{7.42}$$

where the slopes s^{Y} are defined by

$$s^{\mathrm{Y}}_{\alpha\delta} = \left(p^{\mathrm{Y}}_{\delta\text{-start}} - p^{\mathrm{Y}}_{\alpha\text{-end}}\right) / \left(c^{\mathrm{Y}}_{\delta\text{-start}} - c^{\mathrm{Y}}_{\alpha\text{-end}}\right) \tag{7.43}$$

$$s^{\mathrm{Y}}_{\delta\delta} = \left(p^{\mathrm{Y}}_{\delta\text{-end}} - p^{\mathrm{Y}}_{\delta\text{-start}}\right) / \left(c^{\mathrm{Y}}_{\delta\text{-end}} - c^{\mathrm{Y}}_{\delta\text{-start}}\right) \tag{7.44}$$

$$s^{\mathrm{Y}}_{\delta\varepsilon} = \left(p^{\mathrm{Y}}_{\varepsilon\text{-start}} - p^{\mathrm{Y}}_{\delta\text{-end}}\right) / \left(c^{\mathrm{Y}}_{\varepsilon\text{-start}} - c^{\mathrm{Y}}_{\delta\text{-end}}\right) \tag{7.45}$$

$$s^{\mathrm{Y}}_{\varepsilon\epsilon} = \left(p^{\mathrm{Y}}_{\varepsilon\text{-end}} - p^{\mathrm{Y}}_{\varepsilon\text{-start}}\right) / \left(c^{\mathrm{Y}}_{\varepsilon\text{-end}} - c^{\mathrm{Y}}_{\varepsilon\text{-start}}\right)\,. \tag{7.46}$$

The maximum theoretically achievable concentration in the Y-H system is considered to be $c^{\mathrm{Y}}_{\varepsilon\text{-end}} \approx 3 \cdot \delta_{\mathrm{Y}}/M_{\mathrm{Y}}$. To reproduce an almost infinite pressure increase in the ε-YH_{3-y} phase, the model assumes a hypothetical equilibrium pressure of $p^{\mathrm{Y}}_{\varepsilon\text{-end}} \approx 10^{10}$Pa. The left-hand plot in figure 7.9 shows the fully assembled PCIs of the Y-H system for $T = 523\,\mathrm{K}$, $T = 573\,\mathrm{K}$ and $T = 623\,\mathrm{K}$ as mathematically defined by relation (7.42).

Finally, a generalized expression of boundary condition (7.19) is numerically determined after inserting the relations (7.27) and (7.42) into equation (7.19). The result is plotted in the right-hand graph in figure 7.9. It reveals the value of $c^{\mathrm{Y}}_{\mathrm{int}}$ which occurs at the pebble surface at a given value of $c^{\mathrm{Li}}_{\mathrm{int}}$. In addition, the visualized boundary condition indicates the homogeneous equilibrium concentration that would occur inside the yttrium pebbles $c^{\mathrm{Y}}_{\mathrm{eq}}$ once a certain constant equilibrium concentration $c^{\mathrm{Li}}_{\mathrm{eq}}$ in the lithium is established at thermodynamic equilibrium.

7.4. Yttrium hydride formation in lithium

The right-hand plot in figure 7.9 reveals that up to a certain temperature-dependent critical concentration c^{Li}_{-} the adjusting interface concentration $c^{\mathrm{Y}}_{\mathrm{int}}$ is determined by equation

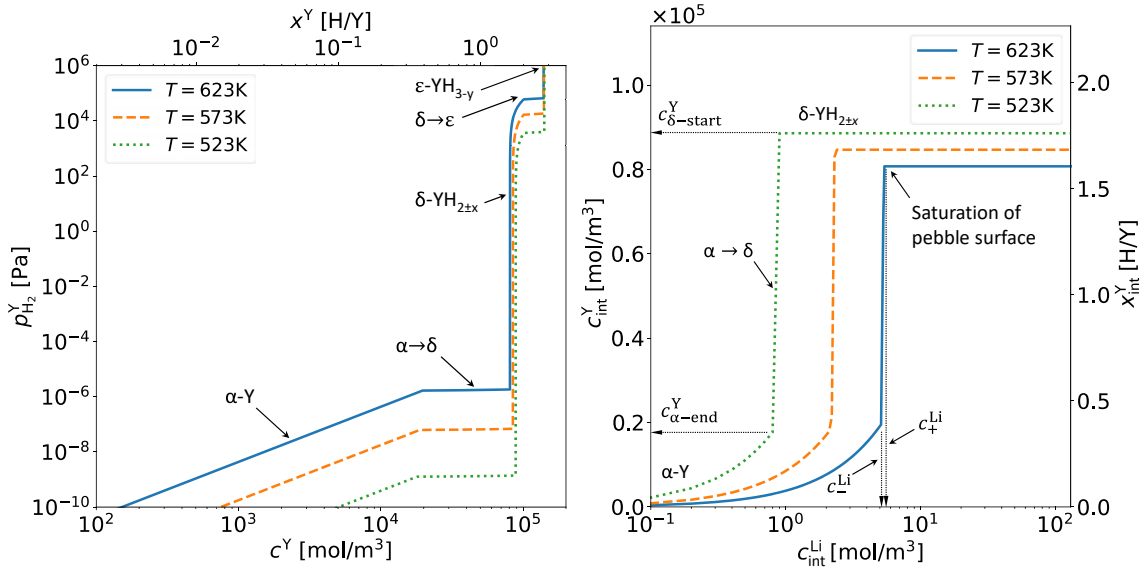

Fig. 7.9. [Left] Theoretically approximated pressure-composition isotherms of the Y-H system at three temperatures relevant for the DONES lithium loop. [Right] Visualization of the numerically calculated concentration boundary condition (7.19). It indicates the hydrogen concentration in yttrium which occurs at the pebble surface at a certain interface concentration in the lithium. Moreover, it depicts the concentration which adjusts in the yttrium pebbles at a certain concentration in the lithium once thermodynamic equilibrium is reached.

(7.21). At a Li-Y interface concentration in lithium of $c^{Li}_{int} > c^{Li}_-$ the concentration at the pebble surface in yttrium satisfies $c^Y_{int} > c^Y_{α\text{-end}}$ and yttrium dihydride formation is triggered. Since $c^{Li}_- < c^{Li}_{α\text{-end}}$ the critical concentration can be calculated by inserting $c^{Li}_{α\text{-end}}$ into equation (7.21)

$$c^{Li}_- = \frac{K^{Li}_s}{K^Y_s} \cdot c^Y_{α\text{-end}} \,. \tag{7.47}$$

Its upper and lower error limits $\Delta^+ c^{Li}_-$ and $\Delta^- c^{Li}_-$ are determined by error propagation

$$\Delta^\pm c^{Li}_- = c^{Li}_- \cdot \sqrt{\left(\frac{\Delta^\pm K^{Li}_s}{K^{Li}_s}\right)^2 + \left(\frac{\Delta^\pm K^Y_s}{K^Y_s}\right)^2 + \left(\frac{\Delta c^Y_{α\text{-end}}}{c^Y_{α\text{-end}}}\right)^2} \tag{7.48}$$

using the errors estimated in the equations (7.23), (7.24), (7.31), (7.32) and (7.34). The right-hand plot in figure 7.9 reveals that yttrium dihydride formation goes hand in hand with a strong increase in hydrogen content at the pebble surface from $c^Y_{int} = c^Y_{α\text{-end}}$ to $c^Y_{int} = c^Y_{δ\text{-start}}$. At the same time, the concentration c^{Li}_{int} increases by only a very small value. The slightly higher concentration that occurs in lithium at the Li-Y interface once the surface region of the yttrium pebbles has fully reached the $δ$-YH$_{2±x}$ phase, is denoted by c^{Li}_+. Since $c^{Li}_+ < c^{Li}_{α\text{-end}}$, it can be calculated by inserting $p^Y_{δ\text{-start}}$ into the Sieverts' law (2.50)

$$c^{Li}_+ = K^{Li}_s \cdot \sqrt{p^Y_{δ\text{-start}}} \,. \tag{7.49}$$

Its error range is given by

$$\Delta^\pm c^{Li}_+ = c^{Li}_+ \cdot \sqrt{\left(\frac{\Delta^\pm K^{Li}_s}{K^{Li}_s}\right)^2 + \left(\frac{1}{2}\frac{\Delta^\pm p^Y_{δ\text{-start}}}{p^Y_{δ\text{-start}}}\right)^2} \,, \tag{7.50}$$

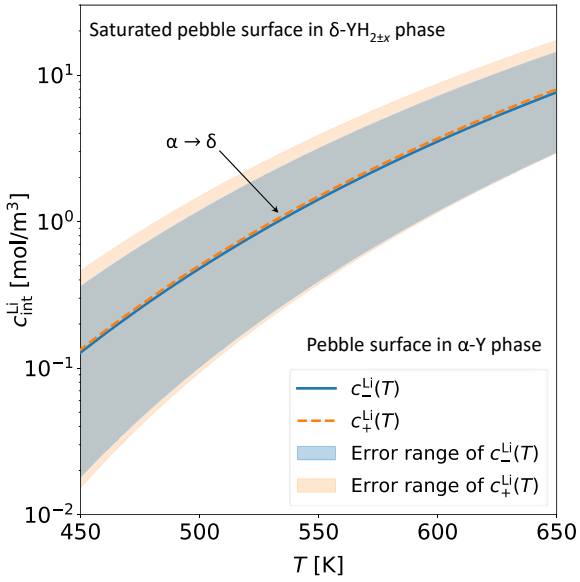

Fig. 7.10. Concentration range in lithium at the Li-Y interface where YH_2 is formed on the pebble surface. Above this concentration range, the pebble surface is in the δ-$YH_{2\pm x}$ phase and below this concentration, it occurs in the α-Y phase.

where $\Delta^{\pm} p^{Y}_{\delta\text{-start}}$ is determined through relation (7.37). In figure 7.10, the calculated critical concentrations c_{-}^{Li} and c_{+}^{Li} are plotted against temperature together with their error ranges.

The right-hand graph in figure 7.9 discloses that at $c_{int}^{Li} > c_{+}^{Li}$, further increasing the concentration in the lithium leads to an almost negligible rise in pebble surface concentration c_{int}^{Y}. This can be attributed to the steep increase of the PCIs in the δ-$YH_{2\pm x}$ phase. By observing figure 7.7 and the left-hand plot in figure 7.9, it is found that in the DONES-relevant temperature range the equilibrium pressure $p_{Li}^{\beta\text{-start}}$, at which a Li-H solution would fully transform to solid β-LiH, is not high enough to trigger a formation of YH_3. For this reason, the formation of YH_3 surrounded by hydrogen-loaded lithium is not possible. In fact, even at a concentration in the lithium of $c_{Li}^{\beta\text{-start}}$, the establishing concentration in the yttrium would remain at a value of approximately $c_{\delta\text{-start}}^{Y}$. Hence, the concentration $c_{\delta\text{-start}}^{Y}$ can be considered as the approximate saturation concentration of hydrogen in lithium-exposed yttrium at DONES-relevant temperatures.

The ratio between the concentrations that adjust in the yttrium pebbles in the lithium at thermodynamic equilibrium is called the general distribution coefficient of the Li-Y-H system K_{D}^{Li-Y}. In contrast to the low-concentration distribution coefficient $K_{D,0}^{Li-Y}$ defined in equation (2.51), the general distribution coefficient is defined for all concentrations. It is evident that the higher the general distribution coefficient, the higher the hydrogen gettering capacity of the yttrium getter at a certain equilibrium concentration in the lithium. The gettering capacity refers to the total amount of hydrogen isotopes the getter bed can absorb at a specific concentration in the lithium. Since the infinitesimal space crossing the Li-Y interfaces of a pebble is assumed to be always at equilibrium, during thermodynamic non-equilibrium the general distribution coefficient writes

$$K_{D}^{Li-Y} \equiv \frac{c_{int}^{Y}}{c_{int}^{Li}} . \tag{7.51}$$

The left-hand plot in figure 7.11 presents the temperature-dependent general distribution coefficient of the Li-Y-H system as a function of c_{int}^{Li} for different temperatures. It is cal-

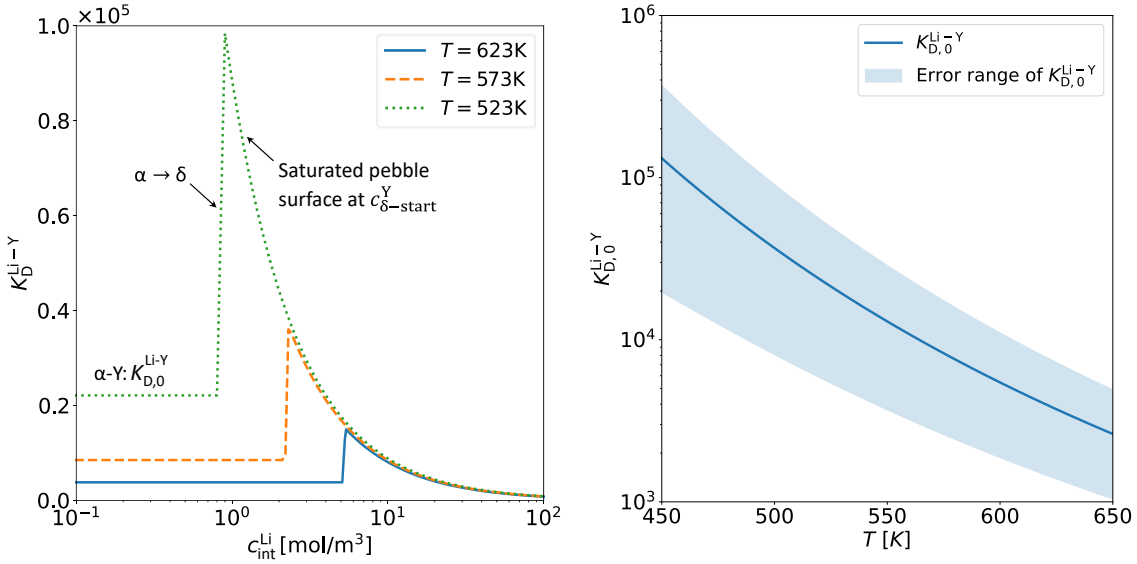

Fig. 7.11. [Left] General distribution coefficient of the Li-Y-H system as a function of the concentration in lithium calculated from the numerically derived concentration boundary condition (7.19) depicted in the right-hand plot in figure 7.9. [Right] Low-concentration distribution coefficient of the Li-Y-H system as a function of the temperature.

culated from the numerically obtained boundary condition (7.19) shown in the right-hand graph in figure 7.9. As the plot reveals, in the Sieverts' regime of the low-concentration α-Y phase the general distribution coefficient takes the constant value $K^{\mathrm{Li-Y}}_{\mathrm{D},0}$ of the low-concentration distribution coefficient. Inserting the low-concentration boundary condition (7.21) into equation (7.51) yields $K^{\mathrm{Li-Y}}_{\mathrm{D},0} = K^{\mathrm{Y}}_{\mathrm{s}}/K^{\mathrm{Li}}_{\mathrm{s}}$ which is conform with equation (2.51). Consequently, with the equations (7.22) and (7.30) it follows that

$$K^{\mathrm{Li-Y}}_{\mathrm{D},0} = \frac{K^{\mathrm{Y}}_{\mathrm{s}}}{K^{\mathrm{Li}}_{\mathrm{s}}} = \frac{1}{\rho_{\mathrm{Li}}} \cdot 1.76 \times 10^{2}\,\mathrm{kg\,m^{-3}} \cdot \exp\left(\frac{48.1\,\mathrm{kJ\,mol^{-1}}}{RT}\right). \tag{7.52}$$

The error of this low-concentration distribution coefficient is calculated by error propagation

$$\Delta^{\pm} K^{\mathrm{Li-Y}}_{\mathrm{D},0} = K^{\mathrm{Li-Y}}_{\mathrm{D},0} \cdot \sqrt{\left(\frac{\Delta^{\pm} K^{\mathrm{Li}}_{\mathrm{s}}}{K^{\mathrm{Li}}_{\mathrm{s}}}\right)^{2} + \left(\frac{\Delta^{\pm} K^{\mathrm{Y}}_{\mathrm{s}}}{K^{\mathrm{Y}}_{\mathrm{s}}}\right)^{2}} \tag{7.53}$$

using the estimated errors (7.23), (7.24), (7.31) and (7.32). It is plotted in the right-hand plot in figure 7.11 together with its error range. Combining equation (7.52) and equation (7.47) yields that the critical concentration in lithium above which hydride formation occurs is related to the low-concentration distribution coefficient according to

$$c^{\mathrm{Li}}_{-} = \frac{c^{\mathrm{Y}}_{\alpha\text{-end}}}{K^{\mathrm{Li-Y}}_{\mathrm{D},0}} \cdot \tag{7.54}$$

Moreover, from the equations (7.48) and (7.53) it is found that the relatively large error range of c^{Li}_{-} yields mainly from the wide error range of the distribution coefficient.

In the concentration range $c^{\mathrm{Li}}_{-} < c^{\mathrm{Li}}_{\mathrm{int}} < c^{\mathrm{Li}}_{+}$, where yttrium dihydride formation occurs, the general distribution coefficient $K^{\mathrm{Li-Y}}_{\mathrm{D}}$ experiences a sharp increase (see left-hand plot

in figure 7.11). Its highest value is reached at the start of the δ-$YH_{2\pm x}$ phase. At concentrations $c_{\mathrm{int}}^{\mathrm{Li}} > c_{+}^{\mathrm{Li}}$ it decreases with increasing $c_{\mathrm{int}}^{\mathrm{Li}}$. Above a certain value of $c_{\mathrm{int}}^{\mathrm{Li}}$ the general distribution coefficient even decreases below its constant value in the α-Y phase $K_{\mathrm{D},0}^{\mathrm{Li-Y}}$. It can therefore be concluded, that in the concentration range $c_{\mathrm{int}}^{\mathrm{Li}} > c_{-}^{\mathrm{Li}}$ where $K_{\mathrm{D}}^{\mathrm{Li-Y}} > K_{\mathrm{D},0}^{\mathrm{Li-Y}}$ the hydrogen gettering capacity of yttrium in lithium is particularly large.

7.5. Determination of the hydrogen diffusivity in yttrium hydride phases

A physical quantity which, according to equation (7.14), strongly determines the retention flux of hydrogen isotopes into the yttrium pebbles, is the diffusion coefficient of hydrogen in yttrium.

As mentioned above, previous experimental studies have shown that the diffusion coefficient in yttrium is dependent on the hydrogen content [68], [277]. This can be attributed to the fact that the driving force for chemical diffusion of hydrogen in metals arises from the gradient of the chemical potential which is expressed by the generalized Fick's first law (2.67). Equation (2.67) allows writing a general expression for the temperature- and concentration-dependent chemical diffusion coefficient of hydrogen in yttrium

$$\overline{D}^{\mathrm{Y}}(c^{\mathrm{Y}}, T) \equiv \frac{D^{\mathrm{Y}} c^{\mathrm{Y}}}{RT} \frac{\partial \mu_{\mathrm{H}}^{\mathrm{Y}}}{\partial c^{\mathrm{Y}}} \,. \tag{7.55}$$

The chemical potential $\mu_{\mathrm{H}}^{\mathrm{Y}}$ of atomic hydrogen at a given position in the yttrium pebble where a certain concentration c^{Y} occurs can be obtained by expressing $\mu_{\mathrm{H}}^{\mathrm{Y}}$ in terms of the corresponding chemical potential of a diatomic H_2 gas that would adjust at thermodynamic equilibrium with the corresponding H-Y solution of concentration c^{Y}. Therefore, equation (2.23) is inserted into equation (2.12) and the equilibrium pressure is replaced by the derived temperature-dependent pressure-composition isotherm $p_{\mathrm{H_2}}^{\mathrm{Y}}(c^{\mathrm{Y}}, T)$, which is expressed by equation (7.42)

$$\mu_{\mathrm{H}}^{\mathrm{Y}} = \frac{1}{2}\mu_{\mathrm{H_2}}^{\circ} + \frac{RT}{2} \ln\left[\frac{p_{\mathrm{H_2}}^{\mathrm{Y}}(c^{\mathrm{Y}}, T)}{p^{\circ}}\right] . \tag{7.56}$$

In this equation, the chemical potential is expressed with the unit [J mol^{-1}]. Consequently, the derivative in equation (7.55) writes

$$\frac{\partial \mu_{\mathrm{H}}^{\mathrm{Y}}}{\partial c^{\mathrm{Y}}} = \frac{RT}{2 p_{\mathrm{H_2}}^{\mathrm{Y}}(c^{\mathrm{Y}}, T)} \frac{\partial p_{\mathrm{H_2}}^{\mathrm{Y}}(c^{\mathrm{Y}}, T)}{\partial c^{\mathrm{Y}}} \,. \tag{7.57}$$

As shown in section 2.1.2, in the low-concentration α phase of a metal-hydrogen solution where the Sievers' constant is assumed to be valid the chemical diffusion coefficient equals the intrinsic diffusion coefficient $\overline{D}^{\mathrm{Y}} = D^{\mathrm{Y}}$, which is concentration-independent.

For the value of the concentration-independent intrinsic diffusion coefficient D^{Y}, this model considers the same diffusion relation of deuterium in yttrium for all three hydrogen

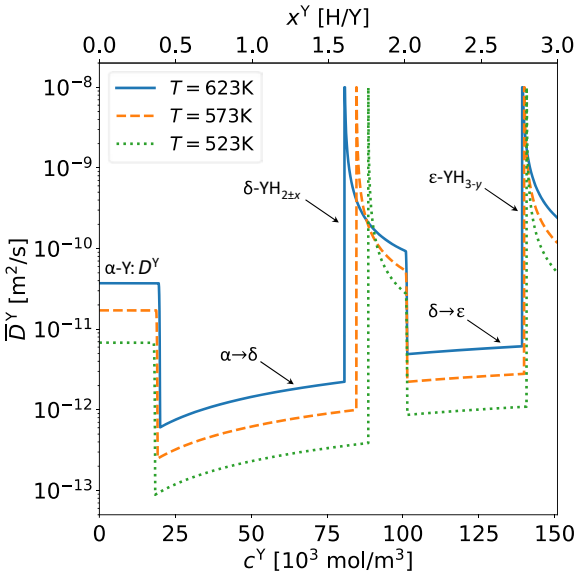

Fig. 7.12. Theoretically derived concentration-dependent diffusion relation of hydrogen in yttrium calculated using the equations (7.59) and (7.42).

isotopes. It is determined from the protium diffusivity relation reported by Buxbaum *et al* in [154] by making use of the isotope effect of diffusion (2.66).

$$D^{\mathrm{Y}} = 2.7 \times 10^{-7}\,\mathrm{m^2\,s^{-1}} \cdot \exp\left(\frac{-46.0\,\mathrm{kJ\,mol^{-1}}}{RT}\right). \tag{7.58}$$

The diffusion relation given by Buxbaum *et al* is chosen for this model since it is valid in a temperature range of $673\,\mathrm{K} < T < 1373\,\mathrm{K}$ that is closest to the temperature range relevant for DONES. All other measured relations that are available in the literature have been measured at significantly higher temperatures [278], [279]. Relation (7.58) is plotted against the temperature in figure 7.3. It is clearly visible that hydrogen diffusion in yttrium is several orders of magnitude slower than in lithium.

Finally, substituting the equations (7.57) into equation (7.55) provides a relation for the concentration-dependent chemical diffusion coefficient of hydrogen in yttrium.

$$\overline{D}^{\mathrm{Y}}(c^{\mathrm{Y}}, T) = D^{\mathrm{Y}}(T) \cdot \frac{c^{\mathrm{Y}}}{2p^{\mathrm{Y}}_{\mathrm{H_2}}(c^{\mathrm{Y}}, T)} \frac{\partial p^{\mathrm{Y}}_{\mathrm{H_2}}(c^{\mathrm{Y}}, T)}{\partial c^{\mathrm{Y}}}. \tag{7.59}$$

In this description, the derivative of the equilibrium pressure $p^{\mathrm{Y}}_{\mathrm{H_2}}(c^{\mathrm{Y}}, T)$ which is described by relation (7.42) equals the phase-specific slopes given by the equations (7.43), (7.44), (7.45) and (7.46).

Figure 7.12 shows the calculated concentration-dependent diffusion coefficient in yttrium for three different temperatures. It can be seen that at concentrations corresponding to the phase transitions the diffusivity plunges. When entering a new phase, it abruptly rises by several orders of magnitude above the constant intrinsic diffusivity D^{Y} of the α-Y phase.

For the finite element description of the yttrium pebbles in this model, the derived relation for $\overline{D}^{\mathrm{Y}}(c^{\mathrm{Y}}, T)$ is inserted into equation (7.16), where $\overline{D}^{\mathrm{Y}}(r_q, y_m, t) = \overline{D}^{\mathrm{Y}}[c^{\mathrm{Y}}(r_q, y_m, t)]$. It is important to emphasize that the concentration $c^{\mathrm{Y}}(r_q, y_m, t)$, which is used to calculate

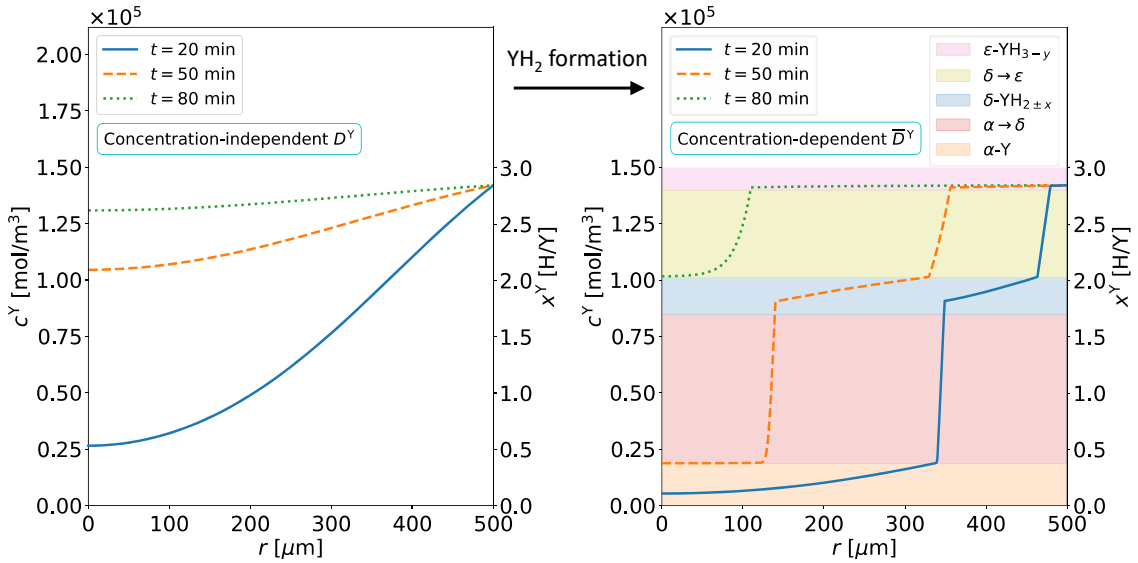

Fig. 7.13. Simulated temporal evolution of the concentration profile inside of an yttrium pebble at $T = 573\,\mathrm{K}$ if its surface is maintained at a constant concentration of $c_{\mathrm{int}}^{\mathrm{Y}} > c_{\mathrm{Y}}^{\varepsilon\text{-start}}$. [Left] The first simulation assumes a concentration-independent diffusion coefficient $\overline{D}^{\mathrm{Y}} = D^{\mathrm{Y}}$ as it would yield from the model if hydride formation was not taken into account. [Right] The second simulation considers the derived concentration-dependent chemical diffusion coefficient (7.59).

the chemical diffusion coefficient, refers to the summed concentration of all isotopes in the corresponding shell of a discretized pebble.

The determination of the chemical diffusion coefficient $\overline{D}^{\mathrm{Y}}$ is the result of a theoretical study that has been performed within the scope of this dissertation. Deriving an expression for the concentration-dependent hydrogen diffusivity in different yttrium hydride phases is a novelty and, to the best of the author's knowledge, has not been done before. The sharp change of the diffusion coefficient in different phases visible in figure 7.12 is a clear indication that hydride formation has a strong influence on the hydrogen absorption kinetics of yttrium and must therefore be considered in the model.

Figure 7.13 presents two simulated diffusion processes of hydrogen into an yttrium pebble of radius $r_{\mathrm{peb}} = 5 \times 10^{-4}\,\mathrm{m}$ at $T = 573\,\mathrm{K}$, assuming that the interface concentration at the pebble surface is constant at $c_{\mathrm{int}}^{\mathrm{Y}} = 1.4 \times 10^5\,\mathrm{mol\,m^{-3}}$. This concentration value is chosen for the simulations because it satisfies the condition $1.4 \times 10^5\,\mathrm{mol\,m^{-3}} > c_{\mathrm{Y}}^{\varepsilon\text{-start}}$. According to figure 7.8, this implies that the pebble surface occurs in the ε-YH_{3-y} phase.

The left plot shows the simulated concentration profile in the pebble after three different times if the diffusion coefficient was concentration-independent and described by relation (7.58) over the entire concentration range. As a result, a continuous concentration profile is observed that increases smoothly with time. It follows the typical solution of Fick's second law for a diffusion process into a homogeneous sphere at constant interface concentration (see chapter 6 in [165]).

The right-hand graph displays a simulation of the same process, this time carried out

considering the derived concentration-dependent chemical diffusion coefficient expressed by equation (7.59). In the plot, areas shaded in color indicate the concentration ranges corresponding to the different yttrium hydride phases. The interrupted concentration scale illustrates the fact that the model considered a maximum hydrogen content of yttrium at a concentration $c^{\mathrm{Y}}_{\varepsilon\text{-end}}$. The simulation reveals that because of the temperature-dependent variation of the diffusivity shown in figure 7.12 the time-evolving concentration profile is no longer continuous. Indeed, in the concentration ranges representing the $\alpha \rightarrow \delta$ and $\delta \rightarrow \varepsilon$ transition regimes, the diffusing atoms pile up and form steep diffusion fronts. Due to the much slower diffusivity in the transition regimes compared to the pure hydride phases, the rate of diffusing atoms entering a transition range from an adjacent higher phase is bigger than the rate of atoms leaving the transition range into a lower phase. Moreover, it is observed that the $\alpha \rightarrow \delta$ front moves faster than the $\delta \rightarrow \varepsilon$ front. These results are in good accordance with measurements made by den Broeder *et al* who experimentally visualized the same behavior of hydrogen diffusion in different yttrium hydride phases at lower temperatures [277].

Whenever in the following reference is made to a simulation that does not take yttrium hydride formation into account (no HyF), what is meant is a simulation that considers boundary condition (7.21) and the intrinsic hydrogen diffusion coefficient in yttrium (7.58) to be valid in an infinite concentration range. This would be the case if the Y-H system remained in the α-Y phase regardless of the concentration.

Possible material-altering effects of the tritium β^- decay on the hydrogen transport properties of the two metals are neglected by this model.

7.6. Simulation results and discussion

In this section, the developed numerical model is applied to simulate the retention of hydrogen isotopes by an yttrium-based hydrogen getter trap installed in the DONES lithium loop. Therefore, the volume flow rate through the main loop is set to $F_{\mathrm{main}} = 1{\times}10^{-1}\,\mathrm{m}^3/\mathrm{s}$. The current design of the DONES lithium loop envisages a total lithium volume of approximately $V_{\mathrm{Li}} = 14\,\mathrm{m}^3$ which is considered as a reference value for the following simulations [280]. Unless otherwise noted, the simulations are executed assuming a flow rate through the trap of $F_{\mathrm{trap}} \approx 2 \times 10^{-3}\,\mathrm{m}^3/\mathrm{s}$, a trap diameter of $d_{\mathrm{trap}} = 0.15\,\mathrm{m}$ and a pebble radius of $r_{\mathrm{peb}} = 5 \times 10^{-4}\,\mathrm{m}$.

The pebble bed void fraction of perfectly round pebbles packed in a cylindrical trap container with $d_{\mathrm{trap}} \gg r_{\mathrm{peb}}$ is usually determined to be approximately $\varepsilon \approx 0.4$ [281]. However, in a real yttrium getter-bed the sizes and shapes of the pebbles are expected to strongly vary. Therefore, a packing density as high as $\varepsilon \approx 0.4$ is probably not achievable. The mass transfer coefficient α_{MT} in equation (7.7) decreases with increasing void fraction [105]. Hence, to obtain conservative simulation results, the following calculations assume a higher void fraction of $\varepsilon = 0.6$.

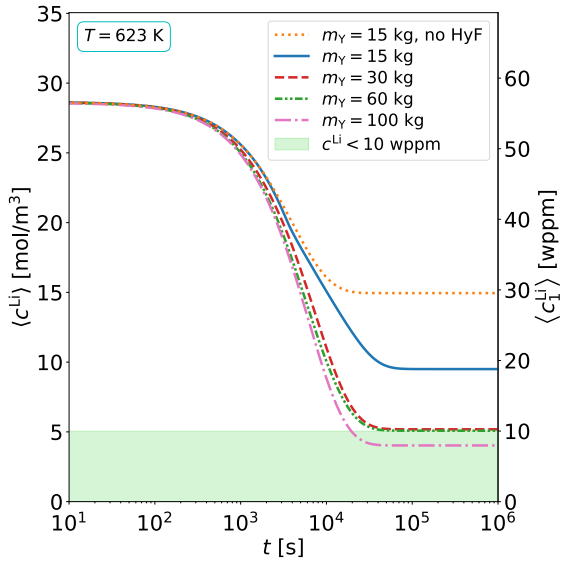

Fig. 7.14. Simulated temporal evolution of the average protium concentration in lithium during initial purification of the DONES lithium loop at $T = 623\,\mathrm{K}$, assuming different yttrium masses in the hydrogen trap. The graph includes a simulation that does not take hydride formation into account (no HyF). The green area marks the required concentration range for DONES operation.

The applied discretization density of the spatial sub-systems considered in the model is set to $\mathcal{Q} = 198$, $\mathcal{M} = 6$, and $U = 3$. To solve the system of equations introduced in the previous section, the finite difference equations (7.2), (7.3), (7.16) and (7.17) are manually solved in for-loops over the indexes q, m and n. As explained in section 5.1, the temporal parts of the differential equations (7.1), (7.2), (7.3) and (7.17) are automatically computed by EcosimPro©.

In order to cope with the imposed safety requirements for DONES, the installed hydrogen trap needs to be capable of maintaining the average total hydrogen isotope concentration in the lithium below $c^{\mathrm{Li}}_{\mathrm{limit}} = 10\,\mathrm{wppm}$. Further radiation safety requirements restrict the inventories of tritium in yttrium to $m^{\mathrm{Y}}_{3,\mathrm{limit}} = 3 \times 10^{-4}\,\mathrm{kg}$ and in lithium to $m^{\mathrm{Li}}_{3,\mathrm{limit}} = 3 \times 10^{-4}\,\mathrm{kg}$ [99]. This is equivalent to $c^{\mathrm{Li}}_{3,\mathrm{limit}} = 7.1 \times 10^{-3}\,\mathrm{mol\,m^{-3}}$ considering that $V_{\mathrm{Li}} = 14\,\mathrm{m^3}$. The current design basis of the DONES impurity control loop envisages $T = 623\,\mathrm{K}$ as the design temperature of the hydrogen trap [256].

7.6.1. Simulation of hydrogen capture during DONES initial purification

It is assumed that the lithium which is going to be purchased to fill the DONES lithium loop for its future experimental campaigns will be contaminated with a relatively high protium concentration. Furthermore, filling the DONES lithium loop the first time will cause the stainless steel walls of the pipes to release an additional significant amount of protium into the lithium. Part of the dissolved protium will be removed by a cold trap which is working at a temperature of $T = 463\,\mathrm{K}$. The cold trap retains solidified lithium hydride (β-LiH) which precipitates above the temperature-dependent terminal solubility $c^{\mathrm{Li}}_{\alpha\text{-end}}$. Equation (7.25) reveals that at $T = 463\,\mathrm{K}$ the terminal solubility of the solid solution α-Li phase is $c^{\mathrm{Li}}_{\alpha\text{-end}} \approx 28.7\,\mathrm{mol\,m^{-3}}$. Hence, it is expected that after the first purification run using only the cold trap, the liquid lithium will have a maximum protium concentration of approximately $c^{\mathrm{Li}}_{1,\mathrm{init}} = 28.7\,\mathrm{mol\,m^{-3}} = 57\,\mathrm{wppm}$.

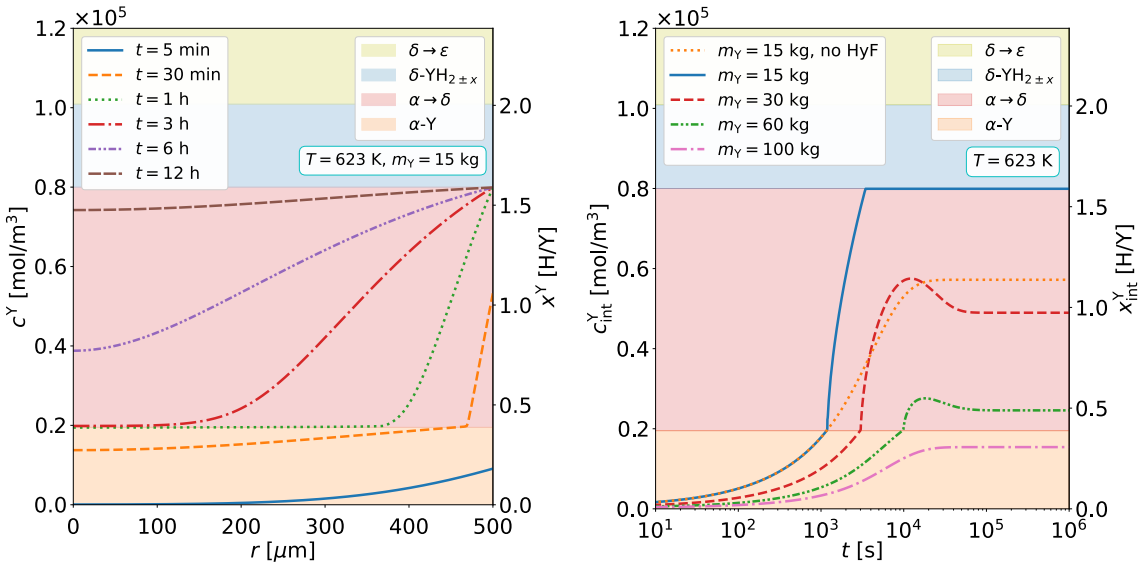

Fig. 7.15. [Left] Simulated temporal evolution of the protium concentration profile inside of an yttrium pebble of the first trap segment, assuming a temperature of $T = 623\,\mathrm{K}$ and a pebble bed mass of $m_\mathrm{Y} = 15\,\mathrm{kg}$. [Right] Simulated temporal evolution of the protium concentration occurring at the surface of an yttrium pebble in the first trap segment during initial purification of the DONES lithium loop, assuming a temperature of $T = 623\,\mathrm{K}$ and a pebble bed mass of $m_\mathrm{Y} = 15\,\mathrm{kg}$. The graph includes a simulation that does not take hydride formation into account (no HyF).

In order to comply with the DONES safety requirements mentioned above, prior to continuous DONES operation, the lithium loop system should undergo another purification run with the hydrogen trap operating in which the average concentration in the loop $\langle c_1^\mathrm{Li}\rangle$ is further reduced to below $\langle c_1^\mathrm{Li}\rangle < 10\,\mathrm{wppm} = 5.1\,\mathrm{mol\,m^{-3}}$. This initial purification process using the hydrogen trap is simulated and analyzed in the following paragraphs. Since protium is assumed to be the only isotope present during the initial purification phase, its average concentration $\langle c_1^\mathrm{Li}\rangle$ equals the total average concentration $\langle c^\mathrm{Li}\rangle$, including all hydrogen isotopes.

Figure 7.14 presents the simulated temporal evolution of the average concentration $\langle c^\mathrm{Li}\rangle$ in the loop during initial purification for different pebble bed masses. The simulation assumes an operating temperature of $T = 623\,\mathrm{K}$. To analyze the observed hydrogen absorption behavior of the trap and the impact of yttrium dihydride formation, it is taken a closer look at the purification process resulting from a trap with an yttrium mass of $m_\mathrm{Y} = 15\,\mathrm{kg}$ (see solid blue curve in figure 7.14). A deep insight into the getter process is obtained by observing the time-evolving concentration profile within an yttrium pebble of the first trap segment y_1. It is simulated and plotted in the left-hand graph of figure 7.15. The analysis is supported by the right-hand graph in figure 7.15 and by the two plots shown in figure 7.16. They show the simulated values of the interface concentrations $c_\mathrm{int}^\mathrm{Y}$, $c_\mathrm{int}^\mathrm{Li}$ and the general distribution coefficient $K_\mathrm{D}^\mathrm{Li-Y}$ in the first trap segment.

It is found that after a period of several minutes in which the empty yttrium pebbles absorb the protium atoms as a solute, the surface concentration $c_\mathrm{int}^\mathrm{Y}$ surpasses the

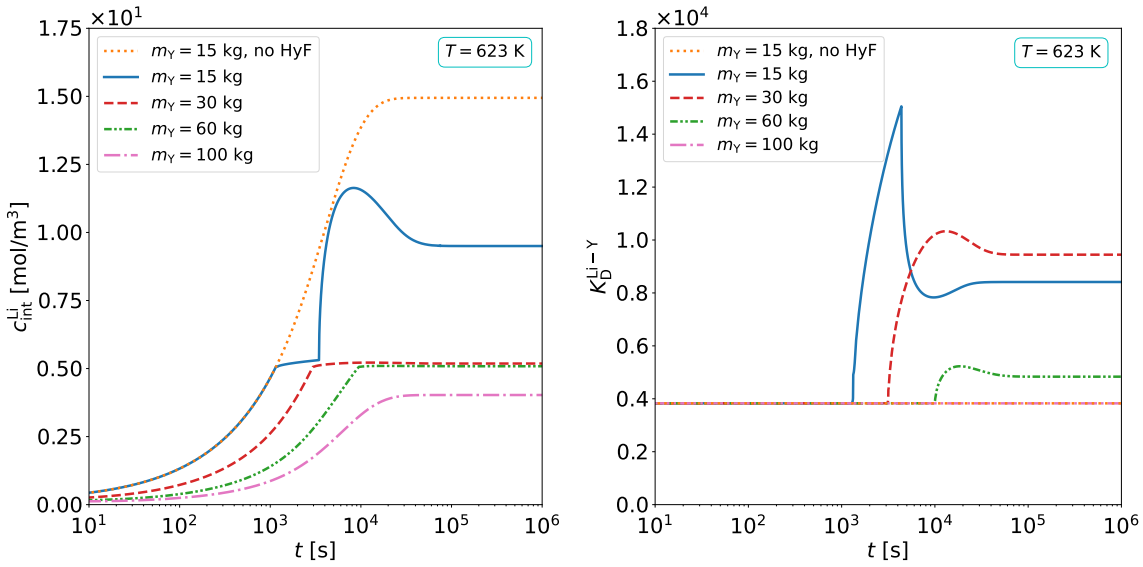

Fig. 7.16. [Left] Simulated temporal evolution of the protium concentration occurring in lithium at the Li-Y interfaces in the first trap segment during initial purification of the DONES lithium loop, assuming a temperature of $T = 623\,\mathrm{K}$ and a pebble bed mass of $m_{\mathrm{Y}} = 15\,\mathrm{kg}$. The graph includes a simulation that does not take hydride formation into account (no HyF). [Right] Simulated temporal evolution of the Li-Y general distribution coefficient in the first segment during initial purification of the DONES lithium loop, assuming a temperature of $T = 623\,\mathrm{K}$ and a pebble bed mass of $m_{\mathrm{Y}} = 15\,\mathrm{kg}$. The graph includes a simulation that does not take hydride formation into account (no HyF).

maximum concentration $c_{\alpha\text{-end}}^{\mathrm{Y}}$ of the pure α-Y phase and hydride formation sets in (see both plots in figure 7.15). The precipitation of high-concentrated yttrium dihydride at the surface is characterized by an abruptly accelerated increase in the average hydrogen concentration in the yttrium at the Li-Y interface $c_{\mathrm{int}}^{\mathrm{Y}}$ (see right-hand plot in figure 7.15). As the left-hand plot in figure 7.16 reveals, during hydride formation, the protium concentration in lithium at the Li-Y interface abides in the concentration range $c_{-}^{\mathrm{Li}} < c_{\mathrm{int}}^{\mathrm{Li}} < c_{+}^{\mathrm{Li}}$. The right-hand graph in figure 7.16 demonstrates how the rapidly growing concentration $c_{\mathrm{int}}^{\mathrm{Y}}$ at almost constant value of $c_{\mathrm{int}}^{\mathrm{Li}}$ causes the general distribution coefficient $K_{\mathrm{D}}^{\mathrm{Li-Y}}$ to increase above its constant value $K_{\mathrm{D},0}^{\mathrm{Li-Y}}$ in the pure α-Y phase (see left-hand plot in figure 7.9). Approximately one hour after the start of the purification process, the increase in interface concentration at the pebble surface comes to a halt at the saturation concentration $c_{\mathrm{int}}^{\mathrm{Y}} = c_{\alpha\text{-end}}^{\mathrm{Y}}$ (see right-hand plot in figure 7.15) and the general distribution coefficient reaches its maximum value (see right-hand plot in figure 7.16). By this time, the yttrium surface has entered the pure δ-$YH_{2\pm x}$ phase. Once surface saturation occurs, the protium concentration in lithium at the Li-Y interface abruptly increases beyond the concentration range $c_{-}^{\mathrm{Li}} < c_{\mathrm{int}}^{\mathrm{Li}} < c_{+}^{\mathrm{Li}}$ where it resided during phase transition. In accordance with the left-hand graph in figure 7.11, the sudden rise in the concentration $c_{\mathrm{int}}^{\mathrm{Li}}$ implies that the general distribution coefficient decreases. At about the same time, the quickly diffusing protium atoms in the α-Y phase have homogeneously distributed in the entire pebble. In contrast, the much slower elapsing diffusion process occurring in the $\alpha \rightarrow \delta$ phase transition

regime closer to the surface leads to the formation of a relatively steep diffusion front (see red shaded area in the left-hand plot of figure 7.15). It slowly flattens out over time while the pebble surface remains at the saturation concentration $c^{\mathrm{Y}}_{\mathrm{int}} = c^{\mathrm{Y}}_{\delta\text{-start}}$. The left-hand plot of figure 7.16 reveals that after approximately three hours, the hydrogen absorption flux induced by the concentration gradient that occurs at the pebble interface has lowered the average concentration in the loop so much that $c^{\mathrm{Li}}_{\mathrm{int}}$ reaches a maximum before decreasing alongside with the average concentration $\langle c^{\mathrm{Li}} \rangle$. According to the left-hand plot in figure 7.11, this results in a slow but persistent rise in the general distribution coefficient back toward its maximum value. The transport processes come to an end once thermodynamic equilibrium establishes and the concentrations in both the Li-H and the Y-H systems have reached steady state values. At this time the concentration profiles in the pebbles are flat. The left-hand graph in figure 7.15 shows that at equilibrium the yttrium pebbles of a getter bed with a mass of $m_{\mathrm{Y}} = 15\,\mathrm{kg}$ have entirely transformed to pure δ-$YH_{2\pm x}$ and occur at a homogeneous concentration of $c^{\mathrm{Y}} = c^{\mathrm{Y}}_{\delta\text{-start}}$.

The influence of the implemented mechanism of hydride formation on the retention dynamics of the trap becomes apparent when comparing the discussed simulation results with a simulation that does not take hydride formation into account (no HyF). The simulation results are plotted in the figures 7.14, 7.15 and 7.16 using an orange dotted line and assuming the same input parameters as before ($m_{\mathrm{Y}} = 15\,\mathrm{kg}$, $T = 623\,\mathrm{K}$). The right-hand plot in figure 7.15 reveals that if the process of hydride formation is ignored, no abruptly accelerated increase in $c^{\mathrm{Y}}_{\mathrm{int}}$ is observed once the concentration in yttrium at the pebble surface surpasses the terminal solubility $c^{\mathrm{Y}}_{\alpha\text{-end}}$. Disregarding hydride formation in the model would mean that even at concentrations $c^{\mathrm{Y}}_{\mathrm{int}} > c^{\mathrm{Y}}_{\alpha\text{-end}}$, the general distribution coefficient remains constant at $K^{\mathrm{Li-Y}}_{\mathrm{D},0} = K^{\mathrm{Y}}_{\mathrm{s}} / K^{\mathrm{Li}}_{\mathrm{s}}$ during the entire simulated time period. In contrast, taking hydride formation into account leads to an increase in the general distribution coefficient which levels out at a value $K^{\mathrm{Li-Y}}_{\mathrm{D}} > K^{\mathrm{Li-Y}}_{\mathrm{D},0}$ (compare solid blue and orange dotted lines in the right-hand plot in figure 7.16). For this reason, the final equilibrium concentration $c^{\mathrm{Li}}_{\mathrm{eq}} \approx 19\,\mathrm{wppm}$ which yields from the simulation that considers hydride formation is much lower than the adjusting equilibrium concentration $c^{\mathrm{Li}}_{\mathrm{eq}} \approx 30\,\mathrm{wppm}$ that adjusts when hydride formation is ignored. The great difference between the two simulated equilibrium concentrations in lithium obtained with and without the consideration of hydride formation illustrates the significant magnitude by which yttrium dihydride formation increases the gettering capacity of yttrium. Ignoring the process of hydride formation would therefore lead to an overestimation of the required trap mass to meet the DONES safety requirements. This example demonstrates the importance of incorporating the thermodynamics of hydride formation into the model.

Observing figure 7.14, it is found that regardless of the pebble bed mass, with the examined parameter set ($T = 623\,\mathrm{K}$, $F_{\mathrm{trap}} = 2{\times}10^{-3}\,\mathrm{m^3\,s^{-1}}$, $r_{\mathrm{peb}} = 5{\times}10^{-4}\,\mathrm{m}$, $d_{\mathrm{trap}} = 0.15\,\mathrm{m}$, $\varepsilon = 0.6$) the purification process takes about twelve hours to reach thermodynamic equilibrium. It is found that the higher the mass of the pebble bed, the lower the concentration $c^{\mathrm{Li}}_{\mathrm{eq}}$ in lithium, which adjusts throughout the loop once thermodynamic equilibrium is

reached. The right-hand plot in figure 7.15 reveals that different pebble bed masses lead to specific equilibrium concentrations $c_{\mathrm{eq}}^{\mathrm{Y}}$ in the pebbles. In fact, three distinct scenarios are identified.

The first scenario describes a case like the one discussed above ($m_{\mathrm{Y}} = 15\,\mathrm{kg}$, $T = 623\,\mathrm{K}$), where, at thermodynamic equilibrium, the entire pebble bed converts to pure δ-$YH_{2\pm x}$. This means that the adjusting equilibrium concentration everywhere in the pebbles is $c_{\mathrm{eq}}^{\mathrm{Y}} = c_{\delta\text{-start}}^{\mathrm{Y}}$. As the derived concentration boundary condition illustrated by the right-hand graph in figure 7.9 indicates, full saturation occurs only if the establishing equilibrium concentration in lithium satisfies $c_{\mathrm{eq}}^{\mathrm{Li}} > c_{+}^{\mathrm{Li}}$. In this case, the final concentration $c_{\mathrm{eq}}^{\mathrm{Li}}$ can be calculated assuming that at thermodynamic equilibrium the mole numbers of hydrogen isotopes in the yttrium $\varkappa_{\mathrm{eq}}^{\mathrm{Y}}$ and in the lithium $\varkappa_{\mathrm{eq}}^{\mathrm{Li}}$ are distributed according to $\varkappa_{\mathrm{init}}^{\mathrm{Li}} = \varkappa_{\mathrm{eq}}^{\mathrm{Y}} + \varkappa_{\mathrm{eq}}^{\mathrm{Li}}$. Here, $\varkappa_{\mathrm{init}}^{\mathrm{Li}}$ is the mole number of hydrogen isotopes present in the lithium prior to purification. With $\varkappa_{\mathrm{init}}^{\mathrm{Li}} = c_{\mathrm{init}}^{\mathrm{Li}} V_{\mathrm{Li}}$, $\varkappa_{\mathrm{eq}}^{\mathrm{Li}} = c_{\mathrm{eq}}^{\mathrm{Li}} V_{\mathrm{Li}}$ and $\varkappa_{\mathrm{eq}}^{\mathrm{Y}} = c_{\delta\text{-start}}^{\mathrm{Y}} V_{\mathrm{Y}}$ the equilibrium concentration yields

$$c_{\mathrm{eq}}^{\mathrm{Li}} = c_{\mathrm{init}}^{\mathrm{Li}} - \frac{V_{\mathrm{Y}}}{V_{\mathrm{Li}}} \cdot c_{\delta\text{-start}}^{\mathrm{Y}}\,, \quad \text{if} \quad c_{\mathrm{eq}}^{\mathrm{Li}} > c_{+}^{\mathrm{Li}}\,. \tag{7.60}$$

According to figure 7.8, the concentration $c_{\delta-\mathrm{start}}^{\mathrm{Y}}$ decreases with increasing temperature. Therefore, in the first scenario, the gettering capacity slightly reduces with increasing temperature. Solving equation (7.60) for m_{Y} yields the pebble bed mass required to reduce the equilibrium concentration from a given initial concentration $c_{\mathrm{init}}^{\mathrm{Li}}$ down to a certain equilibrium value

$$m_{\mathrm{Y}} = \frac{\rho_{\mathrm{Y}} V_{\mathrm{Li}}}{c_{\delta\text{-start}}^{\mathrm{Y}}} \cdot \left(c_{\mathrm{init}}^{\mathrm{Li}} - c_{\mathrm{eq}}^{\mathrm{Li}}\right), \quad \text{if} \quad c_{\mathrm{eq}}^{\mathrm{Li}} > c_{+}^{\mathrm{Li}}\,. \tag{7.61}$$

The error of the required pebble bed mass is determined by the error of the phase boundary $\Delta c_{\delta\text{-start}}^{\mathrm{Y}}$ which was estimated in equation (7.39). Consequently, error propagation yields

$$\Delta m_{\mathrm{Y}} = \frac{\Delta c_{\delta\text{-start}}^{\mathrm{Y}}}{c_{\delta\text{-start}}^{\mathrm{Y}}} \cdot m_{\mathrm{Y}}\,, \quad \text{if} \quad c_{\mathrm{eq}}^{\mathrm{Li}} > c_{+}^{\mathrm{Li}}\,. \tag{7.62}$$

The second scenario refers to a case where during the concentration decrease the value of the average concentration $\langle c^{\mathrm{Li}} \rangle$ falls below the minimum concentration required for hydride formation c_{-}^{Li}, such that $c_{\mathrm{eq}}^{\mathrm{Li}} < c_{-}^{\mathrm{Li}}$. As figure 7.14 shows, such a situation is observed for a trap with a mass of $m_{\mathrm{Y}} = 100\,\mathrm{kg}$ operating at $T = 623\,\mathrm{K}$. The pink dash-dotted lines in the right-hand graphs of the figures 7.15 and 7.16 reveal that if a sufficiently heavy trap is installed the concentration $c_{\mathrm{int}}^{\mathrm{Y}}$ never exceeds $c_{\alpha\text{-end}}^{\mathrm{Y}}$ and no hydride formation takes place. Hence, if $c_{\mathrm{eq}}^{\mathrm{Li}} < c_{-}^{\mathrm{Li}}$ the pebble bed occurs exclusively in the α-Y phase and the concentration boundary condition is described by relation (7.21). With equation (7.51), this implies that at thermodynamic equilibrium the mole number of hydrogen atoms in the pebbles is given by $\varkappa_{\mathrm{eq}}^{\mathrm{Y}} = V_{\mathrm{Y}} c_{\mathrm{eq}}^{\mathrm{Y}} = V_{\mathrm{Y}} c_{\mathrm{eq}}^{\mathrm{Li}} K_{\mathrm{D},0}^{\mathrm{Li-Y}}$. Inserting this relation into the equation $\varkappa_{\mathrm{init}}^{\mathrm{Li}} = \varkappa_{\mathrm{eq}}^{\mathrm{Y}} + \varkappa_{\mathrm{eq}}^{\mathrm{Li}}$ provides an expression for the equilibrium concentration in the lithium

$$c_{\mathrm{eq}}^{\mathrm{Li}} = \frac{V_{\mathrm{Li}} c_{\mathrm{init}}^{\mathrm{Li}}}{V_{\mathrm{Li}} + V_{\mathrm{Y}} K_{\mathrm{D},0}^{\mathrm{Li-Y}}}\,, \quad \text{if} \quad c_{\mathrm{eq}}^{\mathrm{Li}} < c_{-}^{\mathrm{Li}}\,. \tag{7.63}$$

Also in the second scenario, the gettering capacity decreases with increasing temperature. This is attributed to the temperature dependency of $K_{\mathrm{D},0}^{\mathrm{Li-Y}}$ which is visualized in the right-hand graph in figure 7.11 and mathematically expresses with equation (7.52). According to equation (7.63), in the second scenario the required pebble bed mass to lower the concentration in lithium down to a certain equilibrium value is determined by

$$m_{\mathrm{Y}} = \frac{\rho_{\mathrm{Y}} V_{\mathrm{Li}}}{K_{\mathrm{D},0}^{\mathrm{Li-Y}}} \cdot \left(\frac{c_{\mathrm{init}}^{\mathrm{Li}}}{c_{\mathrm{eq}}^{\mathrm{Li}}} - 1 \right), \quad \text{if} \quad c_{\mathrm{eq}}^{\mathrm{Li}} < c_{-}^{\mathrm{Li}} . \tag{7.64}$$

Its error originates from the error of $K_{\mathrm{D},0}^{\mathrm{Li-Y}}$ given by equation (7.53), such that

$$\Delta^{\pm} m_{\mathrm{Y}} = \frac{\Delta^{\pm} K_{\mathrm{D},0}^{\mathrm{Li-Y}}}{K_{\mathrm{D},0}^{\mathrm{Li-Y}}} \cdot m_{\mathrm{Y}} , \quad \text{if} \quad c_{\mathrm{eq}}^{\mathrm{Li}} < c_{-}^{\mathrm{Li}} . \tag{7.65}$$

A third scenario arises when, for the observed temperature and pebble bed mass, the values of $c_{\mathrm{eq}}^{\mathrm{Li}}$ resulting from the equations (7.61) and (7.64) do not satisfy the specified conditions for $c_{\mathrm{eq}}^{\mathrm{Li}}$ written alongside the equations. In this case, the Li-Y-H system levels out at an equilibrium concentration $c_{-}^{\mathrm{Li}} < c_{\mathrm{eq}}^{\mathrm{Li}} < c_{+}^{\mathrm{Li}}$. According to the right-hand plot in figure 7.9, in this regime, the pebbles have only partially transformed to yttrium dihydride once thermodynamic equilibrium is reached. Figure 7.10 shows that both c_{-}^{Li} and c_{+}^{Li} strongly increase with temperature. For this reason, also in the third scenario, the gettering capacity decreases with increasing temperature. Figure 7.14 as well as the right-hand plots in the figures 7.15 and 7.16 show that at $T = 623\,\mathrm{K}$, the third scenario occurs for the traps with the masses $m_{\mathrm{Y}} = 30\,\mathrm{kg}$ and $m_{\mathrm{Y}} = 60\,\mathrm{kg}$. In spite of their large difference in mass, both traps are found to reduce the average concentration in the lithium into the range $c_{-}^{\mathrm{Li}}(623\,\mathrm{K}) < c_{\mathrm{eq}}^{\mathrm{Li}} < c_{+}^{\mathrm{Li}}(623\,\mathrm{K})$ and level out in the $\alpha \rightarrow \delta$ phase transition regime.

The equations (7.61) and (7.64) allow calculating the minimum pebble bed mass which is required to reduce the concentration in the DONES lithium loop from $c_{\mathrm{init}}^{\mathrm{Li}} = 28.7\,\mathrm{mol\,m^{-3}} = 57\,\mathrm{wppm}$ to the limit value $c_{\mathrm{limit}}^{\mathrm{Li}} = 10\,\mathrm{wppm} = 5.1\,\mathrm{mol\,m^{-3}}$. It is plotted in figure 7.17 against the temperature.

From figure 7.10 it can be derived that if the operating temperature is smaller than a critical value $T < T_{\mathrm{crit}}^{-} = (620 \pm {}^{60}_{45})\,\mathrm{K}$ the DONES limit concentration satisfies $c_{\mathrm{limit}}^{\mathrm{Li}} > c_{+}^{\mathrm{Li}}$ and the pebble bed follows the defined first scenario. In this case, the minimum required trap mass is significantly lower than at higher operating temperatures and is described by the equations (7.61) and (7.62). They yield an almost constant value of $m_{\mathrm{Y}} \approx (18 \pm 1)\,\mathrm{kg}$ throughout the temperature regime $T < T_{\mathrm{crit}}^{-}$.

According to figure 7.10, if $T > T_{\mathrm{crit}}^{+} = (623 \pm {}^{60}_{45})\,\mathrm{K}$ the limit concentration satisfies $c_{\mathrm{limit}}^{\mathrm{Li}} = 5.1\,\mathrm{mol\,m^{-3}} < c_{-}^{\mathrm{Li}}$. Consequently, in this regime, any pebble bed will behave as described in the defined second scenario where the minimum required trap mass and its error range are given by the equations (7.64) and (7.65). It can be seen that if $T > T_{\mathrm{crit}}^{+}$ a much larger minimum pebble bed mass $m_{\mathrm{Y}} > 78\,\mathrm{kg}$ is required to comply with the concentration limit than at lower operating temperatures. Such a large pebble bed mass

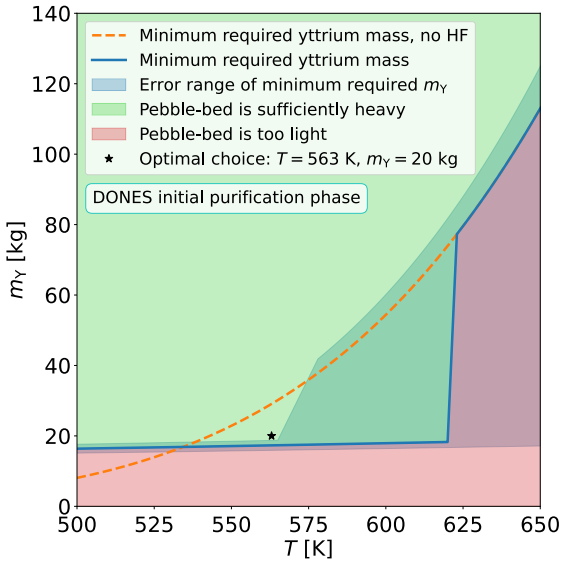

Fig. 7.17. Minimum pebble bed mass as a function of temperature required for the initial purification run of the DONES lithium loop to reduce the concentration from an initial value of $c^{\mathrm{Li}}_{\mathrm{init}} = 57\,\mathrm{wppm}$ to a limit equilibrium value of $c^{\mathrm{Li}}_{\mathrm{limit}} = 10\,\mathrm{wppm}$. The black star marks the optimal design parameters for the hydrogen trap used for the initial purification.

is necessary because, without hydride formation, the gettering capacity remains relatively low.

Figure 7.17 reveals that the defined third scenario occurs if $T^-_{\mathrm{crit}} < T < T^+_{\mathrm{crit}}$. In this regime, the minimum required pebble bed mass is in the range of $18\,\mathrm{kg} < m_Y < 78\,\mathrm{kg}$.

If hydride formation mechanisms were not taken into account the minimum required trap mass would be exclusively given by equation (7.64) regardless of the operating temperature (see orange dashed line). Disregarding hydride formation at temperatures $T > (538 \pm 5)\,\mathrm{K}$ could hence only lead to a non-problematic overestimation of the minimum required trap mass. However, at temperatures $T < (538 \pm 5)\,\mathrm{K}$, ignoring hydride formation would lead to a severe underestimation of the necessary pebble bed mass. That is because below this temperature the orange dashed line falls below the blue curve which takes hydride formation into account. Yet another reason why implementing hydride formation in the model is essential.

In figure 7.17, the green shaded area represents an appropriate combination of operating temperature and pebble bed mass which ensures meeting the safety requirement $\langle c^{\mathrm{Li}} \rangle < c^{\mathrm{Li}}_{\mathrm{limit}}$ during initial purification of the DONES lithium loop. Picking the design parameters from the red area must be avoided, as this would lead to equilibrium concentrations above the concentration limit. The relatively large error range which enters deep into the green shaded area arises from the error ranges of the critical temperatures T^-_{crit} and T^+_{crit}.

An optimal hydrogen trap design for the DONES purification phase should be based on the intention to exploit the gettering capacity-enhancing effect of yttrium dihydride formation. Therefore, the optimal trap should have an operating temperature of $T < T^-_{\mathrm{crit}}$. To ensure that hydride formation occurs and the DONES limit is met under all circumstances, the conservatively estimated error range in figure 7.17 must be taken into account when choosing the design parameters. Considering this, it is found that if $T <$

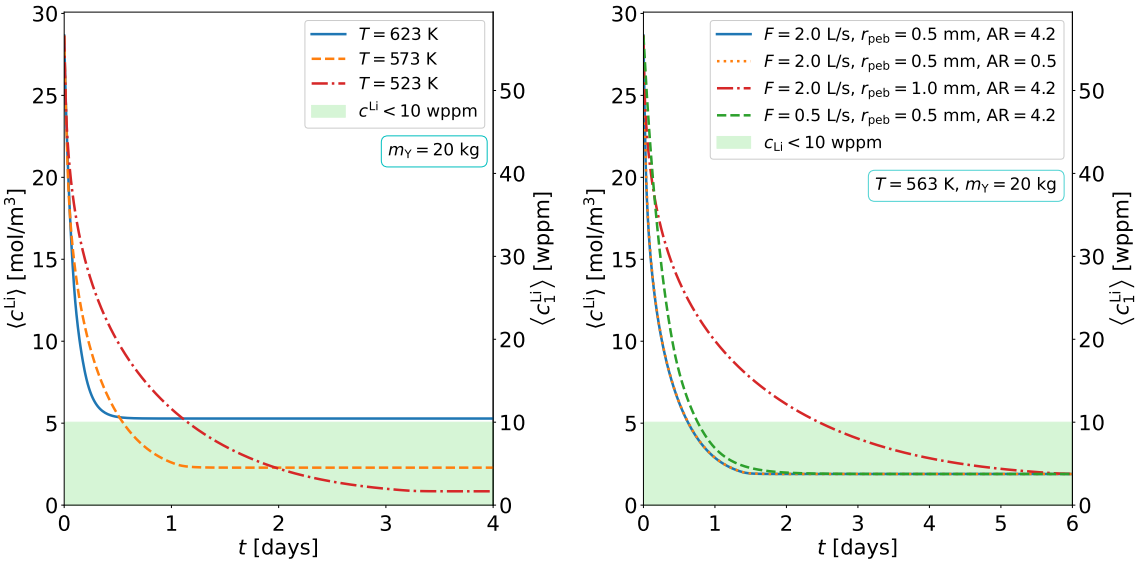

Fig. 7.18. [Left] Simulated temporal evolution of the average protium concentration in the lithium during initial purification of the DONES lithium loop for a pebble bed mass of $m_Y = 20\,\text{kg}$, assuming different operating temperatures. [Right] Simulated temporal evolution of the average protium concentration in the lithium flow during initial purification of the DONES lithium loop for a pebble bed mass of $m_Y = 20\,\text{kg}$ and an operating temperature of $T = 563\,\text{K}$, varying the pebble diameter, the lithium flow rate through the trap or the aspect ratio of the pebble bed.

T^-_{crit}, a trap with a pebble bed mass of $m_Y = 20\,\text{kg}$ would ensure meeting the requirements with the least amount of yttrium.

The left-hand plot in figure 7.18 displays the simulated protium concentration decrease during initial purification at three different temperatures that would result from a trap with a mass of $m_Y = 20\,\text{kg}$. As predicted by figure 7.17, the two temperatures that satisfy $T < T^-_{crit}$ lead to a concentration decrease well below the safety limit. In contrast, $T = 623\,\text{K}$ is above the critical temperature. At this temperature, a pebble bed mass of $m_Y = 20\,\text{kg}$ can be assigned to the red shaded area in figure 7.17 and therefore does not comply with the concentration safety limit (see left-hand plot in figure 7.18). It is found that the higher the temperature, the less time it takes for the system to reach thermodynamic equilibrium. This can be attributed to the fact that the diffusion coefficients in lithium and in yttrium increase with temperature (see figure 7.12).

According to the error range in figure 7.17, an operating temperature of $T = 563\,\text{K}$ is the maximum temperature where hydride formation in a pebble bed with a mass of $m_Y = 20\,\text{kg}$ is guaranteed. Furthermore, with this combination of design parameters, the purification run would be completed in a reasonable period of time of between one and two days (see left-hand plot in figure 7.18).

Having determined the optimal trap mass and working temperature it remains to be investigated how varying the flow rate, pebble diameter and aspect ratio $\text{AR} \equiv l_{trap}/d_{trap}$ affects the purification dynamics. In the following, these quantities are referred to as

secondary design parameters. The right-hand plot in figure 7.18 depicts the simulated temporal evolution of the average concentration in the lithium yielding from the determined optimal trap mass and temperature for different sets of the secondary parameters. The reference parameter set which was assumed for all previous simulations is $F_{\mathrm{trap}} = 2 \times 10^{-3}\,\mathrm{m^3\,s^{-1}}$, $r_{\mathrm{peb}} = 5 \times 10^{-4}\,\mathrm{m}$ and $d_{\mathrm{trap}} = 0.15\,\mathrm{m}$. Given that $m_{\mathrm{Y}} = 20\,\mathrm{kg}$ and $\varepsilon = 0.6$, the trap length yields $l_{\mathrm{trap}} = 0.63\,\mathrm{m}$ and the aspect ratio is AR = 4.2.

The right-hand graph in figure 7.18 discloses that operating a trap at a lower lithium flow rate F_{trap} causes the purification process to finish later. This has the following reasons. According to the equations (7.8) and (7.9), the pebble bed mass transfer coefficient decreases with the lithium flow velocity. Since a smaller flow rate F_{trap} implies a lower lithium flow velocity u_{int}, it leads to a reduced mass transfer coefficient and thus to a lower retention flux into the pebbles. Moreover, at a lower flow rate, the residence time of lithium in the trap container is higher. As a result, the lithium flowing past is exposed to the yttrium getter for a longer time leading to a smaller concentration $c_{\mathrm{trap}}^{\mathrm{Li}}$ in the trap. Consequently, the concentration gradient in yttrium at the pebble surface and thus the retention flux is smaller, so that thermodynamic equilibrium is reached later.

Furthermore, the right-hand plot in figure 7.18 shows that using a trap with wider pebbles also leads to a delay in the purification time. As equation (7.4) discloses, this is due to the fact that a reduced total surface area of the yttrium pebbles at equal pebble bed mass implies a reduced hydrogen retention rate. Moreover, wider pebbles imply a smaller mass transfer coefficient.

Increasing the trap diameter and thus reducing the aspect ratio of the trap container does not increase the residence time. However, it does decrease the lithium flow velocity and thus the mass transfer coefficient of the pebble bed. Therefore, one would expect the time to reach equilibrium to increase with the trap diameter. However, the right-hand plot in figure 7.18 shows no noticeable change in the shape of the concentration decrease as the trap diameter is increased from $d_{\mathrm{trap}} = 0.15\,\mathrm{m}$ to $d_{\mathrm{trap}} = 0.3\,\mathrm{m}$. This is due to a second overlapping effect that increases the retention flux when moving toward wider trap diameters. It arises from the effect a reduced mass transfer coefficient has on the hydride formation dynamics. During $\alpha \rightarrow \delta$ phase transition, the pebble surface concentration in yttrium increases abruptly and the concentration gradients on both sides of the lithium-yttrium pebble increase alongside. This is directly related to an increase in hydrogen retention flux. However, the increased retention flux lasts only until the pebble surface reaches the saturation concentration. A smaller mass transfer coefficient causes hydride formation to proceed slower and surface saturation to happen later. Therefore, in wider traps, the increased retention flux occurring during hydride formation lasts over a longer period of time.

Finally, it is found that in contrast to the pebble bed mass and operating temperature, neither the lithium flow rate, nor the pebble diameter or aspect ratio has an influence on the establishing concentration $c_{\mathrm{eq}}^{\mathrm{Li}}$ in the lithium at thermodynamic equilibrium.

7.6.2. Simulation of hydrogen capture during DONES operation

As soon as the DONES experimental phase is started, nuclear stripping reactions in the target component of the loop lead to an accumulation of hydrogen isotopes in the lithium flow. Current estimations expect the generation rates [99], [101], [256]

$$\dot{\varkappa}_{1,\mathrm{gen}} = 8.26 \times 10^{-8}\,\mathrm{mol\,s^{-1}} \tag{7.66}$$

$$\dot{\varkappa}_{2,\mathrm{gen}} = 1.37 \times 10^{-6}\,\mathrm{mol\,s^{-1}} \tag{7.67}$$

$$\dot{\varkappa}_{3,\mathrm{gen}} = 4.11 \times 10^{-8}\,\mathrm{mol\,s^{-1}}\,. \tag{7.68}$$

The total hydrogen isotope generation rate is defined by $\dot{\varkappa}_{\mathrm{gen}} = \sum_i \dot{\varkappa}_{i,\mathrm{gen}}$. Due to the preliminary purification procedure which was discussed in the last section, the total hydrogen isotope concentration at the start of the DONES experimental phase is expected to satisfy the condition $\langle c^{\mathrm{Li}} \rangle < c^{\mathrm{Li}}_{\mathrm{limit}} = 10\,\mathrm{wppm}$. To provide conservative simulations, this work assumes an initial protium concentration of $\langle c^{\mathrm{Li}}_1 \rangle = 10\,\mathrm{wppm} = 5.1\,\mathrm{mol/m^3}$ in the lithium while the deuterium and tritium concentrations start from zero.

The generation rates yield that without the installation of a hydrogen trap, the tritium inventory limit in lithium ($m^{\mathrm{Li}}_{3,\mathrm{limit}} = 3 \times 10^{-4}\,\mathrm{kg}$) would be exceeded after the time

$$t = \frac{m^{\mathrm{Li}}_{3,\mathrm{limit}}}{\dot{\varkappa}_{3,\mathrm{gen}} \cdot M_3} = 28\,\mathrm{days}\,. \tag{7.69}$$

Without a trap, the total concentration in the lithium would grow over time as indicated by the olive dashed line in figure 7.19.

Case A: Non-replaced hydrogen trap

To demonstrate the effect of hydride formation on the behavior of an yttrium getter trap exposed to a liquid lithium flow with continuous hydrogen isotope generation, a scenario is considered in which a single hydrogen trap is used throughout the entire lifetime of DONES. Figure 7.19 showcases the simulated development of the average total hydrogen isotope concentration in the lithium over an operating time of six years at a fixed temperature of $T = 623\,\mathrm{K}$ considering different pebble bed masses of the hydrogen trap.

The zoom shown in figure 7.19 reveals that the average concentration in the lithium initially drops sharply from a value of $\langle c^{\mathrm{Li}} \rangle = 5.1\,\mathrm{mol/m^3}$ before reaching an intermediate equilibrium state a few hours later. The establishing initial equilibrium concentration can be calculated using the equations (7.60), (7.63) or $c^{\mathrm{Li}}_- < c^{\mathrm{Li}}_{\mathrm{eq}} < c^{\mathrm{Li}}_+$, depending on whether the purification process belongs to the defined first, second or third scenario, respectively (see section 7.6.1). Whether $c^{\mathrm{Li}}_{\mathrm{eq}} < c^{\mathrm{Li}}_-$ or $c^{\mathrm{Li}}_{\mathrm{eq}} > c^{\mathrm{Li}}_+$ also determines the hydride phase in which the yttrium pebbles occur at initial equilibrium. In the example shown in figure 7.19, all three equilibrium concentrations satisfy $c^{\mathrm{Li}}_{\mathrm{eq}} < c^{\mathrm{Li}}_-\,(623\,\mathrm{K})$, which means that the yttrium pebbles must occur in the α-Y phase. Indeed, when examining the process over

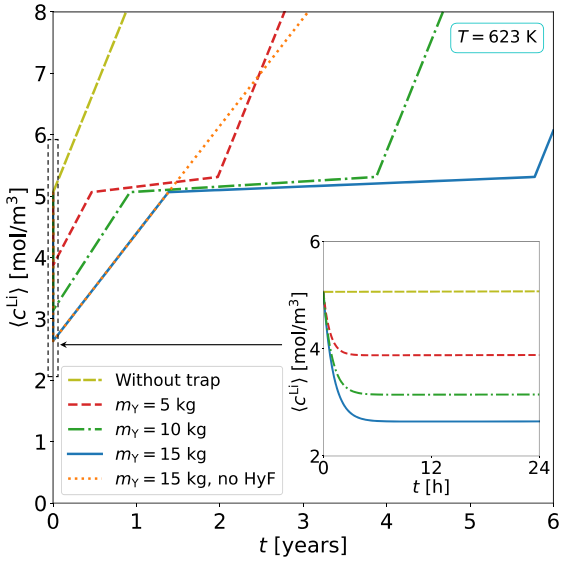

Fig. 7.19. Simulated average total hydrogen isotope concentration in lithium during DONES experimental phase for different pebble bed masses at $T = 623\,\mathrm{K}$ if a single non-replaced trap is used. The graph includes a simulation that does not take hydride formation into account (no HyF).

the scale of a year a concentration increase in the lithium is observed which arises from the proceeding isotope generation in the target. The zoom shows that the increase in lithium concentration is slow compared to the time required to reach initial equilibrium, and therefore has a negligible effect on the value of the equilibrium concentration.

In fact, compared to the scale of a year, the time required for the hydrogen isotopes to diffuse from a pebble surface to the center is negligibly short. Therefore, it can be assumed that despite the continuous hydrogen isotope generation, the Li-Y-H system remains approximately at thermodynamic equilibrium. Consequently, during DONES operation, the concentrations throughout the yttrium pebbles and at different locations in the lithium are approximately homogeneous and very close to their average concentrations $\langle c^{\mathrm{Y}} \rangle$ and $\langle c^{\mathrm{Li}} \rangle$, respectively. This implies that $c^{\mathrm{Y}}_{\mathrm{int}} \approx \langle c^{\mathrm{Y}} \rangle$ and $c^{\mathrm{Li}}_{\mathrm{int}} \approx \langle c^{\mathrm{Li}} \rangle$. Consequently, boundary condition (7.21) visualized in the right-hand plot in figure 7.9 applies to both the lithium system and the yttrium system as a whole, not just to their interfaces.

This means that according to the equations (7.21) and (7.51), the mole numbers of the different hydrogen isotopes in the two metal-hydrogen systems satisfy the condition $\varkappa_i^{\mathrm{Y}}/V_{\mathrm{Y}} = K_{\mathrm{D},0}^{\mathrm{Li-Y}} \varkappa_i^{\mathrm{Li}}/V_{\mathrm{Li}}$. Indeed, a prerequisite for this condition is that the yttrium pebbles occur in the α-Y phase. It is evident that the rates at which the generated isotopes are distributed between the lithium and yttrium systems respect the relation

$$\dot{\varkappa}_{i,\mathrm{gen}} = \dot{\varkappa}_i^{\mathrm{Y}} + \dot{\varkappa}_i^{\mathrm{Li}} \,. \tag{7.70}$$

Therefore, the rates at which the mole numbers of the dissolved isotopes in the two metals increase while the pebbles occur in the α-Y phase are

$$\dot{\varkappa}_{i,\alpha}^{\mathrm{Y}} = \frac{V_{\mathrm{Y}} K_{\mathrm{D},0}^{\mathrm{Li-Y}}}{V_{\mathrm{Li}} + V_{\mathrm{Y}} K_{\mathrm{D},0}^{\mathrm{Li-Y}}} \cdot \dot{\varkappa}_{i,\mathrm{gen}} \tag{7.71}$$

$$\dot{\varkappa}_{i,\alpha}^{\mathrm{Li}} = \frac{V_{\mathrm{Li}}}{V_{\mathrm{Li}} + V_{\mathrm{Y}} K_{\mathrm{D},0}^{\mathrm{Li-Y}}} \cdot \dot{\varkappa}_{i,\mathrm{gen}} \,. \tag{7.72}$$

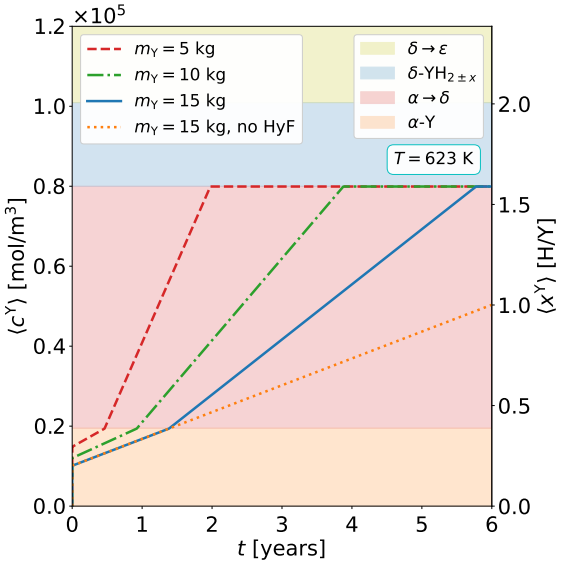

Fig. 7.20. Simulated average total hydrogen isotope concentration within the yttrium pebbles during DONES experimental phase if a single hydrogen trap is used without replacement, assuming different pebble bed masses and $T = 623\,\mathrm{K}$. The graph includes a simulation that does not take hydride formation into account (no HyF).

Figure 7.20 displays the simulated time evolution of the average approximately homogeneous total hydrogen isotope concentration within the yttrium pebbles for the same temperature and pebble bed masses as those plotted in figure 7.19. In accordance with the equations (7.71) and (7.72), both figures show that the increase rates of the average concentrations in the lithium and the yttrium decrease with increasing pebble bed mass. However, they also reveal that while the pebbles occur in the α-Y phase, only an infinitely heavy hydrogen trap would lead to $\dot{\varkappa}^{\mathrm{Li}}_{i,\alpha} = 0$.

Hydride formation is triggered once the concentration in the loop reaches the critical concentration c^{Li}_{-} which coincides with the attainment of the concentration $c^{\mathrm{Y}}_{\alpha\text{-end}}$ in the yttrium pebbles. As figure 7.9 shows, during phase transition the concentration in lithium remains nearly constant, increasing only from c^{Li}_{-} to c^{Li}_{+}. Therefore, as long as hydride formation progresses the concentration in the lithium occurs in a quasi-stationary state. By far the biggest fraction of generated isotopes is absorbed by the yttrium pebbles. During hydride formation, any absorbed hydrogen isotope is directly converted to yttrium dihydride at the pebble surface. Saturation occurs once the nearly homogeneous concentration throughout the pebbles reaches $c^{\mathrm{Y}}_{\delta\text{-start}}$. Hence, the mole numbers of hydrogen isotopes added to the yttrium and lithium during hydride formation are given by

$$\varkappa^{\mathrm{Li}}_{\mathrm{HyF}} = \left(c^{\mathrm{Li}}_{+} - c^{\mathrm{Li}}_{-}\right) \cdot V_{\mathrm{Li}} = c^{\mathrm{Li}}_{-} \cdot \left(\sqrt{f^{\alpha\delta}_{\mathrm{Y}}} - 1\right) \approx 0 \tag{7.73}$$

$$\varkappa^{\mathrm{Y}}_{\mathrm{HyF}} = \left(c^{\mathrm{Y}}_{\delta\text{-start}} - c^{\mathrm{Y}}_{\alpha\text{-end}}\right) \cdot V_{\mathrm{Y}}\,, \tag{7.74}$$

where $\varkappa^{\mathrm{Li}}_{\mathrm{HyF}} = 0$ and $\varkappa^{\mathrm{Y}}_{\mathrm{HyF}} = 0$ at the moment hydride formation begins. The transformation in expression (7.73) is performed by making use of the equations (7.35), (7.36), (7.47) and (7.49). From the equations (7.73) and (7.74) it becomes apparent that $\varkappa^{\mathrm{Y}}_{\mathrm{HyF}} \gg \varkappa^{\mathrm{Li}}_{\mathrm{HyF}} \approx 0$. The time τ_{HyF} from the beginning of hydride formation to reaching saturation is obtained by considering that $\tau_{\mathrm{HyF}}\dot{\varkappa}_{\mathrm{gen}} = \varkappa^{\mathrm{Li}}_{\mathrm{HyF}} + \varkappa^{\mathrm{Y}}_{\mathrm{HyF}}$, such that

$$\tau_{\mathrm{HyF}} = \frac{1}{\dot{\varkappa}_{\mathrm{gen}}} \left[\left(c^{\mathrm{Y}}_{\delta\text{-start}} - c^{\mathrm{Y}}_{\alpha\text{-end}}\right) \cdot V_{\mathrm{Y}} + c^{\mathrm{Li}}_{-} \cdot \left(\sqrt{f^{\alpha\delta}_{\mathrm{Y}}} - 1\right)\right]. \tag{7.75}$$

Equation (7.75) and the figures 7.19 and 7.20 demonstrate that τ_{HyF} rises linearly with the pebble bed mass. The rates at which the mole numbers of hydrogen isotopes in the lithium and yttrium grow during hydride formation are given by

$$\dot{\varkappa}^{\mathrm{Li}}_{\mathrm{HyF}} = \frac{\varkappa^{\mathrm{Li}}_{\mathrm{HyF}}}{\tau_{\mathrm{HyF}}} = \dot{\varkappa}_{\mathrm{gen}} - \frac{\varkappa^{\mathrm{Y}}_{\mathrm{HyF}}}{\tau_{\mathrm{HyF}}} \approx 0 \tag{7.76}$$

$$\dot{\varkappa}^{\mathrm{Y}}_{\mathrm{HyF}} = \frac{\varkappa^{\mathrm{Y}}_{\mathrm{HyF}}}{\tau_{\mathrm{HyF}}} = \dot{\varkappa}_{\mathrm{gen}} - \frac{\varkappa^{\mathrm{Li}}_{\mathrm{HyF}}}{\tau_{\mathrm{HyF}}} \approx \dot{\varkappa}_{\mathrm{gen}}\,. \tag{7.77}$$

Since it is assumed that $c^{\mathrm{Y}}_{\mathrm{int}} \approx \langle c^{\mathrm{Y}} \rangle = \varkappa^{\mathrm{Y}}/V_{\mathrm{Y}}$ and $c^{\mathrm{Li}}_{\mathrm{int}} \approx \langle c^{\mathrm{Li}} \rangle = \varkappa^{\mathrm{Li}}/V_{\mathrm{Li}}$, the derivative of equation (7.20) with respect to time provides the following general expression for the growth rate of isotopes of type ^{i}H in yttrium

$$\dot{\varkappa}^{\mathrm{Y}}_i = \frac{\varkappa^{\mathrm{Li}}_i}{\varkappa^{\mathrm{Li}}} \cdot \dot{\varkappa}^{\mathrm{Y}} + \frac{\partial}{\partial t}\left(\frac{\varkappa^{\mathrm{Li}}_i}{\varkappa^{\mathrm{Li}}}\right) \cdot \varkappa^{\mathrm{Y}}\,. \tag{7.78}$$

By considering that during hydride formation $\dot{\varkappa}^{\mathrm{Y}}_{\mathrm{HyF}} \approx \dot{\varkappa}_{\mathrm{gen}}$ and $\dot{\varkappa}^{\mathrm{Y}}_{\mathrm{HyF}} \approx 0$, inserting relation (7.78) into equation (7.70) yields the following expression for the growth rates of the mole numbers of the isotopes ^{i}H in lithium during hydride formation

$$\dot{\varkappa}^{\mathrm{Li}}_{i,\mathrm{HyF}} \approx \frac{\varkappa^{\mathrm{Li}} \cdot \dot{\varkappa}_{i,\mathrm{gen}} - \varkappa^{\mathrm{Li}}_i \cdot \dot{\varkappa}_{\mathrm{gen}}}{\varkappa^{\mathrm{Li}} + \varkappa^{\mathrm{Y}}}. \tag{7.79}$$

This equation implies that

$$\dot{\varkappa}^{\mathrm{Li}}_{i,\mathrm{HyF}} < 0\,, \quad \text{if} \quad \varkappa^{\mathrm{Li}}_i/\varkappa^{\mathrm{Li}} > \dot{\varkappa}_{i,\mathrm{gen}}/\dot{\varkappa}_{\mathrm{gen}} \tag{7.80}$$

$$\dot{\varkappa}^{\mathrm{Li}}_{i,\mathrm{HyF}} > 0\,, \quad \text{if} \quad \varkappa^{\mathrm{Li}}_i/\varkappa^{\mathrm{Li}} < \dot{\varkappa}_{i,\mathrm{gen}}/\dot{\varkappa}_{\mathrm{gen}}\,. \tag{7.81}$$

Once the pebbles have completely converted to pure δ-$\mathrm{YH}_{2\pm x}$, the pebble bed is exhausted because the concentration in the pebbles cannot get any higher. As a consequence, the total retention rate $\dot{\varkappa}^{\mathrm{Y}}_{\mathrm{sat}} = 0$, which implies that after saturation occurs $\dot{\varkappa}^{\mathrm{Li}}_{\mathrm{sat}} = \dot{\varkappa}_{\mathrm{gen}}$. Substituting the conditions of a saturated trap $\dot{\varkappa}^{\mathrm{Y}}_{\mathrm{sat}} = 0$ and $\varkappa^{\mathrm{Y}}_{\mathrm{sat}} = c^{\mathrm{Y}}_{\delta\text{-start}} V_{\mathrm{Y}}$ into the equations (7.78) and (7.71) provides the growth rates of the mole numbers of isotope species ^{i}H in the lithium after the pebble bed is exhausted

$$\dot{\varkappa}^{\mathrm{Li}}_{i,\mathrm{sat}} = \dot{\varkappa}_{i,\mathrm{gen}} - V_{\mathrm{Y}} \cdot c^{\mathrm{Y}}_{\delta\text{-start}} \cdot \frac{\partial}{\partial t}\left(\frac{\varkappa^{\mathrm{Li}}_i}{\varkappa^{\mathrm{Li}}}\right) \tag{7.82}$$

Hence, if after trap exhaustion the generation of isotopes in the loop keeps changing the ratio $\varkappa^{\mathrm{Li}}_i/\varkappa^{\mathrm{Li}}$ there is an ongoing isotope exchange between the yttrium and the lithium.

Both figures 7.19 and 7.20 contain a simulation that does not incorporate the physics of hydride formation. Consequently, it predicts the curves to continue as if the Y-H system forever remained in the α-Y phase. Moreover, disregarding hydride formation would mean that there is no maximum saturation concentration of the yttrium pebbles and that the pebble bed could take up an infinite amount of hydrogen isotopes. However, the possibility of the trap being exhausted once the pebbles have entirely transformed to yttrium

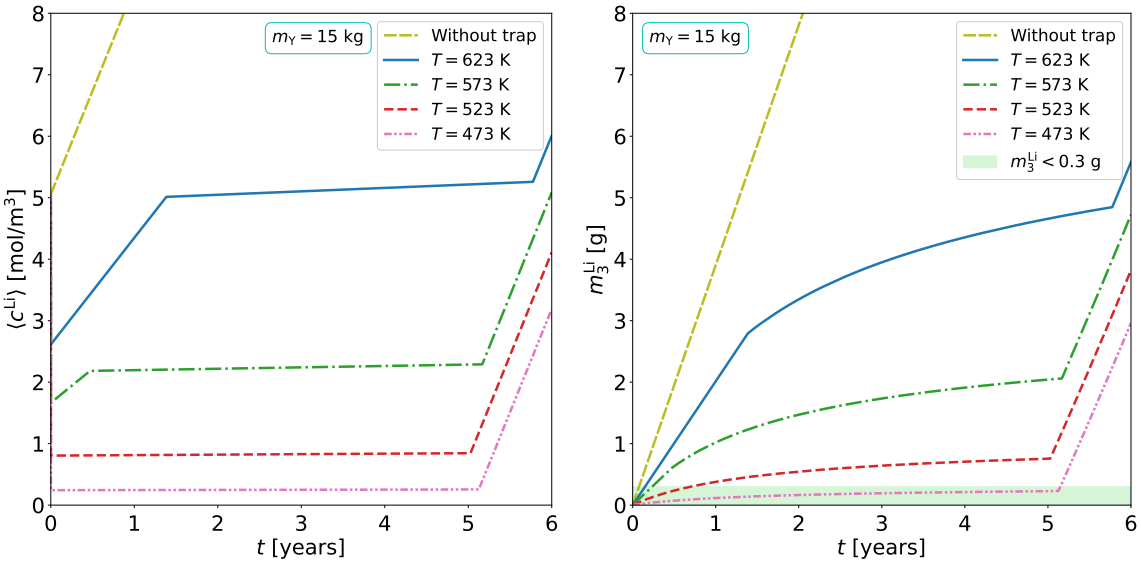

Fig. 7.21. [Left] Simulated average total hydrogen isotope concentration in lithium during DONES experimental phase at different temperatures assuming a single hydrogen trap with a pebble bed mass of $m_Y = 15$ kg is used throughout the lifetime of DONES. [Right] Simulated mass of tritium in the lithium during DONES experimental phase at different temperatures assuming a single hydrogen trap with a pebble bed mass of $m_Y = 15$ kg is used throughout the lifetime of DONES.

dihydride is a critical safety consideration and must be taken into account in the design of the hydrogen trap for DONES. This is another reason why the inclusion of hydride formation in the model is so important.

The left-hand plot in figure 7.21 presents the simulated evolution of the average total hydrogen isotope concentration in the loop at different temperatures, considering a trap with a fixed pebble bed mass of $m_Y = 15$ kg. It is found that at $T = 473$ K and $T = 523$ K, the initial concentration drop proceeds according to the third scenario defined in section 7.6.1, meaning that hydride formation starts right at the beginning. The figure shows that the height of the steady state plateau increases with temperature. This is in accordance with the temperature dependencies of the critical concentrations c_-^{Li} and c_+^{Li} depicted by figure 7.10. Moreover, it is observed that the time period hydride formation lasts decreases with increasing temperature. According to equation (7.75) and figure 7.8, this is due to the fact that the width of the concentration range assigned to the $\alpha \rightarrow \delta$ phase transition regime of the Y-H system narrows with increasing temperature.

The right-hand plot in figure 7.21 displays the simulated evolution of the tritium content dissolved in lithium which results from a trap with a mass of $m_Y = 15$ kg. Instead of abruptly entering into a flat stationary state, during hydride formation, the tritium inventory increase slows down rather smoothly until saturation occurs. This behavior is explained by equation (7.81) considering that due to the large amount of protium in the system $\varkappa_3^{Li}/\varkappa^{Li} < \dot{\varkappa}_{3,gen}/\dot{\varkappa}_{gen}$. It is found that at $T = 473$ K the establishing stationary concentration is low enough to keep the ^{3}H inventory below the DONES safety limit $m_{3,limit}^{Li} = 3 \times 10^{-4}$ kg for more than five years.

Case B: Replaced hydrogen traps

Indeed, since the amount of generated tritium in the loop follows the relation $\dot{\varkappa}_{3,\mathrm{gen}} \cdot t = \varkappa_3^{\mathrm{Li}} + \varkappa_3^{\mathrm{Y}}$, using a single trap for the entire DONES lifetime to satisfy $m_3^{\mathrm{Li}} < m_{3,\mathrm{limit}}^{\mathrm{Li}} = 3 \times 10^{-4}\,\mathrm{kg}$ would at some point violate the second imposed tritium safety requirement $m_3^{\mathrm{Y}} < m_{3,\mathrm{limit}}^{\mathrm{Y}} = 3{\times}10^{-4}\,\mathrm{kg}$. Nevertheless, the calculations in the previous section show that hydride formation in a sufficiently large trap prevents the concentration in the lithium from increasing above a certain temperature-dependent value for several years. This effect can be regarded a natural safety control system that is triggered in the event of an accidental, uncontrolled increase in concentration occurring in the DONES lithium loop.

One proposed method to meet both limits at all times is to frequently replace the installed hydrogen trap before the tritium contents in both the lithium and the yttrium exceed the limits [99].

To determine an appropriate operating temperature, pebble bed mass, and trap replacement period τ_{trap} it is considered that a non-exhausted hydrogen trap operates in a state in which it is least efficient, i.e., when the yttrium pebbles occur in the α-Y phase where no hydride formation occurs.

As the DONES experimental phase starts, the tritium contents in both metals begin to grow. It is imagined that once an arbitrary tritium content $m_{3,\mathrm{max}}^{\mathrm{Li}}$ in the lithium is reached, the trap is replaced by an empty trap. As a result, the tritium content in the lithium decreases within a short period of time before it reaches an equilibrium, similar to the initial concentration decrease shown in figure 7.19. By hypothetically assuming that the concentration decrease occurs instantaneously, the value of the equilibrium tritium content in the lithium can be calculated with equation (7.63)

$$m_{3,\mathrm{eq}}^{\mathrm{Li}} = \frac{m_{3,\mathrm{max}}^{\mathrm{Li}} V_{\mathrm{Li}}}{V_{\mathrm{Li}} + V_{\mathrm{Y}} K_{\mathrm{D},0}^{\mathrm{Li-Y}}} \,. \tag{7.83}$$

While the tritium content in the lithium plunges, the mass of absorbed tritium m_3^{Y} in the new yttrium pebble bed quickly rises until the concentration profiles in the pebbles are flat. For the reasons discussed in the previous subsection Case A, it can be assumed that, in spite of the proceeding hydrogen isotope generation, from this moment onwards the pebbles approximately remain in thermodynamic equilibrium with the lithium system. Therefore, boundary condition (7.21) is approximately satisfied and yields

$$m_3^{\mathrm{Y}} = \frac{V_{\mathrm{Y}}}{V_{\mathrm{Li}}} \cdot K_{\mathrm{D},0}^{\mathrm{Li-Y}} \cdot m_3^{\mathrm{Li}} \,. \tag{7.84}$$

Moreover, the assumed thermodynamic equilibrium implies that the progressive production of hydrogen isotopes in the loop causes the tritium content in the two metals to increase approximately linearly, with slopes given by the equations (7.71) and (7.72). Therefore, the time evolution of the slowly increasing tritium content in the lithium after the trap exchange is approximately described by

$$m_3^{\mathrm{Li}} = \dot{\varkappa}_{3,\alpha}^{\mathrm{Li}} M_3 \cdot t + m_{3,\mathrm{eq}}^{\mathrm{Li}} \,. \tag{7.85}$$

Inserting the equations (7.72) and (7.83) into equation (7.85) and replacing m_3^{Li} with the maximum tritium content $m_{3,\mathrm{max}}^{\mathrm{Li}}$ that occurred in the lithium just before the trap was replaced gives the time τ_{trap} it will take for the tritium content in lithium to rise back to the same maximum value $m_{3,\mathrm{max}}^{\mathrm{Li}}$ as prior to the trap replacement

$$\tau_{\mathrm{trap}} = \frac{m_{3,\mathrm{max}}^{\mathrm{Li}} V_{\mathrm{Y}} K_{\mathrm{D},0}^{\mathrm{Li-Y}}}{M_3 V_{\mathrm{Li}} \dot{\varkappa}_{3,\mathrm{gen}}} \,. \tag{7.86}$$

Transforming equation (7.86) yields the maximum inventory of tritium in the lithium $m_{3,\mathrm{max}}^{\mathrm{Li}}$ that establishes at a given value of τ_{trap}.

$$m_{3,\mathrm{max}}^{\mathrm{Li}} = \frac{V_{\mathrm{Li}} M_3}{V_{\mathrm{Y}} K_{\mathrm{D},0}^{\mathrm{Li-Y}}} \cdot \dot{\varkappa}_{3,\mathrm{gen}} \cdot \tau_{\mathrm{trap}} \,. \tag{7.87}$$

Substituting equation (7.87) into equation (7.84) provides the value of the maximum tritium content which occurs in the yttrium bed after the time τ_{trap} has elapsed

$$m_{3,\mathrm{max}}^{\mathrm{Y}} = M_3 \dot{\varkappa}_{3,\mathrm{gen}} \cdot \tau_{\mathrm{trap}} \,. \tag{7.88}$$

Therefore, if the trap is replaced with a period τ_{trap} the tritium contents in the lithium and the yttrium bed are maintained below their maximum values given by the equations (7.87) and (7.88), respectively.

From equation (7.88) it follows that in order to satisfy the safety condition $m_3^{\mathrm{Y}} < m_{3,\mathrm{limit}}^{\mathrm{Y}} = 3 \times 10^{-4}\,\mathrm{kg}$ the trap needs to be replaced every

$$\tau_{\mathrm{trap}} < \tau_{\mathrm{trap}}^{\mathrm{max}} \equiv \frac{m_{3,\mathrm{limit}}^{\mathrm{Y}}}{\dot{\varkappa}_{3,\mathrm{gen}} M_3} = 28\,\mathrm{days} \,. \tag{7.89}$$

If $\tau_{\mathrm{trap}} = \tau_{\mathrm{trap}}^{\mathrm{max}}$, the adjusting maximum tritium content in the lithium given by equation (7.87) is

$$m_{3,\mathrm{max}}^{\mathrm{Li}} = \frac{V_{\mathrm{Li}} m_{3,\mathrm{limit}}^{\mathrm{Y}}}{V_{\mathrm{Y}} K_{\mathrm{D},0}^{\mathrm{Li-Y}}} \,. \tag{7.90}$$

The requirement for the pebble bed mass to meet the other limit $m_3^{\mathrm{Li}} < m_{3,\mathrm{limit}}^{\mathrm{Li}} = 3{\times}10^{-4}\,\mathrm{kg}$ is determined by inserting $m_{3,\mathrm{limit}}^{\mathrm{Li}}$ into equation (7.87)

$$m_{\mathrm{Y}} > m_{\mathrm{Y}}^{\mathrm{min}}\left(\tau_{\mathrm{trap}}\right) = \frac{V_{\mathrm{Li}} \rho_{\mathrm{Y}} M_3}{m_{3,\mathrm{limit}}^{\mathrm{Li}} K_{\mathrm{D},0}^{\mathrm{Li-Y}}} \cdot \dot{\varkappa}_{3,\mathrm{gen}} \cdot \tau_{\mathrm{trap}} \,. \tag{7.91}$$

The minimum required pebble bed mass is highest in case the maximum permissible replacement period of $\tau_{\mathrm{trap}}^{\mathrm{max}}$ is chosen. In this case, the requirement for the yttrium mass m_{Y} is obtained by inserting equation (7.89) into equation (7.91)

$$m_{\mathrm{Y}} > m_{\mathrm{Y}}^{\mathrm{min}}\left(\tau_{\mathrm{trap}}^{\mathrm{max}}\right) = \frac{V_{\mathrm{Li}} \cdot \rho_{\mathrm{Y}}}{K_{\mathrm{D},0}^{\mathrm{Li-Y}}} \,. \tag{7.92}$$

The relative error of $m_{\mathrm{Y}}^{\mathrm{min}}$ is given by

$$\Delta^{\pm} m_{\mathrm{Y}}^{\mathrm{min}} \equiv \frac{\Delta^{\pm} K_{\mathrm{D},0}^{\mathrm{Li-Y}}}{K_{\mathrm{D},0}^{\mathrm{Li-Y}}} \cdot m_{\mathrm{Y}}^{\mathrm{min}} \,. \tag{7.93}$$

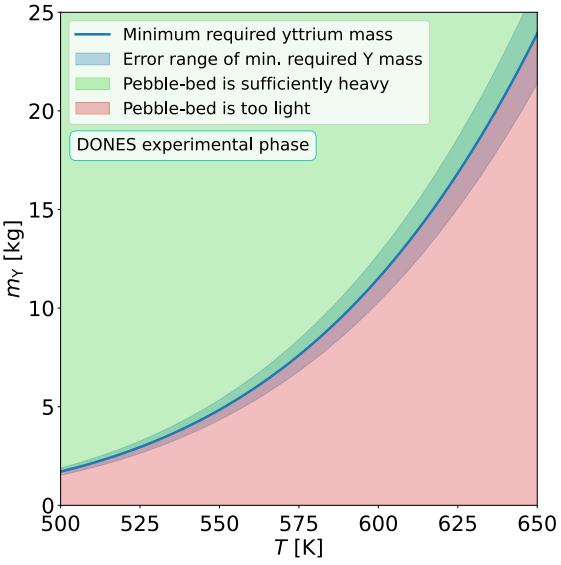

Fig. 7.22. Minimum pebble bed mass required to meet the tritium limits in yttrium and lithium during DONES experimental phase if the trap it is replaced every $\tau_{\text{trap}}^{\text{max}} = 28\,\text{days}$.

Figure 7.22 presents a plot of the temperature-dependent minimum pebble bed mass and its error range required to meet the imposed tritium limits of the DONES experimental phase considering that the trap is replaced every $\tau_{\text{trap}}^{\text{max}} = 28\,\text{days}$. The design parameters should be chosen such that they are located in the green shaded area, outside of the plotted error range. Traps with a mass and operating temperature in the red area would cause the tritium content in the lithium to level out above the limit value $m_{3,\text{limit}}^{\text{Li}}$.

In contrast to the above thought experiment, in a real DONES operating scenario, it is not waited until the tritium contents in the yttrium and lithium reach their maximum permissible values before the trap is exchanged. Instead, the trap replacement procedure is started from the beginning with a fixed replacement period τ_{trap}. As a result, the tritium contents in both lithium and yttrium converge toward their maximum values determined by the equations (7.87) and (7.88) over the course of several replacement iterations.

From the equations (7.92) and (7.93) it follows that if $\tau_{\text{trap}} = \tau_{\text{trap}}^{\text{max}}$, the minimum required yttrium mass at $T = 623\,\text{K}$ is $m_{\text{Y}} = (16.4 \pm 1.7)\,\text{kg}$ (see figure 7.22). The simulated temporal evolutions of the tritium contents in the yttrium and the lithium, that result from such a pebble bed mass and operating temperature, are showcased in the two plots in figure 7.23 for different exchange periods, respectively. It can be seen that the shorter the trap exchange period, the faster the tritium contents in the two metals converge toward their maximum values. The left-hand plot in figure 7.23 confirms the prediction from equation (7.92), that for an exchange period of $\tau_{\text{trap}}^{\text{max}} = 28\,\text{days}$ the maximum tritium content in the pebble bed matches $m_{3,\text{limit}}^{\text{Y}}$. Moreover, the right-hand plot in figure 7.23 verifies that if at $T = 623\,\text{K}$ the yttrium mass is $m_{\text{Y}} = (16.4 \pm 1.7)\,\text{kg}$ and $\tau_{\text{trap}} = \tau_{\text{trap}}^{\text{max}}$ the maximum adjusting concentration in the lithium is indeed converging against the value $m_{3,\text{limit}}^{\text{Li}}$. If the exchange period is longer, the tritium contents in the bed and the lithium level out at higher values $m_3^{\text{Y}} > m_{3,\text{limit}}^{\text{Y}}$ and $m_3^{\text{Li}} > m_{3,\text{limit}}^{\text{Li}}$. This must be prevented at all costs. A shorter replacement period allows maintaining the tritium contents in both metals at values below the limit contents without changing the pebble bed mass or temperature.

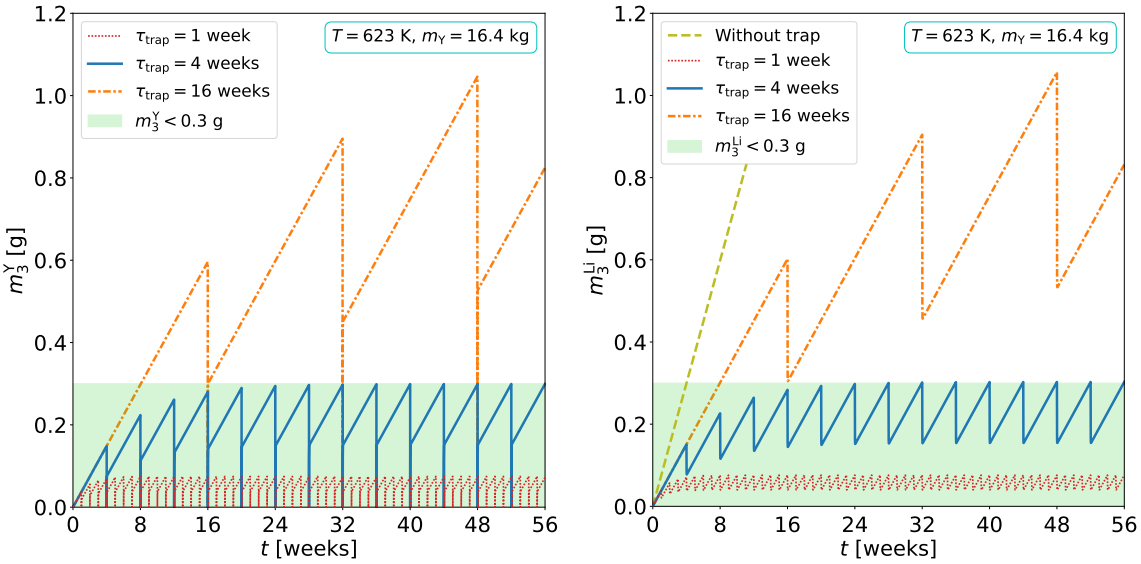

Fig. 7.23. [Left] Simulated evolution of the tritium content in the yttrium pebble bed during DONES experimental phase for different trap exchange periods assuming an yttrium mass of m_Y = 16.4 kg and a temperature of T = 623 K. [Right] Simulated evolution of the tritium content in lithium during DONES experimental phase for different trap exchange periods assuming an yttrium mass of m_Y = 16.4 kg and a temperature of T = 623 K.

The figures also demonstrate that if the pebble bed mass has the value given by equation (7.92) and $\tau_{trap} = \tau_{trap}^{max}$, the maximum tritium contents in the lithium and the yttrium are equal.

The left-hand plot in figure 7.24 presents the simulated time evolution of the tritium content in lithium at a fixed temperature T = 623 K and replacement period $\tau_{trap} = \tau_{trap}^{max}$, varying only the pebble bed mass. The plot validates equation (7.90) according to which the adjusting maximum tritium content in lithium increases with decreasing pebble bed mass. When choosing $\tau_{trap} = \tau_{trap}^{max}$, the maximum tritium content in yttrium is $m_3^Y = m_{3,limit}^Y$, regardless of the observed temperature and yttrium mass [see equation (7.88)].

The variation of the adjusting maximum tritium content in lithium that occurs when changing the temperature at a fixed pebble bed mass of m_Y = 7.5 kg and fix trap replacement period $\tau_{trap} = \tau_{trap}^{max}$ is depicted in the right-hand plot in figure 7.24. In this case, the value of m_3^{Li} is determined by equation (7.90). It is found that m_3^{Li} increases with temperature. The reason for this is that $K_{D,0}^{Li-Y}$ decreases with increasing temperature [see equation (7.52)].

The temporal evolutions of the average protium, deuterium, tritium, and total hydrogen isotope concentrations in the lithium that occur when a trap with m_Y = 16.4 kg operating at T = 623 K is replaced with an exchange period of $\tau_{trap} = \tau_{trap}^{max}$ is shown in the left-hand plot in figure 7.25. The plots reveal that during several trap replacements the average protium concentration which starts at a value of $\langle c_1^{Li} \rangle$ = 5.1 mol/m^3 is gradually reduced before it keeps oscillating at a constant level. In contrast, the average deuterium

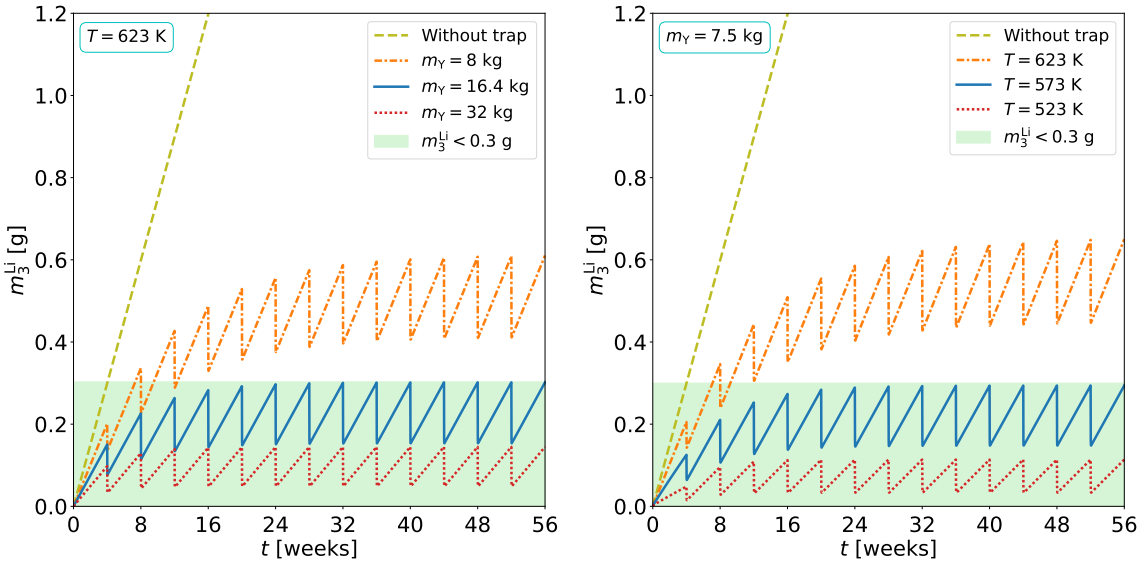

Fig. 7.24. [Left] Simulated evolution of the tritium content in lithium during DONES experimental phase for different pebble bed masses assuming a temperature of $T = 623$ K and a trap replacement period of $\tau_{\text{trap}} = 28$ days. [Right] Simulated evolution of the tritium content in lithium during DONES experimental phase for different temperatures assuming a pebble bed mass of $m_Y = 7.5$ kg and a trap replacement period of $\tau_{\text{trap}} = \tau_{\text{trap}}^{\text{max}}$.

and tritium concentrations approach their equilibrium values from below. Regardless of whether the initial concentration is zero or higher, the maximum concentration values below which the individual average concentrations will oscillate after several replacement iterations are determined by equation (7.87), in which the tritium generation rate and the molar mass must be replaced by the corresponding values of the observed isotope. It is evident that the values to which the concentrations of the different isotopes converge increase with increasing temperature and decreasing mass of the pebble bed. The left-hand plot in figure 7.25 shows that if the tritium limits for both the lithium and the yttrium are satisfied, the average total hydrogen isotope concentration in lithium levels out considerably below a value where hydride formation would be triggered. However, at lower temperatures, hydride formation might occur during the first trap replacement iterations when the total hydrogen isotope concentration is still relatively high. According to the findings of the last section, hydride formation would keep the concentration in lithium stationary until the trap is exchanged.

The simulated effects a changing pebble diameter, the lithium flow rate through the pebble bed, or aspect ratio of the trap container have on the concentration dynamics can be seen in the right-hand graph in figure 7.25. It shows the evolution of the average total hydrogen isotope concentration which is plotted in the left-hand plot in figure 7.25, magnified to day 336. First, it is found that a variation of the secondary parameters only affects the time to reach the intermediate equilibrium each time the trap is exchanged. It has no influence on the maximum establishing concentration in the lithium. For the reasons discussed in section 7.6.1 the time that elapses before the intermediate equilibrium

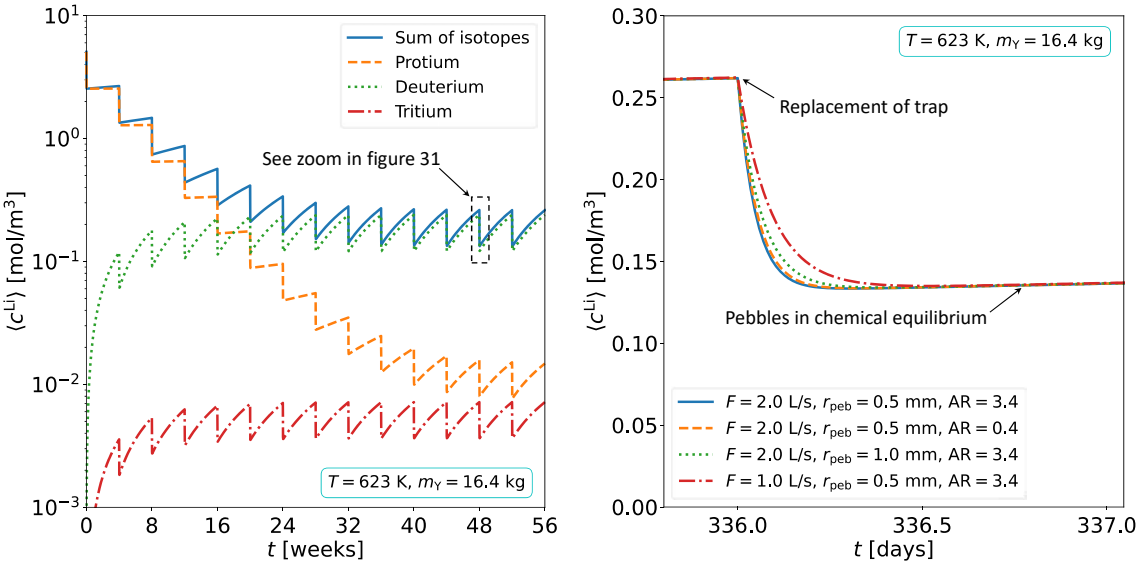

Fig. 7.25. [Left] Simulated evolutions of the average protium, deuterium, tritium, and total hydrogen isotope concentrations in lithium during DONES experimental phase if the yttrium pebble bed mass is $m_Y = 16.4\,\text{kg}$, the temperature is $T = 623\,\text{K}$ and assuming the hydrogen trap is exchanged with the period $\tau_{trap} = 28\,\text{days}$. Such configuration would comply with the DONES safety limits. [Right] Simulated total hydrogen isotope concentration in lithium at the moment of a trap replacement during DONES experimental phase if the yttrium pebble bed mass is $m_Y = 16.4\,\text{kg}$, the temperature is $T = 623\,\text{K}$ and assuming the hydrogen trap is exchanged with the period $\tau_{trap} = 28\,\text{days}$. The simulation is performed for different pebble diameters, lithium flow rates through the pebble bed, and aspect ratios of the trap container.

is established increases with increasing pebble diameter and decreasing flow rate. In contrast to the right-hand plot in figure 7.18, since no hydride formation takes place a reduced aspect ratio is found to slightly delay the concentration drop. Due to a smaller diffusion coefficient a lower temperature would delay the time to reach the intermediate equilibrium (see left-hand plot in figure 7.18).

7.6.3. Experimental validation of the model

Finally, the presented numerical model is tested against experimental results obtained by Yamasaki *et al* [112]. In their experiments, $m_{Li} = 0.6\,\text{kg}$ of liquid lithium at $T = 573\,\text{K}$ is loaded with an initial deuterium concentration of $c^{Li}_{2,init} = 160\,\text{wppm} = 40.1\,\text{mol}\,\text{m}^{-3}$ before it is set in motion through an experimental liquid lithium circuit connected in line with an yttrium getter bed. The trap container used for the experiments has a length of $l_{trap} = 0.3\,\text{m}$ and contains $m_Y = 1 \times 10^{-2}\,\text{kg}$ of thin yttrium chips with a diameter of 2 - 3 mm. The lithium flow rate through the trap is reported to be $F_{trap} = 2.5 \times 10^{-5}\,\text{m}^3\,\text{s}^{-1}$. As soon as the deuterium-loaded lithium passes the pebble bed, its deuterium content is continuously reduced. Yamasaki *et al* measured the decrease in deuterium concentration that occurred after five time periods of different lengths using the chemical dissolution method [112]. Figure 7.26 shows the ratios between the measured concentration $\langle c^{Li}_2 \rangle$ of

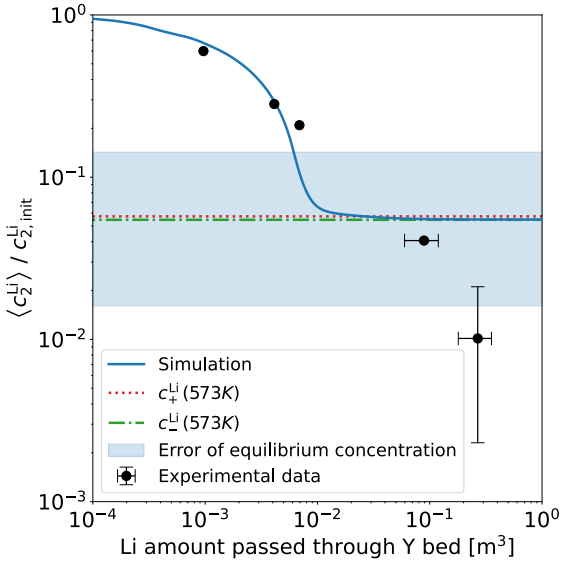

Fig. 7.26. Ratios between the measured average deuterium concentration of extracted lithium samples that were exposed to an yttrium getter bed and the initial deuterium concentration in the lithium prior to the contact with the yttrium. The ratios were measured in deuterium retention experiments performed by Yamasaki *et al* [112]. The graph contains a simulation reproducing the experimental values with the developed numerical model.

the extracted lithium samples and the initial deuterium concentration $c_{2,\text{init}}^{\text{Li}}$ in the lithium as a function of the lithium volume that has passed through the trap [112].

The described experiment is numerically reproduced using the presented EcosimPro© model illustrated in figure 7.1. Therefore, it is assumed that $F_{\text{main}} = F_{\text{trap}} = 2.5 \times 10^{-5}\,\text{m}^3\,\text{s}^{-1}$. Moreover, the simulation considers a pebble radius of $r_{\text{peb}} = 5 \times 10^{-4}\,\text{m}$. The void fraction and diameter of the pebble bed is set to $\varepsilon = 0.6$ and $d_{\text{trap}} = 5 \times 10^{-3}\,\text{m}$ which implies that the simulated trap has a length of $l_{\text{trap}} \approx 2.8 \times 10^{-1}\,\text{m}$. The discretization densities of the trap and pipe segments are set to the same values as in the simulations discussed in the previous sections.

The performed numerical reproduction of Yamasaki's experimental data is plotted with a solid blue line in figure 7.26. It can be seen that the simulation agrees very well with the first four data points. The last data point is located well below the simulated curve.

When analyzing the observed purification process, it can be certainly excluded that the pebbles in Yamasaki's experiment have completely transformed to pure δ-$YH_{2\pm x}$. There is just not enough deuterium in the system to load an yttrium mass of $m_{\text{Y}} = 1 \times 10^{-2}\,\text{kg}$ with a homogeneous saturation concentration of $c_{\delta\text{-start}}^{\text{Y}}$. Therefore, the establishing equilibrium concentration in Yamasaki's experiment must have satisfied the condition $c_{\text{eq}}^{\text{Li}} < c_+^{\text{Li}}(573\,\text{K})$ (see figure 7.10). The two critical concentrations $c_-^{\text{Li}}(573\,\text{K})$ and $c_+^{\text{Li}}(573\,\text{K})$ are plotted together with their overlapped error range (blue shaded area) in figure 7.26. It is found that the simulated concentration levels out in the concentration range $c_-^{\text{Li}} < c_{\text{eq}}^{\text{Li}} < c_+^{\text{Li}}$. Hence, according to the simulation, at thermodynamic equilibrium, the yttrium chips in Yamasaki's experiment occur in the $\alpha \rightarrow \delta$ transition regime. Given that $c_{\text{eq}}^{\text{Li}} < c_+^{\text{Li}}(573\,\text{K})$, an overestimation of the critical concentrations c_-^{Li} and c_+^{Li} implies an overestimation of the simulated equilibrium concentration.

In fact, the error range of the critical concentrations shaded in blue can be considered

as the error range of the simulated equilibrium concentration. As the equations (7.37), (7.48) and (7.50) indicate, this error range is mainly determined by the errors of the Sieverts' constants of the Li-H and Y-H systems and therefore by the error of the low-concentration distribution coefficient (7.52) of the Li-Y-H system. Figure 7.26 shows that the error bar of the last experimental data point enters deep into the error range of the simulated equilibrium concentration (see right-hand plot in figure 7.25). Therefore, it is reasonable to say that the simulation results and the experimental data match within their error ranges.

The experimental data suggests that the model rather underestimates the hydrogen gettering capacity of yttrium in liquid lithium. For this reason, designing the hydrogen trap of DONES based on simulations performed with the presented model would probably lead to a slightly oversized trap. Nevertheless, from a safety point of view, this is beneficial.

8. DEVELOPMENT OF THE LYDER EXPERIMENT

The last chapter proves that a numerical model capable of simulating hydrogen transport from flowing liquid lithium into an yttrium getter trap is a helpful tool to comprehend and simulate the physical mechanisms that determine the dynamics of the occurring hydrogen transport processes. Only by having access to such a tool is it possible to determine appropriate design parameters for the hydrogen trap of DONES that will ensure reaching concentration safety limits in a reasonable period of time. In section 7.6.3, the developed numerical model could be validated by demonstrating that the reproduction of experimental data succeeds when taking into account the error ranges of both experimental data and simulation results. The relatively large error range of the simulated experimental results in figure 7.26 is found to be mainly due to the uncertainty of the low-concentration distribution coefficient $K_{\mathrm{D},0}^{\mathrm{Li-Y}} = K_{\mathrm{s}}^{\mathrm{Y}}/K_{\mathrm{s}}^{\mathrm{Li}}$. In fact, besides the inaccuracies of the assumed low-concentration hydrogen diffusivities in lithium and yttrium, the error of $K_{\mathrm{D},0}^{\mathrm{Li-Y}}$ turns out to be the main source of error of the model. This is because, up to the critical concentration $c_{-}^{\mathrm{Li}} = c_{\alpha\text{-end}}^{\mathrm{Y}}/K_{\mathrm{D},0}^{\mathrm{Li-Y}}$, boundary condition (7.19) visualized in the right-hand plot in figure 7.9 is mainly determined by the value of the low-concentration distribution coefficient [see equation (7.21)]. In addition, the error of the critical concentration c_{-}^{Li} (threshold concentration for hydride formation and great increase in gettering capacity) depends entirely on the accuracy of $K_{\mathrm{D},0}^{\mathrm{Li-Y}}$. For these reasons, as long as the pebbles are not fully transformed into the δ-$YH_{2\pm x}$ phase, the error ranges of the minimum required trap masses for DONES shown in the figures 7.17 and 7.22 are mainly due to the uncertainty of $K_{\mathrm{D},0}^{\mathrm{Li-Y}}$. Hence, increasing the accuracy of the model requires reducing the error range of the assumed distribution coefficient and additional experimental validation of the developed model by performing in-situ deuterium retention experiments.

For this purpose, a new liquid lithium experiment is designed and constructed within the scope of this thesis. It is called the LYDER (Lithium system for Yttrium-based DEeuterium Retention experiments) experiment and is part of the liquid metals laboratory of the Ciemat Institute. Besides being designed to validate the numerical model and to measure the distribution coefficient, the LYDER experiment has the goal of testing critical liquid metal technologies that are developed in this work. That is a system for injecting deuterium into liquid lithium, an experimental hydrogen hot trap and a system for sampling from a liquid lithium circuit. The experimental design and planned experimental procedure of the LYDER experiment are described in this chapter.

8.1. Design input parameters

The following paragraphs justify the established input design parameters on which basis the LYDER experiment is designed. They are listed in table 8.1. Since the ultimate goal of

TABLE 8.1
ESTABLISHED INPUT DESIGN PARAMETERS OF THE LYDER EXPERIMENT.

Design parameter	Parameter range / applied technique / materials
Operating temperature	$523\,\mathrm{K} < T < 623\,\mathrm{K}$
Working atmosphere	Argon
Piping material	316 stainless steel
Pressure range in lithium circuit	$1 \times 10^{-2}\,\mathrm{Pa} < p < 2 \times 10^{5}\,\mathrm{Pa}$
Lithium flow propulsion	Differential pressure
Lithium volume	$V_{\mathrm{Li}} = 100\,\mathrm{mL}$
Lithium flow rate	$F_{\mathrm{trap}} = 50\,\mathrm{mL\,min^{-1}}$
Max. injected ^{2}H concentration in Li	$c_2^{\mathrm{Li}} < 40\,\mathrm{mol\,m^{-3}}$
Yttrium capacity of the trap	$m_{\mathrm{Y}}^{\mathrm{max}} = 5 \times 10^{-3}\,\mathrm{kg}$

the research conducted is to gain the knowledge necessary to develop a reliable hydrogen trap for DONES, the LYDER experiment is designed to operate in a DONES-relevant temperature range of $523\,\mathrm{K} < T < 623\,\mathrm{K}$, where lithium is in its liquid state.

Although lithium is the least reactive of the alkali metals, it undergoes many chemical reactions [282]. When catalyzed by the presence of moisture, lithium reactions with the air molecules N_2, O_2, CO_2 become exothermic, resulting in the formation of Li_3N, Li_2O, and Li_2CO_3 compounds. These reactions can cause the lithium to ignite spontaneously. The ignition temperature depends on the pressure, composition and humidity of the surrounding air, but is somewhere in the range of $458\,\mathrm{K} < T < 913\,\mathrm{K}$. Of particular importance is the exothermic reaction of lithium with water molecules, producing LiOH and $^1H_2$ gas. Especially in its liquid state, the lithium-water reactions occur vigorously. However, the main problem associated with this reaction is the generation of $^1H_2$ gas, which in the presence of air can result in an oxyhydrogen explosion. Furthermore, at the operating temperature of the LYDER experiment, the compounds Li_3N, Li_2CO_3, Li_2O, and LiOH are solid and have a higher density than liquid lithium, leading to erosion of these particles on the tube bottoms [282]. As a result, the pipe system can become clogged with solid particles over time. Moreover, elevated concentrations of these compounds in the liquid lithium significantly increases corrosion [282]. Therefore, it is essential to perform the LYDER experiment in an inert gas atmosphere specially purified from N_2, O_2, CO_2, ^1H_2O molecules. The inert working gas chosen for the LYDER experiment is argon.

Very few materials withstand the corrosive nature of liquid lithium. In particular, the presence of Li_3N, Li_2O and LiOH compounds causes most materials to be severely attacked. Metals that show good long-term resistance in the relevant temperature range are Ti, Ta, Mo, Zr, Co-based alloys and austenitic stainless steels such as 316 and 304 stainless steel. However, the best corrosion resistance is found for pure α-iron [282]. To avoid the expensive manufacturing of custom-made tubing parts, the LYDER experiment is de-

signed to be constructed from standard 316 stainless steel piping components chemically pre-treated with pickling and passivation processes.

The operating pressure inside the lithium system is set to range from $p = 1 \times 10^{-2}$ Pa under vacuum conditions to $p = 1 \times 10^{5}$ Pa under pressurized conditions. To prevent exterior impurities from entering the lithium system or lithium from leaking, the chosen flanges and fittings connecting the pipes must be particularly leak-tight and have a reasonable over-pressure safety margin. Moreover, all gaskets, valves and piping components in contact with the lithium must be made of the above-mentioned lithium-resistant materials.

The LYDER facility is designed as a small-scale dynamic liquid metal system that operates with a relatively small volume of lithium in the liquid phase of only $V_{\mathrm{Li}} = 100\,\mathrm{mL}$. Therefore, there is not enough space to include a cold trap to retain O and C impurities or a titanium getter to remove N impurities. To compensate for the accumulation of impurities over time, the contaminated lithium is planned to be drained into a dump tank after each experiment. For this reason, it is necessary to be able to add new lithium to the system in a quick and easy manner without each time having to dismantle the piping system. In general, due to the lack of additional trap systems, it is important that the purchased lithium is very pure and contains only minimal amounts of N, C, O and ^{1}H impurities.

In order to study the performance of an experimental hydrogen trap exposed to flowing liquid lithium, it is necessary to set the lithium in motion by technical means. One possibility would be to install an electromagnetic liquid metal pump as used in the LIFUS (LIthium for FUSion) 6 experiment or planned for the DONES liquid lithium loop [283], [284]. This would allow the lithium to be moved in a closed loop with a well-controlled flow rate. However, due to the small volume of lithium manipulated in the LYDER experiment, this option is excluded. Instead, the movement of the lithium will be realized by differential pressure between two tanks and connected by a pipe and regulating valves for additional control of the flow rate. The experiments are aimed to be performed at a flow rate of about $F_{\mathrm{trap}} \approx 50\,\mathrm{mL\,min^{-1}}$ so that it takes about two minutes for the lithium to move from one tank to the other.

To perform deuterium retention experiments with the LYDER experiments, the liquid lithium must first be loaded with deuterium. Therefore, the LYDER system requires a specially designed deuterium injection system that enables control over the initially injected concentration $c^{\mathrm{Li}}_{2,\mathrm{init}}$. The lithium retention experiments are planned to be executed at concentrations relevant to the DONES lithium loop (see section 7.6). For this reason, the design of the deuterium injection system should allow loading the lithium with deuterium at concentrations in the range $c^{\mathrm{Li}}_{2} < 40\,\mathrm{mol\,m^{-3}}$.

To measure the low concentration distribution coefficient, it is necessary to allow the extraction of lithium samples and measure their deuterium concentrations. This is the purpose of a lithium sample extraction system with a removable sample container. The deuterium concentration in the extracted lithium samples is planned to be measured either by thermal desorption spectroscopy (TDS) as part of the LYDER infrastructure or

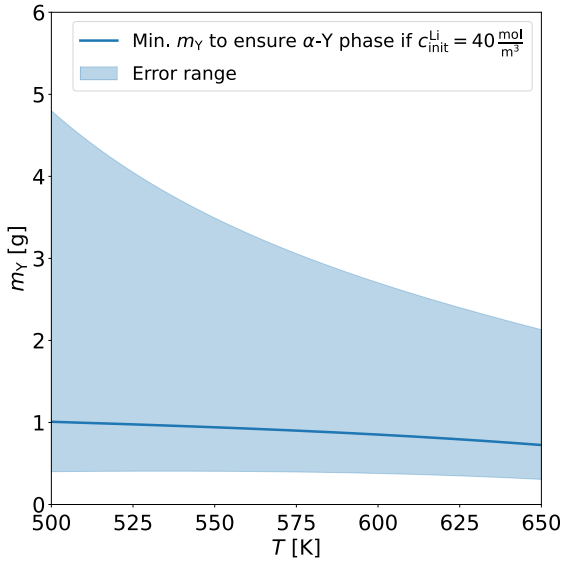

Fig. 8.1. Minimum yttrium bed mass required in the LYDER experiment to ensure a reduction from an initial deuterium concentration of $c^{\mathrm{Li}}_{2,\mathrm{init}} = 40\,\mathrm{mol\,m^{-3}}$ to the critical concentration below which the pebbles occur in the α-Y phase where equation (8.1) is valid.

by chemical dissolution in an external device [111], [285]. Executing deuterium retention experiments requires the installation of an experimental hydrogen trap (HT) with a removable yttrium getter bed. In the following, it is estimated how much yttrium is required to enable measurement of the low-concentration distribution coefficient. The estimation assumes that the level of protium impurities in the lithium is negligibly small compared to the concentration of injected deuterium.

The amount of yttrium exposed to the lithium must be large enough to reduce the concentration in the lithium sufficiently so that the yttrium pebbles occur in the α-Y phase after thermodynamic equilibrium is reached. According to the right-hand graph in figure 7.9, this is the case when the concentration in the lithium at equilibrium satisfies $c^{\mathrm{Li}}_{2,\mathrm{eq}} < c^{\mathrm{Li}}_{-}$. Only in this case, no yttrium dihydride formation occurs and the adjusting equilibrium concentration during a deuterium retention process is described by equation (7.64) which allows the low-concentration distribution coefficient to be expressed by

$$K^{\mathrm{Li-Y}}_{\mathrm{D},0} = \frac{\rho_{\mathrm{Y}} V_{\mathrm{Li}}}{m_{\mathrm{Y}}} \cdot \left(\frac{c^{\mathrm{Li}}_{2,\mathrm{init}}}{c^{\mathrm{Li}}_{2,\mathrm{eq}}} - 1 \right) \quad \text{if } c^{\mathrm{Li}}_{2,\mathrm{eq}} < c^{\mathrm{Li}}_{-} \,. \tag{8.1}$$

The formula shows that as long as $c^{\mathrm{Li}}_{2,\mathrm{eq}} < c^{\mathrm{Li}}_{-}$, the distribution coefficient can be calculated directly from the measured ratio $c^{\mathrm{Li}}_{2,\mathrm{eq}}/c^{\mathrm{Li}}_{2,\mathrm{init}}$ between the initial concentration and the equilibrium concentration. The minimum yttrium mass required to ensure $c^{\mathrm{Li}}_{2,\mathrm{eq}} < c^{\mathrm{Li}}_{-}$ to be satisfied is calculated with equation (7.64) by substituting $c^{\mathrm{Li}}_{\mathrm{eq}}$ for the temperature-dependent value of c^{Li}_{-} defined by equation (7.47). The minimum required yttrium mass increases with the initial concentration in the lithium and decreases with temperature. It is plotted in figure 8.1 assuming an initial concentration of $c^{\mathrm{Li}}_{2,\mathrm{init}} = 40\,\mathrm{mol\,m^{-3}}$ and a lithium volume of $V_{\mathrm{Li}} = 100\,\mathrm{mL}$. The error of $K^{\mathrm{Li-Y}}_{\mathrm{D},0}$ as assumed in the last chapter is taken into account by the plotted error range. This range suggests designing a trap that is large enough so that it can take up yttrium pieces with a total mass of $m_{\mathrm{Y}} = 5\,\mathrm{g}$.

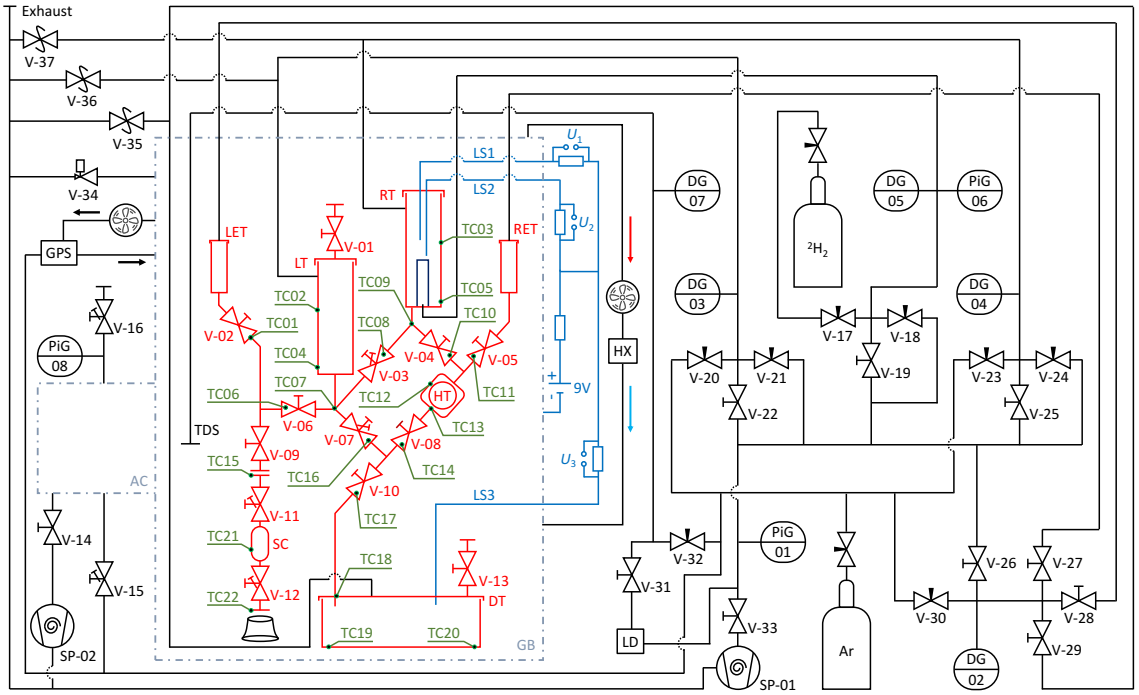

Fig. 8.2. Process flow diagram of the LYDER experiment.

8.2. Engineering design

The process flow diagram of the LYDER experiment is shown in figure 8.2. It can be seen that it consists of several subsystems. In general, a distinction should be made between those components that are directly in contact with the liquid lithium, the so-called lithium system, and external components that serve as auxiliary systems. In the PFD shown in figure 8.2, the lithium system is drawn in red. This indicates that the lithium system is heated, unlike all other subsystems of the LYDER experiment. A photo of the whole LYDER facility is shown in figure 8.3.

8.2.1. Homemade glove box

To prevent lithium from spilling into the open air in the event of a lithium leak and to avoid oxidation of lithium or yttrium samples during preparation, the lithium system of the LYDER experiment is mounted inside an argon-filled glove box (see dash-dotted line in figure 8.2). It is designed and fabricated on-site to fit the specific dimensions and pipe connections of the lithium system. The preliminary design of the glove box (GB) is developed by the author of this thesis using the CATIAv5 software. It has been reworked together with a professional draftsman of the Ciemat Institute to produce the final fabrication drawings, which can be found in section A.1 in the appendix. A photograph of the glove box immediately after its fabrication is shown in figure A.1. The glove box is made of welded 316 stainless steel plates with a thickness of 4×10^{-3} m and is closed by two polycarbonate windows sealed by FKM gaskets. Due to its large size of 1.6 m x 1.2 m

Fig. 8.3. Photo showing the various components of the LYDER experiment.

x 0.6 m the glove box is equipped with three glove ports in the lower window. A fourth glove port has been added to the top window in the center after the date of the photo.

The glove box incorporated into the LYDER system can be seen in figure 8.3. It has eight 1/2" pipe feedthroughs that pass the glove box roof and is equipped with ISO-40KF, DN40CF and DN100CF flanges at the roof and the side panels. A capacitance diaphragm pressure gauge (DG-07) attached to one of these flanges measures the pressure inside the glove box. The left-hand side of the glove box has an opening that is closed with a gasket-sealed square-shaped cover plate. It is penetrated by a DN250CF round feedthrough designed to be connected to a custom glove box antechamber (AC).

The design and construction of the antechamber has been realized within the scope of this thesis. It enables the insertion and removal of samples or tools into and out of the glove box without having to remove its argon atmosphere during operation. The fabrication drawings of the antechamber based on the three dimensional design developed by the author of this thesis can be found in section A.2 in the appendix. It involves a custom-made stainless steel drawer that can be moved into the glove box via a rail system (see photo in figure A.19). The antechamber can be opened to the inside atmosphere of the glove box and to the exterior environment of the laboratory via round FKM-sealed vacuum chamber doors. One of the DN40CF flanges at the roof of the antechamber is connected to a dry scroll vacuum pump with the name SP-02 via valve V-14 (see figure 8.2). A Pirani gauge (PiG-08) and a mechanical manometer control the pressure in the antechamber. The other DN40CF flange visible in figure A.19 is connected to an argon

gas line via the regulating open/close valve V-15 and to the surrounding air by valve V-16. Thus, the antechamber operates as an airlock which is evacuated before being refilled with either argon gas for sample insertion or air for sample removal.

On the right-hand side, the front panel of the glove box is attached to a stainless steel control panel. Its fabrication plan is made by the author of this thesis and can be found in figure A.18 in the appendix. It is designed to accommodate 3x 3U 19" rack drawers at the top. The large number of small holes in the center of the panel allows for the mounting of a valve tube manifold supported by pipe clamps attached to threaded rods. The panel is designed to allow the tubes to pass through the larger holes to the rear of the panel.

Furthermore, the glove box is connected to a Core-12 glove box purification system (GPS) from Jacomex [286]. It is the white box visible on the left in figure 8.3, standing on the floor next to the glove box. The unit is equipped with a fan that circulates the argon gas from the glove box through a system of getter beds which reduce the O_2 and ^1H_2O concentrations in the glove box atmosphere to below 1 ppm. This is controlled by internal O_2 and ^1H_2O concentration sensors. In addition, the purifier contains a pressure gauge that measures the pressure inside the glove box. The purifier allows the user to adjust the working pressure of the glove box. An internal valve opens and injects argon gas into the glove box when the pressure is too low and releases gas through the check valve V-34 when the pressure exceeds the set value. To reduce the leak rate of air molecules into the box, it is decided to operate the glove box at an argon pressure of approximately 5×10^2 Pa above atmospheric pressure. The purification unit is controlled by a touchscreen display mounted on the outer wall of the glove box in front of the antechamber (see figure 8.3).

The glove box is connected to a heat exchanger (HX) to prevent the temperature of the glove box atmosphere from rising more than a few Kelvins above the ambient temperature when the lithium system is heated. It is designed and developed within the scope of this thesis. The heat exchanger system can be seen mounted inside an aluminum frame at the bottom right-hand side of figure 8.3. It consists of a fan (the round cylinder at the bottom), the inlet of which is connected to the roof of the glove box above the lithium system using an ISO-40KF bellows tube. The gas flow exiting the blower is split into two parallel paths, each of which passes through a cylindrical heat exchanger. Both cylinders contain a spiral-shaped cooling water tube made of copper, the tube ends of which protrude out of the cylinder wall at the top and at the bottom (see figure 8.3). Cold water flows through the cooling pipes of the two heat exchangers where it heats up and thus dissipates about 1600 W of thermal power from the passing gas. The water flow is part of a water cooling cycle that is connected to a chiller that cools down the water before it passes again through the heat exchangers. After passing the heat exchangers the glove box gas reenters the glove box via a ISO-40KF bellows that is connected to a flange in the lower right corner of the glove box. Keeping the temperature of the argon gas low is important so that the pressure and gas sensors of the GPS do not exceed their maximum permissible operating temperature of about $T = 313$ K.

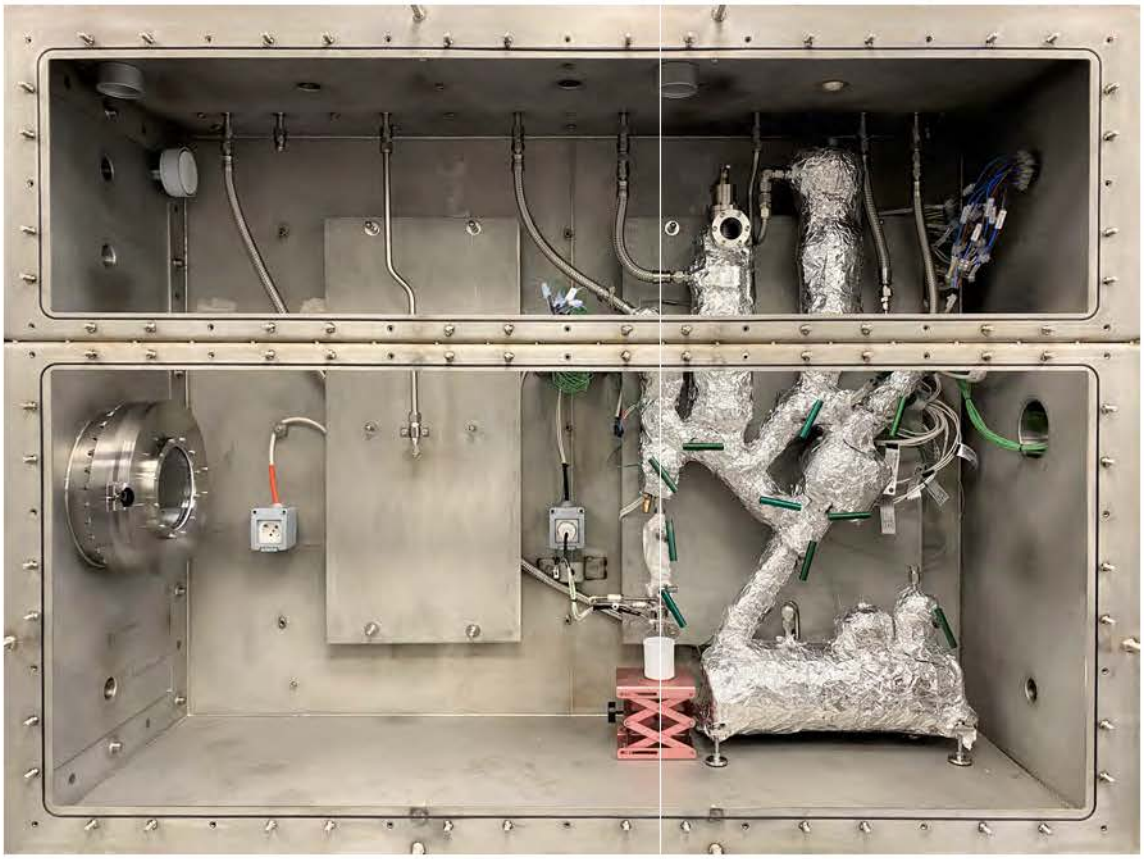

Fig. 8.4. Interior glove box components of the LYDER experiment involving a branch for TDS experiments on the left and the lithium system on the right.

Figure 8.4 shows the interior setup of the glove box. Two steel panels are bolted to the back wall of the glove box at a distance of about 5×10^{-2} m. They support two separate experimental systems. This is the thermal desorption branch on the left and the lithium system wrapped in ceramic thermal insulation wool and aluminum tape on the right. Both systems are described in the following sections.

8.2.2. Experimental lithium system

The engineering design of the lithium system is developed by the author of this dissertation using the CAD software CATIAv5. It is based on the input parameters that are specified in section 8.1. The 3D image of the design is presented in figure 8.5.

The lithium system comprises two tanks, a left tank (LT) and a right tank (RT). Both tanks are supported via stainless steel tube clamps bolted to the right-hand support panel of the lithium system in the back. The tanks consist of two 316 stainless steel CF nipples. Since standard copper CF gaskets would dissolve in liquid lithium, the nipple flanges are sealed with specially designed Helicoflex® gaskets made of an α-iron lining surrounding a Nimonic90 spring from Technetics [287]. They withstand temperatures up to $T = 723$ K and are suitable for pressures from high vacuum to at least $p = 2 \times 10^5$ Pa. To ensure that the CF seals are compressed with the required force regardless of the set operating

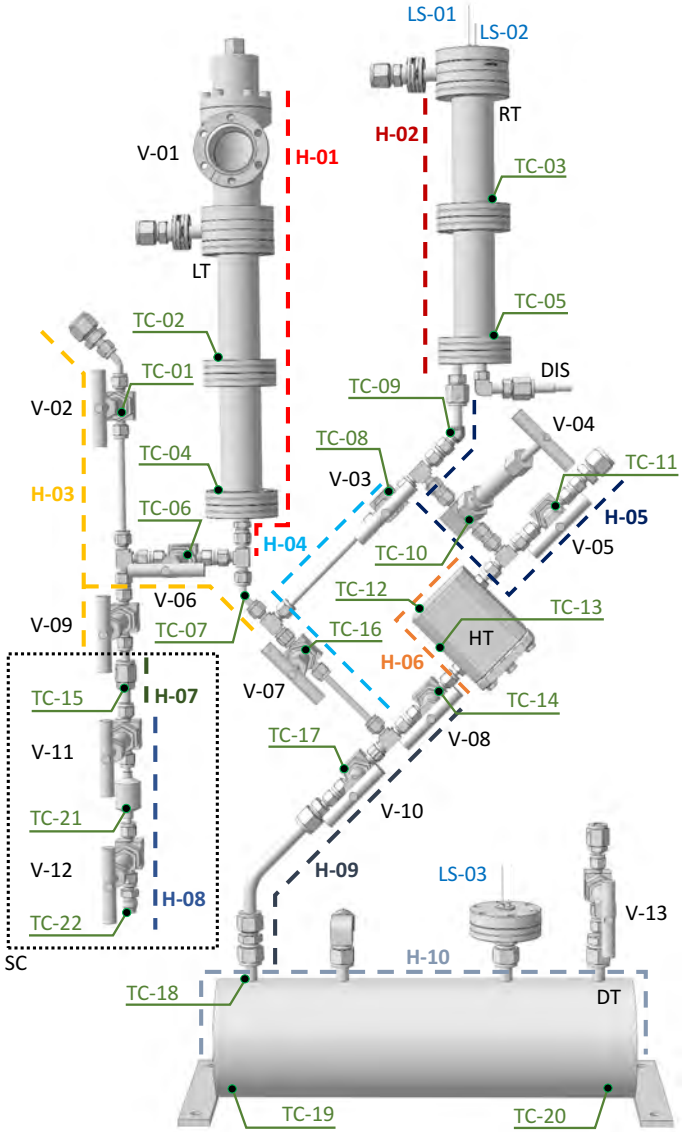

Fig. 8.5. Developed CAD model of the lithium system of the LYDER experiment showing the locations of the heaters, thermocouples, valves and lithium level sensors.

temperature, high-temperature M6 bolts made of Incoloy Alloy® A-286 [250] are used. The inner radius of the CF nipples is $r_{\text{in}}^{40\text{CF}} = 18.75 \times 10^{-3}$ m and each nipple has a length of 1.25×10^{-1} m. This means that a lithium volume of $V_{\text{Li}} = 100$ mL of molten lithium would not even exceed the central flanges of the tanks.

Attached to the top flange of the left tank is an all-metal high-temperature DN40CF open/close valve V-01 of the same type as that shown on the left in figure 3.5. The other flange of the valve is open towards the glove box atmosphere. This valve serves as a gate to insert small solid lithium samples into the left tank. The lithium pallets purchased for this purpose have a cylindrical shape with sizes of approximately ∅ 6 mm x 15 mm. One of the purchased lithium pallets can be seen in figure 8.6. They have a purity of 99.9 % and are packed in small argon-filled bags, each containing about $V_{\text{LI}} = 100$ mL of solid pallets. The impurity list reported by the supplier Neyco is presented in table 8.2. Not shown impurities are either lower than the content of Ni or negligibly small. Therefore, the acquired lithium samples meet the requirement of containing sufficiently low impurity levels of O, N, C, and H. The left tank serves as a lithium injection, melting and storage

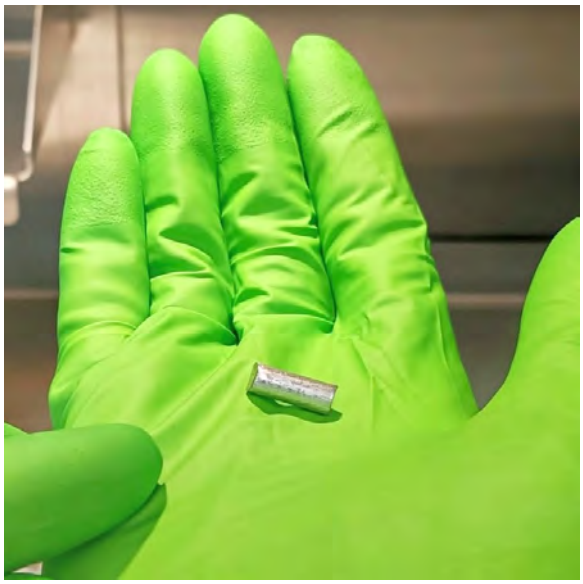

Fig. 8.6. Single lithium pallet with the shape and dimension as those purchased for the experimental campaign of the LYDER experiment.

TABLE 8.2
IMPURITY CONTENT IN [WPPM] OF THE LITHIUM SAMPLES WITH 99.9 % PURITY ACQUIRED TO FILL THE LITHIUM SYSTEM OF THE LYDER EXPERIMENT.

Ca	Na	Si	Fe	K	Al	Cu	Ni
200	200	80	50	50	50	40	30

container. It has an internal volume of about 275 mL. Hence, even if the inserted lithium pallets occupy only 36 % of the space in the tank, the entire volume of $V_{\mathrm{LI}} = 100\,\mathrm{mL}$ may be introduced and melted at once.

The right tank houses the custom-designed deuterium injection system (DIS) at its bottom and two lithium level sensors LS-01 and LS-02. The two level sensors are made of stainless steel conductors that penetrate the cap of the right tank via an electrical feedthrough. The conductor pins of the feedthrough terminate at two different heights in the open space inside the tank. Outside the tank, the pins of the feedthrough are connected to cables that leave the glove box through another electrical feedthrough (see figure 8.2). Here, each of the two cables is connected in line with an electric resistance and a 9V battery whose other pole is put in contact with the glove box stainless steel wall that is electrically connected to the lithium system. As soon as the liquid metal touches one of the level sensor conductor pins the corresponding electrical circuit closes and a voltage drop at the respective resistance is detected (see PFD in figure 8.2). The working principle of the deuterium injection system is addressed in section 8.2.4.

As shown in figure 8.4, both tanks are connected to two separate pipe feedthroughs below the glove box roof by 1/2" stainless steel tubing. Outside the box, the two feedthroughs are linked by long 1/2" flexible stainless steel hoses to the capacitance diaphragm pressure gauges DG-03 and DG-04 (see figure 8.2) before terminating in two identical valve manifolds, each consisting of three valves, (V-20, V-21, V-22) and (V23, V-24, V-25).

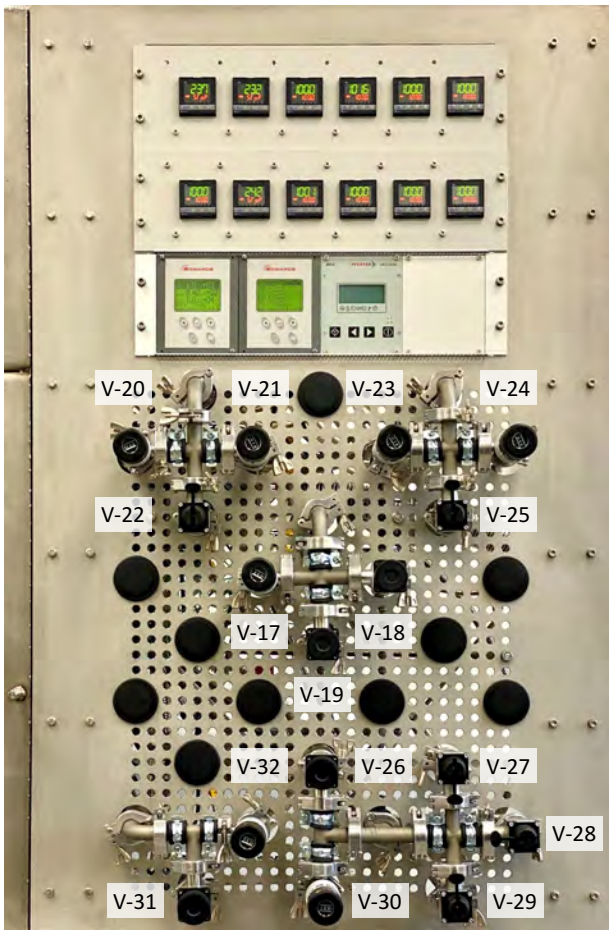

Fig. 8.7. Control panel supporting the temperature controllers, pressure indicators and valve manifold of the LYDER experiment to control the Ar and $^2H_2$ gas pressures in the lithium system and the deuterium injection system.

These valve manifolds are made of ISO-16KF piping components which are attached to the upper left and upper right corners of the control panel where they are held in place by tube clamps. The arrangement of the valves on the control panel can be seen in a close-up view in figure 8.7. The valves V-21, V-22 and V-24, V-25 connect the two tanks to a dry scroll vacuum pump (SP-01) via valve V-33 (see pump to the right of the glove box table in figure 8.3). Both vacuum pumps of the LYDER experiment are the same as those installed in the COOPER experiment, nXDS15i dry scroll pumps from Edwards Vacuum [209]. The open/close valves V-22 and V-25 are opened when the tanks need to be evacuated completely and quickly. If the pressure in the tanks is only to be reduced to a specified lower value in a controlled manner, the gas dosing valves V-21 and V-24 are manipulated instead, while the valves V-22 and V-25 are kept closed. The gas dosing valves are of the type as that shown on the left in figure 3.6, whose specifications are discussed in section 3.1.2. This type of valve is chosen because it allows a pre-set gas flow to be instantly blocked and opened at any time without losing the set flow value. The gas dosing valves V-20 and V-23 are of the same type as the valves V-21 and V-24. They connect the two tanks to an argon gas supply line. This allows the argon pressure in the tanks to be increased in the same controlled manner as it can be decreased by manipulating the valves V-21 and V-24.

Due to the length of the flexible stainless steel tubes coming from the tanks, any lithium vapor will condense on the tube walls and the gas inside will cool to ambient

temperature before reaching the corrosion and heat-sensitive pressure gauges and FKM gaskets of the ISO-KF connections. The readings of all pressure gauges installed in the LYDER experiment are displayed on pressure indicators mounted in the 19" rack drawer directly above the valve manifolds. It should be noted that under normal operating conditions, both tanks are always kept in an argon atmosphere and the path to the vacuum pump is only opened during an evacuation.

The bottoms of the two lithium tanks are linked through 1/4" piping connected by 316 stainless steel double ferrule compression fittings and bellows-sealed high-temperature valves from the Swagelok U-series as that shown on the right in figure 3.5 [201]. Its specifications and inner workings are specified in section 3.1.2. The materials of the valves in contact with the liquid lithium are stainless steel (regulating version) or a cobalt-based alloy (open/close version). According to the discussion in section 8.1, both of these materials are sufficiently chemically compatible with liquid lithium in the relevant temperature range. Only the two valves V-03 and V-07 are of the regulating type, while all other valves of the pipe system between the two tanks are of the open/close type. Each valve, except the slightly angled valve V-04, is bolted to the support panel of the lithium system with threaded rods of 1.5×10^{-1} m length. Thus, the lithium system is held in place. The connection of the threaded rods to the support panel is realized by means of nuts and washers with an FKM damper in between. This provides some horizontal and vertical clearance for the rods which is important to allow the lithium system to thermally expand and contract during the heating and cooling phases. In addition, the FKM dampers provide thermal insulation by reducing the heat flow from the lithium system to the cold backplate.

The pipe connection between the tanks has two different paths. A bypass line interrupted by valve V-03, and a tube line connected to the experimental hydrogen trap via the valves V-04, V-07 and V-08. The connecting tubes are inclined so that no lithium can be stranded at any location in the tube system. In order to transfer liquid lithium from one tank to another, the argon pressure in the target tank is reduced below the argon pressure in the tank from which the lithium is being removed. It is expected that due to the small cross-section of the 1/4" tubes and the high surface tension of liquid lithium in the relevant temperature range, it will be possible to pump the lithium completely out of the thin tube line into the other tank, leaving no lithium in the tubes [282], [288]. It is considered that the maximum height of the lithium column in the LYDER system reaching from the T-piece between the valves V-07, V-08 and V-10 to the center flange of the right tank is approximately $z_{\mathrm{Li}}^{\mathrm{max}} \approx 0.5\,\mathrm{m}$. The minimum pressure difference Δp between the two tanks required to completely pump the lithium from one tank to the other is here estimated with $\Delta p = \rho_{\mathrm{Li}} g_{\mathrm{E}} z_{\mathrm{Li}}^{\mathrm{max}} \approx 2.5 \times 10^{3}\,\mathrm{Pa}$. In this formula, $g_{\mathrm{E}} = 9.81\,\mathrm{m\,s^{-2}}$ is the gravitational acceleration on Earth.

The pressure in the two tanks can be adjusted by manipulating the valves V-20, V-23, V-21 and V-24 on the control panel. The lithium is set in motion when opening the corresponding valves V-03 or V-07, which block the selected path between the tanks. The

liquid lithium will always pass through the bypass path when moved from the left to the right tank. It may be pumped through the trap only when it is moved from the right to the left tank. In this way, it is possible to create a circular trajectory of the lithium through the pipe system. The user is alerted when the lithium in the target tank has reached its maximum level not only by lithium level sensors but also by a sudden gas bubble event in which the pressures in the two tanks abruptly equalize.

The lowest point of the two paths is the T-piece between the valves V-07 and V-08. Therefore, when the valves V-03, V-04, V-07 and V-08 are opened, all liquid lithium will tend to flow to this lowest point where the lithium system has another connection to a lithium dump tank via valve V-10. The dump tank is a round, custom-designed container with an internal volume of approximately four liters. It serves as a receptacle for used liquid lithium. Flexible stainless steel hoses connect the dump tank to valve V-29 on the glove box control panel. This provides a separate connection to the vacuum pump SP-01 via valve V-26 and to the argon gas line via valve V-30. Its internal pressure can be measured with the diaphragm pressure gauge DG-02. To minimize corrosion of the dump tank, the contaminated lithium in the lithium in the dump tank is kept in the hot liquid state as little as possible. Therefore, the dump tank is heated only in rare cases, such as when used lithium is being drained. In almost all operating scenarios of the LYDER experiment, the dump tank is kept in vacuum by maintaining the valves V-29 and V-26 open. The dump tank is also equipped with a level sensor (LS-03) that indicates when the lithium in the dump tank has filled 90 % of its volume. It has the same design as the other two level sensors described above.

For safety reasons, outside the glove box, all three tanks of the lithium system are equipped with pressure relief valves (V-35, V-36 and V-37) that are connected to the exhaust line and open if the pressure in the respective tank exceeds $p = 3 \times 10^5$ Pa.

Above the hydrogen trap, the lithium system has another connection to the argon line and vacuum system via the valves V-05, V-27, V-26, and V-30. This connection provides the ability to push any residual lithium from the hydrogen trap into the dump tank. Before the first lithium is melted, this line will be equipped with a heated expansion tank (RET) consisting of a single DN40CF nipple with a volume of approximately $V = 138$ mL. The expansion vessel will be connected to the upper fitting of valve V-05 as shown in the PFD in figure 8.2. This will prevent lithium from flowing up the gas line to areas outside the glove box in an accidental scenario.

The lithium sample extraction system with the removable sample container is located to the left of the lithium system, connected to valve V-06. Via the valves V-02, V-28, V-26 and V-30 it has a separate connection to the vacuum and argon line. Before the experimental campaign begins, the gas line of the extraction system will be equipped with a heated expansion tank (LET) made of a DN40CF nipple with a volume of $V = 138$ mL, as drawn in figure 8.2. The section of the sample extraction line which is enclosed by the valves V-02, V-06 and V-09 has an interior volume of $V_{\mathrm{Li}}^{\mathrm{SC}} \approx 5$ mL. It determines the

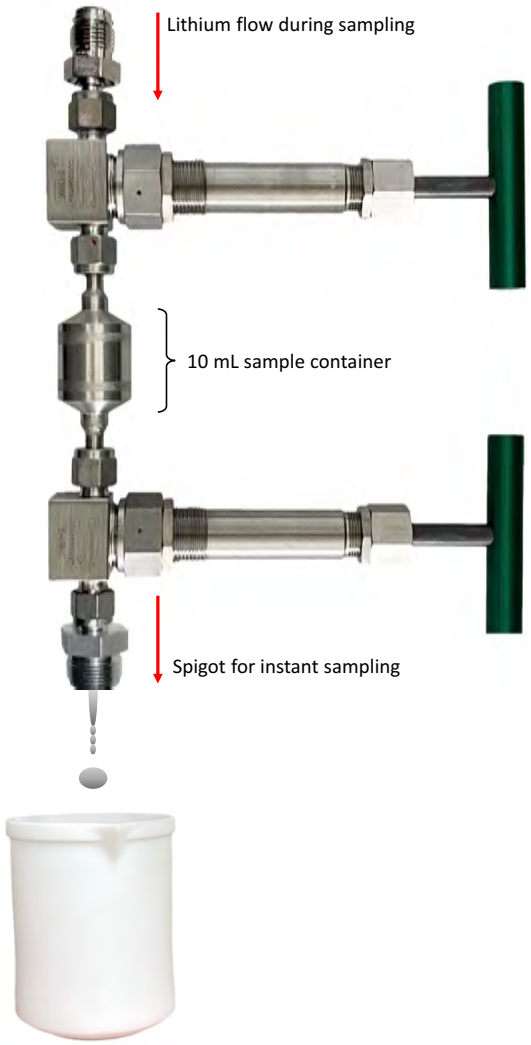

Fig. 8.8. Bare lithium sample container with open VCR male nut disconnected from the lithium system indicating the lithium flow direction into the sample container. The lithium can be filled into a beaker if instant sampling inside the glove box atmosphere is required.

extractable volume of liquid lithium. Below valve V-09 there is a female quick-connect VCR fitting whose sealing principle is described in section 3.1.2 and illustrated in figure 3.3. This connector fitting enables frequently connecting and disconnecting a custom-designed lithium sample container (SC). A photo of the assembled bare sample container disconnected from the sample extraction line is shown in figure 8.8. At the top, it has a male VCR fitting which can be screwed to the female connector of the sample extraction line using two wrenches and a VCR stainless steel gasket (see figure 3.3). The sample container is made of a double-ended stainless steel sample cylinder with an inner volume of $V = 10\,\mathrm{mL}$ whose both ends are connected to high-temperature bellows-sealed regulating valves V-11 and V-12 from the Swagelok U-series [201]. The lower end of valve V-12 serves as a spigot to empty small quantities of liquid lithium into a beaker below. The sample extraction procedure is described in section 8.4.

8.2.3. Heating system

Two electrical plugs are installed inside the glove box (see figure 8.4). The plug on the left is used to power a scale for weighing lithium and yttrium samples that would oxidize

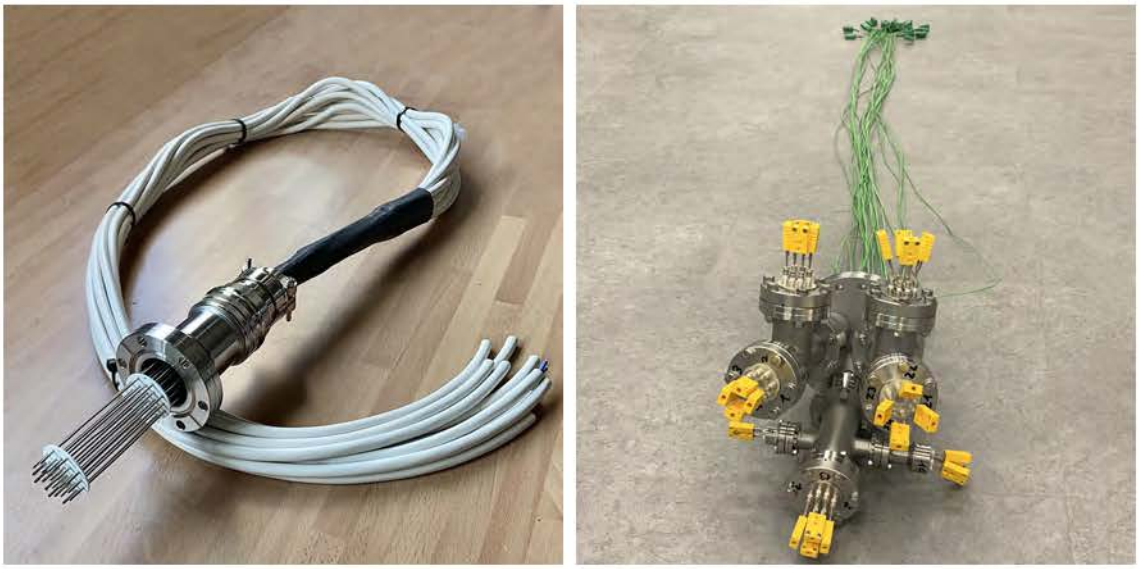

Fig. 8.9. [Left] Constructed 20-pin electric feedthrough to power the ten resistance heaters of the LYDER lithium system. [Right] Assembled feedthrough manifold for the 22 thermocouple cables that penetrate the glove box.

outside the glove box. The other electrical plug is used to power the heating wire of the lithium system's removable sample container. Cables connected to these two plugs exit the glovebox through DN40CF electrical vacuum feedthroughs along with ten other 240 V power cables needed for the lithium heating system. The electrical feedthroughs are of the same type as that shown in figure 3.10. A photo of the constructed 20-pin electrical feedthrough for the lithium heating system can be seen on the left in figure 8.9. Each of the pins is surrounded by a ceramic tube to avoid electrical contact with the glove box walls.

As shown in figure 8.10, the horizontal center column of the glovebox, which supports the horizontal beam of the glovebox window, also serves as a connector strip for 24 female K-type thermocouple connectors. These plugs are connected to thermocouple cables that exit the glovebox through a thermocouple feedthrough manifold attached to a DN100CF flange located on the right-hand glovebox wall. A photo of the constructed thermocouple feedthrough manifold prior to connection to the glove box side wall is shown in the right photo of figure 8.9.

The naked piping of the entire lithium system is wrapped with a layer of fiberglass tape. This acts as electrical insulation and ensures that the sharp edges of the pipe system do not damage the insulation of the heating elements. As shown in figure 8.5, ten heating elements (H-1 through H-10) are required to heat the lithium system. That is nine heating wires with lengths between 0.5 m and 3.5 m and one 200 W cartridge heater (H-07). The heating cords are wrapped around the tanks and the tube system at the locations indicated in figure 8.5. Note that the two expansion vessels that will be installed in the future are going to be covered by the heaters H-03 and H-05. The selected heating wires are grounded HTCE XtremeFLEX® heating cords with a power density of 60 W m^{-2} and a

Fig. 8.10. Thermocouple connector strip mounted on the horizontal beam support in the center of the glove box.

maximum operating temperature of $T = 1033\,\mathrm{K}$ [289]. A total of 12 m of heating cords are installed. This implies a maximum power required to heat the lithium system of about 920 W. The installed heating cables can be seen in the left-hand photo of figure 8.11 prior to the installation of the thermal insulation wool. To ensure good thermal contact between the heating cords and stainless steel surfaces the cords are secured with tube clamps. The location of the cartridge heater can be seen in the right-hand photo of figure 8.11. It is used to heat the VCR connection of the removable sample container. To increase thermal contact the cartridge heater is wrapped with rigid copper foil that adapts to the plane surface of the VCR nut. In addition, the right photo shows a specially shaped gripper arm attached to the stem of the V-12 valve. It has the purpose of holding the sample container in place during operation. The heater grounding leads are connected to the glove box wall, which itself is grounded. On the other hand, their electric power conductors are linked to the mounted 20-pin electrical feedthrough.

Furthermore, there are 22 K-type thermocouples that measure the temperatures at different locations of the lithium system. Their positions are indicated in the figures 8.2 and 8.5. The cables of the thermocouples are connected to the thermocouple connector strip mounted on the horizontal beam support in the center of the glove box (see figure 8.10). The pipes of the lithium system are wrapped with about 3×10^{-2} m thick thermal insulation Superwool® blanket from Morgan Advanced Materials [290], which is secured with high-temperature aluminum tape. The thermal insulation of the removable sample container has yet to be applied. During operation, a removable thermal blanket covers the bare area around the cartridge heater of the sample container's VCR fitting.

The heaters are controlled by ten individual RB100 temperature controllers from RKC Instrument linked to solid-state relays that either open or close the 240V AC power supply to the heaters [291]. They are mounted in the two upper 19" rack drawers on the control panel (see figure 8.7). The internal PID regulation program of each temperature controller uses the temperature measurements of one thermocouple as an input value. Table 8.3

Fig. 8.11. [Left] Assembled liquid lithium system of the LYDER experiment wrapped with fiberglass tape and ten heating wires. [Right] Removable sample holder without thermal insulation surrounded by a heating cable and fiberglass tape. It is connected to the lithium system by a VCR fitting heated by a small cartridge heater.

TABLE 8.3

THERMOCOUPLES ATTACHED TO THE LITHIUM SYSTEM, WHOSE TEMPERATURE MEASUREMENTS ARE USED BY TEN DIFFERENT TEMPERATURE CONTROLLERS AS INPUT PARAMETERS TO CONTROL THE HEATERS WHICH ARE LISTED IN THE FIRST ROW OF THE TABLE (SEE FIGURE 8.5).

Heater	01	02	03	04	05	06	07	08	09	10
Thermocouple	04	05	07	12	09	13	15	21	17	20

lists those thermocouples whose measurements are used for the different heaters. The temperature controllers allow setting individual temperature target values for each heater and specify their temperature ramps during heat-up and cool-down phases.

A LabVIEW program is developed that permits the user to control the settings of the temperature controllers from the computer and store its data. The graphical user interface of the LabVIEW program is shown in figure 8.12. It stores and displays the measured temperatures of all 22 thermocouples and the recorded data of the installed pressure gauges.

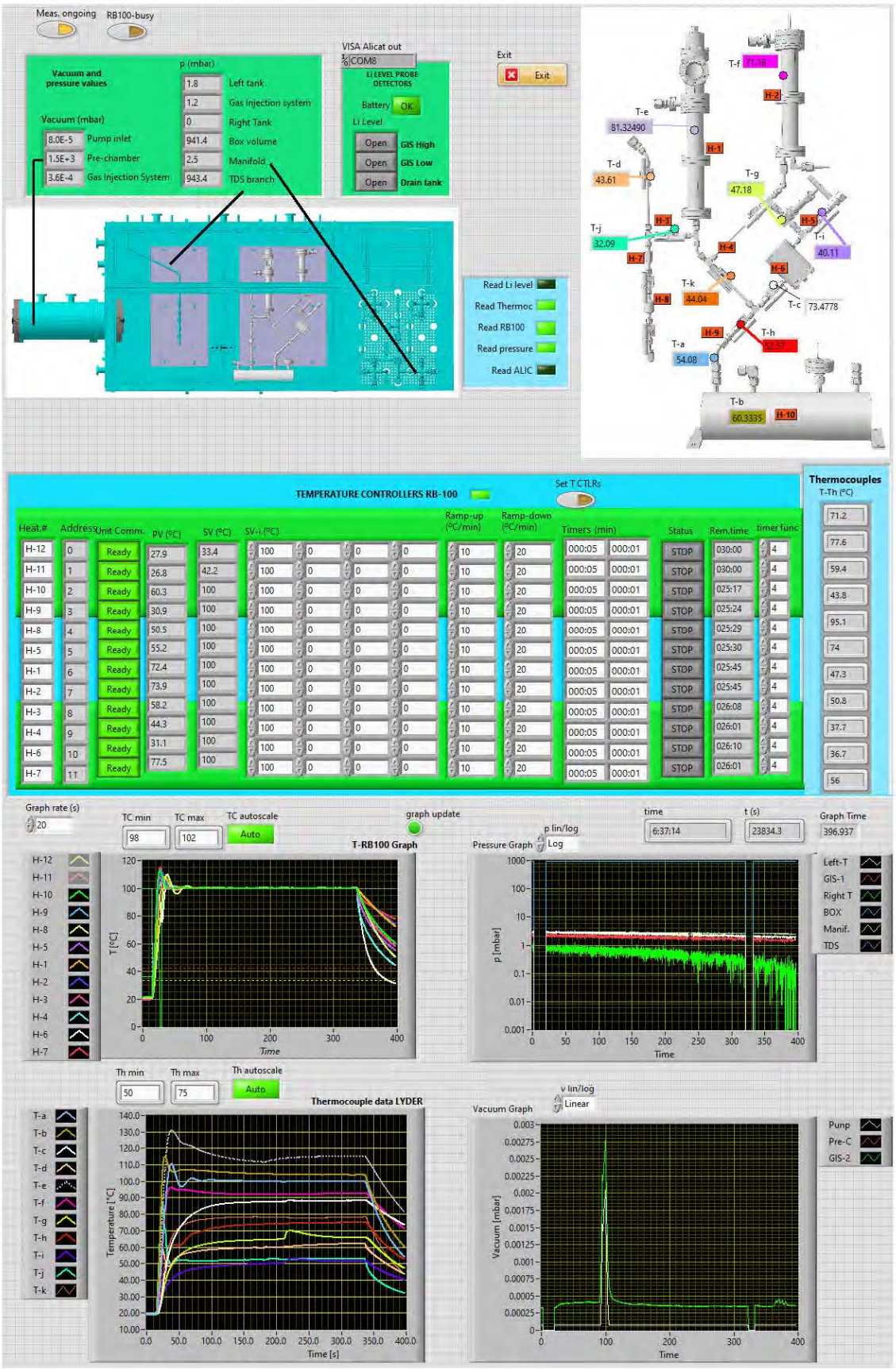

Fig. 8.12. LabVIEW control program of the LYDER facility.

8.2.4. Deuterium injection system

The deuterium injection system, located in the right tank of the LYDER lithium system, is in charge of loading the lithium with a given initial concentration of deuterium prior to the deuterium retention experiments. Injecting deuterium into a liquid metal can be done in several ways.

One may expose the free surface of the lithium to a $^2H_2$ gas atmosphere, or bubble $^2H_2$ gas from below through the liquid metal as done in the experimental campaigns [110]–[112], [292]–[294]. In either case, the deuterium would dissociate at the free surface and diffuse into the liquid metal bulk.

In this work, an alternative deuterium injection technique is applied. It is decided to inject the deuterium by permeation from a $^2H_2$-filled chamber through an α-iron membrane into the liquid lithium. The use of α-iron as the membrane material is reasonable since it has a relatively high hydrogen isotope diffusivity [242], is very corrosion resistant to liquid lithium and is easy to fabricate. In addition, its hydrogen transport parameters are well known, allowing the deuterium injection process to be simulated in advance.

The designed deuterium injection system consists of a modified 316 stainless steel DN40CF blind flange. Its fabrication drawing is created by the author of this thesis and can be seen in figure 8.13 on the right. The performed modification involves the manufacturing of a second DN16CF knife-edge located concentrically within the pre-fabricated DN40CF knife-edge. It is surrounded by six blind internal screw threads. Two holes are drilled through the modified DN40CF blind flange bulk, one inside the circular DN16CF knife-edge and the other between the DN16CF and the DN40CF knife-edges. On the other side of the blind flange, the holes are welded to a straight and an angled male VPN connector fitting. The fabricated modified DN40CF flange can be seen in the upper left photo in figure 8.14.

The fabrication drawing of the α-iron membrane is shown on the left in figure 8.13. It is made of a cylindrical tube with one open and one closed end. The membrane has a length of 6×10^{-2} m and a wall thickness of 5×10^{-4} m. Due to manufacturing limitations, the wall at the closed tube end is considerably thicker than the cylinder wall (about 3×10^{-3} m). The shape of the open α-iron tube end is imitated from a conventional DN16CF nipple with a rotatable flange ring and ends in a manufactured DN16CF knife-edge. A photo of the fabricated α-iron membrane can be seen in the upper right photo in figure 8.14. As visible in the lower left-hand photo in figure 8.14 the tube is fastened to the center of the modified DN40CF blind flange with a conventional DN16CF ring-shaped rotatable flange made of 316 stainless steel. Therefore, it is made use of DN16CF α-iron Helicoflex® gasket from Technetics and six M4 screws made of the high-temperature and corrosion-resistant steel Incoloy Alloy® A-286. At the position of the hole that is drilled through the modified DN40CF blind flange between the inner and outer knife-edges the ring-shaped DN16CF flange has a drilled notch (see upper left corner in figure 8.13). In this configuration, the welded inclined VCR fitting provides a channel into the inner

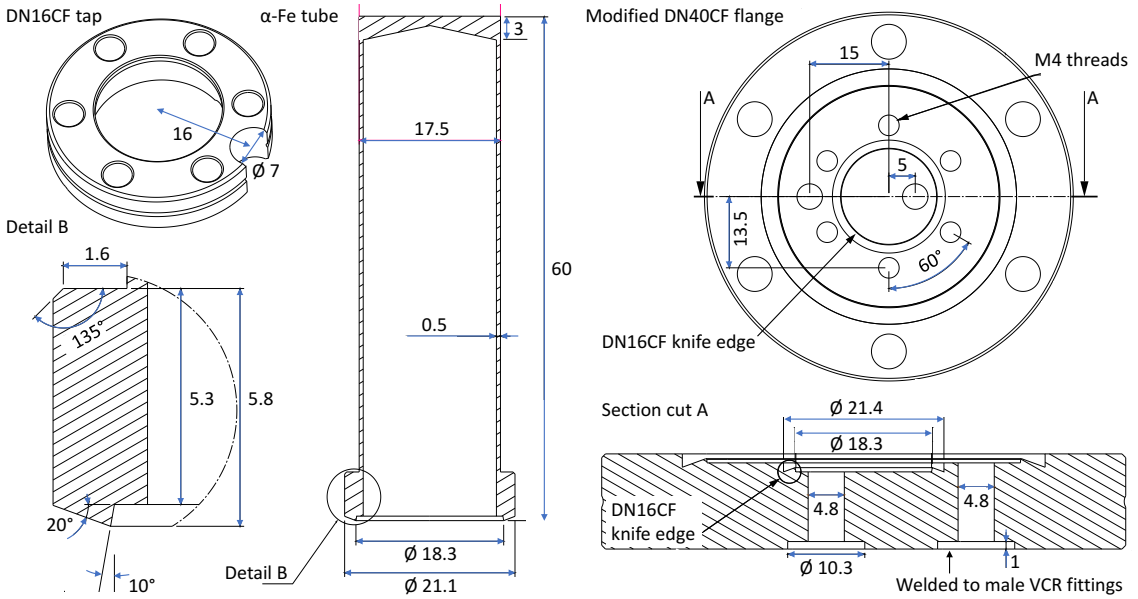

Fig. 8.13. Manufacturing drawing of the developed deuterium injection system for the LYDER experiment. This involves the α-iron membrane, a drilled DN16CF flange ring and a modified DN40CF blind flange.

cavity of the α-iron tube.

On the left, figure 8.15 shows a photo of the bare right tank of the lithium system. It can be seen that the flange of the deuterium injection system is used as the base of the tank. A view from above into the tank with the deuterium injection system at the bottom is shown in the lower right photo in figure 8.14. The lithium passes through the straight VCR connector fitting before entering the tank through the small hole visible at the bottom. The photo in the middle of figure 8.15 shows the positions of the two lithium level sensor pins LS-01 and LS-02. The longer pin LS-01 is cut exactly 7×10^{-2} m above the bottom flange of the tank or 1×10^{-2} m above the plane roof of the permeation membrane. This means that by the time the level sensor LS-01 detects a signal, approximately $V_{\mathrm{LS-01}} = 49$ mL of liquid lithium has entered the right tank, taking into account the space occupied by the permeation membrane. The level sensor LS-01 is designed to indicate when the permeation membrane is completely covered with liquid lithium. This is a requirement for the proper operation of the deuterium injection system. The second level sensor LS-02 is cut 1×10^{-1} m above the bottom flange which corresponds to a volume of liquid lithium in the right tank of $V_{\mathrm{LS-02}} \approx 90$ mL. The distance between the ends of two level sensors is therefore $\Delta z_{\mathrm{LS}} = 3 \times 10^{-2}$ m. Measuring the time Δt between two signals of the level sensors will allow determining the lithium flow rate through the equation

$$F = \pi \left(r_{\mathrm{in}}^{\mathrm{40CF}}\right)^2 \cdot \frac{\Delta z_{\mathrm{LS}}}{\Delta t} = 3.31 \times 10^{-5}\,\mathrm{m}^3 \cdot \frac{1}{\Delta t}\,. \tag{8.2}$$

The right-hand image in figure 8.15 shows a section cut through the deuterium injection system. It depicts the Li and $^2H_2$ inlet holes and the position of the two Helicoflex® gaskets. Moreover, it illustrates the dissociation processes of $^2H_2$ molecules at the inner

Fig. 8.14. [Top left]: Modified DN40CF blind flange used as the base for the deuterium injection system. It has a custom DN16CF knife-edge in the center surrounded by six blind M4 threaded holes. The liquid lithium enters through a drilled hole between the two knife-edges on the left, and the $^2H_2$ gas enters the tube through the hole inside the DN16CF knife-edge. [Top right] Fabricated closed α-iron tube acting as a deuterium permeation membrane with a DN16CF knife-edge at the open end. The tube is attached to the center flange of the base plate by a conventional DN16CF flange ring using a DN16CF α-iron Helicoflex® gasket. [bottom left] Assembled deuterium injection system with a DN40CF α-iron Helicoflex® gasket sitting on the outer knife edge. [bottom right] Top view into the right tank showing the deuterium membrane from above. The picture shows the hole through which the liquid lithium enters.

gas-αFe interface and the diffusion through the membrane into the liquid lithium where it accumulates in atomic form.

The figures 8.2 and 8.15 show that the $^2H_2$ gas inlet of the deuterium injection system is connected via its VCR fitting to a tube line consisting of a 1/2" flexible stainless steel vacuum hose from Swagelok. It passes through the feedthrough at the roof of the glove

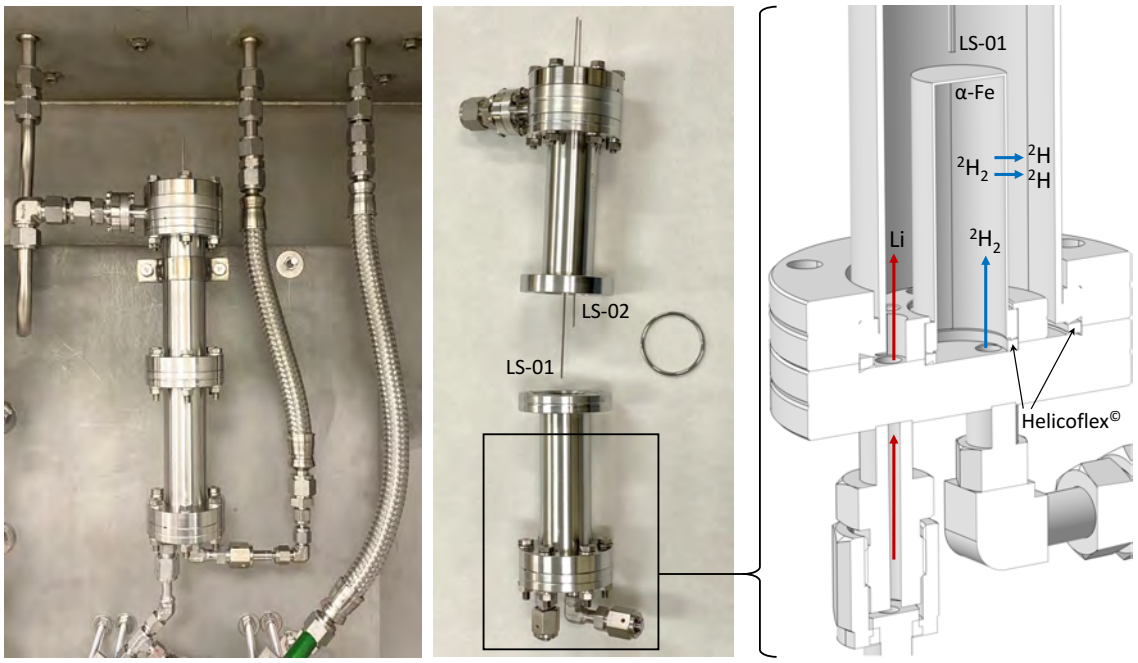

Fig. 8.15. [Left] Assembled right tank of the LYDER lithium system with the deuterium injection system at the bottom flange. [center] Open DN40CF flange in the middle of the right tank showing an α-iron Helicoflex® gasket which is used for the sealing and two lithium level sensors LS-01 and LS-02. [Right] Section cut through a 3D drawing of the custom-designed deuterium injection system illustrating the deuterium permeation process from the interior of a closed α-iron tube into the surrounding liquid lithium.

box. The other end of the feedthrough is connected to the control panel with another hose and terminates at a manifold consisting of the valves V-17, V-18, and V-19.

From now on, the combined internal volume of the α-iron cavity and the piping connected to the valve manifold at the control panel will be referred to as the permeation chamber of the deuterium injection system. The internal volume of the permeation chamber is estimated to be $V_{\mathrm{PC}} \approx (210 \pm 40)\,\mathrm{m}^3$. The relatively large error is due to the uncertainty in the inner radius of the corrugated flexible hoses. The $^2H_2$ gas pressure inside this volume is measured with a capacitance diaphragm gauge (DG-05) for pressures between $1 \times 10^2\,\mathrm{Pa} < p < 2 \times 10^5\,\mathrm{Pa}$ and a Pirani gauge (PiG-05) to cover the range $1 \times 10^{-2}\,\mathrm{Pa} < p < 1 \times 10^3\,\mathrm{Pa}$. The valve manifold has the same design as those used to manipulate the pressure in the left and right tanks. It allows the controlled injection and removal of $^2H_2$ gas through the gas dosing valves V-17 and V-18, respectively. The complete evacuation into the scroll vacuum pump SP-01 is realized by opening the open/close valve V-19.

The deuterium injection procedure established for the LYDER system foresees to pump lithium through the bypass line into the right tank until the lithium has reached its maximum level. As mentioned above, this is indicated by a gas bubble and pressure equalization event that will occur as soon as the argon gas from the left tank begins to enter the right tank. During deuterium injection, the lithium is held motionless at a con-

stant temperature and constant argon pressure with valve V-03 closed. The deuterium injection process into the lithium is started by filling $^2H_2$ into the permeation chamber. Once the desired initial pressure in the permeation chamber $p_{22,\mathrm{init}}$ is set, the valves V-17 and V-18 are closed so that no more $^2H_2$ gas enters or leaves the permeation chamber. The difference between the chemical potentials of deuterium in the high pressure $^2H_2$ gas in the permeation chamber and in the initially deuterium-free lithium triggers a diffusive transport of deuterium from the permeation chamber into the lithium. As deuterium molecules are removed from the gas, the pressure in the permeation chamber decreases until thermodynamic equilibrium is reached. The permeated deuterium isotopes diffuse through the lithium bulk until the concentration is homogeneous. Regardless of the exact deuterium concentration profile in the lithium, its average concentration $\langle c_2^{\mathrm{Li}} \rangle (t)$ is related to the measured pressure drop $\Delta p_{22}(t)$ at a given time t during the deuterium injection process by the equation

$$\left\langle c_2^{\mathrm{Li}} \right\rangle (t) = \frac{V_{\mathrm{PC}}}{RTV_{\mathrm{Li}}} \cdot \Delta p_{22}(t) \ . \tag{8.3}$$

The choice of the height and wall thickness of the designed α-iron membrane is based on numerical simulations of the deuterium permeation process occurring in the described deuterium injection system. Thus, its design is optimized for the injection of deuterium concentrations into the lithium in the range $\langle c_2^{\mathrm{Li}} \rangle < 40\,\mathrm{mol\,m^{-3}}$, which is specified as the desired concentration range in section 8.1. An optimal design allows the desired concentrations to be injected in a reasonable amount of time.

The simulation model of the deuterium injection system is created using EcosimPro©. Its component flow structure is shown in figure 8.16. The applied components are those presented in section 5.1 and graphically illustrated in figure 5.2.

To numerically simulate the pressure decrease in the permeation chamber during the injection procedure, the created higher-level gas chamber component defined in figure 6.24 is used. It is found that due to the significantly greater thickness $\Delta z_{\mathrm{roof}} \approx 3 \times 10^{-3}\,\mathrm{m}$ of the closed end of the α-iron tube compared to its cylindrical wall, the rate at which deuterium isotopes permeate through the horizontal roof of the membrane is negligibly small compared to the rate at which they enter the lithium by permeation through the cylindrical wall. Therefore, the model only takes into account the radial permeation process through the cylindrical part of the α-iron wall, which is represented by a cylindrical wall material component. For the model, it is assumed that the permeation process from the permeation chamber into the lithium happens only along part of the length of the α-iron tube which is estimated by $\Delta z_{\mathrm{per}} = z_{\mathrm{tube}} - \Delta z_{\mathrm{16CF}} - \Delta z_{\mathrm{roof}} = 5.1 \times 10^{-2}\,\mathrm{m}$ (see figure 8.16). Here, $z_{\mathrm{tube}} = 6 \times 10^{-2}\,\mathrm{m}$ is the total length of the α-iron tube and $\Delta z_{\mathrm{16CF}} = 5.8 \times 10^{-3}\,\mathrm{m}$ is the height of the DN16CF flange ring surrounding the α-iron tube at the bottom. In accordance with the fabrication drawing in figure 8.13, the considered inner and outer radii of the cylindrical α-iron wall material component are $r_{\mathrm{in}}^{\alpha\mathrm{Fe}} = 8.25 \times 10^{-3}\,\mathrm{mL}$ and $r_{\mathrm{out}}^{\alpha\mathrm{Fe}} = 8.75 \times 10^{-3}\,\mathrm{mL}$, respectively.

The model uses the Sieverts' constant of hydrogen isotopes in α-iron which is listed

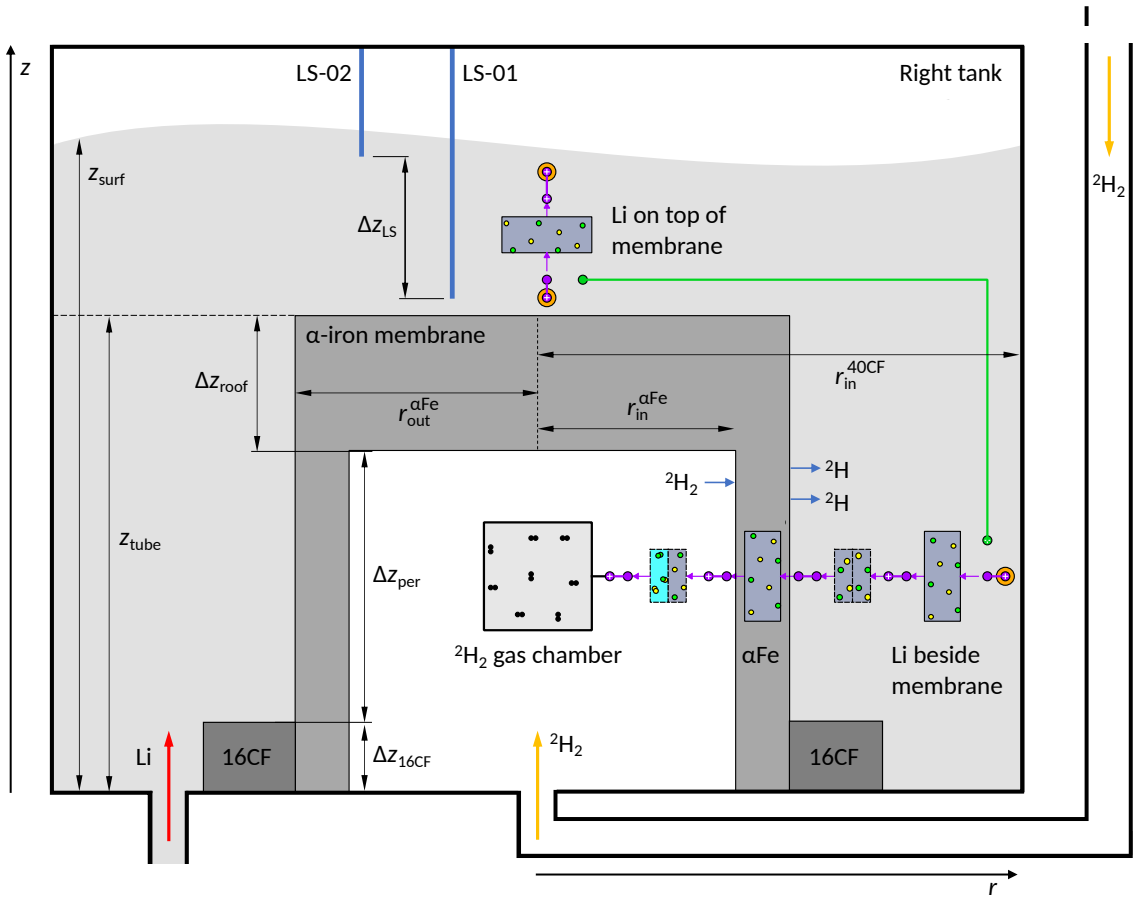

Fig. 8.16. EcosimPro© component structure of the developed numerical model of the deuterium injection system.

in table 5.1 [242]. The protium diffusion coefficient listed in table 5.1 is converted to its value for deuterium using equation (2.66). For the recombination coefficients of $^2H_2$ molecules at a gas-αFe interface, the model assumes the following relation measured by Nagasaki *et al* [295]

$$\sigma k_{r,22}^{\alpha Fe} = 2.77 \cdot \frac{m^4 \sqrt{K}}{mol\, s} \cdot \frac{1}{\sqrt{T}} \cdot \exp\left(\frac{36\,300\,J\,mol^{-1}}{RT}\right). \tag{8.4}$$

The dissociation coefficient is determined from the recombination coefficient and the Sieverts' constant through equation (2.100).

In the model, the lithium bath is divided into two segments. The lower segment is the cylindrical lithium bulk between the α-iron tube and the inner wall of the tank. It is represented by a cylindrical wall material component and calculates the time-dependent concentration profile in the radial r-direction. Up to the total height of the α-iron tube $z_{tube} = 6 \times 10^{-2}$ m, the model assumes the concentration in the lithium to be independent of the vertical z-direction. In this coordinate system $z = 0$ m is the height of the tank floor. Since the DN16CF flange occupies almost the entire width of the tank floor, the volume of lithium reaching from the tank bottom to the end of the α-iron tube is estimated by

$$V_{Li}^{side} \approx \pi \cdot (z_{tube} - \Delta z_{16CF}) \cdot \left[\left(r_{in}^{40CF}\right)^2 - \left(r_{out}^{\alpha Fe}\right)^2\right] = 47\,mL\,. \tag{8.5}$$

The deuterium diffusion process in the liquid lithium bulk that occupies the space between the flat roof of the α-iron tube and the lithium surface at $z = z_{\mathrm{surf}}$ in the range $z_{\mathrm{tube}} < z \leq z_{\mathrm{surf}}$ is modeled with a parallel wall material component (see components above permeation membrane in figure 8.16). Considering that the volume of lithium that enters the right tank is $V_{\mathrm{Li}} = 100\,\mathrm{mL}$ the height of the lithium surface is estimated by

$$z_{\mathrm{surf}} \approx z_{\mathrm{tube}} + \frac{V_{\mathrm{Li}} - V_{\mathrm{Li}}^{\mathrm{side}}}{A_{40\mathrm{CF}}} = 1.08 \times 10^{-1}\,\mathrm{m}\,, \tag{8.6}$$

where $A_{40\mathrm{CF}} = \pi \left(r_{\mathrm{in}}^{40\mathrm{CF}}\right)^2$ is the cross section of the tank. The wall material component, as defined in section 5.1, allows the simulation of the deuterium concentration and diffusion fluxes in only one direction, which is here chosen to be the vertical z-direction. Hence, the deuterium concentration in the radial r-direction is considered to be homogeneous. For this reason, the model assumes that the deuterium concentration at the inlet diffusion port of the parallel wall material component above the tube at $z = z_{\mathrm{surf}}$ is equal to the simulated average concentration in the lithium bulk next to the membrane below. It is assumed that the surface area through which the diffusion into the lithium column above the α-iron tube occurs is equal to the cross-section of the tank $A_{40\mathrm{CF}}$. Since at $T = 623\,\mathrm{K}$ the recombination rate coefficient of hydrogen isotopes at a gas-lithium interface is very small compared to that of other metals, the flux of evaporating deuterium isotopes entering the argon atmosphere is neglected in this model [296], [297].

In order to not violate mass conservation, the particle losses from the lithium beside the membrane into the lithium sitting on top of the membrane need to be taken into account. This is done by treating the deuterium diffusion flux $J_{2,\mathrm{top}}^{\mathrm{d.IN}}(t)$ at the inlet port of the lithium wall material component on top of the membrane as a particle sink that homogeneously removes deuterium isotopes from the lithium sitting beside the membrane. Mathematically, this is expressed by the sink term $\varsigma_2\left(t, r_q\right)$ in equation (5.8) of the cylindrical wall material of the lithium beside the membrane, according to

$$\varsigma_2\left(t, r_q\right) = J_{2,\mathrm{top}}^{\mathrm{d.IN}}(t) \cdot \frac{A_{40\mathrm{CF}}}{V_{\mathrm{Li}}^{\mathrm{side}}}\,. \tag{8.7}$$

For the model, the same diffusion coefficient and Sieverts' constant of deuterium in liquid lithium is applied as used in chapter 7. Since the simulated concentrations in the lithium are sufficiently, low the lithium is considered to occur in the α-Li phase where the Sieverts' law is approximately valid. This is a requirement for the usage of the metal-metal interface component described in section 5.1.

The left-hand graph in figure 8.17 shows the simulated radial concentration profile in the cylindrical lithium bulk next to the membrane after different time periods considering an initial $^2H_2$ pressure in the permeation chamber of $p_{22,\mathrm{init}} = 5 \times 10^4\,\mathrm{Pa}$ and a temperature of $T = 623\,\mathrm{K}$. It can be seen how the concentration profile gradually increases over the course of a day, with a slightly higher concentration at the αFe-Li interface compared to the inner wall of the tank. The concentration profile flattens out when approaching thermodynamic equilibrium.

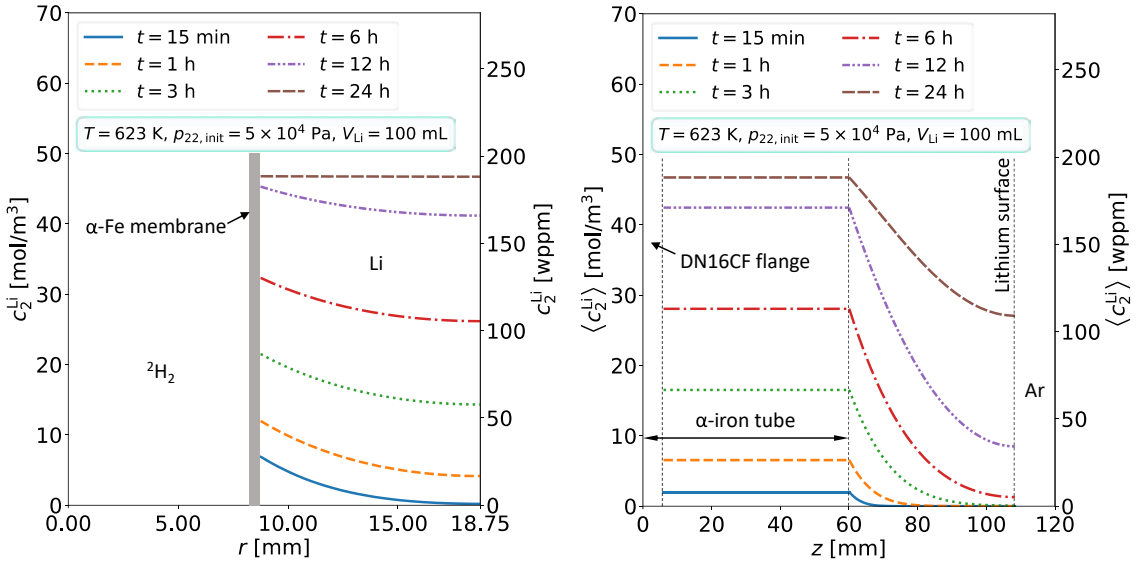

Fig. 8.17. [Left] Simulated evolution of the radial deuterium concentration profile in the lithium between the outer wall of the permeation membrane and the inside wall of the right tank during deuterium injection. [Right] Simulated evolution of the vertical deuterium concentration profile in the lithium during deuterium injection, averaged over the radial direction of the tank.

The right-hand graph in figure 8.17 presents the simulated deuterium concentration in vertical z-direction averaged over the radial r-direction. The plot illustrates how the concentration profile in the column above the permeation membrane rises with time. It can be seen that between $t = 3\,\text{h}$ and $t = 6\,\text{h}$ the first deuterium isotopes have reached the lithium surface. However, it is found that it takes more than $t = 24\,\text{h}$ for the deuterium to homogeneously distribute throughout the entire lithium column. It is worth noting that in this simplified one-dimensional model the average concentration in the vertical direction is a discontinuous function showing a kink at $z = z_{\text{tube}}$. In reality, particle diffusion from the lithium next to the membrane into the lithium column above the membrane would cause a slight decrease of the average concentration closer to the tube head and a smooth transition of the average concentration at the Li-Li interface at $z = z_{\text{tube}}$. Hence, in reality, the gradients of the average concentration across the Li-Li interface at $z = z_{\text{tube}}$ would be the same on both sides. Nevertheless, including this detail in the model would probably have a negligible effect on the calculated deuterium permeation flux across the α-iron membrane.

The simulated total average concentration in the whole $V_{\text{Li}} = 100\,\text{mL}$ of liquid lithium in the right tank is presented in the left graph in figure 8.18 for different initial $^2H_2$ pressures in the permeation chamber. It is found that the lower the initial pressure the smaller is the rate at which the average concentration in the lithium increases. Furthermore, the lower the initial pressure, the earlier is thermodynamic equilibrium reached and the lower is the adjusting constant average concentration at equilibrium. It can be seen that all three simulated $^2H_2$ pressures result in the establishment of a constant equilibrium concentration after a period of time which is reasonable for laboratory experi-

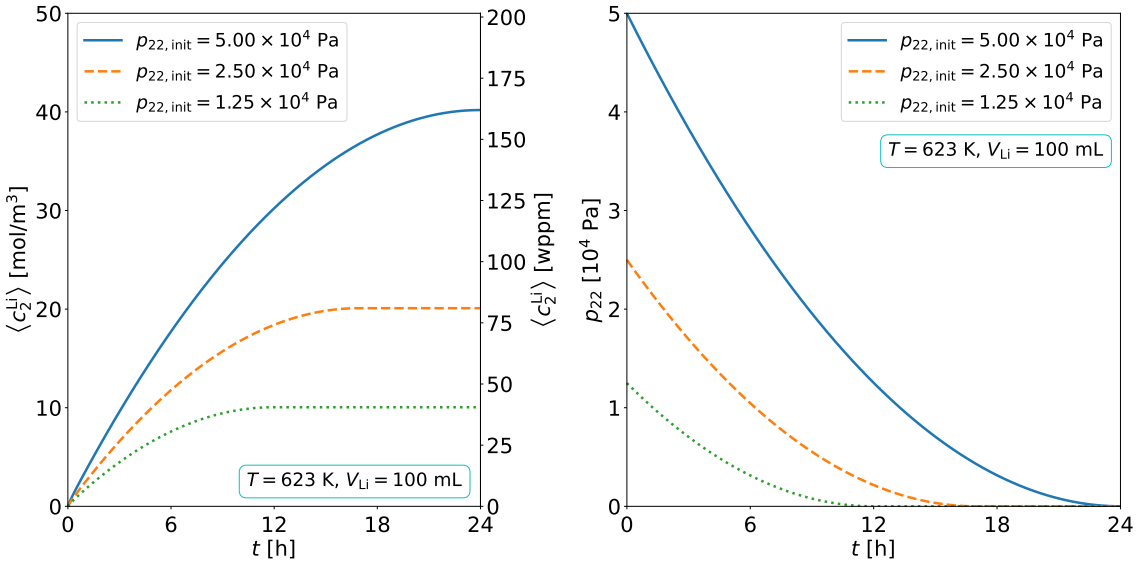

Fig. 8.18. [Left] Simulated evolution of the average deuterium concentration in the lithium of the right tank during deuterium injection considering three different initial $^2H_2$ pressures in the permeation chamber. [Right] Simulated evolution of the $^2H_2$ pressure in the permeation chamber during deuterium injection into the lithium considering three different initial $^2H_2$ pressures.

ments. The deuterium injection process may be stopped at any point during the transient phase towards thermodynamic equilibrium and the momentary average concentration in the lithium would be maintained. According to the simulation that considers an upstream pressure of $p_{22,\mathrm{init}} = 5 \times 10^4$ Pa, removing the gas from the permeation chamber after the times $t = 15$ min, $t = 1.5$ h or $t = 3$ h would allow the establishment of an average initial deuterium concentration of $\langle c_2^{\mathrm{Li}} \rangle = 1\,\mathrm{mol\,m^{-3}}$, $\langle c_2^{\mathrm{Li}} \rangle = 5\,\mathrm{mol\,m^{-3}}$, or $\langle c_2^{\mathrm{Li}} \rangle = 10\,\mathrm{mol\,m^{-3}}$, respectively.

The right-hand graph in figure 8.18 presents the simulated time evolution of the decreasing pressure in the closed permeation chamber. It can be seen that the pressure decrease rate is relatively high and will therefore be well measurable by the pressure gauge DG-05. The $^2H_2$ pressure is found to approach zero at thermodynamic equilibrium. This is consistent with figure 7.7, which shows very low equilibrium pressures in the relevant concentration range.

8.2.5. Deuterium getter trap

The design of the LYDER lithium system allows the deuterium-loaded lithium to be exposed to an yttrium getter bed for deuterium retention experiments. As mentioned above, making this possible is the purpose of an experimental deuterium trap developed as part of this thesis. In section 8.1 it is argued that the trap should have a capacity of up to $m_{\mathrm{Y}} = 5 \times 10^{-3}$ kg of small yttrium pieces and be made exclusively of materials compatible with liquid lithium (see table 8.1). Another requirement is the ability to remove, empty and refill the yttrium basket from the trap container when the system is cold.

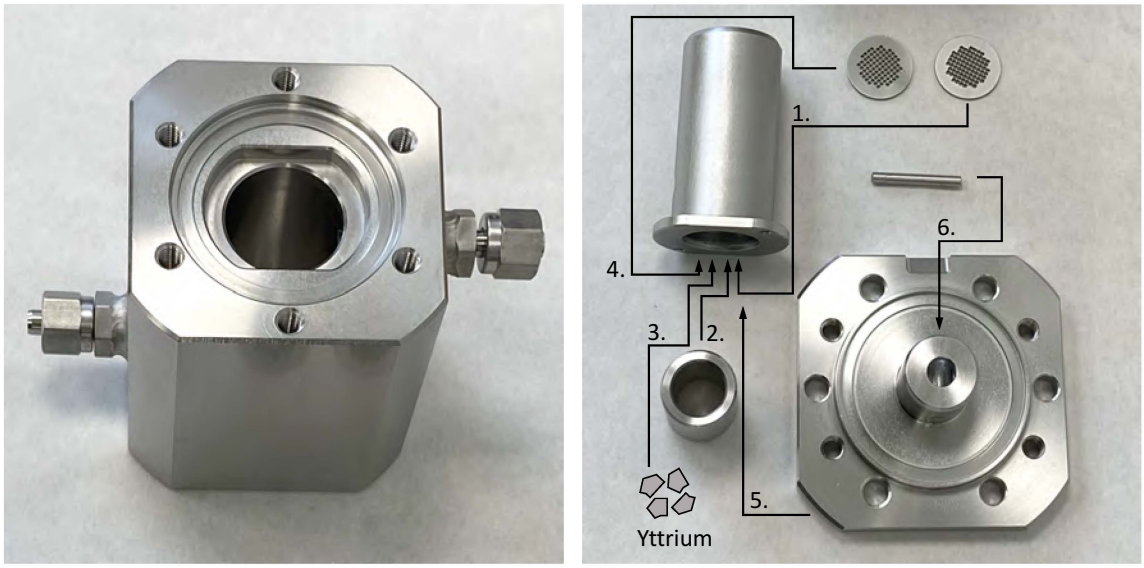

Fig. 8.19. [Left] Thick 316 stainless steel body of the developed deuterium getter trap container for the LYDER experiment. [Right] Fabricated deuterium trap components that make up the yttrium basket. The arrows indicate the assembly steps of the basket attached to the trap lid.

Based on these conditions, a trap design is elaborated by the author of this thesis in collaboration with the company AVS (Added Value Solutions). The prepared manufacturing drawings can be found in section A.3 of the appendix.

Photographs of the various manufactured parts of the trap, made exclusively of 316 stainless steel, are shown in figure 8.19. The photo on the left shows the outer body of the trap container. Two double ferrule compression fittings welded to the opposite side walls of the trap container serve as lithium inlet and outlet ports. The round recess in the center of the trap container is prepared to hold the yttrium sample basket whose individual components are shown in the right photo of figure 8.19. This includes a narrower and a wider open 316 stainless steel cylinder (see center left and top left corner, respectively), two stainless steel meshes with an aperture width of 1×10^{-3} m and a pitch of 1.2×10^{-3} m (see upper right corner), the trap lid made of a custom-designed DN40CF blind flange (see lower right corner) and a small steel pin.

The assembly steps of the yttrium basket are illustrated by the arrows in figure 8.19. First, one of the round steel meshes is inserted into the wider cylinder. At the bottom of the wider cylinder, a slightly narrower opening prevents the mesh from falling through. The second narrower cylinder is then placed on top of the mesh before up to $m_{\mathrm{Y}} = 5 \times 10^{-3}$ kg small pieces of yttrium may be filled into the basket. The second round mesh is placed over the opening of the inner cylinder. In this way, the yttrium will be confined in the space between the two meshes. Finally, the spigot of the trap lid is inserted into the wider cylinder where it is secured with a pin that passes through both parts.

A photograph of the assembled yttrium basket is shown in the left-hand photo in figure 8.20. The yttrium basket is flanged to the manufactured DN40CF knife-edge at the opening of trap container using a DN40CF Helicoflex® α-iron gasket (see left photo in figure

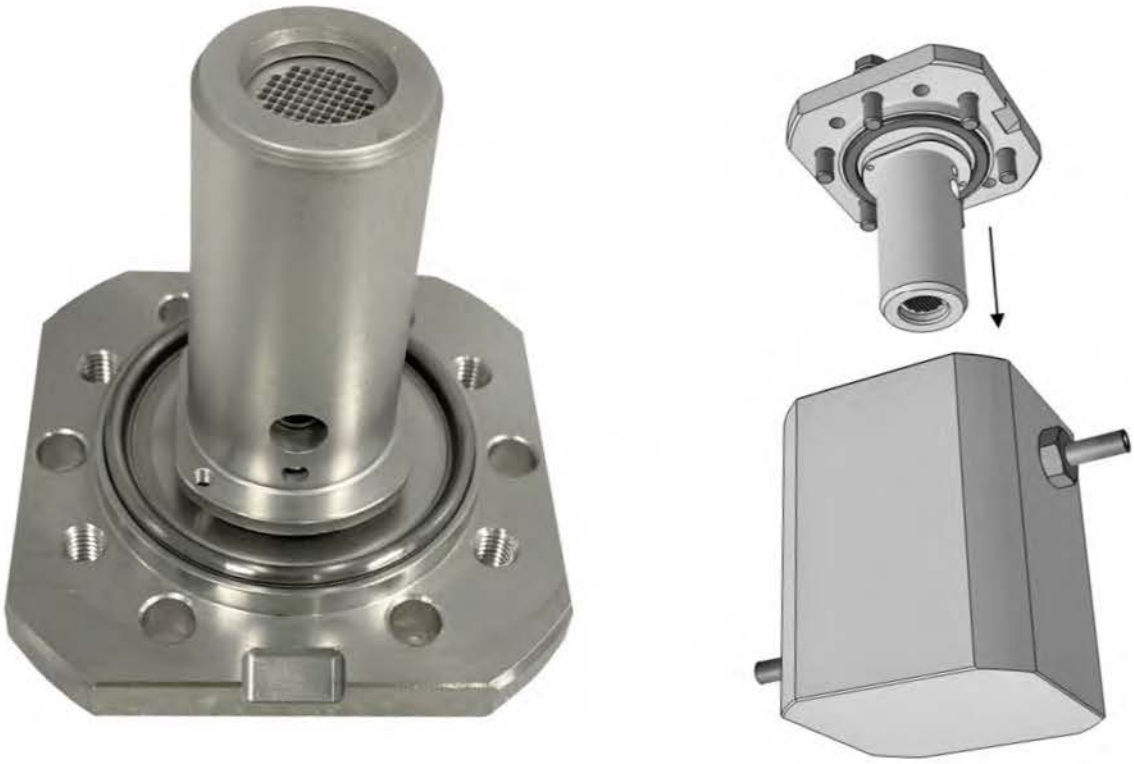

Fig. 8.20. [Left] Assembled yttrium basket of the deuterium trap attached to the trap lid showing the position of a Helicoflex® α-iron gasket [Right] 3D drawing of the deuterium trap design illustrating how the yttrium basket is inserted into the trap container.

8.20) and six high-temperature M6 screws made of Incoloy Alloy® A-286. Therefore, the wider cylinder attached to the trap lid is inserted into the opening of the trap container as illustrated in the 3D drawing of the trap presented in the right-hand image in figure 8.20.

The closed deuterium trap mounted between the valves V-04, V-05 and V-08 into the lithium system can be seen in the left-hand photo in figure 8.21. A 3D drawing showing a cross-sectional view through the trap is shown on the right in figure 8.21. The red arrow indicates the flow path of the liquid lithium through the drilled channels in the trap body and the pebble bed.

The volume of the cylindrical cavity between the meshes that encloses the yttrium pebbles defines the trap volume $V_{\text{trap}} = 3.94 \times 10^{-6}\,\text{m}^3$. It has a diameter of $d_{\text{trap}} = 1.3 \times 10^{-2}\,\text{m}$ and a length of $l_{\text{trap}} = 3 \times 10^{-2}\,\text{m}$. This implies an aspect ratio of AR = 2.28.

The maximum capacity of yttrium pebbles of the trap container is determined by the relation $m_{\text{Y}}^{\text{max}} = (1 - \varepsilon) \cdot \rho_{\text{Y}} V_{\text{trap}}$. Due to the small length and radius of the yttrium-containing cavity compared to the radii of the yttrium pieces ($5 \times 10^{-4}\,\text{m} < r_{\text{peb}} < 1.5 \times 10^{-3}\,\text{m}$) that will be inserted into the basket, a relatively high void fraction of the pebble bed of $\varepsilon \approx 0.7$ should be expected [281]. Such a conservative estimation of the void fraction yields an yttrium capacity of the trap of $m_{\text{Y}}^{\text{max}} = 5.3 \times 10^{-3}\,\text{kg}$. This is consistent with the target yttrium capacity of $m_{\text{Y}}^{\text{max}} = 5 \times 10^{-3}\,\text{kg}$ (see table 8.1).

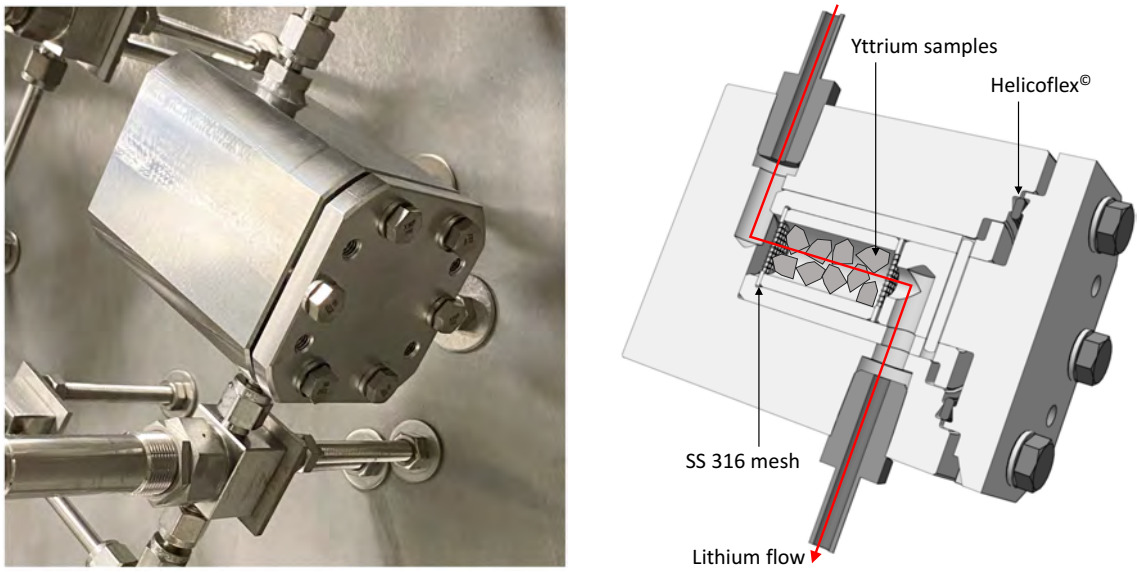

Fig. 8.21. [Left] Closed deuterium trap mounted in the lithium system of the LYDER experiment. [Right] Cross-sectional view into the inner structure of the deuterium getter trap showing the lithium flow path from above through the yttrium getter bed enclosed by two stainless steel meshes.

8.2.6. Thermal desorption branch

One method that might allow the approximate determination of the deuterium content of extracted lithium samples is called thermal desorption spectroscopy [285], [298]. In order to investigate the suitability of this measurement method for the relevant concentration range, it will be tested as part of the LYDER experiment. Therefore, a specially designed TDS branch is designed and constructed within the scope of this work.

It consists of a 1/2" pipe made of 316 stainless steel, which is attached to one of the pipe feedthroughs at the glove box roof by means of a double ferrule compression fitting. The lower end of the pipe terminates in a VCR male fitting that is secured by a pipe clamp in the center of the second support panel in the glove box. The TDS branch mounted to the left of the lithium system can be seen in figure 8.4. Outside the glove box, the TDS branch is attached to the control panel with an ISO-16KF bellows tube where it ends in a valve manifold. It provides a connection to a leak detector (HLT 570 SmartTest leak detector from Pfeiffer Vacuum [216]) via the open/close valve V-31 and to the argon gas line via the gas dosing valve V-32.

When the deuterium content of an extracted lithium sample is to be measured, the removable sample container, previously filled with a fixed volume of $V_{\mathrm{Li}}^{\mathrm{SC}} = 5\,\mathrm{mL}$ of deuterium-loaded liquid lithium, is disconnected from the VCR fitting of the sample extraction system and attached to the VCR fitting of the TDS branch. The measurement is started by opening valve V-11. Thus, the solid lithium in the sample container is exposed to the argon gas in the TDS branch. At this point, valve V-31 is opened and the turbomolecular pump of the leak detector is turned on which leads to an evacuation of the sample container to the high-vacuum regime. The leak detector has an internal pumping

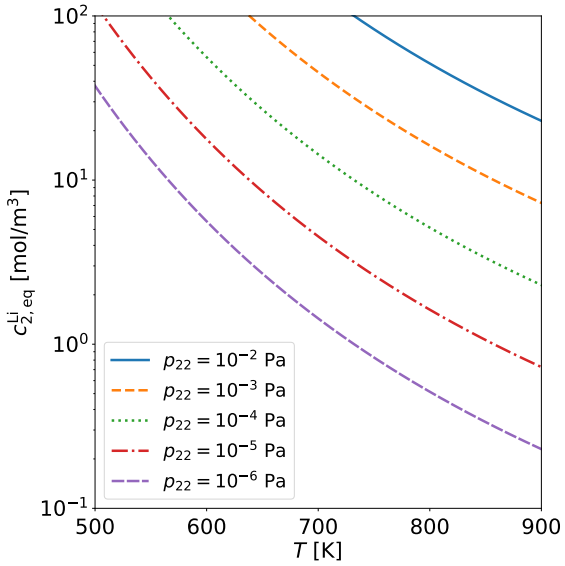

Fig. 8.22. Deuterium equilibrium concentration in liquid lithium as a function of the temperature at different $^2H_2$ partial pressures above the lithium surface.

speed of about $S_{\text{pump}} = 2.5\,\text{L}\,\text{s}^{-1}$ while inside the sample container, the effective pumping speed is calculated to be approximately $S_{\text{eff}} = 0.1\,\text{L}\,\text{s}^{-1}$ using the equations (3.4), (3.5) and (3.6). This relatively low effective pumping speed is mainly due to the thin duct that passes valve V-11 of the sample container.

Figure 8.22 shows the concentration in the lithium sample at thermodynamic equilibrium for different $^2H_2$ partial pressures above the lithium surface as a function of temperature. Since lithium occurs in the α-Li phase in the concentration and temperature range shown in the graph (see figure 7.6), the curves are calculated with the Sieverts' law (2.50). Therefore, the same Sieverts' constant (7.22) for hydrogen isotopes in lithium is used as that considered in the model presented in chapter 7.

The graph reveals that the higher the temperature and the lower the $^2H_2$ partial pressure above the lithium, the lower the concentration that would establish at thermodynamic equilibrium in the lithium sample. Hence, heating the lithium sample in a vacuum environment with a low $^2H_2$ partial pressure to a temperature that implies an equilibrium deuterium concentration that is lower than the initial concentration $c^{\text{Li}}_{2,\text{init}}$ in the extracted sample would cause the deuterium to desorb from the lithium surface.

In the presented experimental setup, the rate at which the deuterium atoms desorb from the sample surface as $^2H_2$ molecules is measured by the leak detector in terms of a desorption flow $q^{\text{desorb}}_{\text{pV},22}$ given in [mbar $\cdot$ L/s]. Therefore, the leak detector must be calibrated for deuterium flux measurements using a calibrated $^2H_2$ leak as described in section 3.2.4.

To determine the deuterium concentration of extracted lithium samples, the sample container is heated to the highest permissible temperature and the desorption flow is measured over time. Indeed, determining the time integral of the measured rate of desorbing deuterium isotopes from the beginning to the end of the desorption measurement gives the cumulative number of desorbed deuterium isotopes $\varkappa^{\text{Li}}_{2,\text{meas}}$ from the sample. In fact, the

measured value of $\varkappa^{\mathrm{Li}}_{2,\mathrm{meas}}$ matches the number of deuterium atoms initially dissolved in the sample $\varkappa^{\mathrm{Li}}_{2,\mathrm{init}} = c^{\mathrm{Li}}_{2,\mathrm{init}} V^{\mathrm{SC}}_{\mathrm{Li}}$ minus the number of deuterium isotopes $\varkappa^{\mathrm{Li}}_{2,\mathrm{final}} = c^{\mathrm{Li}}_{2,\mathrm{final}} V^{\mathrm{SC}}_{\mathrm{Li}}$ that remain in the sample after the measurement is stopped. Consequently, the deuterium concentration in the lithium sample prior to the TDS measurement must satisfy

$$c^{\mathrm{Li}}_{2,\mathrm{init}} = \frac{\varkappa^{\mathrm{Li}}_{2,\mathrm{meas}}}{V^{\mathrm{SC}}_{\mathrm{Li}}} + c^{\mathrm{Li}}_{2,\mathrm{final}} \,. \tag{8.8}$$

This equation shows that to accurately determine the initial concentration $c^{\mathrm{Li}}_{2,\mathrm{init}}$ of the extracted lithium sample from the measured value of $\varkappa^{\mathrm{Li}}_{2,\mathrm{meas}}$, the concentration in the lithium $c^{\mathrm{Li}}_{2,\mathrm{final}}$ at the end of the measurement must be as small as possible. Therefore, the desorption flow must be measured for as long as possible.

The highest temperature to which the sample container of the LYDER experiment may be heated is determined by the temperature limit of the installed high-temperature regulating valves of the sample container, which, according to the discussion in section 3.1.2, is $T = 921\,\mathrm{K}$. Such a high temperature is within the temperature range of the installed heating cables.

When neglecting the rate of $^2H_2$ molecules degassing from the walls of the sample container, the $^2H_2$ partial pressure p_{22} above the lithium surface that occurs during a thermal desorption experiment is determined by the relationship $p_{22} = q^{\mathrm{desorb}}_{\mathrm{pV},22}/S_{\mathrm{eff}}$ [see equation (3.9)]. This pressure determines the equilibrium concentration in the lithium sample shown in figure 8.22. As the declining concentration in the lithium sample approaches the momentary equilibrium concentration, the desorption flow $q^{\mathrm{desorb}}_{\mathrm{pV},22}$ decreases because the concentration gradients in the lithium flatten out. Since according to $p_{22} = q^{\mathrm{desorb}}_{\mathrm{pV},22}/S_{\mathrm{eff}}$, a decreasing desorption flow implies a decreasing $^2H_2$ partial pressure above the lithium surface in the sample container, the equilibrium concentration in the lithium will decrease over time. As a consequence, the desorption process will continue indefinitely with an ever decreasing desorption flow until no more deuterium is left in the sample (see 8.22). The time required for this to occur highly depends on the hydrogen surface recombination and dissociation kinetics of a free lithium surface, which in turn depends strongly on its state of oxidation and contamination [296].

Investigating the recombination and dissociation kinetics of hydrogen from a liquid lithium surface is another purpose of the developed TDS branch. This line of investigation is urgently needed to enable estimation of the rate at which tritium would degas from an open lithium surface in the event of an accidental lithium escape from the DONES lithium loop.

8.3. Commissioning

At this stage, the construction of the LYDER experiment is finished and the commissioning phase has begun. Prior to the installation of the thermal insulation, vacuum tests of the lithium system have been conducted. It was found that after the dry scroll pump SP-01

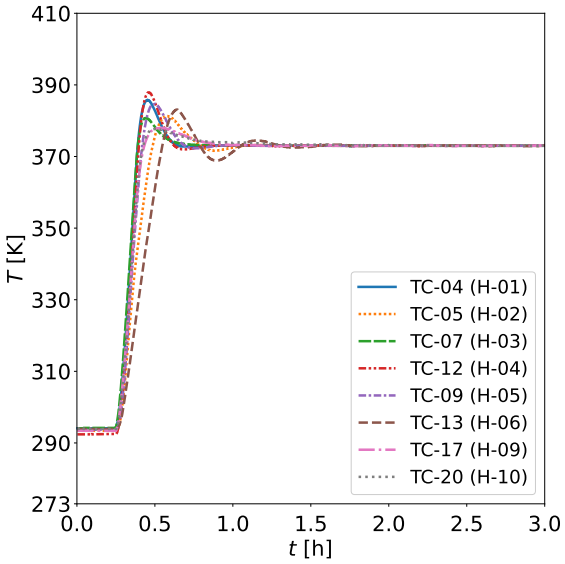

Fig. 8.23. Temperatures measured by thermocouples that are used to control heating elements of the LYDER system during a heating test up to $T = 373\,\mathrm{K}$.

is switched on, it takes only several minutes for the Pirani gauges PiG-01 and PiG-06 to indicate a total pressure of $p < 5 \times 10^{-2}\,\mathrm{Pa}$ which corresponds to the beginning of the high-vacuum regime. Vacuum testing was followed by helium leak testing of the entire vacuum and lithium systems as described in section 3.2.4. During the leak test campaign, the vacuum pump was replaced by the leak detector. The first leak measurements were performed in the cold state where leak rates of maximum $q_{\mathrm{pV}}^{\mathrm{leak}} = 1 \times 10^{-10}\,\mathrm{mbar \cdot L/s}$ could be registered. The leak test was repeated, this time in the warm state by heating the lithium system to a temperature of $T = 353\,\mathrm{K}$. Again, maximum leak rates of at most $q_{\mathrm{pV}}^{\mathrm{leak}} = 5 \times 10^{-10}\,\mathrm{mbar \cdot L/s}$ could be recorded. In conclusion, the constructed lithium and vacuum system of the LYDER experiment can be considered sufficiently leak tight.

Now, as the thermal insulation is attached to the lithium system (see figure 8.4), the heating test campaign is intensified. Figure 8.23 shows the temperature measurements of the thermocouples that are used to control the heating elements of the lithium system during a heating test in which the lithium system is heated to $T = 373\,\mathrm{K}$. Therefore, the temperature controllers are set to a temperature ramp of $5\,\mathrm{K\,min^{-1}}$ using the developed LabVIEW program. Since the thermal insulation of the sample container is not yet installed, the test is performed without the heating elements H-07 and H-08. The graph shows that the developed heating system works as expected as long as the set temperatures are still relatively low. Heating tests up to the lithium system operating temperature of $T = 623\,\mathrm{K}$ remain to be performed.

8.4. Procedure for deuterium retention experiments

This section presents an experimental procedure for deuterium retention experiments using the LYDER experiment. It is established with the goal of measuring the low-concentration distribution coefficient $K_{\mathrm{D,0}}^{\mathrm{Li-Y}}$ using equation (8.1).

The starting point of the procedure is a situation in which the glove box is closed

and the glove box purification and heat exchanger systems are functioning properly. This implies that the glove box contains a cooled, high-purity argon atmosphere. The experimental procedure requires that a scale be connected to the left-hand power plug insight the glove box (see figure 8.4). It is also assumed that all valves of the LYDER experiment are closed at the beginning and that the sample container is connected to the lithium system which is still free of lithium and yttrium. The following experimental procedure is described in sequential order.

First, the lithium system is evacuated. Therefore, the valves V-19, V-22, V-25, V-26, V-27, V-28, V-29, V-33 and all valves of the lithium system (shown in red in figure 8.2) except V-12 and V-13 are opened and the vacuum pump SP-01 is turned on. To degas the lithium system and ensure that it is freed from residual water molecules, it is heated to the maximum operating temperature of $T = 623\,\mathrm{K}$ using the LabVIEW control program and left in the hot state for several hours. Afterwards, it is cooled to ambient temperatures and the valves V-06, V-10, V-22, V-25, V-26, V-27 are closed. By manipulating either valve V-20 or V-23, the lithium system is then filled with argon gas until the pressure gauges DG-03 and DG-04 indicate the same pressure as DG-07 of about $p \approx 1 \times 10^5\,\mathrm{Pa}$. At this point, both the sample extraction system and the lithium dump tank remain evacuated and in direct contact with the vacuum pump SP-01.

In order to insert lithium and yttrium samples into the system, the valves V-03 and V-07 are closed and valve V-01 is opened, exposing the inside of the left tank to the glove box atmosphere. A purchased argon-filled bag containing exactly $V_{\mathrm{Li}} = 100\,\mathrm{mL}$ of lithium pallets (see figure 8.6) is opened and all the pallets are pushed one by one through the opening of valve V-01 before it is closed again.

Yttrium sample insertion is accomplished as follows. The valves V-04, V-05 and V-08 are closed, the flange of the trap container is opened with a wrench and the yttrium basket is pulled out of its socket before being disassembled. The amount of purchased yttrium pebbles to be placed in the trap is weighed beforehand using a scale inside the glove box. To ensure rapid deuterium absorption from the lithium during the experiment, the pebbles should be pre-treated with hydrogen fluoride, which removes any oxide layer that could act as a hydrogen diffusion barrier [299]. The yttrium pebbles are filled into the basket before it is reassembled as described in section 8.2.5. It is then flanged to the trap container using a new Helicoflex® gasket and valves V-04, V-05 and V-08 are opened.

At this point, the lithium system is prepared to be heated to the desired operating temperature which results in the melting of the liquid lithium at $T = 453.54\,\mathrm{K}$. To ensure that all parts of the lithium system are heated at approximately the same rate, it is decided to set the temperature ramp to $2\,\mathrm{K\,min^{-1}}$. This will allow the system to adjust smoothly to the thermal expansion that occurs. It is considered safe to heat the lithium-filled left tank in the presence of the enclosed argon atmosphere because the lithium vapor pressure at the maximum operating temperature of $T = 623\,\mathrm{K}$ is only about $p \approx 4 \times 10^{-4}\,\mathrm{Pa}$ [300].

To inject deuterium into the liquid lithium, it is pumped into the right tank via the

bypass line. Therefore, the valves V-04, V-05 and V-07 are closed and the pressure in the right tank is reduced by a value of $\Delta p > 2.5 \times 10^3$ Pa (see estimation of minimum required pressure difference in section 8.2.2). The lithium is set in motion when the regulating valve V-03 is slightly opened. The level sensors LS-01 and LS-02 will successively signal when the lithium surface has passed their respective heights, allowing the lithium flow rate to be determined using equation (8.2). Valve V-03 is closed when argon gas bubbles from the left tank into the right tank, which can be registered by the pressure gauges DG-03 and DG-04. At this point, the argon pressure in the right tank is brought back to the working pressure of about $p = 1 \times 10^5$ Pa by manipulating valve V-23.

The deuterium injection procedure is started by closing valve V-19 and filling the permeation chamber with a certain $^2H_2$ pressure manipulating valve V-17. It is recommended to perform the deuterium injection procedure at the highest operating temperature of $T = 623$ K. This guarantees the fastest injection flux and the fastest distribution of permeated deuterium in the lithium. The set pressure in the permeation chamber should have a value that, according to the simulation shown in figure 8.18, would allow the injection of the desired deuterium concentration in the lithium in a reasonable time. The pressure decrease in the closed permeation chamber is measured over time and the value of the average concentration of deuterium in the liquid lithium is calculated using equation (8.3). As soon as the desired initial deuterium concentration $c^{\mathrm{Li}}_{2,\mathrm{init}}$ is reached the $^2H_2$ gas is carefully removed from the permeation membrane via the gas dosing valve V-18.

In order to determine the low-concentration distribution coefficient with equation (8.1) it is necessary to measure the ratio of the concentrations in the lithium before and after the deuterium retention experiment. To obtain the most accurate measurement results of this ratio, it is reasonable to measure both the inital and the final concentration with the same experimental technique. Therefore, prior to the retention experiment, a sample of the deuterium-loaded lithium is extracted from the system and its deuterium content is measured with either the presented TDS method or with the chemical dissolution method described in [111]. To extract a sample from the lithium system into the connected sample container after deuterium injection, the lithium is moved from the right into the left tank via the bypass. Then, the valves V-02, V-03 and V-09 are closed. Upon opening valve V-06, a volume of $V^{\mathrm{SC}}_{\mathrm{Li}} \approx 5$ mL of liquid lithium enters the evacuated space between the valves V-02, V-06, and V-09. After closing valve V-06, valve V-09 is opened and the liquid lithium enclosed by the valves V-02, V-06 and V-09 is sucked into the evacuated sample container. To prevent lithium from remaining in the line above valve V-09, it may be pushed into the sample container by pressurized argon gas entering from above by opening the valves V-02, and V-30 after the valves V-26 and V-29 are closed.

To measure the concentration using the chemical dissolution method, the desired amount of liquid lithium is poured into a beaker placed under the sample container by carefully opening the regulating valve V-12 (see figure 8.8). The beaker is then removed from the glove box through the antechamber and transported in a sealed container to the chemical dissolution apparatus. In contrast to the developed TDS branch, the chemi-

cal dissolution measurements will be carried out at an external laboratory that is located within the same research center as the LYDER experiment, the Ciemat Institute in Madrid, Spain. The residual lithium in the sample container not needed for the chemical dissolution experiment is poured into another beaker via valve V-12 and dumped in a sealed container stored inside the glove box.

For concentration measurements using the TDS method, the sample container must be removed from the lithium system and plugged to the TDS branch. To do so, first, the valves V-02, V-09, V-11, and V-12 are closed and the remaining $V_{\mathrm{Li}} = 95\,\mathrm{mL}$ of liquid lithium that resided in the left tank are pumped into the right tank. Here, the lithium is kept in the liquid state at operating temperature. The heaters H-03, H-07, and H-08 are then turned off while all other heating elements are maintained at operating temperature. It is waited until the thermocouples TC-15 and TC-21 indicate that the sample container and the VCR fitting have cooled to ambient temperature before the sample container can be removed safely and plugged to the TDS branch. While the TDS measurement is being executed, a second sample container with the exact same design is connected to the VCR fitting of the sample extraction system. This allows directly continuing with the deuterium retention experiments without having to wait for the TDS measurement to finish. The sample extraction branch including the new sample container is subsequently evacuated via the valves V-02, V-26 and V-28 before the cold heating elements are brought back to operating temperature. After a TDS measurement has finished the residual lithium is pushed into a beaker via valve V-12 by pressurizing the TDS line with argon gas via valve V-32. It is then disposed of in the sealed container, which is stored in the glove box.

The deuterium retention process is initiated by pumping the deuterium-loaded lithium from the right tank through the yttrium pebble bed into the left tank. To do this, the pressure in the left tank is first reduced by a value of $\Delta p > 2.5 \times 10^3\,\mathrm{Pa}$, and the valves V-04 and V-07 are opened. The relationship between the number of turns of the actuator of regulating valve V-04 and the resulting lithium flow rate is to be determined as a function of the set pressure differential Δp during commissioning by performing preliminary lithium flow tests. This will allow a desired flow rate to be deliberately set in future experiments. As a result of the deuterium transport from the liquid lithium into the yttrium pebble bed the deuterium concentration in the lithium reaching the left tank is slightly reduced. Nevertheless, considering that $F_{\mathrm{trap}} \approx 50\,\mathrm{mL\,min^{-1}}$, a single passage of the liquid lithium through the trap would take only 114 seconds, which is not enough time for the two metal-hydrogen systems to reach thermodynamic equilibrium. Therefore, after the first passage is completed the lithium is moved back into the right tank via the bypass and a second passage through the trap is performed. A complete deuterium retention experiment with the LYDER experiment involves multiple passages through the trap until thermodynamic equilibrium is attained. After the last passage through the trap, a second lithium sample is extracted and the equilibrium concentration $c^{\mathrm{Li}}_{2,\mathrm{eq}}$ is measured. The ratio $c^{\mathrm{Li}}_{2,\mathrm{eq}}/c^{\mathrm{Li}}_{2,\mathrm{init}}$ is calculated and inserted in the formula (8.1) which provides a value for the low-concentration distribution coefficient $K^{\mathrm{Li-Y}}_{\mathrm{D},0}$.

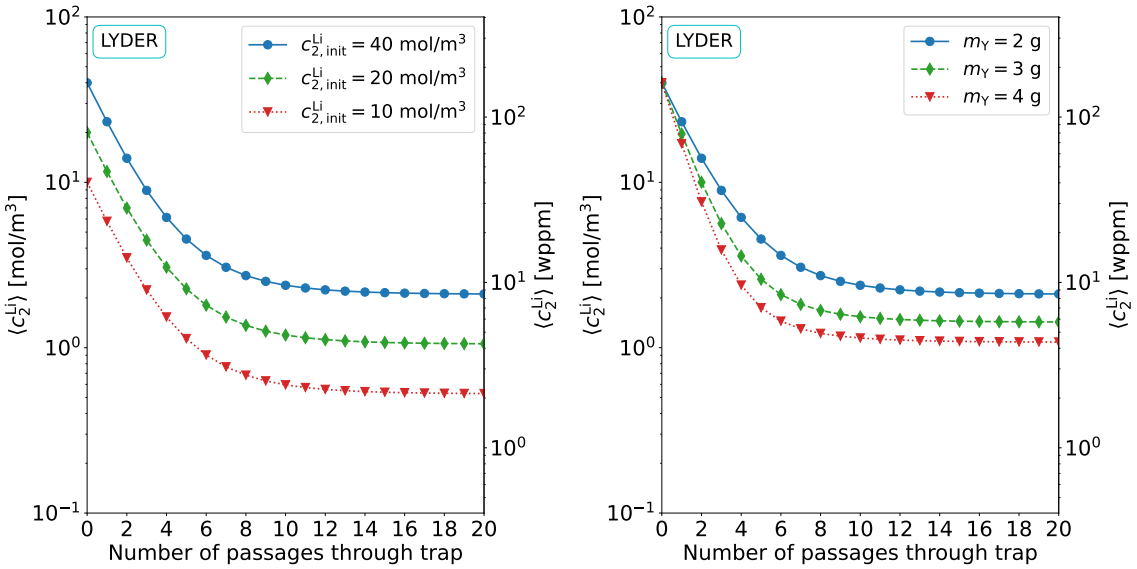

Fig. 8.24. Simulated average deuterium concentration in the lithium during deuterium retention experiments with the LYDER experiment as a function of the number of times the lithium has passed through the trap. [Left] Simulation considering different initial concentrations at $T = 623\,\mathrm{K}$, $m_Y = 2 \times 10^{-3}\,\mathrm{kg}$, $V_{Li} = 95\,\mathrm{mL}$, $F_{trap} = 50\,\mathrm{mL\,min^{-1}}$, $r_{peb} = 7.5 \times 10^{-4}\,\mathrm{m}$ and $d_{trap} = 1.3 \times 10^{-2}\,\mathrm{m}$ [Right] Simulation considering different pebble bed masses at $T = 623\,\mathrm{K}$, $c^{Li}_{2,init} = 40\,\mathrm{mol\,m^{-3}}$, $V_{Li} = 95\,\mathrm{mL}$, $F_{trap} = 50\,\mathrm{mL\,min^{-1}}$, $r_{peb} = 7.5 \times 10^{-4}\,\mathrm{m}$ and $d_{trap} = 1.3 \times 10^{-2}\,\mathrm{m}$.

In order to estimate the number of passages required to reduce the deuterium concentration in the lithium to a value close to the equilibrium concentration $c^{Li}_{2,eq}$, the deuterium retention process occurring in the LYDER experiment is simulated for different experimental conditions. Therefore, it is made use of the developed numerical model of the lithium loop connected to a hydrogen trap presented in chapter 7, whose EcosimPro© component structure is visualized in figure 7.1. The input parameters of the model are adapted to the lithium system of the LYDER experiment considering that $V_{Li} = 95\,\mathrm{mL}$, $F_{main} = F_{trap} = 50\,\mathrm{mL\,min^{-1}}$, $r_{peb} = 7.5 \times 10^{-4}\,\mathrm{m}$ and $d_{trap} = 1.3 \times 10^{-2}\,\mathrm{m}$.

The left-hand plot in figure 8.24 shows a simulation of the average deuterium concentration in the lithium during a retention experiment with the LYDER device for different initial concentrations assuming that $T = 623\,\mathrm{K}$ and $m_Y = 2 \times 10^{-3}\,\mathrm{kg}$. It can be seen that, according to the simulation, thermodynamic equilibrium is reached after about 12 lithium passages through the trap, each lasting about 114 seconds. Since for each of the initial concentrations shown, the simulated retention process takes place in the low-concentration α-Li phase and at the same temperature, the distribution coefficient and thus the ratio of the equilibrium to the initial concentration $c^{Li}_{2,eq}/c^{Li}_{2,init}$ remains equal [see equation (8.1)]. The right-hand plot shows the same simulation with a fixed initial concentration of $c^{Li}_{2,init} = 40\,\mathrm{mol\,m^{-3}}$ but a varying pebble bed mass. The simulation results are in accordance with equation (7.63) which states that an increased pebble bed mass reduces the equilibrium concentration at a constant low-concentration distribution coefficient. It is found that as long as the retention process occurs in the α-Li phase, a variation

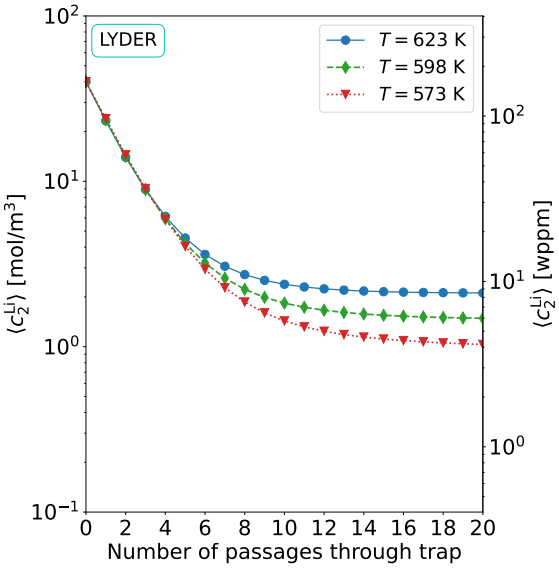

Fig. 8.25. Simulated average deuterium concentration in lithium during a deuterium retention experiment with the LYDER experiment considering different operating temperatures if $c^{\mathrm{Li}}_{2,\mathrm{init}} = 40\,\mathrm{mol\,m^{-3}}$, $m_{\mathrm{Y}} = 2 \times 10^{-3}\,\mathrm{kg}$, $V_{\mathrm{Li}} = 95\,\mathrm{mL}$, $F_{\mathrm{trap}} = 50\,\mathrm{mL\,min^{-1}}$, $r_{\mathrm{peb}} = 7.5 \times 10^{-4}\,\mathrm{m}$ and $d_{\mathrm{trap}} = 1.3 \times 10^{-2}\,\mathrm{m}$ plotted against the number of times the lithium has passed through the trap.

of the pebble bed mass or the initial concentration has no noticeable effect on the number of passages through the trap required to reach equilibrium.

To experimentally determine the temperature dependency of the low-concentration distribution coefficient it is necessary to perform the retention experiments at different temperatures which are simulated and plotted in figure 8.25. It can be seen that the simulated ratio $c^{\mathrm{Li}}_{2,\mathrm{eq}}/c^{\mathrm{Li}}_{2,\mathrm{init}}$ increases with temperature. This is because the low-concentration distribution coefficient decreases with increasing temperature (see figure 7.11). Since the diffusion coefficient decreases with decreasing temperature it requires a higher number of passages through the trap for thermodynamic equilibrium to be attained (about 20 passages at $T = 573\,\mathrm{K}$).

At the end of a deuterium retention experiment, the lithium from the left tank is drained into the evacuated dump tank below. To do this, the valves V-08 and V-29 are closed before the valves V-07 and V-10 are opened. The user will be notified when all the lithium has entered the dump tank because at that moment the pressure in the left tank will drop significantly. To ensure that no lithium remains in the right tank or the deuterium trap before the lithium system is cooled, the valves V-03, V-04, and V-08 are opened and the argon pressure in the right tank pushes the remaining lithium into the dump tank. Then, valve V-10 is closed, the dump tank is evacuated, and the argon pressure in the lithium system is brought back to about $p = 1 \times 10^5\,\mathrm{Pa}$. Finally, the heating elements of the lithium system are turned off. When all thermocouples indicate ambient temperature, the yttrium basket is removed from the trap container.

After the deuterium retention experiment is completed, the used deuterium-containing yttrium pebbles are examined for their deuterium content, surface oxidation state, evidence of yttrium dihydride formation, etc. Therefore, various experimental methods are going to be applied, such as the chemical dissolution method [111], thermal desorption spectroscopy, secondary ion mass spectroscopy, or energy dispersive X-ray spectroscopy.

9. CONCLUSION

Harnessing fusion energy on Earth could make it possible to meet the world's growing energy needs without increasing the use of nuclear fission or fossil fuels. The technical realization of this new energy source in the coming decades depends on the construction of two key experimental fusion devices: DEMO and IFMIF-DONES. For both devices, the release of tritium into external plant systems and ultimately into the environment is a critical safety issue that must be mitigated as much as possible by technical means.

Of special interest are the controlled application of multi-isotopic transport effects as a method to affect the tritium permeation flux into the coolant of a WCLL or an HCPB breeding blanket in DEMO and the use of an yttrium getter bed for tritium capture in the liquid lithium loop of DONES. To date, there is insufficient experimental and theoretical analysis in the available scientific literature to evaluate these methods as suitable tritium mitigation techniques, nor to define the technical requirements for a successful implementation of these methods in the respective facilities.

Therefore, the established general objective of this dissertation has been the development of the scientific framework that allows defining the conditions under which each of these techniques could be implemented as reliable tritium mitigation methods.

For this purpose, theoretical and numerical models have been developed from scratch and used to evaluate the proposed tritium safety measures in DEMO and DONES. Furthermore, two new experimental facilities have been designed and put into operation with the purpose of validating the numerical and theoretical models and measuring critical experimental parameters on which the models are based.

After introducing the research contexts and relevant theoretical foundations in the first three chapters 1 - 3, the chapters 4 - 8 are dedicated to the novel work conducted by the author of this thesis. The following paragraphs summarize, by chapter, the main results obtained and the activities carried out:

Chapter 4 presented a comprehensive theoretical analysis of multi-isotopic hydrogen permeation through metal from gas to gas (relevant for HCPB blankets) and from liquid metal to water (relevant for WCLL blankets). The results of this chapter, listed below, provided the theoretical basis for an evaluation of the potential use of multi-isotope transport effects for tritium control in HCPB and WCLL breeding blankets which was presented in chapter 5.

- It was possible to theoretically demonstrate why the permeation flux of a given hydrogen isotope species through a metal membrane is either enhanced or reduced when a different hydrogen isotope co- or counter-permeates through the membrane. The origin of this isotope effect of multi-isotopic transport could be revealed for both a gas-to-gas and a liquid metal-to-water permeation scenario.

- On the basis of simplifying assumptions, new algebraic formulas have been theoretically derived which provide the permeation flux of a given hydrogen isotope species through a parallel or cylindrical membrane from gas to gas and from liquid metal to water as a function of the concentration of another more abundant, co- or counter-permeating hydrogen isotope species.

- The complete theoretical relationship between the gas-to-gas permeation flux reduction factor of a given hydrogen isotope species permeating in the surface-limited regime and the permeation number of a different co- or counter-permeating hydrogen isotope species could be derived and graphically represented for the first time using a numerically obtained solution of the general equation of steady-state permeation.

- It could be demonstrated that in a multi-isotope gas-to-gas co- or counter-permeation scenario, the flux of a permeating hydrogen isotope species is greatly reduced when a different hydrogen isotope species co- or counter-permeates in the diffusion-limited permeation regime. Gas-to-gas co-permeation is observed to have a stronger permeation flux reducing effect than gas-to-gas counter-permeation.

- It was found that in a multi-isotopic co- or counter-permeation scenario from liquid metal to water, the flux of a permeating hydrogen isotope species increases with increasing concentration of a second distinct co- or counter-permeating hydrogen isotope species. In fact, as the concentration of the second species increases, the permeation flux of the first species approaches a certain maximum value.

- Moreover, an algebraic formula was derived describing the mono-isotopic hydrogen permeation flux from liquid metal to water or vacuum as a function of the hydrogen isotope concentration in the liquid metal. This equation is particularly useful when designing tritium extraction systems or hydrogen concentration sensors for flowing molten metal based on the permeation to vacuum technology.

Chapter 5 was devoted to the numerical investigation of multi-isotopic transport in both an HCPB and a WCLL breeding blanket. Thus, the results obtained in chapter 4 could be numerically validated and a possible application of multi-isotopic permeation as a tritium mitigation method for breeding blankets was critically analyzed.

- A hydrogen transport model of the HCPB breeding blanket purge gas system has been developed. By performing numerical simulations, the multi-isotopic transport effects an injection of protium to the coolant or the purge gas of an HCPB breeding blanket has on the tritium permeation flux into the coolant were analyzed in detail.

- Using the developed model, algebraic equations derived in chapter 4 could be verified numerically by using them to reproduce the numerical results of simulated pure co- and counter-permeation scenarios in an HCPB breeding blanket.

- The performed numerical simulations could show that injecting $^1H_2$ gas into the coolant reduces the tritium permeation flux from the purge gas into the coolant when the partial pressure of the injected $^1H_2$ gas is greater than a critical value. Below this critical value, the tritium permeation flux increases, which must be avoided at all costs. It was found that efficient reduction of the tritium permeation flux would require injecting $^1H_2$ partial pressures into the coolant, which are probably too high to be technically feasible.

- However, it was found that increasing the partial pressure of $^1H_2$ gas in the purge gas instead of in the coolant results in a much more efficient reduction of the tritium permeation flux at still relatively low $^1H_2$ partial pressures. Therefore, the conducted evaluation suggested that injecting additional $^1H_2$ gas into the purge gas should indeed be considered for implementation in an HCPB blanket as an effective and inexpensive tritium permeation mitigation method.

- With the numerical simulations of tritium permeation processes in an HCPB breeding blanket it could also be shown that an addition of water vapor to the purge gas would have a strong decreasing effect on the tritium permeation flux to the coolant.

- Moreover, a numerical model of the tritium permeation processes that occur between the PbLi breeder fluid and the coolant water in a WCLL breeding blanket has been developed. The tritium permeation flux was found to approach a certain maximum value with increasing protium concentration in the system. Therefore, it was concluded that to mitigate tritium permeation in a WCLL breeding blanket, the protium concentration in the water coolant must be kept as low as possible.

- The numerical simulations carried out using the numerical model of the WCLL breeder zone allowed verifying the algebraic formulas for co- and counter permeation from liquid metal to water derived in chapter 4.

- As part of the experimental investigation conducted in this chapter, a numerical model of a gas-to-gas counter-permeation experiment presented in the literature was developed in this thesis. The experimental results were successfully reproduced numerically, demonstrating the experimental validation of the model. In addition, algebraic counter-permeation formulas derived in chapter 4 have been applied to the conditions of the experimental permeation process. It was found that the derived algebraic formulas reproduce the experimental results very well.

To allow for additional in-situ experimental validation of gas-to-gas co- and counter-permeation with Eurofer'97 as the membrane material, a new hydrogen isotope co- and counter-permeation experiment has been designed and was put into operation within the scope of this work. It is called COOPER experiment. Besides, the COOPER experiment is designed to enable measuring hydrogen transport parameters of Eurofer'97 that are

required as input parameters for the models. Chapter 6 presented the design, commissioning and established experimental procedures of the COOPER experiment. Moreover, first mono-isotopic permeation measurements were presented.

- The developed COOPER permeation chamber consists of an upstream and a downstream gas chamber separated by a Eurofer'97 sample disk. A heating system was designed to reach sample disk temperatures of up to $T = 923\,\mathrm{K}$. A gas supply system consisting of two gas tanks permits the user to mix and inject arbitrary partial pressure configurations of $^1H_2$ and $^2H_2$ gas into both the upstream and downstream chambers. The experimental design enables the measurement of deuterium permeation fluxes into an evacuated downstream chamber (for mono-isotopic and co-permeation measurements) or into a $^1H_2$ filled downstream chamber (for counter-permeation measurements) using a calibrated QMS.

- Finite element thermal steady-state calculations of the designed COOPER permeation chamber were executed using the simulation software ANSYS. They anticipated a nearly homogeneous radial temperature profile throughout the disk surface which is important for the accurate measurement of hydrogen transport parameters.

- For the control of the heater and the measurement of the pressures and temperatures of the COOPER experiment, a LabVIEW program was developed from scratch.

- During the commissioning, vacuum and heating tests were conducted that confirmed that the system is sufficiently leak tight and that the heating system works as predicted with the finite element steady-state thermal calculations. In addition, sensitivity tests of the QMS detector were performed to determine the range of $^2H_2$ upstream pressures at which permeation flux measurements can be conducted.

- After an analysis of the material composition of the installed Eurofer'97 sample disk using EDX spectroscopy, a set of mono-isotopic deuterium permeation flux measurements at different temperatures were performed. This involved a previous calibration of the QMS to allow for deuterium permeation flux measurements. The executed experimental procedure established for mono-isotopic permeation measurements was described in detail.

- The experimental data obtained from the conducted mono-isotopic permeation measurements was used to determine the permeability, diffusion coefficient and Sieverts' constant of deuterium in Eurofer'97 in an HCPB-relevant temperature range.

- Established experimental procedures for co- and counter-permeation measurements with the COOPER experiment were described in detail.

- Simulations of co- and counter-permeation flux measurements were performed with a numerical hydrogen transport model of the COOPER permeation chamber that was developed within the scope of this work.

An appropriate design of the hydrogen hot trap for the DONES liquid lithium loop depends on the development of an accurate numerical simulation tool that can predict the hydrogen isotope absorption behavior of an yttrium pebble bed exposed to hydrogen-loaded flowing liquid lithium. This has been the objective of the work presented in chapter 7 of this dissertation. The obtained results presented in this chapter are listed below.

- A new numerical model of hydrogen isotope transport in an yttrium-based hydrogen getter trap connected to the liquid lithium loop of DONES has been developed from scratch using EcosimPro©. It incorporates the physics of yttrium hydride formation into a system-level hydrogen transport model, which has never been done before.
- A generalized concentration boundary condition for the Li-Y interface was derived by approximating the courses of complete PCIs of the Y-H and Li-H systems in the DONES-relevant temperature range. This allowed determining the solubility of hydrogen in yttrium as a function of the concentration in the surrounding liquid lithium. It was found to highly increase when yttrium dihydride forms.
- Moreover, a relation for the concentration dependency of the diffusion coefficient in different yttrium hydride phases could be derived for the first time.
- By simulating the evolving hydrogen isotope concentrations in the lithium loop and the yttrium pebble bed during different DONES operating phases, the effects of yttrium dihydride formation on the trap performance were analyzed in detail.
- It has been found that the formation of yttrium dihydride during DONES operation would greatly increase the hydrogen gettering capacity of the trap and prevent the tritium concentration in the lithium loop from rising above a critical value.
- It is discovered that by selecting an appropriate operating temperature of the trap, the formation of yttrium dihydride can be deliberately induced which highly reduces the yttrium mass in the trap required to meet DONES safety limits.
- A mode of operation relevant to the DONES experimental phase could be identified that involves replacing the hydrogen trap after at least every 28 days so that the tritium contents in the lithium and the yttrium remain below safety limits.
- Furthermore, this work defined the conditions for the mass of the yttrium pebble bed and the temperature of the installed trap that would allow keeping hydrogen isotope concentrations in the lithium and the trap below DONES safety limits.
- Analytical formulas have been derived that enable calculating the minimum required trap mass at any given temperature for both the initial purification phase and the experimental phase of DONES, taking into account error ranges.
- The developed model was tested against experimental results. Simulation and measurement data were found to be in good accordance within each other's error limits.

Measuring critical experimental parameters that determine the hydrogen capacity of an yttrium getter bed exposed to hydrogen loaded-liquid lithium and further experimental validation of the developed numerical model which was presented in chapter 7 are the objectives of a new liquid lithium experiment, called LYDER. It was developed as part of this thesis and presented in chapter 8 of this thesis.

- The development of the LYDER experiment involved the construction of a specially designed glove box with an attached antechamber.
- A new experimental liquid lithium system has been designed and constructed inside the developed glove box. It allows the circular movement of up to $V_{\mathrm{Li}} = 100\,\mathrm{mL}$ of deuterium-loaded liquid lithium between two tanks.
- A deuterium injection system has been designed as part of the lithium system. It enables loading the liquid lithium with a controlled concentration of deuterium. The chosen injection method is permeation from a $^2H_2$ filled chamber through a custom-designed α-iron membrane into the lithium.
- A numerical model of the deuterium injection system was developed to allow numerical simulation of the deuterium injection process. The numerical model has been used to define the appropriate size and thickness of the permeation membrane and allows the calculation of the required $^2H_2$ upstream pressure in the permeation chamber to load the lithium with a given concentration in a reasonable time.
- To enable yttrium-based deuterium retention experiments with the LYDER system, the deuterium-loaded liquid lithium will be pumped through an experimental deuterium trap filled with yttrium pebbles. The trap was designed and manufactured within the scope of this work.
- The lithium system has been equipped with a specially designed lithium extraction system that allows small lithium samples to be taken for subsequent measurement of their deuterium content.
- An experimental branch for thermal desorption spectroscopy of the extracted lithium samples was designed and mounted inside the glove box. Is purpose is to measure the deuterium content in the lithium samples and to study the kinetics of hydrogen desorption from liquid lithium.
- With the LYDER system fully assembled, the first heating and vacuum tests of the lithium system were conducted. They showed that the lithium system is leak tight and that the heating system is working well.
- An established procedure for performing deuterium retention experiments with the LYDER system was presented and supported by numerical simulations.

In conclusion, the general research objectives of this dissertation, defined in section 1.3, have been achieved.

10. FUTURE WORK

This dissertation presented the development of new numerical models and experimental devices for the study of multi-isotopic hydrogen permeation and gettering in fusion-relevant materials. However, their potential applications have only been partially exploited in this work. In fact, the activities carried out have opened several new lines of research that should be pursued in future research campaigns. Some of the numerical and experimental work that remains to be done is presented below:

Among other activities, within the scope of this work, first mono-isotope permeation measurements with the developed COOPER experiment were carried out. In the future, the mono-isotopic permeation measurements will be extended to characterize in which driving pressure ranges the observed permeation processes occur in the diffusion-limited and in the surface-limited regime. This helps to ensure that hydrogen transport parameters are being measured in the appropriate permeation regime. Furthermore, it will be verified whether the installation of a mirror polished Eurofer'97 permeation membrane results in the measurement of hydrogen transport parameters closer to the literature values than those obtained in the preliminary measurements. In addition, mono-isotopic permeation measurements in the surface-limited regime will be performed to measure the dissociation rate coefficient of $^2H_2$ molecules on a Eurofer'97 surface.

Moreover, first co- and counter-permeation measurements with the COOPER experiment will be executed according to the experimental procedures presented in section 6.4. The observation of a decreasing deuterium permeation flux with increasing $^1H_2$ partial pressure would be a major achievement. The obtained experimental data will be compared with the simulation results of the developed model of the COOPER experiment for experimental validation of the model.

The development of the numerical model of hydrogen transport in different yttrium hydride phases presented in chapter 7 has opened the possibility to numerically investigate the hydrogen isotope absorption and desorption kinetics of an yttrium pebble bed exposed to a gas or a vacuum. Thus, it is planned to investigate numerically under which pressure and temperature conditions an exhausted yttrium pebble bed could be degassed and recovered for reuse as a getter trap in the DONES lithium loop. For this purpose, the developed numerical model of the pebble bed will be slightly modified to allow for the simulation of hydrogen transport across a gas-yttrium interface.

However, performing a numerical simulation of a hydrogen degassing process from an yttrium pebble bed would require the unknown temperature relations of the hydrogen recombination and dissociation coefficients at a gas-yttrium interface as input parameters. These parameters are planned to be experimentally determined with the COOPER experiment by performing mono-isotopic permeation measurements of deuterium through an yttrium membrane in the surface-limited permeation regime. The influence of the yttrium

surface condition on the degassing rate will also be investigated experimentally and the results will be incorporated into the model. Finally, the modified numerical model of hydrogen isotopes degassing from an yttrium pebble will be experimentally validated by reproducing TDS measurements of deuterium-loaded yttrium samples.

The development of the LYDER experiment has opened up another line of research. In the near future, the commissioning phase of the LYDER experiment will be completed by testing the heating system at higher temperatures and the functioning of all glove box auxiliary systems. Afterwards, the proper movement of molten lithium between the two tanks will be verified. In addition, the deuterium injection system will be tested and the first lithium samples will be extracted. The designed TDS branch of the LYDER experiment will be evaluated as an appropriate method to measure the deuterium concentration in lithium. Preliminary deuterium retention experiments will be performed with the LYDER experiment. Thus, it will be intended to determine the low-concentration distribution coefficient of the H-Li-Y system. To validate the numerical model presented in chapter 7, future experimental results with the LYDER experiment will be compared with the simulation results of the deuterium retention measurements shown in chapter 8.

The developed TDS branch of the LYDER experiment enables the experimental investigation of the hydrogen isotope desorption kinetics from a free liquid lithium surface. To date, there is insufficient information in the literature to estimate the rate at which tritium would degas from a liberated tritium-loaded lithium surface in an accidental scenario of DONES. Performing TDS measurements with the developed TDS branch may provide sufficient information to make such an estimation possible.

BIBLIOGRAPHY

[1] United Nations - Department of Economic and Social Affairs, *World population prospects 2022*, Data Table, 2022. [Online]. Available: https://population.un.org/wpp/Download/Standard/CSV/.

[2] BP, "Statistical review of world energy - 71st edition," The British Petroleum Company plc, Tech. Rep., 2022. [Online]. Available: https://www.bp.com/content/dam/bp/business-sites/en/global/corporate/pdfs/energy-economics/statistical-review/bp-stats-review-2022-full-report.pdf.

[3] U.S. Energy Information Administration, *International Energy Outlook - World total energy consumption by region and fuel*, Data Table, 2021. [Online]. Available: https://www.eia.gov/outlooks/ieo/tables_side_pdf.php.

[4] M. Kikuchi, K. Lackner, and M. Quang Tran, *Fusion Physics*. Vienna, Austria: International Atomic Energy Agency, 2012. [Online]. Available: https://www-pub.iaea.org/MTCD/Publications/PDF/Pub1562_web.pdf.

[5] Core Writing Team, R.K. Pachauri and L.A. Meyer (eds.), *Climate Change 2014: Synthesis Report. Contribution of Working Groups I, II and III to the Fifth Assessment Report of the Intergovernmental Panel on Climate Change*. Geneva, Switzerland: IPCC, 2014. [Online]. Available: https://www.ipcc.ch/site/assets/uploads/2018/05/SYR_AR5_FINAL_full_wcover.pdf#page=22.

[6] A. Gabbard, "Coal combustion: Nuclear resource or danger," *Oak Ridge National Laboratory Review; (United States)*, vol. 26:3-4, Jan. 1993. [Online]. Available: https://www.osti.gov/biblio/6686041.

[7] R. D. Griffin, *Alternative energy : can renewable energy sources replace fossil fuels?* Washington, D.C.: Congressional Quarterly, Inc, 1992.

[8] M. Stephenson, *Energy and Climate Change*. Washington, D.C.: Elsevier, 1992. DOI: https://doi.org/10.1016/C2016-0-02166-6.

[9] United Nations - Treaty Collection. "Paris agreement." Accessed: 22-02-2023. (2021), [Online]. Available: https://treaties.un.org/Pages/ViewDetails.aspx?src=IND&mtdsg_no=XXVII-7-d&chapter=27&clang=_en.

[10] IAEA, "The Chernobyl accident," Vienna, Austria, Tech. Rep., 1992. [Online]. Available: https://www-pub.iaea.org/MTCD/publications/PDF/Pub913e_web.pdf.

[11] IAEA, "The Fukushima Daiichi accident," Vienna, Austria, Tech. Rep., 2015. [Online]. Available: https://www.iaea.org/publications/10962/the-fukushima-daiichi-accident.

[12] ITER Organization. “Fueling the fusion reaction.” Accessed: 01-03-2023. (2023), [Online]. Available: https://www.iter.org/sci/FusionFuels.

[13] S. Okada and N. Momoshima, “Overview of tritium: Characteristics, sources, and problems,” *Health Physics; (United States)*, vol. 65, Dec. 1993. DOI: https://doi.org/10.1097/00004032-199312000-00001.

[14] M. Kovari, M. Coleman, I. Cristescu, and R. Smith, “Tritium resources available for fusion reactors,” *Nuclear Fusion*, vol. 58, no. 2, p. 026 010, 2017. DOI: https://dx.doi.org/10.1088/1741-4326/aa9d25.

[15] I. E. Lyublinski, A. V. Vertkov, and V. A. Evtikhin, “Application of lithium in systems of fusion reactors. 1. physical and chemical properties of lithium,” *Plasma Devices and Operations*, vol. 17, no. 1, pp. 42–72, 2009. DOI: https://doi.org/10.1080/10519990802703277.

[16] U. Wietelmann and M. Steinbild, “Lithium and lithium compounds,” in *Ullmann’s Encyclopedia of Industrial Chemistry*. John Wiley & Sons, Ltd, 2014, pp. 1–38. DOI: https://doi.org/10.1002/14356007.a15_393.pub2.

[17] U.S. Geological Survey, “Lithium,” Mineral Commodity Summaries 2021, Tech. Rep., 2021. [Online]. Available: https://pubs.usgs.gov/periodicals/mcs2021/mcs2021-lithium.pdf.

[18] D. Fasel and M. Tran, “Availability of lithium in the context of future D–T fusion reactors,” *Fusion Engineering and Design*, vol. 75-79, pp. 1163–1168, 2005, Proceedings of the 23rd Symposium of Fusion Technology. DOI: https://doi.org/10.1016/j.fusengdes.2005.06.345.

[19] A. Hishinuma, A. Kohyama, R. L. Klueh, D. S. Gelles, W. Dietz, and K. Ehrlich, “Current status and future R&D for reduced-activation ferritic/martensitic steels,” *Journal of Nuclear Materials*, vol. 258263, pp. 193–204, 1998.

[20] M. Zucchetti, L. Candido, V. Khripunov, B. Kolbasov, and R. Testoni, “Fusion power plants, fission and conventional power plants. Radioactivity, radiotoxicity, radioactive waste,” *Fusion Engineering and Design*, vol. 136, pp. 1529–1533, 2018, Special Issue: Proceedings of the 13th International Symposium on Fusion Nuclear Technology (ISFNT-13). DOI: https://doi.org/10.1016/j.fusengdes.2018.05.049.

[21] B. Povh, K. Rith, C. Scholz, F. Zetsche, and M. Lavelle, *Particles and Nuclei - An Introduction to the Physical Concepts*. Berlin, Heidelberg, Germany: Springer, 2008. DOI: https://doi.org/10.1007/978-3-540-79368-7.

[22] A. Einstein, “Ist die Trägheit eines Körpers von seinem Energieinhalt abhängig?” *Annalen der Physik*, vol. 323, no. 13, pp. 639–641, 1905. DOI: https://doi.org/10.1002/andp.19053231314.

[23] G. Audi, A. H. Wapstra, and C. Thibault, "The AME2003 atomic mass evaluation: (II). Tables, graphs and references," *Nuclear Physics A*, vol. 729, no. 1, pp. 337–676, 2003. DOI: https://doi.org/10.1016/j.nuclphysa.2003.11.003.

[24] International Atomic Energy Agency. "Evaluated Nuclear Data File." Accessed: 20-02-2023. (2023), [Online]. Available: https://www-nds.iaea.org/exfor/endf.htm.

[25] J. D. Lawson, "Some criteria for a power producing thermonuclear reactor," *Proceedings of the Physical Society. Section B*, vol. 70, no. 1, p. 6, 1957. DOI: https://doi.org/10.1088/0370-1301/70/1/303.

[26] J. Wesson, *Tokamaks*. Oxford, UK: Oxford University Press, 2004.

[27] R. Betti, "A milestone in fusion research is reached," *Nature Reviews Physics*, vol. 5, pp. 6–8, 2023. DOI: https://doi.org/10.1038/s42254-022-00547-y.

[28] W. Meier, A. Dunne, K. Kramer, S. Reyes, and T. M. Anklam, "Fusion technology aspects of laser inertial fusion energy (life)," vol. 89, Sep. 2013. [Online]. Available: https://www.osti.gov/biblio/1256449.

[29] A. Einstein, "Zur Elektrodynamik bewegter Körper," *Annalen der Physik*, vol. 322, pp. 891–921, 10 1905. DOI: https://doi.org/10.1002/andp.19053221004.

[30] K. Miyamoto, *Controlled Fusion and Plasma Physics*. Boca Raton, Florida: CRC Press, 2006. DOI: https://doi.org/10.1201/b15898.

[31] Max-Planck-Institut für Plasmaphysik, *Kernfusion - Berichte aus der Forschung*, Booklet, 2002. [Online]. Available: https://www.ipp.mpg.de/46732/3_berichte.

[32] J. G. Roederer, "Early cosmic-ray research in Argentina," *Physics Today 56*, vol. 57, pp. 32–37, 2003. DOI: https://doi.org/10.1063/1.1554134.

[33] S. Mayo, "More on the value of Ronald Richter's work," *Physics Today 57*, vol. 57, pp. 14–15, 2004. DOI: https://doi.org/10.1063/1.1712480.

[34] I. E. Tamm, "Theory of a magnetic thermonuclear reactor," in *Selected Papers*, B. M. Bolotovskii, V. Y. Frenkel, and R. Peierls, Eds. Berlin, Heidelberg: Springer Berlin Heidelberg, 1991, pp. 213–238. DOI: https://doi.org/10.1007/978-3-642-74626-0_16.

[35] L. Spitzer, "The stellarator concept," *The Physics of Fluids*, vol. 1, no. 4, pp. 253–264, 1958. DOI: https://aip.scitation.org/doi/abs/10.1063/1.1705883.

[36] C. Alejaldre *et al.*, "First plasmas in the TJ-II flexible Heliac," *Plasma Physics and Controlled Fusion*, vol. 41, no. 3A, A539, 1999. DOI: https://dx.doi.org/10.1088/0741-3335/41/3A/047.

[37] T. S. Pedersen *et al.*, "Confirmation of the topology of the Wendelstein 7-X magnetic field to better than 1:100,000," *Nature Communications*, vol. 7, p. 13 493, 2016. DOI: https://doi.org/10.1038/ncomms13493.

[38] Max-Planck-Institut für Plasmaphysik, *Fusion Basics - Nuclear fusion status and prospects*, Booklet, 2019. [Online]. Available: https://www.ipp.mpg.de/986335/1_faltblatt.

[39] C. Gliss, *June-2017 DEMO Reference Configuration Model*, CAD model, 2017. [Online]. Available: https://idm.euro-fusion.org/default.aspx?uid=2N4EZW.

[40] A. Del Nevo and P. Arena, "2020 WCLL DDD - Participation to the PCDR and updating of the documentation," EUROfusion, EFDA_D_2NX3NV, Tech. Rep., 2021. [Online]. Available: https://idm.euro-fusion.org/default.aspx?uid=2NX3NV.

[41] R. Aymar, P. Barabaschi, and Y. Shimomura, "The ITER design," *Plasma Physics and Controlled Fusion*, vol. 44, no. 5, p. 519, 2002. DOI: https://dx.doi.org/10.1088/0741-3335/44/5/304.

[42] L. Giancarli *et al.*, "Overview of the ITER TBM program," *Fusion Engineering and Design*, vol. 87, no. 5, pp. 395–402, 2012, Tenth International Symposium on Fusion Nuclear Technology (ISFNT-10). DOI: https://doi.org/10.1016/j.fusengdes.2011.11.005.

[43] G. Federici, C. Baylard, A. Beaumont, and J. Holden, "The plan forward for EU DEMO," *Fusion Engineering and Design*, vol. 173, p. 112 960, 2021. DOI: https://doi.org/10.1016/j.fusengdes.2021.112960.

[44] A. J. Creely *et al.*, "Overview of the SPARC tokamak," *Journal of Plasma Physics*, vol. 86, no. 5, p. 865 860 502, 2020. DOI: 10.1017/S0022377820001257.

[45] R. Srinivasan, "Design and analysis of SST-2 fusion reactor," *Fusion Engineering and Design*, vol. 112, pp. 240–243, 2016. DOI: https://doi.org/10.1016/j.fusengdes.2015.12.044.

[46] G. Zhuang *et al.*, "Progress of the CFETR design," *Nuclear Fusion*, vol. 59, no. 11, p. 112 010, 2019. DOI: https://dx.doi.org/10.1088/1741-4326/ab0e27.

[47] EUROfusion Consortium Research Institutions, *European research roadmap to the realisation of fusion energy*, 2018. [Online]. Available: https://euro-fusion.org/wp-content/uploads/2022/10/2018_Research_roadmap_long_version_01.pdf.

[48] A. J. H. Donné, "The European roadmap towards fusion electricity," *Philosophical Transactions of the Royal Society A: Mathematical, Physical and Engineering Sciences*, vol. 377, no. 2141, p. 20 170 432, 2019. DOI: https://doi.org/10.1098/rsta.2017.0432.

[49] G. Federici *et al.*, "DEMO design activity in Europe: Progress and updates," *Fusion Engineering and Design*, vol. 136, pp. 729–741, 2018, Special Issue: Proceedings of the 13th International Symposium on Fusion Nuclear Technology (ISFNT-13). DOI: https://doi.org/10.1016/j.fusengdes.2018.04.001.

[50] G. Federici, J. Holden, C. Baylard, and A. Beaumont, "The EU DEMO staged design approach in the pre-concept design phase," *Fusion Engineering and Design*, vol. 173, p. 112 959, 2021. DOI: https://doi.org/10.1016/j.fusengdes.2021.112959.

[51] W. Ronald, "DEMO1 Reference design - 2017 March (EU DEMO1 2017)," EUROfusion, EFDA_D_2NE9JA, Tech. Rep., 2017. [Online]. Available: https://idm.euro-fusion.org/default.aspx?uid=2NE9JA.

[52] C. Bachmann, "Plant description document," EUROfusion, EFDA_D_2KVWQZ, Tech. Rep., 2020. [Online]. Available: https://idm.euro-fusion.org/default.aspx?uid=2KVWQZ.

[53] C. Bachmann *et al.*, "Overview over DEMO design integration challenges and their impact on component design concepts," *Fusion Engineering and Design*, vol. 136, pp. 87–95, 2018, Special Issue: Proceedings of the 13th International Symposium on Fusion Nuclear Technology (ISFNT-13). DOI: https://doi.org/10.1016/j.fusengdes.2017.12.040.

[54] E. Martelli *et al.*, "Study of EU DEMO WCLL breeding blanket and primary heat transfer system integration," *Fusion Engineering and Design*, vol. 136, pp. 828–833, 2018, Special Issue: Proceedings of the 13th International Symposium on Fusion Nuclear Technology (ISFNT-13). DOI: https://doi.org/10.1016/j.fusengdes.2018.04.016.

[55] I. Moscato, L. Barucca, S. Ciattaglia, P. Di Maio, and G. Federici, "Preliminary design of eu demo helium-cooled breeding blanket primary heat transfer system," *Fusion Engineering and Design*, vol. 136, pp. 1567–1571, 2018, Special Issue: Proceedings of the 13th International Symposium on Fusion Nuclear Technology (ISFNT-13). DOI: https://doi.org/10.1016/j.fusengdes.2018.05.058.

[56] Y. N. Hörstensmeyer, B. Butler, C. Day, and F. Franza, "Analysis of the EU-DEMO fuel cycle elements: Intrinsic impact of technology choices," *Fusion Engineering and Design*, vol. 136, pp. 314–318, 2018, Special Issue: Proceedings of the 13th International Symposium on Fusion Nuclear Technology (ISFNT-13). DOI: https://doi.org/10.1016/j.fusengdes.2018.02.015.

[57] Ł. Ciupiński, T. Zagrajek, P. Marek, G. Krzesiński, C. Bachmann, and R. Mozzillo, "Design and verification of a non-self-supported cryostat for the DEMO tokamak," *Fusion Engineering and Design*, vol. 161, p. 111 964, 2020. DOI: https://doi.org/10.1016/j.fusengdes.2020.111964.

[58] O. Crofts *et al.*, "EU DEMO remote maintenance system development during the pre-concept design phase," *Fusion Engineering and Design*, vol. 179, p. 113 121, 2022. DOI: https://doi.org/10.1016/j.fusengdes.2022.113121.

[59] V. Corato *et al.*, "The DEMO magnet system – status and future challenges," *Fusion Engineering and Design*, vol. 174, p. 112 971, 2022. DOI: https://doi.org/10.1016/j.fusengdes.2021.112971.

[60] J. You *et al.*, "Divertor of the european DEMO: Engineering and technologies for power exhaust," *Fusion Engineering and Design*, vol. 175, p. 113 010, 2022. DOI: https://doi.org/10.1016/j.fusengdes.2022.113010.

[61] T. Franke *et al.*, "The EU DEMO equatorial outboard limiter - design and port integration concept," *Fusion Engineering and Design*, vol. 158, p. 111 647, 2020. DOI: https://doi.org/10.1016/j.fusengdes.2020.111647.

[62] G. Federici, L. Boccaccini, F. Cismondi, M. Gasparotto, Y. Poitevin, and I. Ricapito, "An overview of the EU breeding blanket design strategy as an integral part of the DEMO design effort," *Fusion Engineering and Design*, vol. 141, pp. 30–42, 2019. DOI: https://doi.org/10.1016/j.fusengdes.2019.01.141.

[63] M. Roldán, P. Fernández, J. Rams, D. Jiménez-Rey, C. Ortiz, and R. Vila, "Effect of helium implantation on mechanical properties of EUROFER97 evaluated by nanoindentation," *Journal of Nuclear Materials*, vol. 448, no. 1, pp. 301–309, 2014. DOI: https://doi.org/10.1016/j.jnucmat.2014.02.020.

[64] F. Tavassoli, "Eurofer steel, development to full code qualification," *Procedia Engineering*, vol. 55, pp. 300–308, 2013, 6th International Conference on Creep, Fatigue and Creep-Fatigue Interaction. DOI: https://doi.org/10.1016/j.proeng.2013.03.258.

[65] Z. Sun, X. Li, and Z. Wang, "Microstructure and mechanical properties of low activation Fe–Ti–Cr–V–W multi-principal element alloys," *Journal of Nuclear Materials*, vol. 533, p. 152 078, 2020. DOI: https://doi.org/10.1016/j.jnucmat.2020.152078.

[66] R.-D. Penzhorn, M. devillers, and M. Sirch, "Evaluation of ZrCo and other getters for tritium handling and storage," *Journal of Nuclear Materials*, vol. 170, no. 3, pp. 217–231, 1990. DOI: https://doi.org/10.1016/0022-3115(90)90292-U.

[67] C. E. Lundin and J. P. Blackledge, "Pressure-temperature-composition relationships of the yttrium-hydrogen system," *Journal of The Electrochemical Society*, vol. 109, no. 9, p. 838, 1962. DOI: https://doi.org/10.1149/1.2425565.

[68] D. Khatamian and F. D. Manchester, "The H-Y (hydrogen-yttrium) system," *Bulletin of Alloy Phase Diagrams*, vol. 9, pp. 252–260, 1988. DOI: https://doi.org/10.1007/BF02881276.

[69] R. E. Buxbaum and E. F. Johnson, "The use of yttrium for the recovery of tritium from lithium at low concentrations," *Nuclear Technology*, vol. 49, no. 2, pp. 307–314, 1980. DOI: https://doi.org/10.13182/NT80-A32492.

[70] M. Sawan and M. Abdou, "Physics and technology conditions for attaining tritium self-sufficiency for the DT fuel cycle," *Fusion Engineering and Design*, vol. 81, no. 8, pp. 1131–1144, 2006, Proceedings of the Seventh International Symposium on Fusion Nuclear Technology. DOI: https://doi.org/10.1016/j.fusengdes.2005.07.035.

[71] F. Hernández, "HCPB design report 2018," EUROfusion, EFDA_D_2NUTXK, Tech. Rep., 2018. [Online]. Available: https://idm.euro-fusion.org/default.aspx?uid=2NUTXK.

[72] E. Carella and T. Hernández, "Ceramics for fusion reactors: The role of the lithium orthosilicate as breeder," *Physica B: Condensed Matter*, vol. 407, no. 22, pp. 4431–4435, 2012. DOI: https://doi.org/10.1016/j.physb.2012.07.013.

[73] F. A. Hernández *et al.*, "Overview of the HCPB research activities in EUROfusion," *IEEE Transactions on Plasma Science*, vol. 46, no. 6, pp. 2247–2261, 2018. DOI: https://doi.org/10.1109/TPS.2018.2830813.

[74] F. A. Hernández *et al.*, "Consolidated design of the HCPB breeding blanket for the pre-conceptual design phase of the EU DEMO and harmonization with the ITER HCPB TBM program," *Fusion Engineering and Design*, vol. 157, p. 111 614, 2020. DOI: https://doi.org/10.1016/j.fusengdes.2020.111614.

[75] G. Federici, A. Raffray, and M. Abdou, "Mistral: A comprehensive model for tritium transport in lithium-base ceramics: Part I: Theory and description of model capabilities," *Journal of Nuclear Materials*, vol. 173, no. 2, pp. 185–213, 1990. DOI: https://doi.org/10.1016/0022-3115(90)90257-N.

[76] C. Johnson, "Tritium behavior in lithium ceramics," *Journal of Nuclear Materials*, vol. 270, no. 1, pp. 212–220, 1999. DOI: https://doi.org/10.1016/S0022-3115(98)00905-2.

[77] T. Kinjyo and M. Nishikawa, "Tritium release behavior from Li_4SiO_4," *Fusion Science and Technology*, vol. 46, no. 4, pp. 561–570, 2004. DOI: https://doi.org/10.13182/FST04-A591.

[78] E. Carella, C. Moreno, F. R. Urgorri, D. Rapisarda, and A. Ibarra, "Tritium modelling in HCPB breeder blanket at a system level," *Fusion Engineering and Design*, vol. 124, pp. 687–691, 2017. DOI: https://doi.org/10.1016/j.fusengdes.2017.01.051.

[79] F. Cismondi, *Solid and liquid breeder blankets [lecture]*. Italy: Politécnico de Turín, 2011. DOI: https://staff.polito.it/roberto.zanino/sub1/teach.html.

[80] P. Arena and R. Burlon, "WCLL BB design and integration studies 2019 activities," EUROfusion, EFDA_D_2P5NE5, Tech. Rep., 2020. [Online]. Available: https://idm.euro-fusion.org/default.aspx?uid=2P5NE5.

[81] A. Del Nevo *et al.*, "WCLL BB design and integration studies 2020 activities," EUROfusion, EFDA_D_2NTP7J, Tech. Rep., 2020. [Online]. Available: https://idm.euro-fusion.org/default.aspx?uid=2NTP7J.

[82] E. Mas de les Valls *et al.*, "Lead–lithium eutectic material database for nuclear fusion technology," *Journal of Nuclear Materials*, vol. 376, no. 3, pp. 353–357, 2008. DOI: https://doi.org/10.1016/j.jnucmat.2008.02.016.

[83] B. Garcinuño, D. Rapisarda, I. Fernández-Berceruelo, E. Carella, and J. Sanz, "The CIEMAT LiPb loop permeation experiment," *Fusion Engineering and Design*, vol. 146, pp. 1228–1232, 2019. DOI: https://doi.org/10.1016/j.fusengdes.2019.02.045.

[84] E. Carella, D. Rapisarda, and S. Lenk, "Design of the CIEMAT corrosion loop for liquid metal experiments," *Applied Sciences*, vol. 12, no. 6, 2022. DOI: https://www.mdpi.com/2076-3417/12/6/3104.

[85] A. Perujo and K. Forcey, "Tritium permeation barriers for fusion technology," *Fusion Engineering and Design*, vol. 28, pp. 252–257, 1995. DOI: https://doi.org/10.1016/0920-3796(95)90045-4.

[86] T. Hernández, F. Sánchez, F. Di Fonzo, M. Vanazzi, M. Panizo, and R. González-Arrabal, "Corrosion protective action of different coatings for the helium cooled pebble bed breeder concept," *Journal of Nuclear Materials*, vol. 516, pp. 160–168, 2019. DOI: https://doi.org/10.1016/j.jnucmat.2019.01.009.

[87] M. Utili *et al.*, "Development of anti-permeation and corrosion barrier coatings for the WCLL breeding blanket of the European DEMO," *Fusion Engineering and Design*, vol. 170, p. 112 453, 2021. DOI: https://doi.org/10.1016/j.fusengdes.2021.112453.

[88] K. Kizu and T. Tanabe, "Counter-diffusion and counter-permeation of deuterium and hydrogen through palladium," *Journal of Nuclear Materials*, vol. 258, pp. 1133–1137, 1998. DOI: https://doi.org/10.1016/S0022-3115(98)00393-6.

[89] K. Kizu and T. Tanabe, "Deuterium permeation through metals under hydrogen counter flow," *Journal of Nuclear Materials*, vol. 266, pp. 561–565, Mar. 1999. DOI: https://doi.org/10.1016/S0022-3115(98)00589-3.

[90] T. Takeda and J. Iwatsuki, "Counter-permeation of deuterium and hydrogen through Inconel 600®," *Nuclear Technology*, vol. 146, pp. 83–95, Apr. 2004. DOI: https://doi.org/10.13182/NT04-A3490.

[91] K. Kizu, A. Pisarev, and T. Tanabe, "Co-permeation of deuterium and hydrogen through Pd," *Journal of Nuclear Materials*, vol. 289, no. 3, pp. 291–302, 2001. DOI: https://doi.org/10.1016/S0022-3115(01)00428-7.

[92] W. Królas *et al.*, "The IFMIF-DONES fusion oriented neutron source: Evolution of the design," *Nuclear Fusion*, vol. 61, no. 12, p. 125 002, 2021. DOI: https://dx.doi.org/10.1088/1741-4326/ac318f.

[93] A. Ibarra *et al.*, "The european approach to the fusion-like neutron source: The IFMIF-DONES project," *Nuclear Fusion*, vol. 59, no. 6, p. 065 002, 2019. DOI: https://doi.org/10.1088/1741-4326/ab0d57.

[94] J. Molla, M. Yamamoto, A. Polato, M. Soldaini, H. Takeuchi, and E. Wakai, "Workload foreseen for the IFMIF post irradiation examination facility," *Fusion Engineering and Design*, vol. 86, pp. 2522–2525, 2011, Proceedings of the 26th Symposium of Fusion Technology (SOFT-26). DOI: https://doi.org/10.1016/j.fusengdes.2011.03.037.

[95] H. Nakamura, M. Ida, M. Sugimoto, T. Yutani, and H. Takeuchi, "Removal and control of tritium in lithium target for international fusion materials irradiation facility (IFMIF)," *Fusion Science and Technology*, vol. 41, no. 3P2, pp. 845–849, 2002. DOI: https://doi.org/10.13182/FST02-A22704.

[96] S. Simakov, U. Fischer, and U. von Möllendorff, "Assessment of the ^{3}H and ^{7}Be generation in the IFMIF lithium loop," *Journal of Nuclear Materials*, vol. 329-333, pp. 213–217, 2004. DOI: https://doi.org/10.1016/j.jnucmat.2004.04.024.

[97] K. Matsuhiro, H. Nakamura, T. Hayashi, H. Nakamura, and M. Sugimoto, "Evaluation of tritium permeation from lithium loop of IFMIF target system," *Fusion Science and Technology*, vol. 48, no. 1, pp. 625–628, 2005. DOI: https://doi.org/10.13182/FST05-A1003.

[98] G. D'Ovidio and F. Martín-Fuertes, "Accident analysis with MELCOR-fusion code for DONES lithium loop and accelerator," *Fusion Engineering and Design*, vol. 146, pp. 473–477, 2019. DOI: https://doi.org/10.1016/j.fusengdes.2018.12.093.

[99] F. Martín-Fuertes *et al.*, "Integration of safety in IFMIF-DONES design," *Safety*, vol. 5, no. 4, 2019. DOI: https://doi.org/10.3390/safety5040074.

[100] K. Natesan, "Influence of nonmetallic elements on the compatibility of structural materials with liquid alkali metals," *Journal of Nuclear Materials*, vol. 115, pp. 251–262, 1983. DOI: https://doi.org/10.1016/0022-3115(83)90316-1.

[101] B. Garcinuño *et al.*, "Development of an on-line sensor for hydrogen isotopes monitoring in flowing lithium at DONES," *Fusion Engineering and Design* , vol. 161, p. 112 010, 2020. DOI: https://doi.org/10.1016/j.fusengdes.2020.112010.

[102] H. Kondo *et al.*, "Design of purification loop and traps for the IFMIF/EVEDA Li test loop: Design of cold trap," *Fusion Engineering and Design*, vol. 86, no. 9, pp. 2437–2441, 2011. DOI: https://doi.org/10.1016/j.fusengdes.2010.12.021.

[103] S. Hirakane, T. Yoneoka, and S. Tanaka, "Gettering of nitrogen in liquid lithium," *Fusion Engineering and Design*, vol. 75-79, pp. 721–724, 2005. DOI: https://doi.org/10.1016/j.fusengdes.2005.06.080.

[104] S. J. Hendricks, J. Molla, F. R. Urgorri, and E. Carella, "Impact of yttrium hydride formation on multi-isotopic hydrogen retention by a getter trap for the DONES lithium loop," *Nuclear Fusion*, vol. 63, no. 5, p. 056 012, 2023. DOI: https://dx.doi.org/10.1088/1741-4326/acc31a.

[105] S. J. Hendricks, E. Carella, C. Moreno, and J. Molla, "Numerical investigation of hydrogen isotope retention by an yttrium pebble-bed from flowing liquid lithium," *Nuclear Fusion*, vol. 60, no. 10, p. 106 017, 2020. DOI: https://dx.doi.org/10.1088/1741-4326/aba672.

[106] J. Yagi and A. Suzuki, "Nitrogen contamination effect on yttrium gettering of hydrogen in liquid lithium," *Journal of Nuclear Materials*, vol. 417, pp. 710–712, 2011. DOI: https://doi.org/10.1016/j.jnucmat.2010.12.136.

[107] M. Kinoshita, S. Fukada, N. Yamashita, T. Muroga, and M. Nishikawa, "Experimental study of tritium recovery from liquid lithium by yttrium," *Fusion Engineering and Design*, vol. 81, no. 1, pp. 567–571, 2006, Proceedings of the Seventh International Symposium on Fusion Nuclear Technology. DOI: https://doi.org/10.1016/j.fusengdes.2005.04.003.

[108] S. Fukada, Y. Maeda, and Y. Edao, "Experiment of recovery of tritium from Li by Y and design of hot trap," *Fusion Science and Technology*, vol. 54, no. 1, pp. 117–121, 2008. DOI: https://doi.org/10.13182/FST08-A1777.

[109] Y. Edao, S. Fukada, S. Yamaguchi, Y. Wu, and H. Nakamura, "Tritium removal by Y hot trap for purification of IFMIF Li target," *Fusion Engineering and Design*, vol. 85, no. 1, pp. 53–57, 2010. DOI: https://doi.org/10.1016/j.fusengdes.2009.06.002.

[110] S. Fukada, T. Hiromoto, S. Shigeharu, K. Sugie, and Y. Edao, "Trapping of deuterium dissolved in fluidized Li by Y," *Fusion Engineering and Design*, vol. 89, no. 7, pp. 1346–1350, 2014, Proceedings of the 11th International Symposium on Fusion Nuclear Technology-11 (ISFNT-11) Barcelona, Spain, 15-20 September, 2013. DOI: https://doi.org/10.1016/j.fusengdes.2014.02.030.

[111] K. Hiyane, S. Fukada, Y. Yamasaki, K. Katayama, and E. Wakai, "Removal of low-concentration deuterium from fluidized Li loop for IFMIF," *Fusion Engineering and Design*, vol. 109-111, pp. 1340–1344, 2016, Proceedings of the 12th International Symposium on Fusion Nuclear Technology-12 (ISFNT-12). DOI: https://doi.org/10.1016/j.fusengdes.2015.12.030.

[112] Y. Yamasaki, S. Fukada, K. Hiyane, and K. Katayama, "Study on transfer behavior of hydrogen isotopes from fluidized Li to Y for Li blanket," *Fusion Science and Technology*, vol. 71, no. 4, pp. 501–506, 2017. DOI: https://doi.org/10.1080/15361055.2017.1291028.

[113] Empresarios Agrupados, *Ecosimpro - System modelling and simulation software*, EA Internacional website, 2023. [Online]. Available: https://www.ecosimpro.com/products/ecosimpro/#ECOSIMPRO_description.

[114] Y. Fukai, *The Metal-Hydrogen System*. Berlin, Heidelberg, Germany: Springer Berlin Heidelberg, 2005. DOI: https://doi.org/10.1007/3-540-28883-X.

[115] K. Fu *et al.*, "Experimental investigation and thermodynamic assessment of the yttrium-hydrogen binary system," *Progress in Natural Science: Materials International*, vol. 28, no. 3, pp. 332–336, 2018. DOI: https://doi.org/10.1016/j.pnsc.2018.04.001.

[116] J. Peng *et al.*, "Thermodynamic modelling of Y–H and Y–Zr–H system aided by first-principles and its application in bulk hydride moderator fabrication," *Journal of Nuclear Materials*, vol. 531, p. 152 035, 2020. DOI: https://doi.org/10.1016/j.jnucmat.2020.152035.

[117] C. K. Gupta, *Chemical Metallurgy: Principles and Practice*. Weinheim, Germany: WILEY-VCH Verlag GmbHr, 2003.

[118] B. S. Bokstein, M. I. Mendelev, and D. J. Srolovitz, *Thermodynamics and Kinetics in Materials Science*. Oxford, UK: Oxford University Press, 2005. DOI: https://doi.org/10.1093/oso/9780198528036.001.0001.

[119] F. J. Smith, J. F. Land, G. M. Begun, and A. M. La Gamma de Batistoni, "The solubility and isotopic exchange equilibrium for hydrogen isotopes in lithium," *Journal of Inorganic and Nuclear Chemistry*, vol. 41, no. 7, pp. 1001–1009, 1979. DOI: https://doi.org/10.1016/0022-1902(79)80077-9.

[120] P. Atkins and J. de Paula, *Physical Chemistry*. New York City, USA: W. H. Freeman and Company, 2010.

[121] L. D. Landau and E. M. Lifshitz, *Course of Theoretical Physics: Vol. 5, Statistical Physics, Part 1*, 3th Edition. Oxford, UK: Butterworth-Heinemann, 1980.

[122] R. Griessen and A. Züttel, *Lecture notes: Thermodynamics and kinetics in materials science*, 2003. [Online]. Available: https://www.nat.vu.nl/%7egriessen/STofHinM/.

[123] M. Dornheim, "Thermodynamics of metal hydrides: Tailoring reaction enthalpies of hydrogen storage materials," in *Thermodynamics*, J. C. Moreno-Pirajan, Ed., Rijeka: IntechOpen, 2011, ch. 33. DOI: https://doi.org/10.5772/21662.

[124] P. C. Souers, *Hydrogen Properties for Fusion Energy*. Barkeley, Los Angeles, California and London, UK: University of California Press, 1986. DOI: https://doi.org/10.1525/9780520338401.

[125] T. D. Lee and C. N. Yang, "Statistical theory of equations of state and phase transitions. II. Lattice gas and Ising model," *Phys. Rev.*, vol. 87, pp. 410–419, 3 1952. DOI: https://doi.org/10.1103/PhysRev.87.410.

[126] R. H. Fowler, "Adsorption isotherms. Critical conditions," *Mathematical Proceedings of the Cambridge Philosophical Society*, vol. 32, no. 1, pp. 144–151, 1936. DOI: https://doi.org/10.1017/S0305004100018946.

[127] J. R. Lacher, "A theoretical formula for the solubility of hydrogen in palladium," *Proceedings of the Royal Society*, vol. 161, pp. 525–545, 1937. DOI: https://doi.org/10.1098/rspa.1937.0160.

[128] R. Kirchheim and A. Pundt, "25 - Hydrogen in metals," in *Physical Metallurgy (Fifth Edition)*, D. E. Laughlin and K. Hono, Eds., Fifth Edition, Oxford: Elsevier, 2014, pp. 2597–2705. DOI: https://doi.org/10.1016/B978-0-444-53770-6.00025-3.

[129] W. L. Bragg and E. J. Williams, "The effect of thermal agitation on atomic arrangement in alloys," *Proc. R. Soc. Lond. A*, vol. 145, p. 699 730, 1934. DOI: https://doi.org/10.1098/rspa.1934.0132.

[130] A. Züttel, "Fuels – Hydrogen storage," in *Encyclopedia of Electrochemical Power Sources*, J. Garche, Ed., Amsterdam, Netherlands: Elsevier, 2009, pp. 440–458. DOI: https://doi.org/10.1016/B978-044452745-5.00325-7.

[131] A. Driessen, H. Hemmes, and R. Griessen, "Hydride formation at very high hydrogen pressure," *Zeitschrift für Physikalische Chemie*, vol. 143, pp. 145–159, Jan. 1985. DOI: https://doi.org/10.1524/zpch.1985.143.143.145.

[132] R. Lässer and G. Powell, "Solubility of protium, deuterium and tritium in palladium-silver alloys at low hydrogen concentrations," *Journal of the Less Common Metals*, vol. 130, pp. 387–394, 1987. DOI: https://doi.org/10.1016/0022-5088(87)90133-0.

[133] R. Griessen and T. Riesterer, "Heat of formation models," in *Hydrogen in Intermetallic Compounds I: Electronic, Thermodynamic, and Crystallographic Properties, Preparation*, L. Schlapbach, Ed. Berlin, Heidelberg: Springer, 1988, pp. 219–284. DOI: https://doi.org/10.1007/3540183337_13.

[134] H. Sugimoto and F. Fukai, "Solubility of hydrogen in metals under high hydrogen pressures: Thermodynamical calculations," *Acta Metallurgica et Materialia*, vol. 40, no. 9, pp. 2327–2336, 1992. DOI: https://doi.org/10.1016/0956-7151(92)90151-4.

[135] H. A. Kierstead, "A theory of multiplateau hydrogen absorption isotherms," *Journal of the Less Common Metals*, vol. 71, no. 2, pp. 303–309, 1980. DOI: https://doi.org/10.1016/0022-5088(80)90213-1.

[136] W. M. Mueller, J. P. Blackledge, and G. G. Libowitz, *Metal Hydrides*. New York City, USA, and London, UK: Academic Press, 1968.

[137] A. Sieverts, "Absorption of gases by metals," *Zeitschrift für Metallkunde*, vol. 21, pp. 37–46, 1929.

[138] L. Haar, A. S. Friedman, and C. W. Beckett, *Ideal Gas Thermodynamic Functions and Isotope Exchange Functions for the Diatomic Hydrides, Deuterides, and Tritides*. Washington D. C., USA: U.S. National Bureau of Standards, Monograph 20, 1961. [Online]. Available: https://www.osti.gov/biblio/4067290.

[139] K. P. Huber and G. Herzberg, "Constants of diatomic molecules," in *Molecular Spectra and Molecular Structure: IV. Constants of Diatomic Molecules*. Boston, USA: Springer US, 1979, pp. 8–689. DOI: https://doi.org/10.1007/978-1-4757-0961-2_2.

[140] G. Alefeld and J. Völkl, *Hydrogen in Metals I: Basic Properties*. Berlin, Heidelberg, Germany: Springer, 1978. DOI: https://doi.org/10.1007/3-540-08705-2.

[141] G. Alefeld and J. Völkl, *Hydrogen in Metals II: Application-Oriented Properties*. Berlin, Heidelberg, Germany: Springer, 1978. DOI: https://doi.org/10.1007/3-540-08883-0.

[142] L. Schlapbach, *Hydrogen in Intermetallic Compounds I: Electronic, Thermodynamic, and Crystallographic Properties, Preparation*. Berlin, Germany: Springer, 1988. DOI: https://doi.org/10.1007/3-540-18333-7.

[143] L. Schlapbach, *Hydrogen in Intermetallic Compounds II: Surface and Dynamic Properties, Applications*. Berlin, Germany: Springer, 1988. DOI: https://doi.org/10.1007/3-540-54668-5.

[144] A. L. G. Rees, "Statistical mechanics of two-component interstitial solid solutions," *Trans. Faraday Soc.*, vol. 50, pp. 335–342, 1954. DOI: https://doi.org/10.1039/TF9545000335.

[145] H. A. Kierstead, "Application of the Rees theory to multiplateau hydrogen absorption isotherms," *Journal of the Less Common Metals*, vol. 75, no. 2, pp. 267–271, 1980. DOI: https://doi.org/10.1016/0022-5088(80)90124-1.

[146] H. A. Kierstead, "Calculation of phase diagrams from Lacher or Rees theory parameters," *Journal of the Less Common Metals*, vol. 78, no. 1, pp. 81–90, 1981. DOI: https://doi.org/10.1016/0022-5088(81)90116-8.

[147] P. Shewmon, *Diffusion in Solids*. Cham, Switzerland: Springer, 2016. DOI: https://doi.org/10.1007/978-3-319-48206-4.

[148] J. K. Paul Heitjans, *Diffusion in Condensed Matter*. Berlin, Heidelberg, Germany: Springer, 2005. DOI: https://doi.org/10.1007/3-540-30970-5.

[149] J. Philibert, *Atom movements - Diffusion and mass transport in solids*. Les Ulis Cedex A, France: Les Éditions de Physique, 1991.

[150] J. Völkl and G. Alefeld, "Diffusion of hydrogen in metals," in *Hydrogen in Metals I: Basic Properties*, G. Alefeld and J. Völkl, Eds. Berlin, Heidelberg: Springer Berlin Heidelberg, 1978, pp. 321–348. DOI: https://doi.org/10.1007/3540087052_51.

[151] R. Swalin and V. Leak, "Diffusion of heterovalent solutes in liquid silver," *Acta Metallurgica*, vol. 13, no. 5, pp. 471–478, 1965. DOI: https://doi.org/10.1016/0001-6160(65)90096-9.

[152] Y. Gupta, "Solute diffusion in liquid metals," *Advances in Physics*, vol. 16, no. 62, pp. 333–350, 1967. DOI: https://doi.org/10.1080/00018736700101445.

[153] B. N. Bhat, "Solute diffusion in liquid metals," National Aeronautics and Space Administration, Washington, D. C., Tech. Rep., 1973. [Online]. Available: https://ntrs.nasa.gov/citations/19730023300.

[154] R. E. Buxbaum and E. F. Johnson, "Diffusivity of hydrogen isotopes in liquid lithium and in solid yttrium," *Industrial & Engineering Chemistry Fundamentals*, vol. 24, no. 2, pp. 180–182, 1985. DOI: https://pubs.acs.org/doi/10.1021/i100018a007.

[155] J. R. Cahoon, "A modified "hole" theory for solute impurity diffusion in liquid metals," *Metallurgical and Materials Transactions A*, vol. 28, pp. 583–593, 1997. DOI: https://doi.org/10.1007/s11661-997-0044-3.

[156] Q. Yang, Y. Liu, and Y. Li, "Hydrogen diffusion coefficient in liquid metals evaluated by solid–gas eutectic unidirectional solidification," *Transactions of Nonferrous Metals Society of China*, vol. 24, no. 12, pp. 4030–4037, 2014. DOI: https://doi.org/10.1016/S1003-6326(14)63565-2.

[157] R. Causey, R. Karnesky, and C. San Marchi, "Tritium barriers and tritium diffusion in fusion reactors," in *Comprehensive Nuclear Materials*, R. J. Konings, Ed., Oxford: Elsevier, 2012, pp. 511–549. DOI: https://doi.org/10.1016/B978-0-08-056033-5.00116-6.

[158] R. Oriani, "The diffusion and trapping of hydrogen in steel," *Acta Metallurgica*, vol. 18, no. 1, pp. 147–157, 1970. DOI: https://doi.org/10.1016/0001-6160(70)90078-7.

[159] G. Esteban, A. Peña, F. Legarda, and R. Lindau, "Hydrogen transport and trapping in ODS-EUROFER," *Fusion Engineering and Design*, vol. 82, no. 15, pp. 2634–2640, 2007, Proceedings of the 24th Symposium on Fusion Technology. DOI: https://doi.org/10.1016/j.fusengdes.2007.02.002.

[160] I. Peñalva, G. Alberro, F. Legarda, C. Ortiz, and R. Vila, "Influence of the P content on the transport parameters of hydrogen in Fe alloys," *Fusion Engineering and Design*, vol. 98-99, pp. 2058–2062, 2015, Proceedings of the 28th Symposium On Fusion Technology (SOFT-28). DOI: https://doi.org/10.1016/j.fusengdes.2015.06.188.

[161] F. Montupet-Leblond *et al.*, "Permeation and trapping of hydrogen in Eurofer97," *Nuclear Materials and Energy*, vol. 29, p. 101 062, 2021. DOI: https://doi.org/10.1016/j.nme.2021.101062.

[162] H. Johnson, N. Quick, and A. Kumnick, "Hydrogen trapping mechanisms by permeation techniques," *Scripta Metallurgica*, vol. 13, no. 1, pp. 67–72, 1979. DOI: https://doi.org/10.1016/0036-9748(79)90392-2.

[163] F. R. Urgorri *et al.*, "Tritium transport modeling at system level for the EUROfusion dual coolant lithium-lead breeding blanket," *Nuclear Fusion*, vol. 57, no. 11, p. 116 045, 2017. DOI: https://doi.org/10.1088/1741-4326/aa7f9d.

[164] F. P. Incropera and D. P. DeWitt, *Fundamentals of Heat and Mass Transfer*, 4th Edition. New York City, USA: John Wiley & Sons, Inc., 1996.

[165] J. Crank, *The Mathematics of Diffusion*. UK: Oxford University Press, 1956.

[166] T. Takeda, A. Ying, and M. A. Abdou, "Analysis of tritium extraction from liquid lithium by permeation window and solid gettering processes," *Fusion Engineering and Design*, vol. 28, pp. 278–285, 1995. DOI: https://doi.org/10.1016/0920-3796(95)90049-7.

[167] İ. Tosun, "Chapter 3 - Interphase transport and transfer coefficients," in *Modelling in Transport Phenomena*, İ. Tosun, Ed., Amsterdam: Elsevier, 2002, pp. 41–64. DOI: https://doi.org/10.1016/B978-044451052-5/50003-X.

[168] E. J. Wilson and C. J. Geankoplis, "Liquid mass transfer at very low reynolds numbers in packed beds," *Industrial & Engineering Chemistry Fundamentals*, vol. 5, no. 1, pp. 9–14, 1966. DOI: https://doi.org/10.1021/i160017a002.

[169] F. P. Berger and K. F. Hau, "Mass transfer in turbulent pipe flow measured by the electrochemical method," *International Journal of Heat and Mass Transfer*, vol. 20, no. 11, pp. 1185–1194, 1977. DOI: https://doi.org/10.1016/0017-9310(77)90127-2.

[170] F. Waelbrock, "Influence of bulk and surface phenomena on the hydrogen permeation through metals," Jülich, Tech. Rep. Juel-1966, 1984, p. 187. [Online]. Available: https://juser.fz-juelich.de/record/819273.

[171] L. Schlapbach, "Surface properties and activation," in *Hydrogen in Intermetallic Compunds II: Surface and Dynamic Properties, Applications*, L. Schlapbach, Ed. Berlin, Heidelberg: Springer Berlin Heidelberg, 1992, pp. 15–95. DOI: 10.1007/3-540-54668-5_9.

[172] K. Christmann, "Some general aspects of hydrogen chemisorption on metal surfaces," *Progress in Surface Science*, vol. 48, no. 1, pp. 15–26, 1995, Proceedings of the Seventeenth International Seminar on Surface Physics. DOI: https://doi.org/10.1016/0079-6816(95)93412-Z.

[173] J. A. Becker, "Adsorption on metal surfaces and its bearing on catalysis," in ser. Advances in Catalysis, W. Frankenburg, V. Komarewsky, and E. Rideal, Eds., vol. 7, Academic Press, 1955, pp. 135–211. DOI: https://doi.org/10.1016/S0360-0564(08)60527-1.

[174] M. Pick and K. Sonnenberg, "A model for atomic hydrogen-metal interactions - application to recycling, recombination and permeation," *Journal of Nuclear Materials*, vol. 131, pp. 208–220, 1985. DOI: https://doi.org/10.1016/0022-3115(85)90459-3.

[175] R. Speiser, "Chapter 3 - The thermodynamics of metal–hydrogen systems," in *Metal Hydrides*, W. M. Mueller, J. P. Blackledge, and G. G. Libowitz, Eds., Academic Press, 1968, pp. 51–89. DOI: https://doi.org/10.1016/B978-1-4832-3215-7.50007-1.

[176] C. P. E. Wolfgang Pauli, *Pauli lectures on physics - Thermodynamics and the kinetic theory of gases Vol. 3* (Pauli lectures on physics vol. 3). Cambridge, Massachusetts, and London, UK: MIT, 1973.

[177] K. H. Rieder, M. Baumberger, and W. Stocker, "Selective transition of chemisorbed hydrogen to subsurface sites on Pd(110)," *Phys. Rev. Lett.*, vol. 51, pp. 1799–1802, 1983. DOI: https://doi.org/10.1103/PhysRevLett.51.1799.

[178] A. Pundt and R. Kirchheim, "Hydrogen in metals: Microstructural aspects," *Annual Review of Materials Research*, vol. 36, no. 1, pp. 555–608, 2006. DOI: https://doi.org/10.1146/annurev.matsci.36.090804.094451.

[179] R. J. Behm, V. Penka, M.-G. Cattania, K. Christmann, and G. Ertl, "Evidence for "subsurface" hydrogen on Pd(110): An intermediate between chemisorbed and dissolved species," *The Journal of Chemical Physics*, vol. 78, no. 12, pp. 7486–7490, 1983. DOI: https://doi.org/10.1063/1.444739.

[180] I. Ali-Khan, K. Dietz, F. Waelbroeck, and P. Wienhold, "The rate of hydrogen release out of clean metallic surfaces," *Journal of Nuclear Materials*, vol. 76-77, pp. 337–343, 1978. DOI: https://doi.org/10.1016/0022-3115(78)90167-8.

[181] J. Wang, "On the diffusion of gases through metals," *Mathematical Proceedings of the Cambridge Philosophical Society*, vol. 32, no. 4, pp. 657–662, 1936. DOI: https://doi.org/10.1017/S030500410001940X.

[182] M. Baskes, "A calculation of the surface recombination rate constant for hydrogen isotopes on metals," *Journal of Nuclear Materials*, vol. 92, no. 2, pp. 318–324, 1980. DOI: https://doi.org/10.1016/0022-3115(80)90117-8.

[183] P. M. Richards, "Surface-limited hydrogen release and uptake in metals," *Journal of Nuclear Materials*, vol. 152, no. 2, pp. 246–258, 1988. DOI: https://doi.org/10.1016/0022-3115(88)90333-9.

[184] T. Uda, K. Okuno, and Y. Naruse, "Hydrogen isotope exchange reaction rates in tritium, hydrogen and deuterium mixed gases," *Radiochimica Acta*, vol. 56, no. 4, pp. 209–214, 1992. DOI: https://doi.org/10.1524/ract.1992.56.4.209.

[185] I. Shavitt, R. M. Stevens, F. L. Minn, and M. Karplus, "Potential-energy surface for H3," *The Journal of Chemical Physics*, vol. 48, no. 6, pp. 2700–2713, 1968. DOI: https://doi.org/10.1063/1.1669504.

[186] K. J. Laidler, "A glossary of terms used in chemical kinetics, including reaction dynamics," *Pure and Applied Chemistry*, vol. 68, no. 1, pp. 149–192, 1996. DOI: https://doi.org/10.1351/pac199668010149.

[187] R. Sander, "Compilation of Henry's law constants (version 4.0) for water as solvent," *Atmospheric Chemistry and Physics*, vol. 15, no. 8, pp. 4399–4981, 2015. DOI: https://doi.org/10.5194/acp-15-4399-2015.

[188] G. R. Longhurst, "Tritiated water interaction with stainless steel," Idaho National Lab., Tech. Rep., 2007. DOI: https://doi.org/10.2172/912459.

[189] W. F. Libby, "Vibrational frequencies of the isotopic water molecules; equilibria with the isotopic hydrogens," *The Journal of Chemical Physics*, vol. 11, no. 3, pp. 101–109, 1943. DOI: https://doi.org/10.1063/1.1723810.

[190] G. Esteban, A. Perujo, K. Douglas, and L. Sedano, "Tritium diffusive transport parameters and trapping effects in the reduced activating martensitic steel OPTIFER-IVb," *Journal of Nuclear Materials*, vol. 281, no. 1, pp. 34–41, 2000. DOI: https://doi.org/10.1016/S0022-3115(00)00188-4.

[191] Y. Hatano, "Permeation and permeation barrier," in *Tritium: Fuel of Fusion Reactors*, T. Tanabe, Ed. Tokyo: Springer Japan, 2017, pp. 207–229. DOI: https://doi.org/10.1007/978-4-431-56460-7_9.

[192] E. Serra and A. Perujo, "The surface rate constants of deuterium in the martensitic steel DIN 1.4914 (manet)," *Journal of Nuclear Materials*, vol. 223, no. 2, pp. 157–162, 1995. DOI: https://doi.org/10.1016/0022-3115(94)00438-2.

[193] E. Serra and A. Perujo, "Influence of the surface conditions on permeation in the deuterium–manet system," *Journal of Nuclear Materials*, vol. 240, no. 3, pp. 215–220, 1997. DOI: https://doi.org/10.1016/S0022-3115(96)00679-4.

[194] P. W. Humrickhouse and B. J. Merrill, "Vacuum permeator analysis for extraction of tritium from DCLL blankets," *Fusion Science and Technology*, vol. 68, no. 2, pp. 295–302, 2015. DOI: https://doi.org/10.13182/FST14-941.

[195] W. Umrath, *Fundamentals of Vacuum Technology*. Colone, Germany: Leybold Vacuum GmbH, 1998.

[196] J. Lafferty, *Foundations of Vacuum Science and Technology*. New York City, USA: John Wiley & Sons, Inc., 1998. [Online]. Available: https://www.wiley.com/en-ie/Foundations+of+Vacuum+Science+and+Technology-p-9780471175933.

[197] Pfeiffer Vacuum GmbH, *The Vacuum Technology Book - Volume II*. Asslar, Germany, 2013.

[198] M. Sefa and J. Setina, "Comparison of permeation of atmospheric gases through Viton O-ring gaskets for different initial conditions," *Journal of Vacuum Science Technology A: Vacuum Surfaces and Films*, vol. 35, no. 4, p. 041 603, 2017. DOI: https://doi.org/10.1116/1.4984292.

[199] Z. Chen, C. Gautier, F. Hemez, and N. K. Bultman, "Vacuum seals design and testing or a linear accelerator of the national spallation neutron source," Los Alamos National Laboratory, Tech. Rep., 2000. [Online]. Available: https://www.osti.gov/servlets/purl/752382.

[200] Swagelok Company, *VCR® Metal Gasket Face Seal Fittings*, Catalog, 2022. [Online]. Available: https://www.swagelok.com/downloads/webcatalogs/en/MS-01-24.pdf.

[201] Swagelok Company, *Bellows-Sealed Valves - U Series*, Catalog, 2022. [Online]. Available: https://www.swagelok.com/downloads/webcatalogs/en/ms-01-38.pdf.

[202] Swagelok Company, *Gaugeable Tube Fittings and Adapter Fittings*, Catalog, 2021. [Online]. Available: https://www.swagelok.com/downloads/webcatalogs/en/ms-01-140.pdf.

[203] Technetics Group, *Helicoflex® Spring-Energized Metal Seals*, Catalog, 2020. [Online]. Available: https://technetics.com/wp-content/uploads/2020/11/TECH_HELICOFLEX-Brochure_v1r3_fnl_low-res.pdf.

[204] Garlok, *Helicoflex - High Performance Seals and Sealing Systems*, Catalog, 2022. [Online]. Available: http://www.sppsrl.com.ar/catalogos/Helicoflex.pdf.

[205] VAT Group AG. "54.1 UHV All-Metal Angle Valve - Easy Close." Accessed: 07-01-2023. (2022), [Online]. Available: https://www.vatvalve.com/series/ultra-high-vacuum-all-metal-angle-valve-easy-close.

[206] VAT Group AG. "24.4 FV Angle Valve." Accessed: 07-01-2023. (2022), [Online]. Available: https://www.vatvalve.com/series/fine-vacuum-angle-valve.

[207] VAT Group AG. "21.1 Gas Dosing Valve." Accessed: 07-01-2023. (2022), [Online]. Available: https://www.vatvalve.com/series/gas-dosing-valve.

[208] VAT Group AG. "59.0 UHV All-Metal Variable Leak Valve." Accessed: 07-01-2023. (2022), [Online]. Available: https://www.vatvalve.com/series/ultra-high-vacuum-all-metal-variable-leak-valve.

[209] Ideal Vacuum Products, *Ideal Vacuum 2017 Catalog - Dry Scroll Pumps*, Catalog, 2017. [Online]. Available: https://www.idealvac.com/files/literature/Sec_03_Ideal_Vacuum%20_Dry_Scroll.pdf.

[210] Pfeiffer Vacuum GmbH. "Video - Functional principle of the HiPace turbopump in 3D." Accessed: 10-01-2023. (2023), [Online]. Available: https://www.pfeiffer-vacuum.com/en/products/vacuum-generation/turbopumps/.

[211] T. J. Seebeck, "Magnetische Polarisation der Metalle und Erze durch Temperatur-Differenz," *Abhandlungen der Königlichen Akademie der Wissenschaften zu Berlin*, pp. 265–373, 1822.

[212] R. P. Benedict and H. Hoersch, *Manual on - The use of thermocouples in temperature measurement*. Philadelphia, USA: ASTM Special Technical Publications, 1974.

[213] TC Ltd, *Mineral Insulated Thermocouples - Type 12*, Catalog, 2019. [Online]. Available: https://www.tc.co.uk/downloads/Mineral-Insulated-Thermocouples-Type-12.pdf.

[214] Spectite Inc, *Pressure and vacuum sealed feedthroughs for sensors, probes, electrodes and wires*, Catalog, 2008. [Online]. Available: https://www.spectite.com/SPECTITE%20Inc%20Cat1.pdf.

[215] Hiden Analytical, *Mass Spectrometers for Residual Gas Analysis Applications*, Catalog, 2020. [Online]. Available: https://www.hidenanalytical.com/wp-content/uploads/2020/11/TDS-188-8-RGA-CATALOGUE_High-Res.pdf.

[216] Pfeiffer Vacuum GmbH, *SmartTest HLT 550, HLT 560, HLT 570 - Operating Instructions*. Asslar, Germany, 2010. [Online]. Available: https://www.idealvac.com/files/ManualsII/Pfeiffer_SmartTest_Instruction_Manual_2.pdf.

[217] B. Garcinuño *et al.*, "Design and fabrication of a permeator against vacuum prototype for small scale testing at lead-lithium facility," *Fusion Engineering and Design*, vol. 124, pp. 871–875, 2017, Proceedings of the 29th Symposium on Fusion Technology (SOFT-29) Prague, Czech Republic, September 5-9, 2016. DOI: https://doi.org/10.1016/j.fusengdes.2017.02.060.

[218] VAT Group AG, *59.0 UHV All-Metal Variable Leak Valve*. 2022, Accessed: 07-01-2023. [Online]. Available: https://www.vatvalve.com/series/ultra-high-vacuum-all-metal-variable-leak-valve.

[219] L. R. Petzold, *Description of DASSL: a differential/algebraic system solver*. United States, 1982. [Online]. Available: https://www.osti.gov/biblio/5882821.

[220] P. Martínez, C. Moreno, and Á. Ibarra, "Parametric analysis of LIBRETTO-4 and 5 in-pile tritium transport model on EcosimPro," *Fusion Engineering and Design*, vol. 89, no. 7, pp. 1510–1515, 2014, Proceedings of the 11th International Symposium on Fusion Nuclear Technology-11. DOI: https://doi.org/10.1016/j.fusengdes.2014.04.060.

[221] Z. Chen, X. Hu, M. Ye, and B. D. Wirth, "Deuterium transport and retention properties of representative fusion blanket structural materials," *Journal of Nuclear Materials*, vol. 549, p. 152 904, 2021. DOI: https://doi.org/10.1016/j.jnucmat.2021.152904.

[222] A. Aiello, I. Ricapito, G. Benamati, and R. Valentini, "Hydrogen isotopes permeability in Eurofer 97 martensitic steel," *Fusion Science and Technology*, vol. 41, no. 3P2, pp. 872–876, 2002. DOI: https://doi.org/10.13182/FST41-872.

[223] W. Eichenauer and H. Künzig, "Diffusion und Löslichkeit von Wasserstoff in α-Eisen und Silber," *International Journal of Materials Research*, vol. 49, pp. 220–225, 1958. DOI: https://doi.org/10.1515/ijmr-1958-490502.

[224] F. Reiter, "Solubility and diffusivity of hydrogen isotopes in liquid Pb-17Li," *Fusion Engineering and Design*, vol. 14, no. 3, pp. 207–211, 1991. DOI: https://doi.org/10.1016/0920-3796(91)90003-9.

[225] A. Tahara and Y. Hayashi, "Measurements of permeation of hydrogen isotopes through α-iron by pressure modulation and ion bombarding," *Materials Transactions*, vol. 26, pp. 869–875, 1985. DOI: https://doi.org/10.2320/matertrans1960.26.869.

[226] F. A. Hernández *et al.*, "An enhanced, near-term HCPB design as driver blanket for the EU DEMO," *Fusion Engineering and Design*, vol. 146, pp. 1186–1191, 2019. DOI: https://doi.org/10.1016/j.fusengdes.2019.02.037.

[227] F. A. Hernández *et al.*, "Advancements in the helium-cooled pebble bed breeding blanket for the EU DEMO: Holistic design approach and lessons learned," *Fusion Science and Technology*, vol. 75, no. 5, pp. 352–364, 2019. DOI: https://doi.org/10.1080/15361055.2019.1607695.

[228] E. Carella, C. Moreno, F. R. Urgorri, D. Demange, J. Castellanos, and D. Rapisarda, "Tritium behavior in HCPB breeder blanket unit: Modeling and experiments," *Fusion Science and Technology*, vol. 71, no. 3, pp. 357–362, 2017. DOI: https://doi.org/10.1080/15361055.2017.1289584.

[229] C. Bachmann *et al.*, "Initial DEMO tokamak design configuration studies," *Fusion Engineering and Design*, vol. 98-99, pp. 1423–1426, 2015. DOI: https://doi.org/10.1016/j.fusengdes.2015.05.027.

[230] D. G. Jacobs, *Sources of tritium*. Oak Ridge, Tennessee: U.S. Department of Commerce, 1968.

[231] J. F. Black and H. S. Taylor, "Equilibrium in hydrogen-water systems containing tritium," *The Journal of Chemical Physics*, vol. 11, no. 9, pp. 395–402, 1943. DOI: https://doi.org/10.1063/1.1723864.

[232] C. Moreno and F. R. Urgorri, "Analyses of HCPB and WCLL for the review meeting - 2019," EUROfusion, EFDA_D_2PLELC, Tech. Rep., 2021. [Online]. Available: https://idm.euro-fusion.org/default.aspx?uid=2PLELC.

[233] P. Arena *et al.*, "The DEMO water-cooled lead-lithium breeding blanket: Design status at the end of the pre-conceptual design phase," *Applied Sciences*, vol. 11, no. 24, 2021. DOI: https://doi.org/10.3390/app112411592.

[234] A. Del Nevo *et al.*, "Recent progress in developing a feasible and integrated conceptual design of the WCLL BB in EUROfusion project," *Fusion Engineering and Design*, vol. 146, pp. 1805–1809, 2019, SI:SOFT-30. DOI: https://doi.org/10.1016/j.fusengdes.2019.03.040.

[235] F. R. Urgorri, C. Moreno, E. Carella, J. Castellanos, A. Del Nevo, and Á. Ibarra, "Preliminary system modeling for the EUROfusion water cooled lithium lead blanket," *Fusion Science and Technology*, vol. 71, no. 3, pp. 444–449, 2017. DOI: https://doi.org/10.1080/15361055.2016.1273712.

[236] L. Haar, J. S. Gallagher, and G. S. Kell, "NBS/NRC steam tables thermodynamic and transport properties and computer programs for vapor and liquid states of water in SI units," Jan. 1984. [Online]. Available: https://www.osti.gov/biblio/5614915.

[237] F. R. Urgorri, I. Fernández-Berceruelo, and D. Rapisarda, "Magneto-convective analyses of the PbLi flow for the EU-WCLL fusion breeding blanket," *Energies*, vol. 14, no. 19, 2021. DOI: https://doi.org/10.3390/en14196192.

[238] G. A. Al-Enezi and M. S. E. Abdo, "Mass transfer measurements around a single cylinder in cross flow at low Reynolds numbers," *Chemie Ingenieur Technik*, vol. 63, no. 4, pp. 381–384, 1991. DOI: https://doi.org/10.1002/cite.330630421.

[239] N. Bošković-Vragolović, R. Garić-Grulović, R. Pjanović, and Ž. Grbavčić, "Mass transfer and fluid flow visualization for single cylinder by the adsorption method," *International Journal of Heat and Mass Transfer*, vol. 59, pp. 155–160, 2013. DOI: https://doi.org/10.1016/j.ijheatmasstransfer.2012.11.077.

[240] B. Schulz, "Thermophysical properties of the Li(17)Pb(83)alloy," *Fusion Engineering and Design*, vol. 14, no. 3, pp. 199–205, 1991. DOI: https://doi.org/10.1016/0920-3796(91)90002-8.

[241] P. Hubberstey and T. Sample, "Thermodynamic and experimental evaluation of the sensitivity of Pb-17Li breeder blankets to atmospheric contamination," *Journal of Nuclear Materials*, vol. 191-194, pp. 277–282, 1992, Fusion Reactor Materials Part A. DOI: https://doi.org/10.1016/S0022-3115(09)80050-0.

[242] F. Reiter, K. Forcey, and G. Gervasini, *A Compilation of Tritium-material Interaction Parameters in Fusion Reactor Materials*. Milano, Italy: Commission of the European Communities, 1993.

[243] W. Geller and T.-H. Sun, "Einfluß von Legierungszusätzen auf die Wasserstoffdiffusion im Eisen und Beitrag zum System Eisen -Wasserstoff," *Archiv für das Eisenhüttenwesen*, vol. 21, no. 11-12, pp. 423–430, 1950. DOI: https://doi.org/10.1002/srin.195002917.

[244] N. Quick and H. Johnson, "Hydrogen and deuterium in iron, 49–506°C," *Acta Metallurgica*, vol. 26, no. 6, pp. 903–907, 1978. DOI: https://doi.org/10.1016/0001-6160(78)90041-X.

[245] T. Tanabe, Y. Yamanishi, and S. Imoto, "Hydrogen transport through highly purified iron," *Materials Transactions Jim*, vol. 25, pp. 1–10, 1984.

[246] H. Katsuta, H. Iwamoto, and H. Ohno, "Hydrogen solubility in liquid $Li_{17}Pb_{83}$," *Journal of Nuclear Materials*, vol. 133-134, pp. 167–170, 1985. DOI: https://doi.org/10.1016/0022-3115(85)90127-8.

[247] C. C. Lin, "Hydrogen water chemistry technology in boiling water reactors," *Nuclear Technology*, vol. 130, no. 1, pp. 59–70, 2000. DOI: https://doi.org/10.13182/NT00-A3077.

[248] E. Rota, F. Waelbroeck, P. Wienhold, and J. Winter, "Measurements of surface and bulk properties for the interaction of hydrogen with inconel 600," *Journal of Nuclear Materials*, vol. 111-112, pp. 233–239, 1982. DOI: https://doi.org/10.1016/0022-3115(82)90214-8.

[249] S. J. Hendricks, E. Carella, D. Jimenez, J. M. Garcia, and J. Molla, "Design of a multi-isotopic hydrogen co- and counter-permeation experiment for HCPB related tritium mitigation studies," *Fusion Engineering and Design*, vol. 175, p. 112 991, 2022. DOI: https://doi.org/10.1016/j.fusengdes.2021.112991.

[250] Extreme Bolt & Fastener, *Technical data A286*, 2016. [Online]. Available: https://www.extreme-bolt.com/images/Datasheets/Datasheet_-_A286.pdf.

[251] Watlow, *Mineral insulated (MI) band heaters*, Catalog, 2022. [Online]. Available: https://www.watlow.com/products/heaters/mineral-insulated-band-heaters.

[252] Pfeiffer Vacuum GmbH, *HiPace® 300 with TC 400, DN 100CF-F*, 2022. [Online]. Available: https://static.pfeiffer-vacuum.com/productPdfs/PMP03901.en.pdf.

[253] Hiden Analytical. "Cracking patterns." Accessed: 13-03-2023. (2021), [Online]. Available: https://www.hidenanalytical.com/tech-data/cracking-patterns/.

[254] N. W. M. Ritchie, D. Newbury, D. C. Joy, J. Michael, J. Goldstein, and J. H. Scott, *Scanning electron microscopy and X-ray microanalysis (4th ed.)* New York City, USA: Springer, 2018. [Online]. Available: https://doi.org/10.1017/S1431927618015271.

[255] D. W. Green and M. Z. Southard, *Perry's Chemical Engineers' Handbook, 9th Edition*. New York City, USA: McGraw-Hill Education, 2019. [Online]. Available: https://www.accessengineeringlibrary.com/content/book/9780071834087.

[256] F. Nitti *et al.*, "Lithium loop and purification system of DONES: Preliminary design," WPENS-CPR(18)19806, Tech. Rep., 2018. [Online]. Available: https://scipub.euro-fusion.org/archives/eurofusion/lithium-loop-and-purification-system-of-dones-preliminary-design.

[257] H. W. Davison, "Compilation of thermophysical properties of liquid lithium," NASA Lewis Research Center, Tech. Rep., 1968.

[258] M. Rhodes, *Introduction to Particle Technology*. Chichester, UK: John Wiley & Sons, Ltd, 2008. DOI: https://doi.org/10.1002/9780470727102.

[259] H. Moriyama, K. Iwasaki, and Y. Ito, "Transport of tritium in liquid lithium," *Journal of Nuclear Materials*, vol. 191-194, pp. 190–193, 1992. DOI: https://doi.org/10.1016/S0022-3115(09)80031-7.

[260] J. Völkl and G. Alefeld, "5 - Hydrogen diffusion in metals," in *Diffusion in Solids*, A. Nowick and J. Burton, Eds., Academic Press, 1975, pp. 231–302. DOI: 10.1016/B978-0-12-522660-8.50010-6.

[261] R. M. Alire, "Transport of hydrogen in liquid lithium," *The Journal of Chemical Physics*, vol. 65, no. 3, pp. 1134–1137, 1976. DOI: https://doi.org/10.1063/1.433188.

[262] S. Fukada, M. Kinoshita, K. Kuroki, and T. Muroga, "Hydrogen diffusion in liquid lithium from 500°C to 650°C," *Journal of Nuclear Materials*, vol. 346, pp. 293–297, 2005. DOI: https://doi.org/10.1016/j.jnucmat.2005.06.021.

[263] T. L. Bergmann, A. S. Lavine, D. P. DeWitt, and F. P. Incropera, *Fundamentals of Heat and Mass Transfer*, 8th Edition. New York City, USA: John Wiley & Sons, Inc., 2018. [Online]. Available: https://www.wiley.com/en-us/Fundamentals+of+Heat+and+Mass+Transfer,+8th+Edition-p-9781119722489.

[264] E. Veleckis, E. H. Van Deventer, and M. Blander, "Lithium-lithium hydride system," *The Journal of Physical Chemistry*, vol. 78, no. 19, pp. 1933–1940, 1974. DOI: https://doi.org/10.1021/j100612a013.

[265] H. Katsuta, T. Ishigai, and K. Furukawa, "Equilibrium pressure and solubility of hydrogen in liquid lithium," *Nuclear Technology*, vol. 32, no. 3, pp. 297–303, 1977. DOI: https://doi.org/10.13182/NT77-A31753.

[266] E. Veleckis, "Decomposition pressures in the (α + β) fields of the Li-LiH, Li-LiD, and Li-LiT systems," *Journal of Nuclear Materials*, vol. 79, no. 1, pp. 20–27, 1979. DOI: https://doi.org/10.1016/0022-3115(79)90430-6.

[267] E. Veleckis, "Thermodynamics of the lithium - lithium deuteride system," *Journal of Physical Chemistry*, vol. 81, no. 6, pp. 526–531, 1977. DOI: https://doi.org/10.1021/j100521a007.

[268] G. M. Begun, J. F. Land, and J. T. Bell, "High temperature equilibrium measurements of the yttrium–hydrogen isotope (H_2, D_2, T_2) systems," *The Journal of Chemical Physics*, vol. 72, no. 5, pp. 2959–2966, 1980. DOI: https://doi.org/10.1063/1.439496.

[269] P. F. Adams, M. G. Down, P. Hubberstey, and R. J. Pulham, "Solubilities, and solution and solvation enthalpies, for nitrogen and hydrogen in liquid lithium," *Journal of the Less Common Metals*, vol. 42, no. 3, pp. 325–334, 1975. DOI: https://doi.org/10.1016/0022-5088(75)90052-1.

[270] P. Hubberstey, P. Adams, R. Pulham, M. Down, and A. Thunder, "Hydrogen in liquid alkali metals," *Journal of the Less Common Metals*, vol. 49, pp. 253–269, 1976. DOI: https://doi.org/10.1016/0022-5088(76)90039-4.

[271] P. F. Adams, P. Hubberstey, and R. J. Pulham, "Review of the solubility of nonmetals in liquid lithium," *Journal of the Less Common Metals*, vol. 42, no. 1, pp. 1–11, 1975. DOI: https://doi.org/10.1016/0022-5088(75)90014-4.

[272] K. A. Yakimovich, "Phase equilibrium diagrams in a system of the Li-LiH type," *Russian Journal of Physical Chemistry A*, vol. 87, pp. 895–900, 2013. DOI: https://doi.org/10.1134/S0036024413060320.

[273] L. N. Yannopoulos, R. K. Edwards, and P. G. Wahlbeck, "The thermodynamics of the yttrium-hydrogen system," *Journal of Physical Chemistry*, vol. 69, no. 8, pp. 2510–2515, 1965. DOI: https://doi.org/10.1021/j100892a004.

[274] B. J. Beaudry and F. H. Spedding, "The solubility of RH_{2-x} in Gd, Er, Tm, Lu, and Y from ambient to 850°C," *Metall Trans B*, vol. 6, pp. 419–427, 1975. DOI: https://doi.org/10.1007/BF02913827.

[275] J. E. Bonnet, C. Juckum, and A. Lucasson, "Solid solutions of H and D in yttrium metal," *Journal of Physics F: Metal Physics*, vol. 12, no. 4, pp. 699–711, 1982. DOI: https://doi.org/10.1088/0305-4608/12/4/012.

[276] S. D. Clinton and J. S. Watson, "The solubility of tritium in yttrium at temperatures from 250 to 400 °C," *Journal of the Less Common Metals*, vol. 66, no. 1, pp. 51–57, 1979. DOI: https://doi.org/10.1016/0022-5088(79)90194-2.

[277] F. J. A. den Broeder *et al.*, "Visualization of hydrogen migration in solids using switchable mirrors," *Nature*, vol. 394, no. 5, pp. 656–658, 1998. DOI: https://doi.org/10.1038/29250.

[278] J. B. Talbot and S. D. Clinton, "Liquid lithium blanket processing studies," Tech. Rep., 1979, pp. 278–285. [Online]. Available: https://inis.iaea.org/collection/NCLCollectionStore/_Public/11/519/11519449.pdf.

[279] P. W. Fisher and M. Tanase, "Diffusivities of hydrogen in yttrium and yttrium alloys," *Journal of Nuclear Materials*, vol. 123, no. 1, pp. 1536–1540, 1984. DOI: https://doi.org/10.1016/0022-3115(84)90297-6.

[280] G. D'Ovidio, F. Martín-Fuertes, J. Marugán, S. Bermejo, and F. Nitti, "Lithium fire protection design approach in IFMIF-DONES facility," *Fusion Engineering and Design*, vol. 189, p. 113 446, 2023. DOI: https://doi.org/10.1016/j.fusengdes.2023.113446.

[281] N. Jurtz, M. Kraume, and G. D. Wehinger, "Advances in fixed-bed reactor modeling using particle-resolved computational fluid dynamics (CFD)," *Reviews in Chemical Engineering*, vol. 35, no. 2, pp. 139–190, 2019. DOI: 10.1515/revce-2017-0059.

[282] D. W. Jeppson, J. L. Ballif, W. W. Yuan, and B. E. Chou, "Lithium literature review: Lithium's properties and interactions," Apr. 1978. DOI: https://www.osti.gov/biblio/6885395.

[283] A. Aiello *et al.*, "Lifus (lithium for fusion) 6 loop design and construction," *Fusion Engineering and Design*, vol. 88, no. 6, pp. 769–773, 2013, Proceedings of the 27th Symposium On Fusion Technology. DOI: https://doi.org/10.1016/j.fusengdes.2013.02.129.

[284] P. Arena *et al.*, "The design of the DONES lithium target system," *Fusion Engineering and Design*, vol. 146, pp. 1135–1139, 2019, SI:SOFT-30. DOI: https://doi.org/10.1016/j.fusengdes.2019.02.024.

[285] E. Oyarzabal, A. Martín-Rojo, and F. Tabarés, "Comparative studies of h absorption/desorption kinetics and evaporation of liquid lithium in different porous systems and free surfaces," *Fusion Engineering and Design*, vol. 117, pp. 217–221, 2017. DOI: https://doi.org/10.1016/j.fusengdes.2016.08.009.

[286] Jacomex, *Jacomex - pure safety*, Catalog, 2021. [Online]. Available: https://laboline.fi/wp-content/uploads/woocommerce_uploads/2022/01/catalogue_jacomex_en_2021_web-apihsi.pdf.

[287] Technetics Group, *Ultra high purity & ultra high vacuum seals*, Catalog, 2021. [Online]. Available: https://technetics.com/wp-content/uploads/2021/02/UHP-UHV.pdf.

[288] J. Wang *et al.*, "Fundamental study on the wetting property of liquid lithium," *Energy Storage Materials*, vol. 14, pp. 345–350, 2018. DOI: https://doi.org/10.1016/j.ensm.2018.05.021.

[289] BriskHeat, *Heating tapes & cords*, Catalog, 2023. [Online]. Available: https://www.briskheat.com/mwdownloads/download/link/id/602.

[290] Morgan Advanced Materials, *Superwool plus blanket*, Catalog, 2022. [Online]. Available: https://www.morganadvancedmaterials.com/media/8946/superwool-plus-blankets_eng.pdf.

[291] RKC Instrument, *Temperature controller RB series*, Catalog, 2020. [Online]. Available: https://www.rkcinst.co.jp/english/downloads/8936/crb05e/.

[292] J. Yagi, A. Suzuki, T. Terai, T. Muroga, and S. Tanaka, "In-situ observation of hydrogen hot trapping from molten lithium with yttrium," *Fusion Engineering and Design*, vol. 84, no. 7, pp. 1993–1996, 2009. DOI: https://doi.org/10.1016/j.fusengdes.2009.01.084.

[293] S. Shigeharu, Y. Hatachi, T. Hiromoto, Y. Edao, and S. Fukada, "Hydrogen recovery from liquid Li with Y hot trap," *Plasma and Fusion Research*, vol. 7, pp. 2 405 080–2 405 080, 2012. DOI: https://doi.org/10.1585/pfr.7.2405080.

[294] T. Hiromoto *et al.*, "Chemical analysis of hydrogen isotopes dissolved in Li and Y for hot trap of IFMIF target loop," *Fusion Science and Technology*, vol. 64, no. 3, pp. 533–537, 2013. DOI: https://doi.org/10.13182/FST13-A19148.

[295] T. Nagasaki, M. Saidoh, R. Yamada, and H. Ohno, "Ion-driven permeation and surface recombination coefficient of deuterium for ion," *Journal of Nuclear Materials*, vol. 202, no. 3, pp. 228–238, 1993. DOI: https://doi.org/10.1016/0022-3115(93)90392-C.

[296] M. Baldwin, R. Doerner, R. Causey, S. Luckhardt, and R. Conn, "Recombination of deuterium atoms on the surface of molten Li–LiD," *Journal of Nuclear Materials*, vol. 306, no. 1, pp. 15–20, 2002. DOI: https://doi.org/10.1016/S0022-3115(02)01232-1.

[297] H. Bi, Y. Hirooka, J. Yagi, and Y. Xu, "A study on hydrogen isotopes transport in a liquid metal GaInSn by plasma-driven permeation method," *Nuclear Materials and Energy*, vol. 12, pp. 329–333, 2017, Proceedings of the 22nd International Conference on Plasma Surface Interactions 2016, 22nd PSI. DOI: https://doi.org/10.1016/j.nme.2017.02.018.

[298] A. Stern, A. Resnik, and D. Shaltiel, "Thermal desorption spectra of the PdHx system in a powder form," *Journal of Physics F: Metal Physics*, vol. 14, no. 7, p. 1625, 1984. DOI: 10.1088/0305-4608/14/7/012.

[299] Y. Wu, Y. Edao, S. Fukada, H. Nakamura, and H. Kondo, "Removal rates of hydrogen isotope from liquid Li by HF-treated Y plate," *Fusion Engineering and Design*, vol. 85, no. 7, pp. 1484–1487, 2010. DOI: https://doi.org/10.1016/j.fusengdes.2010.04.022.

[300] W. T. Hicks, "Evaluation of vapor-pressure data for mercury, lithium, sodium, and potassium," *The Journal of Chemical Physics*, vol. 38, no. 8, pp. 1873–1880, 1963. DOI: https://doi.org/10.1063/1.1733889.

APPENDIX

The appendix presents fabrication drawings of various technical components developed during this dissertation. The final drawings were prepared by professional CAD draftsmen of the Ciemat Institute and AVS company. They are fully based on preliminary designs made by the author of this thesis.

A.1. Fabrication drawings of glove box

Fig. A.1. Foto of the manufactured glove box.

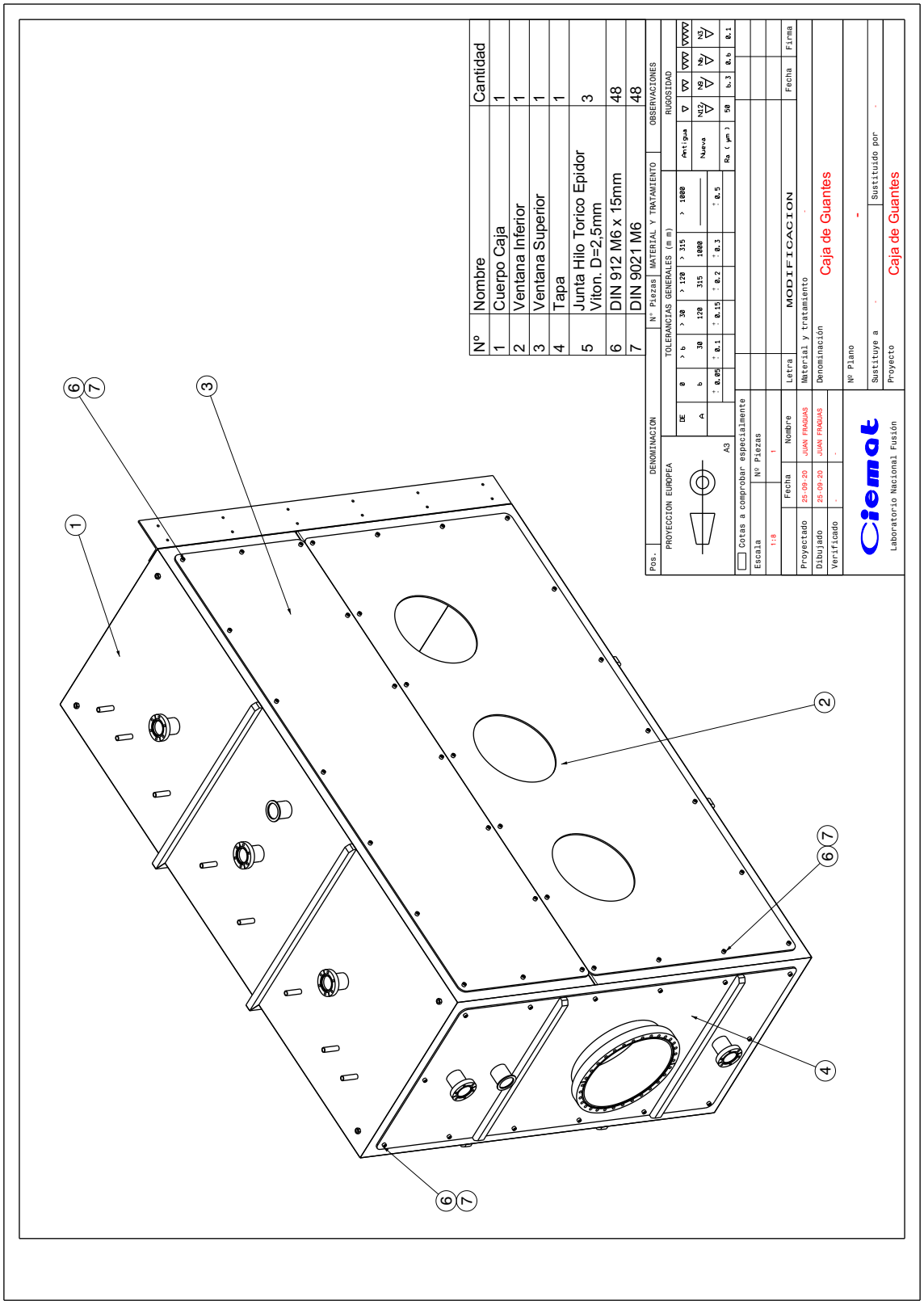

Fig. A.2. General component structure of the glove box.

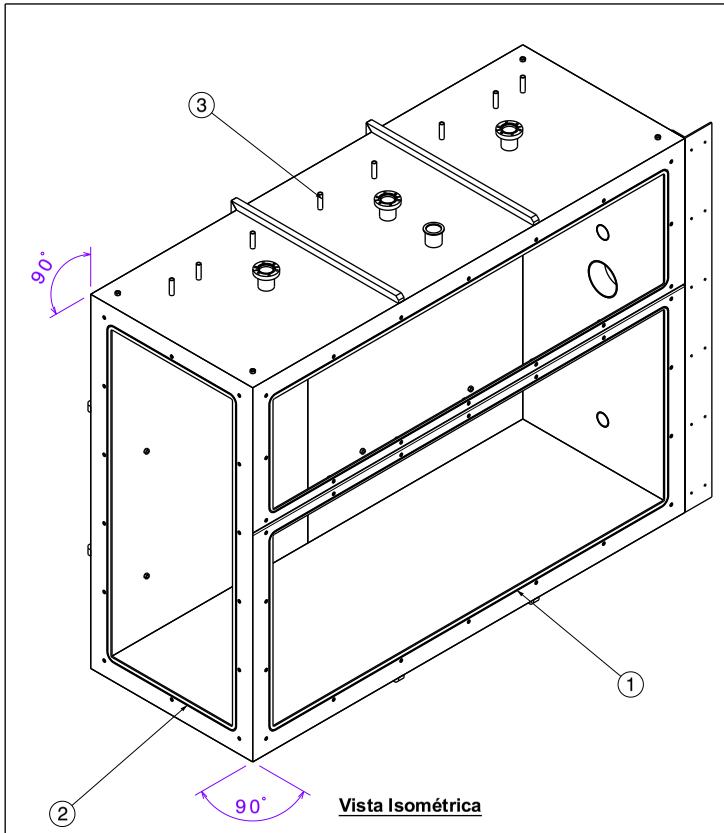

Vista Isométrica

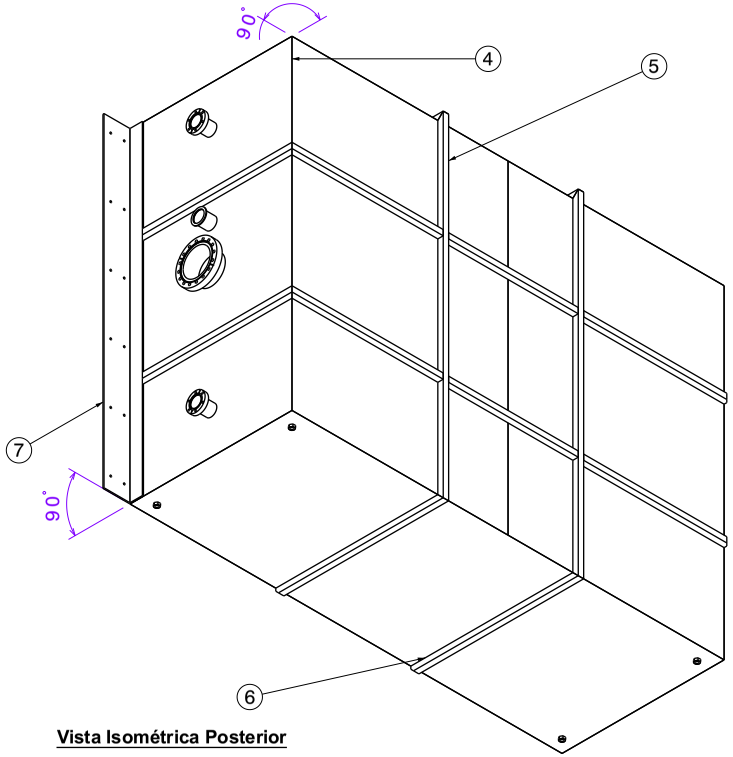

Vista Isométrica Posterior

Nº	Nombre	Cantidad
1	Pared Frontal	1
2	Pared Izquierda	1
3	Pared Superior	1
4	Pared Derecha	1
5	Pared Posterior	1
6	Pared Inferior	1
7	Perfil	1

*Soldar herméticamente todas las piezas

Pos.	DENOMINACION	Nº Piezas	MATERIAL Y TRATAMIENTO	OBSERVACIONES

PROYECCION EUROPEA — A3

TOLERANCIAS GENERALES (mm)

DE	0	> 6	> 30	> 120	> 315	> 1000
A	6	30	120	315	1000	———
	± 0.05	± 0.1	± 0.15	± 0.2	± 0.3	± 0.5

RUGOSIDAD

	Antigua	▽	▽▽	▽▽▽	▽▽▽▽
Nueva		N12	N9	N6	N3
Ra (µm)		50	6.3	0.6	0.1

Cotas a comprobar especialmente

Escala	Nº Piezas
1:10	1

	Fecha	Nombre
Proyectado	24-09-20	JUAN FRAGUAS
Dibujado	24-09-20	JUAN FRAGUAS
Verificado	-	-

Ciemat
Laboratorio Nacional Fusión

Letra	MODIFICACION	Fecha	Firma

Material y tratamiento -

Denominación: Cuerpo Caja

Nº Plano: -

Sustituye a - | Sustituido por -

Proyecto: Caja de Guantes

Fig. A.3. Complete glove box frame.

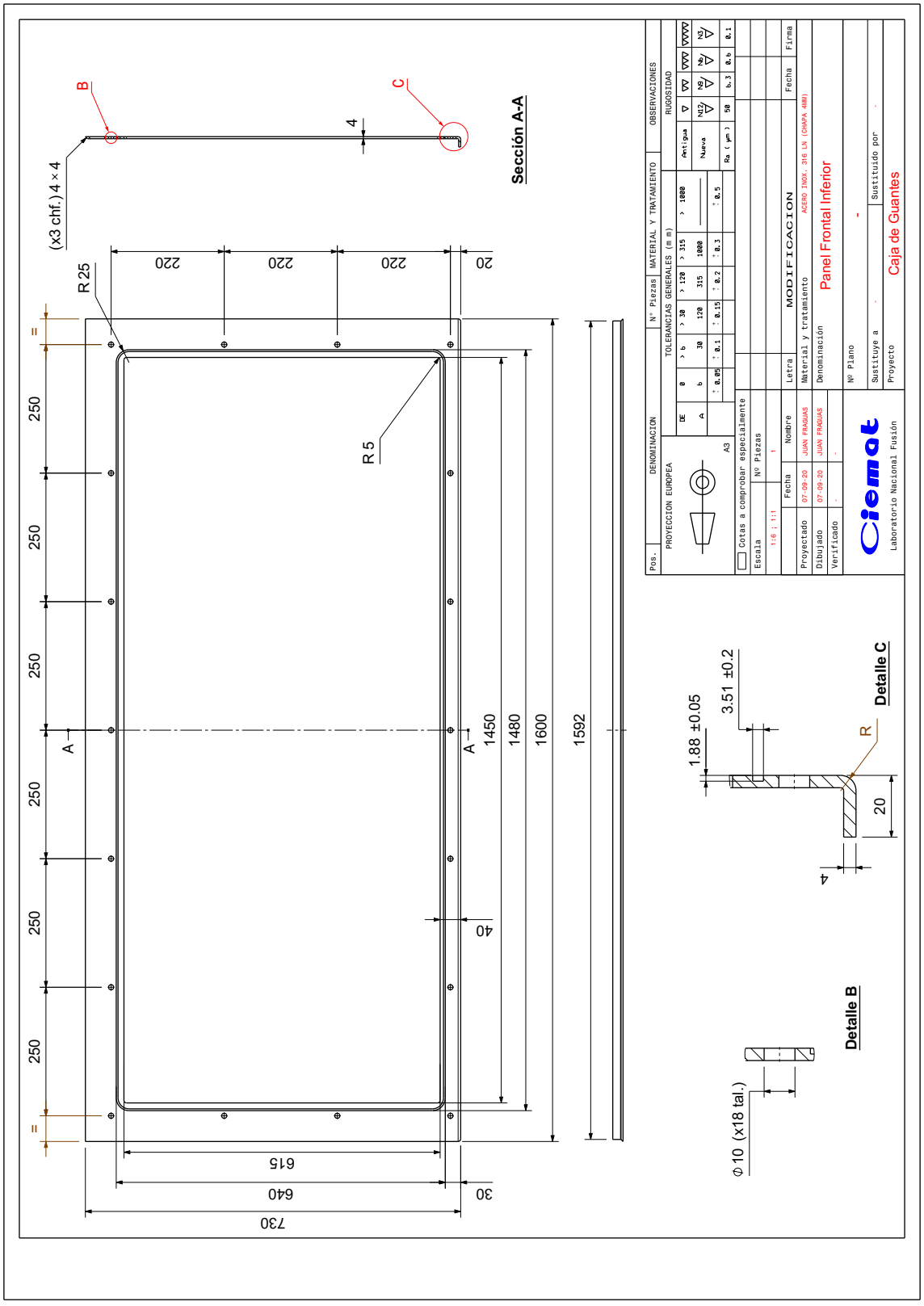

Fig. A.4. Lower front panel of the glove box.

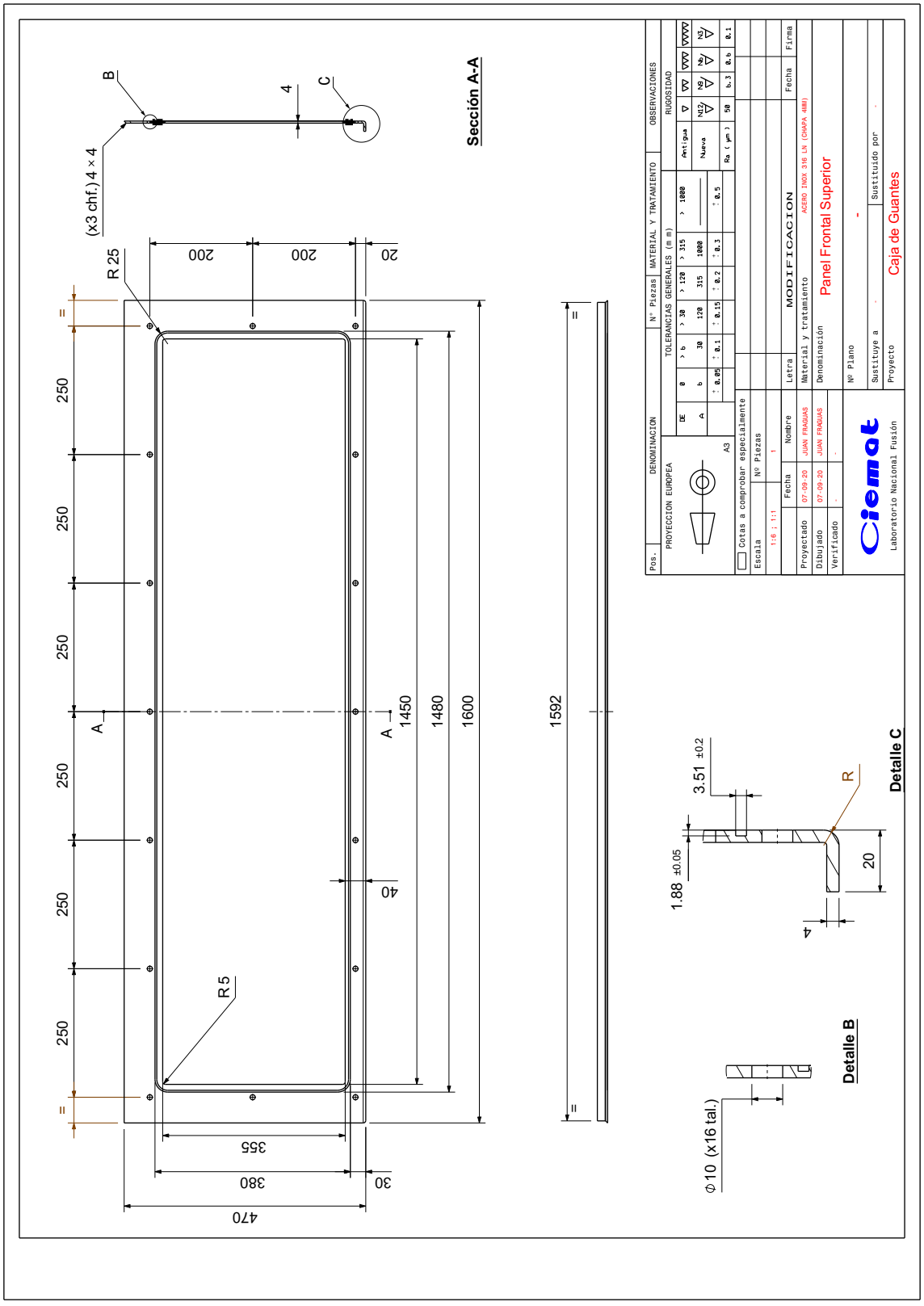

Fig. A.5. Upper front panel of the glove box.

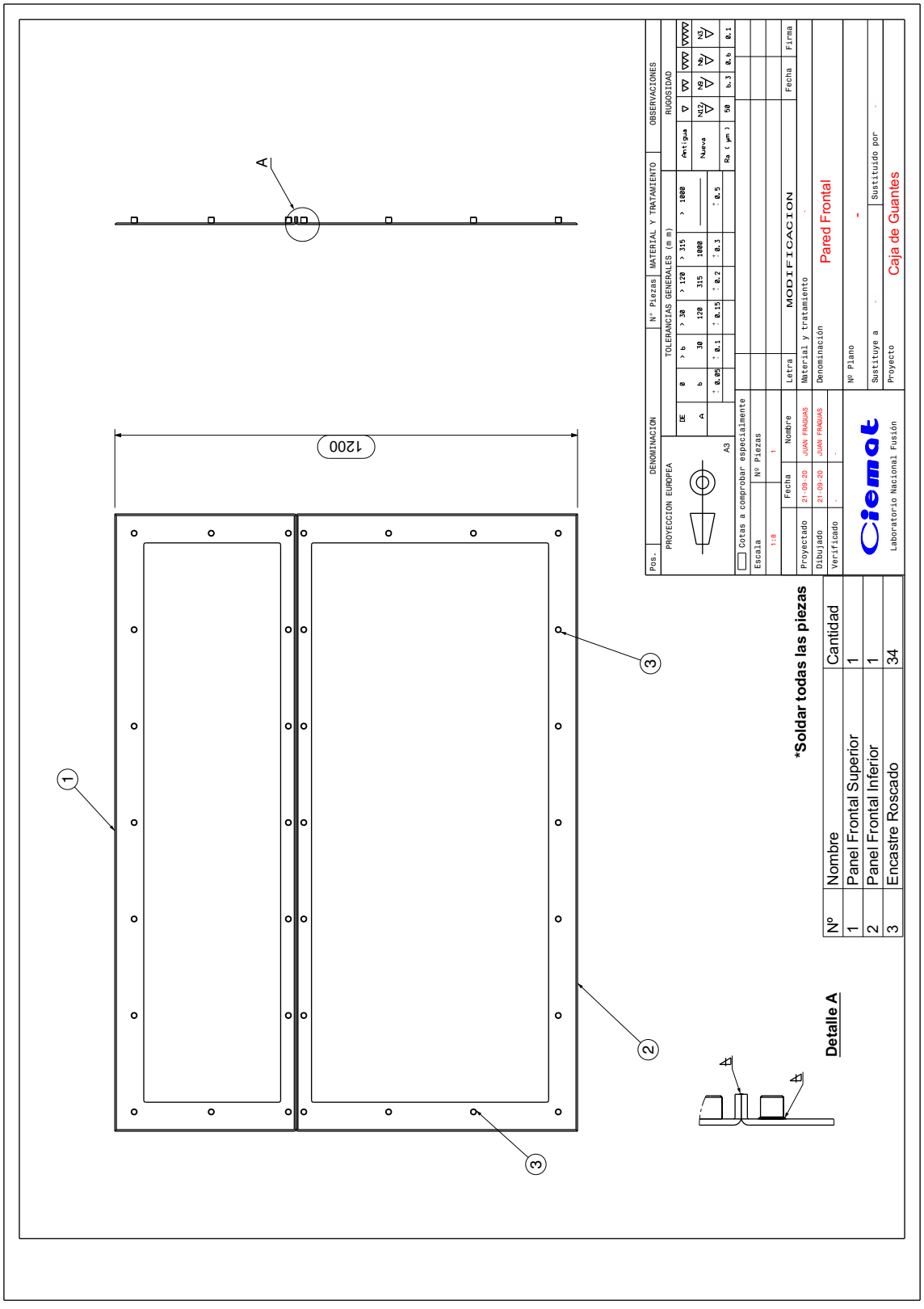

Fig. A.6. Welded lower and upper front panels of the glove box.

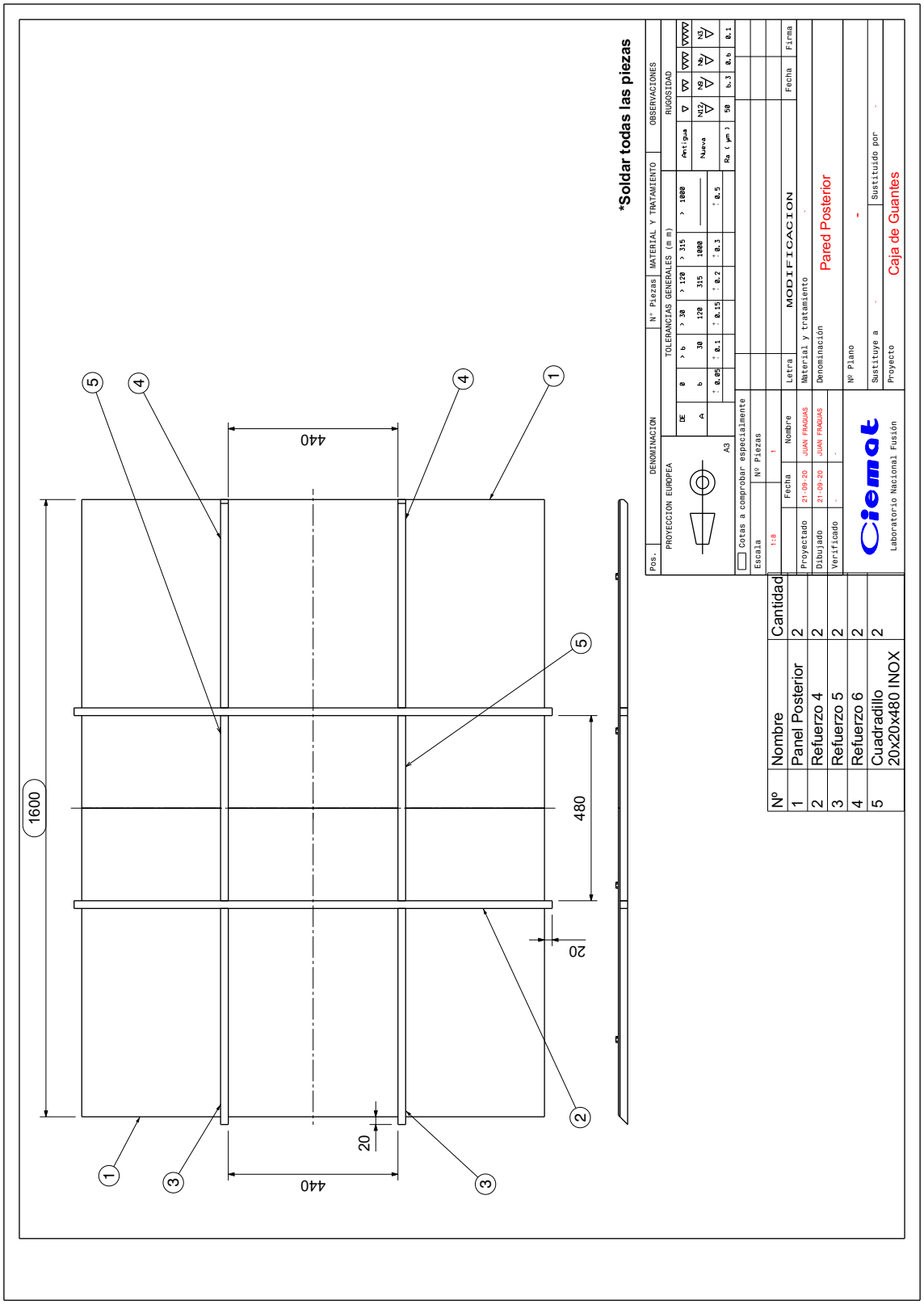

Fig. A.7. Rear wall of the glove box.

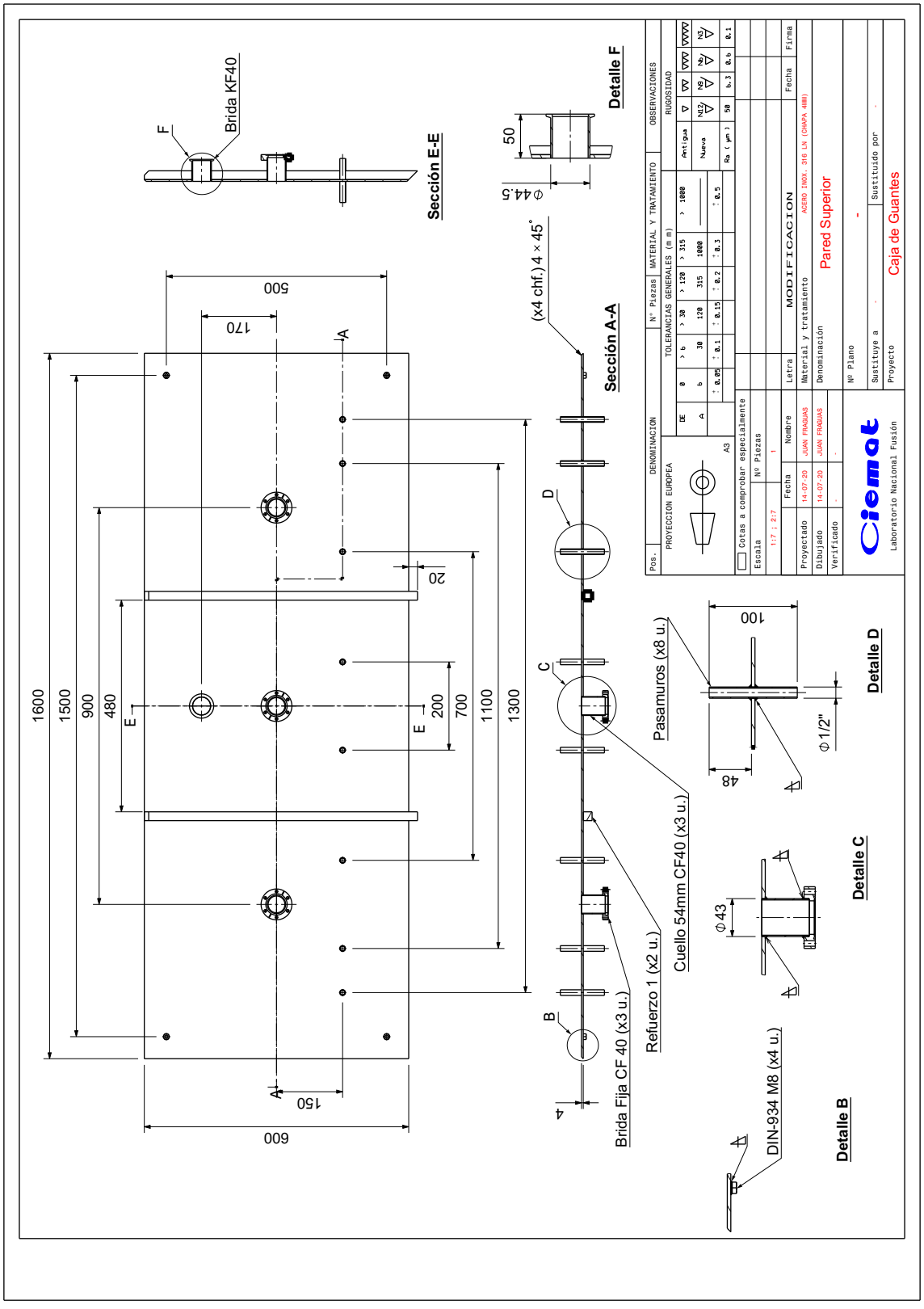

Fig. A.8. Roof plate of the glove box.

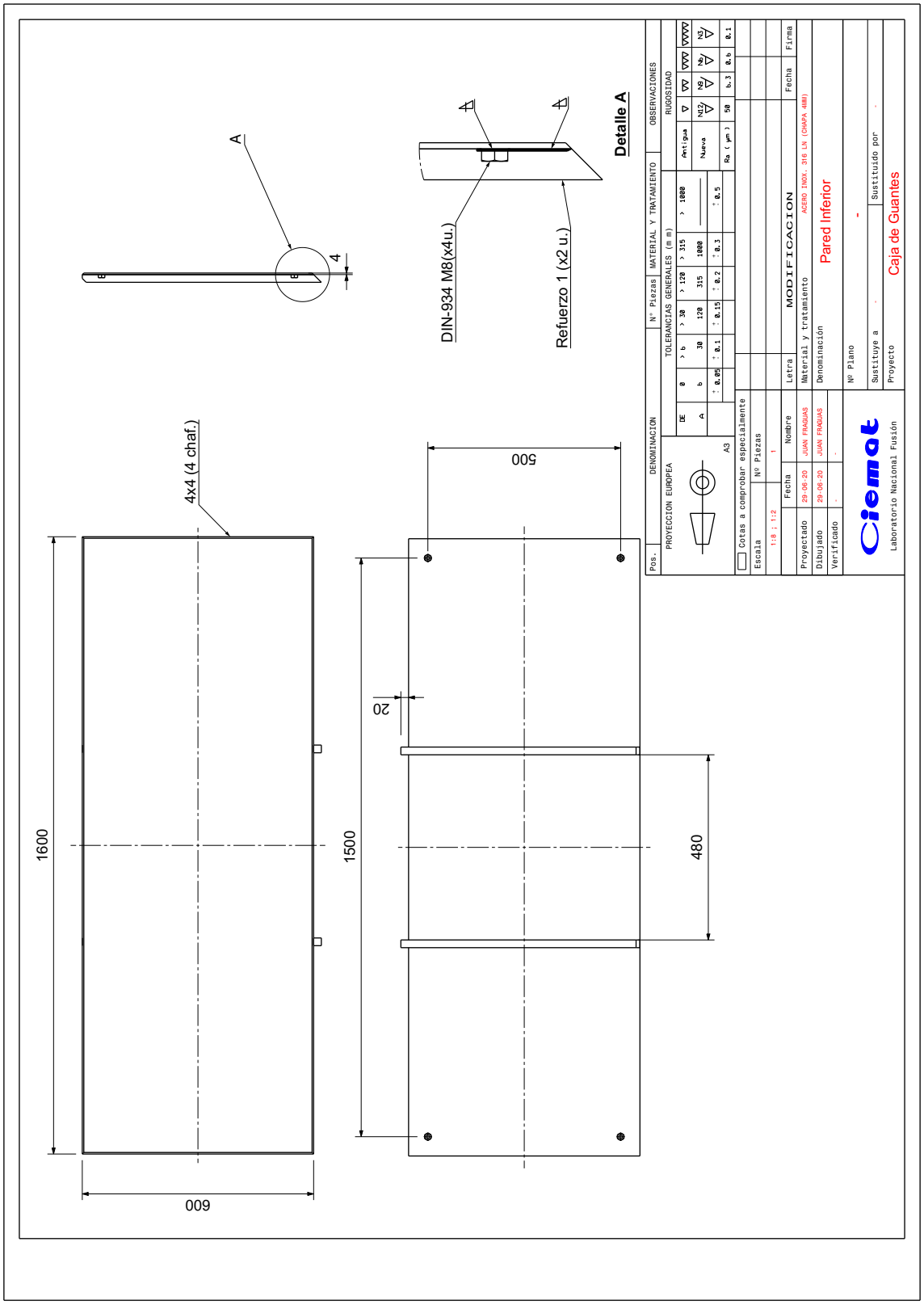

Fig. A.9. Floor plate of the glove box.

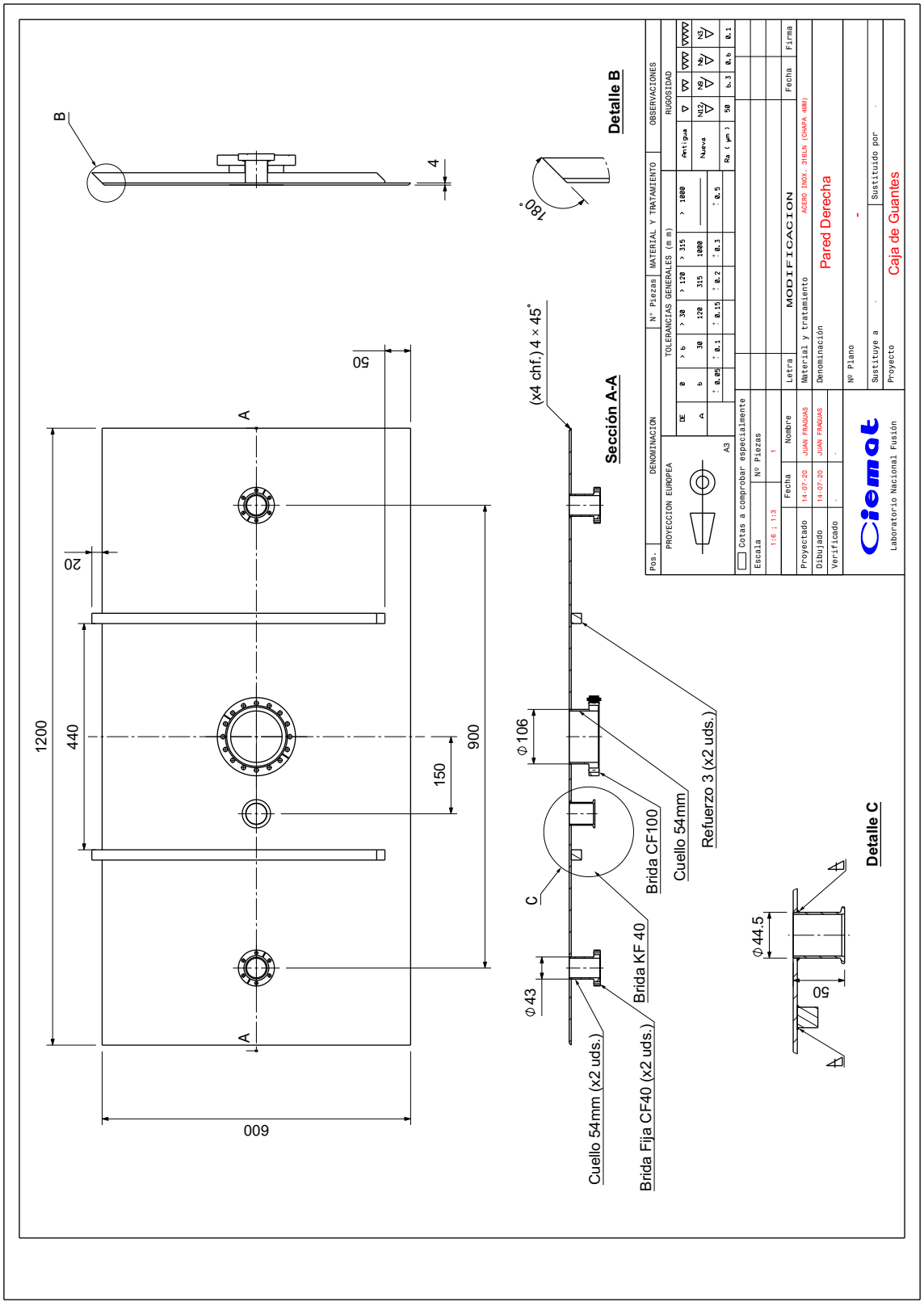

Fig. A.10. Right wall of the glove box.

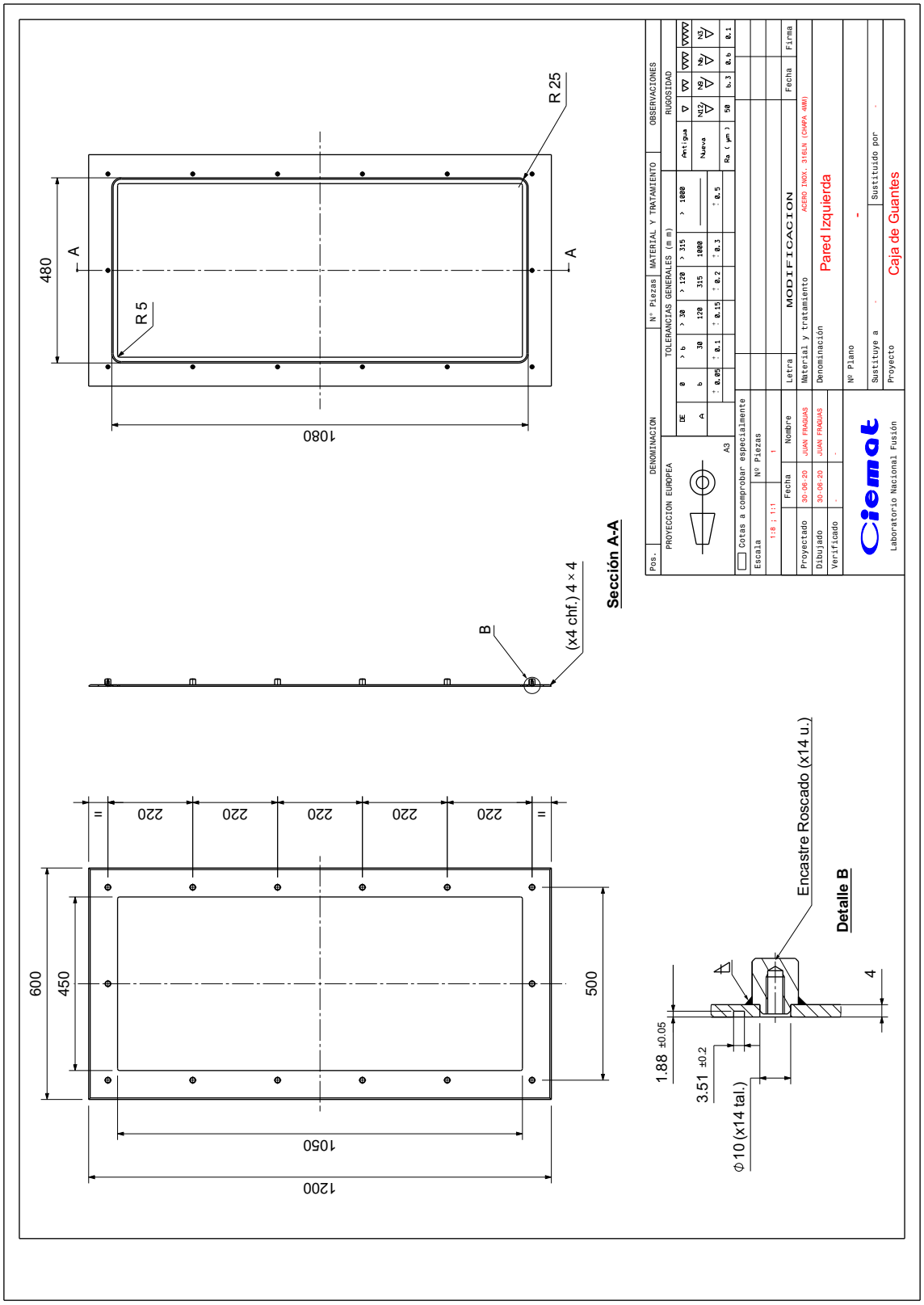

Fig. A.11. Left wall of the glove box.

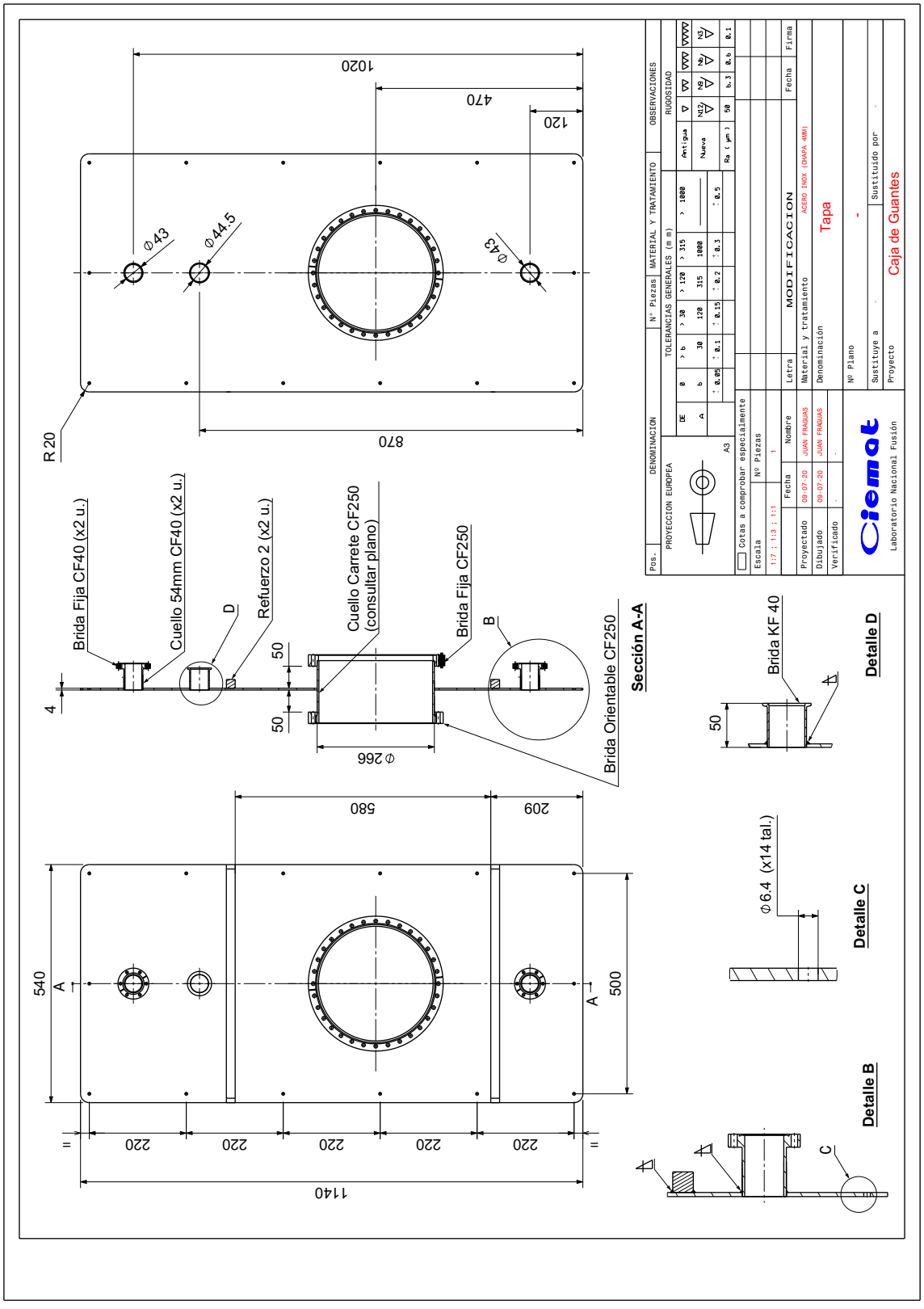

Fig. A.12. Removable cover plate for the opening at the left wall of the glove box.

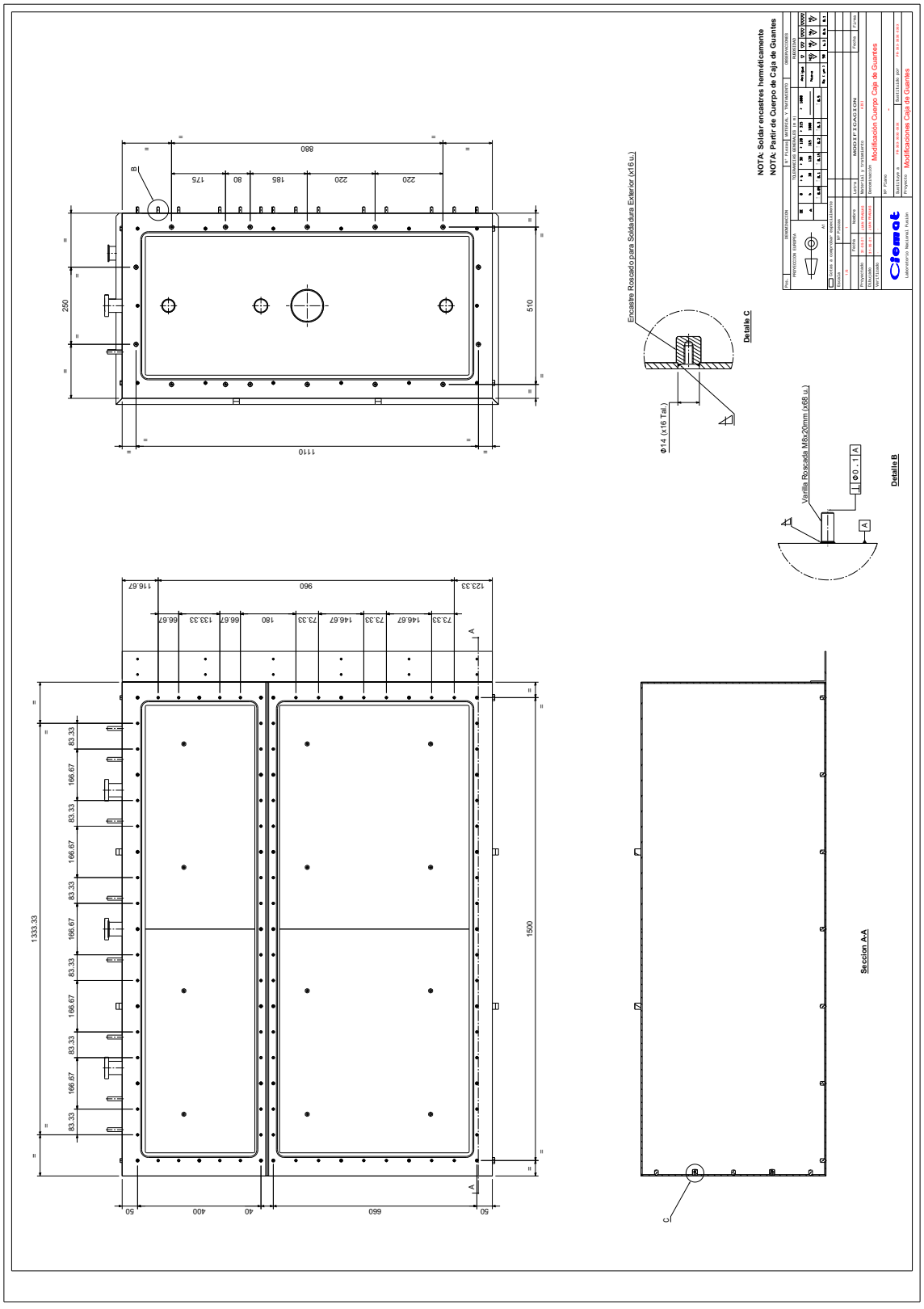

Fig. A.13. Additional modifications of the glove box frame.

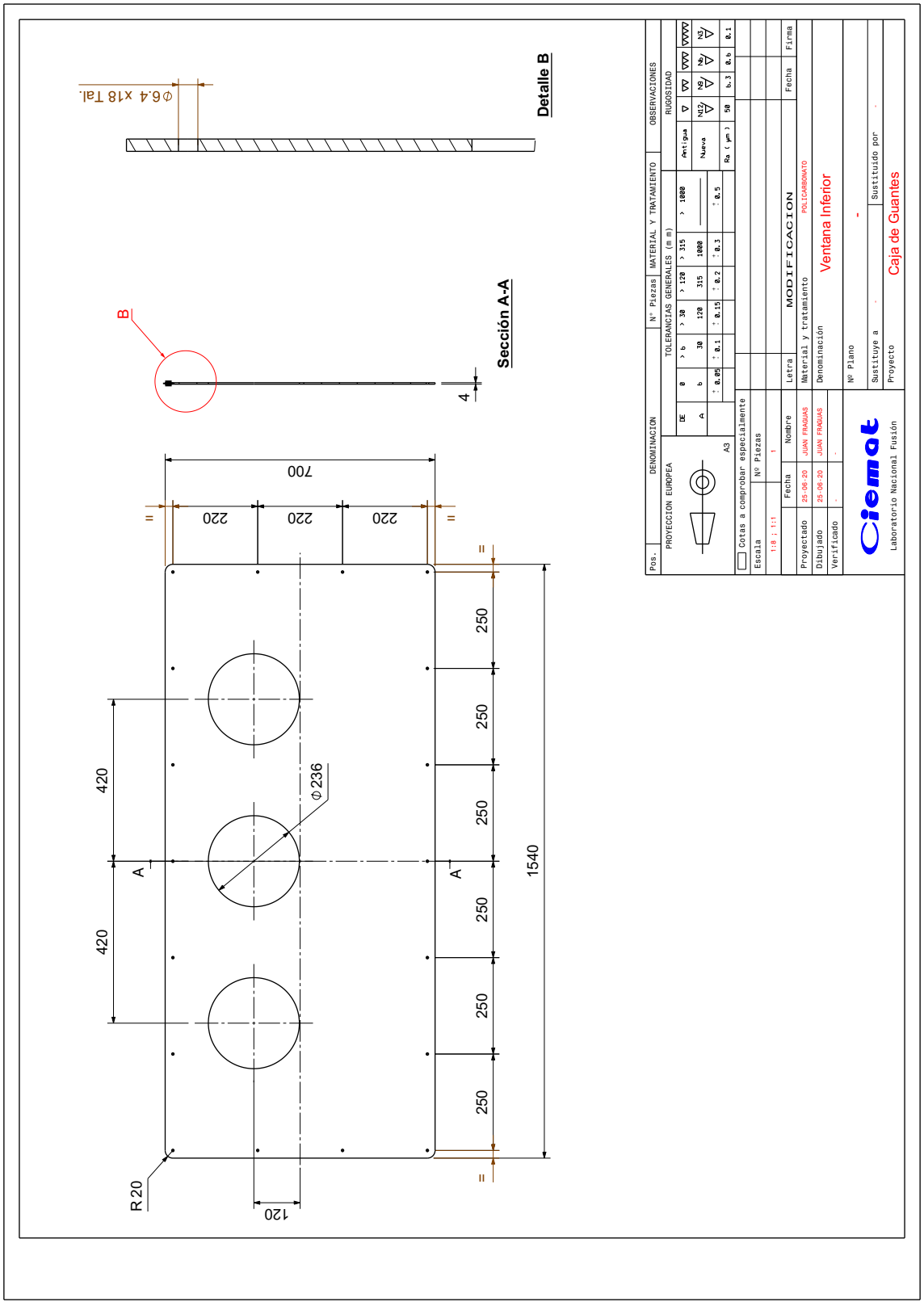

Fig. A.14. Lower polycarbonate window for the glove box.

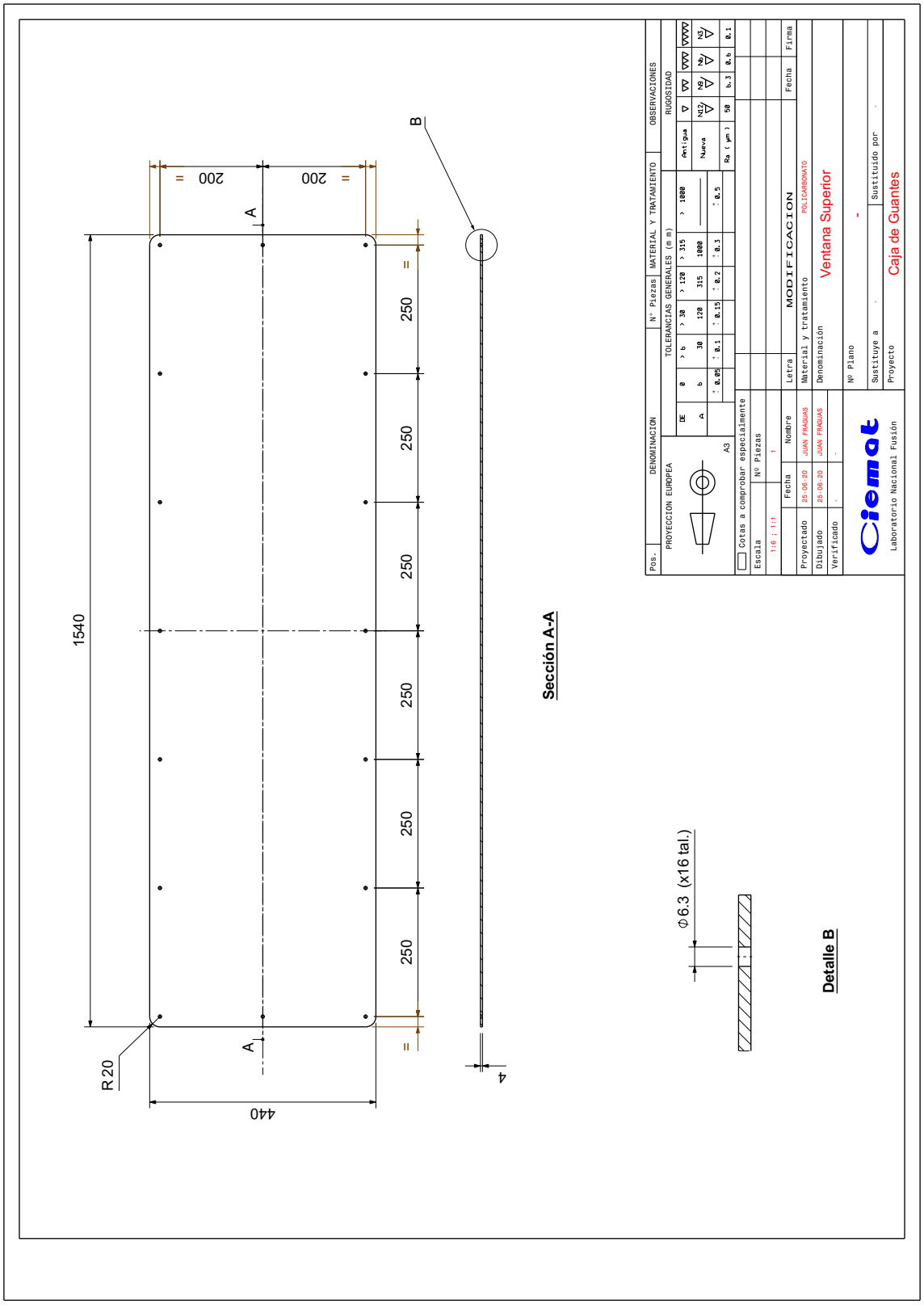

Fig. A.15. Upper polycarbonate window for the glove box.

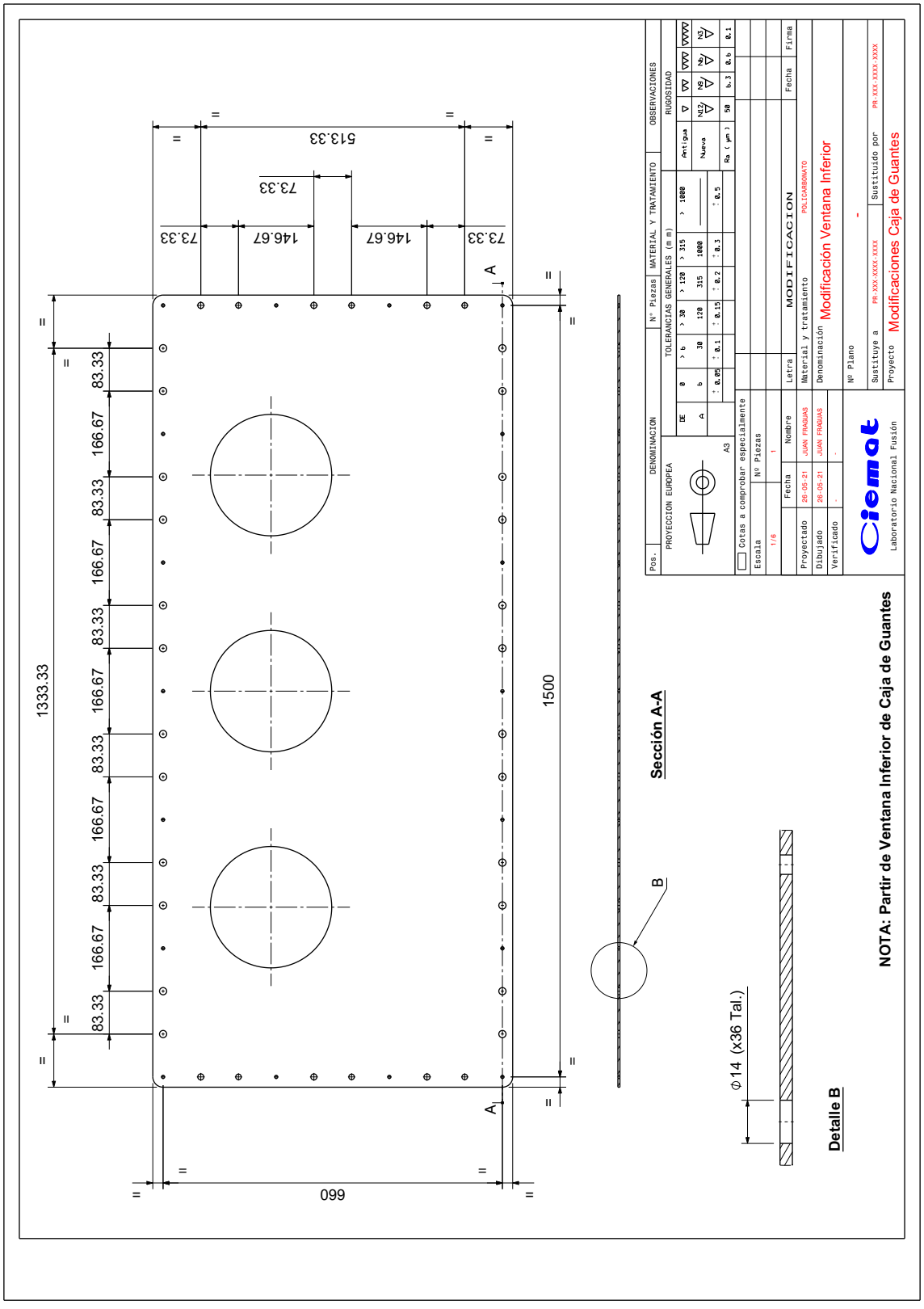

Fig. A.16. Additional modifications of the lower polycarbonate window.

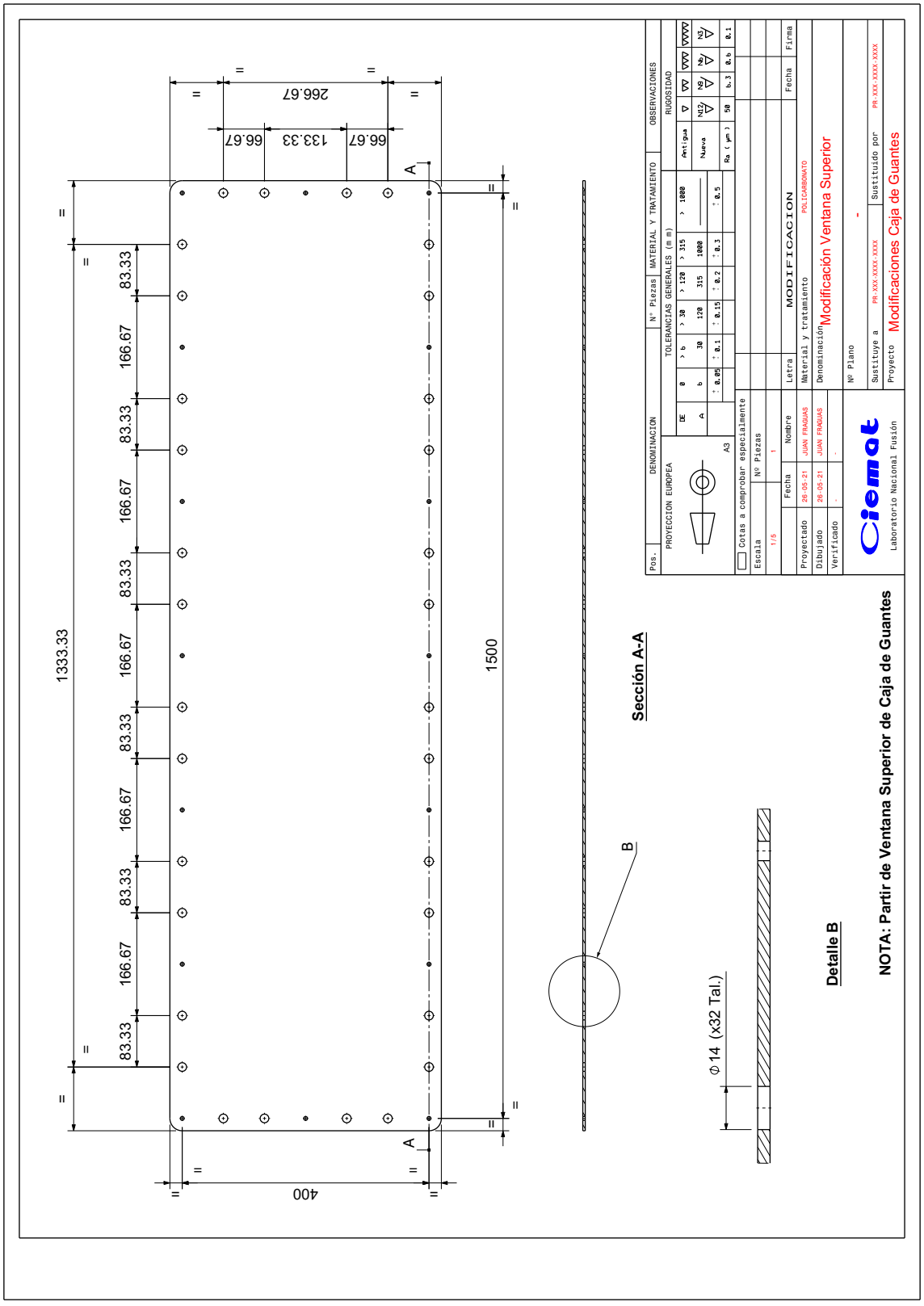

Fig. A.17. Additional modifications of the upper polycarbonate window.

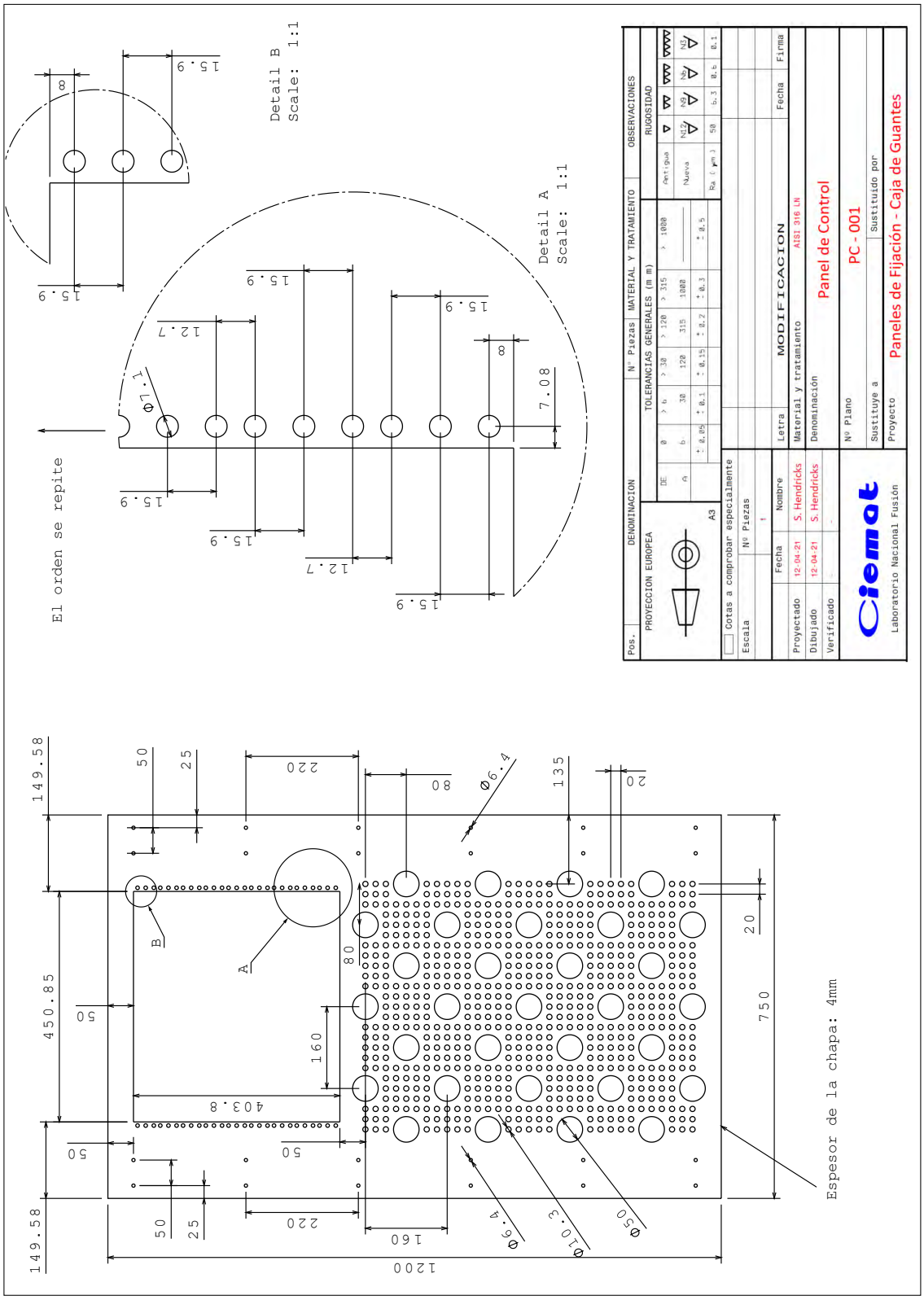

Fig. A.18. Control panel of the LYDER experiment.

A.2. Fabrication drawings of glove box antechamber

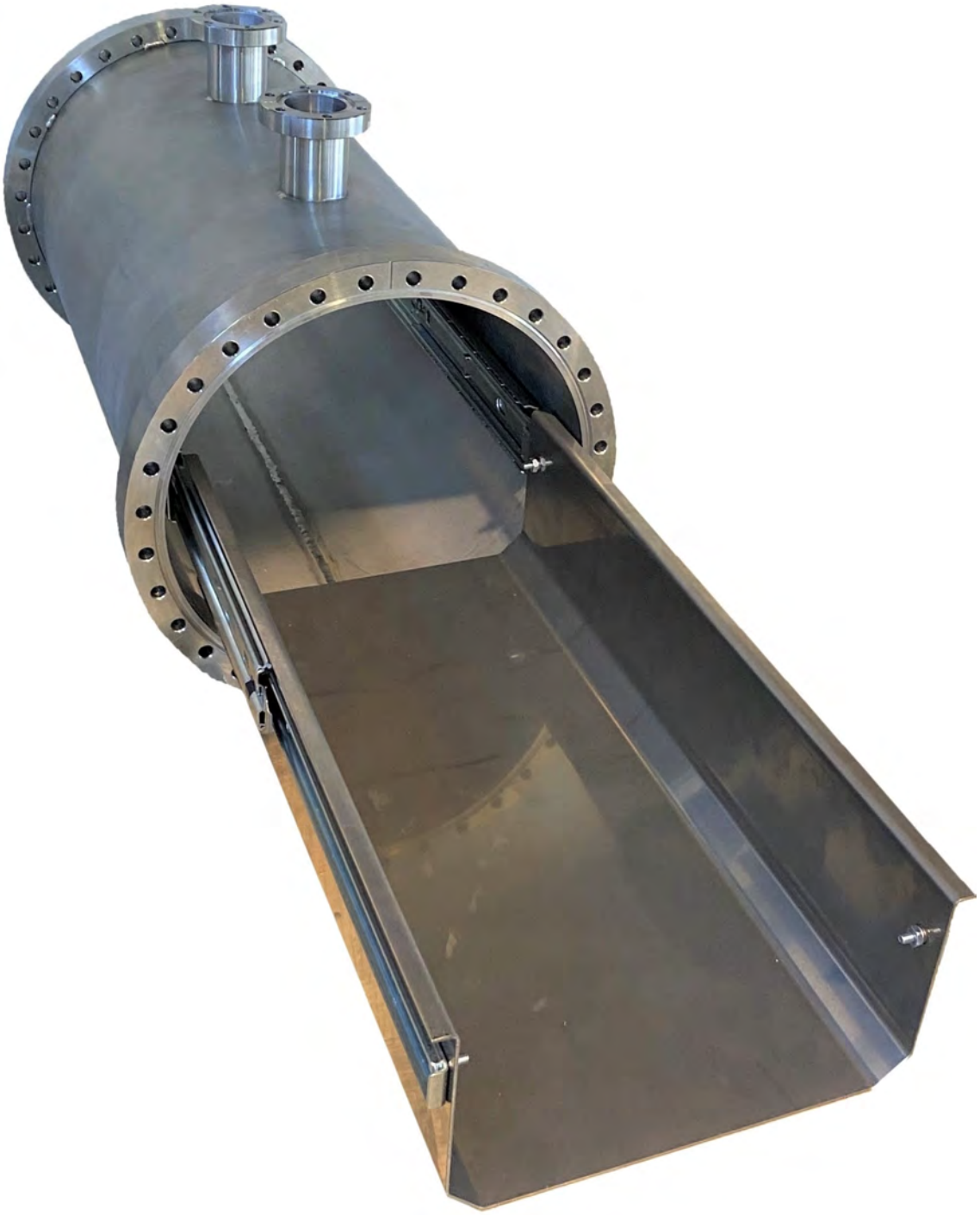

Fig. A.19. Foto of the manufactured glove box antechamber.

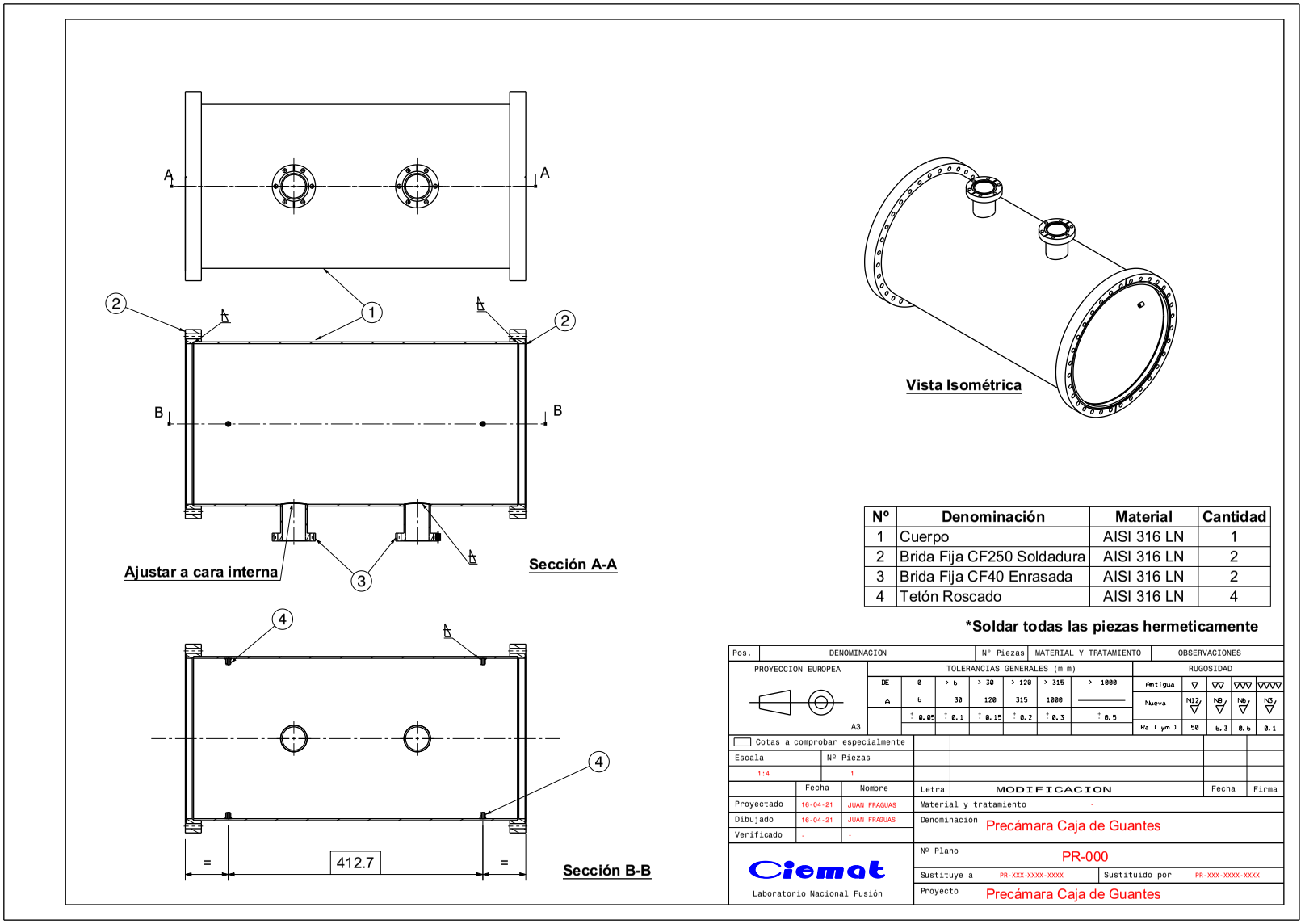

Nº	Denominación	Material	Cantidad
1	Cuerpo	AISI 316 LN	1
2	Brida Fija CF250 Soldadura	AISI 316 LN	2
3	Brida Fija CF40 Enrasada	AISI 316 LN	2
4	Tetón Roscado	AISI 316 LN	4

Fig. A.20. Dimensions and components of the glove box antechamber.

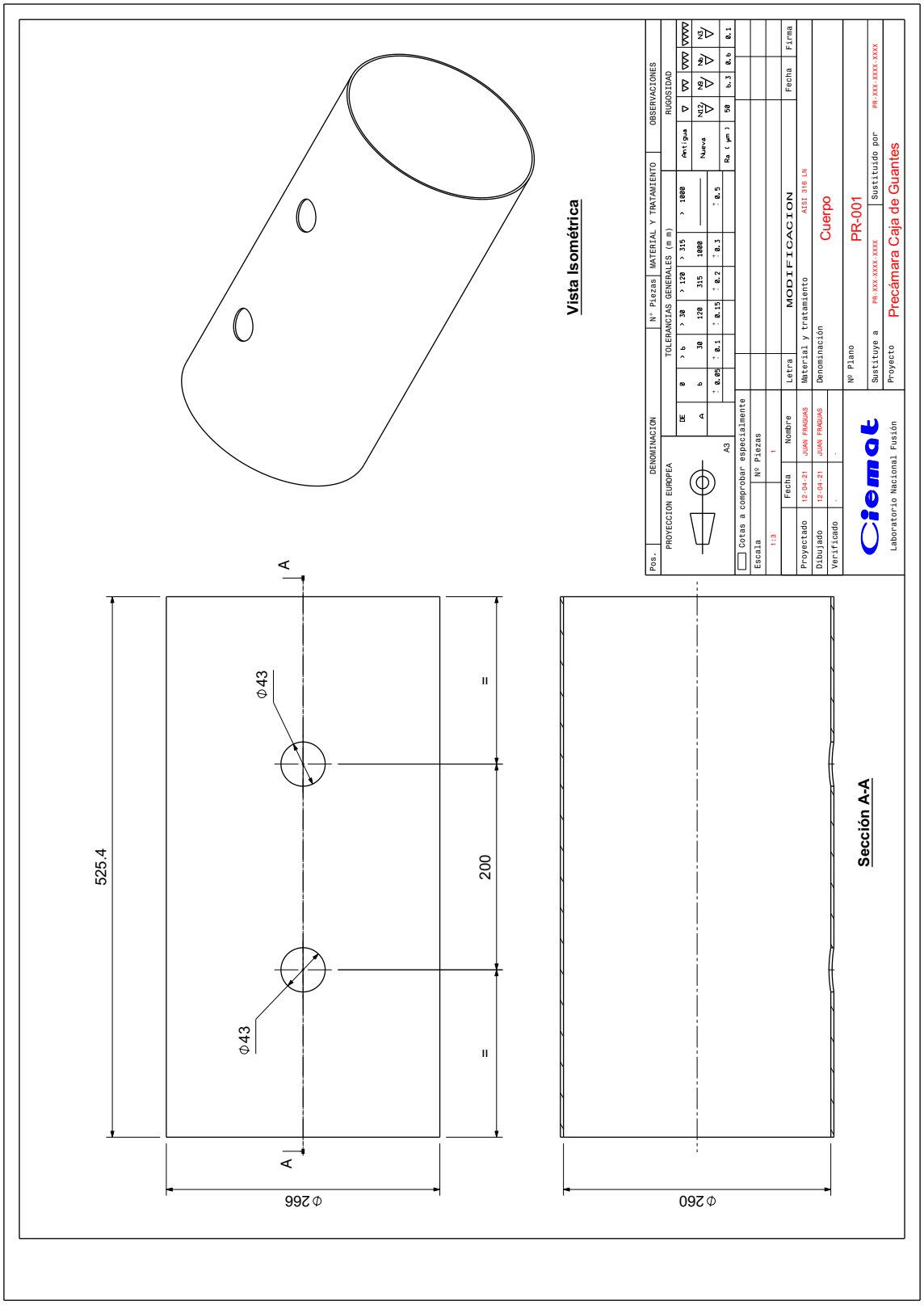

Fig. A.21. Frame of the glove box antechamber.

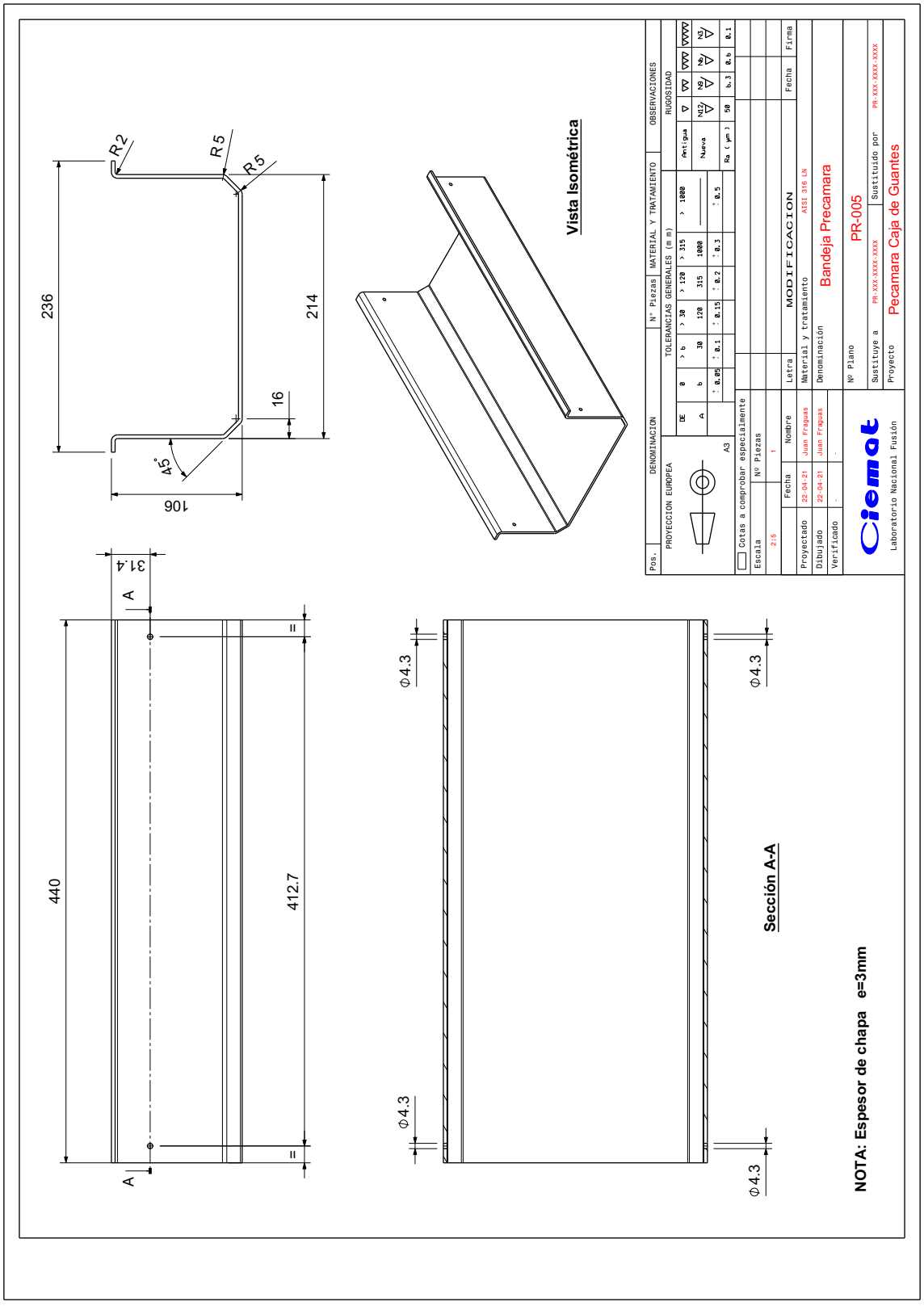

Fig. A.22. Custom-made drawer for the glove box antechamber.

A.3. Fabrication drawings of deuterium getter trap

Fig. A.23. Foto of the manufactured deuterium trap components.

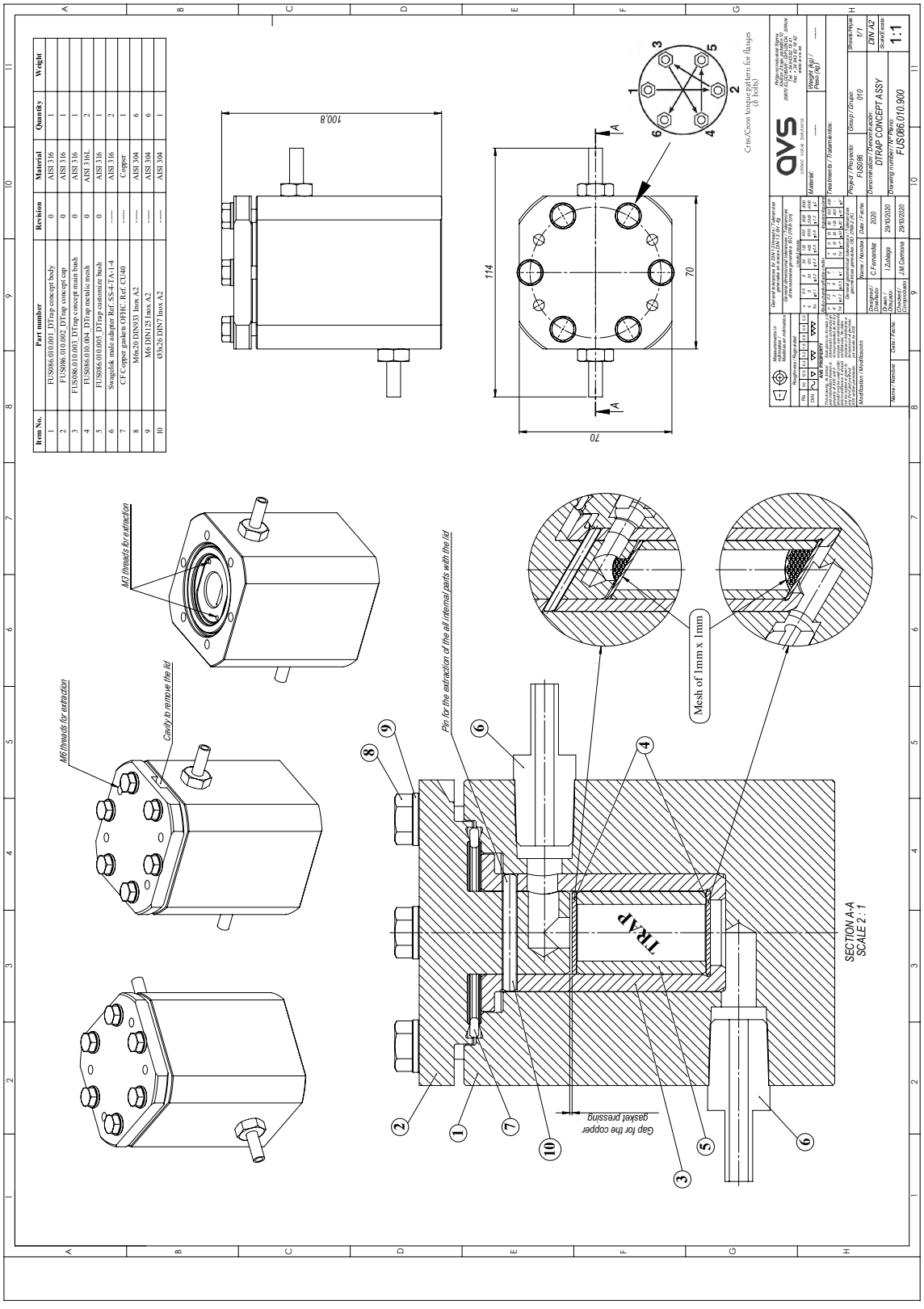

Fig. A.24. Assembly and structure of the deuterium trap.

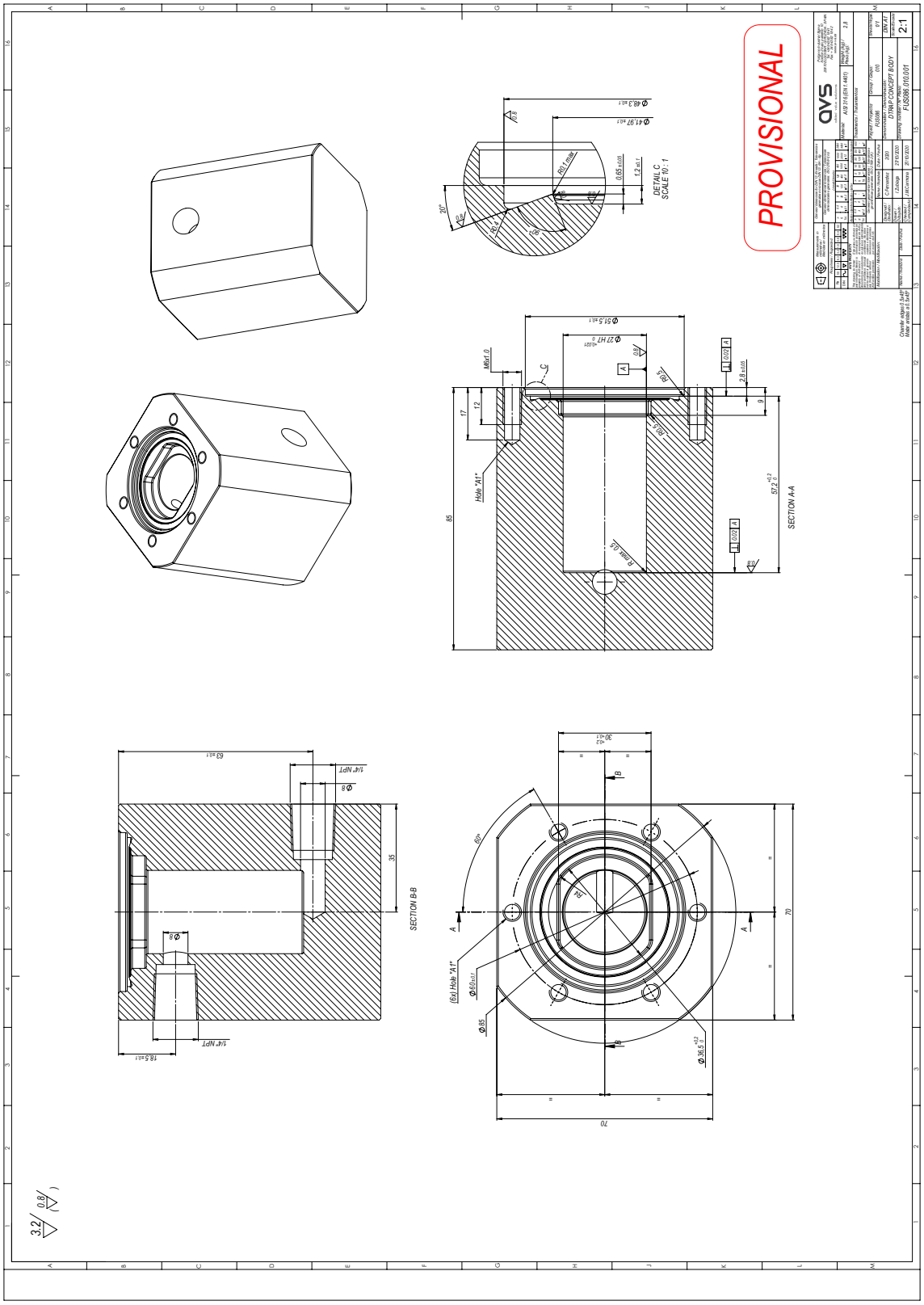

Fig. A.25. Main body of the deuterium trap container.

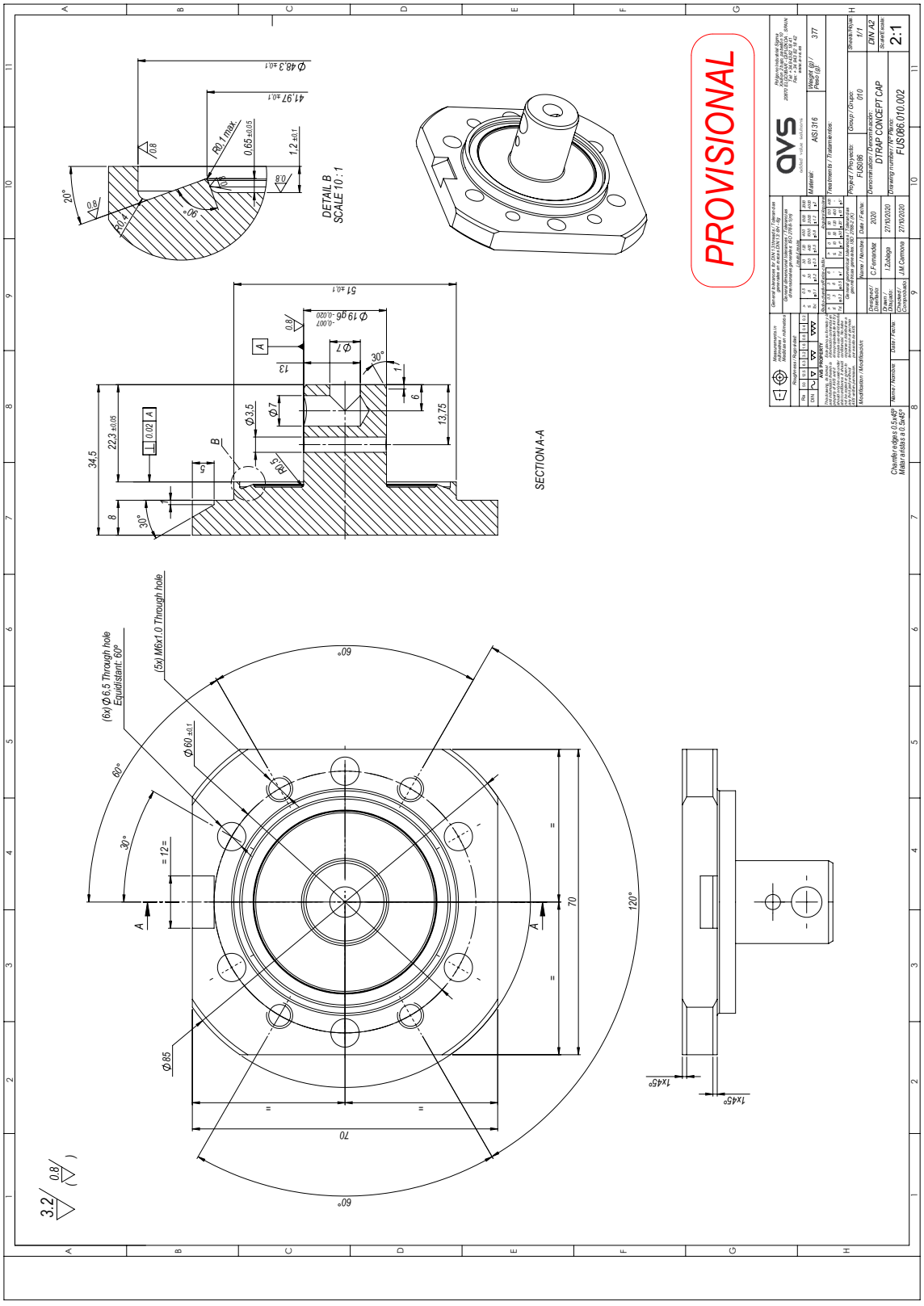

Fig. A.26. Lid with DN40CF flange of the deuterium trap.

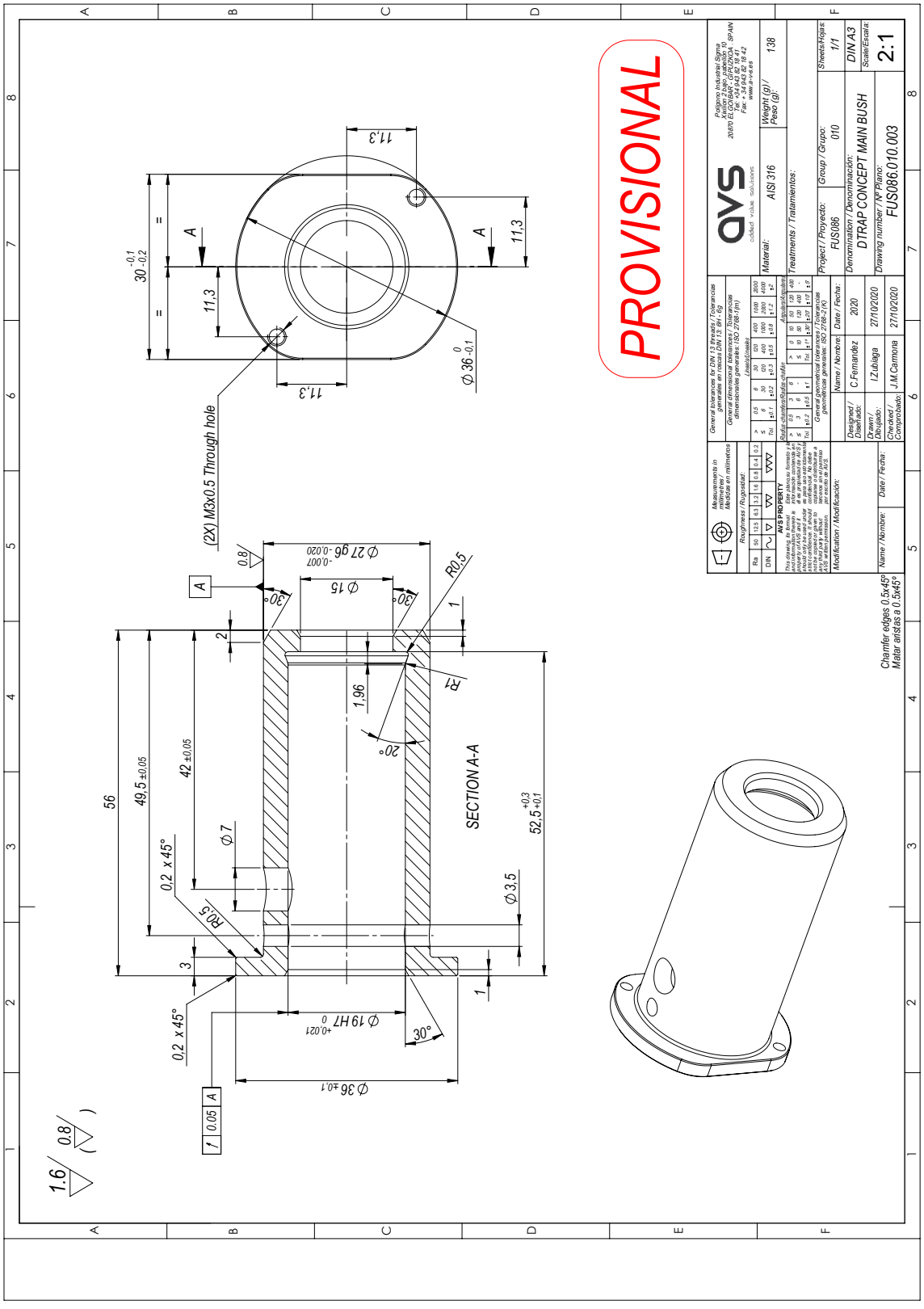

Fig. A.27. Outer cylinder of the yttrium basket of the deuterium trap.

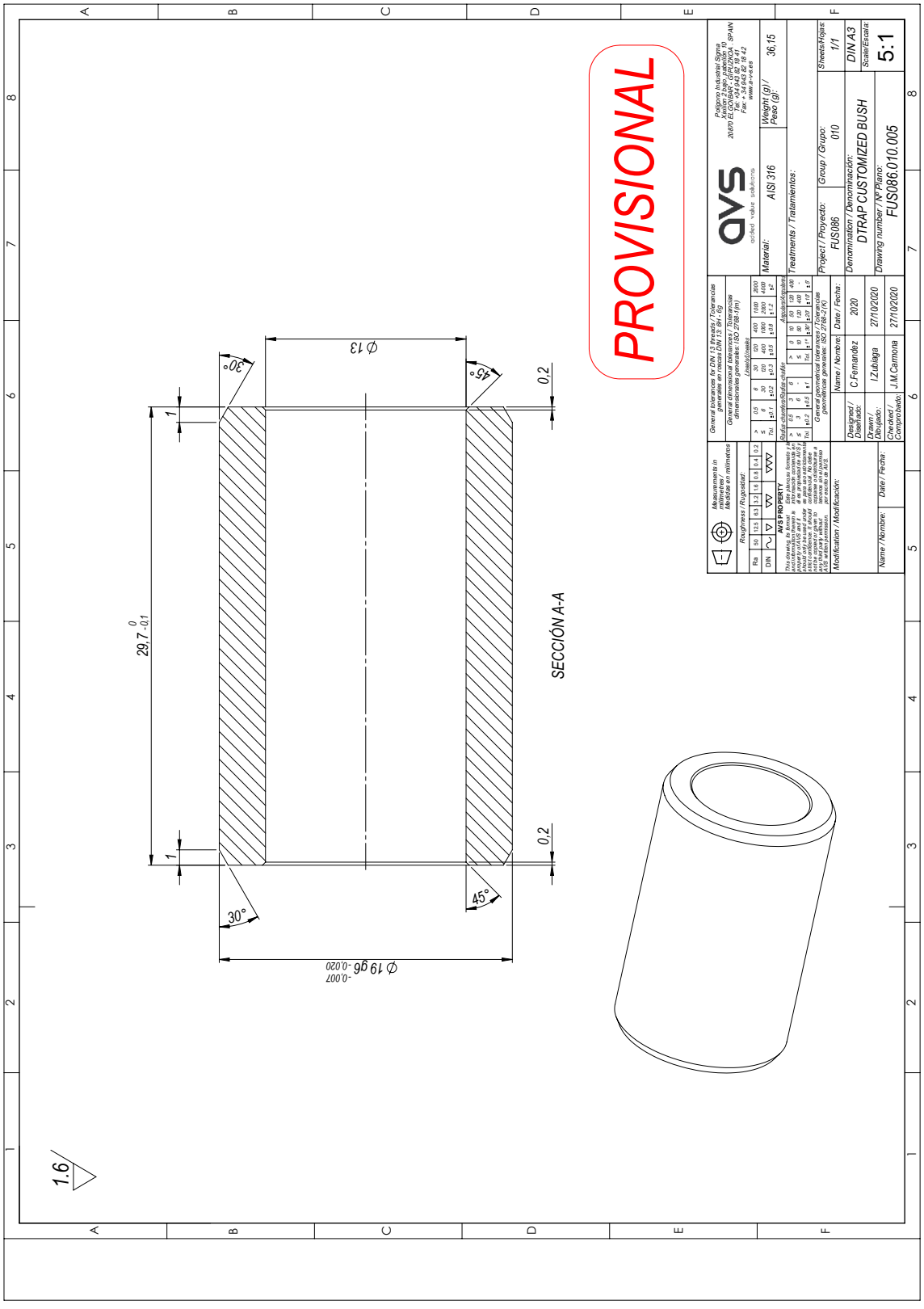

Fig. A.28. Inner cylinder of the yttrium basket of the deuterium trap.

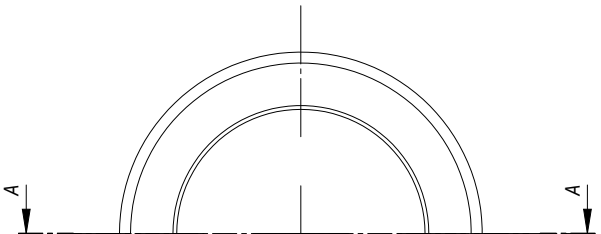

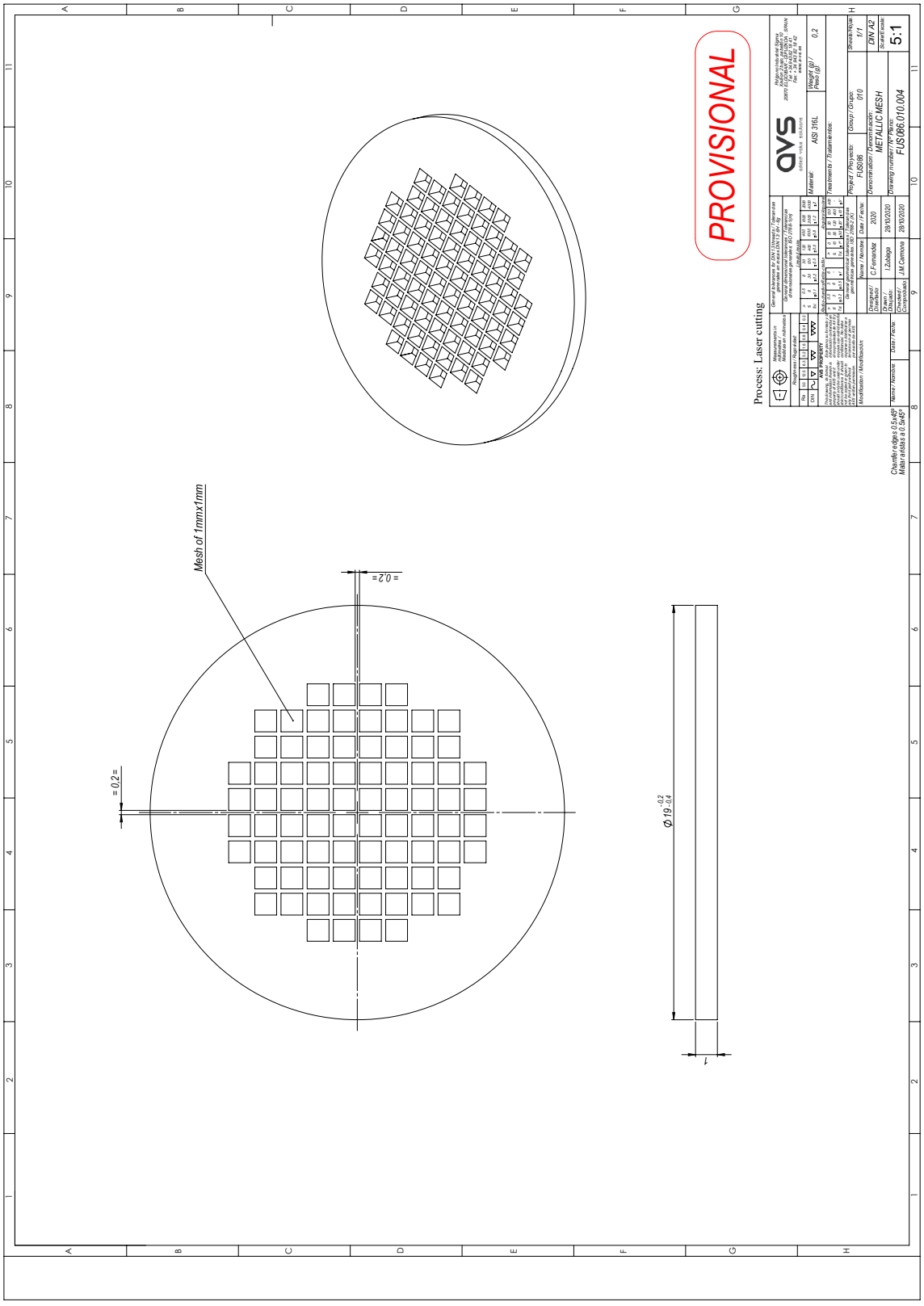

Fig. A.29. Stainless steel mesh of the yttrium basket of the deuterium trap.